Airborne thermography and ground geophysical investigation for detecting shallow ground disturbance under vegetation

Kay Barbara McManus

Airborne thermography and ground geophysical investigation for detecting shallow ground disturbance under vegetation

Thesis submitted for the Degree of Doctor of Philosophy
Department of Geography, University of Durham

Kay Barbara McManus, B.Sc., M.Sc.
June 2004

Abstract

Airborne thermography and ground geophysical investigation for detecting shallow ground disturbance under vegetation

Submitted in September 2003 for the degree of Doctor of Philosophy

K. B. McManus

This thesis discusses the potential of airborne thermal prospection for detecting shallow ground disturbance beneath vegetation based on images acquired by the NERC Airborne Thematic Mapper (ATM) at thermal infrared wavelengths. Shallow ground disturbance creates a differential heat flux due to a variation in the thermal properties between disturbed and undisturbed soils. When observed above a canopy, the effect of vegetation growth on the thermal regime of the underlying soils is poorly understood. The research extends current understanding by examining areas where ground disturbance is known to exist under variable vegetation cover at an archaeological site at Bosworth, Leicestershire and areas of abandoned mine activity on Baildon Moor, W. Yorkshire and in the N. Pennine Orefield, Weardale.

The investigation focuses on qualitative image interpretation techniques, where anomalies on day and night thermal images are compared with those manifest on the multispectral images, and a more quantitative approach of Apparent Thermal Inertia (ATI) modelling. Physical thermal inertia is a parameter that is sensitive to volumetric variations in the soil, but cannot be measured directly using remote sensing techniques. However, an *apparent* thermal inertia is determined by examining the day and night temperature contrast of the surface, where spatial variations can signify potential features buried in the near-surface environment. Ground temperature profiling at the Bosworth site indicates that diurnal heat dissipates between 0.20-0.50m at an early stage in vegetation development with progressively lower diurnal amplitudes observed at 0.20m as the vegetation develops. Results also show that the time of diurnal maximum temperature occurs progressively later as vegetation develops, implying an importance for thermal image acquisition.

The quantitative investigation concentrates on the Bosworth site where extensive ground geophysical prospection was performed and vertical soil samples extracted across features of variable multispectral, thermal and ATI response to enable comparison of the observed airborne thermal response with physical soil properties. Results suggest that there is a high correlation between ATI and soil moisture properties at 0.15-0.25m depth (R^2=0.99) at an early stage in cereal crop development but has a high correlation at a wider depth range (0.10-0.30m) at a later stage in development (R^2=0.98). The high correlation between physical ground disturbance and the thermal response is also corroborated qualitatively with the results of the resistivity surveys.

The ATI modelling reveals similar features to those evident on day or night thermal images at an early stage in vegetation growth, suggesting that thermal imaging during the day at an early stage in vegetation growth may supply sufficient information on features buried in the near-surface environment. Airborne thermal imaging therefore provides a useful complementary prospection tool for archaeological and geological applications for surfaces covered by vegetation.

CONTENTS

Abstract i

Declaration xiv

Statement of Copyright xiv

Acknowledgements xv

Chapter 1:INTRODUCTION TO THESIS 1
1.1 INTRODUCTION 1
1.2 RESEARCH AIMS 1
1.3 OBJECTIVES 3
1.4 RESEARCH FRAMEWORK 4
1.5 STRUCTURE OF THESIS 5

Chapter 2:THEORY and METHODOLOGY 6
2.1 THERMAL REMOTE SENSING 7
2.1.1 Thermal Detection 8
2.1.2 Land Surface Determination 9
2.2 SURFACE ENERGY FLUXES 18
2.3 THERMAL PROPERTIES 24
2.4 THERMAL MODELLING 30
2.4.1 Apparent Thermal Inertia Modelling 31
2.4.2 Energy Flux Modelling 35
2.4.3 Thermal Modelling of Soil-Vegetation Systems 42
2.5 SUMMARY of THERMAL RESEARCH 47

Chapter 3:CONTEXT of SUBSURFACE FEATURES and TECHNIQUES for ASSESSMENT 49
3.1 ENVIRONMENTAL SETTING: BURIED ARCHAEOLOGY BOSWORTH BATTLEFIELD, LEICESTERSHIRE 53
3.2 ENVIRONMENTAL SETTING: ABANDONED MINES on BAILDON MOOR, W. YORKSHIRE 56
3.3 ENVIRONMENTAL SETTING: ABANDONED MINE ACTIVITY on NORTH PENNINE OREFIELD, WEARDALE 60
3.4 REMOTELY-SENSED AIRBORNE DIGITAL IMAGERY 62
3.4.1 Digital Imagery: Bosworth, Leicestershire 63
3.4.2 Digital Imagery: Baildon Moor, W. Yorkshire 64
3.4.3 Digital Imagery: North Pennine Orefield, Weardale 64
3.5 GROUND GEOPHYSICAL PROSPECTION 65
3.5.1 Geophysical Surveying: Magnetometry 66
3.5.2 Geophysical Surveying: Resistivity 68
3.5.3 Geophysical Surveying:Electromagnetometry 71
3.6 GEOPHYSICAL EVALUATION of BOSWORTH 74
3.6.1 Alternative Ground Investigations: Field Walking and Metal Detecting 85
3.7 GEOPHYSICAL EVALUATION of BAILDON MOOR 86
3.8 SUMMARY of SHALLOW SUBSURFACE FEATURES and their PHYSICAL CHARACTERISTICS 98

Chapter 4:AIRBORNE THERMAL DATA PROCESSING 100
4.1 MULTISPECTRAL ATM DATA 100
4.2 RADIOMETRIC CORRECTION 102
4.3 GEOMETRIC CORRECTION 103
4.3.1 Ground Control Point Collection 105
4.3.2 Parametric Geocorrection 110
4.4 SPATIAL RESIZING 113
4.5 ATMOSPHERIC CORRECTION 117

4.5.1 Empirical Line Calibration 118
4.5.1.1 Empirical Line Temperature Calibration 121
4.5.2 IMAGE NORMALISATION 122
4.6 SUMMARY of IMAGE PROCESSING TECHNIQUES 124

Chapter 5: QUALITATIVE IMAGE INTERPRETATION 126
5.1 INTERPRETATION from SINGLE BAND VISUALISATION 127
5.1.1 Bosworth 127
5.1.2 Baildon Moor 132
5.1.3 Weardale 135
5.2 CONTRAST ENHANCEMENT 138
5.3 INTERPRETATION of THERMAL IMAGES 141
5.3.1 Visualisation and Detection of Bosworth Thermal Anomalies 141
5.3.1.1 Ambion Field Interpretation 150
5.3.1.2 Arena Field Interpretation 156
5.3.1.3 Helipad Field Interpretation 158
5.3.1.4 Picnic Field Interpretation 160
5.3.1.5 South Field Interpretation 162
5.3.1.6 Summary of Bosworth Interpretation 165
5.3.2 Visualisation and Detection of Baildon Moor Thermal Anomalies 168
5.3.2.1 Shaft of Topographic Expression 170
5.3.2.2 Shaft of Variable Vegetation 172
5.3.2.3 Suspected Shaft Feature 175
5.3.3 Visualisation and Detection of Weardale Thermal Anomalies 178
5.3.4 Summary of Single Band Assessment 181
5.4 COMPARISON of TIR EMITTANCE with VISIBLE, NEAR-INFRARED and SHORTWAVE INFRARED 183
5.4.1 Natural Colour Composites 184
5.4.2 Near-Infrared False-Colour Composites 188
5.4.3 Thermal Day Colour Composites 192
5.4.4 Thermal Night Colour Composites 193
5.4.5 Summary of Colour Composite Visualisations 195
5.5 FURTHER IMAGE ENHANCEMENT 196
5.5.1 Edge Detection Filtration 197
5.5.1.1 Low Pass Filtration 197
5.5.1.2 High Pass Filtration 198
5.5.1.3 Directional Filtration 199
5.5.2 Image Arithmetic 202
5.5.2.1 Diurnal Thermal Contrast at Bosworth 204
5.5.2.2 Diurnal Thermal Contrast on Baildon Moor 206
5.5.2.3 Diurnal Thermal Contrast in Weardale 211
5.5.3 Spectral Enhancement through Principal Component Analysis 213
5.6 SUMMARY of QUALITATIVE ANALYSIS 227

Chapter 6: NUMERICAL THERMAL MODELLING 232
6.1 QUANTITATIVE TEMPERATURE CALIBRATION 234
6.1.1 Sensitivity Analysis 235
6.2 CONVERTING RADIANCE to TEMPERATURE USING THE PLANCK RELATIONSHIP 244
6.3 CONVERSION of ATM RADIANCE to PRICE RADIANCE 246
6.4 APPARENT THERMAL INERTIA MODELLING 250
6.5 SUMMARY of NUMERICAL MODELLING 275

Chapter 7: BOSWORTH SOIL CHARACTERISTICS 281
7.1 CONTACT TEMPERATURE MEASUREMENTS 281
7.2 THERMAL PROFILE CHARACTERISTICS: SITE A 286
7.2.1 Stage I: Soil Fraction Dominates 288

7.2.2 Stage II: Equal Soil and Vegetation Dominates ... 289
7.2.3 Stage III: Vegetation Fraction Dominates ... 289
7.2.4 Stage IV: Mature Vegetation ... 290
7.2.5 Summary of Site A Thermal Characteristics ... 295
7.3 THERMAL PROFILE CHARACTERISTICS: SITE B ... 297
7.3.1 Stage I: Soil Fraction Dominates ... 298
7.3.2 Stage II: Equal Soil and Vegetation Dominates ... 298
7.3.3 Stage III: Vegetation Fraction Dominates ... 299
7.3.4 Stage IV: Mature Vegetation ... 299
7.3.5 Summary of Site B Thermal Characteristics ... 305
7.4 SOIL COMPOSITIONAL CHARACTERISTICS ... 307
7.4.1 Feature A ... 310
7.4.2 Feature B ... 312
7.4.3 Feature C ... 313
7.4.4 Feature D ... 315
7.4.5 Location E ... 317
7.4.6 Summary of Compositional Characteristics ... 318

Chapter 8: DISCUSSION ... 321

Chapter 9: CONCLUSIONS and RECOMMENDATIONS ... 335
9.1 EVALUATION of AIMS and OBJECTIVES ... 335
9.2 CONCLUSIONS ... 344
9.3 FUTURE RESEARCH DIRECTIONS ... 345

References ... 347

Appendix A: INSTRUMENTATION ... A1
A1 AIRBORNE THEMATIC MAPPER ... A1
A2 WILD RC-10 SURVEY CAMERA ... A4
A3 GER1500 SPECTRORADIOMETER ... A5
A4 GER3700 SPECTRORADIOMETER ... A5
A5 TEMPCON® HOBO-H8 DATA LOGGER ... A6

Appendix B: ENVI PROCESSING ... A8
B1 BASIC IMAGE IMPORTATION ... A8
B2 IMAGE VISUALISATION ... A9
B3 EDIT FILE HEADER DETAILS ... A9
B4 DEFINE REGIONS of INTEREST for SPECTRAL EXTRACTION ... A10
B5 EMPIRICAL LINE CALIBRATION ... A11
B6 IMAGE MASKING ... A14
B7 BAND MATHEMATICS ... A15
B8 IMAGE RESIZING ... A16
B9 HISTOGRAM EXTRACTION ... A17
B10 PRINCIPAL COMPONENT ANALYSIS ... A18
B11 COMPUTE IMAGE STATISTICS ... A19

Appendix C: ATM IMAGES & AERIAL PHOTOGRAPHS ... A20
C1 BOSWORTH IMAGES ... A20
C2 BAILDON MOOR IMAGES ... A36
C3 WEARDALE IMAGES ... A38

Appendix D: FLIGHT DETAILS ... A39
D1 BOSWORTH ... A39
D2 BAILDON MOOR ... A41
D3 WEARDALE ... A42
D4 SUMMARY FLIGHT DETAILS for SUN ANGLE CALCULATION ... A44

Appendix E: SUN ANGLE ... A45

E1 BOSWORTH SUN ANGLE VALUES A45
E2 BAILDON MOOR SUN ANGLE VALUES A47
E3 WEARDALE SUN ANGLE VALUES A47
E4 SOLAR DECLINATION VALUES from SUN ANGLE PROGRAM A47

Appendix F: C++ PROGRAMS A48
F1 SENSITIVITY of PLANCK RADIANCE to VARIABLE WAVELENGTH, SPECIFYING TEMPERATURE and EMISSIVITY A48
F2 SENSITIVITY of PLANCK RADIANCE to VARIABLE EMISSIVITY, SPECIFYING TEMPERATURE and WAVELENGTH A49
F3 SENSITIVITY of PLANCK TEMPERATURE to VARIABLE WAVELENGTH, SPECIFYING RADIANCE and EMISSIVITY A50
F4 SENSITIVITY of PLANCK TEMPERATURE to VARIABLE EMISSIVITY, SPECIFYING RADIANCE and EMISSIVITY A51
F5 CALCULATION of ATI from CRACKNELL & XUE (1996) USING IMAGE DIURNAL TEMPERATURE, SPECIFYING ALBEDO A52
F6 SENSITIVITY of CRACKNELL & XUE (1996) ATI to VARIABLE ALBEDO A55
F7 CALCULATION of ATI from KAHLE & ALLEY (1985) USING IMAGE DIURNAL TEMPERATURES, SPECIFYING ALBEDO, DECLINATION and LATITUDE A56
F8 CALCULATION of ATI from PRICE (1985) USING IMAGE DIURNAL TEMPERATURES, SPECIFYING ALBEDO, DECLINATION and LATITUDE A59
F9 CALCULATION of SOIL MAXIMUM and MINIMUM TEMPRATURES and their DIURNAL TIMES from a TIME-SERIES A62

Appendix G: SOIL ANALYSIS A69
G1 PARTICLE SIZE ANALYSIS A69
G2 MOISTURE CONTENT A71
G3 ORGANIC CONTENT (LOSS on IGNITION) A71

FIGURES

Figure 2.1: Comparison of natural thermal emission of the Sun and Earth, taken from Lillesand and Kiefer (2000) 7
Figure 2.2: Thermal radiation emitted by a blackbody, greybody and a natural material, taken from Elachi (1987) 13
Figure 2.3: Sensitivity of temperature to variable emissivity for constant radiance 16
Figure 2.4: Energy Flux interactions occurring at the surface, taken from Price (1985) 19
Figure 2.5: Diurnal temperature response with respect to thermal inertia, taken from Kahle (1980) 24
Figure 2.6: Thermal inertia of a dry soil with variable sand content and porosity, taken from Pratt & Ellyett (1979) 26
Figure 2.7: Thermal inertia of soils with variable sand and moisture content for porosities ranging from 30%-60%, taken from Pratt & Ellyett (1979) 27
Figure 2.8: Evolution of temperature through time and depth for low thermal inertia (solid line) and high thermal inertia (dashed line), taken from Kahle (1980) 28
Figure 2.9: Thermal inertia as a function of depth and time for variable conductivity, taken from Kahle (1980) 29
Figure 2.10: Thermal inertia as a function of depth and time for variable density, taken from Kahle (1980) 29
Figure 2.11: Sensitivity of diurnal temperature to variations in (A) thermal inertia, (B) geothermal heat flux, (C) albedo and (D) surface emissivity. DC indicates mean diurnal temperature, taken from Kahle (1980) 37
Figure 2.12: Sensitivity of diurnal temperature to variations in (A) albedo, (B) slope, (C) slope azimuth and (D) thermal inertia, taken from Kahle (1977) 38
Figure 2.13: Thermal inertia calibration chart from known diurnal temperature and albedo for specific meteorological conditions, taken from Pratt & Ellyett (1979) 39
Figure 2.14: Thermal properties (A) heat capacity, (B) thermal conductivity, (C) thermal diffusivity and (D) thermal inertia for variable sand-clay fraction and water content for a fixed porosity, taken from Pratt & Ellyett (1979) 40
Figure 3.1: Effect of buried feature on thermal response detected at the surface 49
Figure 3.2: Diurnal thermal response of bare soil, vegetation and water 50
Figure 3.3: Effect of short vegetation on thermal response at the surface 50
Figure 3.4: Effect of vegetation on thermal response detected at the surface 51
Figure 3.5: Two-layer and three-layer models representing subsurface structure, taken from Perriset & Tabbagh (1981) 52
Figure 3.6: Location of Bosworth scheduled monument (www.multimap.co.uk) 53
Figure 3.7: Location of Baildon Moor, W. Yorkshire (www.multimap.co.uk) 56
Figure 3.8: Examples of (A) bell pit and (B) room and pillar shaft formations. Both examples show a narrow shaft-head with wide base for coal extraction 58
Figure 3.9: Crown-hole development above a room and pillar working 59
Figure 3.10: Location of North Pennine Orefield (www.multimap.co.uk) 60
Figure 3.11: Geoscan FM36 Fluxgate Gradiometer operated by James Lyall, Landscape Research Centre 67
Figure 3.12: Twin-electrode array provided by the Geoscan RM15 Resistance apparatus (www.geoscan-research.co.uk) 69
Figure 3.13: Four-electrode Wenner configuration where a current is passed into the ground through a pair of electrodes (C1 and C2) and the potential measured across a secondary pair of electrodes (P1 and P2), taken from Griffiths & Barker (1994) 70
Figure 3.14: Dual-loop EM31 electromagnetic system with transmitting and receiving coils mounted on horizontal pole 72
Figure 3.15: Dual-loop EM34 electromagnetic system with moving transmitting and receiving coils connected by reference cable at fixed coil separation 72
Figure 3.16: Horizontal (A) and Vertical (B) magnetic dipole configurations 73

Figure 3.17: Results of the Fluxgate Gradiometer survey of Bosworth. Dark grey indicates low magnetic response 75
Figure 3.18: Results of the RM15 resistivity survey of Bosworth 78
Figure 3.19: Resistivity survey of the Picnic field 79
Figure 3.20: Resistivity survey of the Arena field 80
Figure 3.21: Resistivity survey of the Re-enactment field 80
Figure 3.22: Resistivity survey of the South field: West section 81
Figure 3.23: Resistivity survey of the South field: East section 82
Figure 3.24: Resistivity survey of the Helipad field 83
Figure 3.25: Example finds from field-walking in Bosworth 85
Figure 3.26: Location of Wenner transect line and representation of features on natural colour composite and day thermal image 86
Figure 3.27: Prominent vegetation anomaly observed over known mine shaft 87
Figure 3.28: Resistivity profile trending WNW from origin (0m) beside road 88
Figure 3.29: EM31 profile for horizontal and vertical coil configurations 89
Figure 3.30: Profile of EM34 survey at 20m coil separation for both horizontal and vertical coil configurations 91
Figure 3.31: Location of Area B transect line on Baildon Moor and representation of features on natural colour composite and thermal imagery 92
Figure 3.32: Known shaft of pronounced topographic expression 93
Figure 3.33: Suspected shaft of circular vegetation and thermal anomaly 93
Figure 3.34: EM31 profile for both horizontal and vertical coil configurations 94
Figure 3.35: EM34 profile for both horizontal and vertical coil configurations 95
Figure 3.36: Location of EM31 secondary profile over suspected shaft 96
Figure 3.37: Wenner resistivity profile over thermal anomaly 97
Figure 4.1: Geometric distortions of imagery compared to base map (right) 104
Figure 4.2: GCP collection using PCI GCPWorks software. GCP pairs are selected at points recognisable on (A) image and (B) vector layer 106
Figure 4.3: Change in field boundary position between vector layer and its potential position on image 107
Figure 4.4: Nearest Neighbour Resampling where uncorrected pixel values are transferred to the closest corresponding pixel location 108
Figure 4.5: Geocorrection of image (A) using GCP pairs to generate geocorrected image (B) 109
Figure 4.6: Day (upper) and night (lower) masks generated for Bosworth 113
Figure 4.7: (A) Overlap of Bosworth masks generating mask (B) for overlap 114
Figure 4.8: Spatial subset generated for Bosworth 115
Figure 4.9: Spatial subset of Baildon Moor abandoned mine activity 115
Figure 4.10: Spatial subset generated for Weardale abandoned mine activity 116
Figure 4.11: Location of field reflectance spectra for Bosworth study site 119
Figure 4.12: Resampling of 512-channel field spectra to the 8-channel resolution of the image in the visible and near-infrared wavelength region 120
Figure 4.13: Spectrally flat reference material for Bosworth multi-temporal data 123
Figure 5.1: Monochrome images of spectral channels of Bosworth May 1998 128
Figure 5.2: Monochrome images of spectral channels of Bosworth June 1998 129
Figure 5.3: Monochrome images of spectral channels of Bosworth August 1998 130
Figure 5.4: Monochrome images of spectral channels of Bosworth March 2002 131
Figure 5.5: Monochrome images of spectral channels for Baildon Moor 134
Figure 5.6: Monochrome images of spectral channels for Weardale 137
Figure 5.7: Histogram manipulation on Bosworth August 1998 day thermal image 140
Figure 5.8: Thermal features on Bosworth May 1998 day thermal image 142
Figure 5.9: Thermal features on Bosworth June 1998 day thermal image 143
Figure 5.10: Thermal features on Bosworth June 1998 night thermal image 144
Figure 5.11: Thermal features on Bosworth August 1998 day thermal image 145
Figure 5.12: Thermal features on Bosworth August 1998 night thermal image 146

Figure 5.13: Thermal features on Bosworth March 2002 day thermal image 147
Figure 5.14: Thermal features on Bosworth March 2002 night thermal image 148
Figure 5.15: Display of complex relationship of Bosworth thermal interpretation 149
Figure 5.16: Field nomenclature for Bosworth study site 149
Figure 5.17: Plateau on Bosworth Ambion field 150
Figure 5.18: Northeast corner of Bosworth Ambion field 150
Figure 5.19: Southwest corner of Bosworth Ambion field 151
Figure 5.20: Anomalies on Bosworth day thermal images of Ambion field 153
Figure 5.21: Anomalies on Bosworth night thermal images of Ambion field 154
Figure 5.22: Comparison of Bosworth August 1998 thermal images with magnetic survey of Ambion field 155
Figure 5.23: Thermal anomalies in Bosworth Arena field 156
Figure 5.24: Area of hard-standing in Bosworth Arena field 157
Figure 5.25: Comparison of Bosworth August 1998 day thermal image with results of geophysical surveys of the Arena field 158
Figure 5.26: Topography of Bosworth Helipad field 158
Figure 5.27: Thermal anomalies in Bosworth Helipad field 159
Figure 5.28: Comparison of Bosworth May 1998 day thermal image with results of the geophysical surveys of the Helipad field 160
Figure 5.29: Topography of Bosworth Picnic field 160
Figure 5.30: Thermal anomalies in Bosworth Picnic field 161
Figure 5.31: Comparison of Bosworth August 1998 day thermal image with results of the geophysical surveys of the Picnic field 162
Figure 5.32: Thermal anomalies of Bosworth South field 163
Figure 5.33: Hummock in Bosworth South field 164
Figure 5.34: Comparison of Bosworth August 1998 day thermal image with results of magnetic survey of the South field 165
Figure 5.35: Thermal anomalies on Baildon Moor 168
Figure 5.36: Baildon shaft of pronounced topographic expression (radius 8m) 169
Figure 5.37: Baildon shaft of pronounced vegetation expression (radius 11m) 169
Figure 5.38: Baildon suspected shaft feature (radius 2m) 169
Figure 5.39: Thermal profiles generated across topographic shaft from Baildon day thermal image 171
Figure 5.40: Thermal profiles generated across topographic shaft from Baildon night thermal image 171
Figure 5.41: Comparison of thermal profiles with EM31 electromagnetic profile across Baildon topographic shaft 172
Figure 5.42: Thermal profiles generated across vegetation feature from Baildon day thermal image 174
Figure 5.43: Thermal profiles generated across vegetation feature from Baildon night thermal image 174
Figure 5.44: Comparison of thermal profile with resistivity profile across Baildon vegetation feature 175
Figure 5.45: Comparison of thermal profile with resistivity profile across Baildon suspected shaft feature 176
Figure 5.46: Thermal profiles generated across suspected shaft feature from Baildon day thermal image 177
Figure 5.47: Thermal profiles generated across suspected shaft feature from Baildon night thermal image 177
Figure 5.48: Thermal anomalies in Weardale 178
Figure 5.49: Scour marks on north-eastern flank of valley in Weardale 179
Figure 5.50: N-S thermal profiles of mineral extraction features from Weardale day thermal image 180
Figure 5.51: N-S thermal profiles of mineral extraction feature from Weardale night thermal image 180

Figure 5.52: Natural colour composites of Bosworth 185
Figure 5.53: Near-infrared false-colour composites of Bosworth 189
Figure 5.54: Thermal day colour composites of Bosworth 192
Figure 5.55: Thermal night colour composites of Bosworth 194
Figure 5.56: Field subset and nomenclature for Bosworth 196
Figure 5.57: Standard averaging low pass 3x3 filter kernel 197
Figure 5.58: Results of low pass filtration on Bosworth August 1998 day thermal image 198
Figure 5.59: Standard high pass 3x3 filter kernel 198
Figure 5.60: Results of high pass filtration on Bosworth August 198 day thermal image 199
Figure 5.61: Standard 3x3 directional filter kernels 200
Figure 5.62: Results of directional filtration on Bosworth August 1998 day thermal image. 201
Figure 5.63: Day, night and thermal contrast of Bosworth Ambion field 205
Figure 5.64: Histograms generated from August thermal images of Bosworth Ambion field 206
Figure 5.65: Day, night and thermal contrast images of Baildon topographic shaft 208
Figure 5.66: Thermal profiles generated across Baildon topographic shaft on thermal contrast image 208
Figure 5.67: Day, night and thermal contrast images of Baildon vegetation feature 209
Figure 5.68: Thermal profiles generated across Baildon vegetation feature from thermal contrast image 209
Figure 5.69: Day, night and thermal contrast images of Baildon suspected shaft 210
Figure 5.70: Thermal profiles generated across Baildon suspected shaft from thermal contrast image 210
Figure 5.71: Day, night and thermal contrast images of Weardale mineral extraction 212
Figure 5.72: Thermal profiles generated across Weardale mineral extraction features from thermal contrast image 212
Figure 5.73: Schematic scatter-plot showing pixel distribution of adjacent spectral bands and location of new PC coordinate system axes (PC1 & PC2) 213
Figure 5.74: Monochrome images of PC transformation bands of Bosworth August 1998 visible and near-infrared bands 215
Figure 5.75: PC transformation of Bosworth August 1998 visible and near-infrared bands of Ambion field 216
Figure 5.76: PC transformation of Bosworth August 1998 visible, near-infrared and thermal bands of Ambion field 217
Figure 5.77: PC transformation of Bosworth August 1998 uncalibrated visible and near-infrared bands of Ambion field 218
Figure 5.78: PC transformation of Bosworth August 1998 uncalibrated visible, near-infrared and thermal bands of Ambion field 219
Figure 5.79: PC band combinations on transformation of Bosworth August 1998 calibrated visible and near-infrared bands of Ambion field 221
Figure 5.80: PC band combinations on transformation of Bosworth August 1998 uncalibrated visible and near-infrared bands of Ambion field 222
Figure 5.81: PC band combinations on transformation of Bosworth August 1998 calibrated visible, near-infrared and thermal bands of Ambion field 223
Figure 5.82: PC band combinations on transformation of Bosworth August 1998 uncalibrated visible, near-infrared and thermal bands of Ambion field 224
Figure 5.83: PC band combinations on transformation of Bosworth March 2002 uncalibrated visible and near-infrared bands of Ambion field 225
Figure 5.84: PC band combinations on transformation of Bosworth March 2002 uncalibrated visible, near-infrared and thermal bands of Ambion field 226
Figure 6.1: Spectral response pattern of ATM thermal channel 235
Figure 6.2: Sensitivity of thermal radiance to variable wavelength at (A) variable temperature and (B) variable emissivity 237
Figure 6.3: Sensitivity of thermal radiance to variable emissivity at (A) variable temperature and (B) variable wavelength 239

Figure 6.4: Sensitivity of temperature to variable wavelength at (A) variable radiance and (B) variable emissivity 241
Figure 6.5: Sensitivity of temperature to variable emissivity at (A) variable radiance and (B) variable wavelength 243
Figure 6.6: Sensitivity of ATI to variable albedo 252
Figure 6.7: Field nomenclature for Bosworth site 253
Figure 6.8: Cracknell & Xue (1996) ATI images for Ambion field at Bosworth 254
Figure 6.9: Comparison of results generated for Bosworth Ambion field from Cracknell & Xue (1996) ATI model and simple image subtraction 255
Figure 6.10: Comparison of results generated for Bosworth Arena field from Cracknell & Xue (1996) ATI model and simple image subtraction 257
Figure 6.11: Comparison of results generated for Bosworth Helipad field from Cracknell & Xue (1996) ATI model and simple image subtraction 258
Figure 6.12: Comparison of results generated for Bosworth Picnic field from Cracknell & Xue (1996) ATI model and simple image subtraction 259
Figure 6.13: Comparison of results generated for Bosworth South field from Cracknell & Xue (1996) ATI model and simple image subtraction 260
Figure 6.14: Comparison of June 1998 results from Kahle & Alley (1985), Cracknell & Xue (1996) ATI models and the image subtraction technique for Bosworth Ambion field 262
Figure 6.15: Comparison of June 1998 results from Price (1985), Kahle & Alley (1985), Cracknell & Xue (1996) ATI models and the image subtraction technique on Bosworth Ambion field 264
Figure 6.16: Comparison of histograms of model outputs for Bosworth Ambion field 265
Figure 6.17: Location of regions of interest for manmade objects at Bosworth 267
Figure 6.18: ATI Histograms extracted from manmade objects at Bosworth 268
Figure 6.19: Bosworth field histograms generated from Cracknell & Xue (1996) ATI model 269
Figure 6.20: Comparison of Bosworth June 1998 Cracknell & Xue ATI with magnetometry 271
Figure 6.21: Comparison of Bosworth August 1998 Cracknell & Xue ATI with magnetometry 272
Figure 6.22: Comparison of Bosworth June 1998 Cracknell & Xue ATI with resistivity 273
Figure 6.23: Comparison of Bosworth August 1998 Cracknell & Xue ATI with resistivity. 274
Figure 7.1: Schematic diurnal response of bare soil, vegetation and water 281
Figure 7.2: Location of Church Lawford Saws meteorological station and the Bosworth study site 284
Figure 7.3: Thermal characteristics with overlay showing moderate daily rainfall 285
Figure 7.4: Thermal characteristics with overlay showing high daily rainfall and high wind speed 285
Figure 7.5: Location of Site A thermal profile observed at Bosworth 287
Figure 7.6: Diurnal thermal profile at Site A under Stage I pasture 2000 291
Figure 7.7: Diurnal thermal profile at Site A under Stage I barley 2001 291
Figure 7.8: Diurnal thermal profile at Site A under Stage II pasture 2000 292
Figure 7.9: Diurnal thermal profile at Site A under Stage II barley 2001 292
Figure 7.10: Diurnal thermal profile at Site A under Stage III pasture 2000 293
Figure 7.11: Diurnal thermal profile at Site A under Stage III barley 2001 293
Figure 7.12: Diurnal thermal profile at Site A under Stage IV pasture 2000 294
Figure 7.13: Diurnal thermal profile at Site A under Stage IV barley 2001 294
Figure 7.14: Location of Site B thermal profile observed at Bosworth 297
Figure 7.15: Diurnal thermal profile at Site B under Stage I pasture 2000 301
Figure 7.16: Diurnal thermal profile at Site B under Stage I barley 2001 301
Figure 7.17: Diurnal thermal profile at Site B under Stage II pasture 2000 302
Figure 7.18: Diurnal thermal profile at Site B under Stage II barley 2001 302
Figure 7.19: Diurnal thermal profile at Site B under Stage III pasture 2000 303

Figure 7.20: Diurnal thermal profile at Site B under Stage III barley 2001 303
Figure 7.21: Diurnal thermal profile at Site B under Stage IV pasture 2000 304
Figure 7.22: Diurnal thermal profile at Site B under Stage IV barley 2001 304
Figure 7.23: Soil classification scheme from Saxton (USDA Agricultural Research Service) 308
Figure 7.24: Location and nomenclature of Bosworth soil extraction profiles 310
Figure 7.25: Vertical soil profile extracted from Bosworth Feature A 311
Figure 7.26: Vertical soil profile extracted from Bosworth Feature B 312
Figure 7.27: Vertical soil profile extracted from Bosworth Feature C 314
Figure 7.28: Vertical soil profile extracted from Bosworth Feature D 316
Figure 7.29: Vertical soil profile extracted from Bosworth Location E 317
Figure 8.1: June and August ATI profiles across specific Bosworth features 324
Figure 8.2: Matrices generated for soil and ATI characteristics for each Bosworth feature .. 329

Figure A1: Daedalus AADS1268 Airborne Thematic Mapper A1
Figure A2: The NERC aircraft (Dornier Do228-101 D-CALM) A3
Figure A3: Wild RC-10 Survey Camera A4
Figure A4: HOBO-H8 outdoor 4-channel data logger with table of characteristics A6
Figure A5: BoxCar® Pro 3.5 launch window enabling channel and sample-interval specifications A6

Insert A: Lateral Soil Profiles for Feature A ..... Back Cover Pocket
Insert B: Lateral Soil Profiles for Feature B ..... Back Cover Pocket
Insert C: Lateral Soil Profiles for Feature C ..... Back Cover Pocket
Insert D: Lateral Soil Profiles for Feature D ..... Back Cover Pocket
Insert E: Lateral Soil Profiles for Location E ..... Back Cover Pocket

TABLES

Table 2.1: Planck's Radiation Law parametric units and values 12
Table 2.2: Emissivity values of common land surface materials, compiled from Rubio et al (1997), Qin & Karnieli (1999) and Lillesand & Kiefer (2000) 15
Table 2.3: Thermal properties of common geological materials, compiled from Kahle (1980) and Elachi (1987) 25
Table 2.4: Thermal properties of common geological materials (Hapke, 1993) 25
Table 2.5: Albedo values of natural surfaces, extracted from Barrett & Curtis (1982) 33
Table 3.1: Spectral characteristics of the Daedalus-1268 Airborne Thematic Mapper 62
Table 6.1 Comparison of Price and ATM radiance values for known temperature values from Bosworth data 248
Table 6.2: Comparison of absolute values from the ATI models on Bosworth Ambion field 266
Table 7.1: Thermal characteristics of Bosworth Site A soil column at Stage I 291
Table 7.2: Thermal characteristics of Bosworth Site A soil column at Stage II 292
Table 7.3: Thermal characteristics of Bosworth Site A soil column at Stage III 293
Table 7.4: Thermal characteristics of Bosworth Site A soil column at Stage IV 294
Table 7.5: Summary of thermal characteristics observed at Bosworth Site A 296
Table 7.6: Thermal characteristics of Bosworth Site B soil column at Stage I 301
Table 7.7: Thermal characteristics of Bosworth Site B soil column at Stage II 302
Table 7.8: Thermal characteristics of Bosworth Site B soil column at Stage III 303
Table 7.9: Thermal characteristics of Bosworth Site B soil column at Stage IV 304
Table 7.10: Summary of thermal characteristics observed at Bosworth Site B 306
Table 7.11: Soil particle size definition 307
Table 8.1: Correlation of ATI with soil properties across Bosworth Feature A 325
Table 8.2: Correlation of ATI with soil properties across Bosworth Feature B 326
Table 8.3: Correlation of ATI with soil properties across Bosworth Feature C 327

Table 8.4: Processing steps for generation of ATI images using Cracknell & Xue (1996) model 331
Table 8.5: Processing steps for assessment of multispectral images 333

Table A1: Spectral characteristics of the Daedalus AADS1268 ATM A1
Table A2: Spectral response details of ATM thermal channel A2
Table A3: Technical characteristics of the Daedalus AADS1268 ATM A3
Table A4: Technical characteristics of the GER1500 Spectroradiometer A5
Table A5: Technical characteristics of the GER3700 Spectroradiometer A5

EQUATIONS

Equation 2.1: 10
Equation 2.2: 10
Equation 2.3: 10
Equation 2.4: 11
Equation 2.5: 13
Equation 2.6: 13
Equation 2.7: 18
Equation 2.8: 19
Equation 2.9: 20
Equation 2.10: 20
Equation 2.11: 20
Equation 2.12: 20
Equation 2.13: 21
Equation 2.14: 21
Equation 2.15: 21
Equation 2.16: 21
Equation 2.17: 22
Equation 2.18: 22
Equation 2.19: 23
Equation 2.20: 24
Equation 2.21: 31
Equation 2.22: 32
Equation 2.23: 34
Equation 2.24: 34
Equation 2.25: 34
Equation 2.26: 36
Equation 2.27: 40
Equation 2.28: 41
Equation 2.29: 41
Equation 2.30: 43
Equation 2.31: 43
Equation 2.32: 43
Equation 2.33: 44
Equation 2.34: 44
Equation 3.1: 69
Equation 4.1: 103
Equation 5.1: 139
Equation 6.1: 234
Equation 6.2: 234
Equation 6.3: 246
Equation 6.4: 250
Equation 6.5: 261

Equation 6.6: 261
Equation 6.7: 263

EXAMPLES

Example 4.1: 101
Example 4.2: 101
Example 4.3: 102
Example 4.4: 106
Example 4.5: 111
Example 4.6: 111
Example 4.7: 111

CALCULATIONS

Calculation 6.1: 247
Calculation 6.2: 247

Declaration

The material contained in this thesis has not been previously submitted by the candidate for a degree in this or any other university.

Statement of Copyright

Acknowledgements

A great number of organisations and individuals have assisted with the research and production of this thesis and thanks must go primarily to the British Geological Survey for part supporting this research under their University Collaboration Scheme. Additional thanks must go to:

The Natural Environmental Research Council Airborne Remote Sensing Facility for provision of the digital imagery and aerial photography without which this research could not be performed and specifically Andrew Wilson at their Centre for Ecology and Hydrology for providing his technical expertise relating to the Airborne Thematic Mapper.

The rangers based at Bosworth Battlefield Centre, most notably Richard MacKinder for his constant interest in the research, without whose invaluable negotiation skills there would have not been access to the study fields at the Bosworth site.

James Lyall at the Landscape Research Centre for his extensive expertise and introducing the concepts and delights of geophysical surveying and the Department of Archaeology, University of Durham for allowing access to their geophysical instrumentation.

The Remote Sensing Division at the British Geological Survey for their assistance in generating a successful research proposal for acquisition of NERC ATM data over Weardale, to Gisela Agar for her assistance with image processing using their remote sensing facilities and David Gunn and Mike Raines for their geophysical field session on Baildon Moor and providing an enjoyable interlude to the research.

Leicestershire County Council for allowing access to existing magnetometry and resistivity reports on the Bosworth study site.

British Atmospheric Data Centre (RAL) for access to their meteorological data archive.

To my brother Neil for his most impressive knowledge of everything to do with C++ programming and for saving my bacon on numerous occasions when all was not what it seemed.....

And in Department of Geography, thanks go to all the Laboratory Technicians for their assistance in the soil analyses and use of the 'wee trowel', IT support especially Terry who managed to make all the computer and printer gremlins miraculously disappear, and of course Stella for just being Stella.

Last, but by no means least, my most sincere thanks must go to supervisors Danny Donoghue and Stuart Marsh for their continual support and guidance.

Chapter 1 : INTRODUCTION to THESIS

1.1 INTRODUCTION

This chapter outlines the concepts behind this thesis, stating the aims and objectives and the reasons for conducting the research and concludes with a brief outline of the structure of the thesis.

1.2 RESEARCH AIMS

The research seeks to assess the value of airborne remote sensing in the context of geological and archaeological applications in the UK environment where the ground surface is covered by a layer of vegetation. Vegetation is a severe limiting factor in detection of variations in surface characteristics since the underlying materials are not exposed at the surface and are masked from direct observation. Airborne remote sensing is becoming more widely used in this style of research as it provides a synoptic view of the ground surface, however, the effect of vegetation is more poorly understood for the detection of surface variations beneath the canopy.

The main aims of the study are:

- To investigate the use of multispectral and thermal airborne remote sensing techniques and ground geophysical prospection for detecting shallow ground disturbance beneath a layer of vegetation

Research to evaluate airborne multispectral remote sensing techniques has been shown to offer considerable potential for landscape assessment in a range of environments (Donoghue & Shennan, 1988; Scollar *et al,* 1990) and have provided interesting results where certain archaeological and geomorphological features are more evident under particular soil and vegetation conditions (Perriset & Tabbagh, 1981; Powlesland *et al*, 1997, Donnelly & McCann, 2000). Conclusions from the research suggest that images acquired at near-infrared and shortwave infrared wavelengths can enhance crop and soil marks when compared with visible wavelengths of standard aerial photography, as these wavelengths are more sensitive to differences in soil moisture and plant health. Images acquired at thermal infrared wavelengths during the day also show an ability to detect features not evident at any other wavelength as this emitted radiation responds in part to subsurface properties of the ground. As a result, thermal prospection techniques are particularly useful in landscape assessment and

archaeological prospection by identifying areas of differential heat flux relating undisturbed and disturbed soils.

Infrared thermography has been used with great success using thermal images for locating shallow ground disturbance in areas devoid of vegetation (Kahle *et al,* 1976; Kahle, 1977; Gillespie & Kahle, 1977; Pratt & Ellyett, 1979; Price, 1980; Watson, 1982; Kahle & Alley, 1985; Price, 1985, Nash, 1988). However, in the intensively farmed areas, such as in UK environment, the ground surface is covered by a layer of vegetation and the response from the underlying material will become affected by the vegetation fraction that masks the soil to some extent from direct heating and cooling processes and the surface will show a more uniform daytime response due to the vegetation regulating its surface temperature through plant evapotranspiration (Perriset & Tabbagh, 1981; Bellerby *et al,* 1990; Scollar, 1990). Although materials underlying the vegetation can affect the thermal response observed from above the vegetation, the behaviour of surfaces masked by a layer of vegetation is poorly understood. The purpose of this research is to understand the effect of vegetation on the visibility of features buried in the near-surface environment, which is important for landscape assessment in the intensively farmed areas in the UK.

A second aim of the study is:

- To examine the relationship between airborne thermal radiance data and the characteristics of surface materials beneath a layer of vegetation

Thermal infrared energy is emitted from the surface materials with different physical materials having different emission characteristics based on the thermal properties of the materials. Materials that are devoid of vegetation typically exhibit a diurnal heating and cooling pattern that is directly influenced by the incoming solar radiation. Materials of different compositions will respond differently to solar heating across the diurnal cycle and will display different values of day-night thermal contrast. This can be used to can give an indication of bulk compositional variations through calculation of a value of Apparent Thermal Inertia (ATI). Therefore, the inclusion of a day-night ATI approach is new and forms an important method that needs to be tested for geological and archaeological applications. However, it is essential to understand the depth to which the diurnal heat can penetrate throughout the vegetation growth and as

such, this aim is directed towards establishing the timing when the thermal regime of the vegetation can be used to detect feature buried in the near-surface environment.

1.3 OBJECTIVES

The study uses multispectral and thermal data measured by the Daedalus 1268 Airborne Thematic Mapper (ATM), which is provided by the Natural Environmental Research Council (NERC), to look at specific sites where suitable airborne thermal and geophysical data exist. The ATM instrument is the only source of airborne thermal imagery available for use by the academic community in the UK and so it is important to assess fully the potential of this instrument for geological and archaeological applications. The main objectives of the research are split into issues addressing technical processing, ground prospection and analysis techniques that may provide assessment of features underlying a layer of vegetation. The main objectives of the study are:

1. To produce fully processed Daedalus-1268 Airborne Thematic Mapper images at visible, near-infrared, shortwave infrared and thermal infrared wavelengths provided by the NERC Airborne Remote Sensing Facility for the study sites
2. To provide co-registered day and night thermal images of the study sites
3. To provide co-registered multi-temporal images of the study sites
4. To calibrate airborne thermal radiance measurements to surface temperature values
5. To assess the suitability of applying published Apparent Thermal Inertia Models to environmental applications
6. To conduct geophysical evaluation of the soil characteristics beneath vegetation at the study sites and compare the results with the airborne survey
7. To assess the effect of vegetation on the detection of near-surface geophysical or archaeological features
8. To analyse the dynamics of the soil-vegetation heat flux based on a time series obtained from ground based contact measurements of soil temperature
9. To determine times when the temperature contrast within the soil column is optimised to conduct an effective thermal survey

10. To determine appropriate processing requirements for conducting assessment of disturbance occurring in the near-surface environment beneath a layer of vegetation using airborne image data

1.4 RESEARCH FRAMEWORK

This research was in part funded by the British Geological Survey under their University Collaboration Scheme where their interest in the use of thermal radiance for site assessment was stimulated from their extensive work on abandoned mineshafts on Baildon Moor. In addition, the Bosworth archaeological community also showed particular interest to understand if this technique would provide an additional prospection tool for detection of buried archaeology. These branches of the scientific community require alternative site assessment where terrains may be potentially dangerous or have restricted access.

The study investigates multispectral airborne remote sensing techniques for detecting shallow ground disturbance and in particular seeks to better understand the value of thermal radiance data. The research uses diurnal airborne imagery acquired by the NERC Daedalus-1268 Airborne Thematic Mapper (ATM) to study a number of examples of disturbed ground in the UK: (1) buried archaeology at Bosworth, (2) abandoned mineshafts on Baildon Moor and (3) abandoned mine spoil heaps and scour marks in Weardale.

Apparent Thermal Inertia (ATI) can detect physical variations in the near-surface environment using a measure of the diurnal contrast in temperature of a material. The research focuses on a particular gap in the current knowledge about the effect of surface vegetation on the heat flux of the soil-vegetation system. The research tests different published Apparent Thermal Inertia models based on pairs of day-night overflights and aims to provide i) an assessment of the methodological steps required to conduct effective thermal surveys of vegetated terrains, ii) an analysis of the dynamics of the soil and vegetation heat flux based on a time-series of instrumented sites and will iii) compare and contrast the relationships between airborne thermal radiometry, ground (soil and vegetation) characteristics and results from ground-based geophysical surveys. The published ATI models take into account variations in temporal, seasonal and vegetation effects of the surface and are used to assess features of disturbed ground in the near-surface environment manifest as voids,

soil texture or soil moisture differences. These ATI models have never been used before for the detection of shallow ground disturbance in terrains covered by a layer of vegetation and so may provide a new approach for detection of ground disturbance. One to the most significant outputs from the research project will be to provide a methodology for selecting the most appropriate conditions where airborne thermal radiance can provide useful additional prospection tool that may benefit the wider scientific community for new geological, archaeological and ecological applications.

1.5 STRUCTURE of THESIS

The thesis opens with a discussion on the theory and methodology behind remote sensing in the thermal infrared and introduces the problem involved with assessing areas covered by vegetation. A chapter that introduces the conceptual framework of the research and introduces the different examples and environmental settings assessed in the research follows this. The different sources of data for conducting the research are also introduced in this chapter together with a detailed discussion on the results of geophysical prospection conducted in two different environmental settings. Chapter 4 presents the methodology for processing the digital airborne images collected for the study sites and points out some of the problems that are encountered where using multitemporal datasets. Chapter 5 introduces qualitative techniques used for image interpretation including a discussion of the features detected on multispectral and thermal images and compares the results with ground geophysical surveys. This is followed by a chapter that assesses the thermal images in a quantitative manner through numerical thermal modelling and includes a discussion on the problems of converting the thermal radiance data to ground temperature values (Chapter 6). Apparent Thermal Inertia is determined for one of the study areas and different models are compared with the results of the ground-based geophysical surveys. Physical soil characteristics observed at the instrumented study site are discussed in Chapter 7 with an analysis of the thermal characteristics observed at different stages of vegetation growth and the physical properties of the soil at sites that showed anomalous spectral and magnetic characteristics. The thesis then moves on to discuss the observed airborne thermal characteristics and their correlation with the physical soil characteristics (Chapter 8) and ends with an evaluation of the research and recommendations for further research (Chapter 9).

2 THEORY and METHODOLOGY

The remote sensing of land surface temperatures has become an important part of environmental studies over the last few decades with methodologies established for retrieval of land surface temperatures from a variety of satellite and airborne remote sensing platforms. Remote sensing in the thermal infrared is a well established technique for environmental investigations and has been applied to a variety of research areas such as lithological mapping (Watson, 1975: Kahle, 1977; Kahle *et al*, 1984), mapping of water surface temperatures (Franca & Cracknell, 1994; Emery & Yu, 1997; McManus *et al*, 1999), calculation of soil moisture content (Deardorff, 1978; Pratt & Ellyett, 1979; Price, 1980), detection of fires (Prakash *et al*, 1999; Giglio, 2000) and the monitoring of volcanic activity (Wright *et al*, 2002 & Flynn *et al*, 2001).

The vast majority of terrestrial studies have been performed in areas where the rock or soils are devoid of vegetation cover and are exposed at the Earth's surface. In these situations, the detected response can be directly related to that of the exposed material. However, when vegetation grows atop of rock or soil, the response will become affected by the vegetation fraction thus preventing direct investigation of the underlying materials. Vegetation also masks the underlying surface from direct heating and cooling processes and impacts upon the thermal study of the underlying surface due to the ability of the overlying plant to regulate is own temperature through the biological process of evapotranspiration. Where a dense vegetation canopy is present, the land surface temperature is generally viewed as the canopy temperature, but where vegetation is more sparse and the surface is heterogeneous in character, formulation for temperature retrieval becomes much more complex due to the combined influences of the materials present. A relationship may be developed to enable the assessment of the underlying soil by examining the diurnal and seasonal thermal response of the vegetation cover.

This chapter introduces the theory of thermal remote sensing, concentrating on the determination of land surface temperature, and is coupled with a discussion of thermal modelling techniques of apparent thermal inertia on the soil-vegetation interface and the thermal properties of surface materials.

2.1 THERMAL REMOTE SENSING

Thermal remote sensing is the study of the interaction of heat from one source to another using non-contact measurements of thermal energy. Thermal infrared radiation occupies the 3.0-50.0μm or middle infrared range of the electromagnetic spectrum. However, atmospheric absorption limits the detection of mid-infrared energy to two principal atmospheric windows at 3-5μm and 8-14μm (Sabins, 1986). Thermal energy of Earth surface materials can be related to either the reflected solar radiation in the 3.0-5.0μm spectral region or the emission of thermal energy generated by an internal heat source or as re-emission of solar radiation that was absorbed by the surface during the day (Figure 2.1).

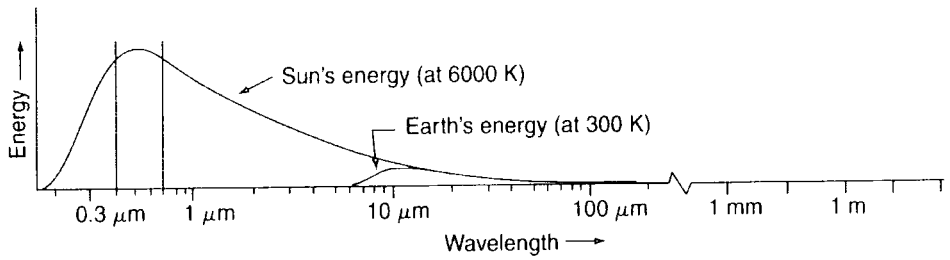

Figure 2.1: Comparison of natural thermal emission of the Sun and Earth, taken from Lillesand & Kiefer (2000)

As the Earth orbits the Sun, the intensity of solar radiation incident on its surface varies as a function of both the geographical location and also the time of observation. The solar declination and solar zenith angles determine the amount of solar radiation incident on surface materials. The amount of solar radiation reaching the surface therefore fluctuates on a diurnal cycle, with heat predominantly being conducted into the ground during the hours of daylight and rising back to the surface nocturnally, and will also fluctuate on a seasonal basis as the relative positions of the Sun and Earth migrate throughout the year.

When incoming solar radiation comes into contact with the Earth's surface, there are three possible interaction processes that can occur, namely reflection, absorption and transmission of the incident energy. The proportions of these interactions will vary as a function of material type and surface condition and variations in the response measured by a remote detector may enable the discrimination of surface material composition. The proportions of reflected and

absorbed radiation will also vary as a function of wavelength thereby enabling some discrimination of materials using different spectral wavelengths. Material discrimination is possible using thermal infrared wavelengths of radiation because the amount of energy emitted by a material is dependent upon its composition, the wavelength of observation, and also the physical temperature of the material. The temperature of the material will increase or decrease as a result of net gain or loss of energy respectively. The spatial variation in thermal response can give an indication of variations in the physical properties of the land surface. The most common method of evaluating the thermal behaviour of the land surface occurs through remote detection of energy from airborne or satellite platforms that give a synoptic view of the land surface.

2.1.1 Thermal Detection

Thermal infrared images can be generated from remote monitoring of the land surface using electromechanical instruments that use a rotating mirror and the motion of the platform to build up an image of the ground as the platform moves across the land surface. Thermal instruments contain detectors that are sensitive to specific wavelengths within the thermal infrared. The thermal radiation emitted from the ground is focussed onto a detector encased within the remote sensor, where the radiant energy is converted into a digital signal proportional to the intensity of thermal radiation received by or at the sensor. The thermal sensor may contain an internal thermal blackbody source whose radiance is measured intermittently throughout observation to give a reference digital signal for a known temperature value (Anderson & Wilson, 1984). The images generated by this type of sensor will give an indication of relative variations in thermal response across the land surface as a direct result of material composition and surface topography, where topography affects emittance values as slopes facing the Sun receive more solar radiation than those facing away from the Sun, with slope angle and elevation also controlling shadow effects and ambient surface temperature. The effects of material composition will be discussed later.

The radiation that is received by the remote detector will not necessarily represent the true amount of radiation emitted by the ground surface. This is due to atmospheric interactions as the energy emitted by the ground surface passes through

the atmosphere towards the sensor (Franca & Cracknell, 1994). The most common atmospheric interactions are the absorption and scattering by atmospheric constituents, mainly water vapour and carbon dioxide, which absorb radiation at different wavelengths that correspond to specific energies required to alter the energy-state of the atmospheric molecules (Hapke, 1993). Atmospheric interactions vary both in time and space, adding further complication to the analysis of thermal data. Prior to evaluation of thermal radiance data, it is often necessary to perform atmospheric correction on the data using an appropriate correction algorithm.

Airborne acquisition gives greater flexibility of viewing the land surface at specific times when the ground conditions are as desired. There is also the additional advantage of being able to acquire data under clear-sky conditions enabling land surface temperatures to be directly retrieved from the measured ground thermal emitted radiation. For the purposes of the research, thermal data was acquired using a modified Daedalus-1268 Airborne Thematic Mapper instrument flown by the Natural Environmental Research Council (see Appendix A). This instrument is an 11-channel multi-spectral scanner that contains 5 channels in the visible (VIS), 3 in the near-infrared (NIR), 2 in the short-wave infrared (SWIR) and 1 in the thermal infrared (TIR). The land surfaces investigated in the research will then be examined through this single thermal channel, to determine land surface temperatures and evaluate the thermal behaviour of the ground materials under investigation.

2.1.2 Land Surface Temperature Determination

Thermal radiation emitted from the land surface can be used to determine the physical temperature of that surface by using a well-established mathematical relationship known as Planck's Law (Equation 2.1) that relates the thermal radiance of a blackbody (L) to its temperature (T) with respect to the wavelength of observation (λ) and constants C1 and C2 (Price, 1989). The values of the constants C1 and C2 can be calculated with the SI values of Planck's constant, $h=6.63\times10^{-34}$ Ws^2, the speed of light, $c=2.99\times10^{8}$ ms^{-1} and the Boltzmann constant, $k=1.38WsK^{-1}$ using Equation 2.2 and Equation 2.3 respectively, as denoted in Kahle (1980).

Equation 2.1

$$L = \frac{C_1}{\lambda^5 \left(e^{\frac{C_2}{\lambda T}} - 1 \right)}$$

Equation 2.2

$$C_1 = 2\pi hc^2$$

Equation 2.3

$$C_2 = \frac{ch}{k}$$

The inference from the Planck radiation law is that the radiant energy emitted by the body will not be the same at all wavelengths for any given temperature and this needs to be taken into account in the determination of land surface temperature from the detected amount and wavelength of thermal radiation. However, some authors have misrepresented the inversion equation (Price, 1989 & Cresswell *et al*, 1999) therefore it is imperative that the correct equation be used for accurate temperature calculation.

The usual outcome of the calibration process to convert raw scanner data into radiances is for the supplier of the data to provide values of $\int\varphi(\lambda)L(\lambda)d\lambda$ where the integral is taken over the wavelength range from λ_1 to λ_2 of the spectral band in question and where $\varphi(\lambda)$ is the transmission function of the filters for this band in the scanner. Therefore to find the temperature what needs to be done is to invert the definite integral $\int\varphi(\lambda)L(\lambda)d\lambda$ (λ_1 to λ_2). This cannot be done explicitly. One has to work the other way round, i.e. to use a range of values of T that is likely to cover all the temperatures one is likely to encounter and use the (assumed known) $\varphi(\lambda)$ (almost certainly as a table of values) to calculate a table of values of $\int\varphi(\lambda)L(\lambda)d\lambda$ (λ_1 to λ_2) versus T. Then to calculate T one can either use this table (stored in one's computer) or develop an empirical equation derived from this table and use that to calculate T. This is clearly a considerable undertaking.

One can make an approximation if the band is narrow, so that $L(\lambda)$ does not vary significantly over the range λ_1 to λ_2, and if $\varphi(\lambda)$ is a perfect filter, i.e. $\varphi(\lambda) = 1$ for $\lambda_1 < \lambda < \lambda_2$ and $\varphi(\lambda) = 0$ elsewhere. Then $\int\varphi(\lambda)L(\lambda)d\lambda$ (λ_1 to λ_2) can be approximated by $L(\lambda)\Delta\lambda$ where $\Delta\lambda = \lambda_2 - \lambda_1$, i.e. the width of the band. One can then determine $L(\lambda)$

by dividing the total radiation detected in the band by $\Delta\lambda$. Then knowing $L(\lambda)$ one can invert the Planck equation (Equation 2.4) to find temperature.

Equation 2.4

$$T = \frac{C_2}{\lambda \ln\left(\frac{C_1}{\lambda^5 L} + 1\right)}$$

In the literature, temperature was consistently stated in units of Kelvin (K) but the units of measurement for radiance, wavelength and the physical constants showed a lack of consistency among the authors. In addition, there was also a variation in the quoted units and magnitudes of the constants C_1 and C_2, which is a direct result of variations in the magnitude of the units associated with the other parameters (Table 2.1). This generates a serious problem in understanding which values of C_1 and C_2 are correct for calculating surface temperature using the quoted values of the radiance obtained from a given scanner. Specific inconsistencies arose for:

(1) radiance, where units were specified in Wm^{-2} (Kahle, 1980; Cresswell *et al*, 1999), Wm^{-3} (Elachi, 1987; Kealy & Hook, 1993; Schmugge *et al*, 1998), Wm^{-2} μm^{-1} (Price, 1989 & 1983; Qin & Karnieli, 1999) or were not specified (Suits, 1983; Hook, 1989; Hapke, 1993; Li *et al,* 1999)

(2) wavelength, where units were specified in m (Suits, 1983; Kealy & Hook, 1993; Schmugge *et al*, 1998; Qin & Karnieli, 1999), cm (Li *et al*, 1999) or otherwise μm

(3) C_1, where units were specified in Wμm (Hook, 1989), Wm^{-2} μm^4 (Price, 1983; Li et al, 1999) or otherwise Wm^2 and values specified as 1.19 (Price, 1983; Li *et al*, 1999) or otherwise 3.74

(4) C_2 where units were specified in μmK (Hook, 1989; Price, 1983), cmK (Li *et al*, 1999) or otherwise mK

As far as the units of the radiance are concerned, it is $L(\lambda)d\lambda$ which is the amount of radiation ($W\ m^{-2}$ in SI units) emitted by a perfect emitter (black body) at temperature T (K) within the wavelength range λ to $\lambda + d\lambda$. The units of $L(\lambda)$ are therefore $W\ m^{-3}$, provided we express $d\lambda$ in metres; if we express $d\lambda$ in μm or nm then

there will be some extra powers of 10 to be applied to these units and this is the reason for some of the differences among the various values of C_1 in Table 2.1. If the SI values for the Planck constant ($h=6.63\times10^{-34}$ Ws^2), the speed of light ($c=2.99\times10^{8}$ ms^{-1}) and the Boltzmann constant, $k=1.38WsK^{-1}$ are used in the calculation of C_1 (Equation 2.2) and C_2 (Equation 2.3) then the values are calculated as $C_1=3.74\times10^{-16}$ Wm^2 and $C_2=0.0144$ mK (to 3 significant figures) and the wavelength λ and the differential wavelength $d\lambda$ will be in metres, see the last line of Table 2.1. It is these values that have been applied for temperature calculations in this research.

AUTHOR	$L(\lambda)d\lambda$	λ	T	C_1	C_2
Kahle (1980)	$W\ m^{-2}$	μm	K	$3.74\times10^{-16}\ Wm^2$	0.0144 m K
Suits (1983)	N/A	m	K	$3.74\times10^{-16}\ Wm^2$	1.44×10^{-2} m K
Elachi (1987)	Wm^{-3}	μm	K	$3.74\times10^{-16}\ Wm^2$	0.0144 m K
Hook (1989)	N/A	μm	K	3.7413×10^{-4} W μm	1.4388×10^{4} μm K
Hapke (1993)	N/A	μm	K	$3.74151\times10^{-16}\ Wm^2$	0.0143879 m K
Kealy & Hook (1993)	Wm^{-3}	m	K	$3.74151\times10^{-16}\ Wm^2$	0.0143879 m K
Price (1983)	$Wm^{-2}\ \mu m^{-1}$	N/A	K	$1.19\times10^{8}\ Wm^{-2}\ \mu m^4$	1.439×10^{4} μm K
Price (1989)	$W\ m^{-2}\ \mu m^{-1}$	μm	K	3.74×10^{8}	1.439×10^{4}
Schmugge et al (1998)	Wm^{-3}	m	K	$3.74151\times10^{-16}\ Wm^2$	0.0143879 m K
Cresswell et al (1999)	$W\ m^{-2}$	N/A	K	3.74×10^{8}	1.439×10^{4}
Li et al (1999)	N/A	cm	K	$1.19\times10^{8}\ Wm^{-2}\ \mu m^4$	1.439 cm K
Qin & Karnieli (1999)	$W\ m^{-2}\ \mu m^{-1}$	m	K	$3.74\times10^{-16}\ Wm^2$	1.43879×10^{-2} m K
SI (m, kg, s)	Wm^{-2}	m	K	$3.74\times10^{-16}\ Wm^2$	0.0144 m K

Table 2.1: Planck's Radiation Law parametric units and values

The Planck Relationship denoted in Equation 2.1 assumed that the thermal radiation was emitted from a surface known as a blackbody that absorbs all wavelengths of energy without preference and re-radiates the stored energy with perfect efficiency. A blackbody is essentially a closed cavity with opaque walls, coated with an absorbing material, that are maintained at equal temperature. The blackbody radiation is then measured from a small opening in the cavity wall, representing a reference radiation of the known wall temperature (Suits, 1983 & Price, 1989). Since the blackbody is a theoretical material introduced solely for the development and formulation of energy relationships, a parameter must be introduced to the Planck relationship, which allows for the fact that natural materials do not exhibit blackbody behaviour. Natural materials re-radiate only a portion of energy that

is absorbed and never emit energy in excess of that of a blackbody at the same temperature (Figure 2.2).

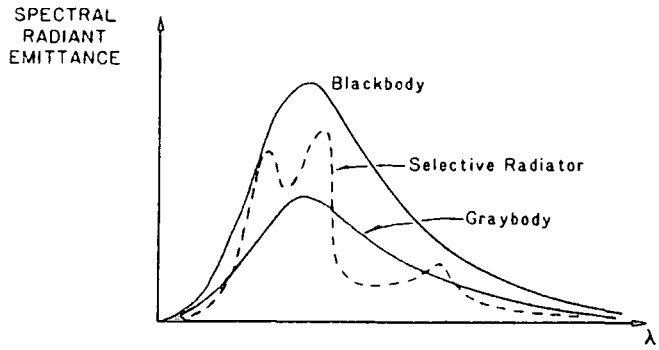

Figure 2.2: Thermal radiation emitted by a blackbody, greybody and a natural material, taken from Elachi (1987)

The efficiency of a material to re-radiate energy is known as the spectral emissivity (ε) with blackbody materials having an emissivity of one. Greybody materials have a constant emissivity value less than one throughout all wavelengths, with natural materials having a value between zero and one that is variable as a function of wavelength (Kahle, 1984; Sabins, 1986; Hapke, 1993 & French *et al*, 2000). Although emissivity varies with wavelength, it is often considered constant across the 8-14μm thermal channel of broad-band sensors like the Daedalus-1268 ATM. Therefore, an emissivity value of 0.97 will be assigned to the mid-channel wavelength of the sensor representing healthy vegetation dominating the surface cover of the study sites with the value taken from empirical measurements by the Jet Propulsion Laboratory. Land surface emissivity is defined as the ratio of the radiation emitted by a natural surface to that emitted by a blackbody at the same temperature and will have a value between zero and one for all natural materials (Equation 2.5). By introducing the emissivity factor to the Planck Radiation Law, the temperature of a natural material can be more accurately evaluated (Equation 2.6).

Equation 2.5

$$\varepsilon = \frac{L_{material}}{L_{blackbody}}$$

Equation 2.6

$$T = \frac{C_2}{\lambda \ln\left(\frac{\varepsilon C_1}{\lambda^5 L} + 1\right)}$$

It is often very difficult to determine the emissivity of a natural surface and a common assumption in many environmental studies is that the surface emissivity is effectively unity, as for a blackbody. This may be appropriate for sea surfaces that are homogeneous with a relatively constant emissivity over a large area, but there may be a greater variation in emissivity on a smaller spatial scale over most natural surfaces due to the heterogeneous nature of the land surface.

There are a variety of factors that affect the emissivity of surface materials, most notably the composition, moisture content, surface roughness and vegetation cover. The most common mineral in geological materials is quartz and an abundance of this mineral results in a decrease in the emissivity of the material (Sabins, 1986; Becker, 1987; French *et al*, 2000). Soil moisture will increase the emissivity of the soil due to an increase in the amount of water-coated particles, which have an emissivity approaching that of water (Schmugge *et al*, 1991; Lillesand & Kiefer, 2000). An increase in surface roughness tends to increase the emissivity of the material when compared with the value of a smooth surface of the same material (Anton & Ross, 1990; Schmugge *et al*, 1991). Emissivity tends to increase with an increase in view angle away from nadir (Qin & Karnieli, 1990; Jupp, 1998; Verbrugghe & Cierniewski, 1998). These factors are important when assessing bare soil surfaces, however, this is rare in the UK environment where the soil tends to be concealed under vegetation. It is therefore important to understand the effects of vegetation on surface emissivity in order to assign an appropriate emissivity for a vegetated surface.

For vegetation canopies, the view angle effects are considered negligible over homogeneous and densely vegetated areas (Anton & Ross, 1990; Carlson *et al*, 1995). In general, the emissivity of a canopy tends to increase with an increase in leaf area index. When the leaf area index is small in the early part of the growing season, there will be a greater proportion of the underlying soil visible through the vegetation canopy than when leaf area index is high late in the growing season. Soils have a lower emissivity than vegetation and so the emissivity of a canopy with a low leaf area index will be lower than that for a high leaf area index due to the greater proportion of the soil visible to the sensor (Guoquan & Zhengzhi, 1992; Sugita *et al*, 1996). Vegetation structure and geometry also affects the emissivity with an

individual leaf having a lower value than that of the whole canopy due to the multiple internal interactions that occur within the canopy structure (Fuchs & Tanner, 1966; Anton & Ross, 1990; Guoquan & Zhengzhi, 1992; French *et al*, 2000). For a homogeneous canopy, the emissivity will have a value that is representative of the proportions of soil and vegetation fractions present for an open canopy with a value representative of the vegetation at full canopy closure (Guoquan & Zhengzhi, 1992; Sugita *et al*, 1996). Heterogeneous canopies require more complex characterisation with emissivity varying as a function of vegetation type, cavity effects and leaf-stem ratio within the canopy (Colton, 1996; Iaquinta & Fouilloux, 1998). Senescent or stressed vegetation can have lower emissivities than associated with healthy green vegetation, thus reducing the canopy emissivity with leaf litter reducing the emissivity of an open canopy (Sugita *et al,* 1996).

A range of emissivity values associated with natural materials is indicated in Table 2.2. From the variability in the published emissivity values, it is suggested that the allocation of a single emissivity value across a heterogeneous terrain may be inappropriate when determining surface temperatures due to the diverse surface composition. The implication is therefore to select an emissivity value representative of each material comprising the surface taking into account the problem of pixel heterogeneity by the proportions of each material that are present. Emissivity can be determined for each surface material (Zilioli *et al,* 1992; Rubio *et al,* 1997). However, since the areas under observation in the research are covered by agricultural crop, the vegetation within each field is considered to have a homogeneous character.

Material	Emissivity	Material	Emissivity
Clear Water	0.98-0.99	Healthy Green Vegetation	0.96-0.99
Wet Sandy Soil	0.95-0.98	Dry Vegetation	0.88-0.94
Dry Sandy Soil	0.92-0.94	Short Grass	0.981
Loamy-Sand Soil	0.914	Deciduous Leaf	0.96
Stony Ground	0.959	Deciduous Tree Crown	0.98

Table 2.2: Emissivity values of common land surface materials, compiled from Rubio et al (1997), Qin & Karnieli (1999) and Lillesand & Kiefer (2000)

The use of an improper emissivity value for a specific material in the Planck Radiation Law will determine an incorrect value of surface temperature. Although the sensitivity of temperature to emissivity is relatively low (Figure 2.3), with Fuchs &

Tanner (1966) and Schmugge *et* al (1998) showing that an uncertainty in emissivity of ±0.03 can translate to an error of ±2.2K.

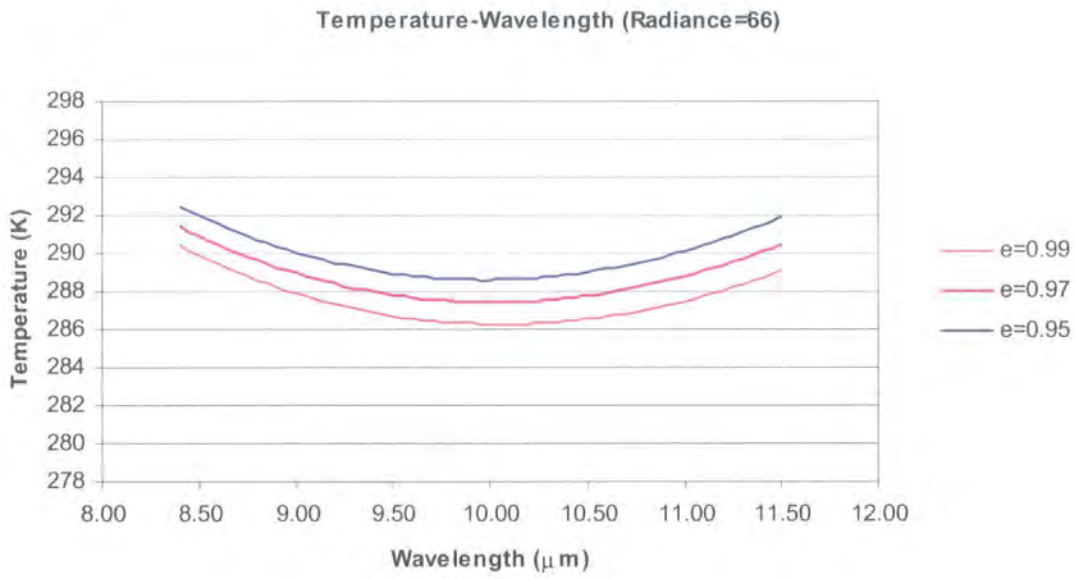

Figure 2.3: Sensitivity of temperature to variable emissivity for constant radiance

Several studies have shown the problem of accurate temperature calculation of a surface by using an incorrect emissivity value, where there was a discrepancy between the calculated value and that measured in situ for the individual materials (Kornfield & Susskind, 1977; Rubio *et al*, 1997 & Platt & Prata, 1993). Therefore, an accurate quantification of emissivity is vital for accurate determination of land surface temperature.

The problem of the unknown surface emissivity can be alleviated by performing a variety of techniques, such as those that have been developed using sensors with multiple thermal channels, such as AVHRR, TIMS and ASTER, thermal with detection across more than one thermal wavelength range. Emissivity values are known to be spectrally variable across thermal wavelengths (Price, 1984 & Schmugge *et al,* 1991), so if the radiance is measured in n spectral channels, there will be $n+1$ unknown emissivities and one temperature value (Kealy & Hook, 1993; Schmugge *et al*, 1998) and this forms the basis of the following techniques with mathematical inversion to calculate surface emissivity from the known temperature.

The *Reference Channel Method* (Kealy & Hook, 1993; Li *et al*, 1999) assumes that the emissivity in one channel has a constant value for all the pixels and the radiance measured for each pixel can then be used to derive the pixel temperature. The temperature is then used to derive the emissivity values for the remaining channels using a simple mathematical inversion. *Emissivity Normalisation* (Kealy & Hook, 1993; Li *et al*, 1999) assumes that a constant emissivity is present in all *n* channels for given pixel, enabling calculation of *n* temperatures for each pixel from the measured radiance. The maximum temperature is then assumed to be the true land surface temperature for the pixel and is used to derive emissivity values for all other channels. The *Spectral Ratio Method* (Li *et al*, 1999) and *Temperature Emissivity Separation Algorithm* (Schmugge *et al,* 1998) are based on the concept that, although the radiances are sensitive to small changes in temperature, their ratios are not and the emissivity can be calculated using the maximum brightness temperature measured through the *n* channels. The *Alpha Emissivity Method* (Kealy & Hook, 1993; Li *et al*, 1999) eliminates surface temperature from calculation by taking natural logarithms of the Planck equation and subtracting one channel from its mean for all *n* channels. The *Split-Window Technique* is the most commonly used technique for emissivity determination (Becker, 1987; Becker & Li, 1990; Franca & Cracknell, 1994; Emery & Yu, 1997; Qin & Karnieli, 1999). This technique assumes that the temperature of a particular pixel has the same value for each thermal channel with the emissivity calculated from a simple mathematical relationship using the different wavelengths and single temperature value.

The techniques discussed assume a radiance measurement in more than one thermal channel. Since the Daedalus-1268 ATM has only a single thermal channel these techniques are not suitable for determination of the land surface emissivity. Alternative approaches for emissivity quantification can be to acquire *in situ* data on the structure and composition of the ground surface, or to even determine the emissivity of every material (Sugita *et al,* 1996). However, empirical measurement is rarely possible due to the complexity of heterogeneous terrain and as a result a value that is representative of the bulk terrain composition is usually estimated for use in the Planck Radiation Law. Although we have seen through previous examples that use of an inaccurate emissivity measure will translate to uncertainties in the calculated temperature, the relatively homogeneous composition of agricultural areas will reduce

the uncertainty in emissivity designation. Since there is a relatively narrow range of emissivities associated with healthy vegetation (Becker, 1987) a single emissivity value representative of healthy vegetation will be assumed for the research.

From the above discussions, it is evident that the emissivity of the material affects the thermal response observed over the land surface. However, emissivity is not the only attribute that affects the thermal response with additional variations due to alterations in the heating and cooling energy fluxes acting on the surface.

2.2 SURFACE ENERGY FLUXES

A surface will increase or decrease in temperature as a direct response to a gain or loss of energy by the material, with the most variable transfer of energy occurring across the surface-atmosphere interface (Kahle, 1980). Surface materials are subjected to a variety of energy fluxes, namely net solar radiation (S), net thermal radiation (R), sensible heat flux (H) and latent heat flux (L) that each interact with the surface of the material, with heat of conduction (G) interacting to depth within the surface layer (Figure 2.4). The surface on which the above energy fluxes occur is represented by a vertical column of material where energy interactions extend to some depth, with negligible lateral energy transfer (Watson, 1982). The value of each flux can be calculated from empirical formulation using data from a combination of physical observation at ground level and meteorological observations (Equation 2.7). Each energy flux is described below with an indication of the relevant parameters that enable accurate determination of the flux, obtained from Kahle (1977).

Equation 2.7 $\mathbf{S + R + H + L + G = 0}$

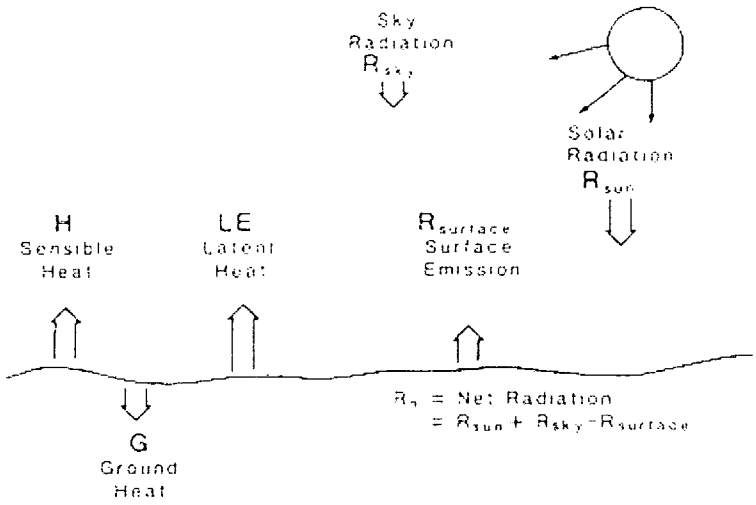

Figure 2.4: Energy flux interactions occurring at the surface, taken from Price (1985)

Solar radiation is the dominant energy flux causing thermal changes at the Earth's surface, with diurnal penetration to a depth of 1m (Kahle, 1980 & Price, 1989). For a cloud-free sky, the solar radiation absorbed by the ground (S) is calculated with knowledge of key topographic and atmospheric factors (Equation 2.8).

Equation 2.8 $$S = (1-\alpha_g)[1 - A(u^*, z)]0.349 S_S \cos z + (1-\alpha_g)\left[\frac{1-\alpha_o}{1-\alpha_o\alpha_g}\right]0.651 S_S \cos z$$

For accurate calculation of the net solar radiation absorbed by a horizontal surface, it is necessary to know the amount of solar radiation incident on top of the atmosphere (S_S) and the fractions of radiation of wavelength greater than 0.9μm that is absorbed (0.349) and of wavelength less than 0.9μm that is scattered (0.651). Atmospheric condition during observation must also be modelled where absorption by atmospheric constituents, mainly water vapour, greatly reduces the amount of solar radiation incident on the Earth. For a cloud-free atmosphere, the effective water content (u*) is the total precipitable water in the atmosphere estimated from meteorological data.

The amount of solar radiation absorbed by the surface will be dependant on the surface reflectivity, or the ground albedo (α_g). Atmospheric albedo (α_o) is also

required, which is dependent on the surface pressure and the relative position of the Sun with respect to the ground surface, known as the zenith angle (z). The solar zenith angle varies with respect to solar declination (δ), latitude (λ), time from noon (t) and the rotation period of the earth (ω) (Equation 2.9).

Equation 2.9 $$\cos z = \sin\lambda \sin\delta + \cos\lambda \cos\delta \cos\omega t$$

Topographic variations also influence the amount of solar radiation incident on the ground where slopes facing the Sun receive more solar radiation than those facing away from the Sun, with slope angle and elevation also controlling shadow effects. The amount of solar radiation received by the ground is modified by the slope and orientation of the surface and requires the calculation of the angle between the normal to the slope and the sun (z') from a given slope angle (s) and azimuth (α) (Equation 2.10).

Equation 2.10 $$\cos z' = \cos s \cos z + \sin s \sin z \cos\alpha$$

The total radiation absorbed by the slanted surface (Sτ) (Equation 2.11) is then calculated with respect to the amount of radiation diffusely scattered by the atmosphere (S_{diff}) due to the surface zenith angle (Equation 2.12).

Equation 2.11 $$S\tau = S_{diff} + (S - S_{diff})\left[\frac{\cos z'}{\cos z}\right]$$

Equation 2.12 $$S_{diff} = 0.05S + 0.10(1 - \cos z)S$$

The net thermal radiative flux (R) is equivalent to the amount of thermal radiation that is detected by a thermal sensor and is calculated as the resultant of thermal energy fluxes between long-wave radiation emitted by the ground towards the atmosphere and the long-wave radiation emitted the by the atmosphere towards the ground (Kahle, 1980 & Price, 1985). The long-wave radiation emitted from the ground towards the atmosphere ($R_{surface}$) is calculated with respect to the Stefan-Boltzmann constant (σ), emissivity (ε) and the ground temperature (T_g) and removes much of the heat from the surface, particularly in the afternoon when the ground is warm (Equation 2.13).

Equation 2.13 $$R_{surface} = \varepsilon\sigma T_g^4$$

Radiation emitted downwards by the atmosphere is dominated by emission from various atmospheric constituents, particularly water vapour, carbon dioxide and ozone (Kahle, 1980). Downwelling radiation can be estimated by the product of the Stefan-Boltzmann constant (σ) and the effective sky temperature (T_{sky}), which is measured in Kelvin, with respect to time from local 1400 hours (t) (Equation 2.14).

Equation 2.14 $$R_{sky} = \sigma T_{sky} = \sigma\left[263 + (10\cos t)\right]$$

The net thermal radiative flux during the day is therefore the sum of the above two equations. Nocturnal atmospheric conditions differ from those occurring during the day and the nocturnal atmospheric flux is expressed as a product of the Stefan-Boltzmann constant (σ), surface temperature (T_g) and the atmospheric water vapour pressure (e) (Equation 2.15). The net thermal radiative flux during the night is the sum of the product of Equation 2.13and Equation 2.15.

Equation 2.15 $$R_{noctural\_sky} = \sigma T_g^4\left(0.61 + 0.05\sqrt{e}\right)$$

The sensible heat flux (H) is often the largest parameter in the energy balance equation, relating to the amount of energy transferred between the surface and the atmosphere through molecular conduction or convection towards the colder medium (Kahle, 1977 & Kahle *et al*, 1984). A negative flux is generated as heat is transferred from the ground to the cold atmosphere during the day, with a positive flux at night. In dry windy conditions, sensible heat can be calculated using a complex combination of specific meteorological parameters (Equation 2.16).

Equation 2.16 $$H = \rho_a c_p C_D W\left(T_a - T_g\right)$$

Meteorological data is required for air density (ρ), specific heat of dry air (c_p), drag coefficient (C_D), wind speed corrected for gustiness (W) and air temperature (Ta). These can be estimated using either an aerodynamic method measuring the atmospheric characteristics at one height, or by a profile method measuring wind speed, air temperature and humidity gradients as a function of height with a

radiosonde (Kahle *et al*, 1984). The drag coefficient (C_D) is an empirical variable that takes into account the elevation (Z) of the feature (Equation 2.17).

Equation 2.17 $$C_D = 0.002 + 0.006\left(\frac{Z}{5000}\right)$$

Sensible heat is the heat removed from or added to the surface through either convective or conductive processes. Convective processes are present due to wind speed, atmospheric temperature and humidity contrast between the ground and atmosphere. Conductive processes are mainly due to the availability of solar radiation varying with solar declination, latitude and slope, together with wavelength-dependent properties of atmospheric transmission and surface reflectivity (Price, 1977). Under dry conditions, the sensible heat flux is the main mechanism for removing heat from the surface.

The latent heat flux (L) is similar to the sensible flux with heat transferred between the surface and the atmosphere. Latent heat is related to the amount of heat removed from the surface under moist conditions through surface evaporation, as well as the release of heat within the atmosphere during cloud formation (Equation 2.18).

Equation 2.18 $$L = \rho_a C_D W l (q_g - q_a)$$

The latent heat flux (L) is heavily dependant on the same parameters as the sensible heat flux, including the latent heat of evaporation (l) and the mixing ratios of air at (q_a) and near (q_g) the ground, determined from the saturation ratio of mixing at the temperature ($q_a(T_a)$) and moisture factor (M_a), both as a function of height. The latent heat flux is therefore heavily dependant on moisture content and its distribution, varying with material composition and porosity. Under wet conditions, the latent heat flux is the main mechanism for removing heat from the surface.

The heat of conduction to the ground (G) is also a very important surface flux. This is strongly related to the material thermal property of thermal conductivity (K) as a function of surface temperature (T) and the depth (z) (Equation 2.19). When the surface is heated during the day, heat is conducted vertically down to the cooler material at depth. If the study site is located in a geothermal area, a small constant

heat source may be added to the heat flow on the deeper layer, as was included by Kahle (1980) to account for the possibility of heat transfer from a depth within the Earth towards the surface.

Equation 2.19

$$G = K\left(\frac{\delta T}{\delta z}\right)$$

As shown above, the heat fluxes acting on the surface clearly incorporate a complex set of meteorological, geographical, topographical and physical parameters. According to Newton's law of conservation, there must be a balance between all of the energy fluxes acting on the surface, with an increase in one heat flux being balanced by a reduction in another in order to retain the state of equilibrium. An understanding of how heat is transported within a material and its surroundings can then be inferred from the relationship between the fluxes acting on the surface (Sabins, 1986), thus enabling the retrieval of land surface temperature with respect to these particular parameters.

The thermal response of a homogeneous surface therefore results from the balance of these energy fluxes with the solution of the surface energy balance equation combining theoretical expressions or measured values for net radiative flux, sensible heat, latent heat and the conduction to the ground. However, the ability to 'solve' the equations will be dependent on the availability of data for insertion into the formulae. Differences in the observed thermal response are therefore dependent upon the surface energy fluxes; when relating the energy fluxes to actual temperature values there will also be a complex relationship between the thermal response and the thermal properties of the surface materials. Thermal properties of surface materials control how the incident solar radiation is distributed through time and depth (Kahle, 1980). The main thermal properties are discussed in the following section.

2.3 THERMAL PROPERTIES

Thermal properties of surface materials determine how the heat from the Sun is distributed through time and depth, and vary as a result of differences in mineralogy, moisture content, particle size, as well as the physical temperature of the material (Price, 1977). The most notable thermal properties include thermal conductivity, thermal diffusivity, specific heat capacity, heat capacity, and thermal inertia. The definitions of the individual thermal properties are that thermal conductivity is a measure of the rate at which heat passes through a material, thermal diffusivity is the temperature change of a volume of material through time and thermal heat capacity determines how well a material stores heat (Curran, 1985; Kahle, 1980; Kahle, 1984; Cracknell & Xue, 1996). Thermal inertia is defined as the resistance of a material to a change in temperature (Price, 1989). Therefore materials with a high thermal inertia will display a small diurnal temperature range (Figure 2.5).

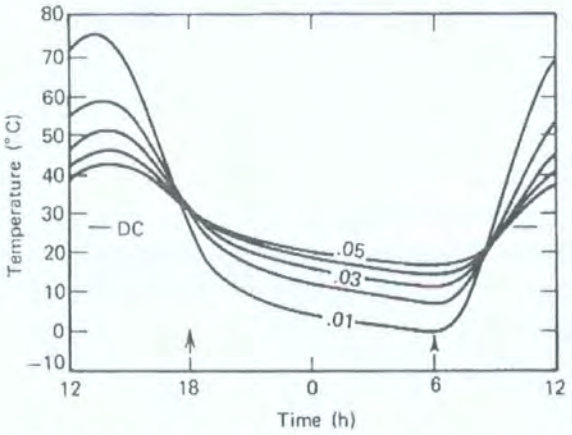

Figure 2.5: Diurnal temperature response with respect to thermal inertia, taken from Kahle (1980)

Physical thermal inertia values (P) can be calculated as the root product of heat capacity (C), thermal conductivity (K) and the material density (ρ), as denoted in Equation 2.20.

Equation 2.20 $$P = \sqrt{CK\rho}$$

The most common geological materials found on the ground surface will vary in their density and thermal properties and as a result, the thermal inertia of the materials will vary with respect to the physical properties of the materials under

investigation. The values associated with thermal properties of a suite of geological materials are indicated in Table 2.3. However is it important that the correct values are used for the appropriate units since there are variations in the values due to conversion from calories to either Joules or Watts (Table 2.4).

	K $calcm^{-1}s^{-1}K^{-1}$	ρ gcm^{-3}	c $cal\ g^{-1}K^{-1}$	k cm^2s^{-1}	P $calcm^{-2}K^{-1}s^{-1/2}$
Clay soil (moist)	0.0030	1.7	0.35	0.005	0.042
Gravel	0.0030	2.0	0.18	0.008	0.033
Limestone	0.0048	2.5	0.17	0.011	0.045
Marble	0.0055	2.7	0.21	0.010	0.036
Sandy gravel	0.0060	2.1	0.20	0.014	0.050
Sandy soil	0.0014	1.8	0.24	0.003	0.024
Shale	0.0030-0.0042	2.3	0.17	0.008	0.034

Table 2.3: Thermal properties of common geological materials, compiled from Kahle (1980) and Elachi (1987)

	K $Wm^{-1}K^{-1}$	ρ $1000kgm^{-3}$	c $1000Jkg^{-1}K^{-1}$	k $10^{-6}m^2s^{-1}$	P $1000Js^{-1/2}\ m^{-2}K^{-1}$
Clay soil (moist)	1.3	1.7	1.5	0.5	1.8
Gravel	1.3	2.0	0.8	0.8	1.4
Limestone	0.9	2.5	0.7	0.5	1.3
Marble	2.5	2.7	0.9	1.0	2.5
Sandy gravel	2.5	2.1	0.8	1.5	2.0
Sandy soil	0.6	1.8	1.0	0.3	1.0
Shale	1.9	2.3	0.7	1.2	1.7

Table 2.4: Thermal properties of common geological materials (Hapke, 1993)

Thermal inertia may be used to distinguish between materials exhibiting similar reflective properties but due to differences in density have different thermal properties (Kahle *et al*, 1976; Price, 1977). Thermal inertia is sensitive to volumetric variations, and as a result, may be particularly useful when attempting to locate features buried at shallow depth through a variation in their thermal properties. However, Pratt & Ellyett (1979) stated that thermal inertia determination is effectively restricted to the upper 0.10m of the surface layer and that changes in thermal inertia below 0.10m depth cannot be effectively detected at the surface. For the vast majority of the research, the upper layer of the ground surface consists of a soil layer with

variable composition, porosity, moisture content and organic content. It is therefore important to understand how each of these parameters affects the physical thermal inertia of the soil.

Pratt & Ellyett (1979) conducted an experiment to examine the thermal inertia values determined for a continuous variation in the sand-clay content, porosity and moisture content for a soil sample. Results of their model showed that as the sand and porosity of the soil increased, the thermal inertia of the soil decreased (Figure 2.6). When moisture infiltrates the pore spaces, the thermal characteristics of the soil begin to alter due to the amount of fluid present therefore the degree of saturation will affect the thermal characteristics of the soil. Results of the thermal simulation performed by Pratt & Ellyett (1979) showed that the thermal inertia of the soil increased with an increase in moisture content. The simulation also showed that the thermal inertia of the soil decreased as the porosity of the soil increased (Figure 2.7).

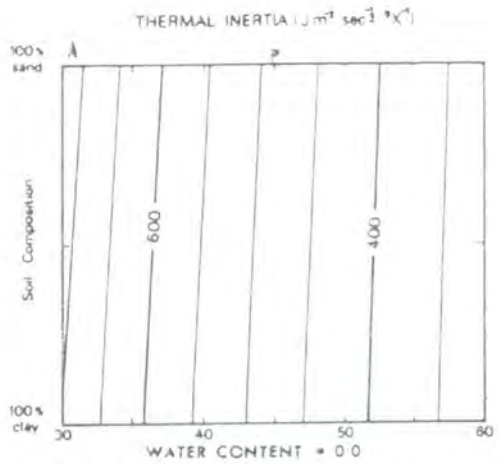

Figure 2.6: Thermal inertia of a dry soil with variable sand content and porosity, taken from Pratt & Ellyett (1979)

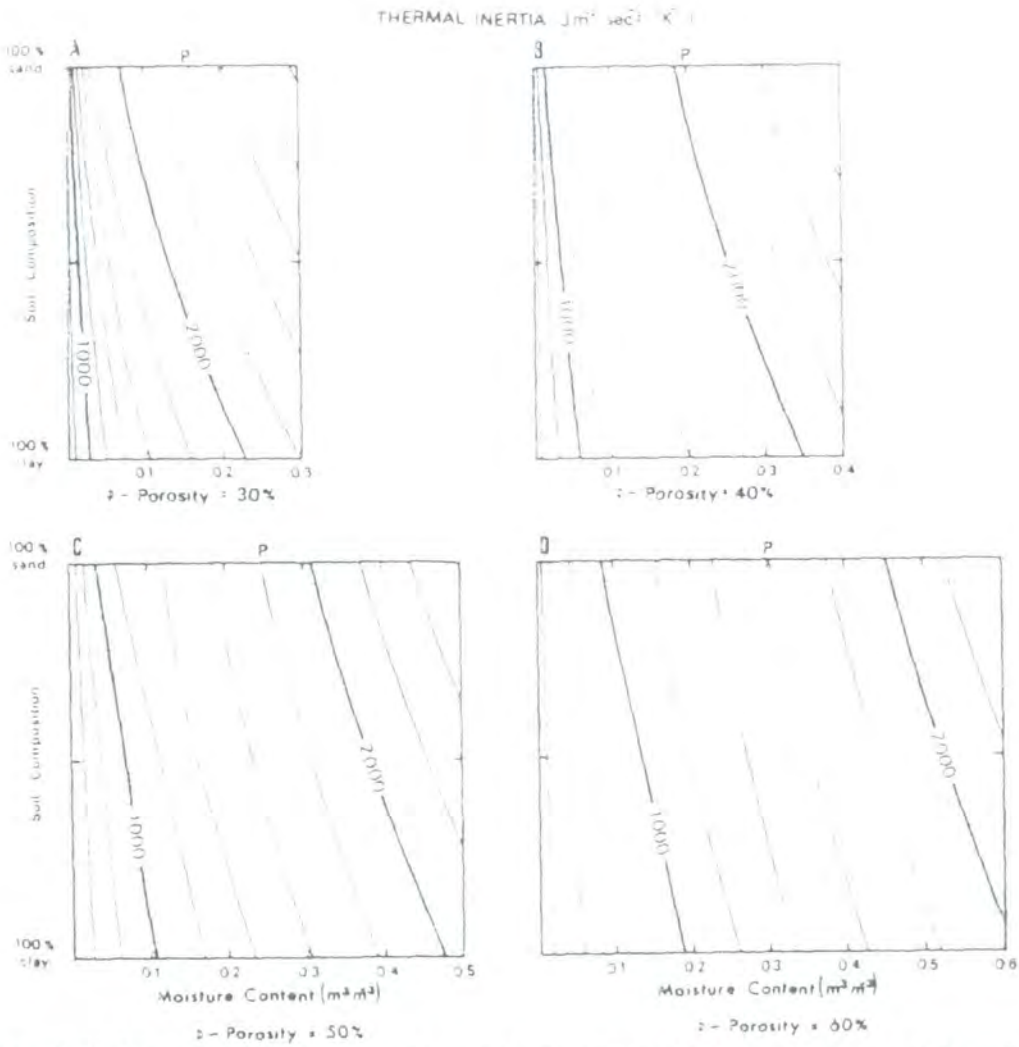

Figure 2.7: Thermal inertia of soils with variable sand and moisture content for porosities ranging from 30%-60%, taken from Pratt & Ellyett (1979)

Since thermal inertia is defined as the resistance of the material to temperature change, the implications of the Pratt & Ellyett (1979) simulation is such that soils that have a high sand fraction, high porosity or low moisture content will have a lower physical thermal inertia than soils of higher clay content, lower porosity or higher moisture content and as a result will display a wider temperature range. This simulation was based on the assumption that the soil was free of vegetation and that the topsoil was uniform in thermal properties to a depth of 0.20m. In nature, it is unlikely that the topsoil will be homogeneous in thermal characteristics to depth and so it is important to understand how the thermal inertia will affect the temperature of the soil through depth and time. The effect of thermal inertia on the temperature evolution through depth and time will therefore be discussed with respect to a heterogeneous material that is devoid of vegetation.

Kahle (1980) assessed the thermal regime of a soil as a function of depth and time for different values of thermal inertia. Results of the depth analysis showed that for a constant thermal inertia, the temperature showed little variation at the surface with a greater degree of temperature separation at depth. The time analysis was assessed at 06:00 and 14:00 in the diurnal cycle corresponding to the times of surface temperature minimum and maximum respectively. Results of the time analysis showed that similar temperatures were observed at the surface independent of the thermal inertia of the soil. However, soils of higher thermal inertia showed lower temperature amplitudes at depth than was observed for the lower thermal inertia soils (Figure 2.8)

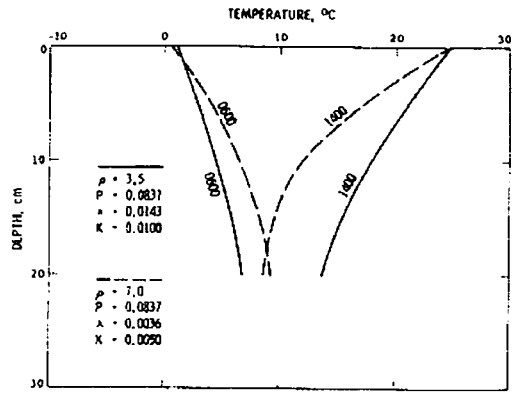

Figure 2.8: Evolution of temperature through time and depth for low thermal inertia (solid line) and high thermal inertia (dashed line), taken from Kahle (1980)

The above temperature evolution through time and depth was calculated using thermal inertia values derived from specific thermal conductivity and density values. However, these parameters will individually affect the thermal regime of the soil and so the temperature of a soil layer was assessed using a variety of thermal inertia values determined from variation in thermal conductivity and density. A variation in thermal inertia was initially assessed with respect to changing conductivity. As the thermal inertia increased, the diurnal temperature amplitude decreased with more heat penetrating to deeper levels in the soil layer (Figure 2.9). The thermal inertia of the soil was also assessed for variable density resulting in a decrease in amplitude as the thermal inertia increased with more heat retained at the surface (Figure 2.10).

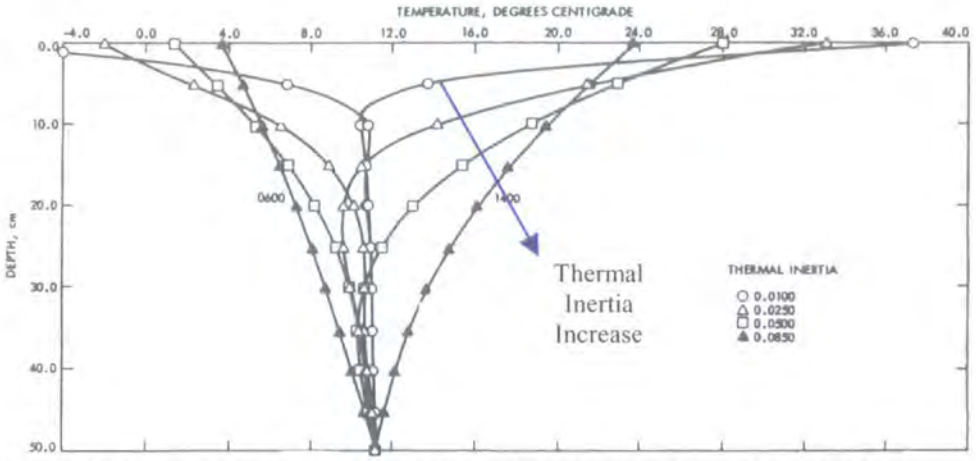

Figure 2.9: Thermal inertia as a function of depth and time for variable conductivity, taken from Kahle (1980)

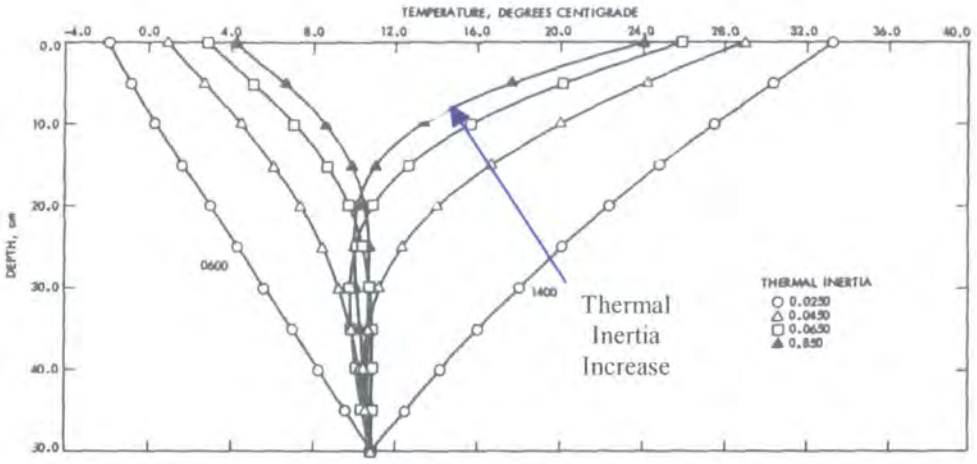

Figure 2.10: Thermal inertia as a function of depth and time for variable density, taken from Kahle (1980)

The above simulations performed by Pratt & Ellyett (1979) and Kahle (1980) were conducted on soils that were devoid of vegetation cover, however, in the UK environment this is rarely the case. Therefore, it is important to understand how the vegetation affects the thermal behaviour of the underlying soil and this has not received much attention in the literature. This research aims to extend knowledge of the effect of vegetation on the thermal behaviour of soil.

Although thermal inertia cannot be directly determined from remotely sensed thermal data, the response of the surface to temperature change can be determined by observing the surface at the times of maximum surface temperature, typically early afternoon, and minimum surface temperature, just before dawn, across the diurnal heating and cooling cycle. The variation between these values gives the diurnal

temperature range expressed at the surface, indicating the resistance of the surface to heating. Although this technique does not give a measure of the physical thermal inertia of the surface, an *Apparent Thermal Inertia (ATI)* of the surface can be determined. ATI modelling can assist investigations of the shallow subsurface where there is insufficient detail on auxiliary atmospheric and topographic parameters for calculation of surface energy fluxes.

The ATI approach can be based on either qualitative or quantitative analyses, the latter aimed at relating the measure thermal response to thermal properties of the surface materials. The following section discusses the models that have been developed for thermal inertia mapping of the land surface.

2.4 THERMAL MODELLING

In order to understand and quantify land surface temperature variations fully, it is necessary to develop an empirical relationship between the response of a surface to solar heating as a function of the thermal properties of the material. The thermal properties of the materials will determine how the heat is distributed as a function of time and depth with both horizontal and vertical spatial variations across a surface. Variations in the temperature response expressed at the surface enables discrimination of materials that display different bulk thermal characteristics. The main thermal properties that control heat distribution include the density, thermal conductivity, specific heat capacity, heat capacity, thermal diffusivity and thermal inertia, which are known to vary with composition, porosity and moisture content.

Several models have been developed to examine the relationship between thermal radiation and the physical properties of materials. However, for remote observation the property that is most amenable to remote thermal investigations is that of *Apparent Thermal Inertia (ATI)*, which can be inferred from the diurnal temperature variations observed at the surface. Variations in ATI will then give an indication of variations in bulk material properties. ATI techniques have been successfully applied to geological exploration and mapping (Kahle *et al,* 1976; Kahle, 1977; Gillespie & Kahle, 1977; Watson, 1982; Kahle & Alley, 1985, Price, 1985) and soil moisture studies (Price, 1977, Pratt & Ellyett, 1979) in areas that are devoid of

vegetation. It is through ATI modelling that the research aims to address the effect of vegetation on the detection of variation in subsurface thermal properties.

2.4.1 Apparent Thermal Inertia Modelling

The design of ATI models is essentially driven by the parametric relationship under investigation and the type of auxiliary data available for incorporation in the model. There is a range of modelling techniques that shall be discussed in detail, from a simplistic image-based approach using images of the maximum and minimum diurnal response of the surface, through to quantitative techniques involving more complex mathematical relationships with knowledge of surface parameters.

The simplest approach to thermal analysis was documented as a part of the Heat Capacity Mapping Mission where a relation was defined between the apparent thermal inertia (ATI) of the surface with respect to the diurnal temperature change (ΔT) and albedo (A) of the surface (Equation 2.21). Although this model essentially relates to the HCMM, it shall be referred to as the Cracknell & Xue (1996) model from this point forward since the model was presented in numerical form in Cracknell & Xue (1996).

Equation 2.21

$$ATI = \frac{(1-A)}{\Delta T}$$

The diurnal temperature range of the surface can be determined by the difference in thermal response between a pair of day and night thermal images acquired when the surface was at its maximum temperature and at its minimum temperature respectively across a 12-hour cycle, or 36-hour cycle if clear-sky conditions prevail (Kahle & Alley, 1985). In addition to the diurnal temperature change, this technique requires knowledge of the surface albedo.

Albedo is a dimensionless measure of the reflectivity of the surface, or the fraction of incident solar radiation that is reflected by the surface (Barrett & Curtis, 1982). From this definition, albedo appears to be the reciprocal of emissivity suggesting that albedo can therefore be determined from a simple relation (Equation 2.22), as defined in Price (1989).

Equation 2.22 $A + \varepsilon = 1$

Albedo is affected by properties similar to those that affect emissivity, such as surface composition, roughness and moisture content as well as vegetation structure, view angle and the solar zenith angle. In general materials with a low albedo will have high surface temperatures. The reflectivity of materials tends to decrease with a darkening of the colour of materials with reflectance of organic-rich soils lower than sands (Snyder *et al*, 1997). Soils will also differentially absorb radiation at discrete spectral wavelengths depending on the mineralogy. The albedo will therefore be wavelength-dependent and will vary with the material under observation (Goetz, 1989). An increase in surface roughness results in a greater portion of radiation that can be scattered back towards the remote sensor, with a resulting increase in albedo. Moisture has a tendency to decrease the albedo with greater absorption of radiation. The albedo varies with view zenith and azimuth angles due to variations in the amount of solar radiation available to interact with the ground (Barnsley *et al*, 1997; Cresswell *et al,* 1999) although Snyder *et al* (1997) determined that the effects were relatively small for all materials except sands. Surface roughness can affect the apparent reflectivity of the material at the remote sensor with slopes facing the sun showing greater reflectivity than those facing away from the sun with a variation in the albedo between nadir and off-nadir depending on the view and solar zenith angles (Verbrugghe & Cierniewski, 1998). The effects of topographic slope and aspect can however be removed by creating ratios of images in two different spectral bands (Goetz, 1989).

Vegetation has a pronounced effect on the surface albedo due to the spectral properties of the canopy elements and particularly the leaf and canopy geometries (Grover *et al,* 2000). In general forest canopies will have a lower albedo than grasslands or erectophile vegetation with a more pronounced seasonality due to an increase in leaf area index of the forest canopy and reduction of the proportion of soil visible through the canopy (Sharratt, 1998). Surface albedo will show a diurnal variation as the solar position moves with respect to the surface. Ideally, albedo shows a symmetrical pattern with peak values at dawn and dusk with low values around solar noon. If the canopy is vertical and stable, there will be a symmetrical pattern in surface albedo. However, there will be a strong asymmetry over vegetation canopies

in windy conditions due to the vegetation leaning in response to the prevailing wind, thus altering the canopy reclination angle and direction with respect to the solar position (Song, 1998).

As discussed in the calculation of emissivity, homogeneous surfaces may be assigned an albedo value that is representative of the surface material. However, where the imaged surface exhibits a heterogeneous composition, the designation of a single albedo over a large spatial area will be inappropriate and so albedo must be determined for each of the pixels in the image. A variety of methods for determining surface albedo are discussed in the literature. These range from the acquisition of field spectral data coincident to image acquisition (Gillespie & Kahle, 1977), the weighting of synchronised visible and near-infrared image data according to the solar illumination curve (Kahle *et al*, 1976; Xue & Cracknell, 1995, Grover *et al*, 2000), the use of the spectral response function of the instrumentation (Gillespie & Kahle, 1977), the use of the reflectance measured in one of the visible or near-infrared spectral channels (Price, 1985), or the combination of reflectance data with topographic information (Watson, 1982). Other authors fail to state their method of albedo determination (Pratt & Ellyett, 1979) or are ambiguous in their descriptions, such as "converting from reflectance" (Price, 1977) or "measurement of the broadband visible and near-infrared radiance" (Kahle & Alley, 1985).

The problem of selecting an appropriate albedo values for the image in the research was therefore alleviated by selecting a single albedo value representative of the grasslands and erectophile crops present in the imagery, on the assumption that non-vegetated materials would be excluded from further analysis. Table 2.5 indicates published albedo values that have been determined for a range of different surface materials over visible spectral wavelengths.

Material	Albedo
Fine Sandy Soil	0.37
Dry Black Soil	0.14
Moist Black Soil	0.08
Wheat	0.16-0.23
Deciduous Forest	0.17
Pine Forest	0.14

Table 2.5: Albedo values of natural surfaces, extracted from Barrett & Curtis (1982)

Once the diurnal temperature range and albedo have been determined for the surface, the ATI can be calculated using a selection of ATI models. The simple relationship denoted in Equation 2.21 forms the basis of most other ATI models, where variations arise in the scaling factor applied to the equation. Price (1977) incorporated parameters on the solar constant (S), atmospheric transmittance (V), angular speed of rotation of the Earth (ω) and the ratio of heat flux transferred to the atmosphere to that towards the ground (α) for the calculation of ATI (Equation 2.23).

Equation 2.23

$$ATI = \frac{2SV}{\sqrt{\omega}\sqrt{\left(1+\alpha^2+\alpha\sqrt{2}\right)}} \bullet \frac{(1-A)}{\Delta T}$$

Kahle & Alley (1985) made a slight modification to the above scaling factor by taking into account a parameter (C) that related to the declination (δ) and latitude (λ) of observation (Equation 2.24).

Equation 2.24

$$ATI = \frac{2SVC}{\sqrt{\omega}\sqrt{\left(1+\alpha^2+\alpha\sqrt{2}\right)}} \bullet \frac{(1-A)}{\Delta T}$$

$$C = \frac{1}{\pi}\left[\sin\delta \sin\lambda \arccos(1-\tan\delta \tan\lambda) + \cos\delta \cos\lambda \sqrt{\left(1-\tan^2\delta \tan^2\lambda\right)}\right]$$

The ATI model developed by Price (1985) gives an advantage of use in situations where the ratio of the heat flux towards and away from the ground is unknown (α). This model also uses the parameter C to take into account the declination and latitude of observation, although there was slight variation in definition from the value used by Kahle & Alley (1985). In this approach, the scaling factor greatly simplifies calculations and essentially brings the values within the standard 0-255 data range associated with 8-bit quantisation of standard satellite imagery (Equation 2.25).

Equation 2.25

$$ATI = 1000\pi \bullet \frac{(1-A)C}{\Delta T}$$

$$C = \frac{1}{\pi}\left[\sin\delta \sin\lambda \sqrt{\left(1-\tan^2\delta \tan^2\lambda\right)} + \cos\delta \cos\lambda \arccos(-\tan\delta \tan\lambda)\right]$$

The ATI models discussed above provide a method of assessing variations in subsurface properties based on the acquisition of day and night thermal image pairs when the surface is at its maximum and at its minimum temperatures respectively. The contrast in thermal response gives an indication of the diurnal temperature change, or the resistance of the surface to heating, and this is incorporated with a measure of the surface albedo in order to calculate the apparent thermal inertia of the surface. The simplest model given in Cracknell & Xue (1996) required no further parameterisation, however, the models by Price (1977) and Kahle & Alley (1985) required some auxiliary detail on the heat flux interaction at the ground surface as well as solar and atmospheric properties, providing a scaling factor to the calculation. The Kahle & Alley (1985) model introduced a parameter to take into account solar variations due to the latitude and the relative position on the surface with respect to the sun at the time of observation. This factor was also incorporated into the Price (1985) model with simplification of the scaling factor to bring the values into the data range associated with standard 8-bit quantisation satellite data and reduces the need for detail on the physical parameters of the surface.

2.4.2 Energy Flux Modelling

A more quantitative approach to thermal modelling can been performed through application of numerical energy flux models that incorporate detailed parameterisation of the surface under investigation. The majority of numerical models are based on the same basic principle, solving the one-dimensional thermal diffusivity heat flow model for periodic heating and cooling of a layer of homogenous material consisting of uniform vertical and lateral thermal characteristics (Watson, 1975; Kahle, 1977; Pratt & Ellyett, 1979; Price, 1980; Watson, 1982; Xue & Cracknell, 1996). The layer represents a vertical section through the surface with an upper boundary condition defined by the surface energy balance equation (Equation 2.7) and a lower boundary characterised by a constant temperature at depth. Solution of the equation occurs by calculating temperature (T) through time (t) and depth (z) for a range of thermal properties such as the thermal diffusivity (k) for the material under investigation (Equation 2.26). Solution of this equation gives the gradient of heating extending to the depth of diurnal heat penetration, with a decrease in temperature through depth.

Equation 2.26

$$\frac{\partial T}{\partial t} = k \frac{\partial^2 T}{\partial z^2}$$

Variations in the numerical model arise from the method of solving the heat flow equation for temperature as a function of time and for a range of thermal properties. In addition, the models vary in the initial assumptions made about the properties of the surface layer. A brief description of each application of the main quantitative thermal models is given below.

Watson (1975) used a finite difference solution to the 1D periodic heating model to determine ground surface temperature variation with respect to atmospheric heating fluxes occurring on the upper boundary of the surface layer. The model used the expression for the upper boundary condition as the balance between geothermal, solar and atmospheric sources of radiation. Initial assumptions for the investigation were that a there was a uniform geothermal flux occurring at depth and that under clear-sky conditions the meteorological parameters were spatially invariant. The model also ignored the effects of sensible and latent heat transfer across the sparsely vegetated surface under investigation. The flux absorbed by the surface was then calculated as a function of albedo, topography, geographical location and surface emissivity with complex formulations for these factors used in the model to predict the thermal response for variations in thermal inertia, albedo, geothermal flux and surface emissivity (Figure 2.11). Results of the model showed that a decrease in the geothermal heat flux and an increase in albedo and emissivity resulted in a progressive decrease in the temperatures calculated at any stage in the diurnal cycle. Variations in thermal inertia, representing materials of different thermal properties, showed the greatest influence on the contrast between day and night diurnal temperatures with a constant mean temperature observed at all values. This suggests that materials of different thermal properties can be discriminated by using the contrast between the day and night temperature values measured over the diurnal cycle.

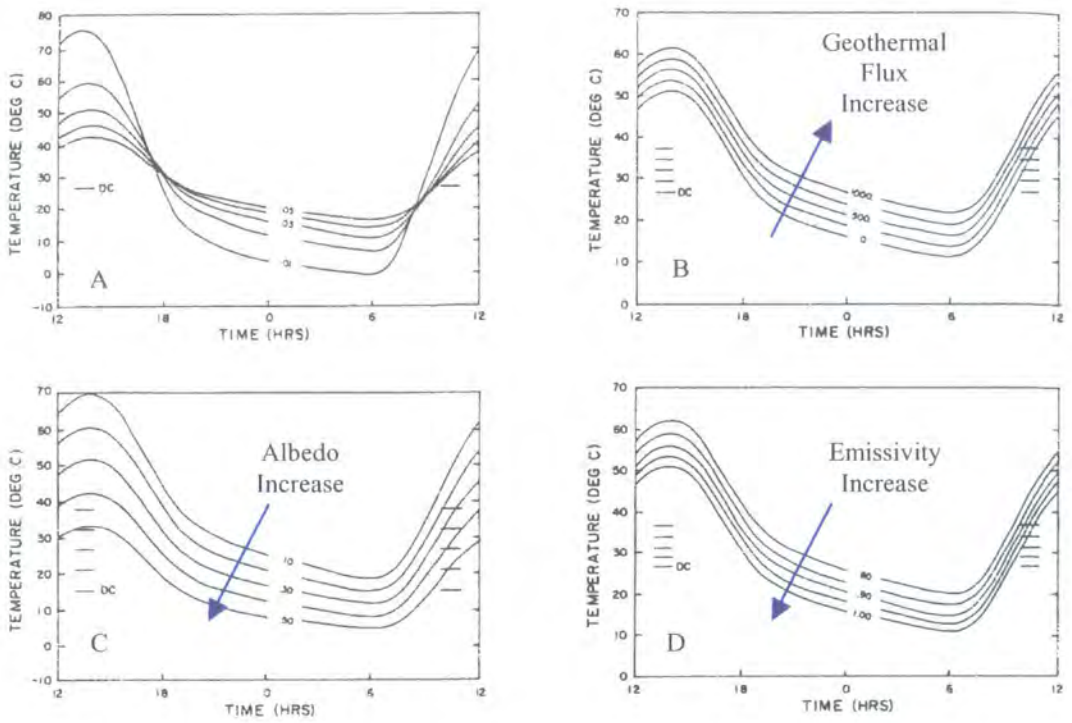

Figure 2.11: Sensitivity of diurnal temperature to variations in (A) thermal inertia, (B) geothermal heat flux, (C) albedo and (D) surface emissivity. DC indicates mean diurnal temperature, taken from Kahle (1980)

Kahle (1977) also used a finite difference solution to the heat flow equation (Equation 2.26) by subdividing the surface layer into finite depth sections and calculating the temperature response of each layer through time. In this model, meteorological conditions were assumed to be uniform with latent heating disregarded due to application in an arid environment. The effects of surface emissivity and atmospheric emission and absorption were also ignored. The model essentially gave a look-up table of diurnal temperature variations calculated as a function of albedo, slope, slope azimuth and thermal inertia, for specific latitude, elevation, time and meteorological conditions in the barren environment (Figure 2.12). The values were then inverted to indicate the thermal inertia of the surface from a measured diurnal temperature range. The results of the analysis showed that there was no variation in the minimum temperature for variations in albedo, slope angle and slope azimuth with a decrease in the maximum temperature on decreasing albedo and increase in slope angle. The thermal inertia results were similar to those in Watson (1975) with values calculated from a range of density, thermal conductivity and diffusivity values.

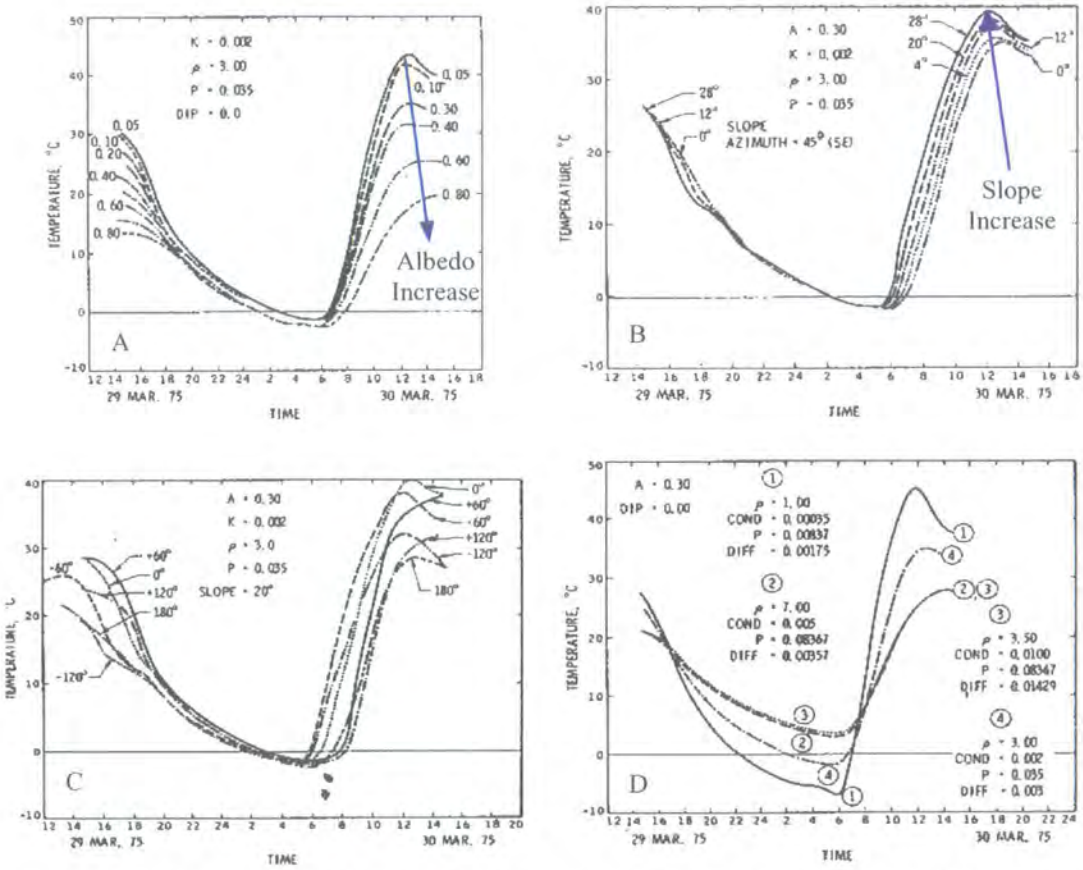

Figure 2.12: Sensitivity of diurnal temperature to variations in (A) albedo, (B) slope, (C) slope azimuth and (D) thermal inertia, taken from Kahle (1977)

Pratt & Ellyett (1979) generated a similar calibration of thermal inertia values with respect to specific values of diurnal temperature and surface albedo. ATI values were then generated by running the one-dimensional heating model specified in Equation 2.26 for a given set of meteorological conditions (Figure 2.13).

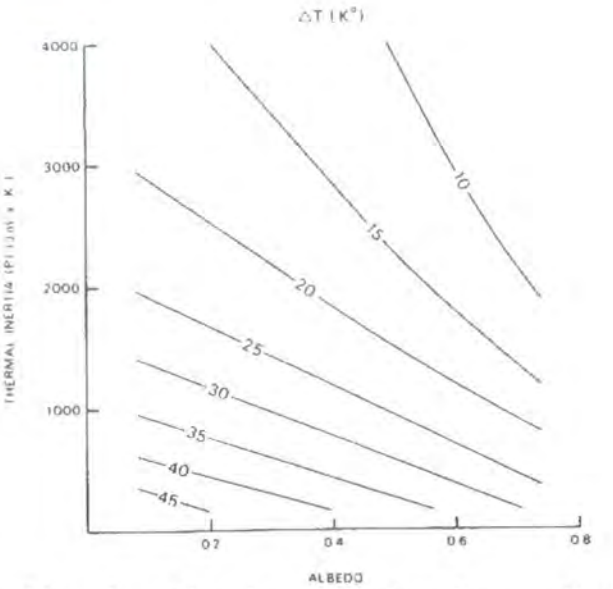

Figure 2.13: Thermal inertia calibration chart from known diurnal temperature and albedo for specific meteorological conditions, taken from Pratt & Ellyett (1979)

The model was then used to predict the influence of particular soil properties on the conductivity of soils, which can be directly related to the thermal inertia and moisture content of the soil. The primary variables for inclusion in the model were the sand-clay fraction, moisture content and porosity of the soil with secondary variables of heat capacity, thermal conductivity, thermal diffusivity and thermal inertia. The initial assumption was that the measurements were representative of a vegetation-free surface with uniform thermal properties to depth. Continuous variations in these parameters were then run through the model and the results showed that the thermal conductivity and diffusivity were dependent on soil type and the water content, whereas the thermal inertia showed a strong dependence on soil moisture with only a small dependence on soil type (Figure 2.14). In the previous discussion on thermal inertia (Chapter 2.3), the Pratt & Ellyett (1979) model also showed that the thermal inertia decreased as the porosity of the soil increased (Figure 2.7).

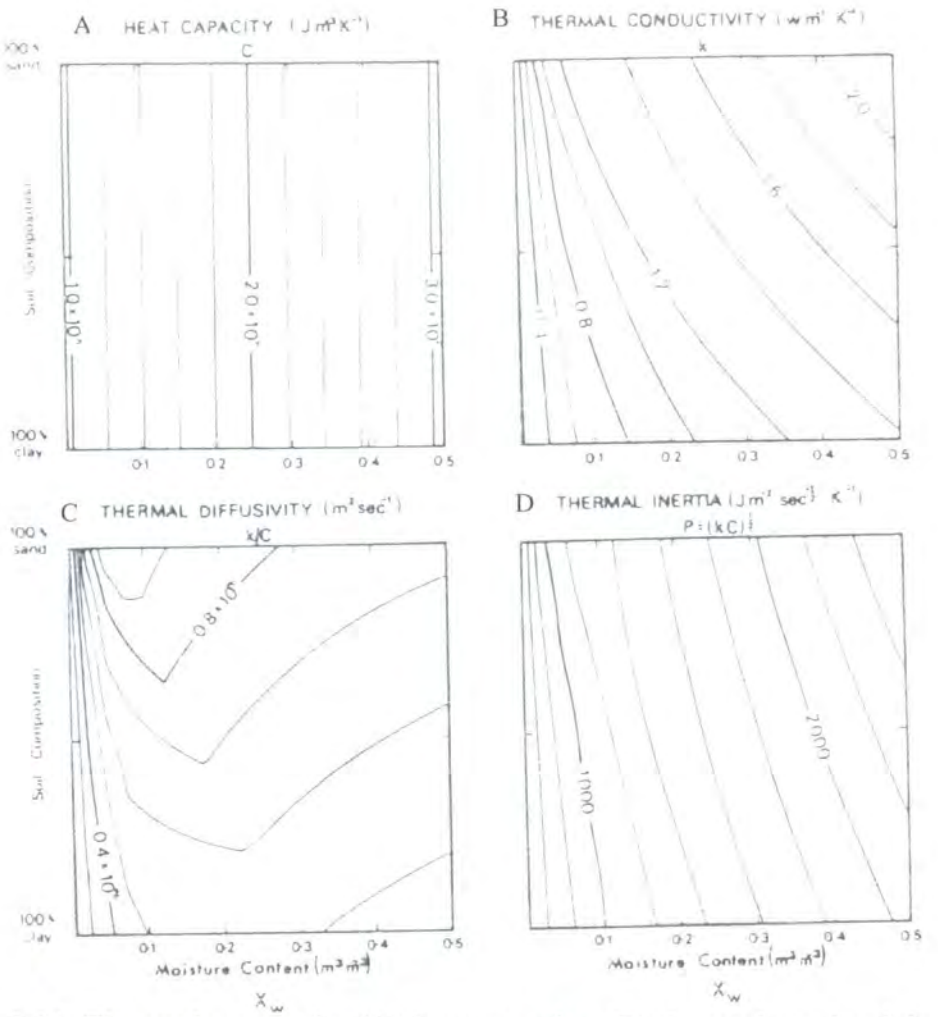

Figure 2.14: Thermal properties (A) heat capacity, (B) thermal conductivity, (C) thermal diffusivity and (D) thermal inertia for variable sand-clay fraction and water content for a fixed porosity, taken from Pratt & Ellyett (1979)

The thermal model developed by Price (1980) assessed the effect of soil moisture and near-surface humidity on the amplitude of the diurnal temperature range and mean surface temperature for specific surface conditions. This model provided a slight variation on the earlier models with solution of the 1D thermal conductivity equation, not the thermal diffusivity previously used, for uniform material of density (ρ), heat capacity (c), thermal conductivity (K) and depth (z) beneath the surface (Equation 2.27).

Equation 2.27

$$\rho\, c \frac{\partial T}{\partial t} = K \frac{\partial^2 T}{\partial z^2}$$

The diurnal temperature range expected at the surface was estimated from the amplitude of the solar variation (S), atmospheric transmittance (V), albedo (A) and diurnal heat capacity, which is a parameter based on Earth's rotation (ω), density (ρ), heat capacity (c) and the thermal conductivity (K), Equation 2.28.

Equation 2.28

$$\Delta T = \frac{2SV(1-A)}{\sqrt{(\varpi \rho\, cK)}}$$

The diurnal temperature range and surface evaporation were calculated using a step-wise multiple regression of this model for a given solar input, meteorological data, surface albedo, emissivity, humidity, roughness and diurnal heat capacity and was performed for a range of soil moisture properties. Results of the model showed that the diurnal heat capacity is directly proportional to the temperature range where heat stored in the soil and the surface albedo are affected the amplitude of the temperature contrast. Surface humidity was observed to be the factor that affected the observed mean temperature most.

Xue & Cracknell (1996) presented a mathematical model of near-surface conductive heat transfer for interpretation of physical properties in areas of variable soil moisture and vegetation cover. The model was based on a Fourier series solution of the one-dimensional thermal diffusion equation (Equation 2.19) satisfying surface boundary conditions to the depth where the temperature remains constant. Solution of the model was mathematically complex with the requirement for detail on flux parameters, surface albedo and topographic parameters. If the time of maximum temperature is known, the phase difference (δ_1) can be calculated with respect to the rotation of the earth (ω), as shown in Equation 2.29.

Equation 2.29

$$T_{max} = \cos(\varpi\, t - \delta_1)$$

The model used the phase of the diurnal temperature change calculated from both apparent and real information on the times of maximum and minimum surface temperatures. The apparent times were associated with image data assumed to have been acquired at peak times, with real assessment using the real times of thermal data acquisition. This diurnal phase could then be related, through a very complex

mathematical formulation, to the apparent thermal inertia of the surface. The thermal properties of the surface can then be inferred from this result.

The models described above have been developed for a homogeneous surface layer with uniform vertical and lateral characteristics. This poorly characterises the natural environment where there is often a very diverse composition at the surface and ignore the effects of partial vegetation fractions on the retrieved land surface temperatures. These single-source models also have a tendency to overestimate sensible heat flux over sparse canopies where there is a greater resistance of heat transport from the underlying soils compared with that occurring above the canopy (Anderson *et al,* 1997). Models are therefore required that incorporate the more complex characterisation of heterogeneous surfaces and further take into account the effects of variable vegetation cover.

2.4.3 Thermal Modelling of Soil-Vegetation Systems

The soil and vegetation components comprising a heterogeneous surface will each contribute to the energy fluxes acting on the surface layer and will have individual effects on the brightness temperature and also on surface albedo (Grover *et al*, 2000) in proportion to the fraction of pixel that is occupied by each component. Thermal models have then been extended to include the effects of a vegetation layer on surface temperature determination (Norman *et al,* 1995; Zhan *et al,* 1996; Kustas & Norman, 1999 & Anderson *et al,* 1997). These dual-source models enable the determination of the view-angle dependence of land surface temperature with respect to variations in the soil and vegetation fractions viewed over sparse canopies for a range of different view angles (Otterman *et al,* 1999). The view angle-dependency is not discussed in the thesis since the data acquired from an airborne system is viewed at nadir.

Norman *et al* (1995) presented a dual-layer model to relieve problems of canopy architecture and fractional vegetation cover on the retrieval of surface temperature from a soil-vegetation system. Their approach examined the contributions of the soil and vegetation layers to the sensible and latent energy exchanges between the layers by including details on the fractional vegetation cover or leaf area index, vegetation height, net radiation, air temperature and wind speed associated with the

radiometric temperatures. The model also assessed the contribution of individual soil and vegetation fractions on the radiometric and aerodynamic temperatures, the latter dependent on the temperature difference between each layer and the atmosphere and on the coupling between layers.

The radiometric temperature (T_{RAD}) of a surface can be obtained from the measured brightness temperature (T_B) with respect to the sky temperature (T_{SKY}) where the power n is assumed to have a value of 4 appropriate for thermal wavelengths. Although soil and vegetation exhibit different individual emissivities the multiple reflections between the soil and leaves tend to equalise the component emissivities in a soil-canopy system and therefore a single emissivity (ε) was assumed for the partially vegetated surface (Equation 2.30).

Equation 2.30

$$T_B = \left[\varepsilon T_{RAD}{}^n + (1-\varepsilon) T_{SKY}{}^n\right]^{\frac{1}{n}}$$

The radiometric temperature (T_{RAD}) of the vegetation surface was then determined as a function of the individual temperatures of the soil (T_S) and vegetation (T_C) within the field of view, weighted by their contributions to the brightness temperature (Equation 2.31).

Equation 2.31

$$T_{RAD}(\theta) = \left[f(\theta)\, T_{Canopy}{}^n + (1 - f(\theta))\, T_{Soil}{}^n\right]^{\frac{1}{n}}$$

The vegetation fraction ($f(\theta)$) was calculated with respect to the view zenith angle (θ) and leaf area index (F), assuming a random canopy of spherical leaf distribution and uniform emissivity (Equation 2.32).

Equation 2.32

$$f(\theta) = 1 - \exp\left(\frac{-0.5F}{\cos\theta}\right)$$

The sensible heat flux for the soil-vegetation system was calculated as the combination of the sensible heat determined for each soil and vegetation present in the partial canopy. These were calculated with respect to the volumetric heat capacity of air, aerodynamic temperature and aerodynamic resistance, which took into account the resistance of heat transport between the soil surface and the heights of wind speed

and air temperature measurements, canopy height, roughness length for momentum and diabatic correction factors for momentum and heat. The complex formulation for the sensible heat flux can be found in Norman *et al* (1995).

The latent heat flux of the soil-vegetation system was estimated from the canopy-soil energy balance equation (Equation 2.33), where latent heat (LE) is proportional to the net radiation (R_n), sensible heat (H) and the soil heat conduction flux (G) with respect to the individual soil and canopy fractions.

Equation 2.33

$$LE = R_n - H - G \qquad G = 0.35R_n \text{ AT NOON}$$

$$LE_{SOIL} = R_S - H_{SOIL} - G \qquad R_S \text{ penetrating soil}$$

$$LE_C = R_C - H_C \qquad R_C \text{ absorbed by canopy}$$

Latent heat flux of the canopy (LE_C) was then determined as a function of the difference in net radiation observed for the soil and that of the vegetation (ΔR_n) with respect to the fraction of green leaf area index present (f_g), slope of saturation vapour-temperature curve (S), psychrometer constant (γ), where the fraction of vegetation (f_C) is calculated with respect to the leaf area index (F), Equation 2.34.

Equation 2.34

$$LE_C = 1.3 f_g \frac{S}{S+\gamma} \Delta R_n$$

$$\Delta R_n = R_n - R_n \exp(0.9 \ln(1 - f_C))$$

$$f_C = 1 - \exp(-0.5F)$$

The above dual-source model examined the individual contributions of the soil and vegetation fractions of a partial canopy on the sensible and latent heat fluxes, the latter being used to determine radiometric temperatures in the majority of the numerical thermal models. Anderson *et al* (1997) modified this dual-source model to eliminate the need for measurement of local meteorological conditions, specifically eliminating air temperature since this factor was common to both the surface energy fluxes and the boundary layer condition at the time of observation. The model presented a series of expressions that described the transport of sensible heat from a

partially vegetated surface to the overlying boundary layer using the time differential of land surface temperature as the surface heated up in the morning. This model did not take into account the effects of a partial canopy on the energy interactions between evaporation from the soil and transpiration from the overlying canopy.

Daamen (1997) assessed the effect of a partial canopy on the network of interactions between the soil, canopy and atmosphere. Results showed that when the leaf area index was 1.0 the sensible heat flux was highly sensitive to the aerodynamic resistance and as the leaf area index increased there was an increase in the absorption of the sensible heat from the soil by the canopy, with subsequent dissipation as latent heat. When the leaf area index increased to 2.0, the soil-vegetation system could be sufficiently characterised by the dual-source model.

Kustas & Norman (1999) also assessed the effect of a partial canopy on the network of interactions between the soil, canopy and atmosphere, in particularly focussing on clumped vegetation. A row crop will possess a difference between along-row and across-row parameters, such as wind speed, and as a result these significantly influence the sensible and latent heat exchanges both inside the canopy layer and above the soil surface. Results showed that forest vegetation had a much higher aerodynamic resistance than a row crop, mainly due to the leaf area index of the vegetation.

A sensitivity analysis of the Norman *et al* (1995) model was performed by Zhan *et al* (1997) to assess parametric variation on the heat fluxes. Results showed that the model was insensitive to most parameters suggesting that the model has great potential where parameters are not easily determined for heterogeneous surfaces. The dual-source models are general enough to predict surface energy fluxes over a wide variety of surfaces, but operate on a single measurement of brightness temperature. The models also require detailed characterisation of soil and vegetation properties of the heterogeneous surface and also auxiliary detail on the local meteorological conditions during observation. The Norman *et al* (1995) model presented a solution to variable canopy architecture and fractional vegetation on the temperature retrieval by assessing their effect on the sensible and latent heat fluxes of the partially vegetated surface. The sensitivity analysis performed by Zhan *et al* (1997) showed that this dual-source model was relatively insensitive to variations in the majority of

parameters with Anderson *et al* (1997) modifying this dual-source model to eliminate the need for measurement of local meteorological conditions, specifically eliminating the need for air temperature. Daamen (1997) and Kustas (1999) examined the effects of clumped vegetation on the sensible and latent heat fluxes showing that a dual-source model was sufficient to characterise the soil-vegetation system when the vegetation had a leaf area index greater than 2.0.

The need for ancillary data on vegetation condition, meteorological and topographic parameters is still of considerable importance for application of these dual-source models. Although values can be assumed for some of the parameters, others will remain uncharacterised and as a result will be a source of uncertainty when retrieving land surface temperatures. The application of coupled soil-vegetation models would therefore be appropriate to the vegetated surfaces under investigation in the research, however, the insufficient auxiliary data on meteorological, topographic and surface parameters involved in the energy flux calculations suggests that the dual-source models will therefore be ineffective when quantifying the temperatures of the vegetated surfaces.

This following section summarises the important principles that have been discussed on the parameters involved in temperature characterisation of the land surface and its application to surfaces covered by vegetation.

2.5 *SUMMARY of THERMAL RESEARCH*

All natural surfaces emit radiation at middle infrared wavelengths that can be measured by a remote detector sensitive to these wavelengths. The detected radiation can be converted to land surface temperature using Planck's Radiation Law, which relates thermal radiation to temperature with respect to the wavelength of observation and the emissivity of the material under observation. Homogeneous surfaces will be sufficiently represented by a single emissivity value over a large area. Where vegetation completely covers the land surface, a single emissivity value that is representative of the bulk vegetation canopy may be assumed. Heterogeneous surfaces require much more complex characterisation and therefore the assumption of a single emissivity value may be inappropriate. The emissivity must therefore reflect the proportions of the various land surface materials, such as soil and vegetation, which comprise the land surface. With sufficient emissivity characterisation, the temperatures of the land surface may then be determined using the Planck relationship. Spatial variations in the thermal response will suggest variations in the thermal characteristics of the surface and it is therefore important to be able to relate the detected response to the thermal properties of the materials under investigation. The main thermal property that is most amenable to remote thermal investigations for single-channel remote sensing instruments is that of thermal inertia, which is a volumetric thermal property and can give an indication of variations in material properties to some depth beneath the surface. Thermal inertia was shown to have an inverse relationship to sand content and soil porosity, but was proportional to the moisture content of the soil. In addition, thermal inertia increases due to conductivity resulted in a greater penetration of heat to depth, but increases due to density resulted in a greater retention of heat at the surface.

These initial assessments refer to surfaces that were horizontally and vertically homogeneous and devoid of vegetation and so alternative approaches were investigated to study the effect of heterogeneity. Numerical energy flux models enabled detailed parameterisation of the surface under investigation with variation in the material properties with depth. These models ignored the effects of vegetation on the surface and so alternative dual-source models were discussed that incorporate the soil-vegetation coupling in their assessments. However, both the energy flux and

dual-source models require auxiliary data on meteorological and atmospheric properties that are not normally available.

The solution to thermal modelling when there is insufficient auxiliary data is to perform an assessment based on the thermal response of the surface across the diurnal heating and cooling cycle. This provides a measure of the resistance of the surface to temperature change, otherwise known as the thermal inertia. Although the physical thermal inertia cannot be directly measured from remote detection, a related property of *Apparent Thermal Inertia* (ATI) can be inferred from the thermal response measured at specific points in the diurnal cycle. ATI can be evaluated using a range of techniques that vary in the parameters incorporated in their calculation. The simplest approach analysed the temperature response of a day and night thermal image pair with respect to the albedo of the surface, but this did not take into account diurnal and seasonal variations in solar properties. A more appropriate model was therefore one that included the position and timing of observation in the calculations.

The ATI model that incorporated position and timing of observation as well as the day and night temperature response was therefore adopted for the research in order to identify areas of variable subsurface bulk thermal characteristics that could infer the presence of shallow buried features. The thermal response was also assessed at different stages in vegetation growth to determine the effect of vegetation growth on the detected response.

3 CONTEXT of SUBSURFACE FEATURES and TECHNIQUES for ASSESSMENT

The main aims of the thesis are to investigate the use of multispectral airborne remote sensing techniques and ground geophysical prospection for detecting shallow ground disturbance beneath a layer of vegetation and to examine the relationship between airborne thermal radiance data and the characteristics of surface materials beneath a layer of vegetation. Previous published research has evaluated airborne multispectral airborne remote sensing techniques for archaeological prospection and landscape assessment with conclusions that results from aerial photography are dependent on the time of imaging for revealing crop and soil marks associated with buried materials in intensively farmed areas, such as exist in the UK. Images acquired at near-infrared and shortwave-infrared wavelengths can aid crop mark detection, as they are sensitive to soil moisture differences with the imagery less seasonally constrained, but often add little additional detail to the results from aerial photography. Remote sensing in the thermal infrared has become an important non-contact tool for locating shallow ground disturbance with successful application to investigations on bare rock or soil surfaces that are devoid of vegetation cover. Shallow ground disturbance creates a differential heat flux between undisturbed and disturbed soils (Figure 3.1) and this provides the potential for detection using thermal imagery with improvement in differentiation due to variable moisture content of the soil above the feature compared with the surrounding matrix (Pickerill & Malthus, 1998).

Figure 3.1: Effect of buried feature on thermal response detected at the surface

The temperature contrast between the buried feature and the surrounding matrix will vary across the diurnal cycle in response to the variation in thermal properties of the materials. Under clear-sky conditions the diurnal thermal response of

surface materials shows a minimum temperature in the pre-dawn time period, rising in response to solar heating to a peak at solar-noon, after which the temperature gradually decreases towards the minimum temperature at pre-dawn the following morning (Figure 3.2).

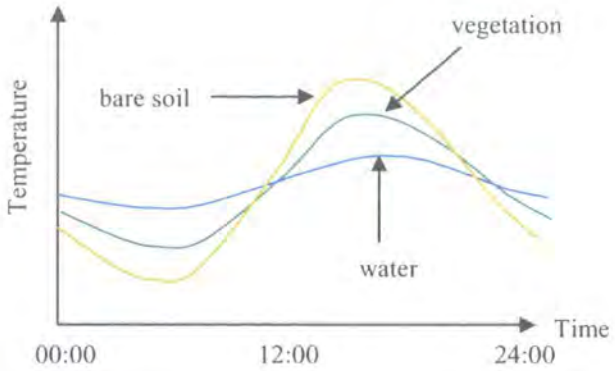

Figure 3.2: Diurnal thermal response of bare soil, vegetation and water

From this thermal response pattern it can be seen that there will be certain times in the day when there will be a minimal thermal contrast between materials of different thermal properties. An image acquired at one point in the diurnal cycle may therefore have a different thermal response than that acquired at a second point in the cycle due to the differential heating properties of the different materials. In order to maximise the contrast between the materials, it is therefore appropriate to acquire images at the times when the surface is at its maximum temperature and when it is at its minimum temperature to reveal features that are otherwise hidden on one-time-of-day thermal images.

Sparse vegetation growing over a buried feature will have little influence on the temperature response compared with that over bare soil due to the low fraction of vegetation present at the surface (Figure 3.3) and has been successful for the detection of buried waste in areas of sparse vegetation (Zilioli *et al,* 1992; Irvine *et al,* 1997).

Figure 3.3: Effect of short vegetation on thermal response at the surface

As the vegetation canopy closes, the thermal response of the soil is masked by the thermal response of the overlying vegetation with an increase in interaction of the energy fluxes within the canopy structure. Features buried in the subsurface will therefore be less likely to be detected unless there is a pronounced contrast in thermal properties between the buried feature and the surrounding matrix with respect to the more uniform thermal characteristics of the vegetation canopy (Figure 3.4).

Figure 3.4: Effect of vegetation on thermal response detected at the surface

The temperature of anomalies in the subsurface varies from that observed over the surrounding matrix across the diurnal cycle in response to the variation in thermal properties of the materials (Figure 3.2). Thermal imaging therefore has the potential to delineate features buried in the shallow subsurface using the thermal contrast over the diurnal cycle. Results of previous work have shown that shallow subsurface variations have sometimes been detected beneath vegetation when assessed across the diurnal cycle at different stages in crop maturity, which were otherwise hidden on visualisation of other spectral wavelengths (Bellerby *et al,* 1990). Where vegetation covers the soil during thermal prospection, the observed thermal response may not be directly representative of variations in the soil surface as vegetation regulates its own temperature through plant transpiration and this results in a more uniform canopy temperature above soil containing buried features (Perriset & Tabbagh, 1981; Scollar, 1990). Vegetation will also show a strong seasonality in thermal response due to growth properties so that seasonal variations in thermal response may reveal additional subsurface variations.

The temperature contrast between the buried feature and the overlying materials will decrease with depth to a certain depth below which the buried horizon will have no measurable effect on the surface temperature. This is known as the damping depth. The depth at which thermal damping occurs will depend on the contrast in thermal properties of the buried feature and the overlying materials. The

influence of the subsurface layer on the surface temperature will be a function of the variation in thermal properties between the two layers. Where a more complex three-layer subsurface structure is present, the variation in thermal response will depend on the contrast between the individual materials forming the surface (Figure 3.5).

Figure 3.5: Two-layer and three-layer models representing subsurface structure, taken from Perriset & Tabbagh (1981)

For the two-layer example, the contrast between the properties of the upper and lower layers provides suitable separation of the materials however in the three-layer model the important contrast is that between the two materials blanketed by the same material (Perriset & Tabbagh, 1981). This differential in properties of the underlying materials has been particularly successfully in geological applications where subsurface topographic variations (Nash, 1985) or buried horizons (Nash, 1988) can be detected beneath a layer of material where surfaces are devoid of vegetation. Vegetation alters the heat flux into the underlying soil and internally regulates the temperature of the canopy. Variations in subsurface characteristics would be more easily detected if temperatures are measured in direct contact with the soil rather than above the canopy (Noel & Bellerby, 1990). However, this technique is not very feasible for conducting a site survey since contact soil temperatures would have to be measured over a large area for widespread characterisation of the subsurface. Thermal imaging therefore provides a potential technique for site survey due to the synoptic view of the ground surface and control on the timing of imaging.

The research focuses on a particular gap in the current knowledge about the effect of surface vegetation cover on heat flux measurements of soil and overlying vegetation canopies and aims to assess the possibility of detecting shallow ground disturbance in vegetated terrains. Two examples of environmental settings in which shallow ground disturbance is known to occur under variable vegetation are buried archaeology and abandoned mine activity. The individual settings are discussed in the following sections together with the data that have been gathered for their analysis.

3.1 ENVIRONMENTAL SETTING: BURIED ARCHAEOLOGY BOSWORTH BATTLEFIELD, LEICESTERSHIRE

The Battle of Bosworth took place on 22nd August 1485 during the War of the Roses, a struggle for power between the royal houses of Lancaster and York. The battle had a major impact on the course of British history with the death of King Richard III, the last English King to be killed in battle. The scheduled ancient monument at Bosworth Battlefield marks the site of a deserted medieval village with earthwork remains and associated ridge and furrow field systems. The monument is located 2 miles south of Market Bosworth, Leicestershire, adjacent to the site of the Battle of Bosworth, in an area of intensively farmed land (Figure 3.6).

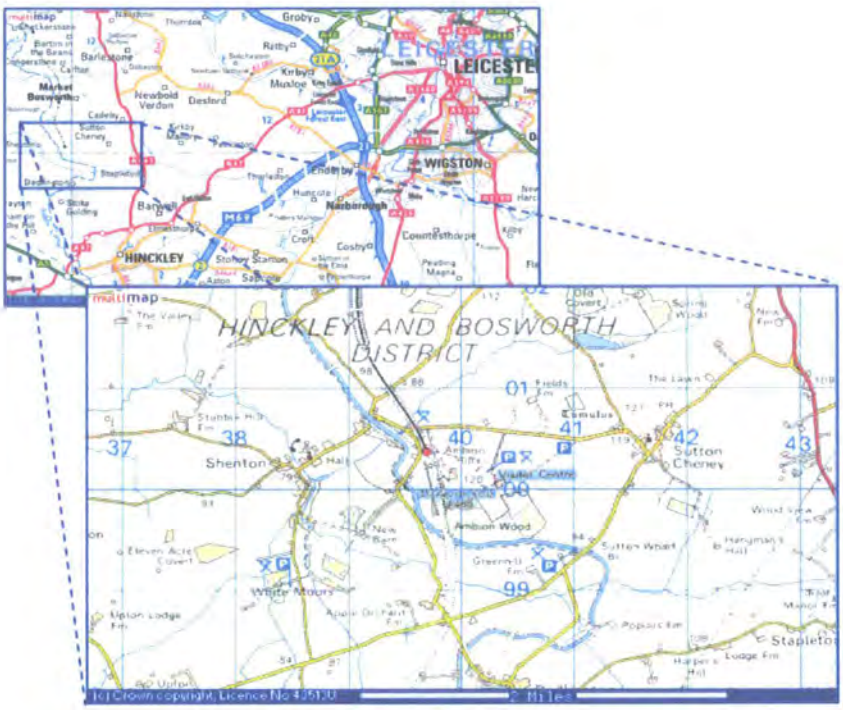

Figure 3.6: Location of Bosworth scheduled monument (www.multimap.co.uk)

The battlefield lies between the villages of Sutton Cheney, Shenton and Dadlington. However, the precise location of Bosworth battlefield is a contentious issue with historical sources indicating a variety of different possible locations of the battle (English Heritage, Proposed Battlefields Register: Bosworth 1485). The modern landscape differs markedly from that of the 15th century with draining of the marshes that were known to exist. In addition to this, a canal and a railway line were introduced in the 19th century. This site was specifically chosen since it was known to

be on the site of a deserted medieval village with associated earthworks and ridge and furrow field systems that were not immediately recognised on standard aerial photography. At this location, buried archaeology is known to exist under variable vegetation cover and authorised access to the land enabled the acquisition of auxiliary ground data.

Buried archaeology, such as walls and ditches, differs in their physical properties from the surrounding soil matrix, which make their detection and mapping possible using investigative techniques that identify variations in the physical properties of the subsurface materials. The most common techniques used in the detection of potential buried archaeology involve geophysical prospection techniques, such as magnetometry, resistivity and electromagnetometry (Chapter 3.5). In addition, vertical or oblique aerial photography has been used for site detection with analysis of multispectral data acquired across the visible and near-infrared spectral wavelengths. The potential use of thermal infrared wavelengths for buried archaeological investigations is addressed in the thesis and forms the basis for assessment.

In the past, the use of digital imagery in investigations of buried archaeology has stemmed from the identification of subtle soil and crop marks evident on vertical or oblique aerial photography, which may give an indication of the presence of potential buried walls or ditches due to stress of the overlying vegetation (Wilson, 1982; Jones & Elgy, 1994). These investigations have yielded excellent results in a variety of natural environments, however, the visibility of the crop marks appears highly dependant on vegetation type and status, and the condition of the underlying soil. Therefore, it is important to consider the vegetation effect when prospecting for subsurface structures in intensively farmed areas where the optimum visibility of crop markings will be dependent on the time of imaging and the maturity of the crop.

Research has shown that near and short-wave infrared multispectral imagery can enhance crop marks as these wavelengths are much more sensitive to the absorption and reflectance properties associated with vegetation status and moisture content than the visible spectral region (Donoghue & Shennan, 1988; Scollar *et al*, 1990). As a result, the imagery is less seasonally constrained however these wavelengths provide only minor additional detail to that extracted from a standard aerial photographic survey.

Thermal infrared imagery is sensitive to emitted rather than reflected radiation and this spectral region has been little studied where features in the shallow subsurface are hidden under vegetation canopies. Previous research suggests that thermal imagery significantly enhances soil marks in a variety of bare soil environments where the soil temperature depends on the direct interaction with solar radiation (Perriset & Tabbagh, 1981). The thermal heat flux into the ground will vary with the properties of the materials with a buried feature causing a different heat flux to that of the surrounding undisturbed soil matrix.

3.2 ENVIRONMENTAL SETTING: ABANDONED MINES on BAILDON MOOR, W. YORKSHIRE

The area of abandoned mine activity on Baildon Moor, W. Yorkshire marks a section of the Yorkshire Coalfield covered mainly by open grassland and bracken where coal was extracted from the Lower Coal Measures of Upper Carboniferous period (Figure 3.7).

Figure 3.7: Location of Baildon Moor, W. Yorkshire (www.multimap.co.uk)

Abandoned mineshafts represent a potential hazard in the rural and urban environment, where there is a need for information on the location and extent to which previous mining activity occurred in the near-surface environment. Over the past few decades, a range of geophysical and other investigative techniques have had variable success in the detection of mineshafts with development of efficient data collection and interpretation techniques. However, the physical characteristics about a site can be limited through insufficient surveying, inappropriate survey techniques, individual data interpretation and also poor integration of the geophysical results into the overall site investigation.

Mining legislation was introduced in its earliest form in 1850, where details on proposed mine activity were required to be submitted only a short time before excavation in order to update the records and maps. It was not until 1872 that mine abandonment plans were also submitted, with the addition of surface features added to

the maps in 1896. However, these plans remained inaccurate until 1911 when the detail on the spatial relationships between surface features was introduced. Additionally, spatial scale was only introduced to mine documentation in 1952 (Donnelly & McCann, 2000). This history shows that even when mine activities were recorded on maps and plans, their position was not always accurately known and furthermore, the maps would not have indicated whether the abandoned mine shafts had been capped to reduce the risk of collapse and if so, how effectively the capping had been carried out. In other circumstances, shafts were marked on plans that did not actually exist.

The potential hazards represented by abandoned mine activity can include the sudden collapse or gradual deformation of the ground surface, which may result in an accidental fall into a shaft by an individual, and the contamination of groundwater through the discharge of mine waters or through the mineral waste deposits. In addition to these, there can often be an efflux of hazardous mine gases, such as methane or radon that exist in certain rock formations and are known to expand and contract with changes in atmospheric pressure (Kearey & Brooks, 1991; Donnelly & McCann, 2000). The hazardous nature of abandoned mine activity outlined above therefore demonstrates a need to develop a more effective method of mineshaft and mineral waste deposit detection and mapping. The most common techniques of assessing mine abandonment sites tend to involve the use of geophysical prospection techniques (Chapter 3.5). These techniques can be time-consuming and so a more efficient method can be adopted through the development of digital image interpretation techniques.

The potential for using thermal imaging in mine abandonment studies was recognised during an airborne survey to observe mining-induced fault reactivation in the Lancashire Coalfield (Donnelly & McCann, 2000). At the time of the survey a ground frost prevailed at the site and circular features could be seen from the air. These corresponded to the approximate location of shafts on the mine plan, but on immediate ground inspection there was no evidence of surface expression usually associated with mine shafts. This suggested that there was a potential temperature increase over the shaft sufficient to alter the crystal structure of the frost, but insufficient to melt the frost completely, in addition to this where gases are emitted

from shafts, there is often an increase in temperature due to an exothermic reaction between the mine gas and the air. Shafts that display a clear topographic expression may also display a thermal anomaly during the day due to the differential heating of the shaft slopes that face both towards and away from the sun. From these characteristics, a temperature gradient may exist between a mineshaft and its surrounding soil generating a thermal anomaly associated with mine activity that may be detected using thermal imagery. However, thermal anomalies may not necessarily be evident over all mineshafts where there may be no variation in the physical characteristics between the shaft and surrounding material with vegetation potentially masking subtle material variations. Thermal anomalies may also exist over mineral waste deposits, which are created mainly from soil moisture effects of the loose spoil material when compared with the undisturbed soil. There may also be a vegetation anomaly associated with the spoil material, where soils extracted from the mine may contain a higher concentration of heavy-minerals in which normal vegetation struggles to grow, with potential growth of rare types of vegetation.

Some mineshafts on Baildon Moor can be identified on the ground from the mine plans, but the true geographical location of others is often poorly identified due to both a lack of accurate documentation and also poor topographic expression associated with the shafts. The coal measures on Baildon Moor are pseudo-horizontal in occurrence with a slight 1-4° dip to the south, with the relative depth to the coal working being a function of the topography. There are two main types of shafts that dominate Baildon Moor, known as the Bell Pits and Room & Pillar workings (Figure 3.8).

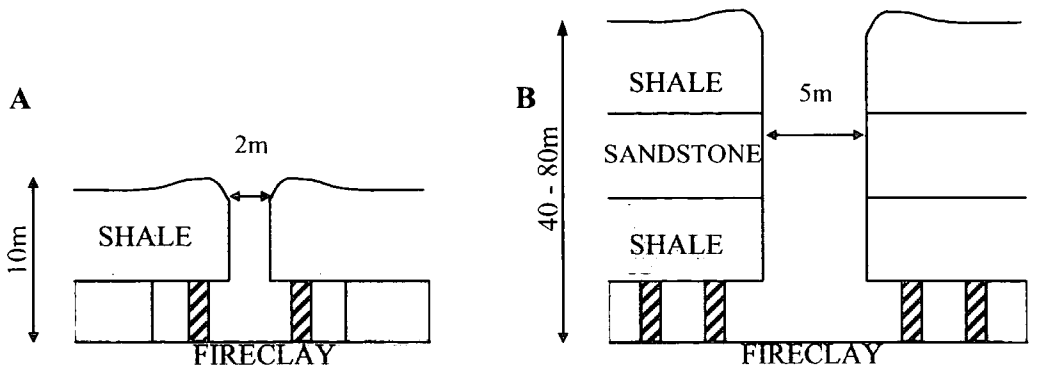

Figure 3.8: Examples of (A) bell pit and (B) room and pillar shaft formations. Both examples show a narrow shaft-head with wide base for coal extraction

Bell pits are relatively shallow workings with 2m diameter shaft heads of up to 10m in depth. The base of a typical shaft is excavated to a width of around 6m with mounds of spoil material forming a lip around the shaft. These shafts were often uncapped and were backfilled using the spoil material. The room and pillar structures are much larger with often 5m diameter shafts, sufficient to accommodate mining equipment. These workings often extended to 40-80m in depth with a 200m excavation at the base. To provide stability, wood, bricks or concrete often lined the shafts and when mine activity ceased they were often backfilled. In the case of shallow workings they were completely backfilled, but deeper workings were often capped at a level below the surface, by timber or mine carts, and spoil material placed on top. In the latter structures crown-hole development is commonplace when variable compaction of the materials result in subsidence (Figure 3.9).

Figure 3.9: Crown-hole development above a room and pillar working

At this location, abandoned mine shafts were known to exist under variable vegetation and open access to land enabled the acquisition of auxiliary ground data. The main objective of the study on Baildon Moor is to examine the properties of mineshafts of known surface expression and compare their response with areas of anomalies. The ground investigation will then be extended to where thermal anomalies occur in the imagery but where there is no obvious surface expression, and geophysical profiling may verify that the observed thermal anomaly can be related to shallow ground disturbance associated with mine activity.

3.3 ENVIRONMENTAL SETTING: ABANDONED MINE ACTIVITY on NORTH PENNINE OREFIELD, WEARDALE

The area of abandoned mine activity in the North Pennine Orefield, Weardale marks an area where there was a sustained period of mining activity, with lead, iron, zinc and silver mineral extraction (Figure 3.10). The area is covered by fields with a varying vegetation cover that are separated by dry-stone dykes and are used for agricultural crops and sheep-grazing.

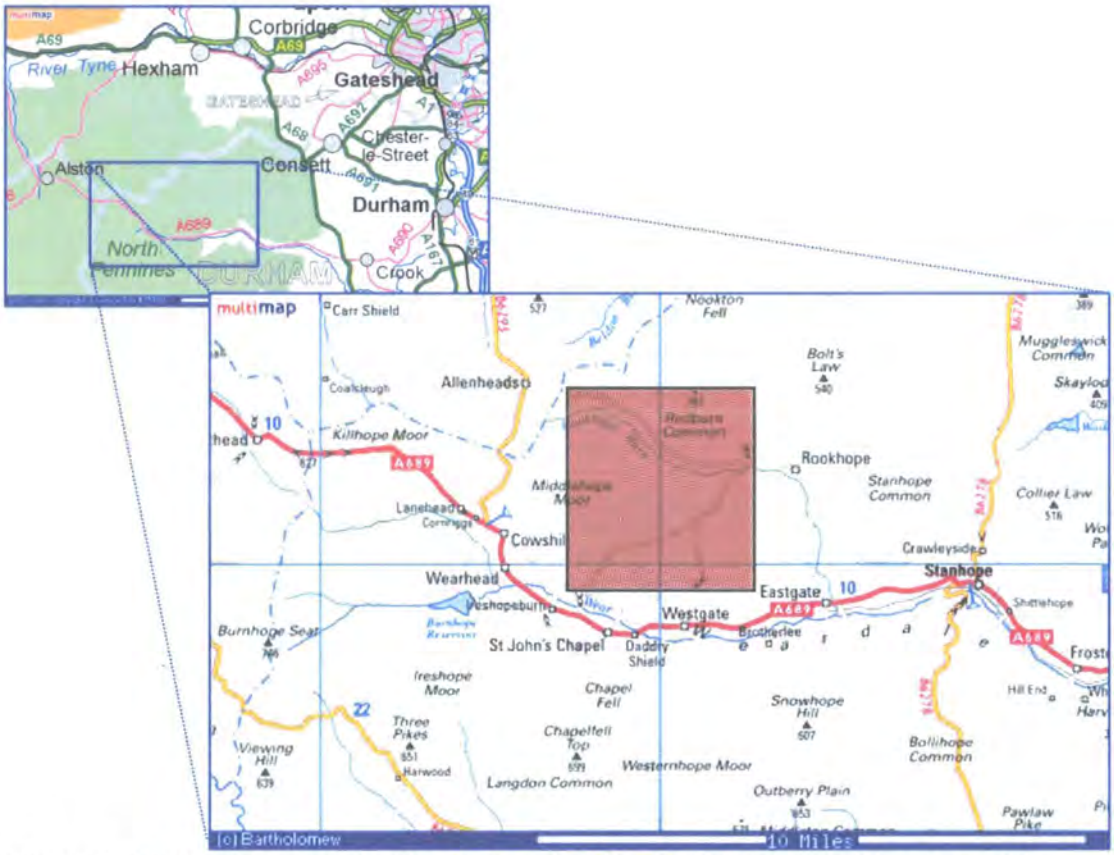

Figure 3.10: Location of the North Pennine Orefield (www.multimap.co.uk)

Mining techniques across the region have resulted in a series of bell pits and shallow shafts similar to those occurring on Baildon Moor. In addition to the shafts, adits and hushes are also common, which can be directly associated with the industrial archaeology of the region. Hushes are scour features created through hydraulic action in opencast mining activities where water is used to flush broken rock out of an excavation. The classic hush is created where water is stored behind a dam at the top of a steep-sided valley on the sides of which the mineral vein outcrops. When the dam is breached, the water cascades downslope scouring the loose soil and rock away to

expose the mineral vein. An adit is essentially a small shaft-like feature created to provide ventilation or access into a shaft and tends to be positioned at an angle to the main shaft. In addition to these features, there are also spoil heaps and scours relating to the mineral extraction, forming a series of topographic features where vegetation struggles to become established in the contaminated loose soils. These features litter the landscape of the region with a varying degree of visibility both on the ground and on digital imagery. At this location, abandoned mineshafts and spoil heaps are known to exist under variable vegetation but prohibited access to land prevented acquisition of auxiliary ground data.

3.4 REMOTELY-SENSED AIRBORNE DIGITAL IMAGERY

The research is performed using digital imagery acquired by the Airborne Remote Sensing Facility of the Natural Environmental Research Council. The NERC Airborne Remote Sensing Facility (ARSF) managed by NERC Scientific Services and Programme Management provides the UK scientific community and other potential users with the means to obtain spatially referenced remotely sensed data as a component of environmental research, survey and monitoring programmes. The NERC Airborne Remote Sensing Facility (ARSF) deploys a dedicated and highly modified research aircraft capable of providing researchers with synoptic digital and analogue imagery of high spatial and spectral resolution.

Multispectral digital imagery was acquired using a Daedalus-1268 Airborne Thematic Mapper (ATM). This is an 11-channel multispectral passive remote sensor designed to measure surface radiation from an airborne platform (Appendix A1). Radiation is captured by the rotating scan mirror of the ATM and is split by dichroic filters into a number of radiation paths. The ATM separates the incoming radiation into 11 spectral bands with 5 bands in the visible (VIS), 3 bands in the near-infrared (NIR), 2 bands in the short-wave infrared (SWIR) and a single band in the thermal infrared (TIR). Detail of the spectral characteristics of the Daedalus-1268 ATM configuration is shown in Table 3.1.

Channel	Daedalus AADS1268
1	0.424 - 0.448
2	0.469 - 0.518
3	0.522 - 0.601
4	0.594 – 0.635
5	0.627 – 0.694
6	0.691 – 0.761
7	0.754 – 0.924
8	0.879 – 1.027
9	1.600 – 1.785
10	2.097 – 2.391
11	8.400 – 11.500

Table 3.1: Spectral characteristics of the Daedalus-1268 Airborne Thematic Mapper

Unlike the data detected in the VIS, NIR and SWIR bands, the data in the TIR band is calibrated in 'real-time' by comparing the response to two on-board blackbodies set at known high and low temperatures. The blackbodies are imaged immediately before and after the scene pixels of every scan line together to enable

calibration of the TIR radiance to known temperature. The data acquired by the ATM was provided in digital format together with details on the specific file format and extraction procedures.

The ATM was deployed aboard a Piper Chieftain for the 1997-1998 flight seasons with upgrade to a Dornier 228-101 for later flights. Both configurations incorporated a 3-axial GPS mounted on the aircraft. This provided detail on the attitude and position of the aircraft during flight, which was synchronised with the timing of image acquisition. The integrated system enables the compensation of errors due to the motion of the aircraft by the synchronisation of the scan lines with the detailed navigational and attitude data on the platform.

As a complement to the multispectral data, high-resolution vertical aerial photographs were acquired simultaneous to the ATM imagery using a Wild RC-10 survey camera mounted on the airborne platform (Appendix A2). The camera is operated in basic mode with minimal forward overlap over Bosworth and in stereo mode with an overlap of 60% between photographs over Weardale. Details on the camera optics and calibration properties are provided along with the hard-copy output format to enable correction for lens distortions occurring across the aerial photographs. The aerial photographs can be scanned, ideally on a photogrammetric scanner to minimise optical distortions, and provide a digital format for the photographs.

3.4.1 Digital Imagery: Bosworth, Leicestershire

Airborne multispectral imagery was acquired using the ATM over the intensively farmed land at Bosworth on four separate dates. A day thermal image was acquired in May 1998 during early barley growth, with day and night image pairs acquired in June 1998 and August 1998 at progressively later stages in barley growth. A third day and night pair was acquired in March 2002 during winter conditions to complete the seasonal coverage. The large gap between the summer and winter data arose from technical problems relating to aircraft and also poor weather conditions, which prevented winter acquisition until 2002. In addition to this, winter data was intended to provide imagery when crop growth was at its minimum so a larger proportion of soil fraction would be present. However, oil seed rape had been planted

early on this site resulting in a closed vegetation canopy overlying the region during the winter acquisition. The multispectral data gave a good response across all multispectral channels, with sufficiently noise-free thermal imagery on all corresponding dates (Appendix C1). The data acquired over Bosworth therefore provided suitable multispectral and thermal data for both diurnal and seasonal analyses for the area of buried archaeology.

3.4.2 Digital Imagery: Baildon Moor, W. Yorkshire

Airborne multispectral imagery was acquired using the ATM over Baildon Moor on two separate dates. A day and night thermal pair was acquired in September 1996 however this data was excessively noisy throughout all channels and therefore rejected from further analysis. A second day and night thermal pair was acquired in May 1997 and this gave a good response across all multispectral channels, with sufficiently noise-free imagery (Appendix C2). The data acquired over Baildon Moor therefore provided suitable multispectral and thermal data for only a diurnal analysis for the area of abandoned mine activity.

3.4.3 Digital Imagery: North Pennine Orefield, Weardale

Airborne multispectral imagery was acquired using the ATM over the North Pennine Orefield in August 2001. The day imagery was of moderate to poor quality with excessive noise in Band 1 (VIS) and Band 9 (SWIR), the latter consistent with electrical discharge across the instrument. The remaining bands from the day imagery were sufficiently noise-free however the night thermal imagery contained a moderate to high amount of banded noise (Appendix C3). The data acquired over the North Pennine Orefield therefore provided a poor multispectral and thermal dataset for a diurnal analysis for the area of abandoned mine activity.

3.5 GROUND GEOPHYSICAL PROSPECTION

In order to understand fully the nature of the features that may be identified on the diurnal and seasonal multispectral imagery, a series of ground validation exercises were performed over the study areas relating to the buried archaeology of Bosworth and on only one of the areas of abandoned mine activity at Baildon Moor. No geophysical survey was performed in Weardale due to restricted access to land and was not followed up as a consequence of the poor data quality of the imagery. The purpose of conducting the ground investigations through geophysical surveying is to determine the physical characteristics of the shallow subsurface and relate the position of geophysical anomalies to features detected on aerial photographs, multispectral and thermal images acquired over the study areas. In addition to geophysical surveying, alternative approaches to ground investigations at Bosworth include field walking and metal detecting, however, the position of artefacts detected through these methods are often poorly recorded. Ground investigation at this site is therefore performed through geophysical prospection due to the accuracy of feature location.

Geophysical prospection is the application of a range of geophysical surveying techniques to the investigation of subsurface materials by making and interpreting measurements of physical properties. The main advantage of using geophysical techniques is that there is no disturbance of subsurface materials during investigation, an important factor where excavation would result in loss of artefact stratigraphy when looking for buried archaeology or result in a sudden collapse of the ground surface in areas of abandoned mine activity. Another advantage of conducting geophysical surveys is that anomalous areas can then be targeted for further investigation at a finer level of detail using other ground validation techniques to obtain more information on the subsurface structure.

Geophysical methods identify variations in physical properties of materials within the subsurface by locating a spatial or vertical boundary across which there is a distinct contrast in response (Reynolds, 1997). Such a contrast gives rise to a geophysical anomaly indicating variations in physical properties relative to some background value. There are both passive and active geophysical techniques where passive techniques detect variations in the Earth's ambient geophysical fields and active techniques transmit a field that is modified by the ground before detection.

The main geophysical techniques measure variations in the magnetic, electrical resistance and electromagnetic properties of the surface materials with additional attenuation and transmittance properties observed using ground penetrating radar. The success of each technique can be very site specific and its effectiveness may even vary within a site, depending on the nature of physical variations of the surface materials that vary with local geology and soil characteristics. From this it is clear that a combination of techniques may be needed since each method will be sensitive to different physical properties and so a more integrated approach will provide a more complete site investigation.

The geophysical prospection techniques that were applied in the study sites include magnetic, resistivity and electro-magnetic surveying, all of which provide the ability of generating a 2D representation of the subsurface structure. Other techniques exist that provide a 3D representation of the subsurface, such as ground penetrating radar and resistance tomography, but such equipment was not available during the period of study. The main techniques of magnetometry, resistivity and electromagnetometry shall be discussed in detail before discussing the results of surveys performed on the two contrasting environments of buried archaeology at Bosworth and abandoned mine activity on Baildon Moor.

3.5.1 Geophysical Surveying: Magnetometry

Magnetic surveys are often used for rapid site assessment where areas showing anomalous magnetic properties can then be targeted for further investigation using other geophysical and excavational techniques. The aim of a magnetic survey is to identify variations in the magnetic properties of subsurface materials, mainly magnetic susceptibility, which is a measure of how susceptible a material is to becoming magnetised (Scollar, 1990; Kearey & Brooks, 1991). The most common rock-forming minerals exhibit a very low magnetic susceptibility, however, certain rock types contain a sufficient proportion of magnetic minerals and produce a greater magnetic response. Similarly, man-made ferrous objects and human activity can locally enhance the magnetic properties of soils and generate local anomalies in the Earth's magnetic field resulting from the contrasting levels of magnetism between the material and the surrounding soil or geology.

There are a variety of highly sensitive instruments known as magnetometers that are designed to measure the subtle variations in magnetic properties of the subsurface. For soil prospection, the two most commonly used instruments are CS and Fluxgate gradiometers. Magnetometers are often used in a prospecting role for generating 2D maps of magnetic susceptibility at a specific observation depth. Areas of anomalous magnetic activity can then be located and identified as possible buried features. Magnetic prospection has provided excellent results in a wide variety of environmental situations. Examples include the prospection of silo-pits in limestone soils (Marshall, 1999), the analysis of ditch enclosures in loess deposits (Doneus & Neubauer, 1998), the determination of the depths of kiln sites and infilled pits (Desvignes, *et al*, 1999) and the identification of anthropogenic materials in leached brown soils (Dalan & Banerjee, 1996; Marmet *et al,* 1999).

The majority of these surveys were undertaken with a FM36 Fluxgate Gradiometer, a passive magnetometer that measures the magnetic gradient between two identical magnetic sensors (Figure 3.11).

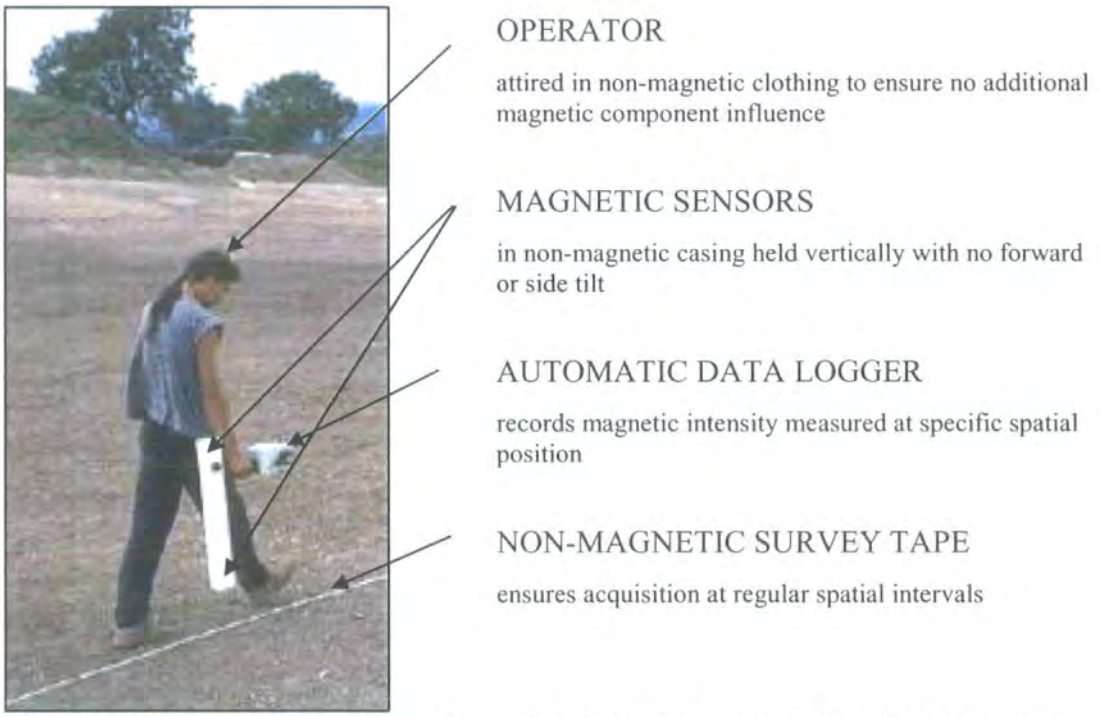

Figure 3.11: Geoscan FM36 Fluxgate Gradiometer operated by James Lyall, Landscape Research Centre

The sensors are encased in a non-magnetic rigid structure that is positioned vertically so that the sensors have zero horizontal displacement and are aligned directly above each. The sensors measure the magnetic field component and the magnetic gradient is calculated as the difference in the intensity between the sensors. Prior to conducting the survey, the local magnetic field component must be determined so that all magnetic readings measured within the survey area are observed as positive or negative readings to this background value. The magnetometer is then carried with unit pointing North along a set of parallel survey lines marking out the survey area with measurements of the magnetic gradient automatically recorded at regular spatial intervals. Once measurements have been obtained over the complete survey area, a prospection map is generated by visualising the adjacent transects to give an indication of areas of anomalously high or low magnetic readings. The small vertical separation between the sensors limits magnetic detection to relatively shallow depths and so any anomalous readings can be associated with material variations located in the shallow subsurface that can then targeted for further investigation using other geophysical or excavation techniques.

3.5.2 Geophysical Surveying: Resistivity

Resistivity surveys are commonly used in a similar manner to magnetic surveying to obtain an accurate depiction of the subsurface structure by identifying spatial variations in the ability of the subsurface materials to conduct an electrical current. All materials allow movement of electrical current to some extent, however, most rock-forming minerals are insulators and current is conducted through a material by the passage of ions present in pore waters, with conduction increasing with porosity (Kearey & Brooks, 1991; Reynolds, 1997). Soil resistivity depends on the structural and chemical characteristics of the soil and when an induced electric current encounters a solid buried feature the resistance is greatly increased. Conversely, where looser material is located within the soil layer a lower resistance is recorded due to an increased moisture content associated with a higher porosity than the surrounding undisturbed soil.

There are a variety of techniques that can be adopted for measurement of the resistivity of the subsurface. The most common technique examines the potential difference of the surface measured between a set of electrodes. An electric current is

passed into the ground by a pair of electrodes and the current radiates outwards equally in all directions towards a second set of electrodes (Griffiths & Barker, 1994). The relationship between induced and received current gives an indication of the resistance of the ground between the electrodes and will depend very much on the material properties through which it travels and also on the geometry of the electrode array. Ground resistance can then be calculated using Ohm's Law where resistance (R) is the ratio of the current (I) injected into the ground to the voltage (V) measured across a second pair of electrodes, positioned at some distance away (Equation 3.1).

Equation 3.1

$$R = \frac{V}{I}$$

Resistivity surveys are usually restricted to relatively small-scale investigations due to the labour-intensive approach of implanting electrodes in the ground for each measurement. The simplest electrode configuration is that of a twin-electrode array where the electrical potential is measured between a pair of electrodes mounted on a rigid frame at a fixed separation. Measurements are taken with respect to a remote pair of electrodes that are fixed at a position external to the survey area that record the ambient electric potential (Figure 3.12).

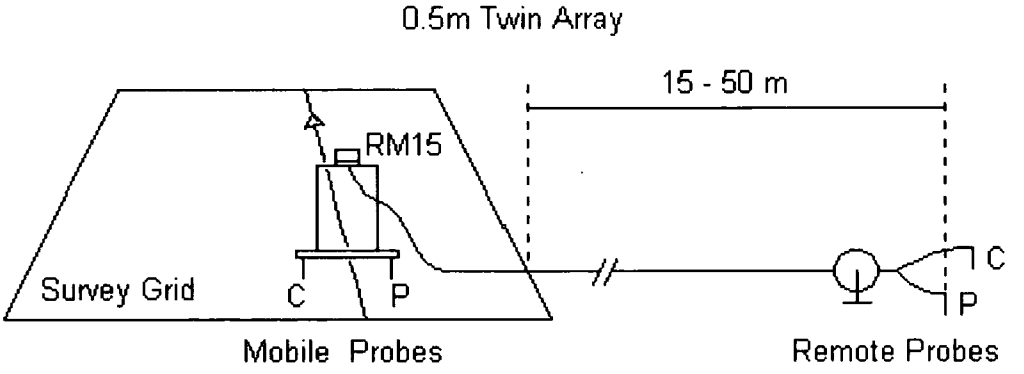

Figure 3.12: Twin-electrode array provided by the Geoscan RM15 Resistance apparatus (www.geoscan-research.co.uk)

The twin-electrode frame is carried along a set of parallel survey lines marking out the survey area with measurements of the electrical resistance automatically recorded at regular spatial intervals. This design enables rapid detailed area surveys to be performed for observation depth roughly equal to the electrode spacing. Once measurements have been obtained along parallel survey lines over the complete

survey area, a prospection map is generated by visualising the adjacent transects values as a grid of resistance to give an indication of the spatial distribution of subsurface features that show anomalously high or low electrical resistance in the survey (Mori, *et al*, 1999). These anomalous areas can then targeted for further investigation using other geophysical and excavational techniques.

Another common electrode configuration is that of a four-electrode Wenner array where pairs of current (C) and potential (P) electrodes are moved in unison at equal spacing (a) along the survey transect (Figure 3.13).

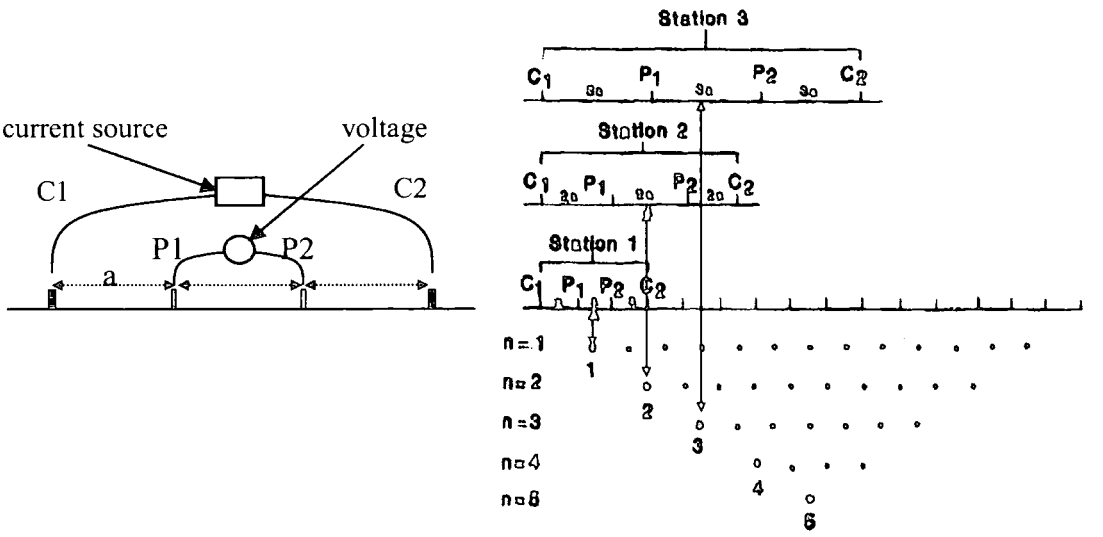

Figure 3.13: Four-electrode Wenner configuration where a current is passed into the ground through a pair of electrodes (C1 and C2) and the potential measured across a secondary pair of electrodes (P1 and P2), taken from Griffiths & Barker (1994)

This mobile four-electrode configuration does not require that use of remote electrodes and can be moved as a complete unit across the survey area. Although the unit is less easily moved than the twin-electrode array that is mounted on a rigid frame, the separation between current and potential electrodes can be more easily varied to represent different investigative depths (Noel & Walker, 1990; Griffiths & Barker, 1994; Mori, *et al*, 1999). The electrode array is moved along a survey transect line at a fixed electrode separation. The spacing can be increased, giving a greater volume traversed by the current and providing a greater depth of observation, or alternatively decreased along the traverse to give shallower depth of observation. The multiple electrode spacing generates a series of vertical cross-sections for the survey

transect line that can be used to determine the depth and geometry of buried features that can then targeted for further investigation using other geophysical and excavational techniques.

3.5.3 Geophysical Surveying: Electromagnetometry

Electromagnetic surveys are less labour-intensive than electrical resistivity surveys as they do not require the constant moving of electrodes into and out of the ground and surveying can therefore be relatively rapid. Electromagnetic surveys are used to delineate subsurface discontinuities by identifying variations in the response of the ground to the propagation of electromagnetic waves. Electromagnetic waves are composed of two orthogonal components, an electric intensity and a magnetising force, which propagate along a plane perpendicular to the direction of travel (Reynolds, 1997). A primary electromagnetic field is generated by passing an alternating current through a wire coil, known as a transmitter coil, with field propagation via paths above and below the ground. When electromagnetic radiation travels through subsurface materials it is modified slightly relative to that which travels through air. If the electromagnetic wave encounters a conductive medium, the magnetic component of the incident wave induces a current within the conductive material, which generates secondary electromagnetic field components that are detected at a receiver coil. The receiver coil also detects the primary field components that travelled through the air, so the overall detected response is the combined effect of both the primary and secondary field components. Consequently, the measured response differs in both phase and amplitude relative to the primary field and this can be used to reveal information about the size, geometry and electrical properties of the subsurface materials.

The most common electromagnetic techniques used for environmental geophysics is the dual-loop system where primary electromagnetic waves are generated in a transmitter coil and are measured at a receiver coil at some distance away. This gives an indication of the conductivity of the material at the mid-coil position. There are two common coil configurations for the dual-loop systems that are simple to operate and provide rapid surveying of the study site.

The first is a simple EM31 coil configuration where transmitting and receiving coils are mounted on a horizontal pole with an integrated data logger capable of automatically recording the conductivity measurements (Figure 3.14). The second is a moving-source EM34 dual-coil configuration where the transmitting and receiving coils are independently mobile and are connected by a reference cable (Figure 3.15).

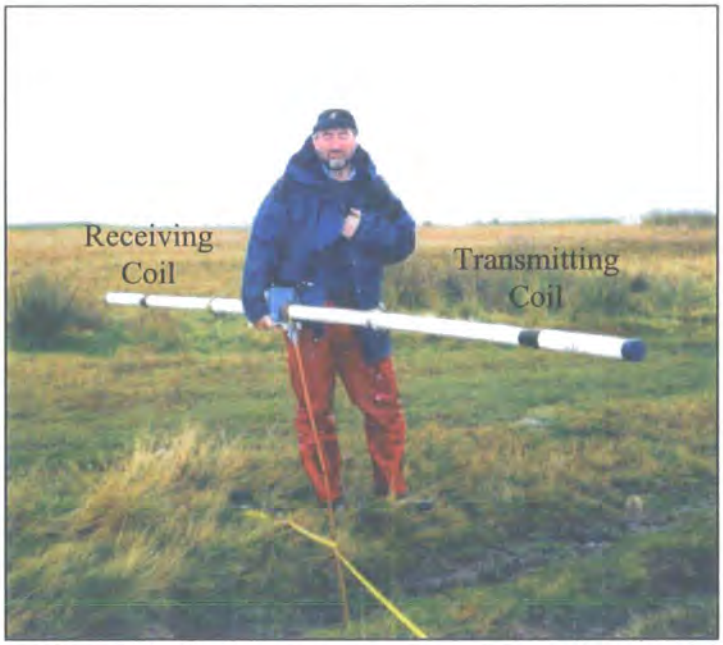

Figure 3.14: Dual-loop EM31 electromagnetic system with transmitting and receiving coils mounted on horizontal pole

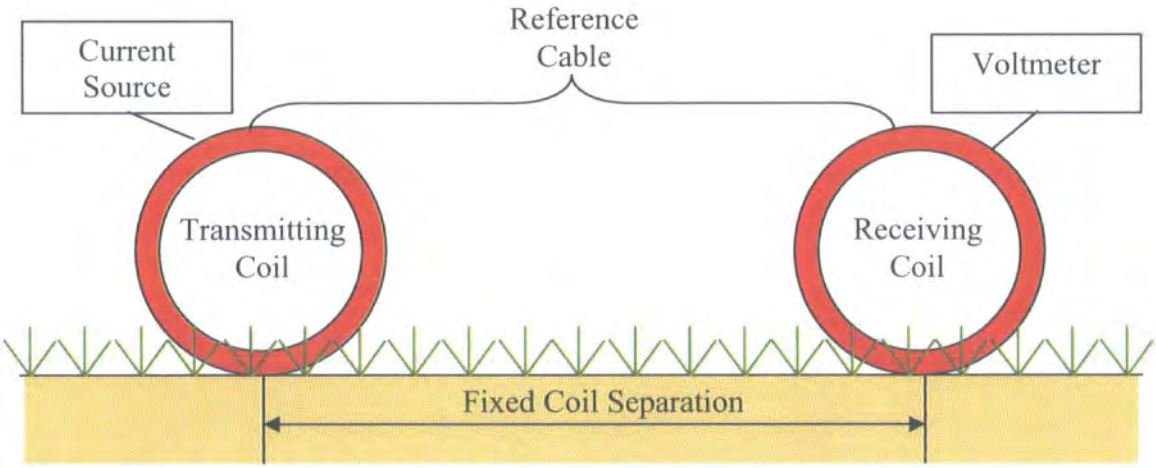

Figure 3.15: Dual-loop EM34 electromagnetic system with moving transmitting and receiving coils connected by reference cable at fixed coil separation

In both dual-loop systems, the transmitting and receiving coils lie in-line with the survey transect with the separation between the coils giving a variable depth of

observation. The coils are then moved along the transect line at a fixed separating distance to build up a profile of variations in electromagnetic response. The coils can be aligned as either horizontal coils to measure the vertical magnetic dipole or vertical coils to measure the horizontal magnetic dipole. The EM31 is rotated clockwise or anticlockwise to change between coil configurations whereas the coils in the EM34 require a rotation about the vertical axis (Figure 3.16).

Figure 3.16: Horizontal (A) and Vertical (B) magnetic dipole configurations

In the horizontal configuration, there is relatively very little response from the near surface materials, increasing with depth to a maximum at depth approximately 0.4 intercoil spacing. As a result, the horizontal configuration is insensitive to near-surface features. In contrast, the relative response for a horizontal magnetic dipole decreases with depth from a maximum at the surface, making the vertical coil system very sensitive to near surface features (Reynolds, 1997). The depth of penetration of the electromagnetic fields also depends on the electrical conductivity of the material through which it is propagating, with attenuation through the ground resulting in a decrease in received resistance exponentially with depth (Kearey & Brooks, 1991). Since the transmitting and receiving coils do not penetrate the ground surface, these electromagnetic surveys are less labour intensive than resistivity surveying and provide a rapid assessment of the depth and structure of the subsurface features. Electromagnetic surveying is rarely applied to archaeological prospection but was

successfully applied by Luck & Eisenreich (1999) as an additional source of information on the features revealed on application of the other forms of geophysical prospection.

3.6 GEOPHYSICAL EVALUATION of BOSWORTH

A geophysical evaluation was commissioned by Leicestershire County Council on a section of the Bosworth scheduled monument in 1999 This was extended in late 1999 and 2000 to provide a complete magnetic survey of the Bosworth scheduled monument and surrounding area. The magnetic survey was performed using the passive Geoscan FM36 Fluxgate Gradiometer that detected anomalies in the local geomagnetic field component associated with anomalous buried materials of anthropogenic activity. The ideal situation for detection is where the buried materials have a reasonably high contrast in magnetic response compared with the surrounding soil matrix. Since the magnetic survey was designed to detect buried ferromagnetic materials associated with anthropogenic activity, the machine sensitivity was set to detect magnetic intensity variations in the order of 0.1 nT, the nanotesla (nT) being the standard unit of magnetic flux. The local geomagnetic field component was determined prior to surveying, represented by an area where the local magnetic field gradient is relatively flat. This is assigned a zero base value so that all subsequent magnetic readings within the survey are positive or negative of this value, due to the dipolar nature of magnetism.

The Fluxgate Gradiometer was used to survey a series of 30m x 30m grids, with magnetic intensity automatically measured at 0.25m spatial intervals along survey transect lines at a spatial separation of 1m. The automatic data logger attached to the instrument allows the specification of the dimensions of the desired survey grid area and will continue to collect magnetic intensity readings until the memory reaches full capacity. For best results, magnetic readings were avoided in areas containing highly metallic objects such as wire fencing, telegraph poles and buildings as these perturb the local geomagnetic field component and can often mask the response of the buried features by influencing several readings in the vicinity of the highly magnetic feature. The survey grids were then downloaded and visualised as series of grey-scale images with goepositioning of the corner points. Each individual survey grid could then be examined for the presence of buried features. However, it is much more

beneficial to generate a single grey-scale image layer of the complete surveyed area in order to identify structures and features of potential interest. In order to achieve this, the geographical coordinates of each grid require to be measured at the same time as they are surveyed in order to create a georeferenced mosaic of the survey area for integration with other georeferenced datasets. The results of the gradiometer survey were displayed in grey-scale image format to identify contrasts in grey-scale intensity values associated with the potential buried features. The most prominent features on the magnetic survey are a series of linear magnetic anomalies and also some point anomalies of anomalously high and low paired response (Figure 3.17).

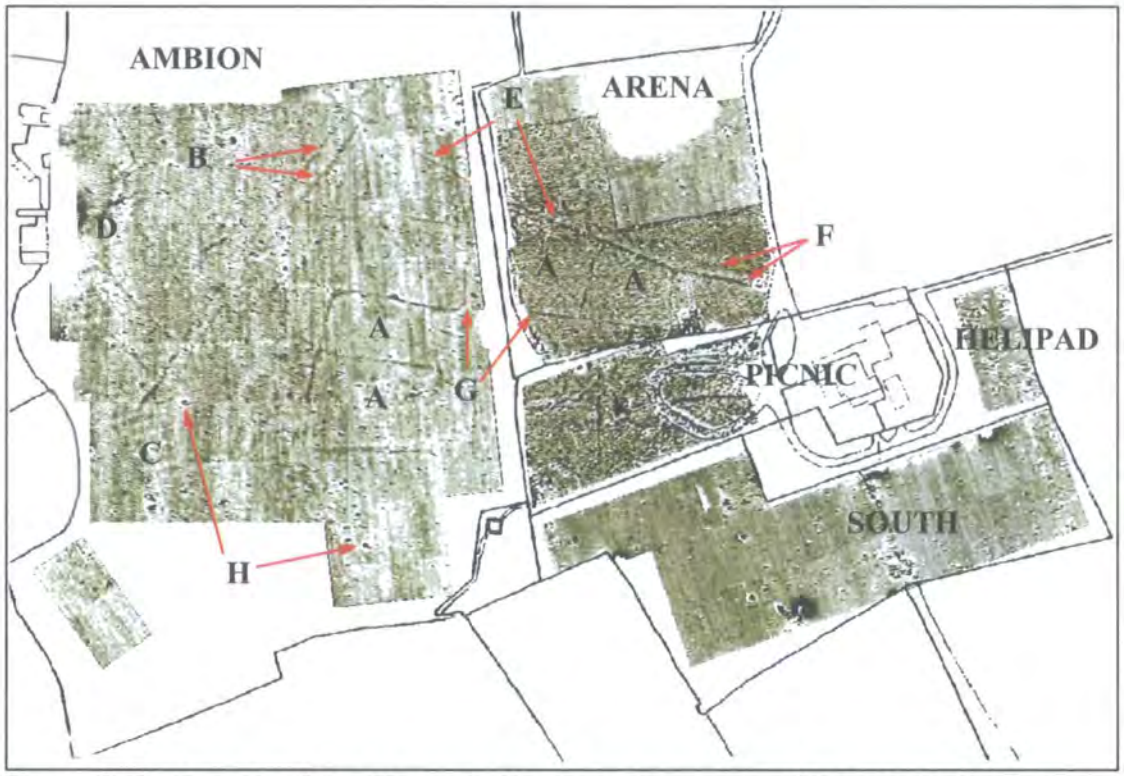

Figure 3.17: Results of the Fluxgate Gradiometer survey of Bosworth. Dark grey indicates low magnetic response

There are a wide variety of linear magnetic anomalies present in Ambion field. The most prominent magnetic anomalies are a series of rectangular anomalies (A) located in the eastern section of the field. These are thought to represent field enclosure systems. There is also a prominent double linear NE-SW anomaly that runs across Ambion field and this is may represent a trackway (B), although the second linear feature is incomplete along its length. On the western section of Ambion field there are a series of narrowly-spaced E-W parallel linear anomalies of relatively high

magnetic response (C). These represent the presence of a ridge and furrow system. In the northern section of the field there is a very low magnetic feature (D), however this feature is very close to the farm buildings to the west and may be a direct result of the highly magnetic character of the tin-roof structures and would therefore require further investigation. There is a faint linear NW-SE anomaly located in the northern section of Ambion field (E) that continues into the adjacent Arena field, showing a double linear anomaly at its eastern end (F) representative of a trackway. In the southern section of the Arena field there is a similar continuation anomaly that marks the boundary of a field enclosure system (G). Throughout all the fields there are a number of small circular bright and dark magnetic spikes (H). The origin of these point features is may relate to the position of burned tree stumps that have been removed since generation of the 1st edition OS map (MacKinder, *pers. comm.*), but this is only one possible explanation and therefore the features require further investigation.

There are no strong magnetic anomalies evident in the Picnic, Helipad or South fields. The implications of this is threefold in that (1) there may be no magnetic features buried in the near-surface in these fields, (2) the features may be deeper than the technique can investigate, or that (3) the magnetic properties of the background soils in these fields are similar to those of the buried materials and therefore magnetometry appears to have its limitations.

The Bosworth magnetic survey revealed a wide variety of anomalies that suggest the presence of enclosure systems. There are some DMV earthwork remains and ridge and furrow marks that are represented by slight topographic features at the ground surface and are visible on the aerial photography or multispectral imagery. However, not all of these features give rise to magnetic anomalies. Magnetometry appears therefore to have its limitations in this physical setting so an alternative geophysical technique was applied to further understand the full extent of anthropogenic activity.

Leicestershire County Council commissioned a resistivity survey over small sub-sections of the Bosworth scheduled monument in late 1999 where the magnetic survey showed variable results. The resistivity survey was performed using a Geoscan RM15 Resistivity Meter to detect anomalies in the electrical conductivity of the soil

associated with anomalous buried materials of anthropogenic activity. As for the magnetometry survey, the ideal condition for feature detection was where the buried materials would have a reasonably high contrast in electrical response compared with the surrounding soil matrix.

The twin-electrode array was mounted on a frame with a fixed electrode separation of 0.5m to measure the electrical resistivity of the soil occurring at 0.5m depth. The RM15 resistivity meter was used to survey a series of 30m x 30m grids, with resistance automatically measured at 1m spatial intervals along survey transect lines at a spatial separation of 1m. The automatic data logger attached to the instrument allows the specification of the dimensions of the desired survey grid area and will continue to collect readings of electrical conductivity until the memory reaches full capacity. For best results, resistivity readings were avoided in water-logged areas as these can often mask the response of the buried features. The survey grid data was then downloaded and visualised as a series of grey-scale images. The geographical coordinates of the corner points of each grid were recorded during data acquisition to enable the generation of a georeferenced image mosaic of the complete survey area for integration with other georeferenced datasets. The results of the resistivity survey were displayed in grey-scale image format to identify contrasts in intensity values associated with the potential buried features (Figure 3.18).

Figure 3.18: Results of the RM15 resistivity survey of Bosworth

The survey performed in the Picnic field covered a 60m x 60m area consisting of nine 20m x 20m grids. The area was situated to the west of the car park on a south-east facing slope containing what appeared to be the remains of earthworks. The results of the survey (Figure 3.19) show a cluster of high resistance anomalies forming a curved feature on the southern edge of the survey area on the flatter ground, suggesting an area of former building materials. There is also an individual high resistance feature in the south-eastern corner possibly indicating the presence of a building structure. There is a rectangle of medium resistance situated on the north side of the cluster that may represent a field surrounded by removed hedgerows that lies in an area of low resistance that appears to pre-date the high resistance clusters. There is also a linear E-W trending low resistance feature situated parallel to the fence-line in the northern section that is bounded on its north and southern edges by high resistance anomalies and this may represent a hollow-way or possibly a walled feature leading to

the area of low resistance. These results lead to the suggestion of an agricultural area surrounding a former building.

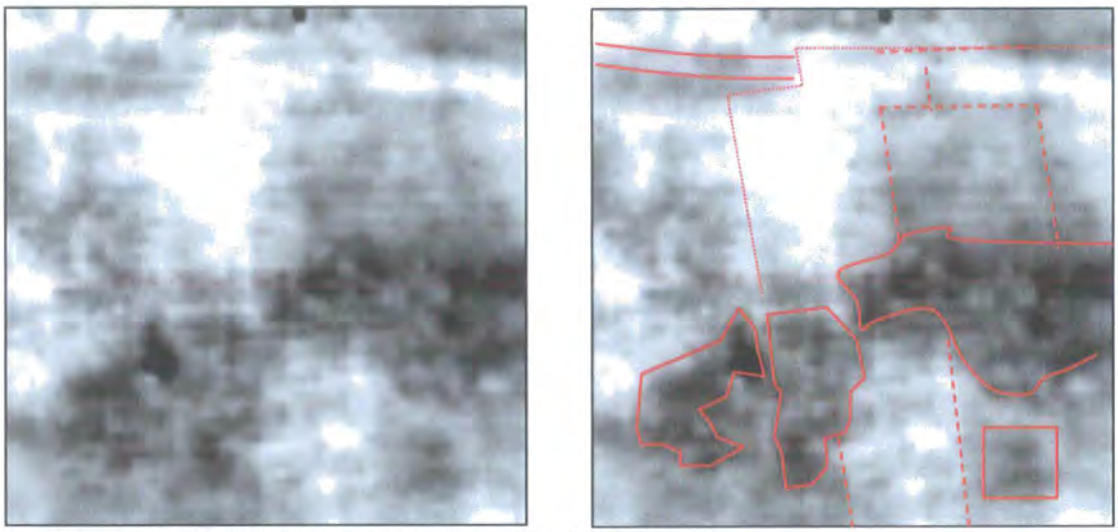

Figure 3.19: Resistivity survey of the Picnic field

The survey performed in the Arena field covered a 100m x 40m area consisting of ten 20m x 20m grids. The area was situated on a south-east facing slope that was covered by grass, annually cultivated for silage, with no trace of man-made features at the surface except for a square of modern hard-standing near the south-east corner. The results of the survey (Figure 3.20) show a prominent linear high resistance anomaly trending E-W close to the southern boundary of the survey area, broken only by the area of low-resistance modern hard-standing. This feature possibly represents a boundary wall. In the north-west corner there is a square of high resistance that is surrounded by an area of low resistance bounded on three sides by high resistance linear features. This is indicative of a building structure surrounded by a walled field. In the north-east corner there is an area of intersecting double linear features that is typical of the presence of hollow-ways associated with different phases of development, however, the discontinuous nature of these features makes interpretation difficult.

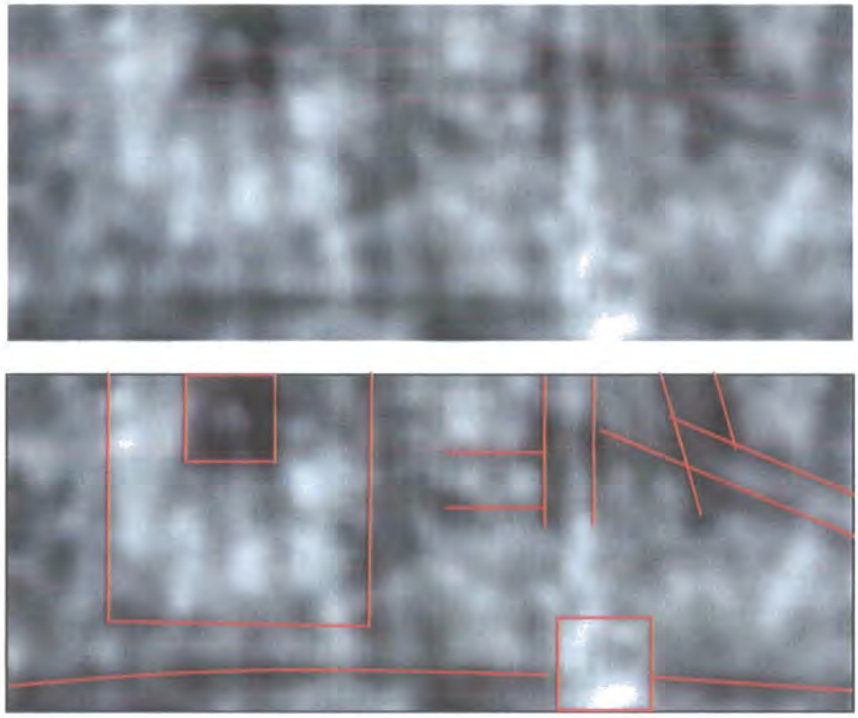

Figure 3.20: Resistivity survey of the Arena field

The survey performed in the re-enactment field covered a 60m x 60m area consisting of seven 20m x 20m grids with two dummy grids containing no data. The area is situated on a slight west facing slope covered by grass with an area of modern hard-standing. The results of the survey (Figure 3.21) show a high resistance feature in the north where the soil was very thin above a rocky outcrop. There was a similar high resistance feature on the eastern section surrounded by an area of small circular high and medium resistance anomalies. This is possibly representative of a mound of rubble with dispersal of material. The broad low resistance feature on the west can be attributed to the area of modern hard-standing that is truncated at the south-western end where the hard-standing gives way to soil and grass.

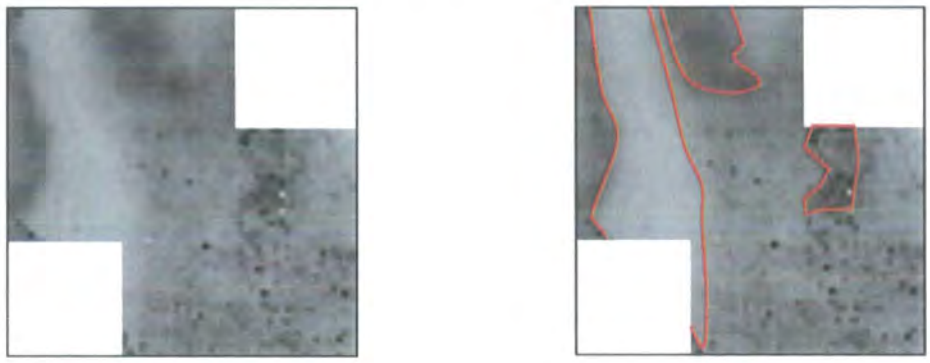

Figure 3.21: Resistivity survey of the Re-enactment field

The survey performed in the South field covered two main areas. The western survey covered a 30m x 90m area consisting of three 30m x 30m grids bounded by a fence-line on the northern, southern and north-eastern boundaries. The site was covered by grass with patches of nettles and thistles and was situated on a southern facing slope where there was evidence of earthworks suggested by prominent topographic hummocks. The results of the survey (Figure 3.22) show a rectangular feature of high resistance in the north, bounded by linear features of low resistance. This coincided with the hummocky ground. At the western edge there was a double linear anomaly of high resistance possibly representing a narrow track or wall. A prominent linear feature of medium resistance trended N-S through the centre of the survey area leading to a large circular feature of high resistance that was surrounded by small high and low resistance anomalies, possibly representing rubble. To the south there was a feature of medium resistance that coincided with the site of a modern watering hole for livestock, with an area of well-trampled surrounding ground. The east generally showed lower response than the west with a low resistance feature in the north-east marking a modern track through the grass.

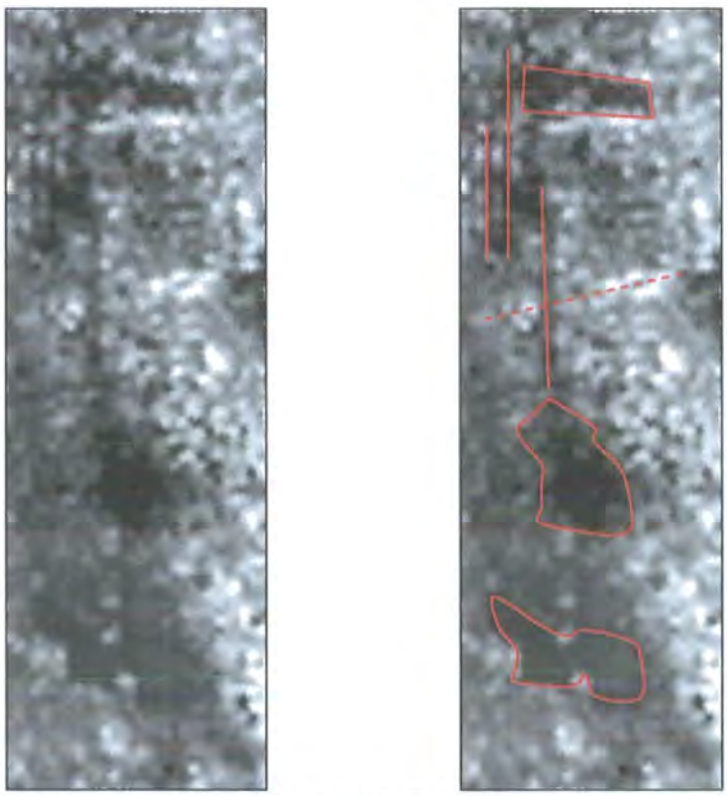

Figure 3.22: Resistivity survey of the South field: West section

The eastern survey consisted of a single 30m x 30m grid situated in the north-eastern corner of the field, bounded by an oak tree on the western edge and by hedgerows on the northern and eastern boundaries. The site was relatively flat with slight topographic linear features suggesting ridge and furrow farming. The results of the survey (Figure 3.23) show a rectangular feature of high resistance in the east representing a man-made structure with a medium resistance section on its eastern wall suggesting an entranceway. In close proximity to the main feature there are additional high resistance rectangular features, possibly representing outbuildings. In the south-west internal corner of the main feature there is a curved medium resistance anomaly that may represent a furnace. The survey also revealed a double linear feature of medium resistance trending NNW-SSE that suggested the presence of a track.

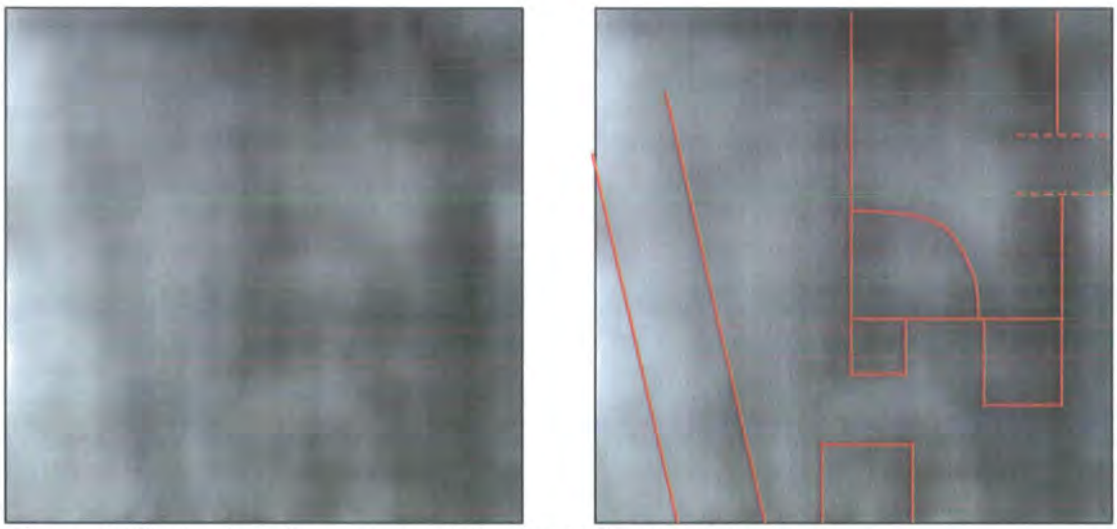

Figure 3.23: Resistivity survey of the South field: East section

The survey performed in the Helipad field covered a 20m x 60m area consisting of six 20m x 20m grids bounded by a fence-line on the southern and eastern edges and gravel tracks on the northern and western edges. The site was situated on a very slight south-east facing slope that was covered by grass. The results of the survey (Figure 3.24) show a rectangular feature of high resistance in the south-west with a second rectangular feature of higher resistance in the east, the dimensions of which was similar to the structural feature present in the East section of the South field. These suggest the presence of man-made structural features that are separated by an area of low resistance. There is a curved feature of low resistance in the north-west, bounded by medium resistance anomalies, that possibly represents a track. This feature intersects the main rectangular structure in the east, giving an indication of relative timing of occurrence of the anomalies. Although there is clear evidence from the resistivity survey as to the presence of structural anomalies in this field, there are no topographic anomalies at the surface associated with these features.

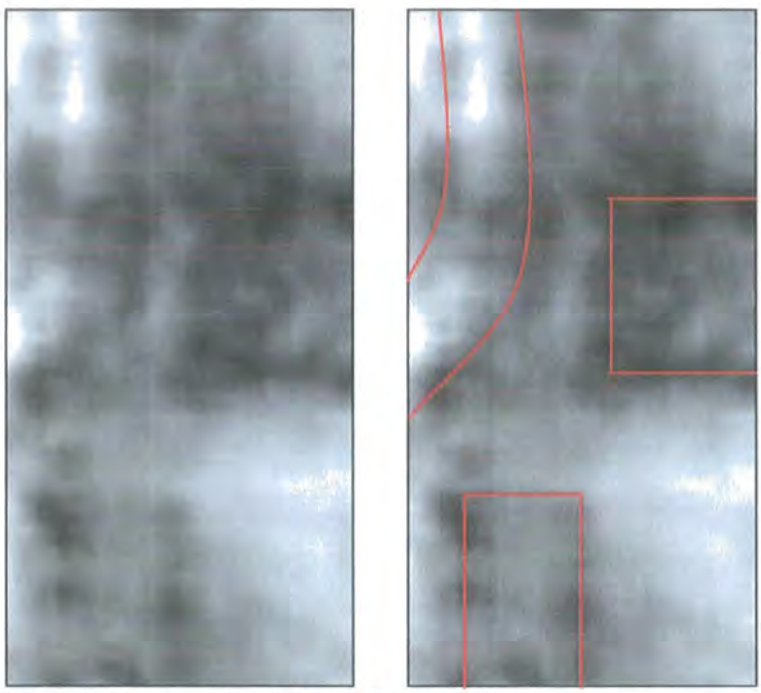

Figure 3.24: Resistivity survey of the Helipad field

The results of the resistivity survey have indicated that there were a number of building structures, boundary walls, hollow-ways and fields present in the area surrounding the scheduled monument of Bosworth. Interpretation provided in the Leicestershire County Council Report suggests the presence of a deserted medieval village of variable use. Although there is little topographic trace of earthworks associated with anthropogenic activity, the resistivity showed evidence of buildings concentrated in the eastern surveys of the Helipad and South-East fields where there were numerous outbuildings and fields associated with the main structure suggesting the presence of a possible farmstead. Additional field systems were identified from orthogonal walled structures in the Arena and Picnic fields. There were numerous tracks and possible hollow-ways that connected the various field surveys with the superimposition of a number of these features suggesting several phases of habitation was associated with the village. These features were located in an area where there was little topographic trace of earthworks associated with anthropogenic activity viewed at ground level. The exception to this was the hummock feature in the western section of the South field, which clearly marked the site of earthwork remains.

When the results of the resistivity survey were compared with the results of the magnetometry survey, it was clear that the features revealed on the resistivity survey did not correspond with the features of magnetic characteristics suggesting that resistivity is an important complimentary technique when surveying for potential archaeological remains. The results are also compared with the results from field walking and metal detecting.

3.6.1 Alternative Ground Investigations: Field Walking And Metal Detecting

Field walking and metal detecting involves the search for artefacts at the ground surface within a series of 20m x 10m grid squares. In both situations, the field-walker records any artefacts found within the grid square, such as pottery, coins and other objects that may be related to anthropogenic activity (Figure 3.25). Much of these features are brought to the surface from depth due to extensive plough activity. Some of the more interesting artefacts are extracted and identified by Leicestershire County Council with respect to the period of anthropogenic activity. Due to the inaccuracy of the documentation of the precise location of the finds within the survey area and also the transportation of artefacts within the field due to plough activity, maps of the field-walking and metal detecting show only general concentrations of specific periods of activity and show poor correlation with the geophysical results. The maps generated from the field-walking are held at County Hall by Leicestershire County Council.

Figure 3.25: Example finds from field-walking in Bosworth

In order to understand fully the nature of the detected features, further investigations are required with extraction and analysis of soil samples across the features that show variable characteristics. In addition, it is important to assess the use of the multispectral and the thermal data to reduce the necessity for invasive investigative techniques. This shall be discussed in later chapters.

3.7 GEOPHYSICAL EVALUATION of BAILDON MOOR

The British Geological Survey commissioned a resistivity evaluation of a section of Baildon Moor using a four-electrode Wenner configuration to detect anomalies in the electrical conductivity of the soil associated with the abandoned mine activity. The Wenner array formed a complete electrical circuit with transmitting electrodes connected to a current source and observing the electrical conductivity across a pair of potential electrodes using a voltmeter. The electrodes were separated by 5m to enable measurement of the ground resistance at a depth of 2.5m at the mid-electrode position, thus enabling the detection of both capped and uncapped mine shafts.

The Wenner-electrode array was deployed at a single site in the northern section of Baildon Moor adjacent to the golf course (Figure 3.26) where there were prominent circular vegetation features with moderate topographic expression. One of the features was known to represent an abandoned mine shaft (Figure 3.27) and the resistivity profile observed over this feature was compared with that observed over a secondary feature of similar topographic and vegetation expression to determine whether this feature also represented an abandoned mine shaft. Resistivity was measured along a transect line that intersected the features of distinct topographic and vegetation expression to compare the resistivity response observed over the known and suspected shaft features.

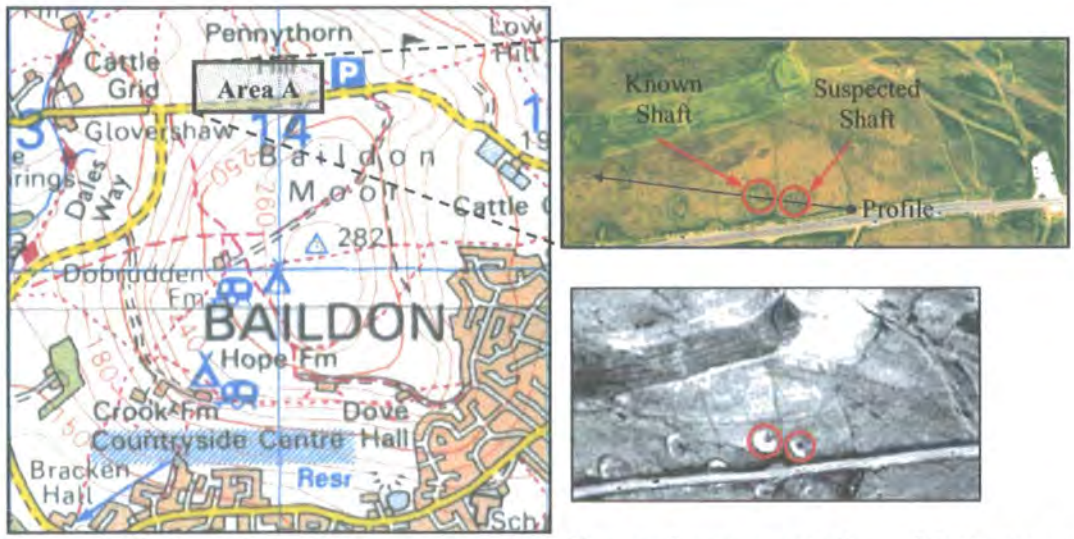

Figure 3.26: Location of Wenner transect line and representation of features on natural colour composite and day thermal image

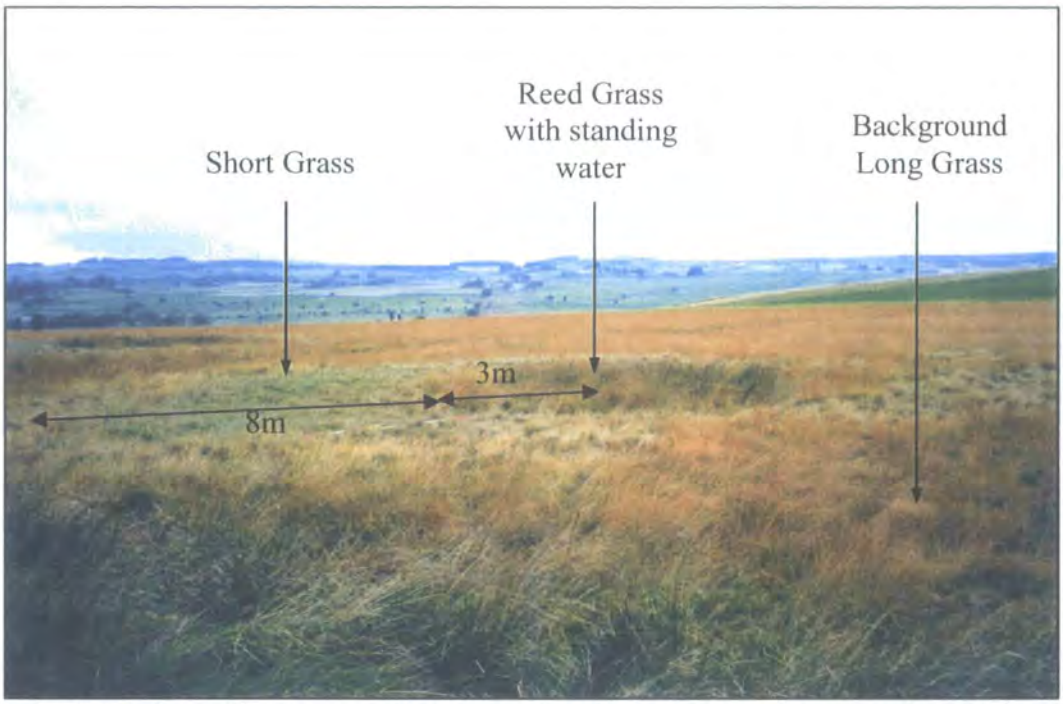

Figure 3.27: Prominent vegetation anomaly observed over known mine shaft

Ground resistivity was measured at 2m intervals along the survey line with transmitting and potential electrodes moved at equal spatial intervals to generate a profile of ground resistivity measured at 2.5m observation depth for the specific electrode separation. The survey line originated beside the main road and passed through the background vegetation, intersecting the prominent circular vegetation features at a distance of 92m and 50m from the profile origin. These were also observed as anomalies in the thermal imagery due to the presence of standing water at the centre of each feature. Results of the Wenner survey were displayed in graphical format showing the resistivity of the ground measured at a distance from the origin of the profile (Figure 3.28).

Figure 3.28: Resistivity profile trending WNW from origin (0m) beside road

The above graph shows a clear resistivity anomaly at 92m from the origin, which was observed as a pair of raised resistivity values at 85m and 100m on either side of a relatively lower resistivity value at 92m. The raised resistivity levels correspond to the position of flat areas of short vegetation that immediately surround the topographical low of the shaft, which was itself marked on the ground by an area of tall reed grass and standing water. The known shaft situated at 92m from the origin therefore shows a clear resistivity anomaly, implying that there was a contrast in the resistivity characteristics observed at the 2.5m observation depth for the shaft when compared with the background vegetation.

The suspected shaft feature at 50m from the origin that was observed as a topographic anomaly on the ground and a vegetation anomaly on the digital colour composites did not show a prominent resistivity anomaly, as would have been expected if the anomaly represented a shaft similar in nature to that observed at 92m from the origin. At 50m from the origin, the observed resistivity was similar to the surrounding background material suggesting that there was no difference in resistivity characteristics of the suspected shaft feature and the surrounding material at the 2.5m observation depth. The suspected shaft feature therefore displays a different physical characteristic than the shaft observed at 92m and this may represent a different

method of capping of the shaft head, or that the shaft was backfilled with the same material as the surrounding soil or that the shaft is insensitive at the specific electrode separation. In order to understand fully the nature of the feature observed at 50m further investigation was required using other geophysical techniques.

An electromagnetic evaluation was performed in Area A. Vertical profiles of the electromagnetic field properties over the known and suspected features were acquired using EM31 and EM34 techniques. Ground conductivity was measured in Area A at 2m intervals along the same transect line over which resistivity was measured using the EM31 technique with coil separation of 3m to give an observation depth of 1.5m. The survey line originated beside the main road and passed through the background vegetation intersecting the prominent circular vegetation features at a distance of 92m and 50m from the profile origin. These were also observed as anomalies in the thermal imagery due to the presence of standing water at the centre of each feature. Results of the EM31 survey were displayed in graphical format showing the conductivity of the ground measured at a distance from the origin of the profile (Figure 3.29).

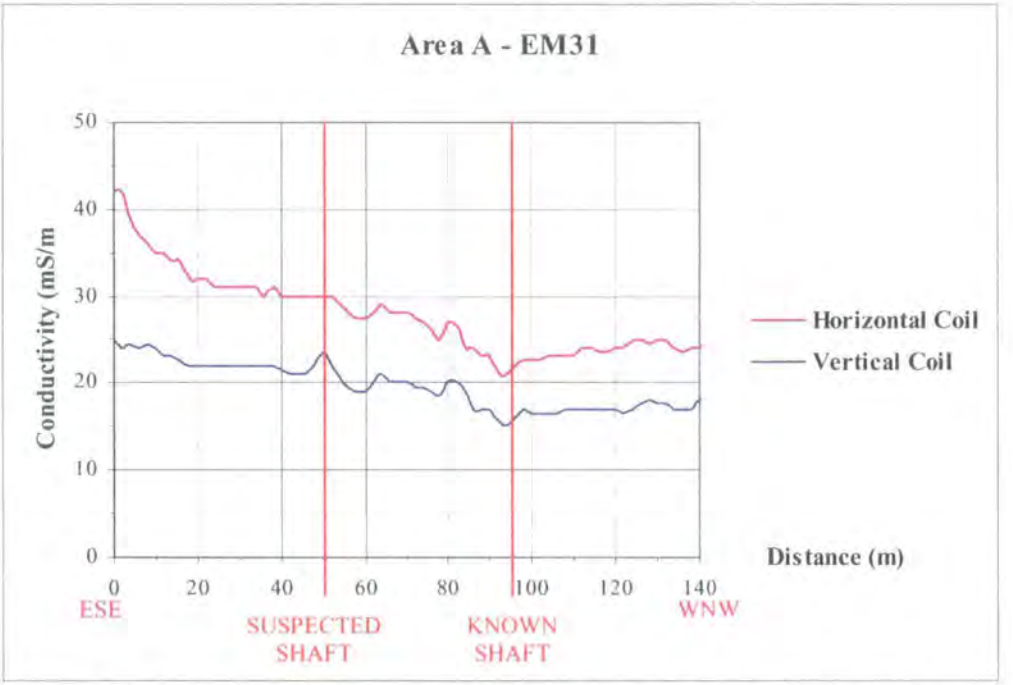

Figure 3.29: EM31 profile for horizontal and vertical coil configurations

The conductivity profiles observed by the horizontal and vertical coil configurations are very similar in characteristics, with a gradual decrease in conductivity level to a trough at 92m before returning to a relatively constant moderate conductivity level away from the origin of the profile. The initial high values can be attributed to the acquisition of conductivity readings in close proximity to the main road. The low conductivity values measured at 92m correspond to the position of the prominent circular vegetation feature with moderate topographic expression that was known to represent a mine shaft. In contrast to the results of the resistivity survey, there are no anomalies associated with the flat vegetation rims surrounding the known shaft. This suggests that there is no anomalous variation in soil properties at the 1.5m observation depth across the rims compared to the background vegetation. There was no conductivity anomaly evident in the horizontal coil configuration corresponding to the suspected shaft at 50m from the profile origin, however there was an anomalously elevated conductivity level in the vertical coil configuration at this position when compared to the surrounding background vegetation measurements.

Since both features occur in soils of the same composition, the results of the EM31 survey suggest that the shaft at 92m displays a variation in electrical properties at both shallow and deep observation depths, as detected by the vertical and horizontal coil configurations respectively, suggesting that the shaft remained uncapped and was not backfilled with material. The suspected shaft feature at 50m shows a variation in electrical properties at only shallow observation depth associated with the vertical coil configuration and this may suggest that the secondary feature was capped and backfilled with material at a level between the horizontal and vertical coil sensitivities. However, in order to understand fully the nature of the suspected feature at 50m, further geophysical investigation must be performed.

Ground conductivity was measured using the EM34 technique along the EM31 survey line at 2m intervals intersecting the prominent circular vegetation features. Coil separation was selected at 20m to give a maximum observation depth of 8m and 6m for the horizontal and vertical coil configurations respectively. Results of the EM34 survey were displayed in graphical format showing the conductivity of the ground measured at a distance from the origin of the profile (Figure 3.30).

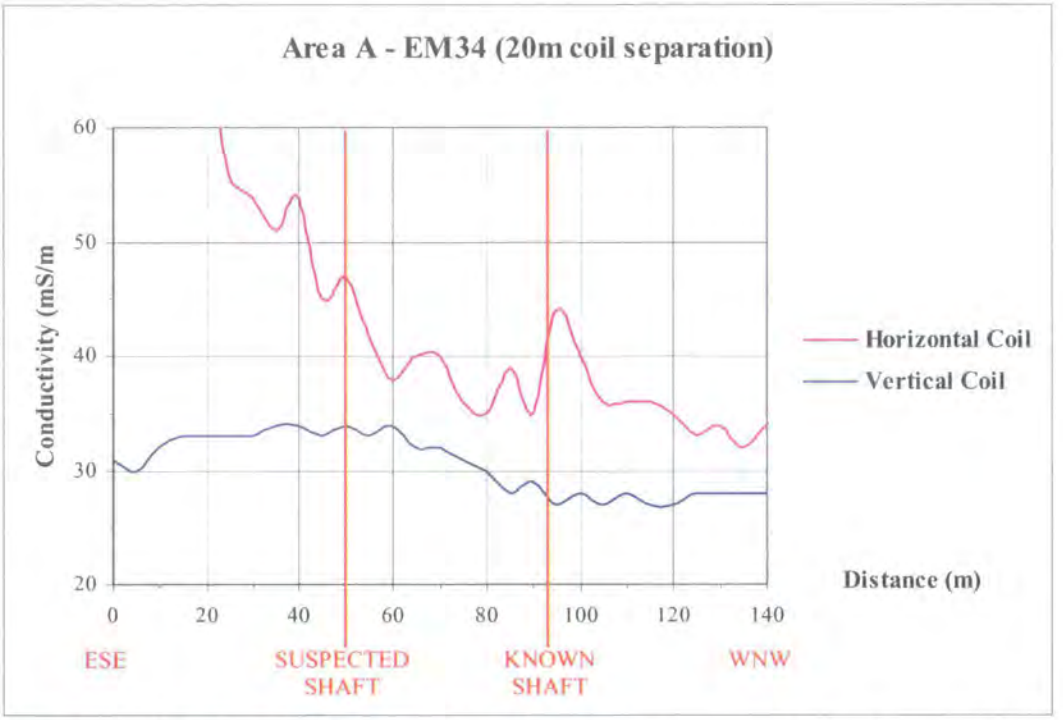

Figure 3.30: Profile of EM34 survey at 20m coil separation for both horizontal and vertical coil configurations

The horizontal coil configuration shows an exponential decline in conductivity with an anomalous conductivity peak at 95m corresponding to WNW flank of the documented shaft. There is no anomaly observed at 50m over the suspected shaft suggesting that the feature shows no variation in electrical properties compared with the surrounding material for the 8m observation depth. The conductivity profile observed by the vertical coil configuration shows less overall fluctuation in response than that observed with the horizontal coil configuration. The electrical response shows a gradual increase in conductivity to a peak around 50m before decreasing gradually to a wide trough centred around 105m before rising again to an intermediate conductivity level associated with the background vegetation. The fluctuation in conductivity levels about the maximum or minimum values observed for the known and suspected shaft features suggests that the features show similar characteristics to the background vegetation at the 6m observation depth. The observed fluctuation may therefore be associated with the flat vegetation rims surrounding the shaft features.

In summary, the known shaft at 92m displayed anomalies in both vertical and horizontal coil configurations for the EM31, with a prominent anomaly observed in only the horizontal coil configuration for the EM34 coil separation of 20m. The

known shaft therefore displays a variation in soil characteristics at 1.5m and 8m depths of observation. The suspected shaft at 50m displays anomalies in only the vertical coil configurations for both the EM31 and EM34 techniques. The suspected shaft therefore displays a variation in soil characteristics for 1.5m and 6m depths of observation. The implication of this is that although the surface vegetation and thermal characteristics are identical for both features, the variation in electromagnetic properties at shallow depth for the suspected shaft may result from a variation in the method of capping and backfilling between the features.

Comparing the results of the EM31 and EM34 surveys with those from the resistivity survey, it becomes evident that a combination of geophysical techniques was necessary in order to be confident about detection of both the known 92m shaft and suspected 50m shaft.

A secondary geophysical survey was performed over a documented shaft in Area B of different physical attributes than those presented in Area A. EM31 and EM34 techniques were deployed across a transect line in Area B (Figure 3.31) to intersect a shaft of pronounced topographic expression (Figure 3.32) and suspected shaft showing a 6m-wide vegetation and thermal anomaly (Figure 3.33).

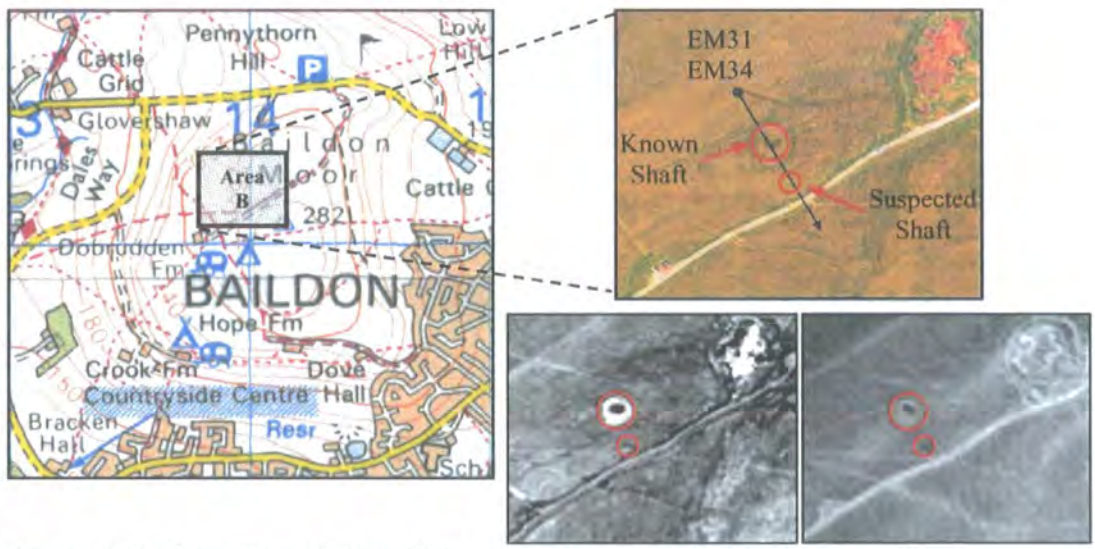

Figure 3.31: Location of Area B transect line on Baildon Moor and representation of features on natural colour composite and thermal imagery

Figure 3.32: Known shaft of pronounced topographic expression

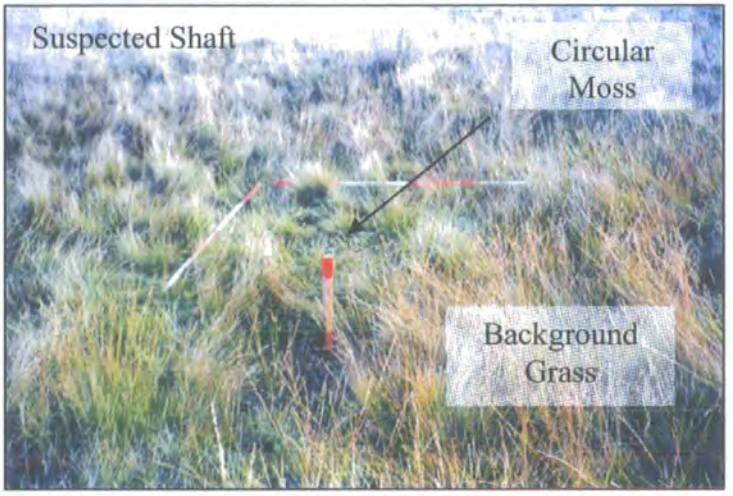

Figure 3.33: Suspected shaft of circular vegetation and thermal anomaly

Ground conductivity was measured in Area B at 2m intervals along the survey line using the EM31 technique with coil separation of 3m to give an observation depth of 1.5m. The survey line intersected the pronounced topographic feature known to represent an abandoned mine shaft at 50m from the profile origin and the suspected shaft at 80m from the profile origin represented by an anomaly on the thermal imagery and represented an area of ground moister than the surrounding moorland. Results of the EM31 survey were displayed in graphical format showing the conductivity of the ground measured at a distance from the origin of the profile to enable the comparison of the electromagnetic field properties of the known and suspected shaft features (Figure 3.34).

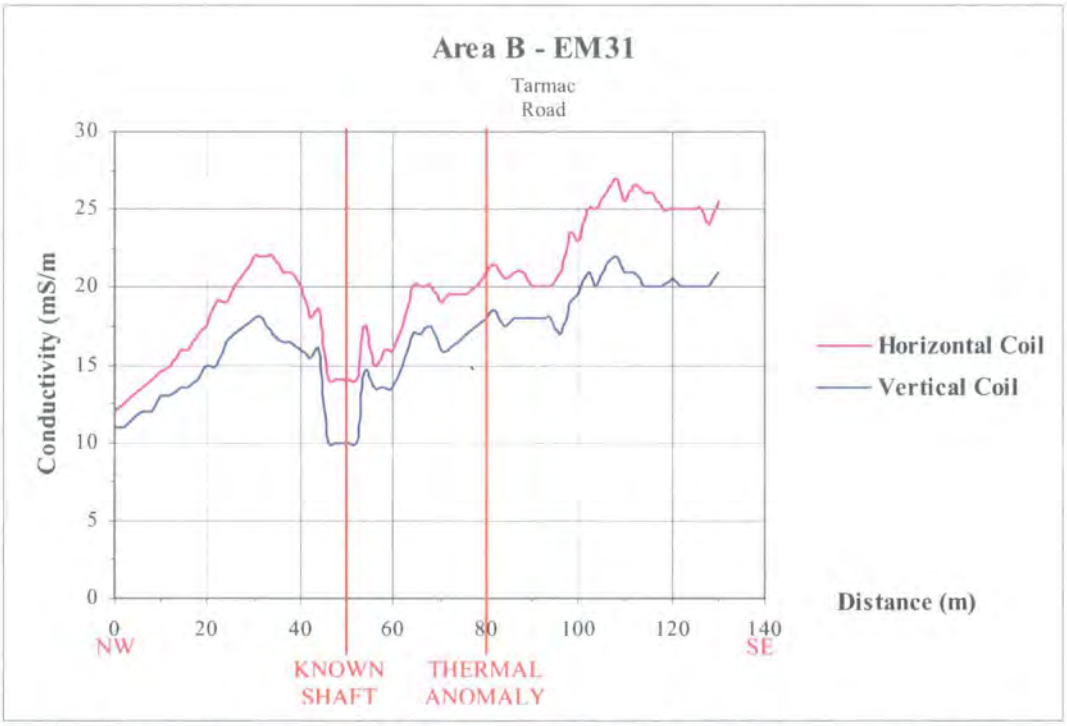

Figure 3.34: EM31 profile for both horizontal and vertical coil configurations

The conductivity profiles observed by the horizontal and vertical coil configurations are very similar in characteristic, with a gradual rise in conductivity from the profile origin and a prominent negative anomaly at 50m, corresponding to the position of the topographically pronounced shaft. This suggests that there is a strong variation in physical characteristics associated with the topographic shaft at the 1.5m observation depth. The conductivity then rises gradually from the shaft towards the background vegetation with a slight plateau of conductivity at 91-95m corresponding to the position of a tarmac road before measurements continue to rise over the background vegetation. There is no obvious anomaly observed through either horizontal or vertical coil configurations relating to the suspected shaft at 80m from the profile origin, suggesting that there is no physical variation associated with the suspected shaft at this observation depth. The suspected shaft therefore requires further geophysical investigation in order to determine whether the thermal anomaly represents a true physical variation beneath the surface.

Ground conductivity was measured using the EM34 in both horizontal and vertical coil configurations at 2m intervals along the same survey line for the EM31 technique. Coil separation was selected at 20m to give an observation depth of 8m and also at a separation of 10m to give an observation depth of 6m. Results of the

EM34 survey were displayed in graphical format showing the conductivity of the ground measured at a distance from the origin of the profile (Figure 3.35).

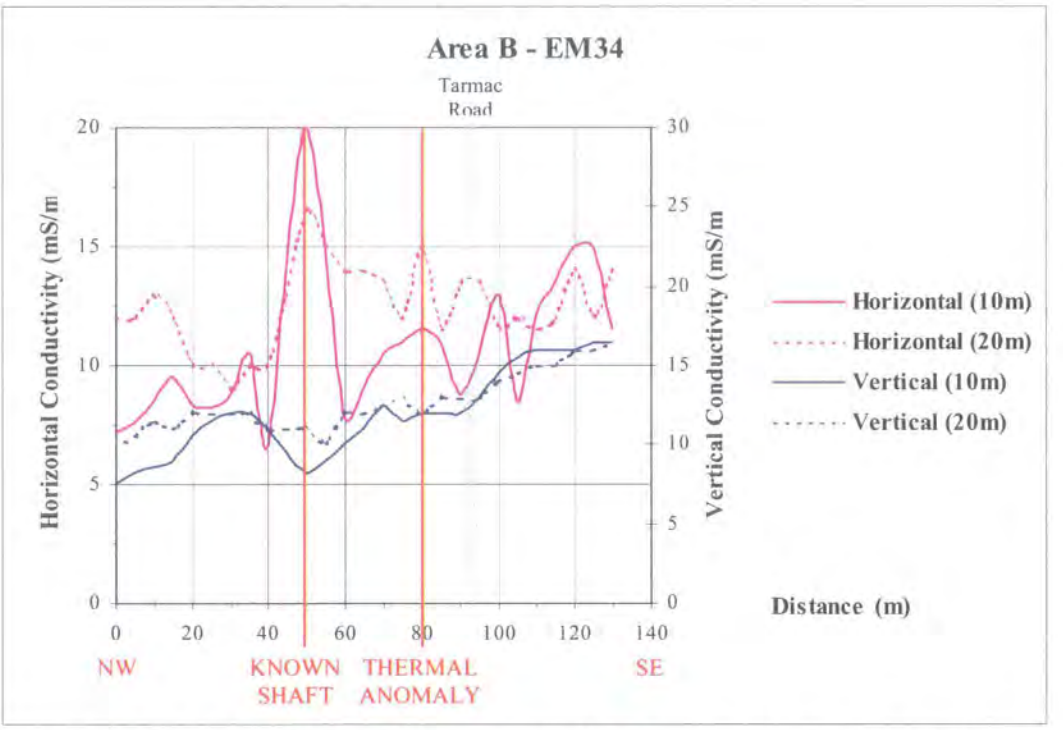

Figure 3.35: EM34 profile for both horizontal and vertical coil configurations

The conductivity profiles observed by the horizontal coil configurations showed a strong positive anomaly at both observation depths corresponding to the position of the pronounced topographic shaft, with a moderate negative anomaly observed at both observation depths through the vertical coil configurations. This suggests that there was a strong variation in physical characteristics associated with the topographic shaft and that the shaft was probably not backfilled with material at either observation depth. There was a slight rise in conductivity towards the suspected shaft feature in the shallower-viewing horizontal and vertical coil configurations with the deeper-viewing coil configurations showing a more pronounced positive anomaly in the horizontal configuration and a negative anomaly in the vertical configuration. Since the vertical coil configuration is more sensitive to near-surface variations, the results of the EM34 evaluation suggest that the suspected shaft may possess a variation in physical characteristics at depth. In this survey, the tarmac road was less easily observed in either coil configuration.

The results of the EM31 and EM34 surveys over the thermal anomaly were inconclusive for all coil configurations and observation depths. Therefore, further geophysical investigation was required to determine the nature of the thermal anomaly. A Wenner resistivity profile was surveyed with an electrode separation of 5m to give an observation depth of 2.5m. The survey line was selected perpendicular to the original survey line to intersect the thermal anomaly (Figure 3.36).

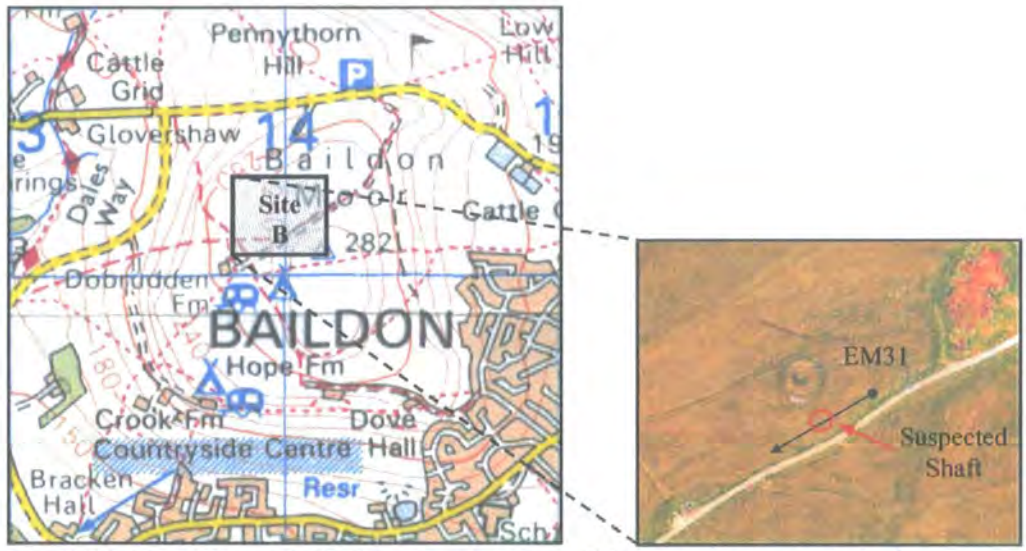

Figure 3.36: Location of EM31 secondary profile over suspected shaft

Results of the resistivity survey (Figure 3.37) show a gradual decrease in resistivity across the background vegetation with a strong positive anomaly at 30m, at a 2m offset to the position of the thermal anomaly. The suggestion from this is that the thermal anomaly may represent a ventilation shaft since these are known to be generated at an angle to a mine shaft and may explain the offset between the thermal anomaly and the variation in soil properties at the 2.5m observation depth. However, there is a secondary positive anomaly at 40m that does not correspond to a thermal anomaly, but coincides with an area of trampled vegetation that may cause a variation in the moisture of the ground at this location. The resistivity measurements therefore cannot be used in isolation to determine the nature of the thermal anomaly at the 2.5m observation depth. Further investigation would therefore be required using additional techniques to determine the nature of the thermal anomaly, however there was insufficient time to conduct additional surveys using the equipment.

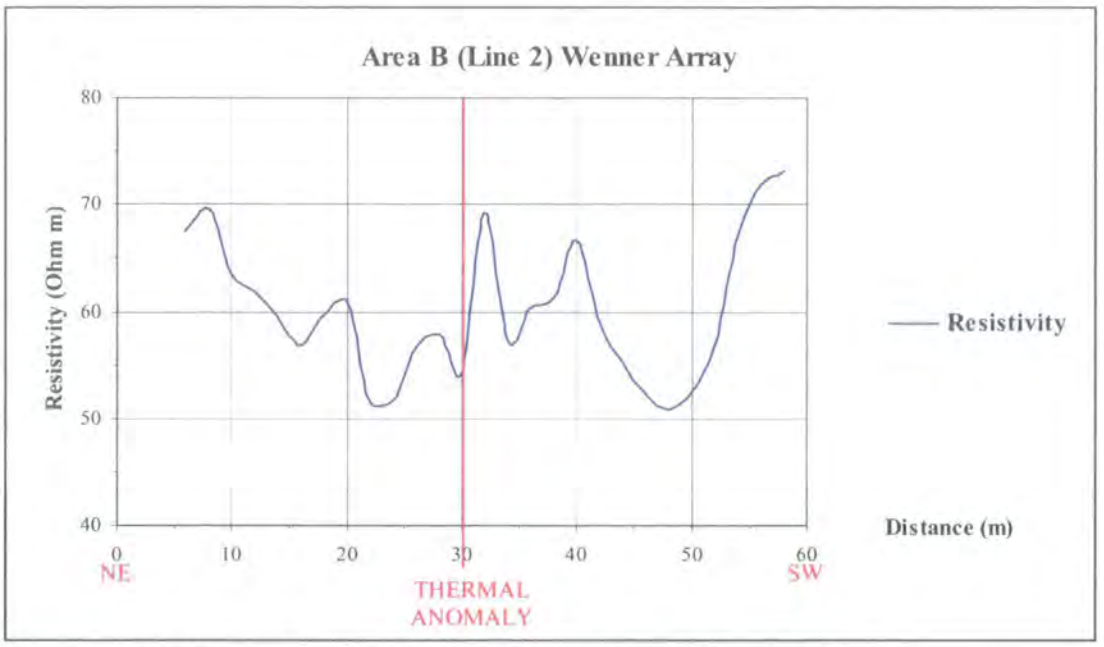

Figure 3.37: Wenner resistivity profile over thermal anomaly

Results of the geophysical evaluation of Baildon Moor have shown that a combination of techniques was essential for the prospection of the suspected shaft features. In Area A, the circular feature of suspected shaft origin showed similar vegetation and thermal characteristics as the documented shaft. Geophysical profiles were measured using Wenner resistivity, EM31 and EM34 techniques across the documented and suspected shaft features. The geophysical characteristics of the documented shaft were compared with the characteristics measured across the secondary feature and the similar response pattern suggested that the secondary feature also represented a shaft. In Area B, the circular thermal anomaly showed a similar thermal anomaly to the documented shaft, but displayed a very different vegetation and topographic expression. Geophysical profiles were measured using EM31 and EM34 electromagnetic techniques in both horizontal and vertical coil configurations at a variety of observation depths across the documented and suspected shaft features. The geophysical characteristics of the documented shaft showed an anomaly through horizontal and vertical coil configurations of both techniques at shallow and deep observation depths. These were very different in comparison with those measured over the suspected shaft where there was only a slight anomaly observed at only the deeper observation depth of the EM34 coil configurations. This suggested that the thermal anomaly was of a different nature to the documented shaft, as suspected by the pronounced difference in topographic expression. An additional

Wenner resistivity survey was performed perpendicular to the original profile line to intersect the thermal anomaly and results showed that there was a variation in resistivity measured across the secondary feature. This corresponded well with the presence of an area of high moisture content however additional geophysical profiles would be required across the same survey line to be sure of the nature of the thermal anomaly. The results of the geophysical surveys performed on Baildon Moor have therefore shown that a combination of techniques was essential for the prospection of the suspected shaft features.

3.8 SUMMARY of SHALLOW SUBSURFACE FEATURES and their PHYSICAL CHARACTERISTICS

Shallow ground disturbance creates a differential heat flux between the undisturbed soil matrix and that of the buried feature and it is this characteristic that provides the potential for detection using thermal imagery. Variations in the temperature observed at the soil surface can be related directly to that of the buried feature where the surface is devoid of vegetation or is covered by very sparse vegetation. As the vegetation canopy closes, the thermal response of the soil will be completely masked by the overlying vegetation resulting in a more complex relationship between the vegetation and the buried feature due to the interactions of the energy fluxes between the soil and vegetation canopy and within the canopy structure.

The temperature contrast between the buried feature and the surrounding matrix will vary across the diurnal cycle in response to the variation in thermal properties of the materials with the greatest contrast occurring when the surface is at its maximum temperature at solar noon and at its minimum temperature just before dawn. The acquisition of a pair of thermal images will therefore improve the ability to detect features when comparing the thermal contrast with a thermal image acquired at a single time in the diurnal cycle. It is difficult to know whether the features detected by the thermal contrast relate to buried features, or whether they relate to structural differences within the vegetation.

The case studies provide a wide range of environmental situations where shallow buried features are known to occur under a variety of vegetation conditions.

In order to understand the structure of the subsurface in each of the settings, a series of geophysical surveys are performed to identify physical variations in the subsurface. Results from the different contexts show that the application of a variety of geophysical techniques is vital in order to identify subsurface variations since certain techniques are more appropriate for specific soil conditions.

The position and structural appearance of the geophysical features are then compared to the position of anomalies identified on the multispectral and thermal imagery to determine the suitability of using this type of data for the detection of shallow buried features. However, prior to analysis the digital data require a series of pre-processing steps in order that any noise or positional variations in the data are removed so that the various datasets can be directly compared and contrasted. The following chapter discusses the data pre-processing techniques that are applied to the digital image data before the qualitative image analysis and thermal assessment are performed.

4 AIRBORNE THERMAL DATA PROCESSING

In its most raw format, data recorded by the NERC Daedalus-1268 Airborne Thematic Mapper contains radiometric, geometric and atmospheric distortions or imperfections that prevent or hinder meaningful interpretation of the raw digital data. The processes of removing the unwanted or distracting features are termed preprocessing techniques as these operations are performed prior to interpretation of the imagery. The main preprocessing techniques applied to the raw image data are radiometric calibration, geometric correction and atmospheric correction procedures. Although radiometric calibration is performed by the NERC Airborne Remote Sensing Facility, there is still a need for further preprocessing to remove geometric distortions and atmospheric effects from the imagery. Geometric correction can be performed using either ground control point collection or through the integration of the image data with information on the aircraft attitude during image acquisition. Atmospheric effects should ideally be removed from the data, however if this is not possible then radiometric normalisation may be performed to provide similar radiometric conditions by matching image spectra to field spectral measurements. If field spectra are not available for a multi-temporal dataset, variations in the illumination conditions may be compensated for by image normalisation. Each of the preprocessing techniques is described below after a brief description of the extraction procedure required before the image data can be visualised.

4.1 MULTISPECTRAL ATM DATA

The image data recorded by the Daedalus-1268 Airborne Thematic Mapper (ATM) is supplied in NASA's Hierarchal Data Format (HDF). This data is available in a range of standard data products that define the amount of processing that has been applied to the raw data before delivery. The NERC Airborne Remote Sensing Facility supply the data in radiometrically-calibrated Level 1b format, if requested. In this format, pixel values correspond to the radiance measured for a particular pixel with detail on the navigational parameters of each scan line appended to enable further processing of the data.

Although HDF data format is supported by most commercially available image processing software, the ATM images cannot be directly visualised as there

appears to be an inconsistency between the format of the data and the structure of the data expected by the image processing software. The images therefore require conversion to a more suitable digital format and this is achieved using the *azexhdf* software provided by NERC along with the image data. The *azexhdf* software operates on a UNIX platform, using command lines to extract the imagery for visualisation. Example 4.1 indicates the standard command line defined to extract a radiometrically-calibrated image (input_1b.hdf) and generate an output file in a band interleaved by line format (-B) whose values represent the radiance (-r) measured for each pixel.

Example 4.1 **azexhdf input_1b.hdf –r –B output_file**

In the above example, there is no file format specified for the output image to enable the data to be exported as a generic binary image that could be read into any commercially available image processing software. During the extraction process, the *azexhdf* software indicates the number of rows, pixels and bands contained within the file, together with the type of data and the type of band sequencing. This detail must be known in order to specify the dimensions of the generic binary image for visualisation and importation into the image processing software. The images are initially imported into PCI® image processing software for subsequent manipulation using the IMAGERD process in XPace.

In addition to the process of image extraction, the *azexhdf* software also enables the determination of supporting information contained in the image header, such as mission, navigational and instrumentation parameters. The entire parametric detail contained in the header can be extracted (-h) to a text file to reveal values associated with specific parameters and the abbreviations required in the command line for more detailed parametric extraction (Example 4.2).

Example 4.2 **azexhdf –h input_1b.hdf input_1b.txt>input_1b.txt**

The most important detail given in the extracted header for the research is the units of radiance associated with the pixel values and the scaling factors applied to the values to ensure that the radiance is measured with the correct number of decimal places. This is very important where the pixel radiance values are used in numerical

models for assessing the apparent thermal inertia of the surface. The units of radiance associated with the imagery are $\mu W\ cm^{-2}\ sr^{-1}\ nm^{-1}$, which are different from the standard units of radiance detailed in Chapter 2 used in Planck's Radiation Law. This problem will be addressed in more detail in Chapter 6.

Other important parameters that are extracted from the header are the upper (ATwavu) and lower (ATwavl) spectral wavelengths associated with each image channel. This is important as the mean spectral wavelength of each channel must be specified in order to perform meaningful spectral analysis of the data (Example 4.3).

Example 4.3 **azexhdf -hd ATwavu -v 11 a194031b.hdf out_u.txt>out_u.txt**

Once the wavelength data was extracted, the spectral information is attached to all subsequent images since the same instrument was used to acquire all the data channels. It is very important to be aware of the units associated with the wavelength data to ensure that there is a consistency between the spectral detail of all the imagery and that of any ancillary spectral data. The wavelengths are initially specified in nanometers, but can be easily converted to other units in the image processing software.

The image header also contains detail on the calibration factors used by the NERC Airborne Remote Sensing Facility to provide the radiometrically-calibrated images. The following section describes the radiometric calibration procedures performed in order to provide the image data in radiance units.

4.2 RADIOMETRIC CALIBRATION

Radiometric calibration is an instrument-specific and inter-channel correction that removes systematic or random inconsistencies that degrade the radiometric content of the digital image data (Mather, 1999). The main causes of radiometric inconsistency are the periodic drift, malfunction or electronic interference of the detectors during data acquisition. It is especially important to correct for these problems where studies require the comparison of pixel values from images obtained at different times, or where estimates of surface parameters such as reflectance are required for use in physical models. Calibration can be performed either by imaging

an external calibration target on the ground and relating the measured value to the image data, or by using internal sensor calibration data.

Instrument detectors are designed to produce a linear relationship between the digital number recorded and the spectral radiance measured for a pixel, with the slope and intercept of the line known as the gain and offset calibration factors respectively (Equation 4.1).

Equation 4.1 $Radiance = Offset + Gain * Pixel\ Value$

Each detector has a different set of calibration factors associated with it that are determined prior to instrument deployment, although the factors will vary over time as the response of the detector degrades and therefore substantial differences will occur in radiometric calibration if incorrect calibration factors are applied to the data. Detail on the gain factors for each image channel can be extracted from the image header, but since the images are already radiometrically-calibrated by the NERC Airborne Remote Sensing Facility, there is no need to apply the above equation to the data (Wilson, *pers. comm.*)

Although the images are radiometrically calibrated prior to handling, it is necessary to perform other preprocessing techniques to remove the effects of variations in atmospheric conditions occurring between the images and also to correct for geometric distortions. The topic of geometric correction is discussed in the following section.

4.3 GEOMETRIC CORRECTION

Raw digital images contain geometric distortions that must be removed from the data in order that the structure of the ground surface visualised on the imagery will correspond directly with its appearance on a map. The transformation of images so that they have the scale and projection properties of a map is known as geometric correction and this is especially important when comparing multiple images of an area or where the information extracted from the images requires integration with ancillary data. The main sources of geometric error result from platform instabilities, including variations in altitude and attitude of the platform, and relief effects that cause non-linear distortions during image acquisition (Figure 4.1).

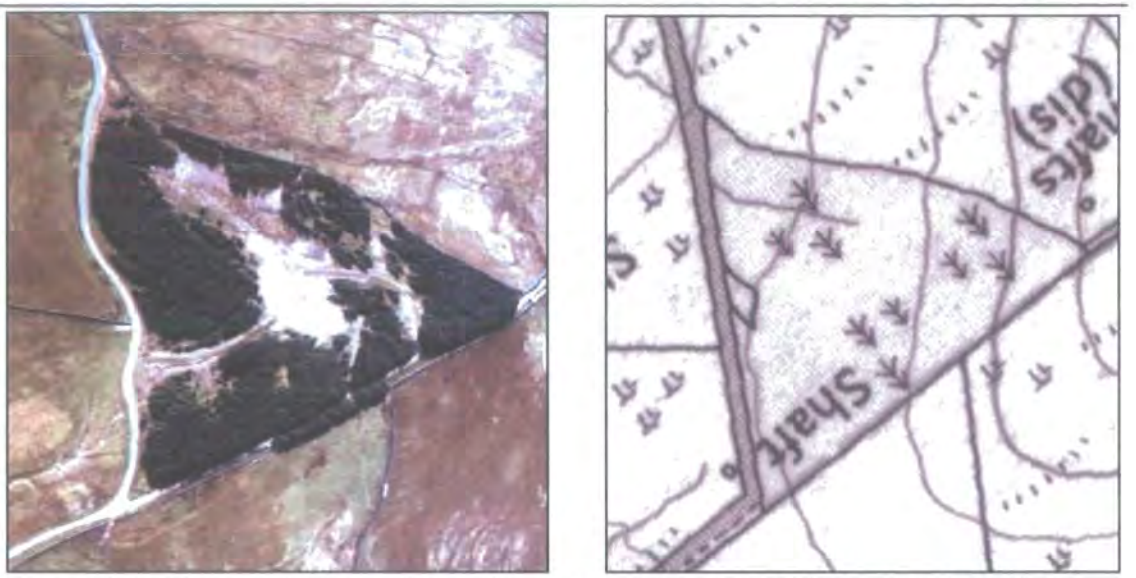

Figure 4.1: Geometric distortions of imagery compared to base map (right)

All sources of geometric distortions must be removed prior to analysis or integration with other datasets. The low altitude airborne platform supporting the ATM was affected by air turbulence and fluctuating winds during data acquisition that cause pitch, roll, yaw and crabbing of the aircraft causing incoherent movement between the sensor and the ground surface. Some of the motion was reduced through gyro-stabilisation of the sensor, but the directional motion of the aircraft required the acquisition of ancillary navigational data, specifically the latitude and longitude of each scan line, in order to transform the image into the specified coordinate system and adjust the image so that it represented the geometric integrity of a map. This technique tends to be more successful where the topography shows little variation, however where surface relief effects are greater the distortions can vary with respect to the distance occurring between the aircraft and the elevation of the terrain. When viewing at nadir, the relief effects tend to be negligible but as the viewing angle increases off-nadir, there may be a greater geometric distortion of sloping surfaces. It was possible to remove relief effects by integrating the image data with a digital elevation model and this process will be discussed in a later section.

Geometric correction involves the determination of the relationship between the two coordinate systems associated with the map and the image. The process defines a set of points representing the pixel centres in the corrected image that, when considered as a rectangular grid, define an image with the desired geometric properties (Mather, 1999). The process then estimates the new pixel values based on some mathematical relationship between the input and output pixel locations.

The following sections describe the two main geometric correction procedures of Ground Control Point Collection and Automated Geocorrection that were applied to transform the images into a grid of pixels with associated coordinates.

4.3.1 Ground Control Point Collection

Ground control point collection is an image-based approach to geometric correction that requires the identification of well-defined features, such as field boundaries, road intersections, building corners or the centre of mineshafts, that can be accurately located on both a the digital image and the base map. These features are termed ground control points (GCPs) and are used to convert the image coordinates to map coordinates. The collection of GCPs requires the presence of a good base map at a suitable scale from which the control coordinates can be obtained. The coordinates can be extracted using a digital map or by manual extraction from an analogue source. Geometric correction is performed on each study site using the PCI® image processing software, with GCP correlation between the digital image and a digital map source.

The initial step in geometric correction is to generate a geocorrected database whose bounding coordinates enclose the study site. The software internally determines the positions of the database pixel centres from the defined pixel resolution, database dimensions and bounding coordinates. The geocorrected database then provides a reference coordinate system for rectification of an image.

Prior to geocorrection, it is first necessary to import a digital base map into the geocorrected database for accurate GCP location and this is achieved by obtaining Digital OS Landline vector data from the EDINA Digimap online facility (www.edina.co.uk). The data obtained through this facility is provided in NTF file format and requires conversion to the standard vector shape (SHP) file format using a file conversion in Map Manager® v6.1. The individual vector tiles covering the study site are viewed in ArcView® and are merged together, specifying details of the vector grids to be merged in the single command line of the Map Calculator available in the Spatial Analyst module (Example 4.4). This provides a single vector layer for the geocorrected database from which to collect the GCPs.

Example 4.4 **([grid1].mosaic({ [grid2],[grid3],[grid4]}))**

The PCI GCPWorks module enables geocorrection of the study images, establishing the Full Processing requirements at the outset for image transformation using GCP collection from a vector source. The Thin Plate Spline algorithm is selected as the desired mathematical model for transformation as this ensures that the warping of the data is exact at each selected control point with errors increasing with distance from the point forming a tessellated surface. Once these details are specified, image geocorrection begins with selection of an uncorrected image, the geocorrected database and the vector layer from which to collect the GCPs. GCP collection begins with the selection of a pair of points, a pair being formed by selecting a feature on the image and then its corresponding location on the vector layer (Figure 4.2).

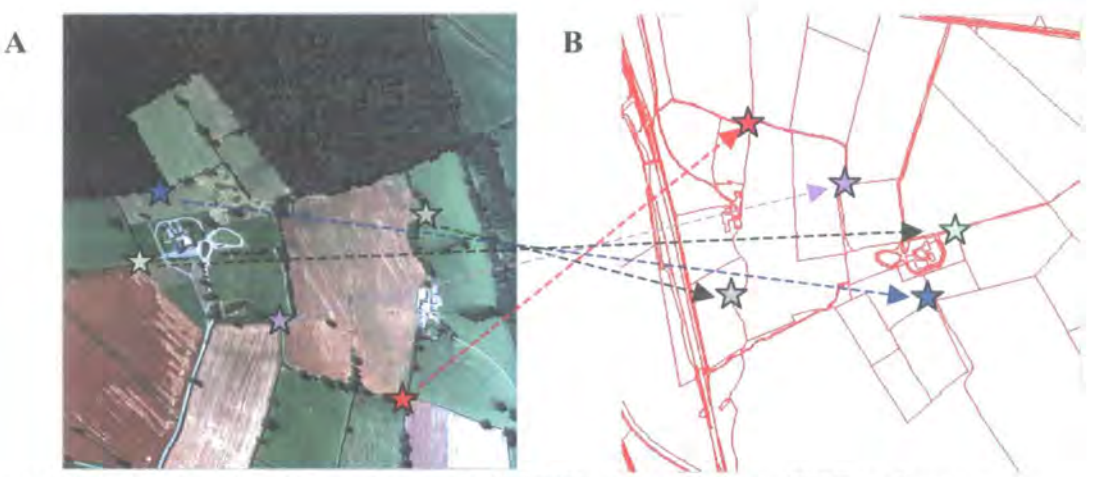

Figure 4.2: GCP collection using PCI GCPWorks software. GCP pairs are selected at points recognisable on (A) image and (B) vector layer

The GCP selection process is straightforward, with points selected at road intersections and field boundaries for Bosworth and at the intersections of roads and paths in Baildon Moor and Weardale. The vast majority of these features are easily recognisable on both datasets. However, problems arise in GCP selection on the Bosworth imagery where the position of some field boundaries on the vector layer has been altered on the ground since generation of the OS map, due to removal of hedgerows since mapping was undertaken (Figure 4.3).

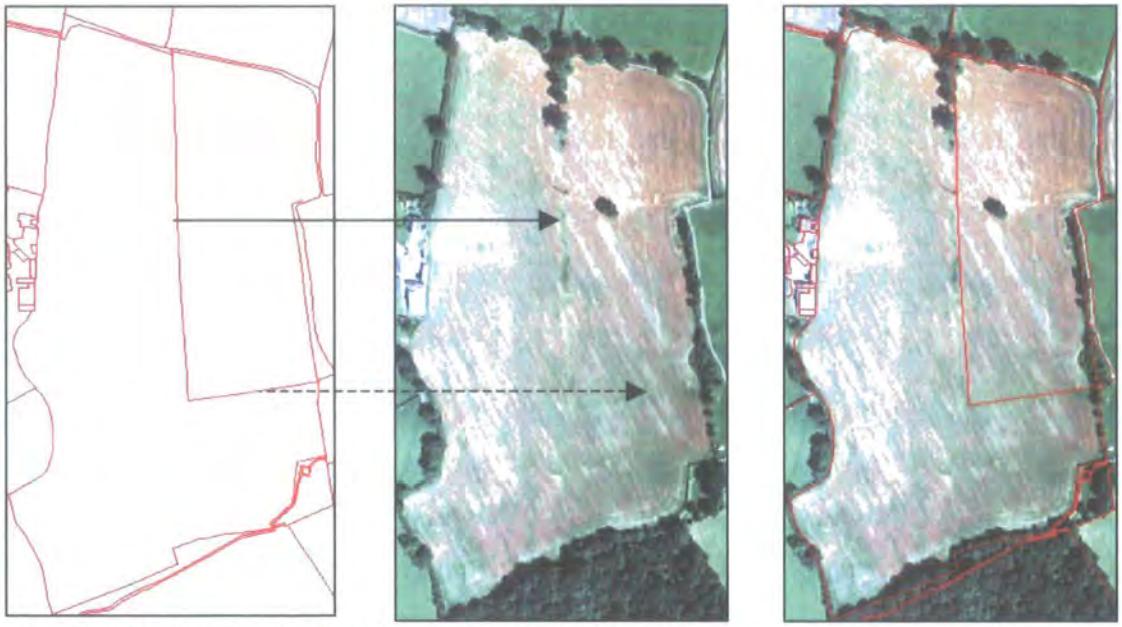

Figure 4.3: Change in field boundary position between vector layer and its potential position on image

Vegetation also causes a problem for GCP selection for Bosworth, especially around the edges of the fields with either the shadow cast by the hedgerow or the crown of the trees masking the position of the field boundary from view on the image. When the foliage is at an early stage in the growth season it is possible to make a reasonable estimate as to the boundary position. However, where the foliage covers a greater surface area later in the growth season, alternative points are selected on either side of the problem feature.

The spatial relationship between the GCP pairs is assumed to represent the image distortion and is used to calculate the transformation required to correct the image into the database coordinates. There is a minimum requirement of three GCP pairs that are defined in order to calculate the mathematical transformation. However, the transformation is more accurate through collection of as many pairs as possible. When the fourth GCP point is selected from either source, the software estimates the position of its corresponding GCP. If the estimated point is positioned far from its true position, the GCP must be moved to the appropriate position. To ensure GCP estimation is as accurate as possible, the initial three GCP pairs are ideally selected with a wide spatial distribution. However the estimation is poorer in accuracy where there is a strong topographic variation. In this case, more GCP pairs are selected around the feature to reduce the errors during transformation. Once a sufficient

number of GCP pairs span the uncorrected image, the points are saved for reference and the image transformed into the coordinate system of the geocorrected database using an appropriate resampling technique.

The software offers a range of different methods for resampling the data into the new coordinate system from Nearest Neighbour and Bilinear Interpolation to Cubic Convolution, with progressively more complex mathematical transformations. Bilinear Interpolation uses a distance-weighted average of the four pixels in the input image nearest to the output pixel. Cubic Convolution evaluates the nearest sixteen input pixels to the output pixel and in both cases the output pixel has a value representing the mathematical relationship of the input pixels. To retain the subtle variations in the absolute pixel values of the uncorrected image, Nearest Neighbour resampling is selected, which assigns the pixel value from the uncorrected image directly to the spatially closest pixel position in the geocorrected database (Figure 4.4). Geocorrection is then performed for the first image of the study region (Figure 4.5).

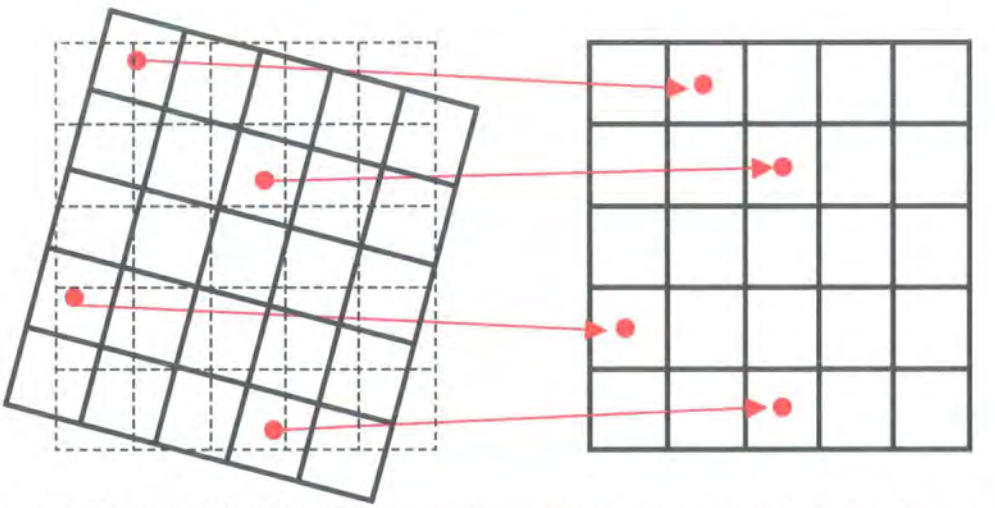

Figure 4.4: Nearest Neighbour Resampling where uncorrected pixel values are transferred to the closest corresponding pixel location

Figure 4.5: Geocorrection of image (A) using GCP pairs to generate geocorrected image (B)

Several images are needed to provide complete coverage for the study site so that once the first image is rectified it is necessary to mosaic together all subsequent images with the geocorrected image. Image mosaicking is achieved by performing the GCP collection routine outlined above for all subsequent images. However, before the final stage in their transformation, an area is defined where the overlap between images is minimal in order to generate a single uninterrupted image of the study site when the images are blended together. Mosaicking involves the creation of a polygon within the uncorrected image that encloses the desired area. The polygon edges are drawn around field boundaries and roads, avoiding fragmentation of individual fields and shaft features. Pixels in the geocorrected database that overlap ones enclosed within the polygon are then replaced by the corresponding pixels from the new image on geocorrection. This ensures that the boundaries between the images are not easily seen in the geocorrected image of the study site.

Once the first mosaic of each study site is generated, the geocorrection process is repeated for the additional acquisition dates. In these cases, GCP collection is performed using the initial geocorrected image mosaic as the base coordinate source, with GCPs selected as features common to the two images. This ensures that co-registration of the images is as precise as possible so that the variability in the diurnal or seasonal response of any feature can be more easily assessed. For consistency in the warp transformation, GCPs are ideally selected at the same positions for all the images but this is not always possible due to variations in feature visibility. This is especially the case for co-registration of the day and night thermal images where features that show a strong thermal contrast with the surrounding material on the day

imagery show a much poorer contrast in the night imagery and are therefore less easily identified. Some of the field boundary hedgerows on the Bosworth imagery and mineshafts on the Baildon Moor imagery display such characteristics where the night thermal response of the features is similar to that of the surrounding vegetation. In this case GCP pairs are selected at the best estimate of the feature location. Although this results in a variation in the number and position of the GCP pairs, there is little visible affect on the warp transformation of the multitemporal images.

Both Bosworth and Baildon Moor represent two situations where there is very little variation in topography over the study sites and the GCP collection procedure generates geocorrected images that display a similar spatial integrity to the base map. When this process is attempted for the Weardale imagery, where there is a much greater topographic expression, the number of GCPs required to correct each image is extremely high and so the process is very time-consuming and produces poor results. An alternative geocorrection method for the Weardale data is then required that incorporates the parametric detail on the aircraft position during scanning. NERC supply an Automatic Geocorrection software package along with the data and this is then applied to the Weardale data.

4.3.2 Parametric Geocorrection

The parametric approach to geometric correction is less dependent on the collection of ground control points from data sources and provides an automated process using detail on the external orientation of the airborne platform (Roy *et al*, 1997). The NERC airborne platform measures sensor orientation using an inertial navigation system integrated with a GPS to give detail on the latitude and longitude during data acquisition. This data is incorporated into the header of the Level 1b HDF image to indicate the position of the aircraft at the start and end of every scan line.

The *azgcorr* Automatic Geocorrection software, supplied by the NERC Airborne Remote Sensing Facility, is designed specifically for the geocorrection of ATM data. The *azgcorr* software uses the navigational information contained in the image header to compensate for the geometric distortions present in the imagery due to the motion of the aircraft.

The *azgcorr* software operates on a UNIX platform, with a distinct set of command lines to generate a geocorrected Level 3b HDF image of the study site. Example 4.5 indicates the standard command line defined to geometrically correct the image (input_1b.hdf) and generate an output image (output_3b.hdf) with a specified pixel resolution (-p) and default settings of Nearest Neighbour resampling and with a geocorrected image orientation with North at the top of the image.

Example 4.5 **azgcorr -1 input_1b.hdf –3 output_3b.hdf –p 2 2**

A suitable output pixel resolution is defined from detail on the spatial resolution given on extraction of the image data using the *azexhdf* software (Example 4.1). As a default, the entire number of image channels present in the data is geocorrected using the command line (Example 4.5). This is only suitable for geocorrection of the day time imagery since the important data in the night imagery is contained in only the thermal channel. The individual thermal channel is then specified (-b) for geocorrection of the night data (Example 4.6).

Example 4.6 **azgcorr -1 input_1b.hdf –3 output_3b.hdf –p 2 2 –b 11**

Further to a basic geocorrection using only the aircraft navigation coordinates, geocorrection is performed by including a digital elevation model of the study site to compensate for the effects of aircraft motion relative to the relief of the terrain. Ordnance Survey 1:50,000 scale Panorama digital elevation model data for Weardale can be obtained from the EDINA Digimap online facility (www.edina.co.uk) in NTF file format, which is converted to a vector SHP file using Map Manager® v6.1. The elevation data is then visualised in ArcView and converted to a grid before exporting to an ASCII text file. In order that the data is recognised as a DEM in the *azgcorr* software, a single line of comma-delimited text is added to the start of the ASCII text file to define the dimensions, bounding coordinates and spatial resolution of the DEM. The geocorrection process is then performed using the DEM (-eh) and the appropriate image (Example 4.7).

Example 4.7 **azgcorr -1 in_1b.hdf –3 out_3b.hdf –p 2 2 –b 11 –eh dem.txt**

The initial DEM obtained for Weardale has a spatial resolution of 50m and on visualisation of the output geocorrected image, it is apparent that this grid resolution is inappropriate for geocorrection since the geocorrected image displays large gaps containing no image data where the spatial data of the image is forced to stretch over a wide area on the DEM. The gaps can be removed by performing the geocorrection using a DEM with smaller spatial resolution, generated using stereo aerial photographs that had been acquired simultaneous to the image data by the Wild RC-10 survey camera mounted on the aircraft. The analogue stereo aerial photos are scanned on a photogrammetric scanner for importation as digital images into the Intergraph® software operating on a Microstation at the British Geological Survey. The calibration and optical properties of the survey camera are provided by the NERC ARSF to compensate for lens distortions on the aerial photography. These parameters are specified at the outset and the software compensates for camera distortions using these values together with the position of the fiducial marks visible on the digital images. Once the general arrangement of the photos is defined, the software automatically identifies points that overlap between the images. The user then checks their absolute positions and assigns elevation values to specific points. The software then generates a DEM with a specified spatial resolution from the images, together with a series of orthophotos with the scale, tilt and relief distortions removed. This DEM is integrated with the Weardale images in the *azgcorr* software to generate a suitably geocorrected image dataset.

The geocorrected Level 3b HDF images once again cannot be directly visualised in the image processing software as the file format is incompatible with the expected structure of the data. The geocorrected images are again extracted to a generic binary format using the *azexhdf* software as for the Level 1b HDF images (Example 4.1). When visualised, the geocorrected images still show a small degree of geometric distortion and therefore it is necessary to perform an additional GCP collection routine on the images to remove further errors and co-register the day and night images. As with the Bosworth and Baildon Moor data, several images cover the Weardale study site and so during the GCP collection process the images were mosaicked together to provide a single uninterrupted image of the site.

The procedures outlined above provide geometrically corrected images for the study sites. When assessing variations in the response of surface materials, it is important to remove all sources of distortions from the data. With the radiometric and geometric distortions removed from the data, atmospheric effects require to be removed in order that the values represent true variations in material response. The geocorrected images are then imported into ENVI® image processing software (Appendix B1) for visualisation (Appendix B2), making sure that the spectral detail of the image channels is accurately defined (Appendix B3).

4.4 SPATIAL RESIZING

When the geometrically corrected images are imported into the ENVI software it is apparent that there is a difference in the spatial coverage of the images associated with each study site. It is therefore necessary to spatially reduce the images and generate a series of output images that represent the area of image overlap. The area overlap of each study site can be determined by generating a series of masks that represent the coverage of each individual image (Appendix B6.1). Mask definition requires the range of data values associated with the individual images to be examined through calculation of the image statistics (Appendix B11) and specifying the minimum and maximum values associated with each image. The results generate a series of masks representing the spatial extent of each image (Figure 4.6).

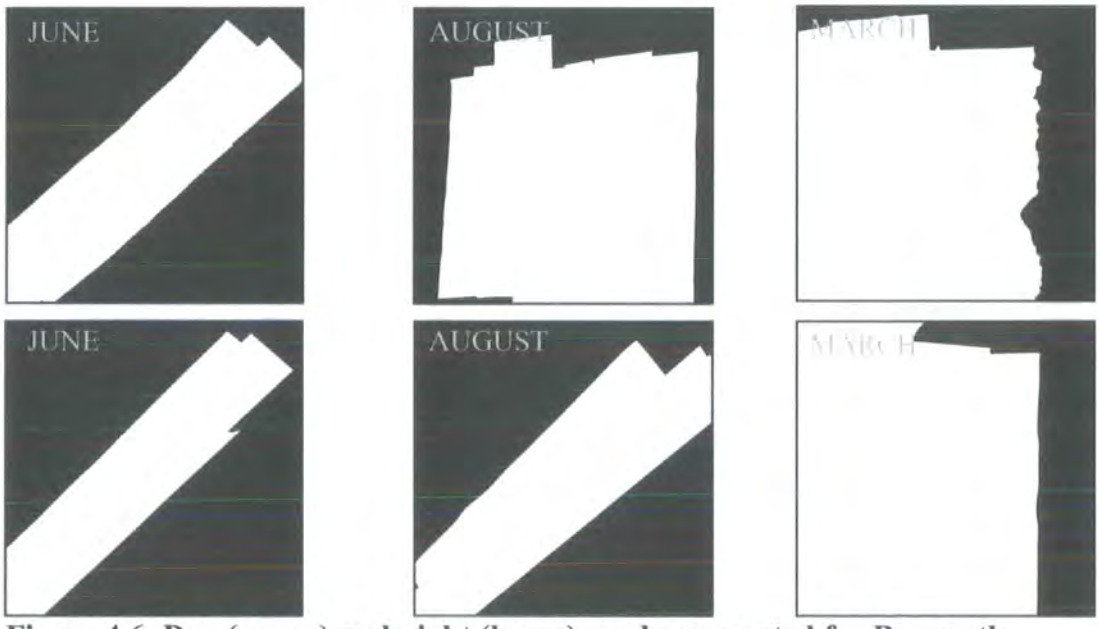

Figure 4.6: Day (upper) and night (lower) masks generated for Bosworth

The overlap between the images is then determined by adding the masks together through simple band arithmetic (Appendix B7). The area of image overlap is then determined from the new mask image (Figure 4.7A) and a secondary mask generated for image overlap by selecting the maximum value associated with added mask (Figure 4.7B). The secondary mask is then applied to the original geocorrected images (Appendix B6.2) to generate a series of images indicating the area of overlap. Similar masks are generated for the Weardale and Baildon Moor datasets though these are not presented.

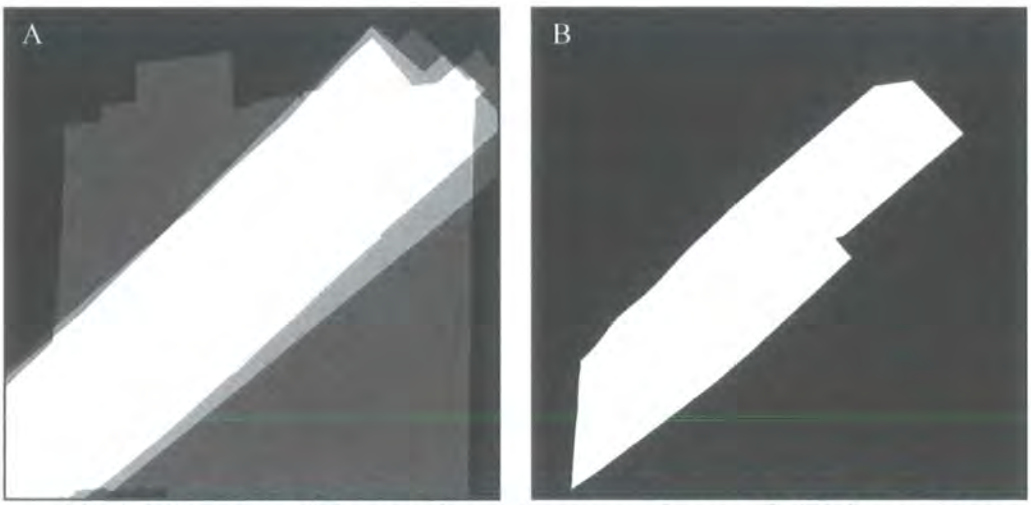

Figure 4.7: (A) Overlap of Bosworth masks generating mask (B) for overlap

When the statistics of the masked images are calculated, it is apparent that a series of 'non-value' pixels are generated outside the overlap area. Since these pixels can produce a problem for further mathematical transformation, the datasets are again reduced in size to exclude these pixels. This gives an added bonus of reducing computation time of the subsequent analyses. Spatial subsets are generated for each site by defining a rectangle on the imagery that contains the surface features of greatest importance, namely the features of archaeological interest and of abandoned mine activity (Appendix B8). The spatial subset generated for the Bosworth study site is selected to incorporate the main fields where geophysical evaluation had been performed surrounding the Battlefield visitor centre (Figure 4.8). The spatial subset of the Baildon Moor imagery concentrates on a small area where mineshaft features are most evident (Figure 4.9) and the spatial subset for Weardale concentrates on an area of mineral extraction scour marks and spoil heaps (Figure 4.10).

Figure 4.8: Spatial subset generated for Bosworth

Baildon Day Thermal

Baildon Night Thermal

Figure 4.9: Spatial subset of Baildon Moor abandoned mine activity

Weardale Day Thermal

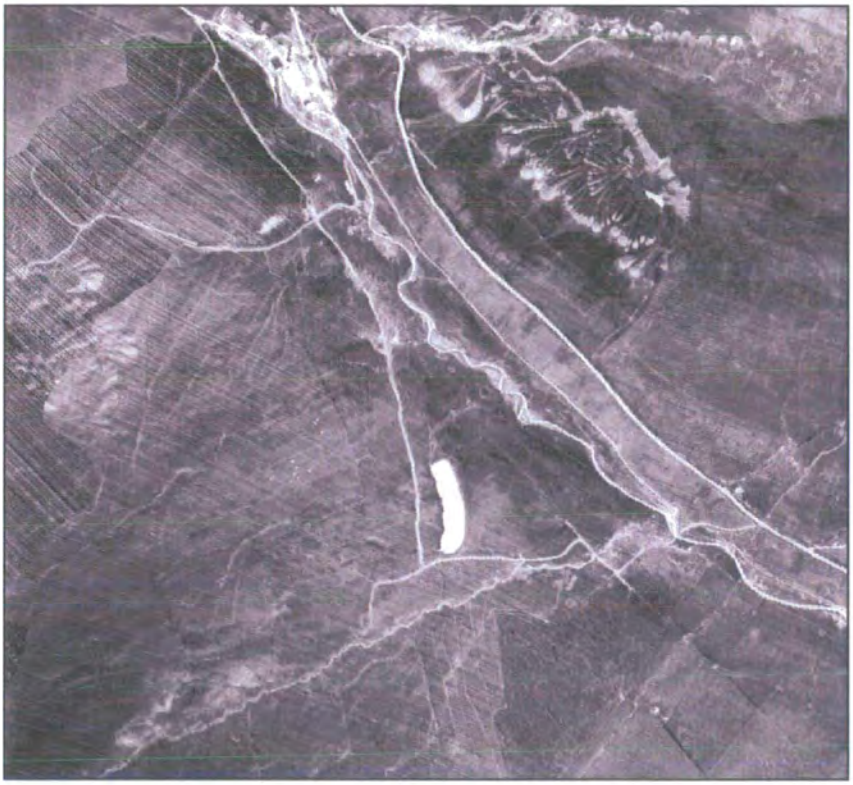

Weardale Night Thermal

Figure 4.10: Spatial subset generated for Weardale abandoned mine activity

4.5 ATMOSPHERIC CORRECTION

The intensity and spectral distribution of energy that is received at the remote sensor will not be the same as the intensity and spectral distribution of energy that left the ground surface. Solar radiation that is reflected by the surface materials passes through the atmosphere before detection and has suffered attenuation by the atmospheric constituents present in the atmosphere. Although greatly reduced under clear-sky conditions, atmospheric attenuation still affects the quality of the ATM data and so a value recorded for a given pixel is representative of the ground-leaving radiance at that point, but may also include atmospheric effects. The problem is then to be able to restore the detected radiation to the characteristics when it left the ground surface to enable pixels radiance values to be related to some physical property of the surface. As the Earth orbits the Sun, the amount of solar radiation reaching the ground surface varies through time and so variations in the solar radiation must also be accounted for when comparing multitemporal data acquired under different solar conditions.

There are a variety of techniques that can be adopted for atmospheric correction of image data. *Radiative Transfer Modelling* can be used to simulate atmospheric conditions at the time of image acquisition by quantifying all the various processes that corrupt the signal from the surface (Hapke, 1993). These models are theoretically sound, but problems arise when values for important atmospheric parameters have to be estimated and inserted into the radiative transfer equations, particularly when detailed meteorological detail is unavailable. Radiative transfer modelling was not pursued because of the lack of meteorological data for accurate quantification of the necessary parameters.

Image Normalisation can be carried out without the need to input additional information and can be used to remove the effects of variations in illumination conditions and solar illumination between the multitemporal images using the spectral response of a spectrally flat target material whose response is assumed to be stable between the times of imaging (Warner & Chen, 2001). *Empirical Line Calibration* is the most commonly used technique where empirical relationships are produced between the radiance values measured at the sensor and reflectance values measured over a number of target materials simultaneous to image acquisition (Smith & Milton,

1999). The main technique adopted for atmospheric correction of the ATM image data was Empirical Line Calibration with Normalisation of the multitemporal images acquired over Bosworth.

4.5.1 Empirical Line Calibration

Empirical Line Calibration (ELC) assumes that there is a range of target materials of different reflectance characteristics present in an image and requires the measurement of the reflectance spectra of each target material at ground level simultaneous to image acquisition (Smith & Milton, 1999). Ideal conditions are that the target materials are homogeneous in composition with a horizontal surface and are devoid of any shadow effects.

The ELC technique compares two sets of spectral data, one measured at the surface over a variety of target materials and the other extracted from the imagery over the same target materials. The ELC algorithm calculates the relationship between the surface and image spectra measured in each spectral channel. The technique therefore matches the sensor spectra with the ground spectral measurements in order to correct for atmospheric effects using a linear regression function.

The use of a single calibration target can provide a simple calibration, but can generate large variations between the expected and measured ground reflectance. Two calibration targets are preferable with a large spectral contrast for removal of atmospheric radiance effects but this still produces a rough approximation for the atmospheric effect. Greater accuracy is achieved by increasing the number of spectral target materials. The method also assumes that there are no differences in illumination conditions across the image with no cloud or topographic shadow effects (Smith & Milton, 1999).

The ELC technique is performed through ENVI® image processing software and requires the acquisition of ground reflectance spectra. Field reflectance spectra are measured concurrent to ATM overflight using a GER1500 spectroradiometer, a hand-held instrument that measures radiance in 512 contiguous spectral bands across visible and near-infrared spectral wavelengths (Appendix A3). The GER1500 is used to measure the radiance spectra of a standard calibration plate and the radiance spectra of a target material. Reflectance is then calculated by taking a ratio of the radiance of

the target material with respect to the radiance of the calibration plate. During spectral measurement, the user specifies whether the spectral reading is associated with either the reference material or the target material with the instrument capable of calculating the reflectance of each target with respect to a single reference reading.

Targets are selected for a wide range of contrasting material types to represent the greatest degree of spectrally diversity between the materials. The targets are also selected with sufficient size that they can be located on the imagery. To ensure accurate target location, the GPS coordinates of each target are measured in the field. The target materials selected for the Bosworth study site consist of dark gravel, light gravel and a range of different vegetation surfaces including pasture, barley, long green grass and short green grass (Figure 4.11).

Figure 4.11: Location of field reflectance spectra for Bosworth study site

Reflectance spectra were measured over these specific targets on three dates of daytime image acquisition. The data acquired during June and August 1998 are downloaded into a text file where the columns of data represented the wavelength of observation, radiance of the calibration plate, radiance of the target material and the automatic calculation of reflectance for the target material. When the data from March 2002 was downloaded it was apparent that the instrument had been unable to differentiate between the radiance recorded for a target material and the radiance of the reference material. As a result, the generated reflectance spectra were incorrect.

Due to insufficient field spectral detail for the March data, an alternative approach to atmospheric correction is therefore sought in order that a direct comparison can be made in the spectral response patterns of a particular material across the multitemporal data. Atmospheric correction using the ELC technique is performed for the June and August Bosworth data using the field reflectance spectra visualised for each of the target materials.

In addition to the field reflectance spectra, image radiance spectra are required for the ELC technique. Radiance spectra are extracted from the appropriate image by defining a region of interest around the target material (Appendix B4). The precise position of the target can be located on the geocorrected image by using the GPS coordinates measure in the field at each target material. The mean spectral signature of the image pixels within each of the defined regions are then visualised and extracted as the image radiance spectra for the suite of target materials. The image radiance spectra are imported into the Data Spectra Collection of the ELC tool together with the field reflectance spectra; pairs of corresponding image and field spectra are matched using regression analysis (Appendix B5.3). Prior to determination of the regression equations, the software resamples the field spectra measured in 512 contiguous channels spanning the visible and near-infrared (0.3044-1.1078μm) to match the spectral overlap of the 8 channels of the visible and near-infrared measured by the ATM (0.4360-0.9620μm), Figure 4.12.

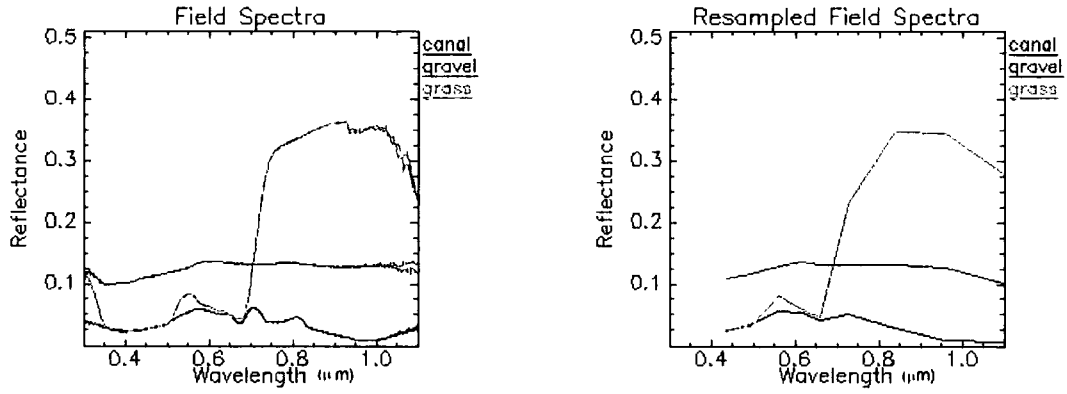

Figure 4.12: Resampling of 512-channel field spectra to the 8-channel resolution of the image in the visible and near-infrared wavelength region

Using the ELC technique, atmospheric effects are therefore removed from visible and near-infrared channels (Bands 1 to Band 8) of the June and August Bosworth data. This technique does not however remove atmospheric effects from data in the short-wave infrared channels (Band 9 and Band 10) nor the thermal infrared channel (Band 11). This is performed through image normalisation and shall be discussed later. In order that the diurnal and seasonal variation in the thermal response of the surface materials can be evaluated, the thermal channel must be calibrated to temperature values.

4.5.1.1 Empirical Line Temperature Calibration

The thermal channel of the ATM is calibrated to surface temperature using the same Empirical Line Calibration technique adopted for atmospheric correction of the visible and near-infrared data. As for the visible and near-infrared multispectral data, the technique forces radiance values measured at thermal infrared wavelengths to match ground temperature values measured in situ over a range of target materials. Ground temperatures are ideally measured simultaneously to image acquisition since the temperature of the materials will vary across the diurnal cycle.

Ground surface temperatures are measured in contact with the same target materials over which ground spectral measurements are acquired. The temperatures are recorded in an ASCII text file together with the wavelength associated with thermal observations (9.9500μm). The ELC algorithm in the ENVI image processing software prohibits the use of a single line of ASCII so another line is added in the text with duplication of the temperature values at a slightly higher observational wavelength (9.9501μm). The new ASCII file then provides ground temperature values suitable for ELC of the data measured in the thermal channel.

Before the calibration is performed, it is necessary to extract the thermal radiance values from the target materials in the image data where ground temperatures are measured. The radiance values are obtained by defining a region of interest around the target material and the mean radiance value extracted for all areas. The values are then imported into the calibration technique and pairs of corresponding image and field values are selected. This provides conversion of the thermal image channel to surface temperature values.

Ground temperature measurements are acquired simultaneous to image acquisition for the Bosworth images. Unfortunately no ground temperatures were measured for the Baildon Moor or Weardale data and as a result the thermal channel remained in units of radiance. An alternative more quantitative approach to temperature calibration can be performed using the radiance values in the Planck equation and this is discussed in Chapter 6.

4.5.2 Image Normalisation

Image normalisation provides an appropriate alternative to the ELC technique where there is insufficient auxiliary detail on the spectral characteristics of the surface. Image normalisation enables the compensation of variations in seasonal illumination effects that occur due to the seasonal variation in the geometrical relationship between the sensor, the Sun and the topographic slope. This technique is especially important when assessing seasonal variations in the reflectance or emission of materials present throughout the multitemporal Bosworth data.

There are a variety of Normalisation procedures that can be applied by using the relative reflectance properties between a horizontal and inclined surface (Warner & Chen, 2001). An alternative technique is to use one image from a multitemporal dataset as the reference spectral response and normalise the other images to it. This is suitable where similar surface conditions are present and the vegetation is at a similar growth stage (Mather, 1999). Normalisation provided a suitable technique to enable the seasonal comparison of the Bosworth dataset for the majority of fields due to similar grassland condition. Ambion field, however, was planted with an agricultural crop that had different vegetation condition at the various times of imaging so normalisation was not necessarily a suitable technique for analysis of this field.

The Bosworth images were normalised by performing a Flat Field Correction algorithm, which normalises the images to an area that is known to contain a spectrally flat reference material that showed very little variation in response throughout the spectral wavelengths and also showed little variation between the image dates. For the normalisation of the Bosworth data, an area of gravel was selected near the visitor centre as a suitable spectrally flat reference material. This material showed the least amount of variation across the visible and near-infrared

wavelengths and also the least amount of variation between the temporal data (Figure 4.13).

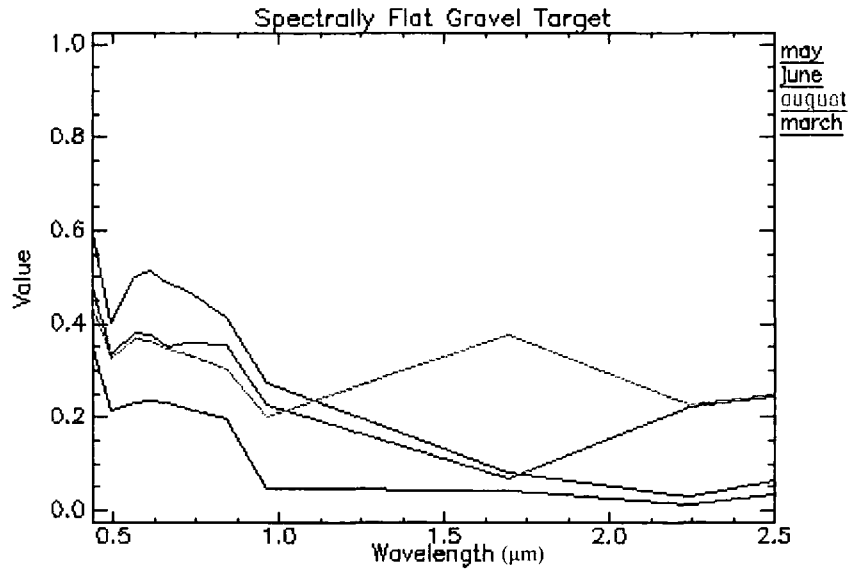

Figure 4.13: Spectrally flat reference material for Bosworth multi-temporal data

Before Flat Field Correction was performed, the radiance spectrum of the target material was extracted from the visible, near-infrared and short-wave infrared spectral channels of the imagery (Band 1 to Band 10) by defining a region of interest around the target material and determining the mean radiance spectra of the image pixels within the define region (Appendix B4). The reference spectral signature was then divided into the spectral signature of every other pixel in the image, thus normalising the multi-temporal Bosworth data using the Flat Field Correction algorithm. The seasonal variation in the particular surface materials was then assessed by comparing the spectral response observed on the multitemporal images.

4.6 SUMMARY of IMAGE PROCESSING TECHNIQUES

The raw image data recorded by the NERC Daedalus-1268 ATM sensor contain radiometric, geometric and atmospheric distortions that prevent meaningful interpretation of the information content of the digital images. These require removal through application of a number of preprocessing steps.

Radiometric calibration, which is specific to the individual sensor, was performed by the NERC ARSF prior to data delivery so that the images extracted from the raw file format were calibrated in terms of radiance. The initial file format was incompatible with the NASA HDF image standard expected by the image processing software so the images required extraction to a more compatible generic binary file format.

Geometric distortions were removed from the data using two different methods in order to provide the geometric integrity of a georeferenced base map and enable the integration with other georeferenced data sources. The initial method involved the collection of ground control points whose position were easily located on both the imagery and a georeferenced Ordnance Survey base map. This technique proved to be most successful for the Bosworth and Baildon Moor images where there was minimal topographic variation across the extent of the imagery and also where there was minimal aircraft motion. The geometric distortions were more dramatic in the Weardale data due to a more pronounced topographic variation and as a result of gusting winds. An alternative approach was therefore adopted through application of an automatic technique that used the auxiliary navigational detail measured by an inertial navigation system that is integrated with each scan line.

Once the spatial extent of the study sites was reduced to represent the overlap between the diurnal or seasonal images, atmospheric effects were removed from the data. These proved more difficult to compensate for than the geometric distortions due to an insufficient characterisation of the atmospheric condition during overflight for application of radiative transfer models. Atmospheric effects were removed from the visible and near-infrared channels of two of the Bosworth images using linear regression functions to relate image radiance data and field reflectance spectra recorded simultaneously to overflight over a series of target materials. This technique

can only be applied where there is sufficient field spectral measurement during overflight. It was not possible to obtain spectral signatures or meteorological data for the Baildon Moor or Weardale data thereby preventing correction of atmospheric effects from these images and as a result, atmospheric effects remained. Although atmospheric effects were removed from two of the Bosworth images, the effects remained in the other images and so evaluation of seasonal variations in surface response must bear this in mind. Image normalisation provided a suitable alternative with compensation of variations in illumination conditions between the images using the spectral response of a spectrally flat target material.

For extraction of information on the thermal properties of the land surface it is useful to convert thermal radiance to surface temperature and this will be discussed in detail in later chapters together with interpretation of the observed temperature response.

These preprocessing techniques have provided a series of seasonal images with normalised visible and near-infrared responses for one of the study sites. These data are now ready to be evaluated using a variety of image analysis techniques with interpretation of the results before the application of the most promising techniques to the uncalibrated data of Baildon Moor and Weardale.

5 QUALITATIVE IMAGE INTERPRETATION

The synoptic view of the ground surface offered by the processed digital airborne images is used for the identification and interpretation of archaeological and geological features. The research uses both qualitative and quantitative methods to assist the process of image interpretation. This chapter concentrates on qualitative image interpretation where surface features are identified by their anomalous spectral response with respect to surrounding pixels.

Initial interpretation of the images involves the visualisation of the individual spectral channels as a series of monochrome images. The range of response values associated with the vegetation covering the ground surface is relatively low compared with the surrounding materials and so the appearance of the images requires enhancement so that the information contained in the monochrome images can be interpreted more easily. This is achieved through a series of *contrast enhancement* techniques, which manipulate the histogram of the display channel to provide improved visualisation. The data can also be visualised as a series of colour composite images, representing a combination of the sensor's spectral channels. Colour composites are initially formed by combining the visible channels to represent the output of a standard aerial photograph, with additional colour composites generated through combination of the visible, near-infrared and thermal-infrared channels. The anomalous features associated with each of the spectral combinations are then compared to assess the amount of additional detail provided by inclusion of the thermal channel. A series of numerical transformations are then applied to the calibrated image data from the Bosworth site through *edge detection, image arithmetic* and *principal component analysis* to enhance the detection of the anomalous features. The techniques that reveal the greatest amount of detail are then applied to the uncalibrated image data from the Bosworth site to determine (i) the necessity of calibration and (ii) the most appropriate processing requirements for feature detection. The most successful techniques are then applied to the images from Baildon Moor and Weardale to locate shallow ground disturbance at each study site. The anomalous features from each site are then compared with the results of the geophysical evaluations to determine whether the thermal anomalies represent variations in the physical nature of the shallow subsurface. The visualisation and

enhancement techniques that are applied to the processed images are described below together with the results of each enhancement technique, with larger versions of the images located in Appendix C.

5.1 INTERPRETATION from SINGLE BAND VISUALISATION

Basic image interpretation begins with the visualisation of the individual spectral channels as a series of separate monochrome images, which are loaded onto a single display channel using the ENVI software (Appendix B2). When viewing the individual spectral channels of the daytime data, it is apparent that some adjacent spectral channels show a very similar response pattern and so performing interpretation of each spectral channel would be time-consuming. However, this visualisation enables an initial assessment of the similarity between adjacent spectral channels and also enables the identification of spectral channels that contain excessive noise. Single band visualisation is also important for the assessment of thermal anomalies and can be used to assess the variation in diurnal and seasonal thermal response of the land surface.

5.1.1 Bosworth

The spectral channels of the Bosworth data are visualised as a series of individual monochrome images showing the spectral response from May 1998 (Figure 5.1), June 1998 (Figure 5.2), August 1998 (Figure 5.3) and March 2002 (Figure 5.4). These visualisations show that Band 1 contains excessive noise on all dates and as a result is excluded from further analysis.

The majority of this site is covered by an agricultural field system that surrounds the Battlefield visitor centre (Figure 5.16) consisting mostly of grass-covered fields (Arena, Helipad, South and Picnic) where the grass varies in height between acquisition dates. The remaining field (Ambion) was covered with barley in 1998 with oil seed rape present in 2002. The other fields surrounding the visitor centre are used for livestock grazing and agricultural crops, but these fields are excluded from analysis due to restricted access.

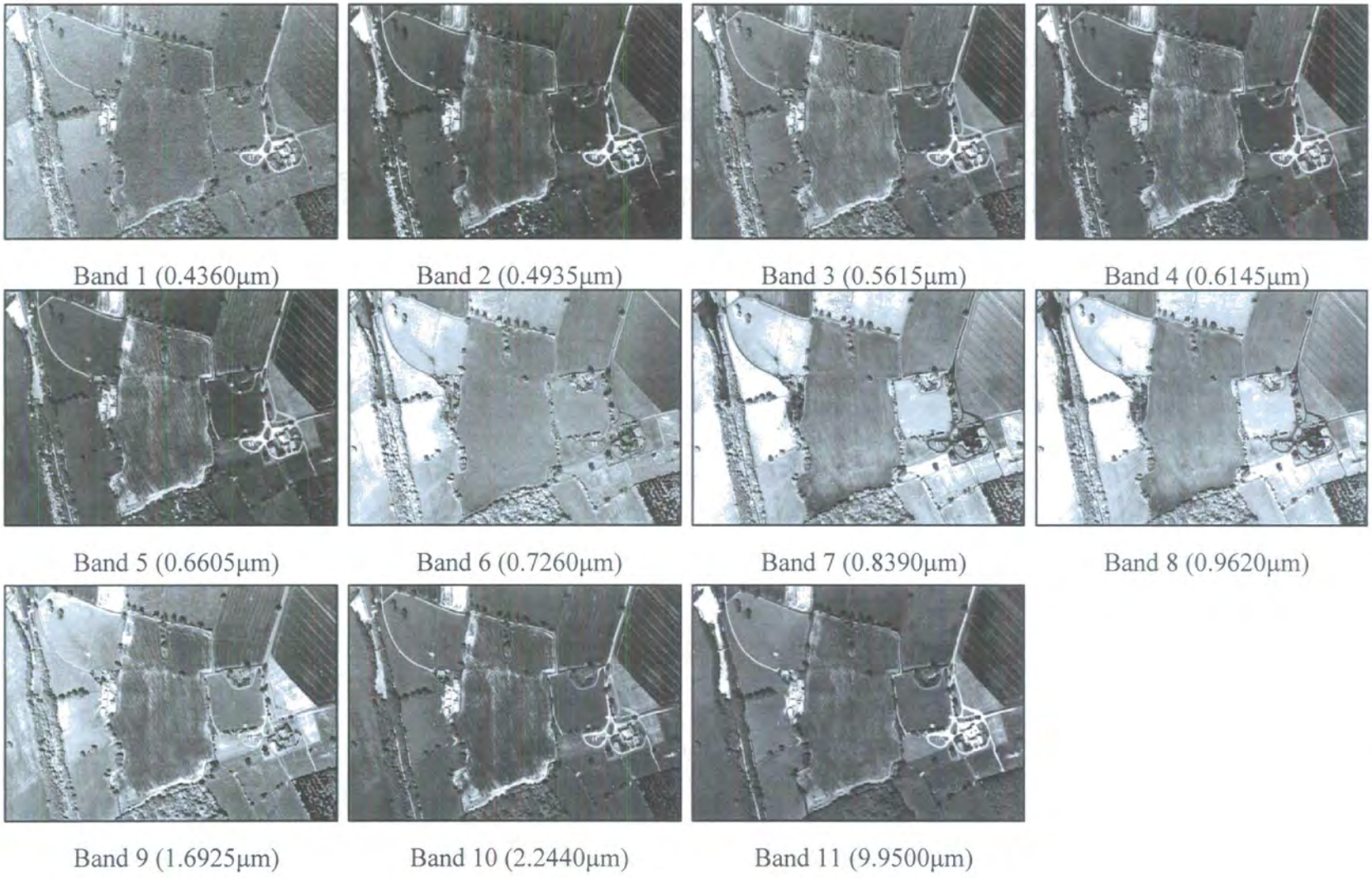

Figure 5.1:: Monochrome images of spectral channels of Bosworth May 1998

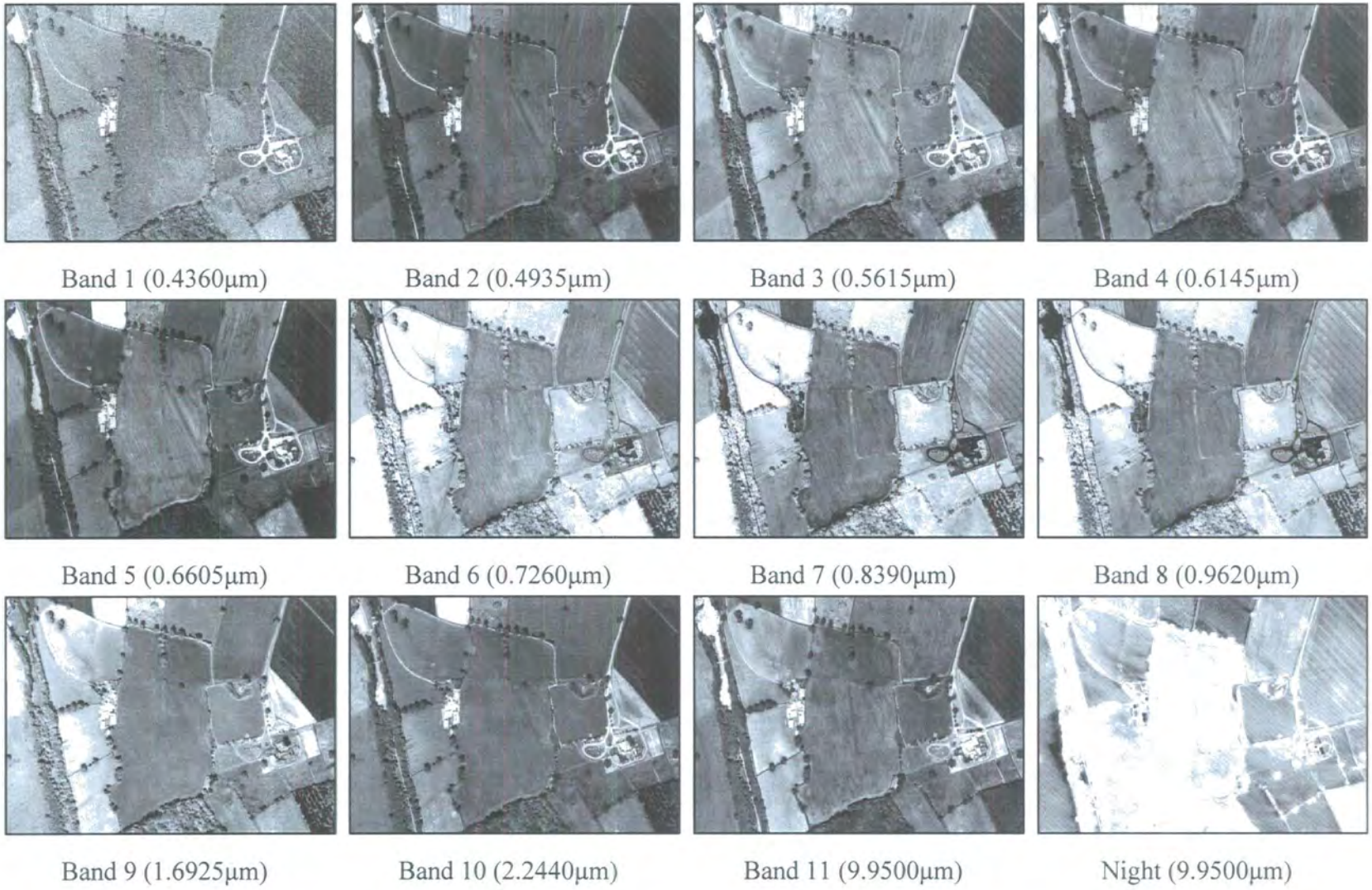

Figure 5.2: Monochrome images of spectral channels of Bosworth June 1998

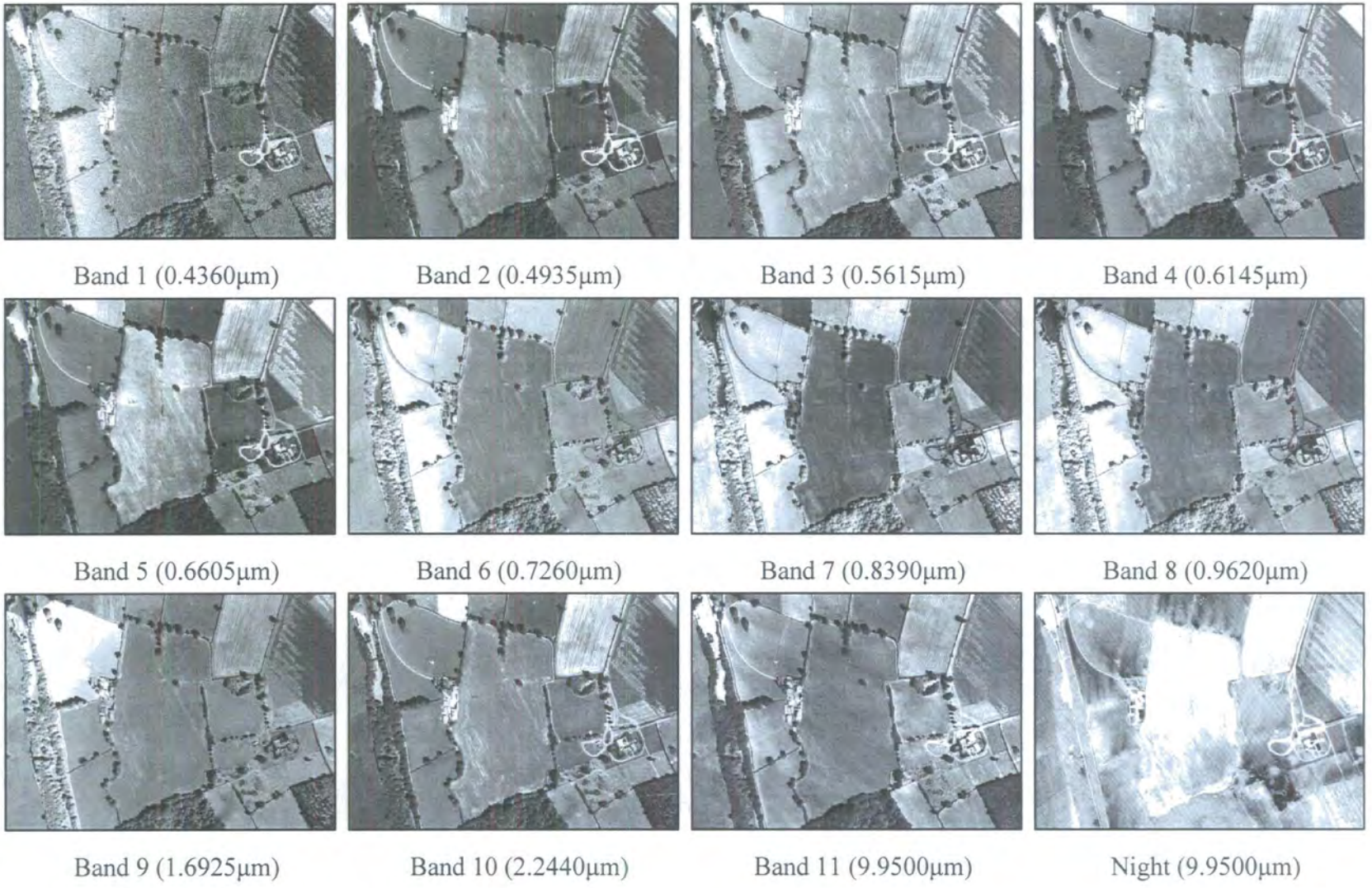

Figure 5.3: Monochrome images of spectral channels of Bosworth August 1998

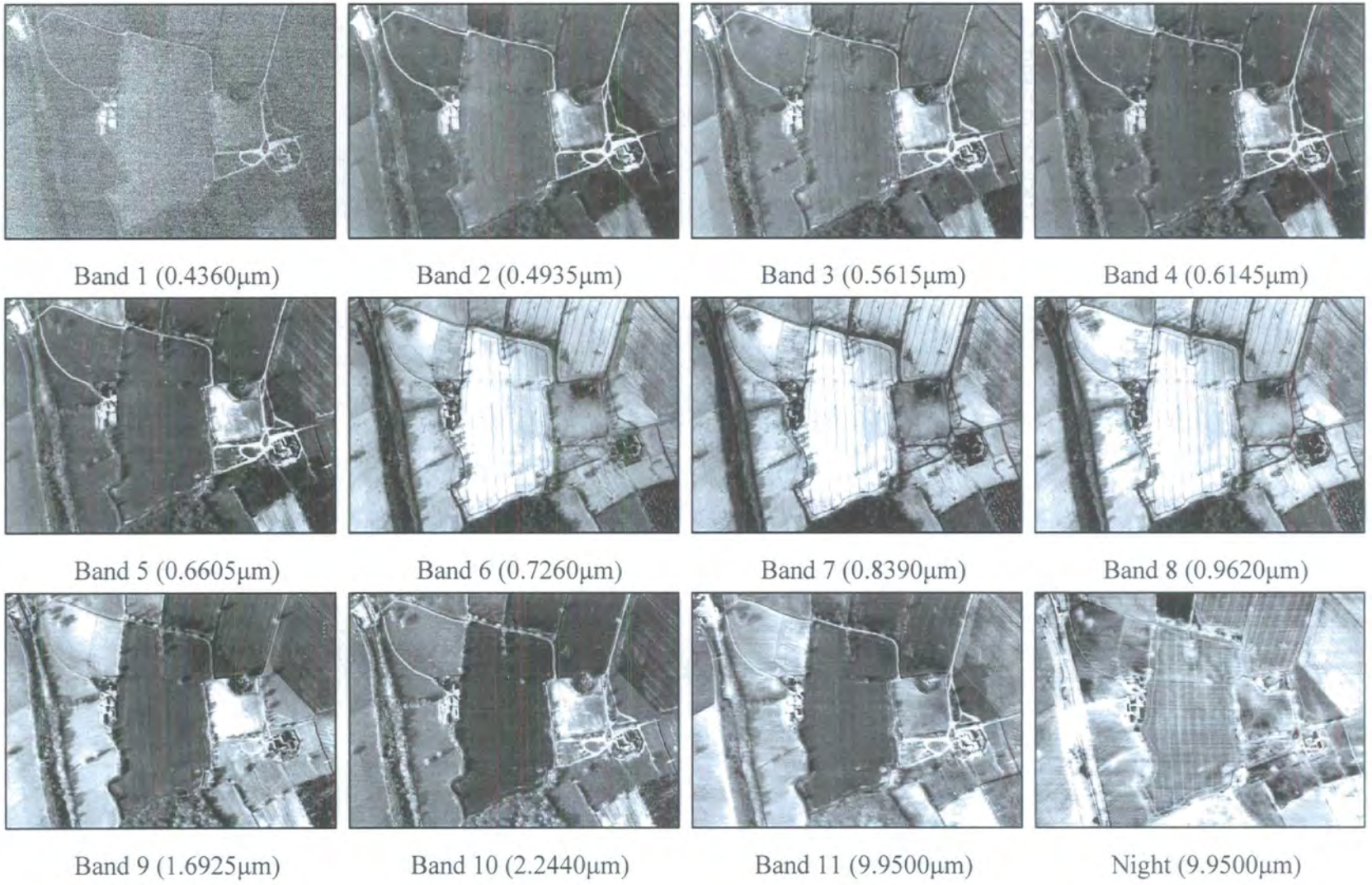

Figure 5.4: Monochrome images of spectral channels of Bosworth March 2002

On initial inspection, the fields that are covered with grasses (Arena, Helipad, South and Picnic) show a gradually more uniform spectral response as the grass height increases from March through to June and masks the underlying soil from observation, with greatest anomaly visibility when the grass is short. Ambion field shows a more variable internal response during barley growth with prominent plough markings evident in May and June 1998 and a more variable degree of crop maturity observed in August 1998. Present day plough markings are also evident in Ambion field in March 2002 during oil seed rape growth where there is a much more uniform vegetation response than observed for the barley.

On initial inspection of the May 1998 data, there appears to be a very similar spectral response between Bands 4 and 5, representing visible red wavelengths of radiation, which is also evident in June and August 1998 and March 2002. There is also a very similar response between Bands 7 and 8, representing near-infrared wavelengths in May, June and August 1998. However, in March 2002 the near-infrared Band 6 also shows a similar spectral response as Bands 7 and 8. From these observations, it is apparent that the spectral response of the adjacent spectral channels is similar and so alternative spectral analysis techniques, discussed later in the chapter, are applied to the data rather than interpreting the individual spectral channel.

5.1.2 Baildon Moor

The spectral channels of the Baildon Moor data are visualised as a series of individual monochrome images showing the spectral response from May 1997 (Figure 5.5). This visualisation shows that Band 1 contains excessive noise and as a result is excluded from further analysis. The majority of this site is covered with moorland grasses with patches of bracken occurring in the central region. The topography of the site is relatively flat with a topographic high occurring to the north with a gradual increase in elevation towards the south-east

On initial inspection, the feature that shows the most prominent spectral characteristic is a linear feature trending east to west in the northern section of the study site. This feature represents a tarmac road and shows a strong low response in Bands 5, 6, 7, 8, 9 and 10 but is indistinguishable from the surrounding materials in the other day channels. The tarmac shows a contrasting response to that of the dirt

track running north-east from the caravan park in the south-west corner. This feature shows a bright response in the visible Bands 2, 3, and 4 but is indistinguishable from the surrounding materials in the other day channels. Another characteristic feature of Baildon Moor is the golf course to the north of the main road. Here the well-kept fairways show a prominent high response across Bands 5, 6, 7, 8 and 9, low response in Bands 2, 3, 4 and 10 compared to the surrounding vegetation. There are two features of unknown origin on the Moor. The first represents a subtle curvilinear feature of low response in Bands 5, 6, 7, 8 and 9 and high response in Band 10 that is otherwise indistinguishable from the surrounding material. The second is represented by an elliptical feature in the west that is evident in only Band 10 with a poor spectral contrast throughout the remaining channels. These may represent variations in the underlying geology, whose mineralogy and porosity affects vegetation growth.

The features that are of most significance in the context of the research are the abandoned mineshafts, which are represented by circular features of low central response surrounded by a rim of high response. These are clearly evident in Band 10 with a very subtle contrast in Bands 5, 6, 7, 8 and 9, but are absent from Bands 2, 3 and 4.

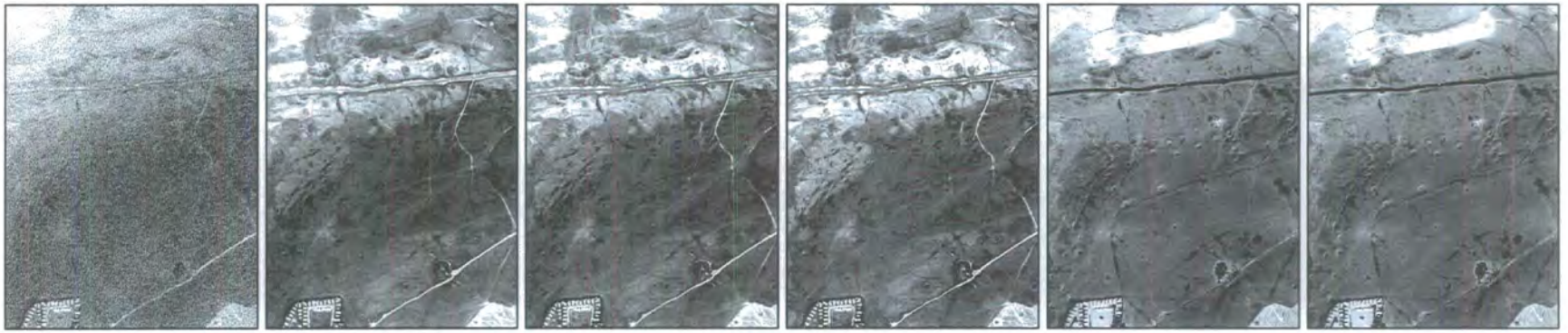

Band 1 (0.4360μm) Band 2 (0.4935μm) Band 3 (0.5615μm) Band 4 (0.6145μm) Band 5 (0.6605μm) Band 6 (0.7260μm)

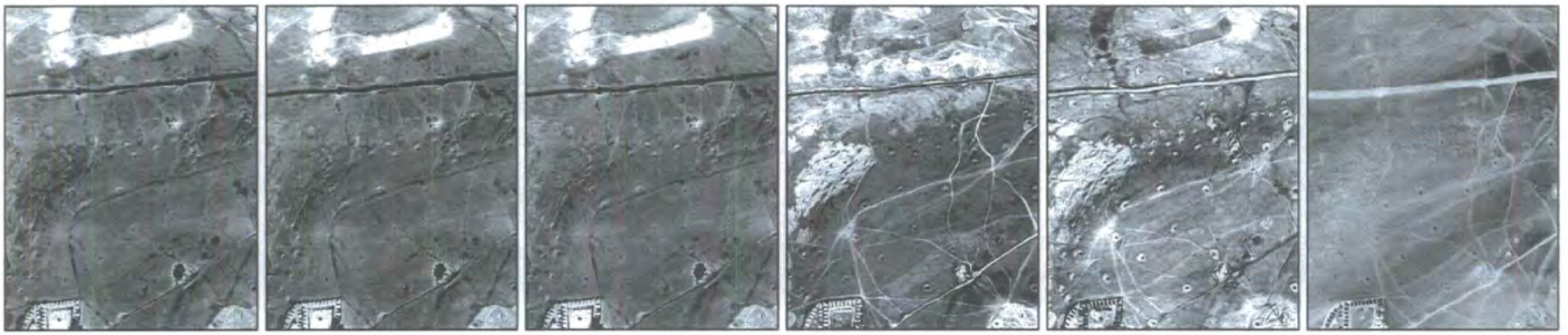

Band 7 (0.8390μm) Band 8 (0.9620μm) Band 9 (1.6925μm) Band 10 (2.2440μm) Band 11 (9.9500μm) Night (9.9500μm)

Figure 5.5: Monochrome images of the spectral channels for Baildon Moor

5.1.3 Weardale

The spectral channels of the Weardale data are visualised as a series of individual monochrome images showing the spectral response from August 2001 (Figure 5.6). This visualisation shows that Band 1 and Band 9 contain excessive noise, the latter representative of electrical discharge across the instrumentation, and as a result these bands are excluded from further analysis. In addition, the night thermal image shows a considerable amount of noise, which is manifest as alternating dark and light banding that shows a variable orientation as a result of the georectification process.

The majority of the site is covered with moorland grasses that occupy fields that are separated by dry-stone dykes. The topographic setting is represented by a v-shaped valley carved out by the Rookhope Burn that flows south-eastwards from an upland area in the north-west

On initial visualisation, the feature that shows the most prominent spectral characteristic is a triangular area in the north-eastern section of the study site. This feature shows a strong high response in Bands 2, 3, 4 and 5 with a more subtle higher response in Bands 6, 7, 8 and 10. This feature represents a variation in solar illumination conditions between the north-eastern and south-western flanks of the valley. There is an additional prominent contrast observed in the eastern section that is a result of a contrast in radiance values between the adjacent flight lines that could not be removed prior to creating a mosaic of the study site during image processing. This is seen in the south-eastern section in Bands 6, 7 and 8. In addition to these immediately apparent features, there is an area of very low response in the centre of the image that is evident on all multispectral bands. This represents an area of cloud shadow that is absent from the day and night thermal images.

The features that are of most significance in the context of the research are the areas of abandoned mineral excavation. There are three main mineral excavation sites in the study site represented by (i) spoil heaps, (ii) scour marks and (iii) abandoned mineshafts. The spoil heaps have a bulbous representation on the images, radiating from a central position, with several phases of heaping of spoil suggested by the overlapping of the radial pattern. There are two main spoil heap sites in the valley,

one on the north-eastern flank and the other on the western flanks. The sites have a contrast in response due to the variable topographic illumination conditions, with the site on the north-eastern flank having a higher response. The extremities of the spoil heaps at both sites show a relatively low response in Bands 6, 7 and 8 and a higher response in Band 10 when compared to the surrounding material with a more prominent response evident in the north-eastern site. The extremities of the spoil heaps also show high day and night thermal response compared to the inner spoil heap materials and also the surrounding moorland due to the exposure of soils at the vertical edge of the spoil heaps where vegetation struggles to grow.

The scour marks are represented by a line of circular features along the northern edge of the image, on the north-eastern flank of the valley. These features display a low near-infrared response and a subtle visible and short-wave infrared response pattern. Each scour mark has a bright north-eastern side and a dark south-western side, which is representative of a differential solar heating due to topographic aspect. This pattern is replicated on the day thermal image with a more uniform night thermal response from both sides of the scour marks.

The abandoned mineshafts are scattered across the western flank of the valley and are represented by high response in the short-wave and thermal infrared bands compared to the surrounding material. This response is highly contrasting to the abandoned mineshafts of Baildon Moor mainly due to the more variable surface composition of the region.

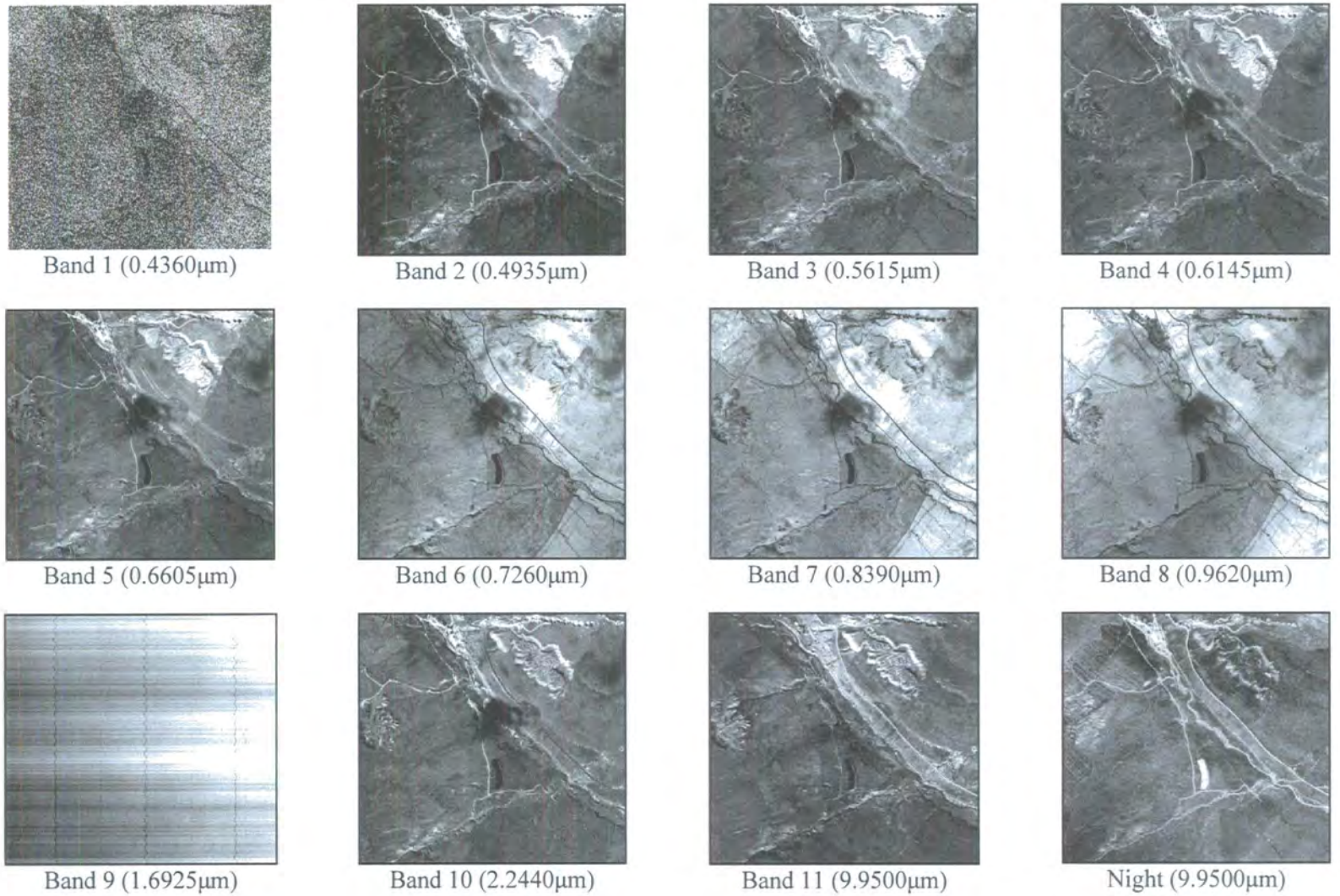

Figure 5.6: Monochrome images of the spectral channels for Weardale

Although visualisation of the individual spectral channels as a series of monochrome images provides initial assessment of some of the more prominent features occurring within the agricultural fields and moorland, subtle variations are much more difficult to detect due to the poor spectral contrast associated with the vegetation. A detailed assessment of the individual spectral channels would be time-consuming and so alternative methods are required to assist with the interpretation of the multispectral data. However, in order to assess the thermal characteristics of each study site, a more detailed analysis of the day and night thermal images is required. Initial visualisation of the individual thermal channels shows poor spectral contrast over the vegetated terrains and requires enhancement prior to interpretation. This is performed through a series of *contrast enhancement* techniques that manipulate the histograms of each thermal image. The techniques are described in the following section with respect to the study site of Bosworth.

5.2 CONTRAST ENHANCEMENT

The poor contrast in thermal response observed over vegetation is often a direct result of anomalously high or low radiance values associated with non-vegetated areas such as farm buildings or roads within the spatial extent of the images. As a result, subtle anomalous features occurring within the vegetation become difficult to detect as the values associated with the vegetation are clustered into a small section of the image histogram. Therefore, the vegetation shows a uniform grey-scale intensity over large areas and lacks contrast and so the identification of the subtle features requires contrast enhancement.

Contrast enhancement techniques are applied to the displayed images so that the contrast between high and low values is enhanced whilst maintaining the relative distribution of the grey-scale intensity levels in the image. The contrast of the displayed image is enhanced by extracting the image histogram (Appendix B9) and by manipulating the range of observed values through a series of contrast stretches, which generate a look-up table to correlate an observed input value to a stretched output value. The overall effect of the histogram manipulation is to brighten an underexposed image or to darken an overexposed image. The most common methods used for contrast stretching are Linear, Gaussian and Histogram Equalisation.

The simplest method is the *Linear* stretch that translates the range of observed pixel values to the full capability of the visual display, which is usually 0-255 for an 8-bit image display (Mather, 1999). The pixel values are scaled so that the lowest observed value is mapped to the minimum visual display value (0) and the largest observed value is mapped to the maximum display value (255), with all intermediate values stretched so that they retain their relative distribution. The Gaussian stretch fits the observed input histogram to a standard Gaussian distribution, where the probability (p) for a value (x) decreases symmetrical away from the mean value ($\bar{x}$), with respect to the standard deviation (σ) of the input values (Equation 5.1). Although image processing software usually provides a default standard deviation value, the user is able to specify the number of standard deviations for the histogram stretch, with larger values decreasing the visual contrast

Equation 5.1

$$p(x) = \frac{1}{\sigma\sqrt{2\pi}} \exp\left(\frac{-(x-\bar{x})^2}{2\sigma^2}\right)$$

Histogram Equalisation automatically scales the data so that each histogram bin in the output image contains an approximately equal number of pixel values. The effect of this stretch is to increase the contrast in the densely populated parts of the histogram and to reduce contrast in the more data sparsely areas (Mather, 1999).

Results from the application of the different contrast enhancement techniques to a thermal image from the Bosworth site are displayed to show the variation in the amount of detail visible through each enhancement (Figure 5.7).

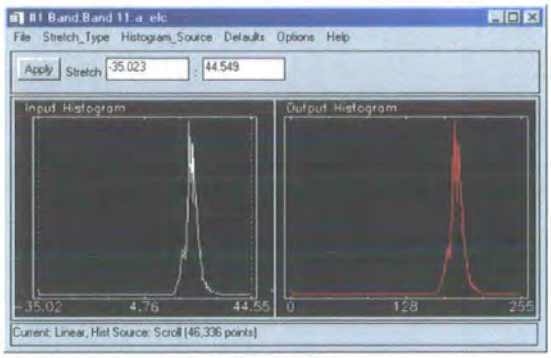

LINEAR

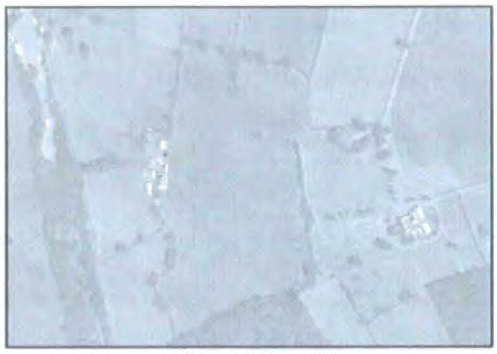

August 1998 Day Thermal

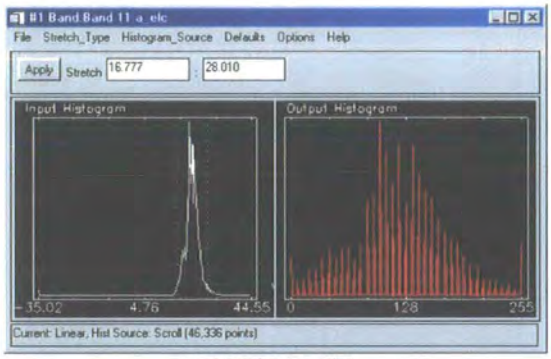

LINEAR 2%

August 1998 Day Thermal

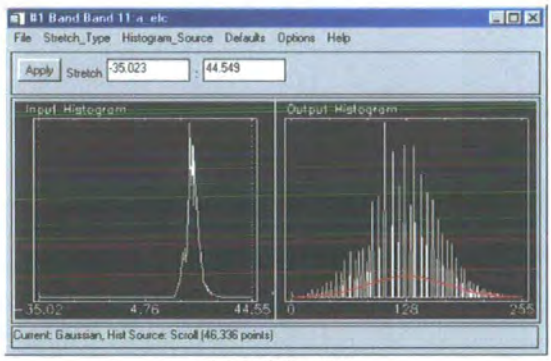

GAUSSIAN

August 1998 Day Thermal

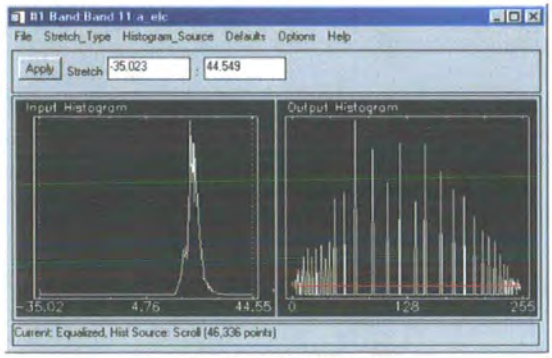

EQUALISATION

August 1998 Day Thermal

Figure 5.7: Histogram manipulation on Bosworth August 1998 day thermal image

The different contrast enhancement techniques are applied to each of the thermal images from the study sites to enable interpretation of the thermal anomalies.

5.3 INTERPRETATION of THERMAL IMAGES

The thermal anomalies from each site are interpreted through application of the contrast enhancements detailed above. However, performing the enhancements on the entire image can often mask subtle features occurring with the vegetation cover. Additional enhancements are therefore performed on specific ranges of data values selected to highlight particular features of the histogram. By specifying the range of values to be stretched, those parts of the image histograms associated with bright or dark features such as buildings and roads are excluded. In addition to specifying a range of data values, the interactive functionality of the software also enables contrast enhancements to be performed on spatial subsets of the image data. Both these techniques provide enhancement of the more subtle features occurring within areas covered by vegetation.

The following section presents the thermal images of each study site displayed using the contrast enhancement that provides optimum visualisation of features observed in areas covered by vegetation. An interpretation layer is also presented for each image displaying the anomalous features that are used to assess the diurnal and seasonal variations in thermal response of the vegetation.

5.3.1 Visualisation and Detection of Bosworth Thermal Anomalies

The optimum visualisation for the May 1998 (Figure 5.8), June 1998 day (Figure 5.9), August 1998 night (Figure 5.12), March 2002 day (Figure 5.13) and March 2002 night (Figure 5.14) thermal images is obtained through a Linear 2% contrast enhancement with the optimum visualisation for June 1998 night (Figure 5.10) and August 1998 day (Figure 5.11) thermal images obtained through Histogram Equalisation.

May 1998 Day

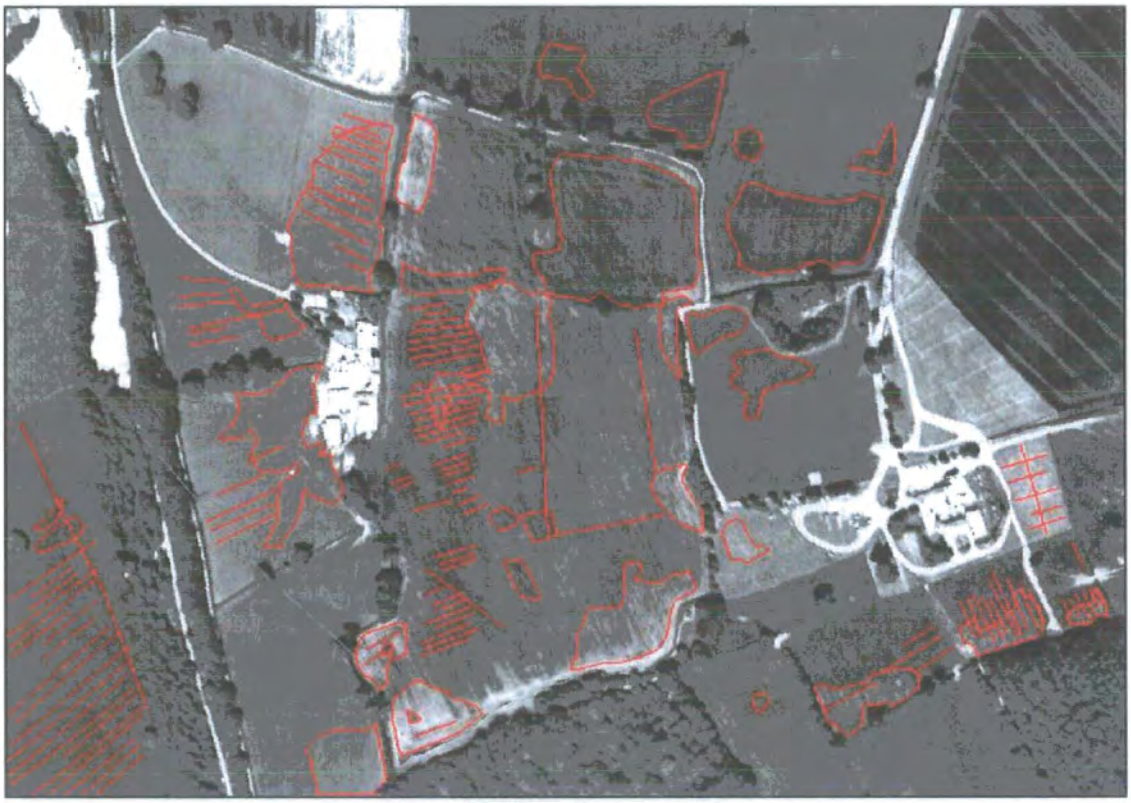

May 1998 Day Interpretation

Figure 5.8: Thermal features on Bosworth May 1998 day thermal image

June 1998 Day

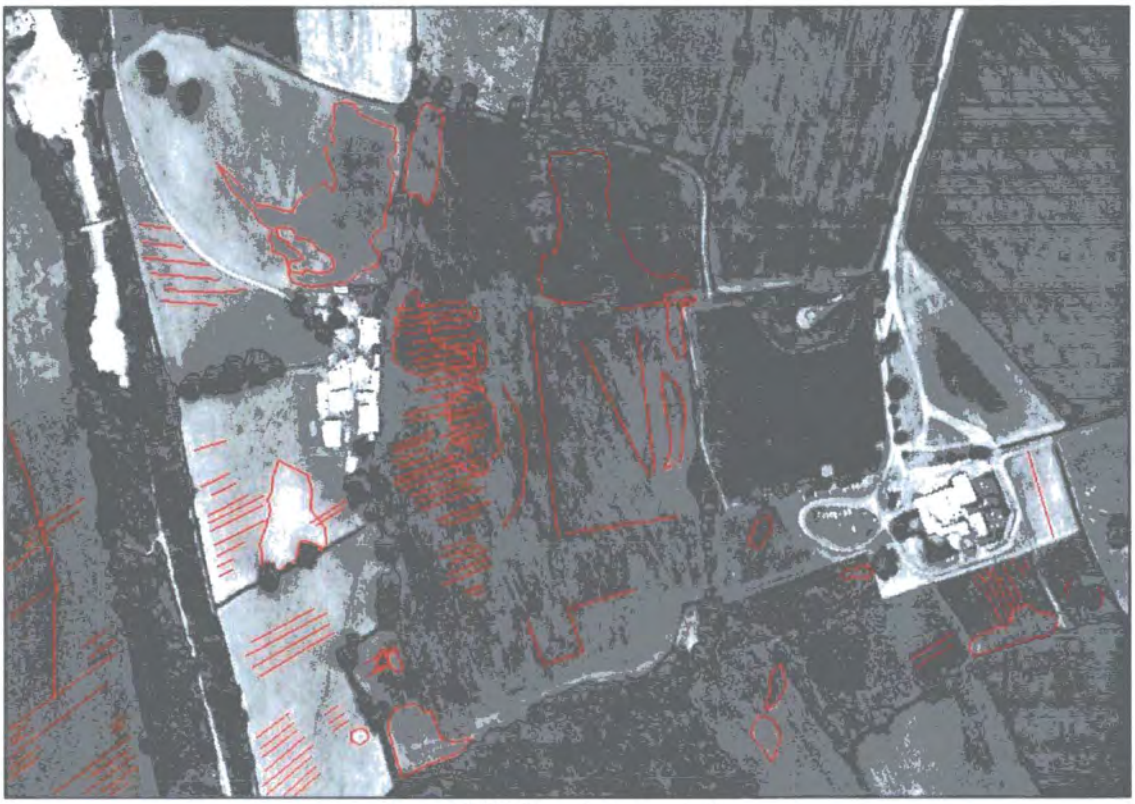

June 1998 Day Interpretation

Figure 5.9: Thermal features on Bosworth June 1998 day thermal image

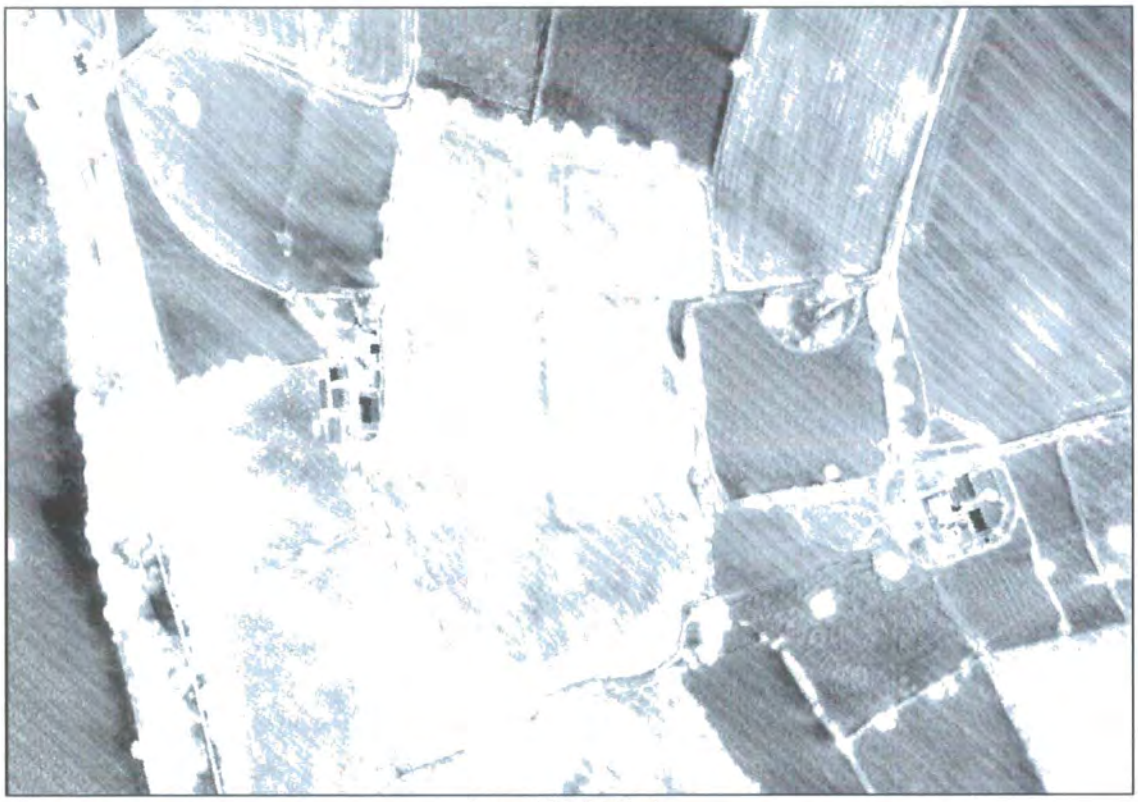

June 1998 Night

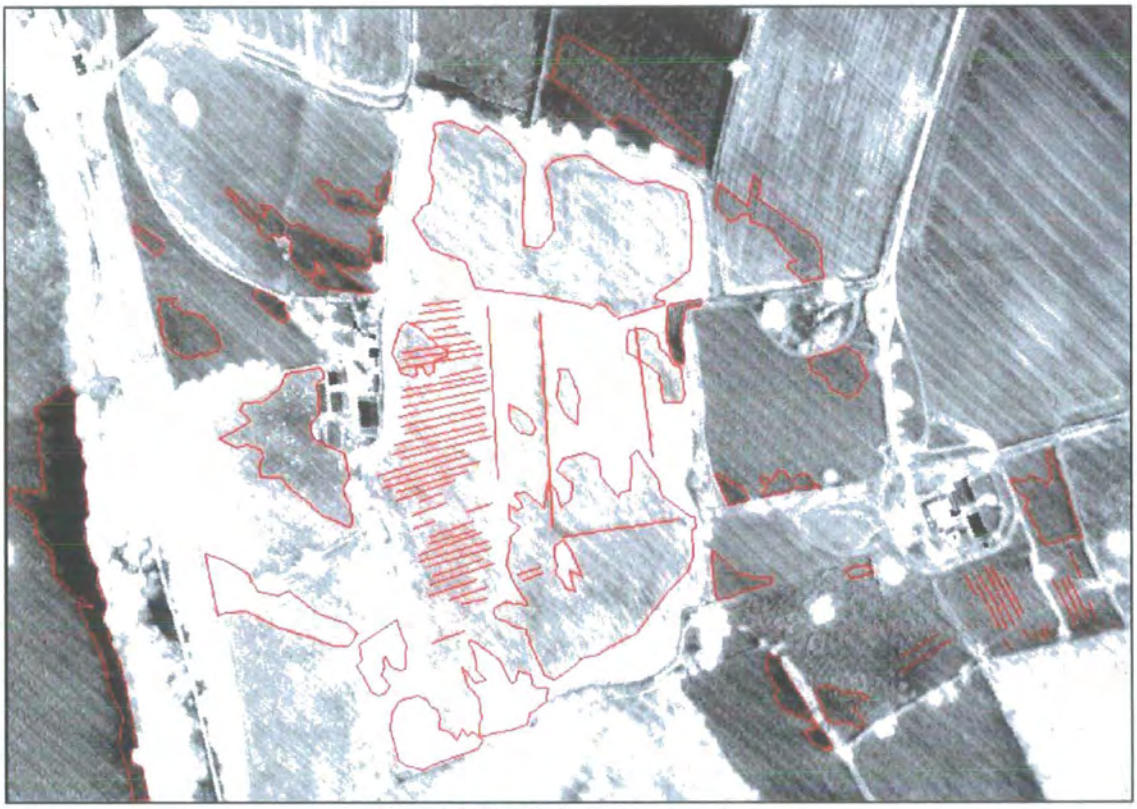

June 1998 Night Interpretation

Figure 5.10: Thermal features on Bosworth June 1998 night thermal image

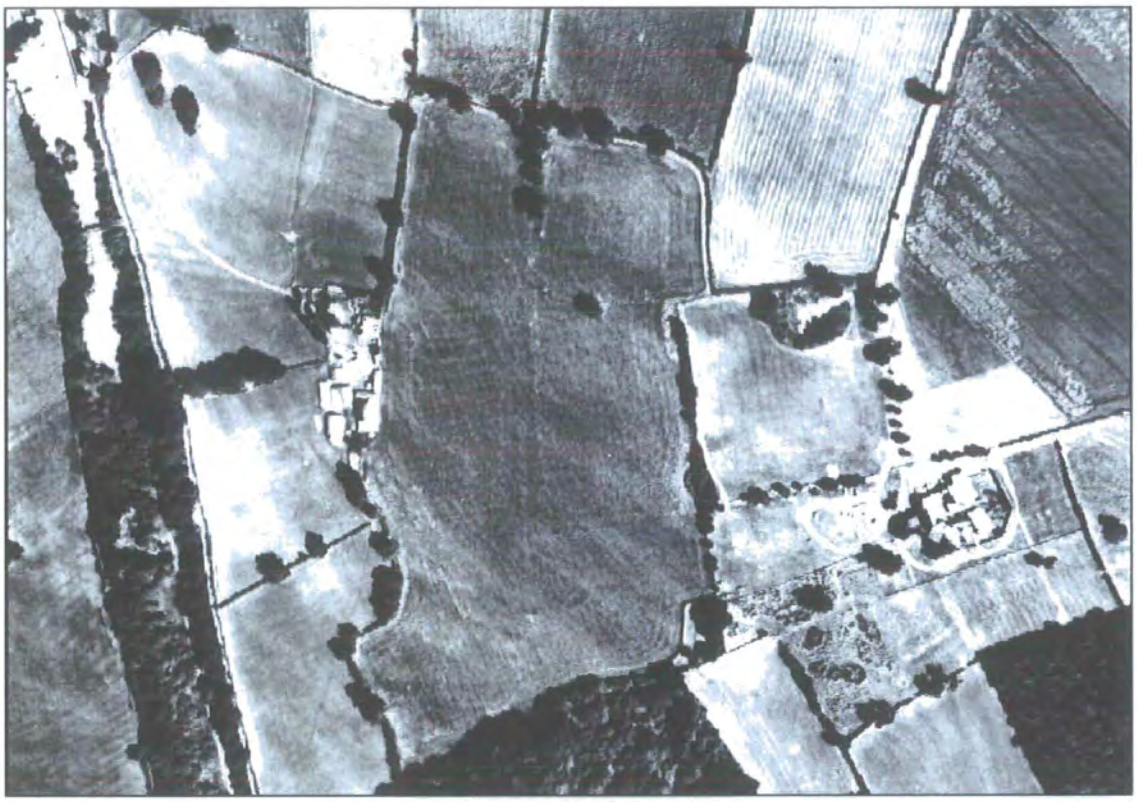

August 1998 Day

August 1998 Day Interpretation

Figure 5.11:Thermal features on Bosworth August 1998 day thermal image

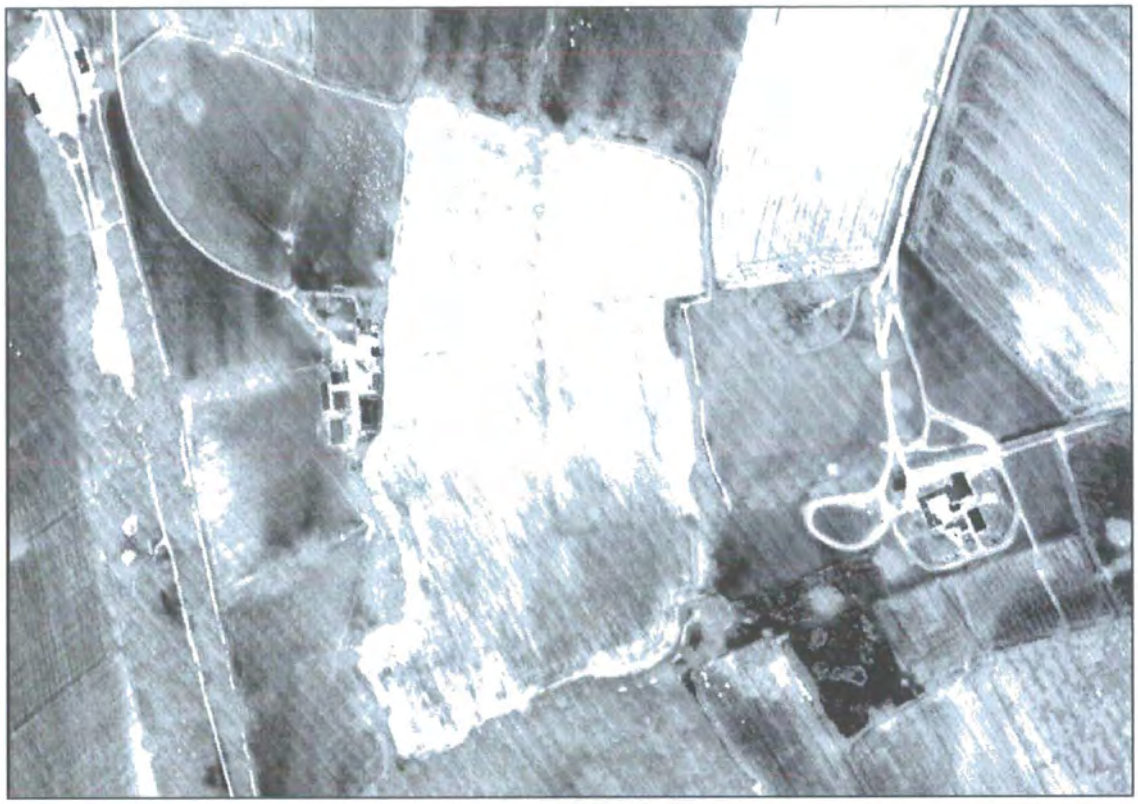

August 1998 Night

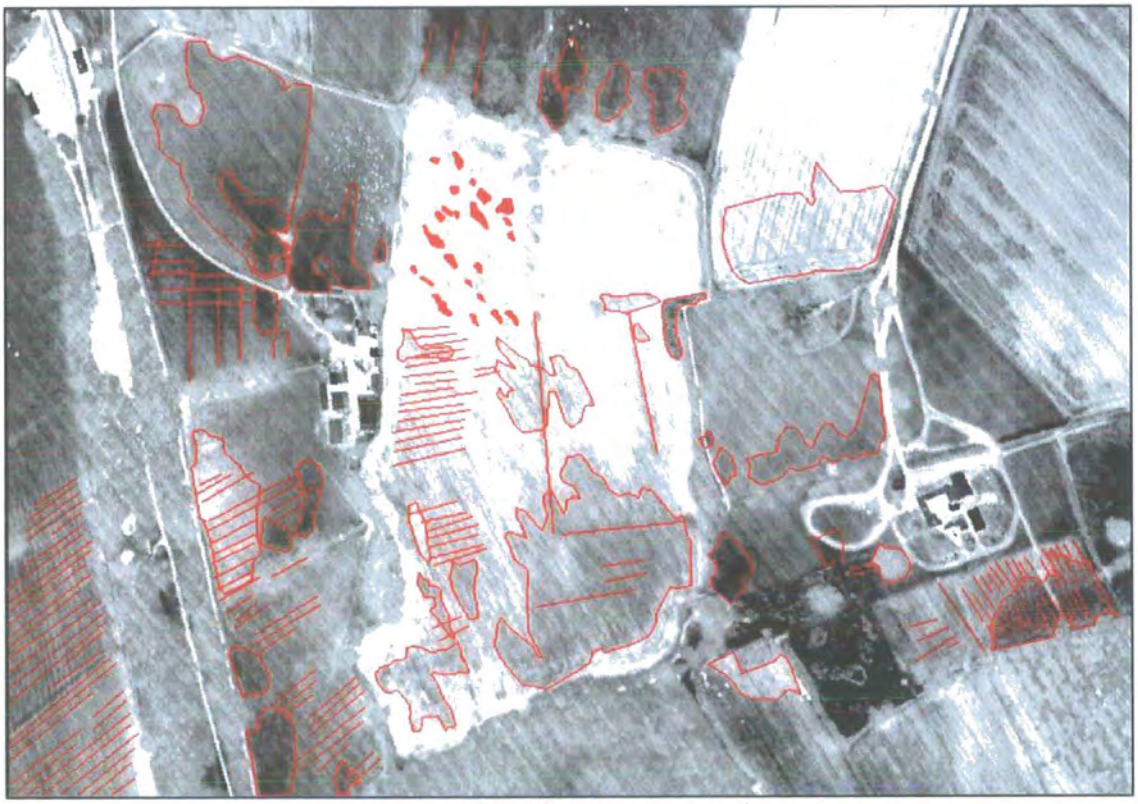

August 1998 Night Interpretation

Figure 5.12: Thermal features on Bosworth August 1998 night thermal image

March 2002 Day

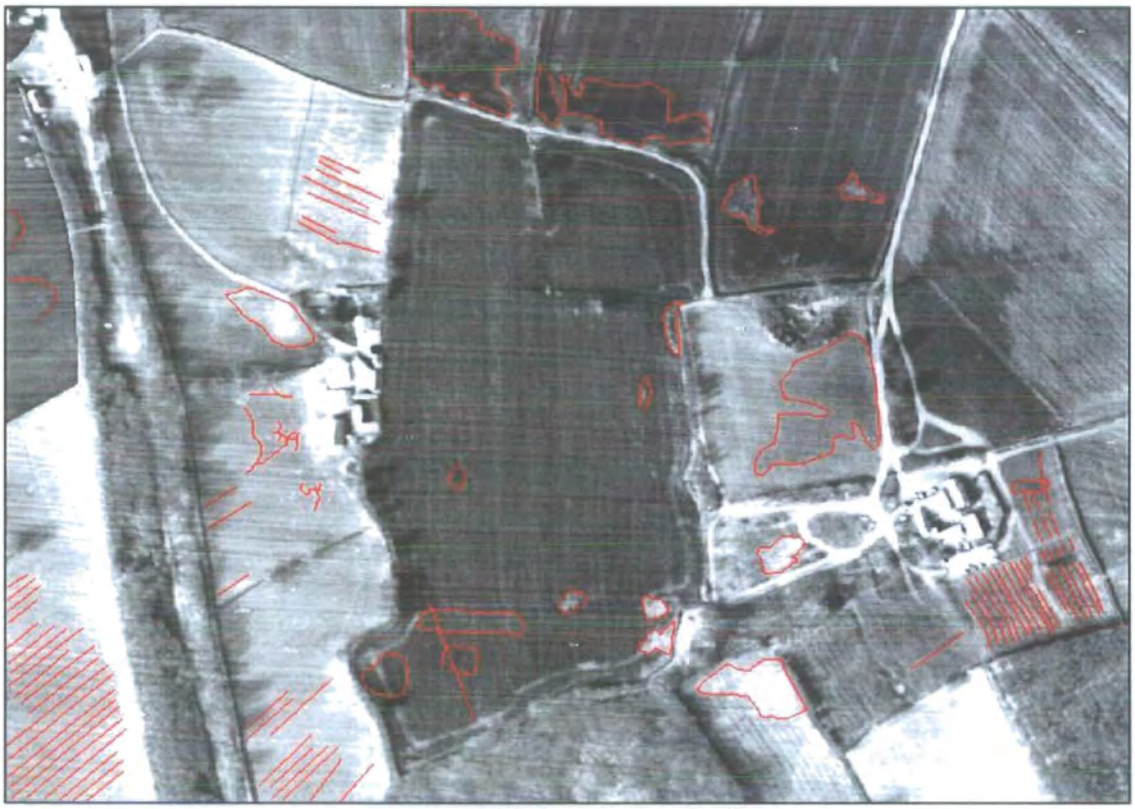

March 2002 Day Interpretation

Figure 5.13: Thermal features on Bosworth March 2002 day thermal image

March 2002 Night

March 2002 Night Interpretation

Figure 5.14: Thermal features on Bosworth March 2002 night thermal image

In order to assess the diurnal and seasonal characteristics of the study site, the interpretation layers from each thermal image are displayed on top of one another (Figure 5.15) to look at similarities and differences in the position and recognition of thermal anomalies. From this visualisation, it becomes apparent that there is a complex relationship between the stage in the vegetation growth and detection of thermal anomalies. In order to develop an understanding of the diurnal and seasonal effects of vegetation on the detection of thermal anomalies, the site is broken down to field level with interpretation concentrating on the fields surrounding the visitor centre where ground geophysical evaluation has been performed (Figure 5.16).

Figure 5.15: Display of complex relationship of Bosworth thermal interpretation

Figure 5.16: Field nomenclature for Bosworth study site

5.3.1.1 Ambion Field Interpretation

The topographic setting of Ambion field is such that there is a plateau in the eastern section of the field in line with the northern boundary of the Arena field. The plateau runs to the mid-field position (Figure 5.17) where there is a steep down slope towards the NW and NE (Figure 5.18) with a more gradual down slope towards all other directions and an area of flat land in the far SW corner (Figure 5.19).

Figure 5.17: Plateau on Bosworth Ambion Field

Figure 5.18: Northeast corner of Bosworth Ambion Field

Figure 5.19: Southwest corner of Bosworth Ambion Field

Visualisation of the day (Figure 5.20) and night (Figure 5.21) thermal images of Ambion field show that the most consistently detected feature under the barley is a N-S linear anomaly that shows a progressively more subtle contrast through May, June and August 1998 with a moderately low night temperature in June and August 1998. This feature is completely absent on the March 2002 diurnal thermal images under the oil seed rape. At the southern end of this feature there are two parallel subtle anomalies trending E-W that are evident on the May and June 1998 day images, with a moderate temperature on the June and August 1998 night images. These linear anomalies mark the position of field hedgerow boundaries that have been removed since generation of the 1st edition OS map. There is a secondary N-S linear anomaly of low temperature to the east of the main feature that is evident on the June and August 1998 night images, with a third N-S linear anomaly of high temperature on the west of the main feature that is evident on the day and night images under the barley. This feature possibly represents the position of an infilled ditch with higher moisture content giving rise to the elevated night signature.

There is a series of parallel E-W linear anomalies on the western region of Ambion field that show moderately contrasting temperatures on the daytime images under a barley crop that are more prominent on the corresponding night images, but are absent under the oil seed rape. These features have a slight topographic expression at ground level suggesting the presence of ancient ridge and furrow plough marks. There is a series of parallel NW-SE linear anomalies spanning the field on the May 1998 image that show progressively more subtle temperature contrast through June and August 1998. These represent present-day plough markings where the high

temperature corresponds to the visible soil fraction that decreases as the vegetation cover masks the soil as the barley crop develops. In March 2002 the present-day plough marks alter to a N-S orientation and are less noticeable due to the higher leaf area of the vegetation.

In the southwest corner of the field there is a patch of low day and high night temperatures under the barley that is absent under the oil seed rape. This marks the position of flat land whose high night temperature may signify high moisture content as the moisture drainage from the main field.

There are two patches of high day temperatures in Ambion field under the barley that have corresponding low night temperatures. The patch in the NE corner of the field adjacent to the Arena field marks an area of recently deposited manure. The similar patch adjacent to SW corner of Arena field marks the position of a badger set. Both features are devoid of vegetation cover and as a result, the response is representative of the soil that underlies the rest of the field.

In the NW corner of Ambion field there is a series of elliptical anomalies evident on the June and August 1998 night images that are absent on the day images and also absent at all times under the oil seed rape. These possibly represent areas where trees have been either removed prior to the present-day cultivation of the field and may be infilled with a different material, or whose stumps have been burned in situ with a different compaction compared to the surrounding material.

All of the anomalies mentioned above are difficult to detect on the August 1998 day thermal image due a wind shear effect. Wind affects the temperature observed for the soil-vegetation system by increasing the movement of cool air through the canopy and removing heat from the underlying soil. As a result there is an increase in heat flux from the canopy towards the soil and a reduction in canopy temperatures.

The results from Ambion field suggest that the anomalous features have a different response at different stages in barley growth and also vary when compared with their response under the oil seed rape. The variation in response under the different vegetation types can be attributed to the different characteristics of the vegetation, such as leaf area where the oil seed rape has a more leafy structure and covers more of the underlying soil.

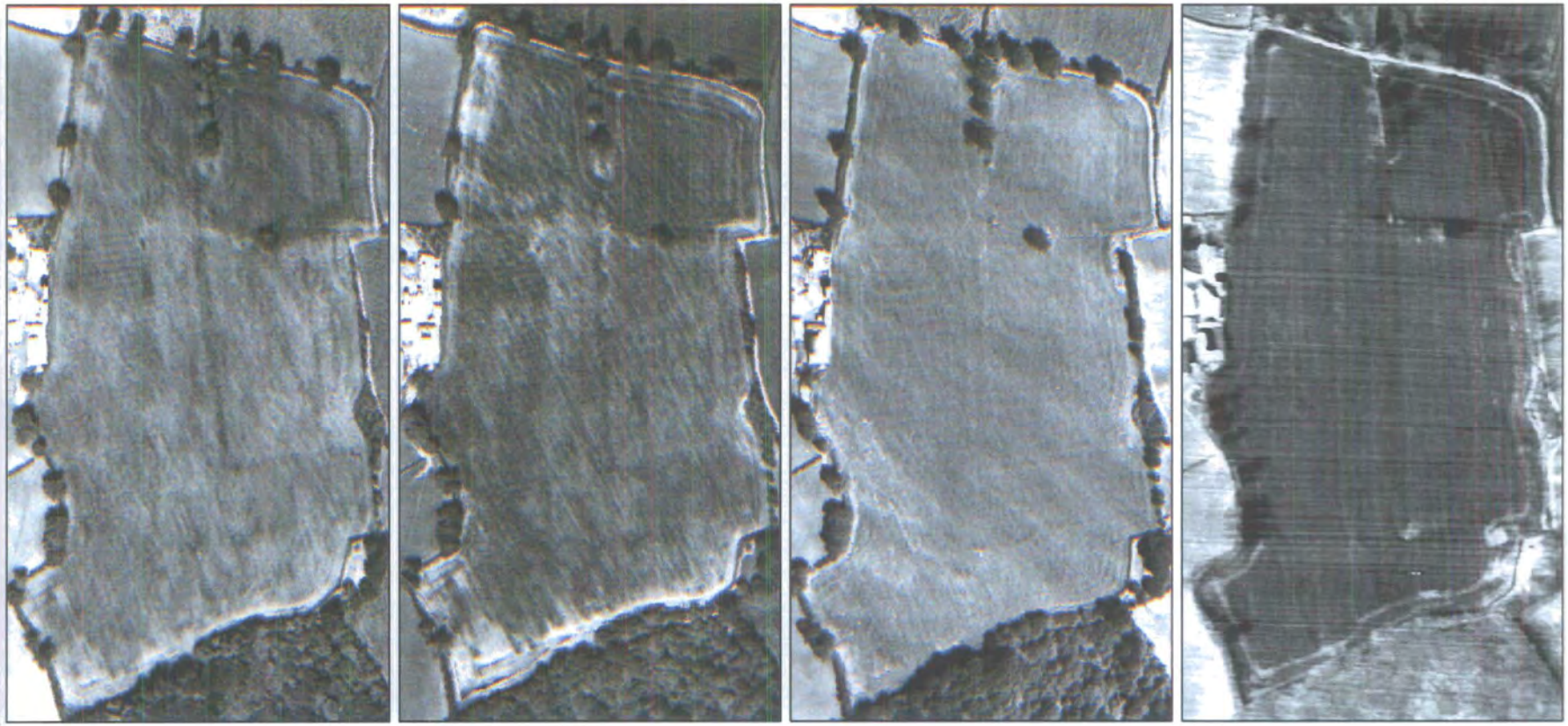

May 1998 Day under barley | June 1998 Day under barley | August 1998 Day under barley | March 2002 Day under oil seed rape

Figure 5.20: Anomalies on Bosworth day thermal images of Ambion field

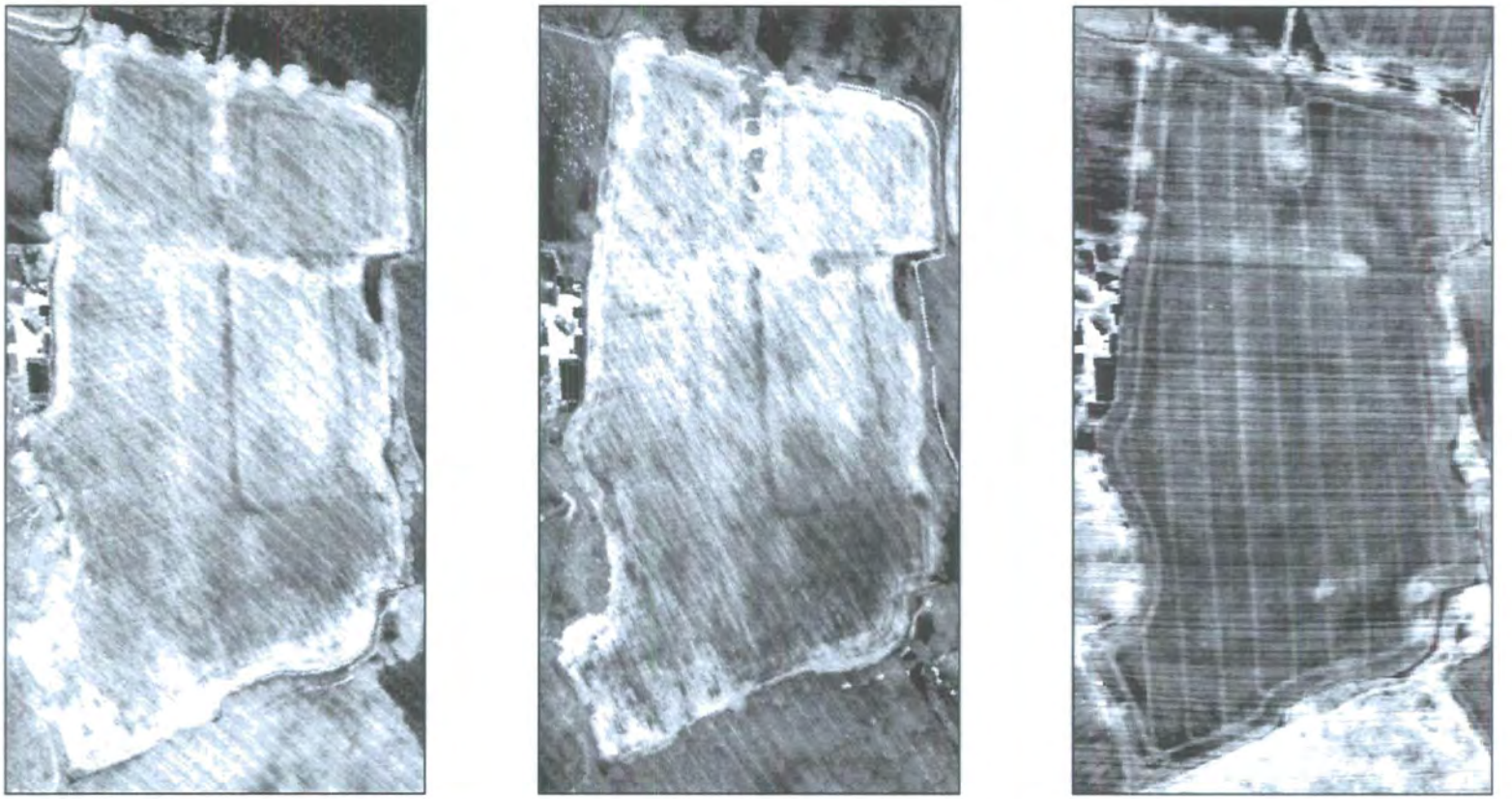

June 1998 Night under barley | August 1998 Night under barley | March 2002 Night under oil seed rape

Figure 5.21: Anomalies on Bosworth night thermal images of Ambion field

When the images that show the most distinct thermal anomalies are compared with the magnetic survey conducted on the field (Figure 5.22), it is apparent that the thermal anomalies representing the old field boundaries and the anomalous area in the south-west corner are not evident on the magnetic survey and so do not represent variations in magnetic properties of the soil. However, the ridge and furrow marks are clearly evident on both sources of data and suggest a concentration of magnetic materials in the plough marks.

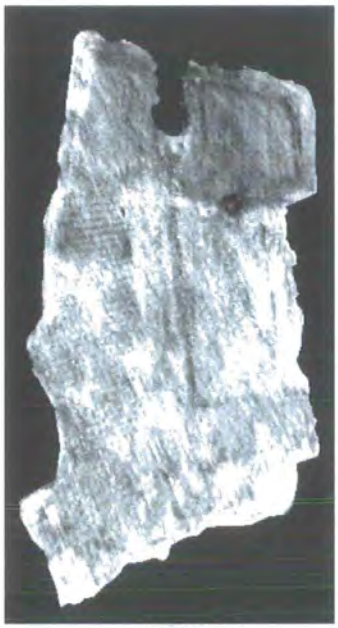

June 1998 Day

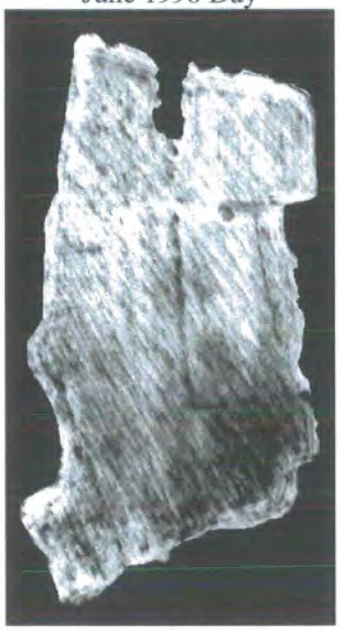

August 1998 Night

Magnetic Survey

Magnetic Survey

Figure 5.22: Comparison of Bosworth August 1998 thermal images with magnetic survey of Ambion field

5.3.1.2 Arena Field Interpretation

The topographic setting of the Arena field is such that there is a topographic high in the NW corner with a gentle downward slope towards all other directions. Visualisation of the day and night thermal response of Arena field (Figure 5.23) show a fairly uniform day response in March, May and June with generally lower temperatures on the eastern side where the topographic slope faces away from the sun resulting in a cooler response. The August image is more variable with a patch of lower temperature near the NW topographic high and in the SW corner where there is a break in the tree-line and shows a continuation of the wind shear effect that dominates Ambion field.

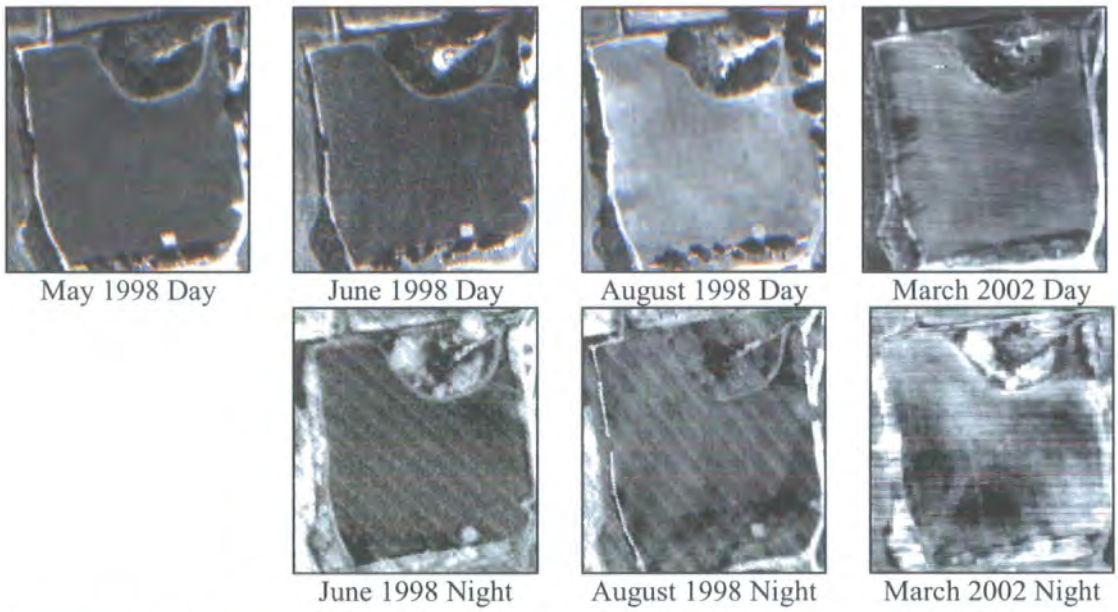

Figure 5.23: Thermal anomalies in Bosworth Arena field

The night thermal images contain more noise than the day thermal images, because at night there is less energy emitted from the ground. The diagonal stripes seen in the June and August 1998 night images are caused by slight inaccuracy in the calibration of the thermal detector, which is set by looking at a hot and cold blackbody at the start and end of each scan line. March 2002 and June 1998 night images show an elongated patch of low temperatures hugging the southern fence line with wider patches occurring between the individual trees where the ground flattens out at the base of the slope. There is a similar pattern on the August 1998 night image slightly further to the north at the break of slope. The March 2002 night image shows an area of low temperature in the NE corner on the steeper E-facing slope with more

pronounced additional patches in the SW corner. These features suggest an affect of wind on the vegetation covering the ground surface.

The August 1998 day image reveals a series of parallel E-W linear anomalies that are not evident at any other point in the vegetation cycle. These possibly represent ridge and furrow plough markings, suggested by their similar temperature pattern and spacing to the ridge and furrow markings observed in the west of Ambion field. Perpendicular to these anomalies there is a small N-S linear feature at the eastern end of the ridge and furrow markings of unknown origin. The linear features present on the August 1998 day image are absent at all other times of imaging. This may be a result of the grass being cut for silage in late July 1998 with a greater visible soil fraction within the field.

The feature that is the most consistent between the images is a rectangular area of bright day and night temperatures at the centre-point of the southern fence line. This marks the position of an area of hard-standing consisting of gravel (Figure 5.24). However this feature is absent from both day and night March images when the area was covered with weeds of similar stand height to the surrounding grass.

Figure 5.24: Area of hard-standing in Bosworth Arena Field

Results from the Arena field suggest that the most variable thermal response occurs when the grass is short suggesting that the underlying soil may have a stronger influence on the thermal response of the surface than when the vegetation fraction dominates. When the image that shows the most distinct thermal contrast is compared

with the geophysical surveys conducted on the field (Figure 5.25), it is apparent that the linear thermal anomalies thought to represent ridge and furrow marks are not evident on the magnetic survey. The resistivity survey shows faint linear anomalies parallel to the more obvious thermal features but did not stretch far enough north to cover their position.

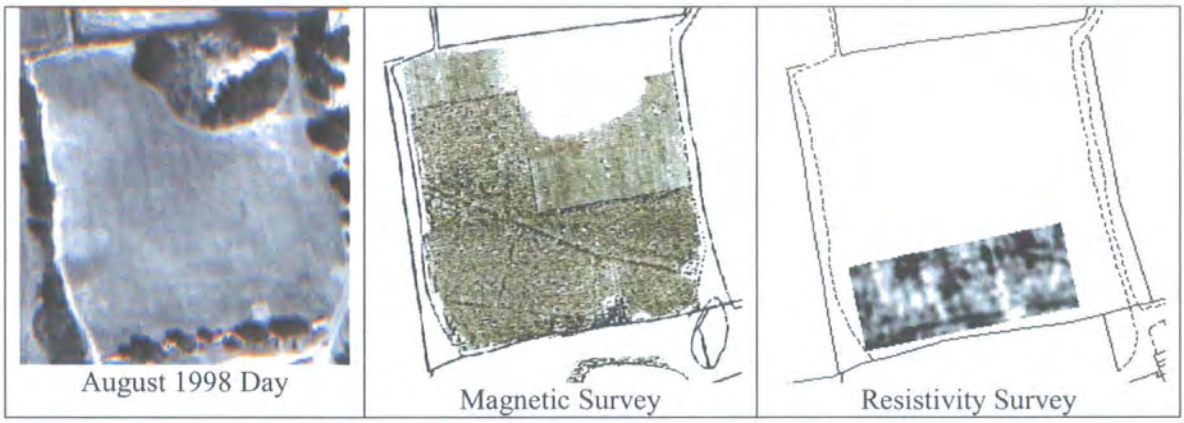

Figure 5.25: Comparison of Bosworth August 1998 day thermal image with results of geophysical surveys of the Arena field

5.3.1.3 Helipad Field Interpretation

The topographic setting of the Helipad field is such that there is a very shallow downward slope towards the south with negligible internal topographic variation (Figure 5.26).

Figure 5.26: Topography of Bosworth Helipad Field

The day and night thermal images of the Helipad field (Figure 5.27) show a prominent NW-SE linear anomaly of high temperature on the May and June 1998 day images with corresponding low temperatures in August 1998 that is absent from the

night images. This feature can be clearly seen on the aerial photography from May and June 1998 (Appendix C1) marking a path trodden by livestock wandering between fields. Perpendicular to this feature there is a series of linear features of alternating high and low temperatures that are prominent on the May 1998 image but are less evident on the June 1998 image and are absent from the other day and night images. Since the grass of this field was kept at a fairly uniform height across the seasonal dataset, the anomalies cannot be explained as a vegetation effect and may therefore represent variations in the moisture content of the soils due to differential compaction of the subsurface by the presence of ditches or tracks. Ditches tend to retain more moisture than the surrounding soil due to the looser infilling material therefore a higher night response would be expected compared to the surrounding soil. Since the night temperatures are fairly uniform across the field, one hypothesis is that the features may represent pipes. There are also areas of low night temperatures in the SE corner of the field and along the eastern fence line that possibly relate to wind and shadow effects caused by the hedgerow.

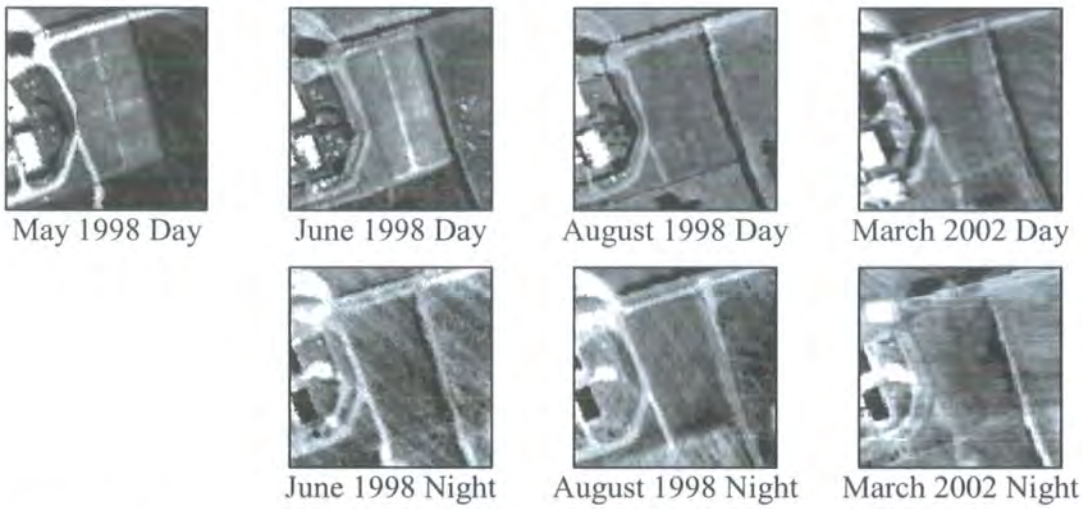

Figure 5.27: Thermal anomalies in Bosworth Helipad field

The results from the Helipad field suggest that the thermal characteristics are likely to represent variations in the moisture content of the ground due to variable compaction. When the image that shows the most distinct thermal anomalies is compared with the geophysical surveys conducted on the field (Figure 5.28), it is apparent that the NE-SW linear thermal anomalies though to represent potential water pipes or ditches are not evident on the magnetic survey, but show a similar pattern to the linear features located on the resistivity survey. Since the resistivity is sensitive to

variations in moisture content, the linear features may well represent ditches where there is a variation in the compaction of the soil infilling the ditch and as a result will have a contrasting response to the undisturbed surrounding soil.

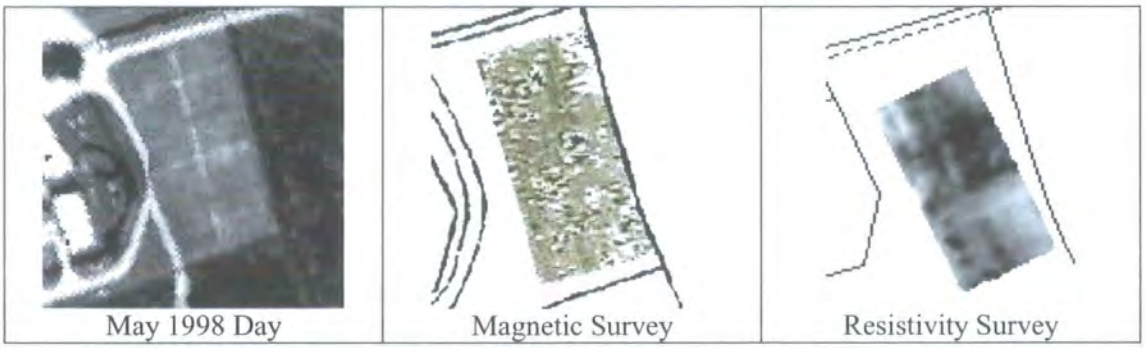

Figure 5.28: Comparison of Bosworth May 1998 day thermal image with results of the geophysical surveys of the Helipad field

5.3.1.4 Picnic Field Interpretation

The topographic setting of the Picnic field is such that there is a moderate downward slope towards the SW corner from the northern fence line with a pronounced NE-SW dip in the topography in the centre of the field (Figure 5.29).

Figure 5.29: Topography of Bosworth Picnic Field

The field shows fairly uniform temperatures on the day images with slightly higher temperatures forming an L-shaped feature observed in the centre of the field on all dates, which corresponds to the position of the topographic hollow (Figure 5.30). The night images are also fairly uniform in response with an area of low temperature observed in the SW corner at the base of the topographic slope in June and August 1998. This marks a thermal shadow effect created by the fully-grown tree adjacent to

this corner of the field. The March 2002 day image shows two pronounced linear features of high temperature along the northern and southern fence lines with moderate temperatures in the SE area to the west of the elliptical car park. The former anomalies mark gravel paths that were created between the 1998 and 2002 flight seasons with the latter marking an area of compacted ground created when the work was being undertaken.

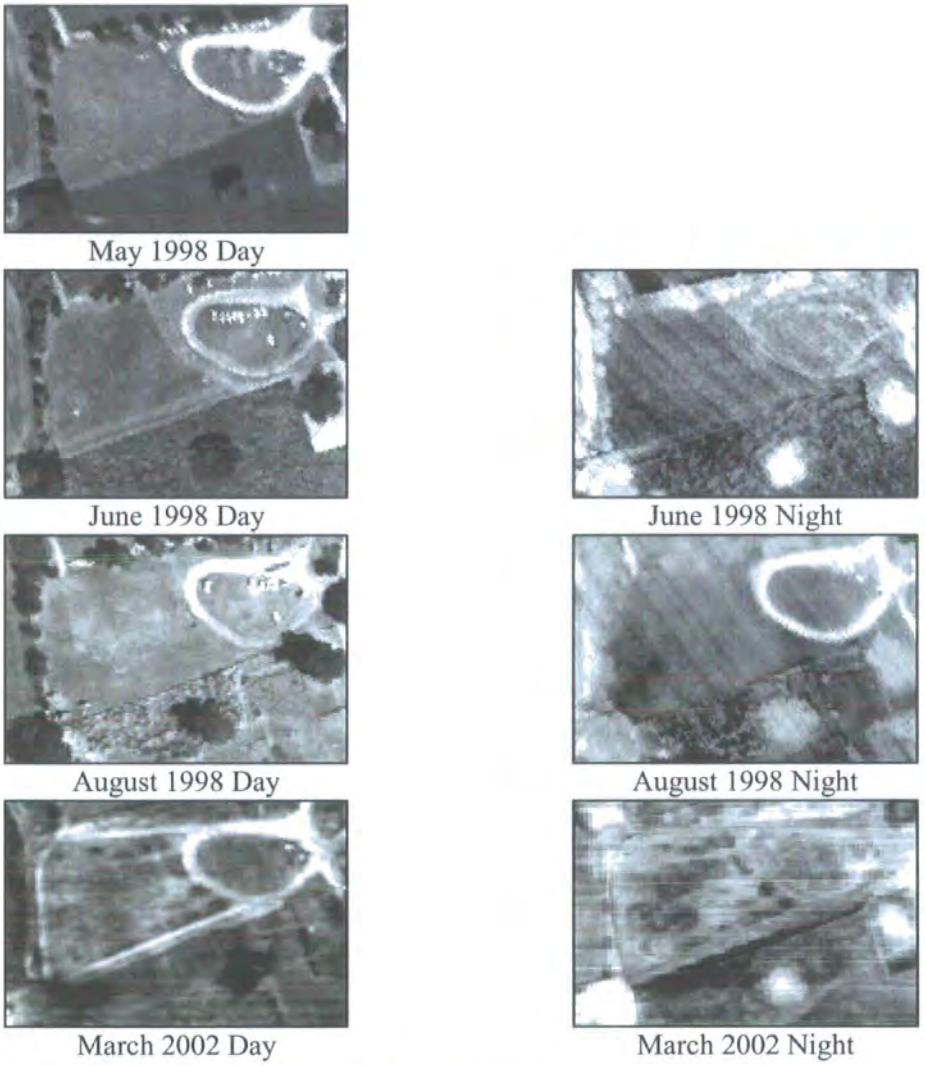

Figure 5.30: Thermal anomalies in Bosworth Picnic field

The results from the Picnic field suggest that the topography of the field results in wind shadow and solar heating effects that influence the observed thermal response. When the image that shows the most distinct thermal anomalies are compared with the geophysical surveys conducted on the field (Figure 5.31), it is apparent that the wide L-shaped thermal anomaly marking the position of the topographic hollow is not evident on the magnetic anomaly. The results of the

resistivity survey show a similar anomalous pattern with a pseudo-vertical area of high resistivity in the northern area and a pseudo-horizontal area of low resistivity along the southern edge of the field possibly representing an intersection of compacted ground. Since resistivity is sensitivity of moisture content and the response pattern is similar to the thermal anomaly, this suggests that when the grass is short, the thermal image is sensitive to variations in moisture content of the soil underneath the vegetation.

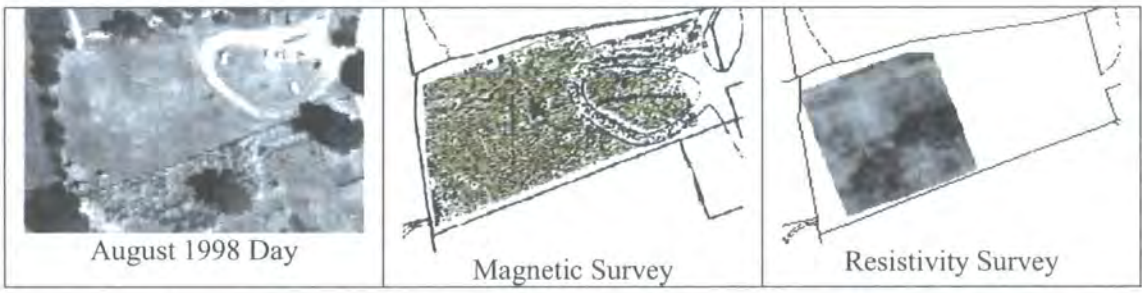

Figure 5.31: Comparison of Bosworth August 1998 day thermal image with results of the geophysical surveys of the Picnic field

5.3.1.5 South Field Interpretation

The topographic setting of the South Field is such that there is a shallow downward slope towards the south over the main part of the field with the NW area having a steeper gradient. The surface vegetation consists mainly of grass that is used for cattle-grazing with scattered thistle and nettle patches in the western section. Visualisation of the day and night thermal response of the South field (Figure 5.32) shows that the nettle patches have lower day and higher night temperatures than the surrounding grasses that increase in contrast with growth. There are two trees within the field, one in the NW and the other in the NE, that result in a lower day temperatures and higher night temperatures than the surrounding materials.

South field is split into three main sections, subdivided by two NW-SE paths of compacted ground that are represented by an elevated day and night temperatures. The field shows fairly uniform temperatures on the May, June and August 1998 images with NW-SE linear anomalies of subtle temperature contrast evident in the two eastern sections and in the far west. These are more prominent on the March 2002 day image when the grass is at its shortest with additional NE-SW linear anomalies cross-cutting these in the western section. These linear anomalies are suggestive of

ancient ridge and furrow markings. There is a pronounced topographic hummock marking earthwork remains in the NE corner adjacent to the car park area (Figure 5.33) and this is represented on all the imagery as a rectangular feature of high temperature with low temperatures on the northern and southern slopes respectively.

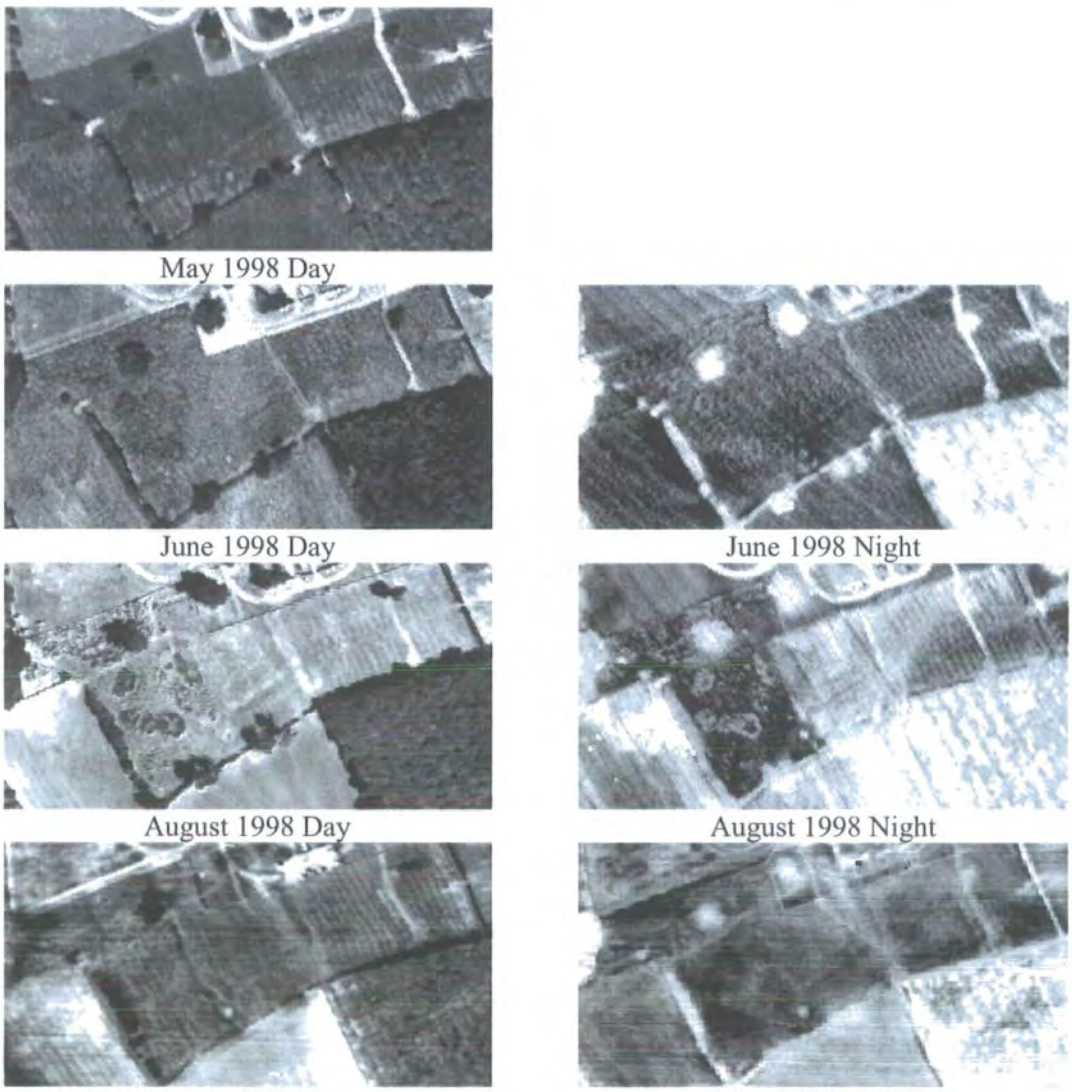

Figure 5.32: Thermal anomalies of Bosworth South field

Figure 5.33: Hummock in Bosworth South Field

The night thermal images reveal an area of low temperatures in the SE section suggesting thermal shadowing effect caused by the adjacent wooded area. There is a circular feature seen in both day and night time thermal images as a warm patch in the SE that marks the position of a water-hole used by the grazing cattle, which are also responsible for the patch of high temperatures by the eastern fence marking the gate between the grazing fields.

Since the grass was at a variable height and condition between the images, the results from the South field suggest that both the vegetation and the topography influence the observed thermal response. When the image that shows the most distinct thermal anomalies are compared with the geophysical surveys conducted on the field (Figure 5.34), it is apparent that the thermal anomalies representing the ridge and furrow markings are evident only as faint linear magnetic anomalies. Since the ridge and furrow marks were clearly evident in the Ambion field on the magnetic survey, this suggests that the soils in the South field may be more clay-rich and as such are less susceptible to magnetic variations. The ridge and furrow marks are absent from the resistivity survey, although there is not sufficient spatial coverage to be confident of detection. The topographic hummock evident on all the thermal images is not seen as an anomaly on the magnetic survey, but is clearly evident on the resistivity survey as an area of low resistance corresponding to the topographic high. This again suggests that the thermal image is sensitive to moisture variations in the near-surface environment.

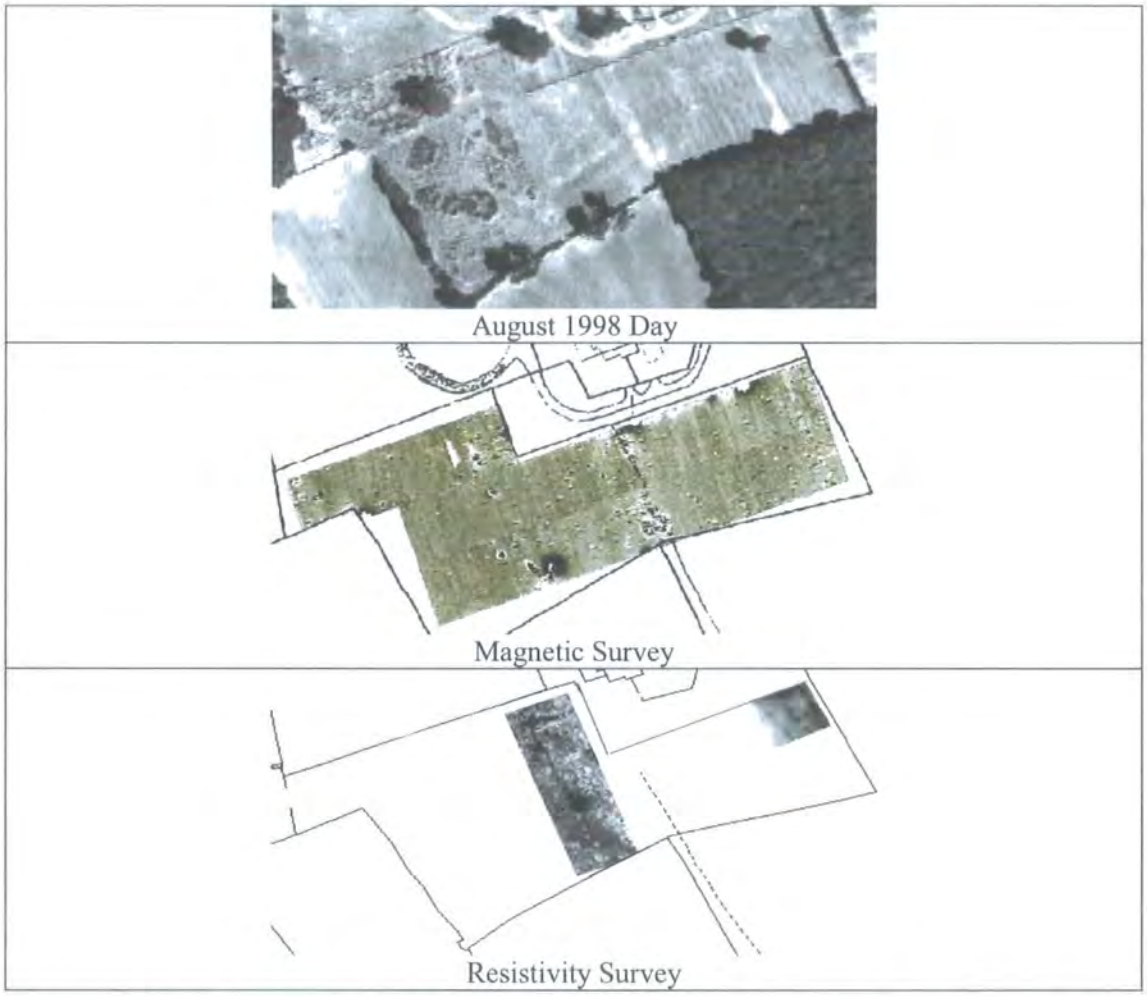

Figure 5.34: Comparison of Bosworth August 1998 day thermal image with results of magnetic survey of the South field

5.3.1.6 Summary of Bosworth Interpretation

The results from the geophysical prospection of the Bosworth site suggested that there is a range of physical features occurring beneath the soil surface in the main fields surrounding the visitor centre (Chapter 3.4). The fields surrounding the visitor centre are covered by fallow grasses and agricultural crops, such as barley and oil seed rape, and are imaged at different stages in the vegetation growth cycle.

The grass-covered Arena field shows few thermal anomalies when the grass is long in May and June 1998, however, when the grass has been shortened in August 1998 there are a few linear thermal anomalies that can be seen on the day thermal image possibly representing non-topographic ridge and furrow marks. The results of the magnetic survey reveal a series of linear features that are different to the thermal anomalies and so the thermal response does not represent variations in magnetic

response of the soil. The results of the resistivity survey reveal some faint linear anomalies the correlate to the position of the ridge and furrow anomalies suggesting that when the grass is short, the thermal response is sensitive to variations in moisture in the near-surface environment. However, both the magnetic and resistivity surveys reveal features that are additional to those evident on the thermal images suggesting that the thermal images cannot be used on their own to describe the shallow subsurface environment.

The grass-covered Helipad field shows strong linear thermal anomalies when the grass is short in May and June 1998, however, when the grass is lengthened these features become masked. The NW-SE and NE-SW linear anomalies are not evident on the magnetic survey. However, both anomalies can be clearly seen on the resistivity survey. As with the Arena field, this suggests that the thermal anomalies may represent variations in the moisture content of the underlying soil when the grass is short. Once again, both the magnetic and resistivity surveys reveal features that are additional to those evident on the thermal images so the thermal images cannot be used on their own to describe the shallow subsurface environment.

The grass-covered Picnic field shows a faint L-shaped feature in May and June 1998 and a much stronger contrast in August 1998 when the grass is shorter. This corresponds to the pronounced variation in the topographic slope and is absent from the magnetic survey. However, the feature is evident on the resistivity survey again suggesting that the thermal images represent variations in the moisture content of the soil and are more readily observed when the grass is short. As for the other fields, the magnetic and resistivity surveys reveal features that are additional to those evident on the thermal images.

The grass-covered South field shows a series of parallel linear anomalies on all thermal images that represent ridge and furrow marks. Although these are evident as only very faint anomalies on the magnetic survey, this may be due to the presence of the clay-rich soils that mask variations in the magnetic response. The features are absent from the resistivity survey, although poor spatial coverage due to insufficient time prevents confidence in their detection. The topographic hummock marking earthwork remains is absent from the magnetic survey, but this is likely to be a factor of the clay-rich soils masking the magnetic response. The feature is clearly evident on

the resistivity survey where there is a variation in the moisture content between the soil above the earthwork remains and the surrounding soil and again suggests that the thermal imagery represents moisture variations in the near-surface environment.

The Ambion field shows a series of parallel linear anomalies on the day and night thermal images during barley growth that represent ridge and furrow marks. These are clearly evident on the magnetic survey. The linear anomalies representing the old field boundaries are progressively less evident on the day thermal images as the barley matures but show similar night response at all stages of barley growth. However, these features are absent from the magnetic survey. The magnetic survey also reveals numerous linear features that are not evident on any thermal image suggesting that the thermal response is sensitive to different physical properties than the magnetic survey. None of these features are detected under the oil seed rape suggesting that the high leaf area of the vegetation completely masks the response from the underlying soil.

The results from the thermal analysis of Bosworth suggest that an optimum detection for thermal anomalies occurs during diurnal maximum temperatures when the soil is covered by a layer of short grass or at an early stage in barley growth when there is a greater visible soil fraction. Thermal detection is poor during diurnal minimum temperatures for the grass-covered fields, but provides a more consistent thermal response when barley is present. When the images are compared with the results of the geophysical surveys, there appears to be poor correlation between the thermal images and the magnetic response. This result leads to simple assumptions that either the depth of observation varies between the thermal and magnetic techniques or that the thermal response is sensitive to different environment properties than the magnetic response. However, when the images are compared with the results of the resistivity survey, there appears to be much better correlation in feature detection. This suggests that the thermal response is likely to represent variations in moisture content of the surface. In order to understand fully the relationship between the physical soil characteristics and the thermal properties in more detail, soil profiles are extracted across some of the features showing variable thermal and geophysical response and the results shall be discussed in later chapters.

5.3.2 Visualisation and Detection of Baildon Moor Thermal Anomalies

Interactive contrast stretching was applied to single-band visualisations of the day and night thermal data obtained over Baildon Moor (Figure 5.35). There are three main features highlighted that shall be discussed in detail: 1) abandoned mineshaft of pronounced topographic expression (Figure 5.36), 2) abandoned mineshaft of distinct concentric vegetation (Figure 5.37) and 3) a thermal feature of no topographic expression but with a different central vegetation (Figure 5.38).

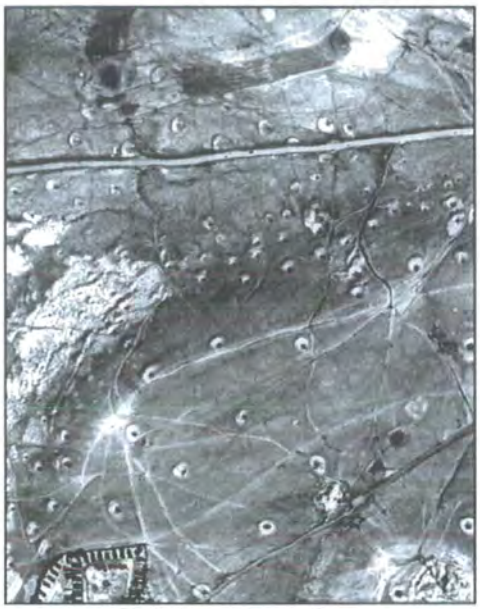

Baildon Moor Day

Baildon Moor Night

Figure 5.35: Thermal anomalies on Baildon Moor

Figure 5.36: Baildon shaft of pronounced topographic expression (radius 8m)

Figure 5.37: Baildon shaft of pronounced vegetation expression (radius 11m)

Figure 5.38: Baildon suspected shaft feature (radius 2m)

5.3.2.1 Shaft of Topographic Expression

The abandoned mineshaft of pronounced topographic expression is represented at ground level by an increase in elevation of the shaft rim compared to the surrounding grassland due to spoil mounding with a topographic hollow at the centre corresponding to the position of the shaft. This is typical of the majority of abandoned mineshafts in the southern region of Baildon Moor. The shaft is represented by a circular thermal feature on both day and night images with a low response at the shaft centre surrounded by a rim of high response on the day image, with only a slight elevation in response compared to the surrounding material on the night thermal image (Figure 5.35). Thermal profiles are generated over the shaft to determine spatial characteristics in response. Since the physical temperature of the surface is unknown due to the lack of auxiliary ground temperature measurements, the profiles of the shaft are discussed in terms of uncalibrated thermal radiance values whose shape will emulate the shape generated when using calibrated temperature values.

Profiles generated across the shaft in the day (Figure 5.39) show a fairly symmetrical W-E and N-S profile with pronounced warming of the rim of the shaft and a decrease in thermal response to a flat response at the centre of the shaft, emulating the topographic expression. Both profiles show a similar width in response of the rim of the shaft and a similar level of response on either side of the shaft corresponding to the area of background vegetation. The profiles show a slightly elevated thermal response on the SE rims of the shaft, which is expected since the topographic slopes face solar heating. Profiles generated across the shaft at night (Figure 5.40) again show a pronounced decrease in thermal response at the base of the shaft on both W-E and N-S profiles. The flat response seen in the daytime imagery has disappeared in the pre-dawn imagery with a warmer response of the SW area of the base of the shaft. The W-E profile shows a slight elevation in thermal response on the western rim, however, the eastern rim is less easily discriminated from the background vegetation. The margins of the shaft are more easily recognised on the N-S profile by their elevated response, however the shape is more asymmetrical with the southern margin having a wider response than that of the northern margin. Therefore, the profiles suggest that the material on the SW margin has the ability to retain more heat and may have a different composition or higher moisture content than the NE slopes.

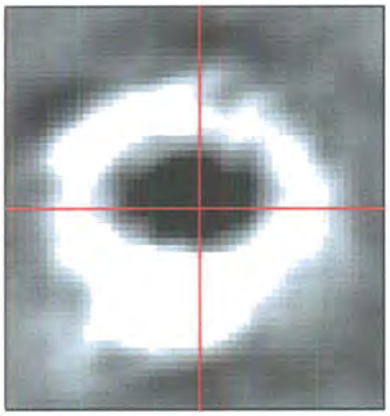

Day

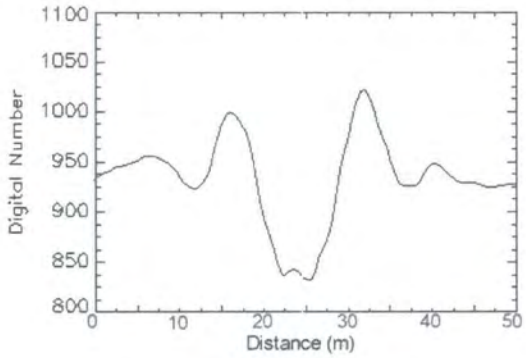

W-E

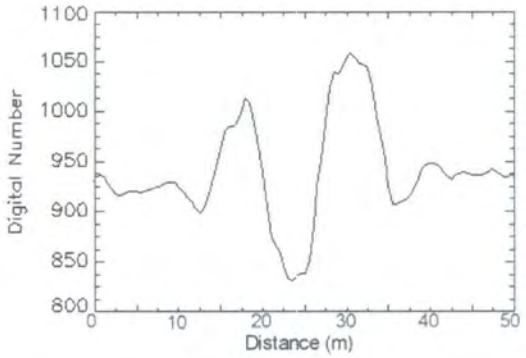

N-S

Figure 5.39: Thermal profiles generated across topographic shaft from Baildon day thermal image

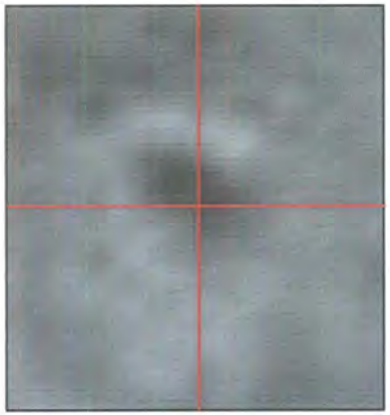

Night

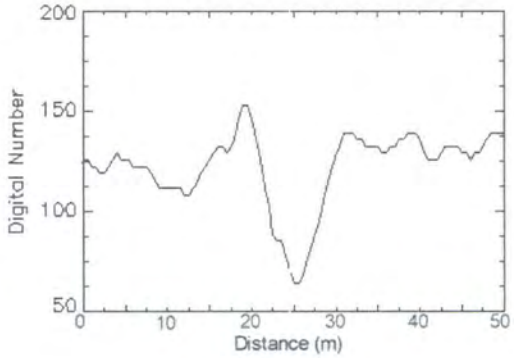

W-E

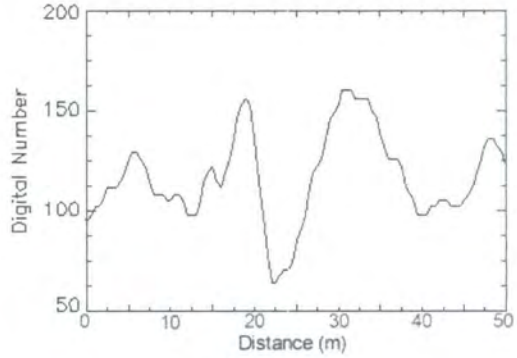

N-S

Figure 5.40: Thermal profiles generated across topographic shaft from Baildon night thermal image

When the day and night thermal profiles are compared with the EM31 electromagnetic profile (Figure 5.41), it is apparent that the observed thermal anomaly corresponds to a variation in the conductivity of the subsurface materials. Since conductivity is sensitive to variations in moisture content, this suggests that the drop in thermal response measured over the topographic shaft may be caused by a decrease in moisture content at the 8m depth of observation possibly due to capping of the shaft. Unfortunately, no alternative geophysical survey techniques were performed at this site to provide greater insight into the nature of the feature.

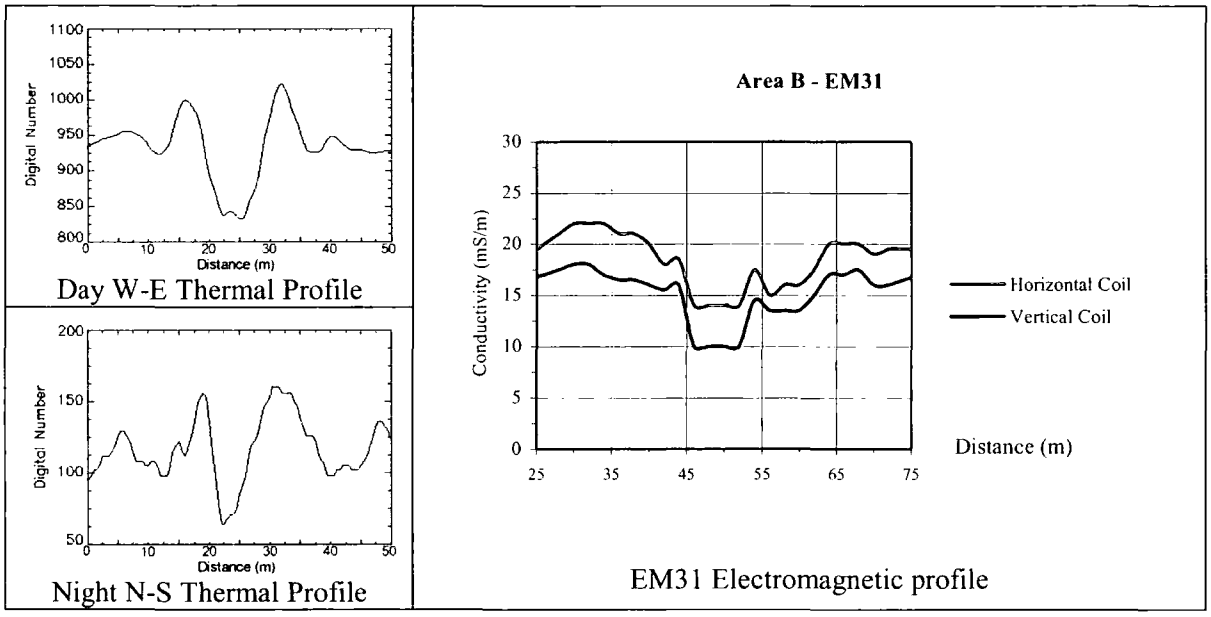

Figure 5.41: Comparison of thermal profiles with EM31 electromagnetic profile across Baildon topographic shaft

5.3.2.2 Shaft of Variable Vegetation

This abandoned mineshaft shows a pronounced concentric vegetation expression with tall reed grass at the centre of the shaft, where there is standing water, that is surrounded by a ring of flat short grass leading to the background vegetation. This is typical of the abandoned mineshafts in the northern region of Baildon Moor. The shaft is represented by a circular thermal feature on both day and night images, with a low response at the shaft centre surrounded by a rim of higher response on both images (Figure 5.35). Thermal profiles are generated over the feature to determine spatial characteristics in response.

Profiles generated across the shaft in the day (Figure 5.42) show an asymmetrical response with pronounced elevated values on the SW margin of the shaft. The centre of the shaft is marked on the N-S profile by a symmetrical U-shape of low response compared to the elevated response provided by the surrounding rim. The background vegetation on the southern margin shows a lower response than the northern margin, which may be a result of the slight topographic slope towards the south. The centre of the shaft shows a more asymmetrical pattern on the W-E profile with higher values evident on the western area of the shaft centre, which may be an indication of variations in the material properties beneath the surface or differential heating of the surface vegetation. Profiles generated across the shaft at night (Figure 5.43) again show an asymmetrical response relating to the rim surrounding the shaft centre with elevated response evident on the SE margin of the shaft. The W-E profile again shows higher values on the western area of the shaft centre. The response patterns recorded over this feature suggest that there may be a wider rim on the SW of the shaft centre suggesting that the entrance to the shaft may be slightly angled towards the NE.

When the day and night thermal profiles are compared with the Wenner resistivity profile (Figure 5.44), it is apparent that the observed thermal anomaly corresponds to a variation in the resistance of the subsurface materials. Since resistance is sensitive to variations in moisture content, this suggests that the drop in thermal response measured over the vegetation feature may be caused by an increase in moisture content, which is corroborated by the presence of standing water at the centre of the feature. However, the results of the electromagnetic survey also show a decrease in the conductivity across the shaft at the 8m depth of observation (Figure 3.29) suggesting a change in physical characteristics of the soil at depth, possibly representing capping of the shaft.

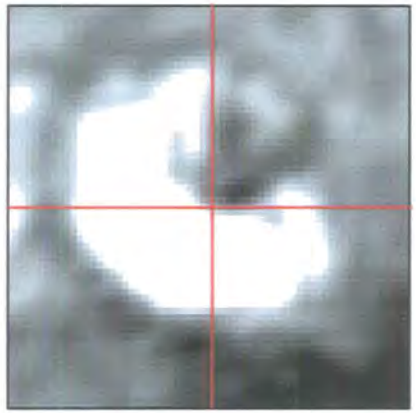

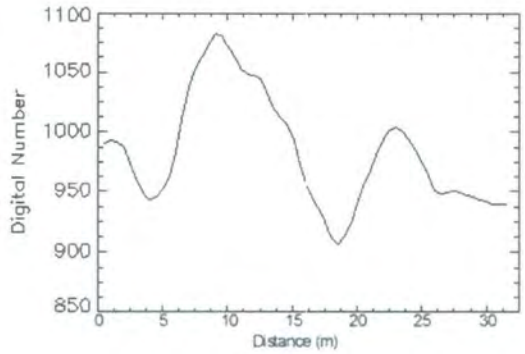

W-E

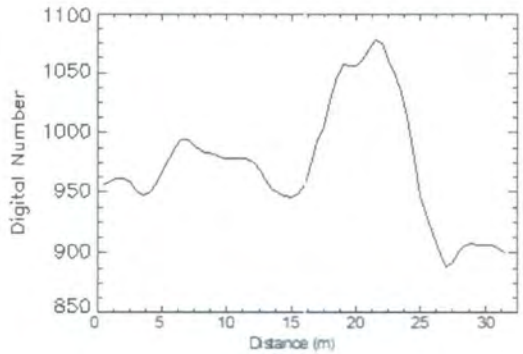

N-S

Day

Figure 5.42: Thermal profiles generated across vegetation feature from Baildon day thermal image

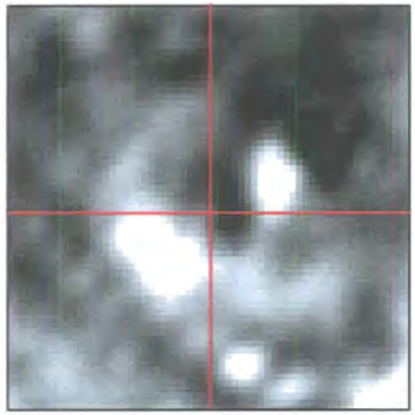

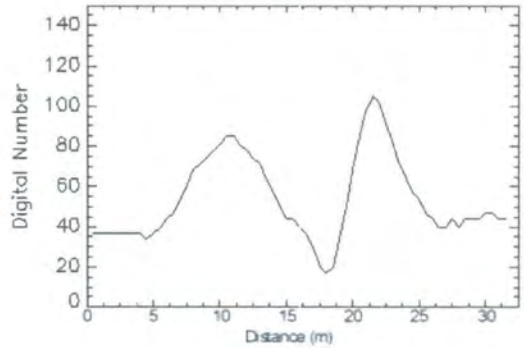

W-E

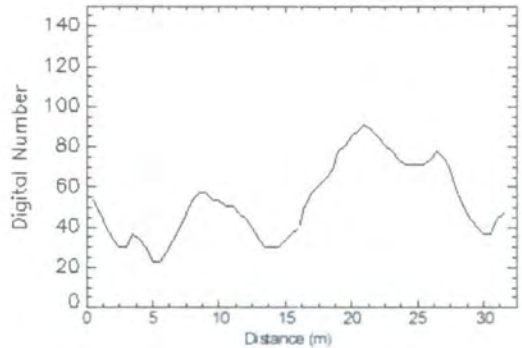

N-S

Night

Figure 5.43: Thermal profiles generated across vegetation feature from Baildon night thermal image

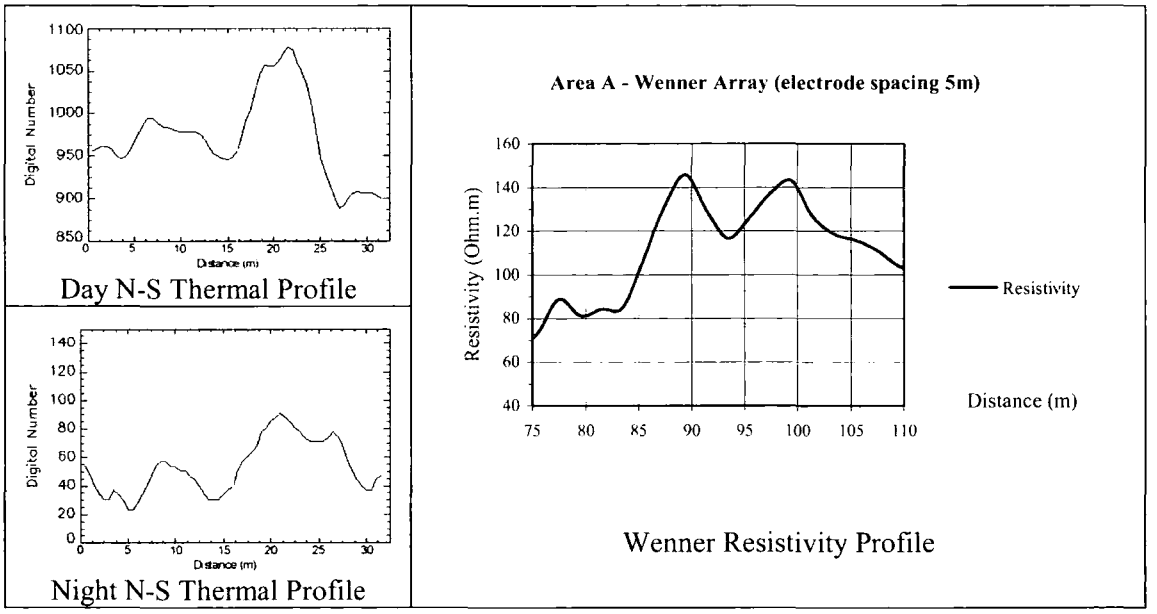

Figure 5.44: Comparison of thermal profile with resistivity profile across Baildon vegetation feature

5.3.2.3 Suspected Shaft Feature

The circular feature that is suspected to relate to mine activity is much smaller in dimension than the previous shaft features being only 4m in diameter. The feature is expressed at the surface by an area of slightly taller reed grasses with a boggy region at the centre. The feature is easily recognised on the night thermal image by an area of slightly lower night response. However, the feature is more difficult to locate on the day imagery since the feature has similar response to the surrounding vegetation (Figure 5.35). There is also the additional problem of co-registration between the day and night images over this feature due to lack of suitable ground control where the adjacent track is similar to the spatial resolution of the data with the wall adjacent to the track causing an additional mixed pixel problem. Thermal profiles are generated over the feature to determine spatial characteristics in response using the position of the feature identified on the night thermal image and the corresponding pixels on the day image.

The W-E profile generated across the feature in the day (Figure 5.46) shows a slight decrease in response across the vegetation with a minor negative anomaly corresponding to the position of the suspect feature. The N-S profile again shows a negative anomaly at the position of the feature, with a pronounced negative anomaly corresponding to the position of the dirt track and a positive anomaly on the

topographically higher southern slope. The profiles across the feature at night (Figure 5.47) show a more pronounced negative anomaly with respect to the background vegetation over the feature with a gradual increase in response over the dirt track towards the SE of the feature. The higher response to the SE suggests potentially higher moisture content of the soil on the SE of the feature.

When the day and night thermal profiles are compared with the Wenner resistivity profile (Figure 5.45), it is apparent that the asymmetry in the observed thermal anomaly also corresponds to an asymmetry in the resistance of the subsurface materials with a decrease in resistance across the suspected shaft feature. Since resistance is sensitive to variations in moisture content, this suggests that the decrease in thermal response to the SE of the suspected shaft feature may be caused by an increase in moisture content. The EM31 electromagnetic profiles show no prominent anomaly at the 8m depth of observation (Figure 3.34) suggesting that the thermal anomaly is present at very shallow depth.

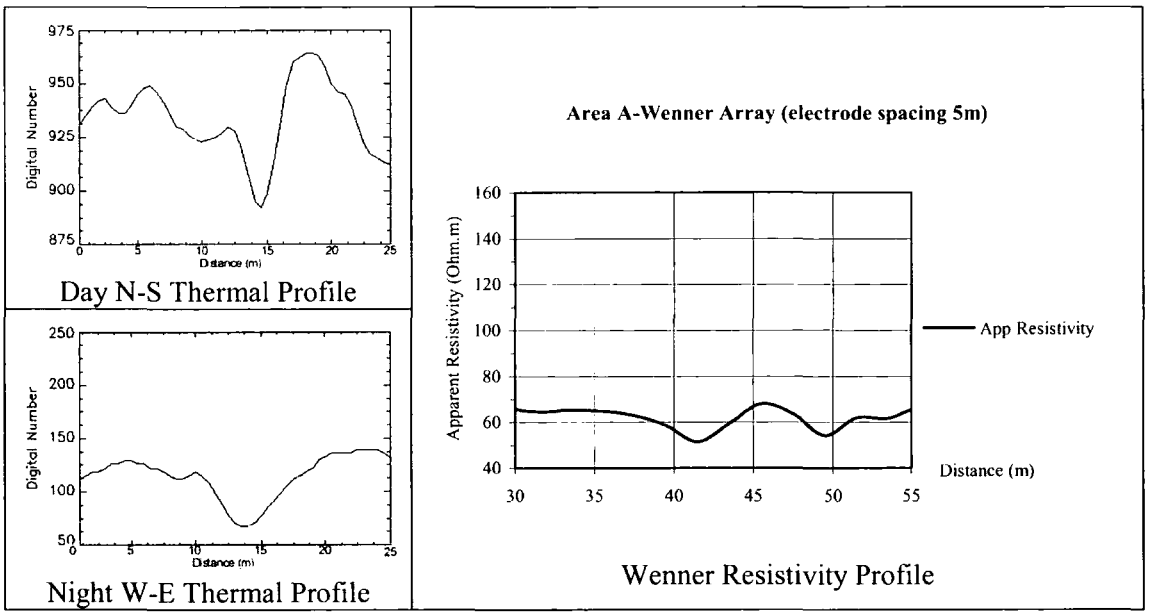

Figure 5.45: Comparison of thermal profile with resistivity profile across Baildon suspected shaft feature

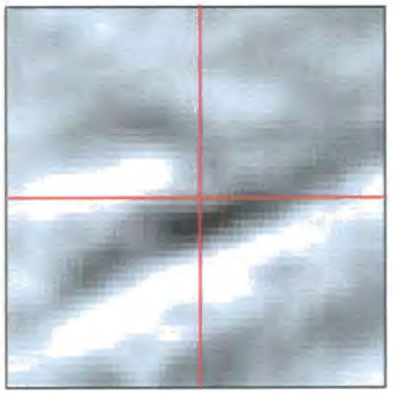

Day

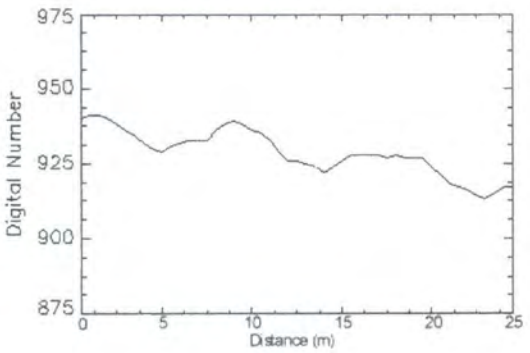

W-E

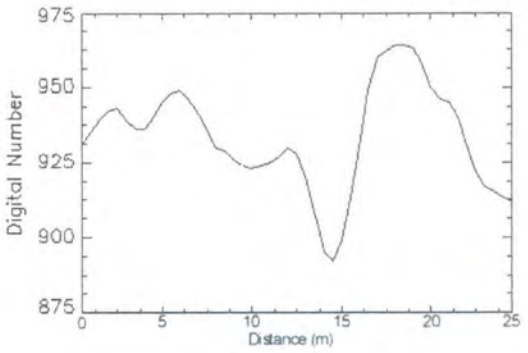

N-S

Figure 5.46: Thermal profiles generated across suspected shaft feature from Baildon day thermal image

Night

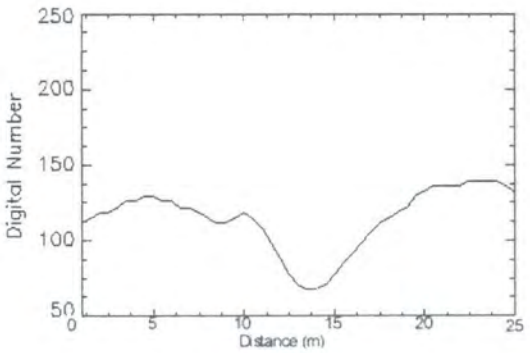

W-E

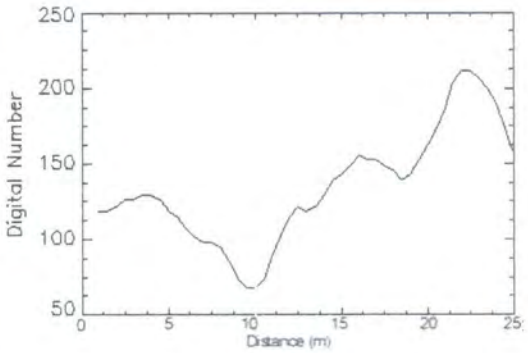

N-S

Figure 5.47: Thermal profiles generated across suspected shaft feature from Baildon night thermal image

5.3.3 Visualisation and Detection of Weardale Thermal Anomalies

The interactive contrast stretching was applied to single-band visualisations of the day and night thermal data obtained over Weardale to identify areas of anomalous thermal response (Figure 5.48). The main features of interest at this site are the areas of scour marks and spoil heaps on the north-eastern flank of the valley, which are created by processes of mineral extraction.

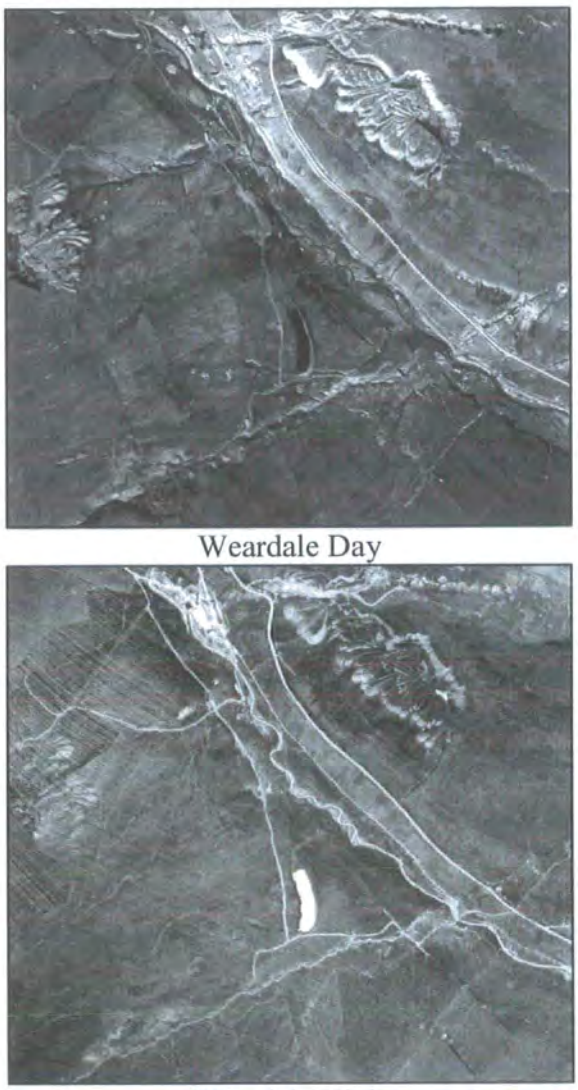

Weardale Day

Weardale Night

Figure 5.48: Thermal anomalies in Weardale

The scour marks are represented at ground level by a series of connected circular features that are excavated from the surface of the moor (Figure 5.49). The scour marks are represented by circular thermal features on both day and night images with a pronounced high thermal response on the side affected by solar heating during the day with a more uniform response from both sides at night.

Scour Mark (height 10m)

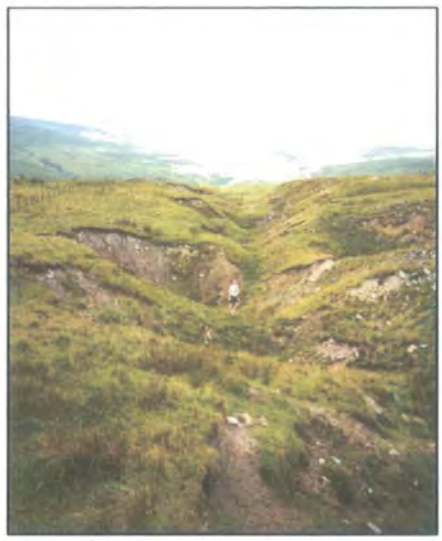

Connected Scour Marks

Connected Scour Marks

Figure 5.49: Scour marks on north-eastern flank of valley in Weardale

The spoil heaps were difficult to assess from ground level due to restricted access to the moorland during the foot and mouth crisis. They have a bulbous appearance on the images spreading out from a central location, with high response at the extremities. There appear to be several phases of heaping on the imagery where more recent heaps cover previous surface patterns. Thermal profiles are extracted across the scour marks and spoil heaps from the day (Figure 5.50) and night (Figure 5.51) thermal imagery to assess thermal response patterns that are typical of such features.

Day

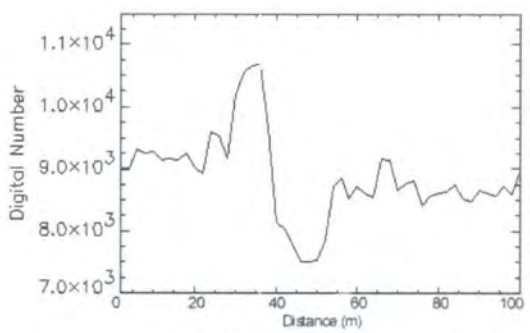

Scour Marks (N-S)

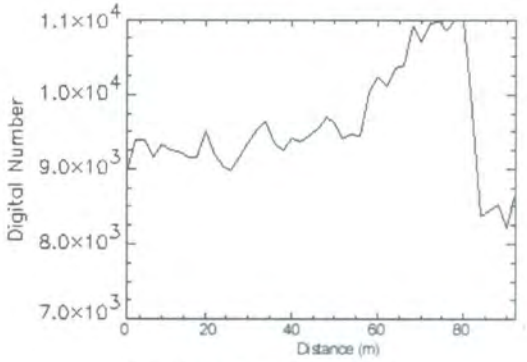

Spoil Heaps (NE-SW)

Figure 5.50: N-S thermal profiles of mineral extraction features from Weardale day thermal image

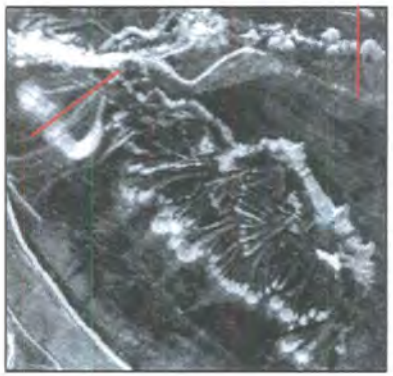

Night

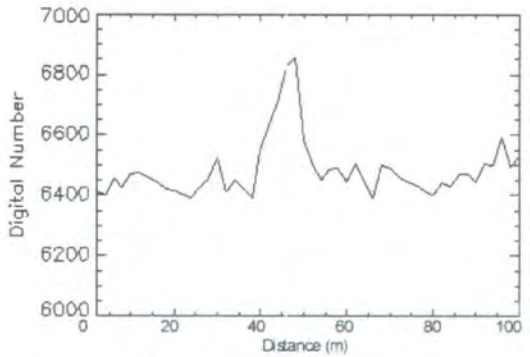

Scour Marks (N-S)

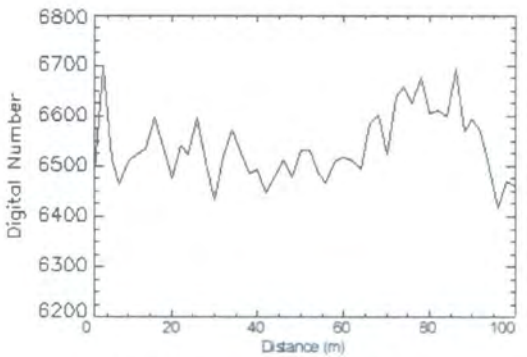

Spoil Heaps (NE-SW)

Figure 5.51: N-S thermal profiles of mineral extraction features from Weardale night thermal image

The profile across the daytime imagery for the scour mark shows a prominent positive and negative thermal anomaly relating to the sides of the scour marks facing towards and away from the sun respectively, with the night thermal profile across the scour mark showing a single positive anomaly corresponding to the side that was facing the sun during the day. The day profile extracted across the spoil heap shows a gradual rise in radiance values towards the edge of the spoil heap that faces the sun and has a prominent positive thermal anomaly. In contrast, the extracted night profile shows a more uniform thermal response with a slight positive thermal anomaly associated with the edge of the spoil heap that was facing the sun during the day. These thermal profiles are consistent across each of the scour marks and spoil heaps.

Unfortunately, due to restricted access to the land during the foot and mouth crisis, no geophysical surveying was performed in the region therefore the physical nature of the thermal anomalies associated with the abandoned mine activity cannot be described fully. Although surveying could have been performed at a later stage, this was not carried out as a result of a combination of the poor quality of the night data and the lack of ground spectral calibration for the day data.

5.3.4 Summary of Single Band Assessment

The diurnal data from Bosworth showed pronounced thermal anomalies in the grass-covered fields during the day when the grass is short, which are not evident on the night thermal images. Thermal anomalies are evident in the barley-covered field on both day and night images during early stages in crop growth but when the crop reached maturity, the thermal anomalies are only evident on the night thermal image. This suggests that the fuller crop masks the thermal response of the underlying soil. However, the diurnal data under the oil seed rape showed no internal field variation, which may be due to the higher leaf area compared with the barley masking the underlying soil. The results from geophysical analysis of these fields revealed a number of linear geophysical anomalies that correlated with the thermal anomalies representing ridge and furrow marks in Ambion field. However, thermal anomalies in the grass-covered fields were closely correlated with resistivity anomalies suggesting that the thermal anomalies can be attributed to variations in moisture content in the shallow subsurface. The lack of correspondence between the magnetic survey and the

thermal anomalies suggests that the thermal images cannot describe fully the features in the shallow subsurface.

The diurnal data from Baildon Moor suggests that the abandoned mineshafts of pronounced topographic or vegetation expression can be identified as circular features on either day or night thermal images, with use of histogram manipulation techniques to enhance the visual contrast of the area surrounding the features. Thermal profiles extracted across the topographic feature show a strong negative day or night anomaly corresponding with the position of the centre of the shaft and this matches the position of pronounced electromagnetic anomaly measured at 8m depth of observation. Since this geophysical technique detects variations in conductivity and moisture content, the thermal anomaly may be related to a physical change in soil structure at depth. Thermal profiles extracted across the vegetation feature, represented by concentric vegetation growth at ground level, again show a strong negative day and night anomaly over the feature with slight asymmetry towards the SE margin of the shaft. The geophysical surveys detected a negative resistance anomaly over the shaft suggesting an increase in moisture content at depth and also an increase in conductivity over the shaft suggesting a change in the physical characteristics of the soil at depth, possibly relating to capping of the shaft at depth. Thermal profiles extracted across the suspected shaft feature, represented at ground level by a minor vegetation change, show a pronounced negative anomaly only on the night thermal image corresponding to the suspected feature, with an asymmetry in response towards the SE. The resistivity survey also showed a slight asymmetry across the feature with an increase in moisture content to the SE of the feature. However, the electromagnetic surveys failed to show an anomaly across this feature, suggesting that the night thermal anomaly corresponds to an increase in moisture content at very shallow depth.

The diurnal data from Weardale suggests that the scour marks of abandoned mine activity can be identified as circular features on either day or night contrast enhanced thermal images with the spoil heaps displaying a radial pattern. Thermal profiles extracted across the scour marks show a positive day and night anomaly on the sides of the scour that face the sun with uniform temperatures representing the surrounding vegetation. Since the scour marks are known to have little internal vegetation growth the thermal response may be characteristics of bare soil. The

thermal profiles extracted across the spoil heaps show a similar positive day and night anomaly at the edge of the spoil heaps suggesting that there is little vegetation growth at the edges. However, it was not possible to verify this due to restricted access to the land and was not followed up at a later date as a consequence of poor data quality.

The archaeological and mining features of interest in the research have shown characteristic thermal response patterns on the day and night monochrome thermal images under different vegetation conditions, some of these features correlate with geophysical survey others do not. However, it is important to compare and contrast the thermal infrared data with that of aerial photography or visible, near-infrared or shortwave infrared spectral wavelength. To investigate this, a series of colour composites are generated using the available spectral wavelengths and the response patterns are compared with the results of the thermal assessment. This is conducted on only the Bosworth dataset due to problems encountered in removal of atmospheric effects from the Baildon Moor and Weardale datasets. By comparing the colour composites with the thermal assessment, this gives both an indication of the amount of additional detail provided by the inclusion of the thermal channel and also if there are particular times in the vegetation growth cycle when the visible, near-infrared or shortwave infrared response matches that of the thermal channel and can be used to provide an adequate depiction of the near-surface environment.

5.4 COMPARISON of TIR EMITTANCE with VISIBLE, NEAR-INFRARED and SHORTWAVE INFRARED

The amount of additional detail provided by the inclusion of the thermal channel is assessed by visualising a series of colour composite images from Bosworth where a combination of spectral bands is displayed on the red, green and blue VDU display channels. The interpretation layer of the Bosworth thermal features generated through the previous thermal band assessment is then displayed on top of each of the appropriate colour composite images to assess the amount of additional detail provided by inclusion of thermal infrared channel. There are two main spectral combinations that are used for assessment with generation of natural colour and near-infrared false-colour composites. In addition, the thermal channel is also displayed as part of the spectral combination to assess the variability in the visualisation techniques.

5.4.1 Natural Colour Composites

Natural Colour Composites for the Daedalus 1268 sensor are generated by displaying a combination of the visible red (Band 5), green (Band 3) and blue (Band 2) spectral wavelengths on the corresponding image display channels to simulate the visualisation of the standard colour aerial photographs of the study site (Appendix C1), which are subsequently overlain by the interpretation of the corresponding day thermal data (Figure 5.52).

In May 1998 the fields surrounding the visitor centre show a fairly uniform surface coverage of healthy green grass. The Helipad field appears to be covered with browner shade of grass, which is a result of recent mowing reducing the height of the grass and revealing a higher visible soil fraction that correspond with areas of higher day thermal response. The strong alternating light and dark brown linear anomalies on the natural colour composite correspond with the position of alternating high and low thermal response respectively. The Arena and Picnic fields show very little internal field variation on the natural colour composite and display a similar uniform thermal response. The natural colour composite reveals a series of NW-SE linear anomalies in the South field that correspond to the position of similar thermal anomalies suggestive of ridge and furrow marks. Ambion field shows a strong linear characteristic of the surface vegetation as a result of present-day ploughing of the agricultural crop, which can also be identified on the thermal image. There are faint N-S and E-W linear anomalies on the natural colour composite that correspond to the positions of linear anomalies on the day thermal image that represent old hedgerow boundaries. The faint E-W linear anomalies on the west of the field are representative of ridge and furrow marks that are also evident on the day thermal image. Results from this stage in vegetation development suggest that thermal infrared does not provide additional detail to natural colour composite at an early stage in barley growth but enhances detail in fields with a cover of grass.

May 1998

May with TIR interpretation overlay

June 1998

June with TIR interpretation overlay

August 1998

August with TIR interpretation overlay

March 2002

March with TIR interpretation overlay

Figure 5.52: Natural colour composites of Bosworth

In June 1998 there is a greater contrast in response between the fields surrounding the visitor centre. The Helipad field has lost much of its brown appearance as the grass has developed and reduced the visible soil fraction. The N-S linear anomaly is still prominent and corresponds to a linear thermal anomaly within this field. The Arena and Picnic fields again show little internal variation with a uniform thermal response. The ridge and furrow marks in the South field are more prominent than in May, which may be a result of differential shadow effects caused by the topographic features, but these features show poor thermal contrast. There is a decrease in the visibility of the present-day plough marks in Ambion field compared with May with a similar reduction in thermal contrast. The N-S and E-W old hedgerow boundaries are represented by continuous linear features on the day and night thermal images, but they have a more disjointed appearance on the natural colour composite with patches of greener vegetation at discrete positions on the boundaries. The E-W ridge and furrow marks are equally visible on the natural colour composite and the thermal images with the edges of the field showing a higher thermal response than within the field due to an increase in the visible soil fraction at the edges. The natural colour composite also reveals a diagonal NW-SE feature, parallel to the plough marks, which is not evident on the thermal data. However, the thermal image reveals a set of N-S linear features on the east of the field that are not evident on the natural colour composite. Results from this stage in vegetation development suggest that thermal infrared does not provide additional detail to natural colour composite in the fields covered by grass, but enhances detail in the barley field. There is also evidence of anomalous features that are specific to the individual spectral wavelengths.

In August 1998 there is no internal variation in the Helipad field, whereas the thermal images shows a series of parallel E-W linear anomalies. The Arena field shows patches of slightly darker green response in the NW at the brow of the hill in the west, adjacent to a gap in the hedgerow, and also in the middle of the field where there is a small N-S linear anomaly. These features correspond to thermal anomalies. The thermal image also shows a series of E-W linear anomalies that are absent from the natural colour composite. The Picnic field again shows a uniform response on the natural colour composite with the thermal image showing a patch of high thermal response at the brow of the topographic slope. The South field shows a greater degree

of internal variation with grazed grass in the eastern section showing a darker response than the grass in the western section, in which there are additional circular features corresponding to thistle and nettle patches that are also evident on the thermal images. Ambion field shows a brown response compared to the surrounding green fields where the barley has reached maturity prior to harvesting. The thermal image shows a prominent wind shadow effect that is absent from the natural colour composite. The N-S and E-W old hedgerow boundaries show a moderate thermal response that are marked by intermittent patches of green vegetation on the natural colour composite. The E-W ridge and furrow marks have a faint appearance on the natural colour composite and correspond to subtle thermal anomalies. The NW-SE diagonal feature shows a strong visible contrast with the surrounding material but is absent from the thermal image. The colour composite also reveals an E-W feature in the west beside the buildings that is not evident at any previous stage in barley growth and is also absent from the thermal image. Results from this stage in vegetation development suggest that thermal infrared provides additional detail to natural colour composite in fields covered by both grass and barley with evidence of features that are specific to the individual spectral wavelengths.

In March 2002 there is again no internal colour or thermal variation in the Helipad field. The Arena field shows a darker visible response on the SE topographic slope that corresponds with a low thermal response. The Picnic field shows areas of brown response at the edge of the car park where the soil fraction dominates and can be correlated with the position of high thermal response. The small white squares on the edges of the field correspond with picnic tables near the gravel paths that display a dark thermal response. The South field shows little internal variation with a similarity in visibility of the ridge and furrow markings between the colour and thermal images. Ambion field again shows present-day plough markings through the agricultural crop, which follow a different orientation than the other images due to crop rotation from barley to oil seed rape. There is little internal variation in Ambion field on either the natural colour composite or on the thermal images. However, there are two areas of brighter response SE corner that correspond to areas of elevated thermal response. Results from this stage in vegetation development suggest that thermal infrared does not provide additional detail to natural colour composite in the fields covered by grass or the oil seed rape.

Results from the comparison between the natural colour composites and the corresponding day thermal images suggest that the thermal infrared enhances the detail in the grass-covered fields at an early stage in growth where there is a higher visible soil fraction and also at later stages in cereal crop development where there is a greater degree in crop stress. The hedgerow and ridge and furrow features previously identified under the barley are noticeably absent from visualisation of the natural colour composite and thermal image under the oil seed rape due to an increase in leaf area masking the underlying surface.

5.4.2 Near-Infrared False-Colour Composites

Near-Infrared False-Colour Composites are generated by displaying a combination of the near-infrared (Band 7), visible green (Band 3) and the blue (Band 2) spectral wavelengths on the corresponding RGB display channels, which are overlain by interpretation of the corresponding thermal images (Figure 5.53).

In May 1998 the Helipad field reveals the N-S linear anomaly but does not reveal the perpendicular features that are evident on the natural colour composite or thermal image. The Arena field is very uniform in response with an area of anomalous blue response adjacent to the fence line that is not evident on the natural colour composite but corresponds to an area of elevated day thermal response and can be associated with a patch of gravel. The Picnic field shows an area of darker response in the NW that corresponds to an area of moderately elevated thermal response and can be associated with the top of a topographic slope. The colour combination does not enhance the visualisation of the ridge and furrow marks in the South field, but enhances visualisation of the hummock in the north shown by a dark linear feature on the north-facing slope of the hummock. The present-day plough markings in Ambion field show less of a contrast with the surrounding vegetation than on the natural colour composite with a higher contrast to the bright blue response around the edges of the field suggesting that there is a greater degree of bare soil at the edges of the field. The N-S and E-W old hedgerow boundaries are less easily identified than on the natural colour composite, but the ridge and furrow marks in the west are more readily delineated. There is an area of bright red response adjacent to the NW corner of the Arena field that is absent from the thermal image.

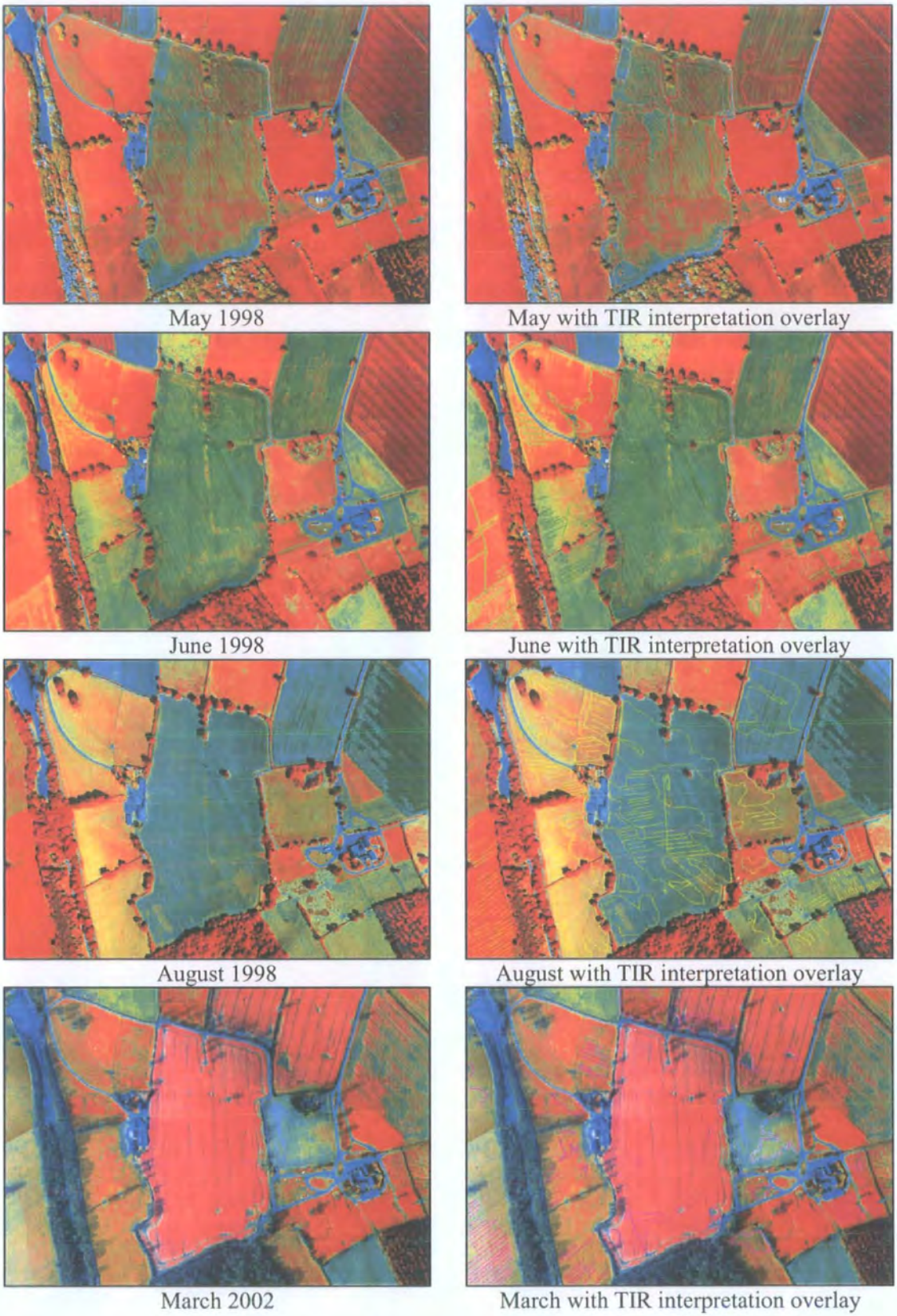

Figure 5.53: Near-infrared false-colour composites of Bosworth

Results from the early stage in vegetation development suggest that near-infrared wavelengths provide detail that is additional to the natural colour composite

in the grass fields but does not enhance features in the barley field and shows a similar variation in visibility compared with the thermal infrared.

In June 1998 the Helipad field again reveals the N-S linear anomaly of the day thermal image, with the Arena and Picnic fields having a more uniform internal response similar to the uniform thermal response. The ridge and furrow marks in the South field are more prominent than on the thermal image and are indicated by alternating dark and light red lines. There is a strong NE-SW linear feature in the western section marking a cattle track across the field that has a low thermal response. The N-S and E-W old hedgerow boundaries in Ambion field show a bright red response compared with the surrounding crop with an intermittent response compared with the response on the thermal image. The ridge and furrow marks in the west are more easily delineated than on the natural colour composite but are better identified on the thermal image. The NW-SE diagonal feature is absent from the thermal image and there is more internal field variation observed in the southern section where there are patches of redder response that are not evident on the thermal image.

In August 1998 the Helipad field shows a series of orthogonal linear feature that are similar to those identified on the thermal image, but that were absent from the natural colour composite. The Arena field shows a similar response pattern to the thermal image with redder areas corresponding with elevated thermal values. The small N-S feature shows an extension on the false colour composite towards the south that was not evident on the natural colour composite or on the thermal image. The Picnic field has no internal variation whereas there is a patch of high thermal response at the top of the topographic slope. The patches of nettles and thistles in the western section of the South field are shown with a dark red response. The ridge and furrow in the eastern section and the E-W linear anomaly show poor internal contrasts compared with the thermal image. The N-S and E-W boundaries in Ambion field show patches of red response on the false colour composite that is in contrast with the continuous feature on the thermal image. Although the ridge and furrow marks are less easily delineated on the false colour composite than the thermal image, the linear feature in the west section near the buildings is absent from the thermal image. In addition, the false colour composite reveals several patches of red in the NW of the

field that were absent from the natural colour composite and can be correlated with anomalies of moderate thermal response.

In March 2002 the Helipad field has a uniform response with no evidence of the linear thermal anomalies. The Arena field shows very similar response with the thermal image with redder areas corresponding to lower thermal values. The Picnic field shows a more variable internal response with blue linear anomalies along the field boundaries corresponding with the position of thermal anomalies with the blue linear anomalies adjacent to the car park correlating with thermal anomalies. The ridge and furrow markings in the South field show poor contrast on the false colour composite compared with the thermal image. The hummock is also poorly visible. There are two prominent patches of blue response in the southern area of Ambion field on the colour composite that correspond with patches of bright response on the thermal image.

The anomalies identified on the near-infrared false colour composite of the main fields vary from those identified on the natural colour composite with a dendritic drainage network evident in the field to the west of Ambion field that was not evident on the natural colour composite. These results suggest that near-infrared wavelengths provide useful additional detail to that provided by a standard aerial colour photograph. Results from the comparison between the near-infrared false colour composites and the corresponding day and night thermal images suggest that there is a good correlation between the day thermal anomalies identified in the fields covered by grass at early times in the growing season when there is a greater visible soil fraction. The day thermal images providing greater detail when the grass is longer and dominates the surface cover and provide enhanced detail at later stages in cereal growth where there is a reduced visible soil fraction. The night thermal images revealed additional features in Ambion field when the cereal crop dominated the surface cover with a greater visibility of the old hedgerow boundaries and ridge and furrow marks. The anomalies identified on the colour composite and thermal images under barley in Ambion field were absent under the oil seed rape suggesting that the complete canopy cover of the vegetation blanketed the soil surface.

The results of the natural and near-infrared colour composites suggest that these specific spectral combinations do not necessarily always reveal the same anomalous

features as detected through visualisation of the thermal infrared data. A more complete spectral assessment will therefore result from inclusion of the thermal channel in the visualisation and will provide a useful complementary spectral dataset for feature identification. A series of thermal day and thermal night colour composites are generated where the thermal infrared data from either the day or night is displayed on the red image display channel.

5.4.3 Thermal Day Colour Composites

Thermal Colour Composites are generated by displaying a combination of the day thermal infrared (Band 11), the near-infrared (Band 7) and the visible red (Band 5) spectral wavelengths on the corresponding RGB display channels (Figure 5.54).

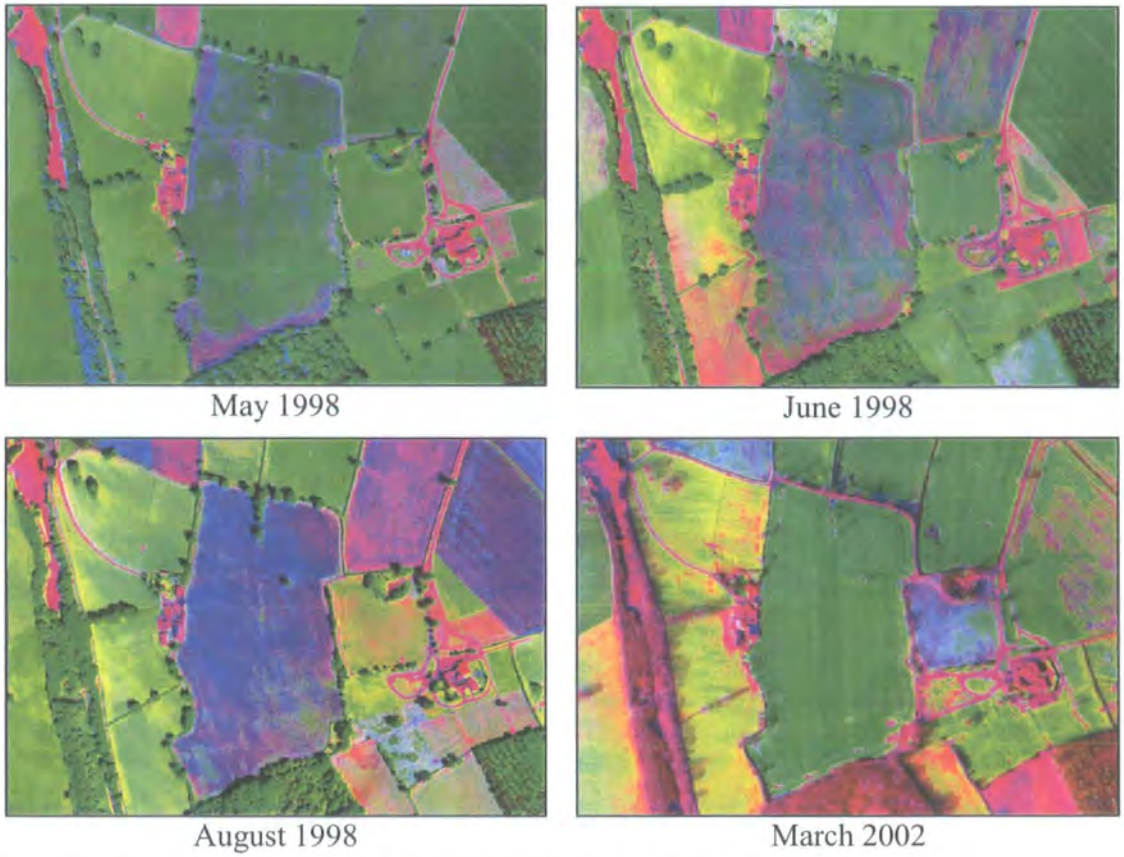

Figure 5.54: Thermal day colour composites of Bosworth

The linear anomalies in the Helipad field show a reduction in visibility across the seasonal dataset even under the uniform height of the grass. Therefore, this may be due to changes in the characteristics of the underlying soil with a variation in moisture content. The anomalies in the Arena field are more prominent in August 1998 after the grass had been cut for silage when there was again a greater visible soil

fraction in the field. This is similar to the response in the Picnic field where thermal anomalies are clearly evident at earlier stages in grass growth. The ridge and furrow marks in the South field are more prominent in March 2002 when the grass is at its shortest and also in August 1998 when the grass in the field has been shortened as a result of grazing. The hummock in the South field shows greatest visibility in August 1998 as a result of topographic shadow but does not show a thermal anomaly. The cattle tracks show strongest visibility in June 1998 when the grass was longer and was trampled flat. The March 2002 image reveals a channel leading from the hummock in the north of the field towards the thermally warm well and this was not evident at any other time of visualisation. The old hedgerow boundaries in Ambion field show their greatest visibility on the June 1998 colour composite with the ridge and furrow markings decreasing in visibility as the cereal crop developed.

5.4.4 Thermal Night Colour Composites

An alternative approach to thermal visualisation is to generate *Night Colour Composites* by displaying the night thermal infrared, the daytime near-infrared (Band 7) and the visible red (Band 5) spectral wavelengths on the corresponding RGB image display channels (Figure 5.55). Generation of the night colour composites requires the accurate georectification and co-registration of the day and night images to prevent the misalignment of field boundaries. The main co-registration problem was caused by variable hedgerow and tree growth resulting in a different degree of shadow on the surface and therefore a greater inaccuracy in field boundary co-registration and misalignment of internal field anomalies. As a result, there may be a misalignment of the internal field anomalies due to the inability to accurately select the same ground control points as used for the day image georectification.

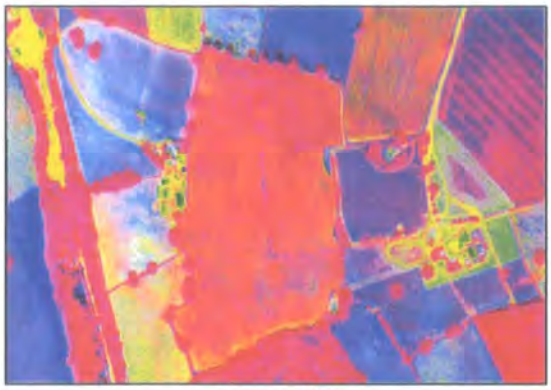

June 1998

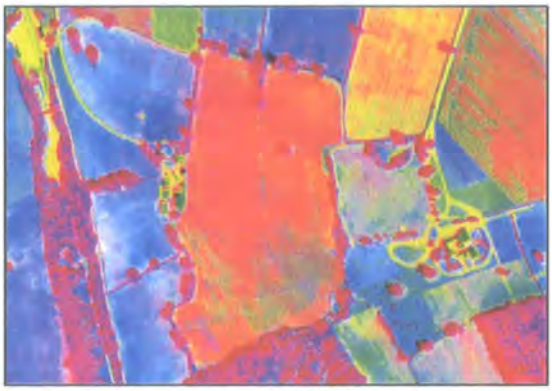

August 1998

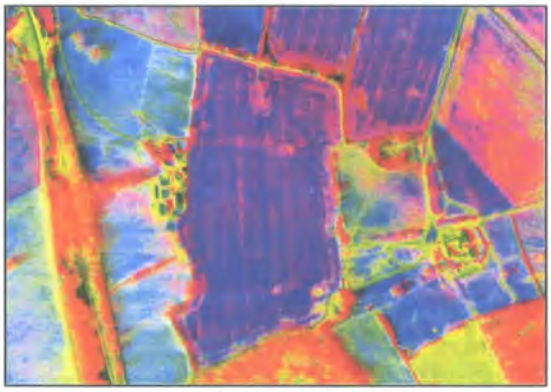

March 2002

Figure 5.55: Thermal night colour composites of Bosworth

The thermal night colour composites reveal no additional features in the Helipad field than the other colour composites with reduction of the visibility of the linear anomaly in June 1998 and enhancement of the hedgerow shadow on the eastern side of the field in March 2002. The Arena field shows a greater degree of internal field variation in August 1998 and March 2002 compared to the day thermal composite with enhancement of the visibility of the linear anomalies in August 1998 and the variation present in March 2002. The gravel paths round the edges of the Picnic field are more prominent on the March 2002 night composite than on any other composite with additional enhancement of the visibility of the topographic effect in June and August 1998. The South field shows little internal variation in June 1998 with enhancement of the visibility of the linear anomalies in August 1998 and March 2002. The hummock shows greatest visibility on the colour composite for August 1998 than on any other spectral combination. The old hedgerow boundaries in Ambion field show a more consistent detection between June and August 1998 than on the other colour combinations but the ridge and furrow marks are less prominent. There is more internal variation evident in March 2002 than on any other combination with an area

of increased night response at the brow of the hill trending from the flagpole towards the western farmhouses with an additional higher night response evident in the NW.

5.4.5 Summary of Colour Composite Visualisations

From these different colour composites of Bosworth it is clear that near-infrared wavelengths provide detail that is additional to that provided by visualisation of a natural colour composite generated to represent a standard colour aerial photograph. This is most evident in the grass fields at an early stage in vegetation growth where the grass is short and there is a greater influence from the visible soil fraction. This is also true at later stages in cereal crop development where the visible variations in crop stress are potentially due to variations in the underlying soil properties. The day thermal data provides greatest additional detail at earlier stages in grass growth and at later stages in cereal crop development, and, is assumed to relate to variations in the moisture properties of the soil and vegetation. The night thermal composite provides a more consistent enhancement of the old hedgerow boundaries in Ambion field throughout cereal crop development with additional features revealed at all stages in grass growth. In addition, the night thermal composite provides an increase in internal field variations under the leafy oil seed rape crop. As a result, the inclusion of the thermal channel appears to provide a more comprehensive depiction of the anomalies in the near-surface environment.

Even though atmospheric correction could not be performed on the Baildon Moor and Weardale datasets, similar results are observed on generation of the same colour composites with the near-infrared and thermal channels providing additional detail to that observed on the natural colour composite.

Interpretation of the colour composite visualisations is still rather time-consuming and so alternative image enhancement techniques are applied to the images to provide a more concise approach to multispectral and thermal evaluation.

5.5 FURTHER IMAGE ENHANCEMENT

Image enhancement operations transform digital data into a more interpretable form. When multi-spectral images are displayed as RGB colour composites, the human eye can distinguish more subtle variations than when displaying a grey-scale image. Enhancement of individual image channels results in only increasing the contrast on the specific image channel. There are a variety of multi-channel spectral enhancement techniques that can be adopted that increase the contrast between highly correlated image channels. The enhancements that are applied to the datasets are *Edge Detection Filtration, Image Arithmetic* and *Principal Component Analysis* techniques that are aimed at enhancing the anomalous features. Once again, the enhancement techniques are applied to only the Bosworth images to assess their effectiveness in feature detection compared with the thermal assessment.

In order to assess the response of features present within the vegetated areas, the non-vegetated areas are masked from the images prior to spectral enhancement (Appendix B6). The vegetated areas that remain are covered by vegetation and represent the fields where ground geophysical investigations were performed (Figure 5.56).

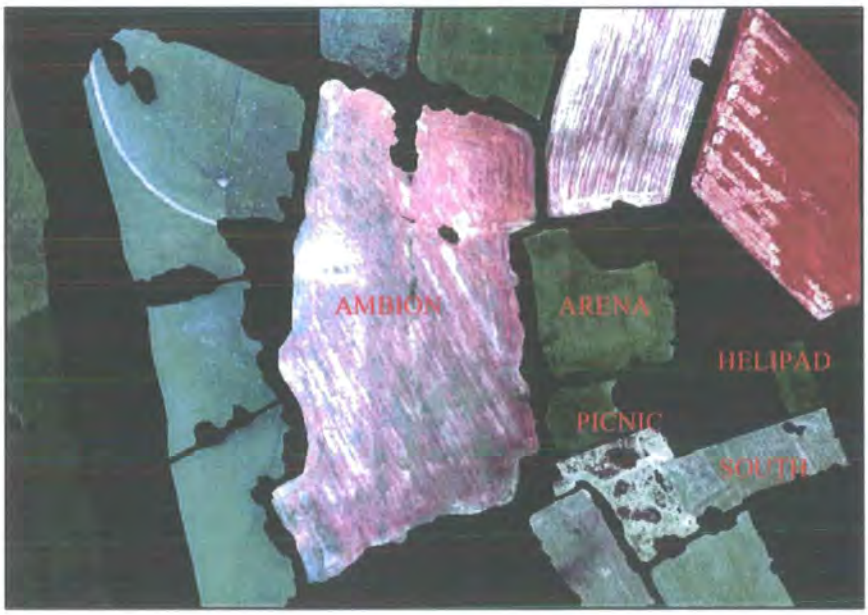

Figure 5.56: Field subset and nomenclature for Bosworth

5.5.1 Edge Detection Filtration

Edge detection filtration is the process of enhancing image data in the spatial domain through numerical transformation of tonal variations contained within an image. Filter operations can be used to smooth or sharpen the information in an image, or to reduce noise while maintaining detail for subsequent processing. A digital image contains both low and high frequency spatial information components with their sum constituting the original image. Low frequency components describe gradual grey-level changes across an image whereas high frequency components describe the more abrupt changes in grey-level intensity from one pixel to the next. Low pass filters preserve low frequency components, effectively smoothing the image and is useful for noise removal. High pass filters remove low frequency components and enhance abrupt edges between pixel intensities and as such are often referred to as edge detection filters. A filter is a defined by a square or rectangular matrix of an odd number of pixels and lines. As the filter kernel is moved across an image, the central pixel is replaced by a value based on a numerical transformation of the kernel coefficients on the original central pixel value. Edge detection techniques are applied to the temperature-calibrated images from Bosworth to assess their effectiveness in feature detection.

5.5.1.1 Low Pass Filtration

Low pass filtration smoothes the central pixel value by an amount that depends on both the size of the filter kernel and also the weighting factor of the kernel elements. The basic low pass filter is a standard 3x3 averaging filter, giving equal weighting to all kernel elements (Figure 5.57).

$$\frac{1}{9}\begin{bmatrix} 1 & 1 & 1 \\ 1 & 1 & 1 \\ 1 & 1 & 1 \end{bmatrix}$$

Figure 5.57: Standard averaging low pass 3x3 filter kernel

Low pass filtration was applied to the August day thermal image of Ambion field in Bosworth (Figure 5.58) to provide an example of the filtration output on application of a 3x3 low pass filter kernel. The results of the filtration provide a smoothed image where the subtle temperature contrast associated with the features is

not enhanced for detection. Low pass filtration is therefore inappropriate for feature detection and as a result was not applied to the other thermal images.

August 1998 day thermal

August 1998 low pass filtration

Figure 5.58: Results of low pass filtration on Bosworth August 1998 day thermal image

5.5.1.2 High Pass Filtration

High pass filtration is designed to emphasise features that are smaller than the size of the filter kernel and de-emphasise features that are greater than the size of the filter kernel. High pass filters have a high central coefficient, surrounding by typically negative values for the other kernel elements and as a result accentuates the central pixel value with respect to the surrounding pixels (Figure 5.59).

-1.0000	-1.0000	-1.0000
-1.0000	8.0000	-1.0000
-1.0000	-1.0000	-1.0000

Figure 5.59: Standard high pass 3x3 filter kernel

High pass filtration was applied to the August day thermal image of Ambion field in Bosworth (Figure 5.60) to provide an example of the filtration output on application of a standard 3x3 high pass filter kernel. The results of the filtration

provide an image where the boundary between the extracted field area and the field hedgerows is greatly enhanced and there is little enhancement of anomalies within the field. This may be due to the subtle temperature contrast between the feature and the surrounding vegetation. High pass filtration is therefore inappropriate for feature detection and as a result was not applied to the other thermal images.

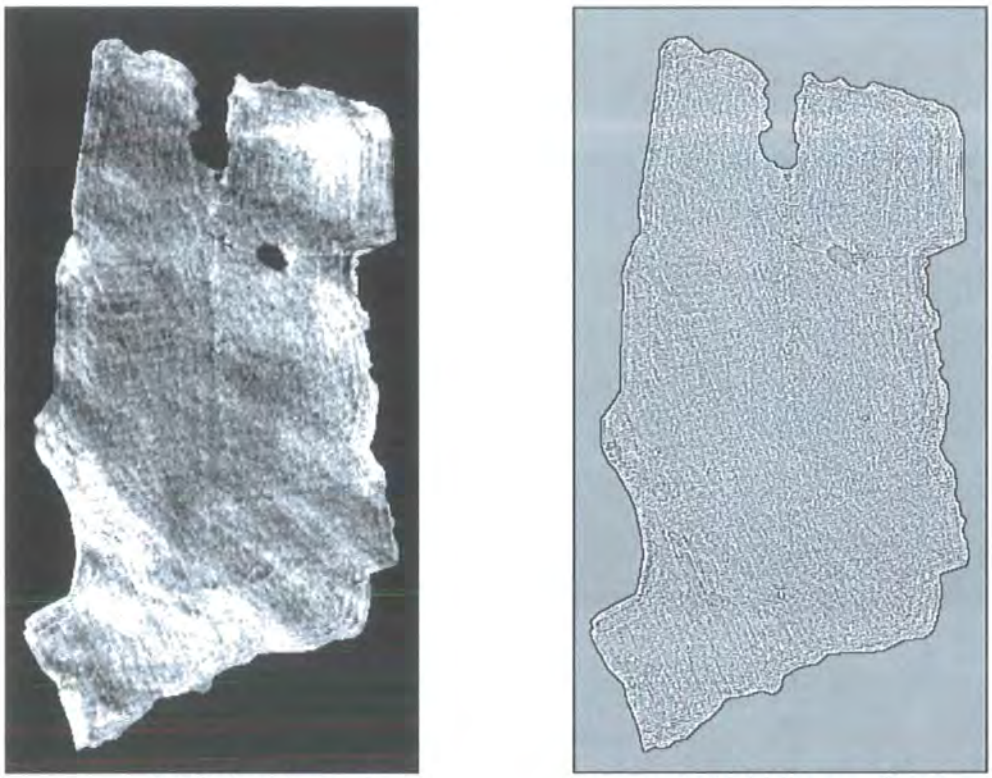

August 1998 day thermal | August 1998 high pass filtration

Figure 5.60: Results of high pass filtration on Bosworth August 1998 day thermal image

Results from the high and low pass filtration suggest that there is no benefit from applying these techniques for feature enhancement due to the subtle nature of the thermal response of the features occurring within the field. As a result, alternative directional filtration techniques are applied to the thermal data to assess their effectiveness for feature detection.

5.5.1.3 Directional Filtration

A directional filter is a specific form of high pass edge enhancement filtration that selectively enhances image features having a specific directional component or gradient between pixel values. Specific filter kernels can be used to enhance features showing strong directional contrasts with respect to the surrounding pixels. In general,

the elements in the kernel have high values along the directional component with the sum of the kernel elements being zero. The result is that areas with similar pixel values have a uniform value in the output image, while pixels that have a high contrast with the surrounding pixels are presented as bright edges. Specific directional filters can be applied to enhance known morphological features if the pixel values show a strong directional contrast with the surrounding pixels. Specific orientations of the directional filter kernel can be applied to the data to enhance the directional component of the images (Figure 5.61).

0° (N-S)		
-1	0	1
-1	0	1
-1	0	1

45° (NE-SW)		
-1.414	-0.707	0
-0.707	0	0.707
0	0.707	1.414

90° (E-W)		
-1	-1	-1
0	0	0
1	1	1

135° (NW-SE)		
0	-0.707	-1.414
0.707	0	-0.707
1.414	0.707	0

Figure 5.61: Standard 3x3 directional filter kernels

Directional filtration was applied to the August day thermal image of Ambion field in Bosworth (Figure 5.62) to provide an example of the variations in feature detection produced on application of various directional filters. The subtle anomaly representing the position of the N-S old hedgerow boundary showed prominent enhancement on all but the E-W filtration, which was expected due to the orthogonal nature of the filter enhancements and the orientation of the field boundary not perfectly N-S. The subtle E-W ridge and furrow marks on the western side of the field showed great enhancement on all but the NE-SW filtration with additional parallel linear features evident on the south-eastern area of the field that were very subtle on visualisation of the thermal image. The thermal effect caused by the wind forcing the vegetation to lean showed enhancement on all but the N-S filtration with most prominence on the southern edge of the field where there is a greater thermal contrast between the leaning and vertical vegetation. The NW-SE present-day field plough marks on the western side of the field show equal prominence on all directional filtrations where the ploughing caused a variation. The SW corner of the field shows a greater degree of variability on all filtration than was visible on the thermal image.

August N-S filtration

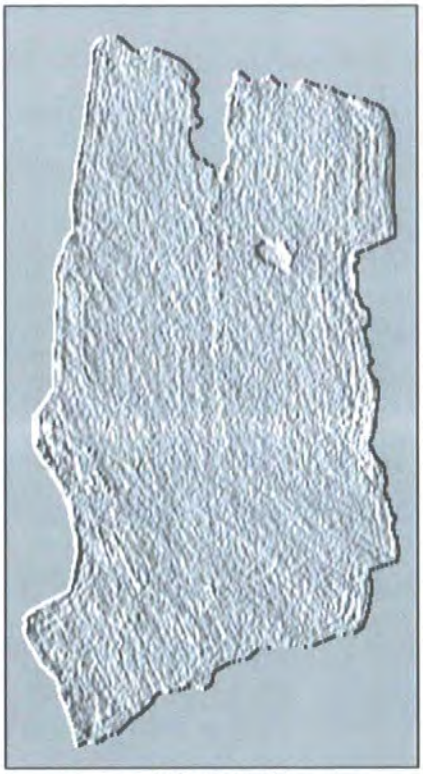

August NE-SW filtration

August E-W filtration

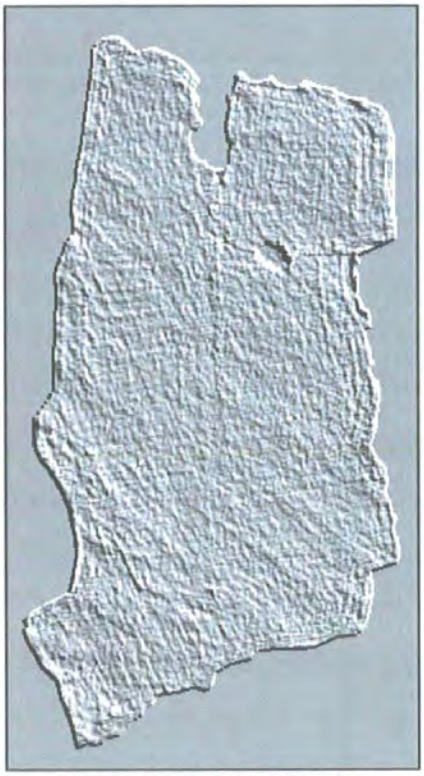

August NW-SE filtration

Figure 5.62: Results of directional filtration on Bosworth August 1998 day thermal image

Results of the filtration suggest that the combination of directional filter is more effective for enhancement of the thermal anomalies within the barley field than is provided by using a single directional filter. The directional filters were also applied to the images obtained at alternative stages in barley growth and the results showed similar features to those revealed at the later stage in barley growth. When the directional filters were applied to the grass-covered Arena, Helipad and Picnic fields and the grass and nettle covered South field, there was little additional detail revealed than provided by the contrast enhancement techniques. This was probably due to the more uniform temperatures of the individual fields than was experienced in the agricultural field where the barley showed a greater thermal variability. When the directional filtration was applied to the oil seed rape field, there were few thermal anomalies revealed suggesting that this crop type and stage in its development was insufficient for delineation of thermal features.

Directional filtration appears to provide a useful technique for rapid assessment of thermal variations occurring within the barley field at any stage in crop growth. However, the directional filtration provided little additional detail to that revealed on standard contrast enhancement in the grass-covered fields at any stage in the vegetation development, and also in the field covered by oil seed rape. When the results of the directional filtration are compared with the results from the geophysical survey, the directional filters did not reveal the geophysical anomalies suggesting that the subtle thermal variations relate to surface vegetation characteristics only.

Directional filtration is one enhancement techniques that provides useful feature detection. However, alternative image enhancement techniques such as image arithmetic operations may also be effective for feature detection.

5.5.2 Image Arithmetic

Basic image arithmetic can be applied to image data to enhance particular features through the combination of specific spectral band. Numerical transformations are applied to any combination of input bands with the association of a particular band to a specific variable in the algorithm. The algorithm is applied across the whole image on a pixel-by-pixel basis, assuming that the selected bands are spatially co-registered and have the same spatial resolution. A new image is then formed

representing the output of the defined algorithm. The four main arithmetic operators are addition, multiplication, division and subtraction.

Addition can be used as a stand-alone function on two images or can be used as part of a more complex mathematical expression. Addition is commonly used as a form of averaging to help reduce noise components between images taken at the same time over the same region. It can also aid feature detection by adding some of the original image back into a filtered image and producing a much more interpretable result.

Multiplication is often used to mask particular image features. Areas of interest are multiplied by a factor of 1 to retain the data, and the areas to be masked or omitted from the output image are multiplied by a factor of zero. This mathematical function is applied during the data pre-processing step to spatially subset the image data based on the areas of image overlap and also to remove data that is not associated with the vegetation surface.

Division acts to reduce the dimensionality of image data and divides pixels in one spectral band by the corresponding pixels in another. This process is also known as a spectral ratio technique and is used to enhance the spectral characteristics of an image by reducing the affects of factors such as topographic shadowing and sun angle. A spectral ratio will enhance extraneous factors that do not act equally on the image channels and factors such as noise must therefore be removed prior to generating a spectral ratio. The technique can also be used in land cover change detection by creating a ratio of two spectral images acquired on different dates with the resulting image showing zero pixel values for no temporal change.

Subtraction is performed on a pixel-by-pixel basis on a pair of co-registered images taken at different times to assess the magnitude of surface change. Where no change has occurred, the radiometric intensity of the normalised images will be the same and the resultant subtraction image will have a grey value of zero. Grey values other than zero, both positive and negative, represent the amount of change that has occurred. This technique can be applied in thermal investigations to determine the variation in diurnal temperature response by subtracting a co-registered day and night thermal image pair. The amplitude of the temperature change gives an indication of

the resistance of the surface to changes in temperature and can indicate variations in the bulk thermal properties of the surface materials through an apparent thermal inertia property of the material (Chapter 2.3) and may provide detection for features buried in the near-surface environment. The following section describes the results of applying a simple day-night image subtraction on the Bosworth thermal images for determination of variations in the Apparent Thermal Inertia of the vegetation-covered fields. A more quantitative approach to Apparent Thermal Inertia modelling is discussed in Chapter 6.

5.5.2.1 Diurnal Thermal Contrast at Bosworth

The contrast in thermal response between the day and night thermal images of Bosworth is calculated by subtracting the night temperature response from the day temperature response for each pixel in the temperature-calibrated thermal image pairs from the study site (Figure 5.63).

The result of the June 1998 subtraction shows a stronger anomaly relating to the N-S old hedgerow boundary and the ridge and furrow marks than is evident on either day or night thermal image. The secondary E-W field boundary is poorly detected through this technique suggesting a difference in physical nature of the feature compared with the other field boundary. The E-W ridge and furrow marks are greatly enhanced on the June image subtraction. There are also additional irregular-shaped features revealed in the NW and SW areas on the contrast image that are not easily recognisable on the single band visualisations. The result from the August 1998 subtraction shows a similar response to that of the August 1998 day thermal image, which is dominated by the wind shear effect. There is poor internal field contrast on this output with only subtle anomalies relating to the old hedgerow boundaries and ridge and furrow marks. The result of the March subtraction again shows poor internal field variation with much more pronounced present-day plough marks.

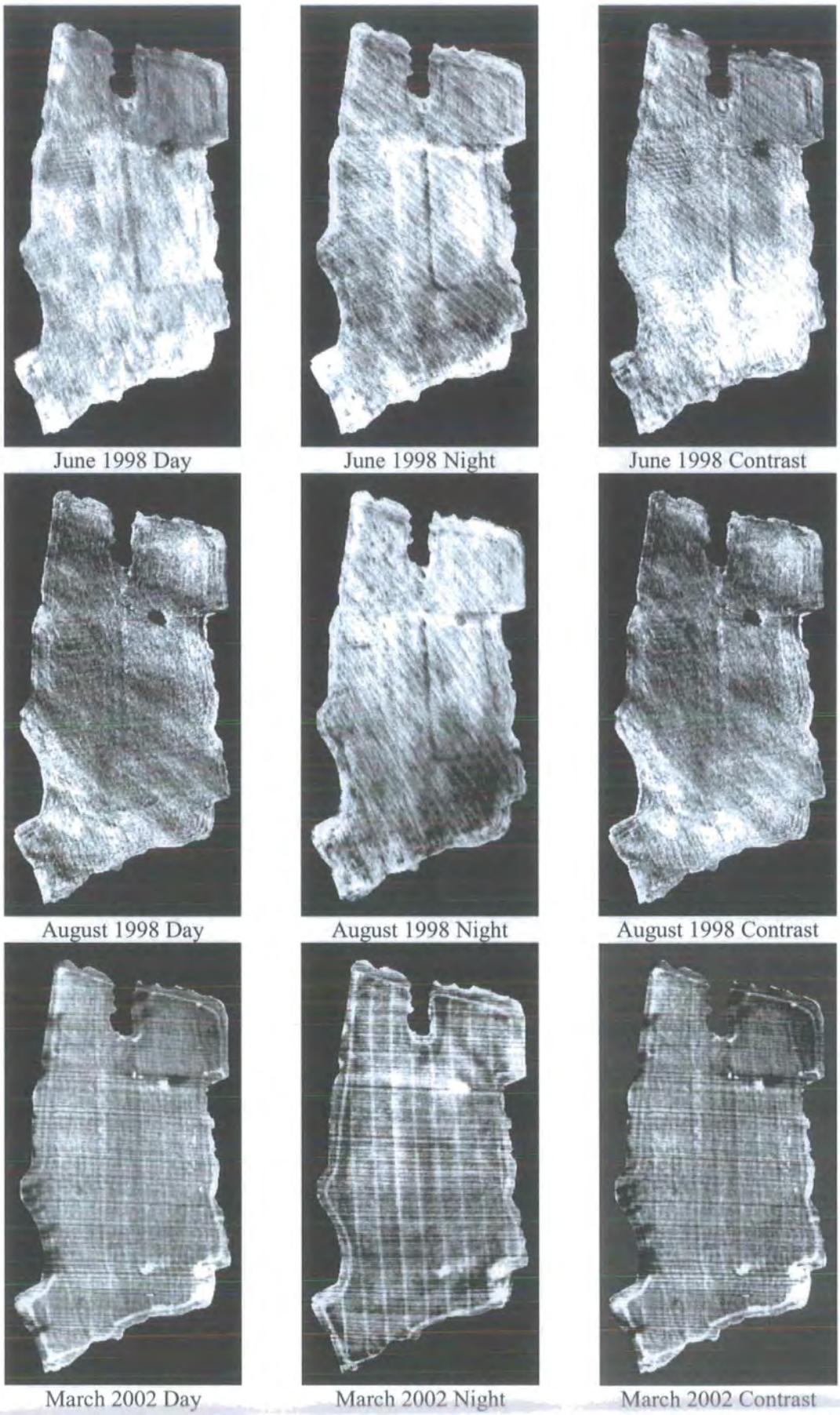

Figure 5.63: Day, night and thermal contrast of Bosworth Ambion field

This simple subtraction technique appears to enhance some features present in the barley-covered field at an early stage in crop growth when compared to single-band visualisation of the day and night thermal images. When the histograms of the Ambion field are extracted from the day and night images from any observation date, the day histogram shows a wider range of temperatures than is evident at night, with much higher temperatures observed during the day. When the histogram of the subtraction image is generated, the distribution of values is similar to that from the day image showing a Gaussian distribution (Figure 5.64).

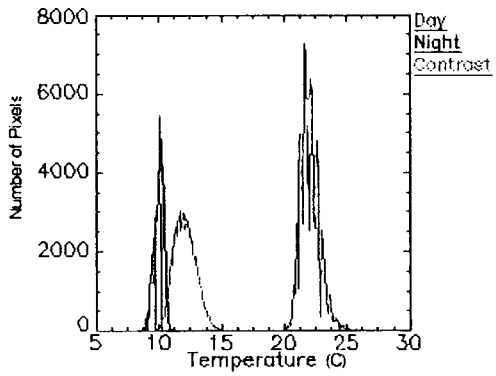

Figure 5.64: Histograms generated from August thermal images of Bosworth Ambion field

The subtraction technique was repeated for the grass-covered fields at the Bosworth site and the results appeared to enhance the thermal anomalies associated with each field when compared to the features detected on single band visualisation of either day or night thermal images, with greater feature enhancement at early stages in grass growth. The results of this technique suggest that image subtraction may be most useful where the vegetation has a low leaf area or is relatively short.

5.5.2.2 Diurnal Thermal Contrast on Baildon Moor

Image subtraction was performed in Baildon Moor on the uncalibrated day and night thermal radiance images of the abandoned mineshaft of pronounced topographic expression (Figure 5.65). W-E and N-S thermal profiles generated from day-night thermal image subtraction (Figure 5.66) show a slight elevation in response of the SE rims with a decrease at the centre of the shaft. There is a slight asymmetry in response with higher values on the NE slope at the base of the shaft. The higher thermal contrast suggests that the materials on the NE slope may have a lower thermal inertia

than the opposite side and may indicate an increase in moisture content. However, due to the acquisition of a single transect of geophysical properties, it was not possible to determine variations in moisture content at depth on this part of the shaft.

Day and night thermal image subtraction was also performed for the vegetation shaft on Baildon Moor (Figure 5.67). W-E and N-S thermal profiles generated from the day-night thermal image subtraction (Figure 5.68) show a slight decrease in response over the vegetation feature with an asymmetric response with a positive skew towards the SW. The W-E and N-S profiles are very similar to those generated from the day thermal image suggesting that the day response dominates the subtraction. The higher thermal contrast in the SW suggests that the materials may have a lower thermal inertia than the surrounding materials and may again indicate an increase in moisture content. This is verified through observation of an area of standing water towards the SW of the vegetation feature and was also corroborated by the results of the geophysical profiles.

Day and night thermal image subtraction was also performed on the suspected shaft feature on Baildon Moor (Figure 5.69). The W-E and N-S thermal profiles generated from the day-night thermal image subtraction show a slight decrease in thermal contrast eastwards with a more pronounced southerly decrease (Figure 5.70). However, there is little difference between the thermal response over the suspected shaft feature and the surrounding vegetation. This is similar to the results of the geophysical analysis.

When the thermal subtraction profile from the suspected shaft feature is compared with the profiles generated over the known topographic and vegetation shafts, the suspected shaft feature shows different profile characteristics suggesting that the feature has a different physical nature than the other shafts.

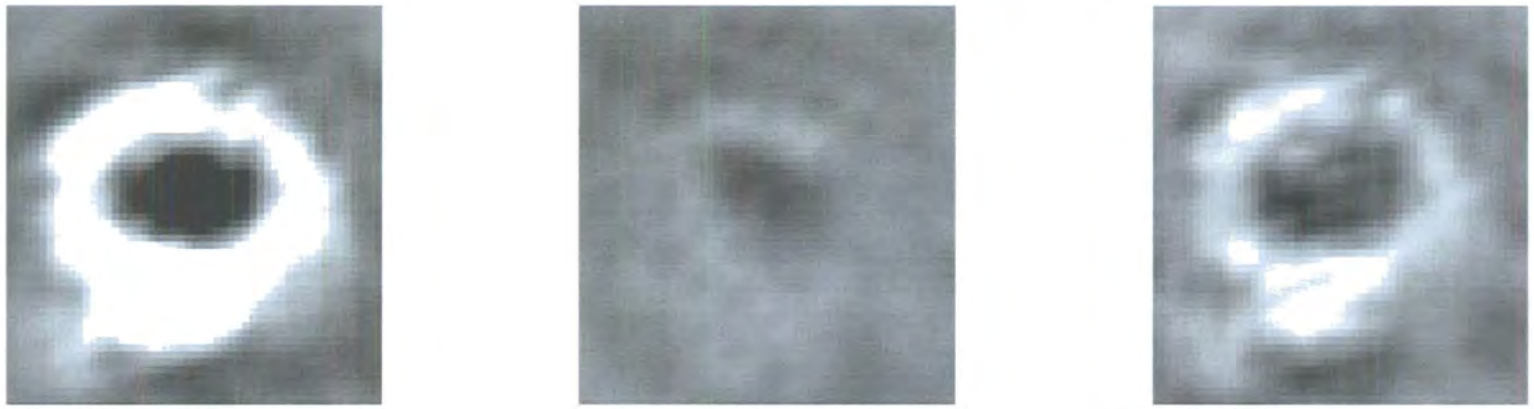

Figure 5.65: Day, night and thermal contrast images of Baildon topographic shaft

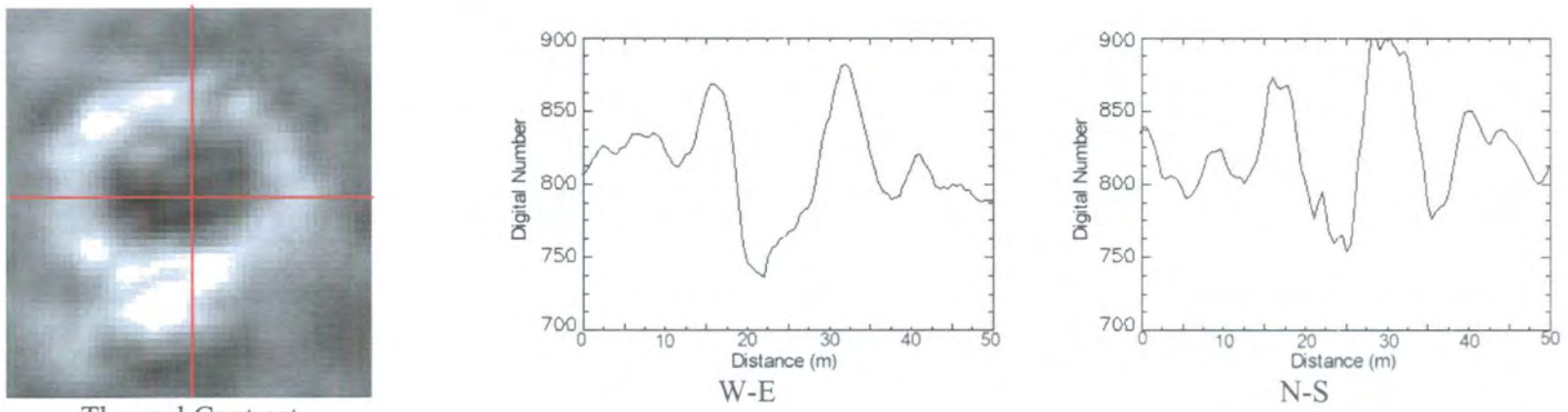

Figure 5.66: Thermal profiles generated across Baildon topographic shaft on thermal contrast image

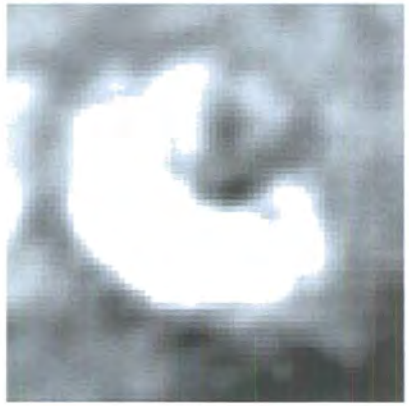

Day

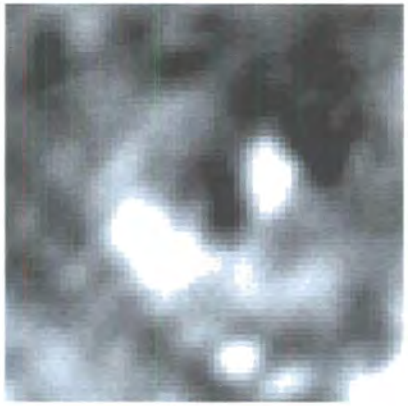

Night

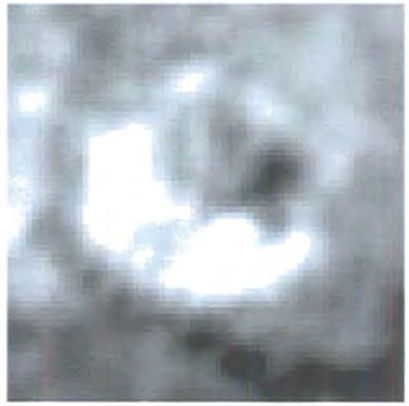

Thermal Contrast

Figure 5.67: Day, night and thermal contrast images of Baildon vegetation feature

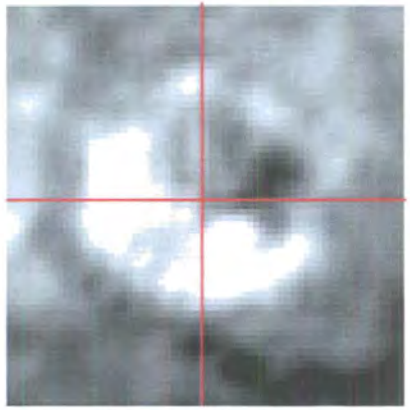

Thermal Contrast

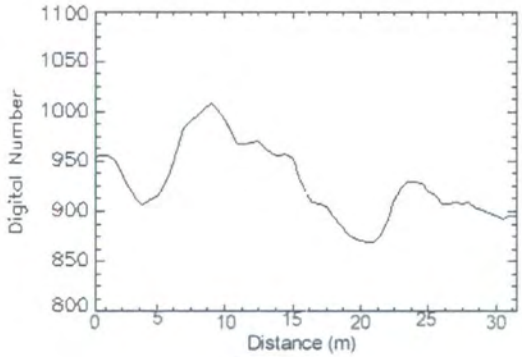

W-E

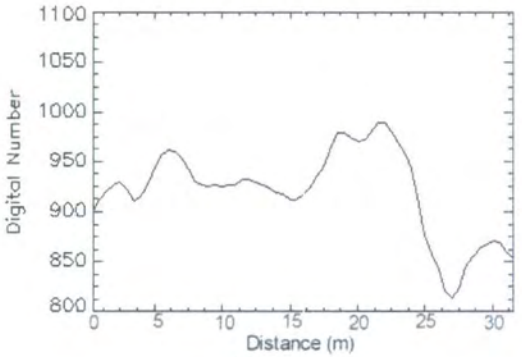

N-S

Figure 5.68: Thermal profiles generated across Baildon vegetation feature from thermal contrast image

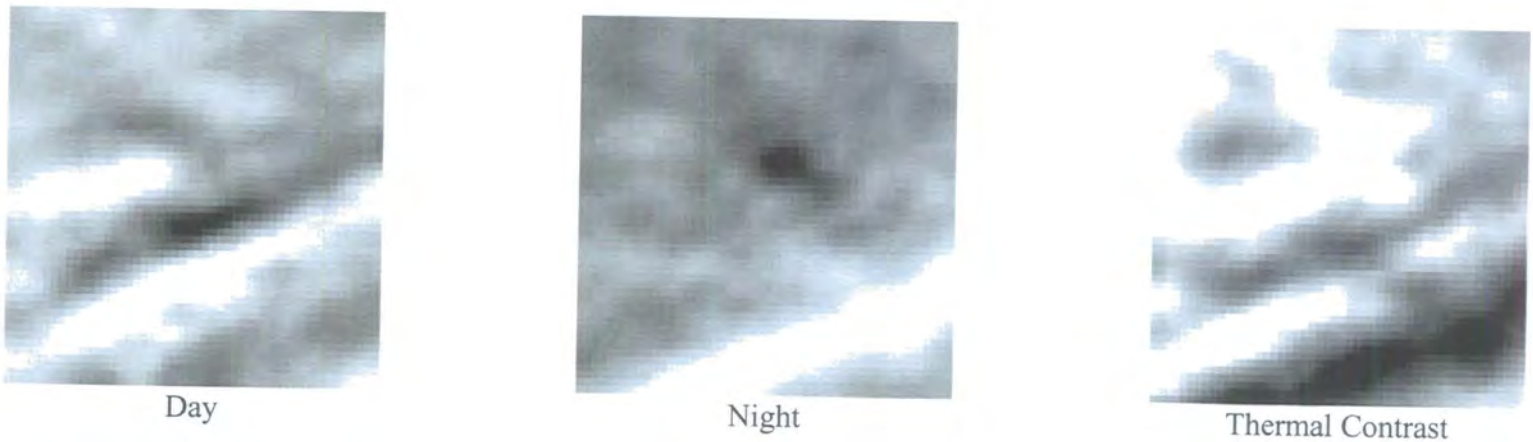

Figure 5.69: Day, night and thermal contrast images of Baildon suspected shaft

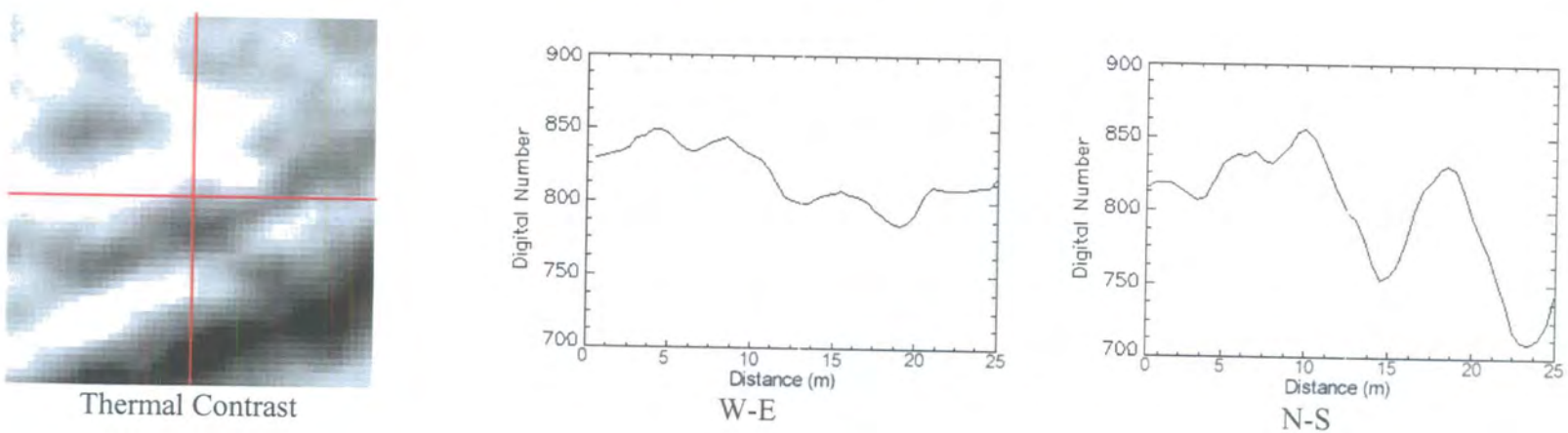

Figure 5.70: Thermal profiles generated across Baildon suspected shaft from thermal contrast image

Results from Baildon Moor suggest that the simple day-night thermal image subtraction technique is useful for detection of thermal anomalies relating to topographic and vegetation shaft features associated with abandoned mine activity, even though the thermal radiance was not calibrated to ground temperature.

5.5.2.3 Diurnal Thermal Contrast in Weardale

Image subtraction was performed on an area of abandoned mining activity in Weardale using the uncalibrated day and night thermal radiance images (Figure 5.71). Thermal profiles extracted over a representative spoil heap and scour mark (Figure 5.72) show similar response pattern to those extracted from the day thermal image (Figure 5.50). As a result, the image subtraction technique does not provide enhancement of these features and suggests that acquisition of a day thermal image is sufficient for detection of spoil heaps and scour marks where there is a strong thermal contrast between the bare soil areas associated with the mine activity and the surrounding vegetation.

Although the thermal image subtraction technique is useful for feature detection in areas covered by vegetation, alternative image enhancement techniques such as spectral enhancement may also be effective for feature detection and prevent the need for the problematic day-night image co-registration.

Day

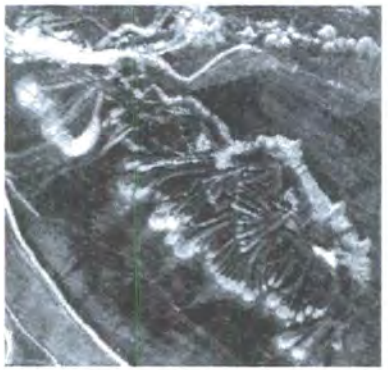

Night

Thermal Contrast

Figure 5.71: Day, night and thermal contrast images of Weardale mineral extraction features

Thermal Contrast

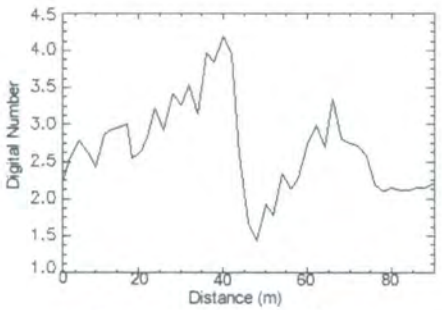

Scour Marks (N-S)

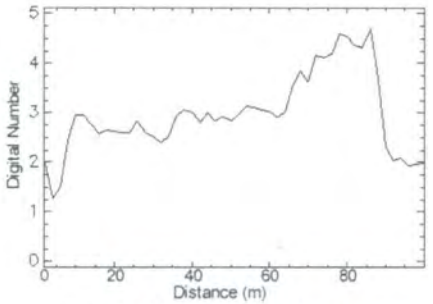

Spoil Heaps (NE-SW)

Figure 5.72: Thermal profiles generated across Weardale mineral extraction features from thermal contrast image

5.5.3 Spectral Enhancement through Principal Component Analysis

It is not uncommon to find strong correlation between adjacent spectral bands in multi-spectral imagery. This is represented by the fact that if the pixel reflectance is high in one band then it is likely to be high for the adjacent spectral band for the same pixel. Principal Component Analysis (PCA) is a statistical analytical technique that reduces the correlation of adjacent spectral bands and enhances the spectral variability contained in the imagery (Mather, 1999, Jia & Richards, 1999). When the pixel distribution of an image band is plotted against the adjacent image band, the majority of the data points form an elongate elliptical cluster centred about a diagonal line representing a high band correlation between the adjacent spectral bands (Figure 5.73).

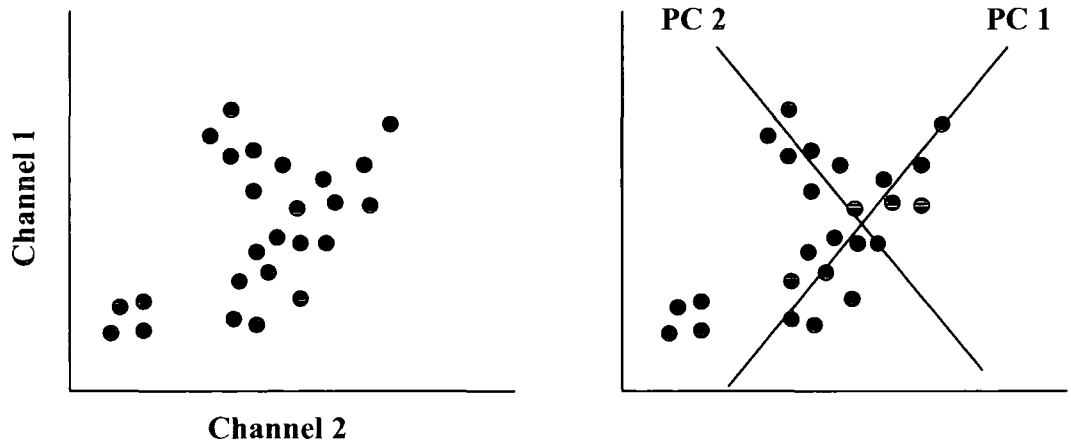

Figure 5.73: Schematic scatter-plot showing pixel distribution of adjacent spectral bands and location of new PC coordinate system axes (PC1 & PC2)

The origin of the principal component coordinate system is centred about the mean of the data distribution with generation of a set of orthogonal axes. The first Principal Component axis (PC1) is directed along the maximum variance of the dataset and the second orthogonal axis (PC2) represents the second greatest variance. The PC transforms the input data into a set of uncorrelated orthogonal components with the greatest amount of information concentrated in the first PC bands with successively less information through to the final PC band where the noise component of the original data is concentrated. PC transformations reduce the dimensionality of the data and generate more 'colourful' composite images because each component is uncorrelated.

The PC transformation is applied to the Empirical Line Calibrated images of the Bosworth site to assess the spectral variability of the vegetation. The grey-scale images display in Figure 5.74 give an example series of the PC bands generated through application of a PC transformation on the calibrated visible and near-infrared bands of the August data, excluding band 1 due its poor quality.

Results from the PC transformation show that the first few PC bands show little internal field variation but show a highly variable contrast between the individual fields. The old hedgerow boundaries in Ambion field are visible as subtle anomalies in most of the PC bands. However, the ridge and furrow marks in the western side of Ambion field are poorly defined. This technique therefore fails to reveal useful detail internal to the individual fields, probably because of the inclusion of the spectral detail associated with the hedgerows, roads and buildings. In order to assess the spectral variability of the individual fields, materials external to the field are masked out and omitted from analysis.

The PC transformation is applied on an individual field basis where areas of interest that are covered by vegetation have been cut out from the rest of the image. As an example, the PC transformation is applied to the August 1998 visible and near-infrared bands from Ambion field (Figure 5.75) and is also performed with inclusion of the thermal band (Figure 5.76). The results of the PC transformation show that the spectral variability within Ambion field is greatly enhanced compared with the visualisation of the same field on transformation of the entire image.

Although the Bosworth dataset has been calibrated to ground-leaving reflectance and surface temperature, this is not always possible to perform without sufficient auxiliary ground calibration as in the case of Baildon Moor and Weardale. The PC transformation was therefore repeated on the August 1998 uncalibrated visible and near-infrared bands of Ambion field (Figure 5.77) and was performed with inclusion of the uncalibrated thermal band (Figure 5.78). This allowed determination of the necessity for spectral calibration prior to using Principal Component Analysis as a suitable method of spectral analysis

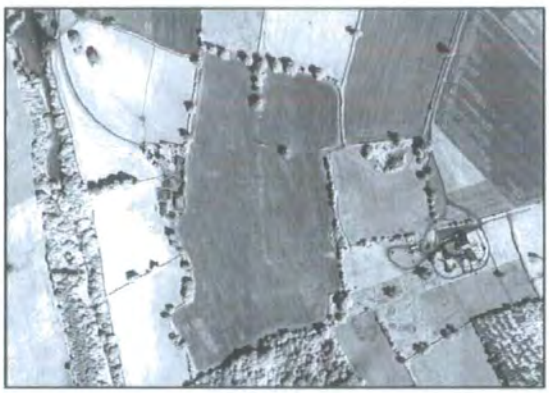

PC 1

PC 2

PC 3

PC 4

PC 5

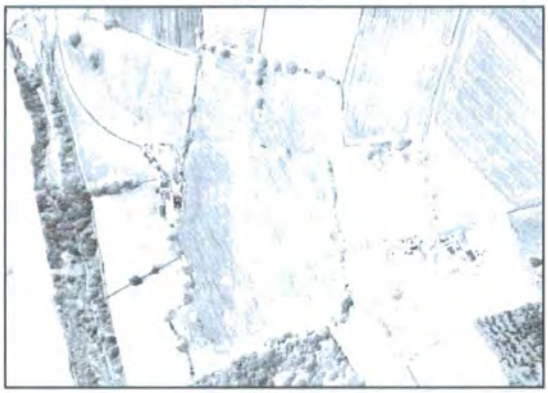

PC 6

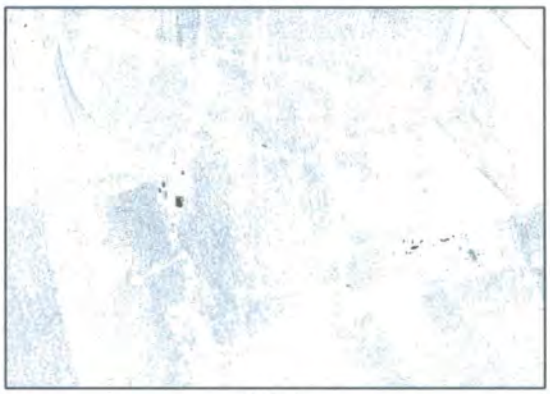

PC 7

Figure 5.74: Monochrome images of PC transformation bands of Bosworth August 1998 visible and near-infrared bands

PC Band 1

PC Band 2

PC Band 3

PC Band 4

PC Band 5

PC Band 6

PC Band 7

Figure 5.75: PC transformation of Bosworth August 1998 visible and near-infrared bands of Ambion field

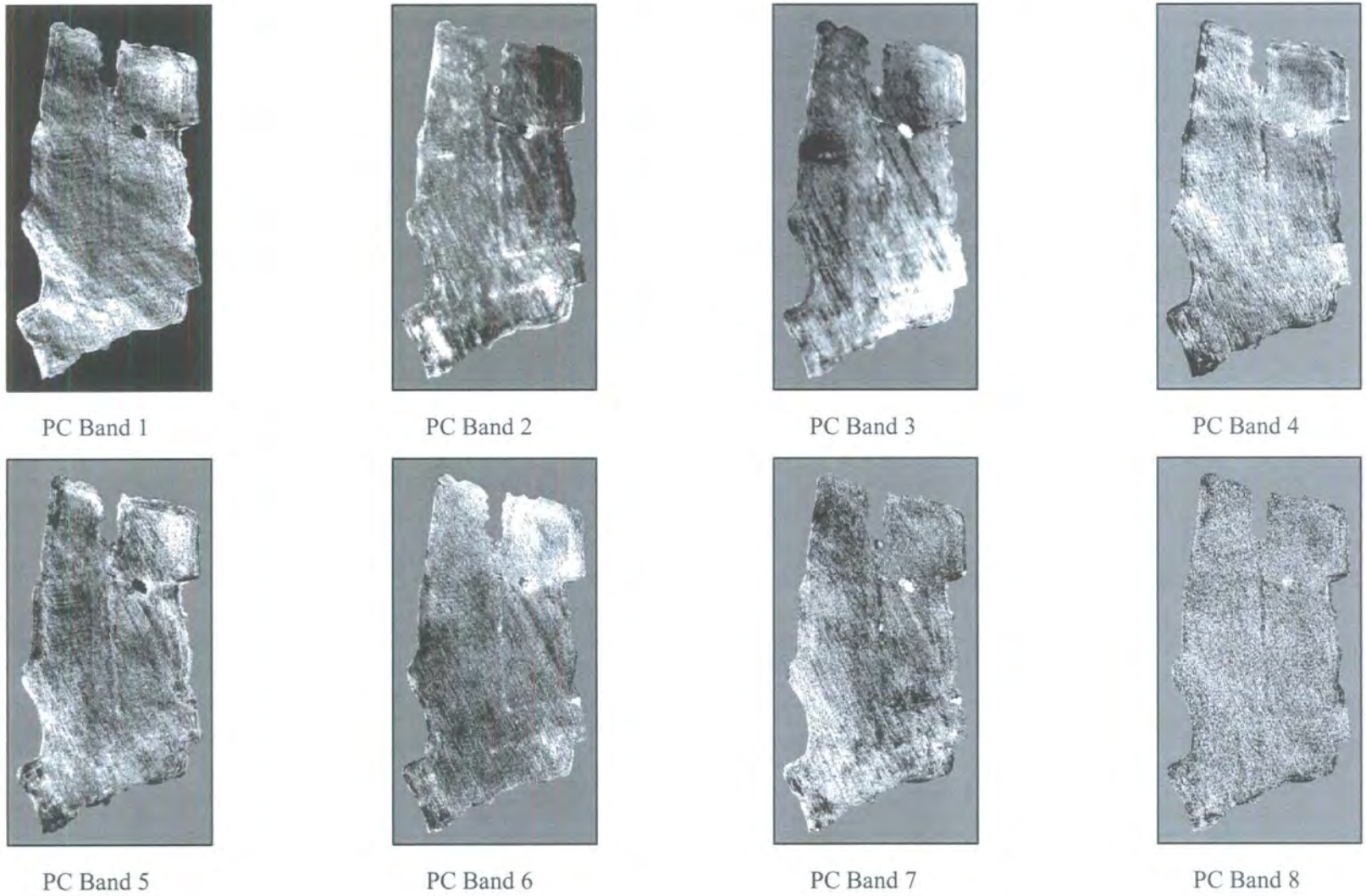

Figure 5.76: PC transformation of Bosworth August 1998 visible, near-infrared and thermal bands of Ambion field

PC Band 1

PC Band 2

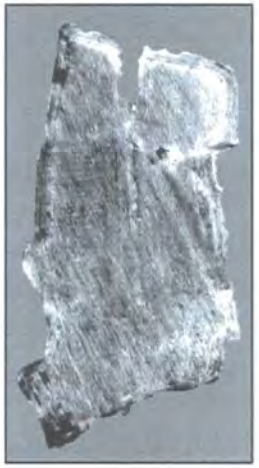

PC Band 3

PC Band 4

PC Band 5

PC Band 6

PC Band 7

Figure 5.77: PC transformation of Bosworth August 1998 uncalibrated visible and near-infrared bands of Ambion field

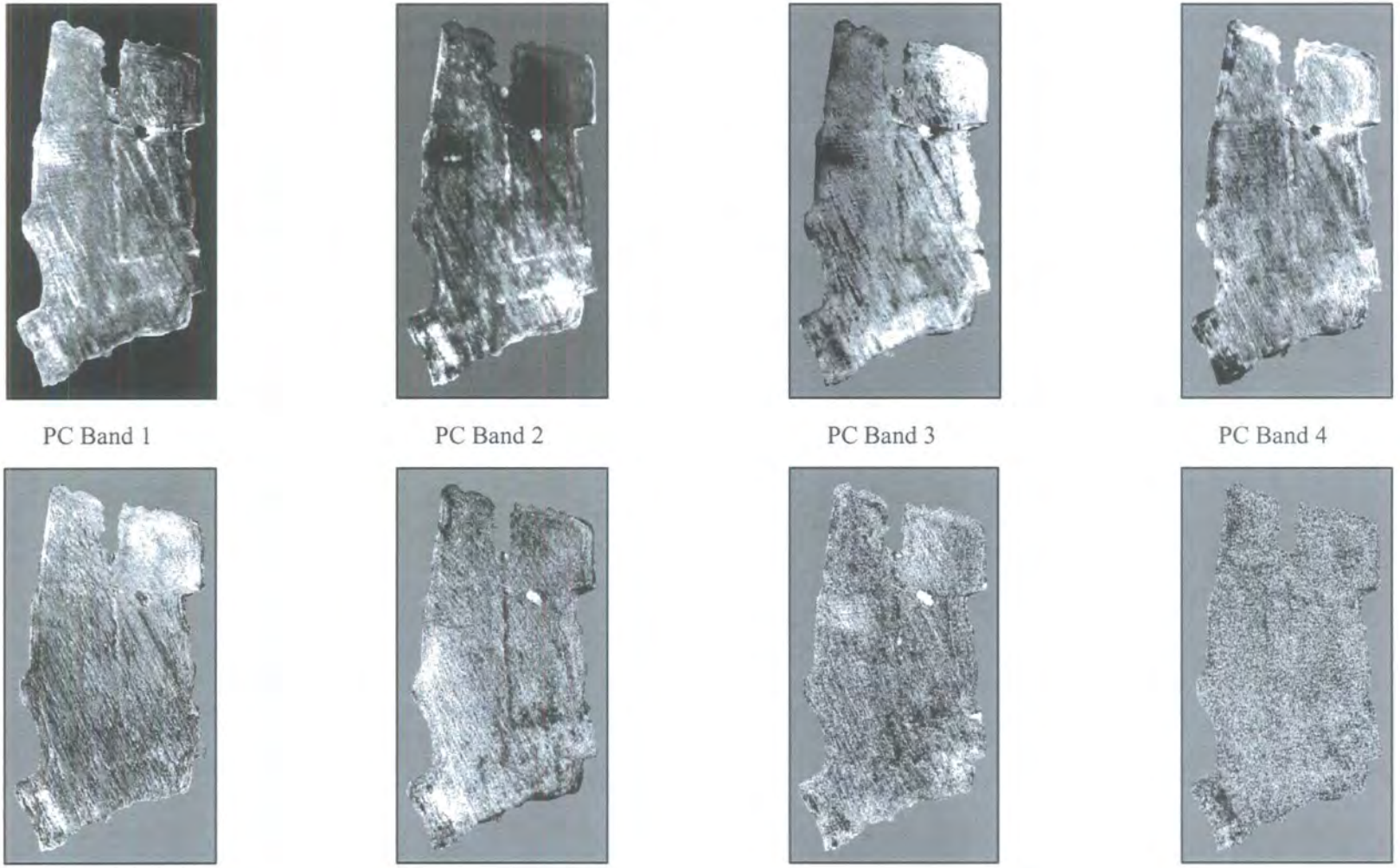

Figure 5.78: PC transformation of Bosworth August 1998 uncalibrated visible, near-infrared and thermal bands of Ambion field

Although the main features of Ambion field are clearly evident on both the calibrated and uncalibrated image datasets, the uncalibrated images contain much more spectral noise in more of the PC bands. As a result the uncalibrated data reduces the number of useful PC bands that can be used for interpretation. However, rather than interpret the monochrome images of each transformation band individually, a more practical method for interpretation is to generate a series of colour composites. A variety of band combinations can be selected for interpretation omitting bands containing excessive noise. The bands selected for colour combination are PC Bands 1-5 from both the calibrated (Figure 5.79) and uncalibrated (Figure 5.80) visible and near-infrared transformations and also the calibrated (Figure 5.81) and uncalibrated (Figure 5.82) visible, near-infrared and thermal transformations. Similar procedures are performed on the June 1998 and March 2002 images from Ambion field and also on the other grass-covered fields, although the results of these visualisations are not illustrated.

The result of the PC band combinations suggest that features internal to the barley field can be more easily delineated on the uncalibrated visible and near-infrared visualisations rather than the calibrated equivalent. However, there is little variation in the results from the uncalibrated and calibrated band combinations of the visible, near-infrared and thermal infrared visualisations. The images from the other stages in both barley growth and the grass-covered fields also show the same results with the uncalibrated visualisation revealing features similar to those revealed on the calibrated equivalents. The implications from the Principal Component Analysis is that it appears to be unnecessary to perform spectral calibration on the noise-free ATM channels prior to sufficient feature delineation in the barley and grass-covered fields using the PC spectral enhancement transformation.

Since the uncalibrated data appears to be sufficient for detection of internal field variations, the PC transformation is performed on the uncalibrated data from Ambion field when the oil seed rape is present. The results show poor internal field variation on either the visible and near-infrared band combinations (Figure 5.83) or from inclusion of the thermal band (Figure 5.84). The oil seed rape is therefore deemed an unsuitable vegetation condition on which to perform feature detection using Principal Component Analysis.

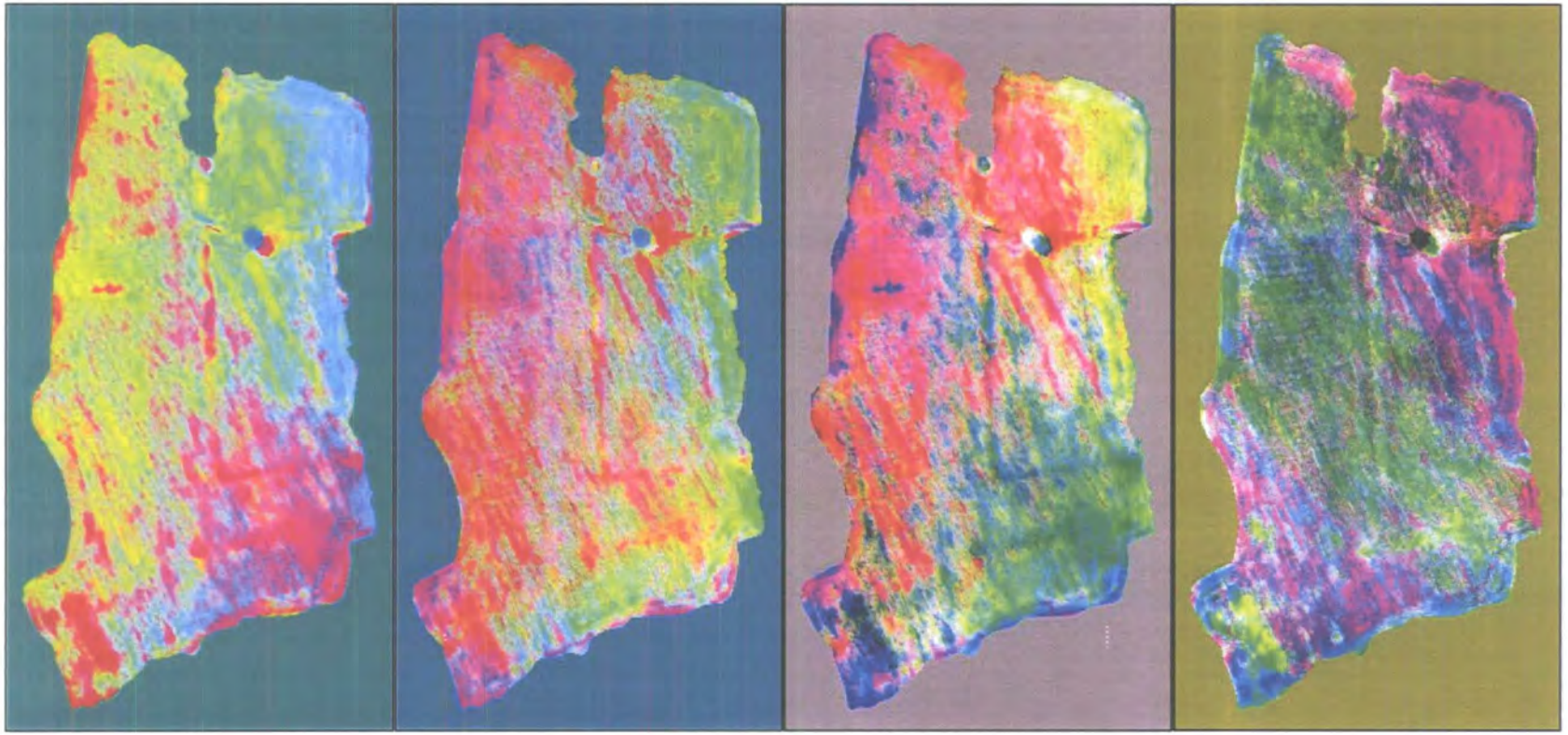

PC 123 PC 134 PC 234 PC 523

Figure 5.79: PC Band combinations on transformation of Bosworth August 1998 calibrated visible and near-infrared bands of Ambion field

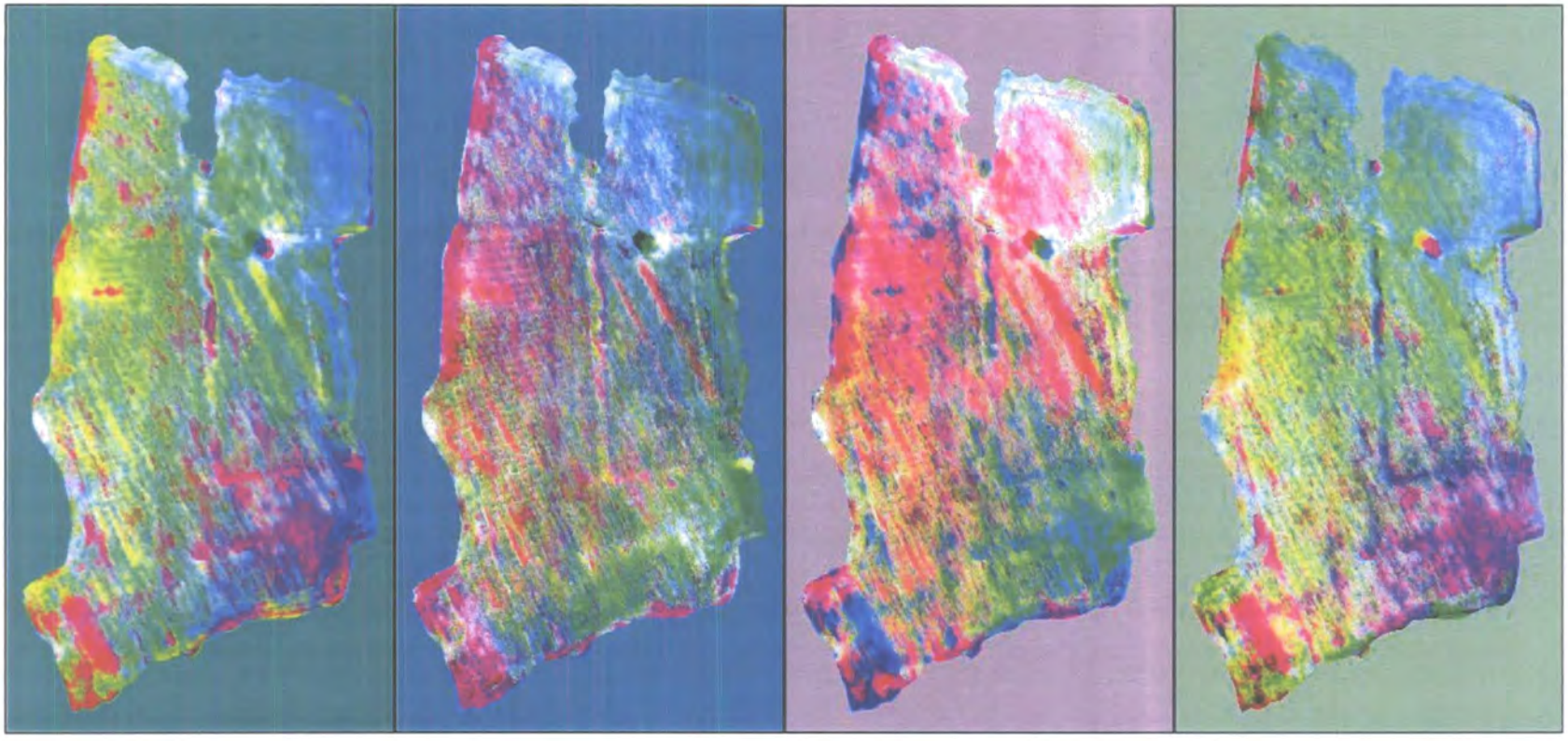

PC 123 PC 134 PC 234 PC 523

Figure 5.80: PC band combinations on transformation of Bosworth August 1998 uncalibrated visible and near-infrared bands of Ambion field

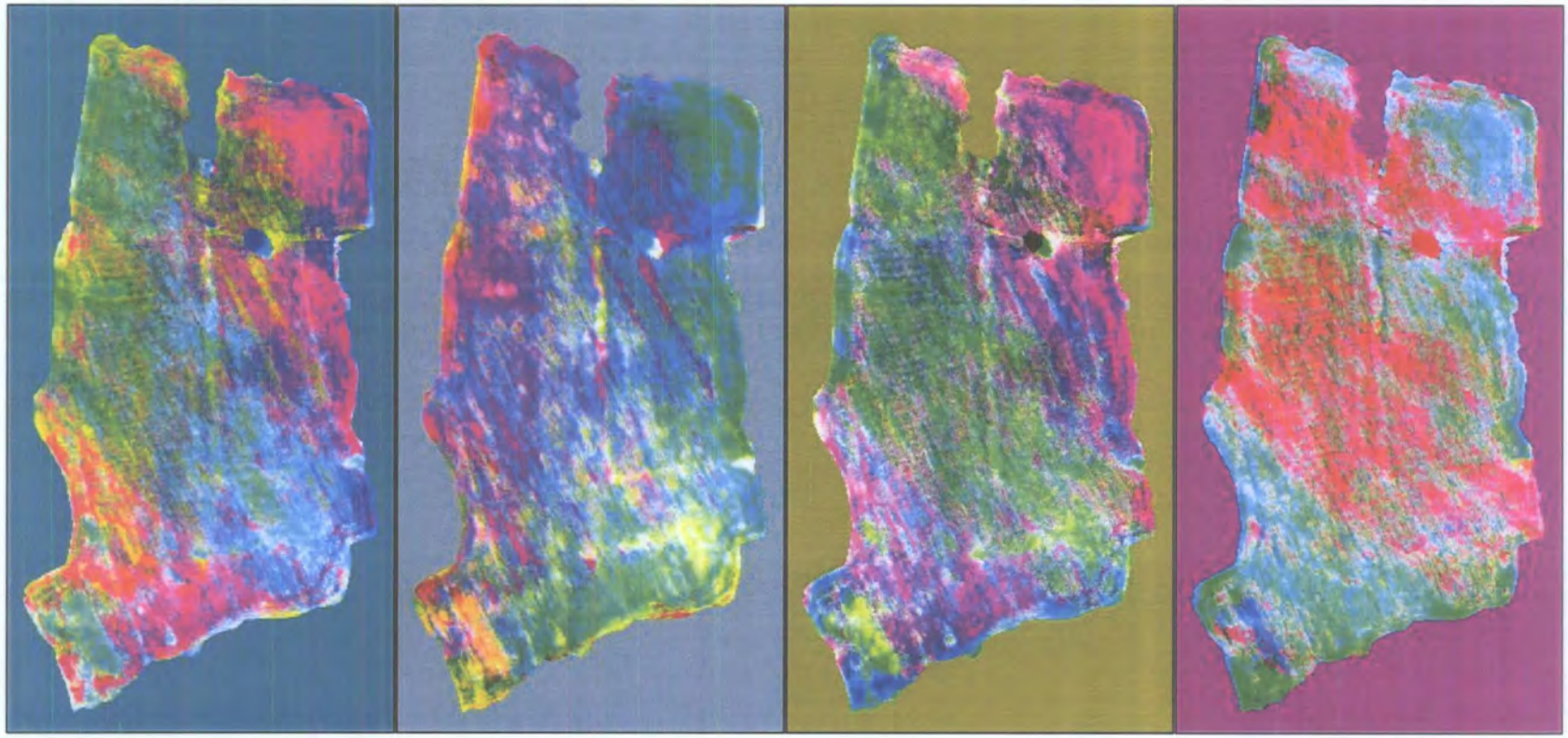

PC 123 PC 234 PC 521 PC 415

Figure 5.81: PC band combination on transformation of Bosworth August 1998 calibrated visible, near-infrared and thermal bands of Ambion field

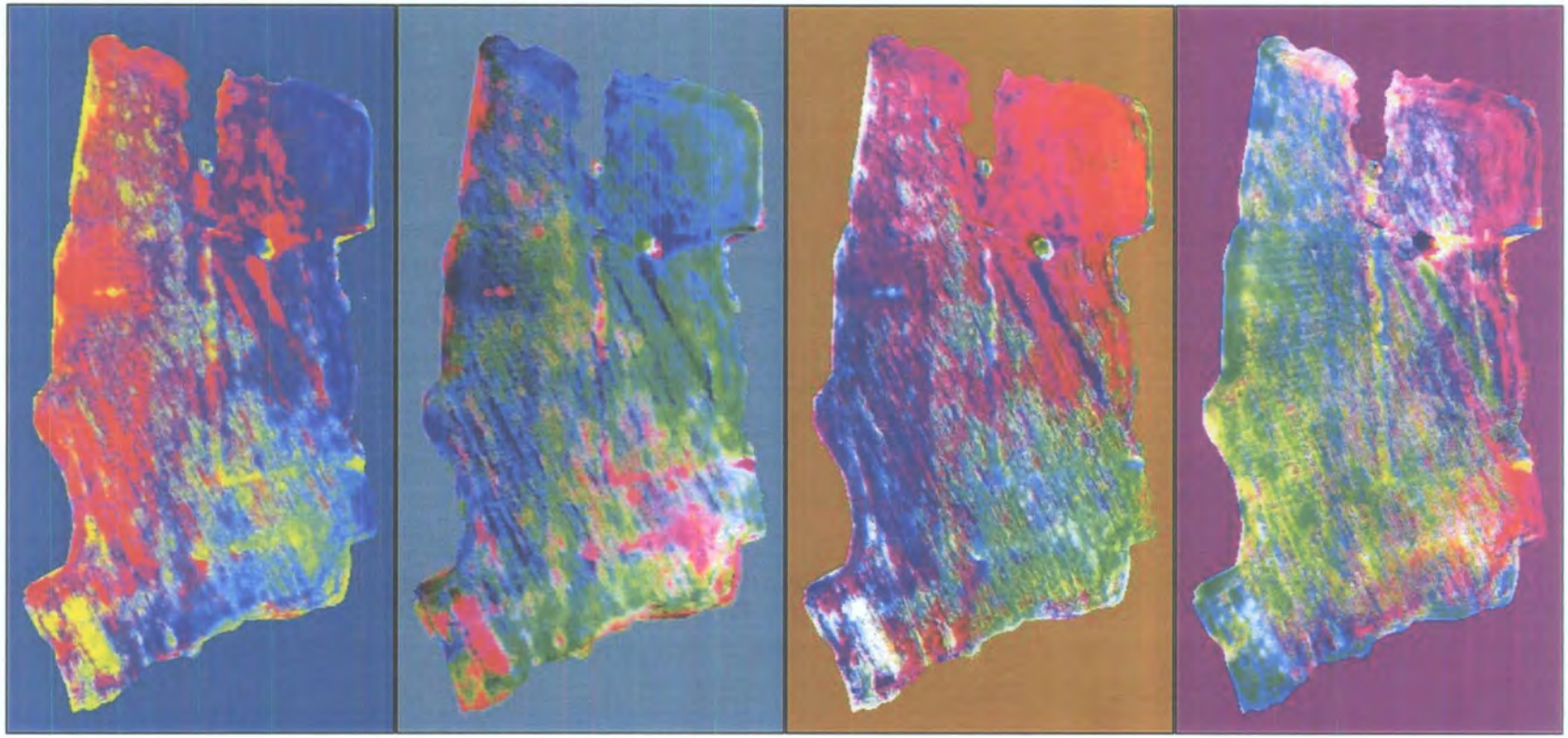

PC 123 PC 234 PC 521 PC 415

Figure 5.82: PC band combination on transformation of Bosworth August 1998 uncalibrated visible, near-infrared and thermal bands of Ambion field

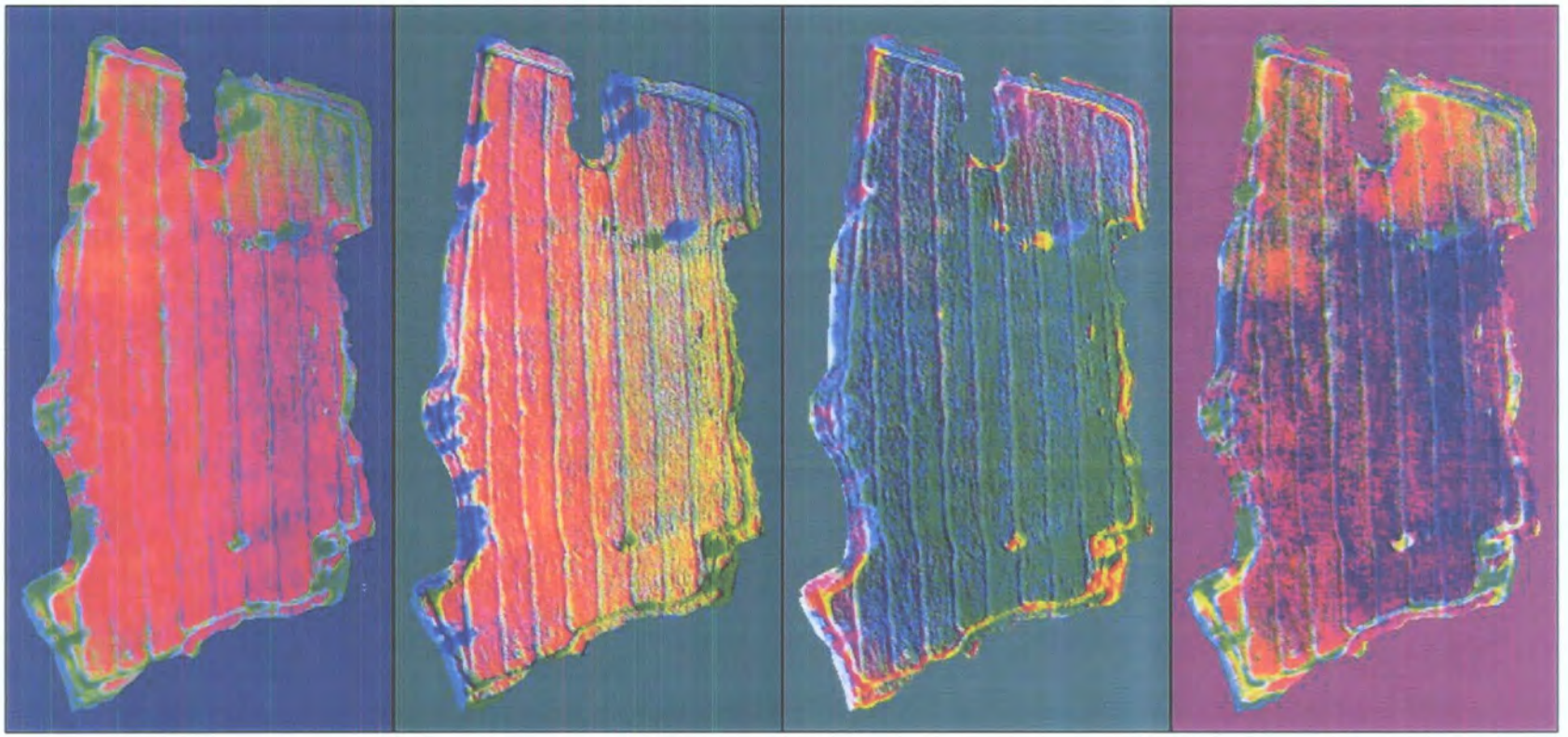

PC 123 PC 134 PC 234 PC 523

Figure 5.83: PC Band combinations on transformation of Bosworth March 2002 uncalibrated visible and near-infrared bands of Ambion field

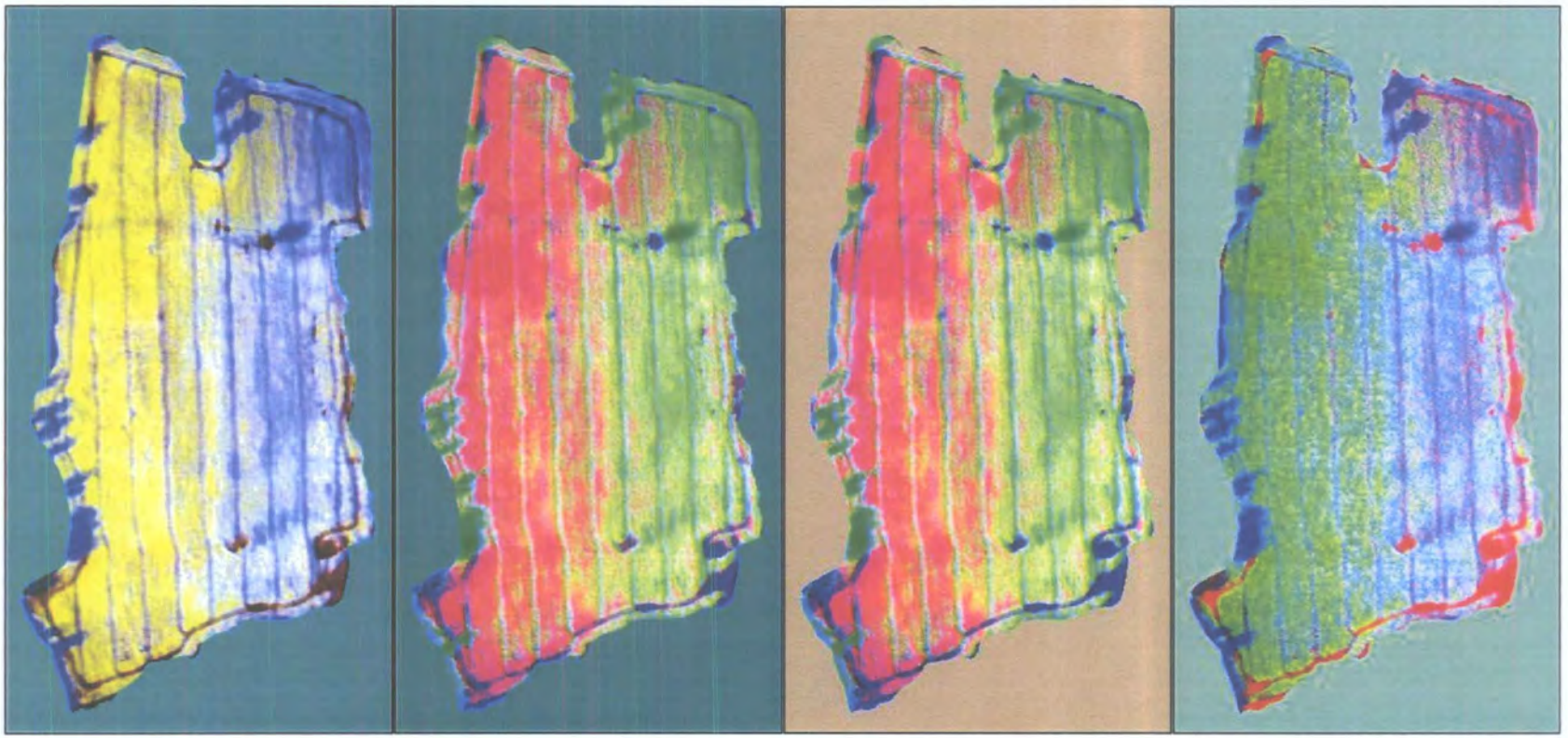

PC 123 PC 134 PC 234 PC 523

Figure 5.84: PC Band combinations on transformation of Bosworth March 2002 uncalibrated visible, near-infrared and thermal bands of Ambion field

5.6 *SUMMARY of QUALITATIVE ANALYSIS*

This chapter has outlined a range of qualitative analysis techniques that can be applied to visible, near-infrared and thermal images to enhance features contained within the spectral data measured by the NERC ATM sensor. The individual spectral channels are initially visualised as a series of monochrome images to assess the similarity in response of adjacent spectral channels and also enables identification of channels that contain excessive noise that are subsequently excluded from further analysis.

Visualisation of the thermal images shows relatively little contrast within the vegetation areas as a direct result of anomalously high and low radiance values associated with non-vegetated areas within the spatial extent of the imagery. This results in the values associated with the vegetation occupying a relatively small section of the image histogram. Subtle variations in response occurring within the vegetation are therefore difficult to detect without performing contrast enhancement techniques. Contrast enhancement techniques are applied to the range of intensity values associated with the vegetation so that there is a greater visual contrast in intensity values. The contrast enchantments that provide the most useful enhancement of the more subtle thermal features in the vegetation areas are the Linear 2% and Histogram Equalisation algorithms that enable the removal of values associated with the non-vegetated pixels.

The single-band visualisation technique allows interpretation of the thermal anomalies present on the diurnal thermal images from all study sites and also the seasonal thermal images obtained at the different stages in vegetation growth at the Bosworth site. Vector layers of the interpretation of the thermal anomalies are generated from the contrast enhanced images and a comparison is made between the diurnal results from each site and also the seasonal results from Bosworth. A seasonal assessment of Baildon Moor and Weardale could not be performed due to the acquisition of a single diurnal pair over these sites. The diurnal results from Baildon Moor suggest that both the abandoned mineshafts of distinct topographic and vegetation expression are more readily distinguished from the surrounding moorland on the day thermal images, with only a subtle contrast evident at night. The scour marks and spoil heaps from Weardale are easily identified on both the day and night

thermal images, mainly due to the lack of vegetation associated with the edges of the features giving rise to a distinct thermal response compared to the surrounding vegetation-covered areas.

The diurnal results from Bosworth show that the grass-covered fields reveal a series of thermal anomalies on the day thermal images when the grass is short, with moisture content and topographic aspect appearing to have the greatest effect on the thermal response. The night thermal images of the grass-covered fields fail to reveal the same detected features. The diurnal results from the barley-covered field showed a similar set of thermal features on the diurnal images obtained at each separate stage in vegetation growth. The night thermal images showed a similar response pattern at the middle and late stages in barley growth. The day thermal images obtained at these times showed a greater variation in response with a greater degree of thermal variation evident at earlier stages in barley growth, although the response from the later stage may be hampered by the wind shear effect. The diurnal response from the oil seed rape failed to reveal features that were revealed under the barley, suggesting that this type of vegetation is unsuitable for feature detection. The complexity in results from the diurnal and seasonal images from Bosworth suggests that the type and stage in vegetation growth can greatly affect the observed response in the vegetation-covered fields. From the single-band visualisations, the optimum observation appears to occur during the day when the grass is relatively short and at early stages in barley or at night in later stages of barley growth.

Although the single-band visualisation is important for the interpretation of the thermal anomalies, it is not very easy to compare the results with the response observed in the other spectral channels. Comparison with each of these bands individually is laborious and so a more suitable method of spectral comparison is to generate colour composite images of selected spectral channels. The series of colour composite images generated for the Bosworth site suggest that the near-infrared enhances the spectral variability of the individual fields with the inclusion of the day thermal channel further enhancing visual interpretation. A similar result is also evident on colour composite visualisation of the Baildon Moor and Weardale data. From the series of the colour composite images it is clear that the inclusion of the

thermal infrared is very important for the interpretation of anomalous features within the study site.

Alternative enhancement techniques are applied to the multispectral imagery, such as *Edge Detection Filtration, Image Arithmetic* and *Principal Component Analysis,* which aim to enhance the variability associated with vegetation cover. In order to enhance the detail associated with the vegetation, areas that did not contain vegetation were omitted from analysis. Spatial enhancement involves the use of mainly Low Pass, High Pass and Directional Filtration techniques that aim to enhance contrasts in the response measured in the vegetation. Results of the Low Pass filtration smoothed the imagery and did not enhance the detail of the vegetation areas. Results of the High Pass and Directional filtration enhanced some of the strong contrast in response within the vegetation, but are only useful as an initial investigation of the thermal contrast occurring within a vegetated area and do not necessarily reveal all thermal anomalies within the vegetation.

Image arithmetic or more specifically image subtraction is important in thermal assessments where the thermal contrast in diurnal response can indicate the resistance of the materials to temperature change, or the apparent thermal inertia, and relate to variations in the bulk properties of the surface materials. This technique can only be successful where radiometric calibration has been performed on the diurnal thermal images and the same thermal response on either diurnal image will have the same digital number. Image subtraction is performed on the calibrated data from Bosworth to detect potential anomalies that may relate to bulk material variations. Results from the barley field showed substantial enhancement of the thermal features at an earlier stage in crop development, whereas the results from later in the barley growth and under the oil seed rape show thermal response patterns similar to the day thermal images, supported by the similarity in histograms generated from the day and contrast images. This characteristic is also evident in the Weardale imagery. However, the Baildon Moor data shows a more variable response pattern across the shafts. When the thermal profiles are extracted across the shaft features in Baildon Moor there appears to be a variation in the shape of the profile between the day and night images, and, as a result, the thermal profile across the mine shaft shows a skew towards one side of the feature, suggesting a variation in the materials beneath the surface. When

the results of the thermal interpretation are compared with the results from the geophysical survey in Baildon Moor, the variation in shape of the thermal profile correlates with a skew in the geophysical properties of the materials at depth. When the results of the thermal interpretation from Bosworth are compared with the results from the geophysical survey, it is apparent that the thermal features no not necessarily correlate with geophysical anomalies suggesting that the thermal anomalies relate to variations in the vegetation rather than variations in the underlying soil characteristics.

Principal Component Analysis is performed on the calibrated and uncalibrated multispectral data from the Bosworth site to determine the necessity for spectral calibration prior to feature detection. The results from the PCA transformation suggest that the uncalibrated dataset provides a suitable spectral basis from which to detect features present in the vegetation areas with inclusion of the thermal channel revealing further features. The promising results from this technique suggest that substantial feature enhancement may be obtained in the Baildon Moor and Weardale areas by performing PCA on the uncalibrated datasets, and omitting the non-vegetated areas from analysis. PCA therefore appears to provide a useful approach to detecting features in vegetated areas where ground data may not be available for spectral calibration.

The different qualitative analyses described in this chapter have shown that a range of visualisation and transformation techniques can provide the basis for feature detection when areas that contain non-vegetated materials are excluded from analysis. In addition, the results from the calibrated and uncalibrated Bosworth data suggest that it is not entirely necessary for spectral calibration of the data in order to detect features, as long as there is linearity in the thermal response across the day and night thermal images. Results from Baildon Moor suggest that the thermal anomalies can be related to strong geophysical anomalies of the soil properties at depth. This is not the case for the Bosworth site where the geophysical anomalies are not associated with thermal anomalies, and vice versa, suggesting that the thermal response may indicate variations in the vegetation cover.

In order to test this hypothesis, soil samples are examined across positions of some of the thermal and geophysical features in the Bosworth site to assess the

relationship between the observed thermal anomaly and variations in the physical characteristics of the underlying soils.

6 NUMERICAL THERMAL MODELLING

The processing requirements for thermal infrared image data is typically dependent on the type of information to be extracted from the data, such as the calibration to absolute surface temperature or the determination of physical thermal properties of the surface (Schott, 1989). Both of these requirements are examples of processing that enable extraction of quantitative information from manipulation of the numerical image data.

When exposed materials are altered by weathering or are covered by a layer of a different material, the observed surface reflectance is unrepresentative of the bulk composition and materials with different compositions will often display similar temperature values when observed at one point in the diurnal cycle. As a result, interpretation of thermal images is often complicated because information on the physical properties of the surface is contained in both the spatial and temporal variations of the data and thermal models are necessary to extract and display this information. Thermal inertia is especially useful in such circumstance as a complement to surface reflectance data because it depends on the volumetric rather than the surface properties of the material. Thermal inertia is a measure of the resistance of a material to a change in temperature and physical thermal inertia can be calculated from the root product of the physical parameters of thermal conductivity, heat capacity and density. Due to the inclusion of density in the calculation, thermal inertia can indicate volumetric variations in surface materials and so thermal inertia may be particularly useful when attempting to locate features buried at shallow depths where there will be a variation in physical and thermal properties of the features compared to the surrounding matrix.

Although thermal inertia cannot be measured directly from remote thermal observation, an Apparent Thermal Inertia (ATI) can be inferred from the diurnal resistance of the surface to temperature change. This requires the acquisition of thermal images at times when there is the greatest difference in temperature response at the surface with an image acquired during the day when the surface is at its maximum temperature, with a complementary image acquired at night when the surface is at its minimum temperature. The apparent thermal inertia can then be

calculated from the contrast between the day and night response and is displayed in image format. However, this technique requires the accurate calibration of the thermal radiance measured at the sensor to temperature values. An empirical surface temperature calibration can be performed on the thermal data using ground temperature values measured at the surface at the time of overflight and is performed on the data during preprocessing. However, if such data is unavailable then an alternative is to perform a *quantitative* temperature calibration where radiance is converted to temperature using the Planck Radiation Law.

Once the thermal data is converted to temperature, quantitative information on the thermal nature of the surface can be extracted by calculating the Apparent Thermal Inertia using a variety of algorithms. Some of the algorithms require auxiliary detail on topographic, meteorological or physical parameters relating to the surface. However, such detail is often unavailable at the time of observation. Alternative algorithms that require limited auxiliary detail are applied to the calibrated diurnal temperature images and the results from the Kahle *et al* (1984) and Price (1989) algorithms are compared with the results from the simple day-night image subtraction performed during qualitative assessment.

The ATI values calculated from the thermal imagery gives a snap-shot of the thermal characteristics of the surface, however, an uncertainty lies in whether the values relate to a combined effect of the soil and surface vegetation or related solely to the vegetation layer. In order to assess this phenomenon, contact soil temperature values are measured at depths within the undisturbed soil column to generate a vertical thermal profile at selected locations in the study area. The thermal behaviour of the soil column is assessed throughout the vegetation growth cycle by measuring the heat flux at specific depths. The purpose of these measurements is to assess the relationship between the vegetation growth and the thermal regime of the surface to identify situations when the response of the vegetation is similar to that of the underlying soil.

6.1 QUANTITATIVE TEMPERATURE CALIBRATION

The data acquired by the 8-12μm channel on the ATM sensor give a measure of the thermal radiance measured for a discrete location on the ground surface. This value can be converted to temperature using an Empirical Line calibration technique during preprocessing where a particular thermal radiance value is assigned to a temperature value measured at the ground location, with interpolation between sets of thermal radiance and known temperature values. However, errors may occur using this calculation because it may be wrong to assume that every surface material behaves in the same way. An alternative approach is therefore adopted, where thermal radiance measured by the remote sensor is converted to temperature values using the mathematical inversion of the Planck Radiation Law (Equation 6.1) to calculate temperature (T) from known radiance (L) with respect to wavelength of observation (λ), emissivity of the surface (ε) and radiation constants C1 and C2 (Equation 6.2).

Equation 6.1

$$L = \frac{\varepsilon C_1}{\lambda^5 \left(\exp\left(\frac{C_2}{\lambda T} \right) - 1 \right)}$$

Equation 6.2

$$T = \frac{C_2}{\lambda \ln\left(\frac{\varepsilon C_1}{\lambda^5 L} + 1 \right)}$$

The above equation can be applied to the whole thermal image since the thermal radiance is known for every pixel in the imagery. However, there are two main factors in this equation that are not precisely known, that of spectral wavelength and surface emissivity. Therefore, prior to accurate temperature calibration of the thermal channel it is necessary to understand the sensitivity of the calculated temperature values to these factors.

6.1.1 Sensitivity Analysis

In order to assess the sensitivity of the Planck Equation to variations in each parameter, a series of C++ programs are written to calculate thermal radiance from a constant temperature with respect to variable wavelength and emissivity. In addition, temperature is also assessed with respect to a constant thermal radiance with variable wavelength and emissivity.

Where sensitivity is assessed with respect to variable wavelength, wavelength values are varied from 8.40μm to 11.50μm in increments of 0.05μm to represent the full spectral response curve of the ATM thermal channel. The spectral response of the ATM thermal channel, provided to NERC by NPL, indicates that the quantised boundary wavelengths associated with the thermal channel are set to an upper limit of 8.40μm and a lower limit of 11.50μm, giving the mid-channel wavelength of 9.95μm for the thermal infrared channel. Therefore all further calculations using thermal wavelengths were performed using this full spectral range, even though the response of the thermal channel varies across this spectral range (Figure 6.1).

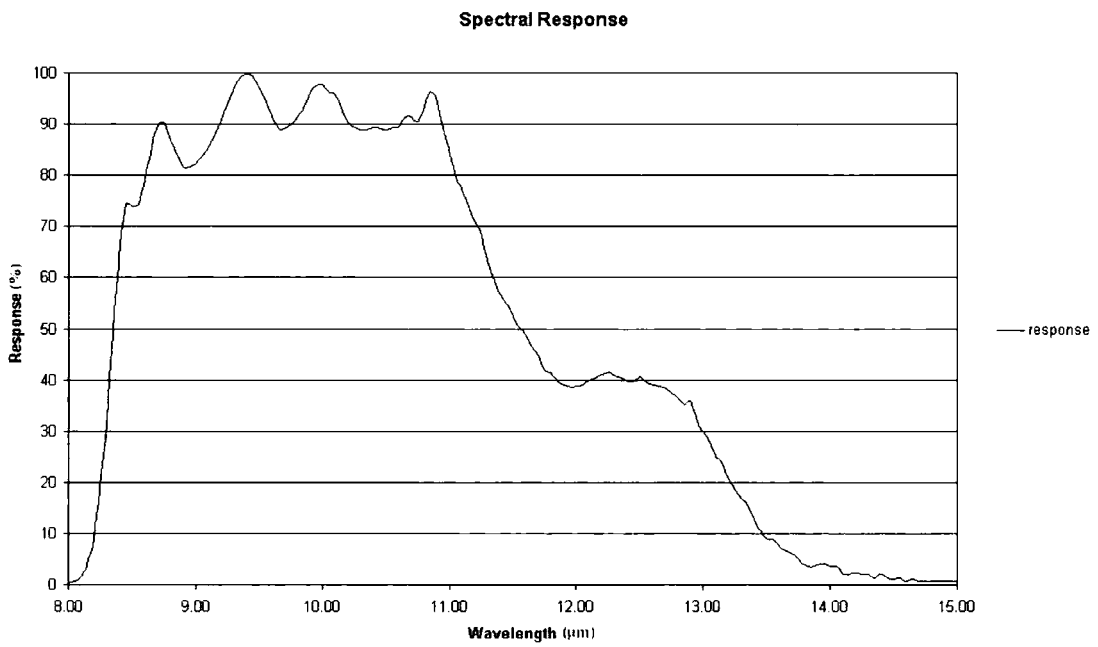

Figure 6.1: Spectral response pattern of ATM thermal channel

When sensitivity is assessed with respect to variable emissivity, the emissivity values are varied from 0.90 to 1.00 in 0.01 increments to represent the full range of possible natural material emissivity values present in the imagery, excluding those of roads and buildings. All sensitivity analyses are performed on the calibrated Bosworth data due to the availability of ancillary ground data.

The first analysis was performed to assess the sensitivity of radiance with respect to variable wavelength (Appendix F1). For this, values are substituted into the Planck equation (Equation 6.1) for a constant emissivity of 0.97, chosen to represent healthy vegetation that dominates the fields in the study site, and a constant temperature of 288K, chosen to represent the mean daytime temperature recorded for the study site. Results of the sensitivity analysis generate a 3rd order polynomial solution, with maximum radiance occurring at a wavelength of 10.00μm (Figure 6.2).

Further analyses are performed, first by varying the temperature and then the emissivity. Results of the temperature variation show that an increase in temperature results in the peak of calculated radiance moving to shorter wavelengths with progressively higher associated radiance values (peak at 9.60μm for 300K). In addition, a decrease in temperature results in the peak of calculated radiance moving to longer wavelengths with a decrease in radiance values (peak at 10.55μm for 273K) (Figure 6.2A). Results of the emissivity variation show an increase in emissivity results in progressively higher calculated radiance values with the peak of radiance always occurring at 10.00μm for a constant temperature of 288K (Figure 6.2B).

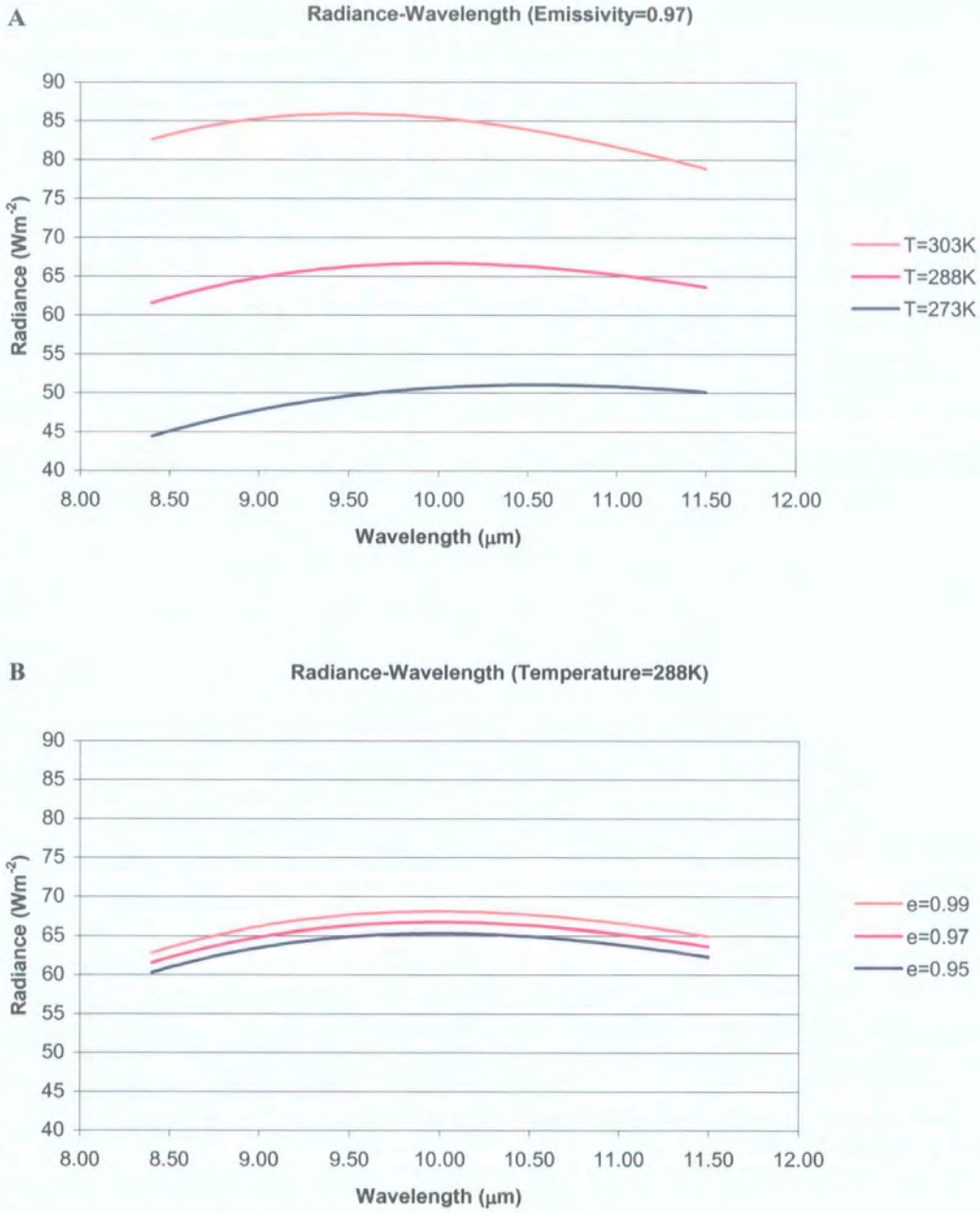

Figure 6.2: Sensitivity of thermal radiance to variable wavelength at (A) variable temperature and (B) variable emissivity

The second analysis was performed to assess the sensitivity of radiance with respect to variable emissivity (Appendix F2). For this, values are substituted into the Planck equation (Equation 6.1) for a constant wavelength of 9.95μm, chosen to represent the mean wavelength of the ATM thermal channel, and a constant temperature of 288K, chosen to represent the mean daytime temperature recorded for the study site. Results of the sensitivity analysis are summarised by an inverse linear relationship between radiance and emissivity for constant temperature and wavelength (Figure 6.3).

Further analyses are performed, first by varying the temperature and then the wavelength. Results of the temperature variation show that the gradient of the line increases with increasing temperature, with calculated radiance values also increasing with temperature (Figure 6.3A). Results of the wavelength variation show that the gradient of the line also increases with increasing wavelength. However, the radiance values do not show a linear increase with wavelength. A wavelength increase from 8.40μm to 10.00μm results in a progressive increase in radiance values. However, wavelength values from 10.00μm to 11.50μm results in a gradual decrease in subsequent radiance values (Figure 6.3B).

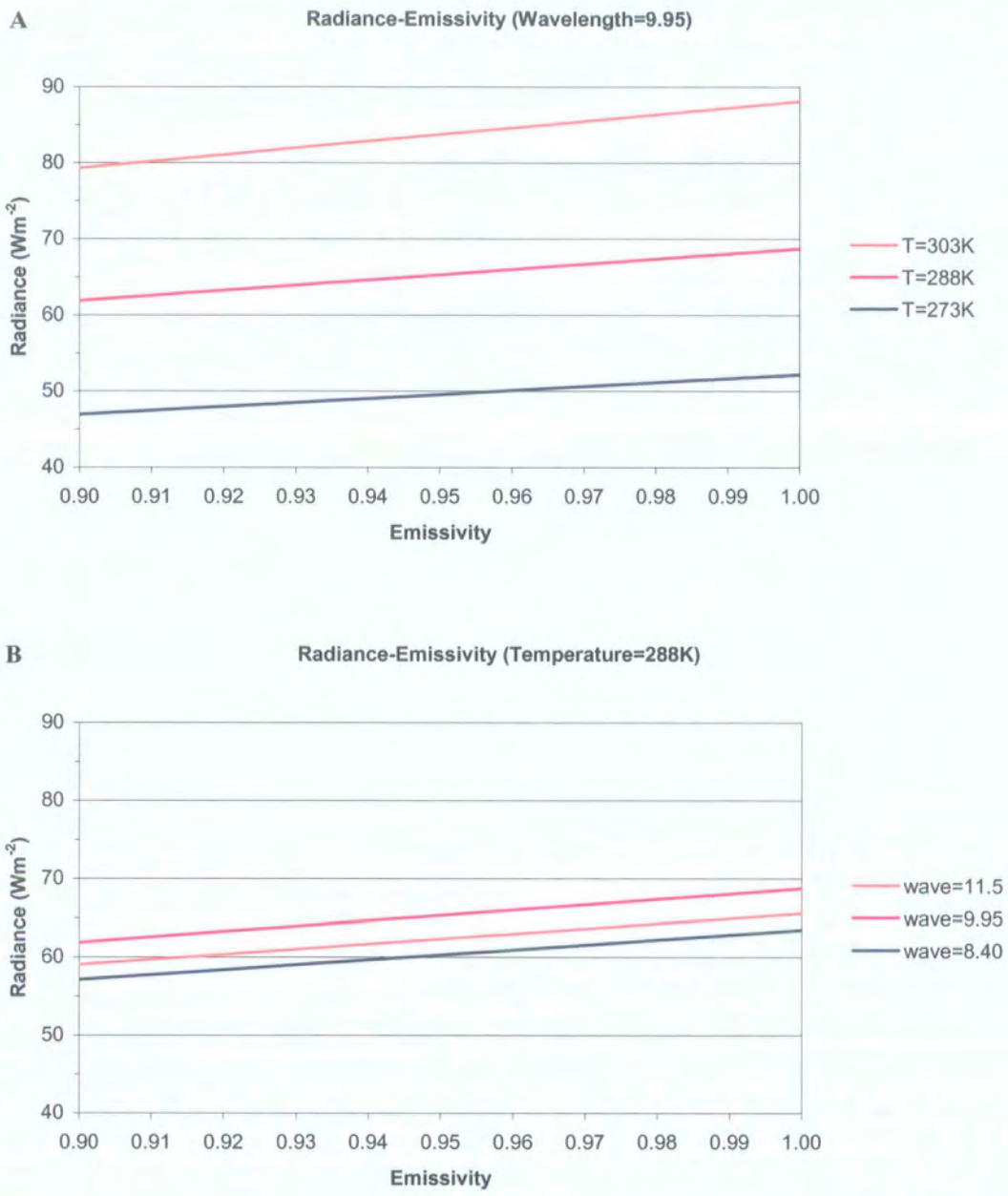

Figure 6.3: Sensitivity of thermal radiance to variable emissivity at (A) variable temperature and (B) variable wavelength

The third analysis was performed to assess the sensitivity of temperature with respect to variable wavelength (Appendix F3). For this, values are substituted into the inverse Planck equation (Equation 6.2) for a constant emissivity of 0.97, chosen to represent healthy vegetation that dominates the surface cover in the study sites. A constant radiance of 66 Wm^{-2} was chosen to represent the radiance calculated by Equation 6.1 using the mean parameter values recorded for the study sites. Results of the sensitivity analysis generate a 3rd order polynomial solution between temperature and wavelength for constant radiance or emissivity (Figure 6.4).

Further analyses are performed, first by varying the radiance and then the emissivity. Results of the radiance variation show that an increase in radiance results in an increase in the associated temperature values, with the minimum temperature moving to shorter wavelengths with an increase in radiance (Figure 6.4A). Results of the emissivity variation show that an increase in emissivity results in a decrease in the associated temperature values, with the minimum temperature occurring at progressively longer wavelengths with an increase in emissivity (Figure 6.4B).

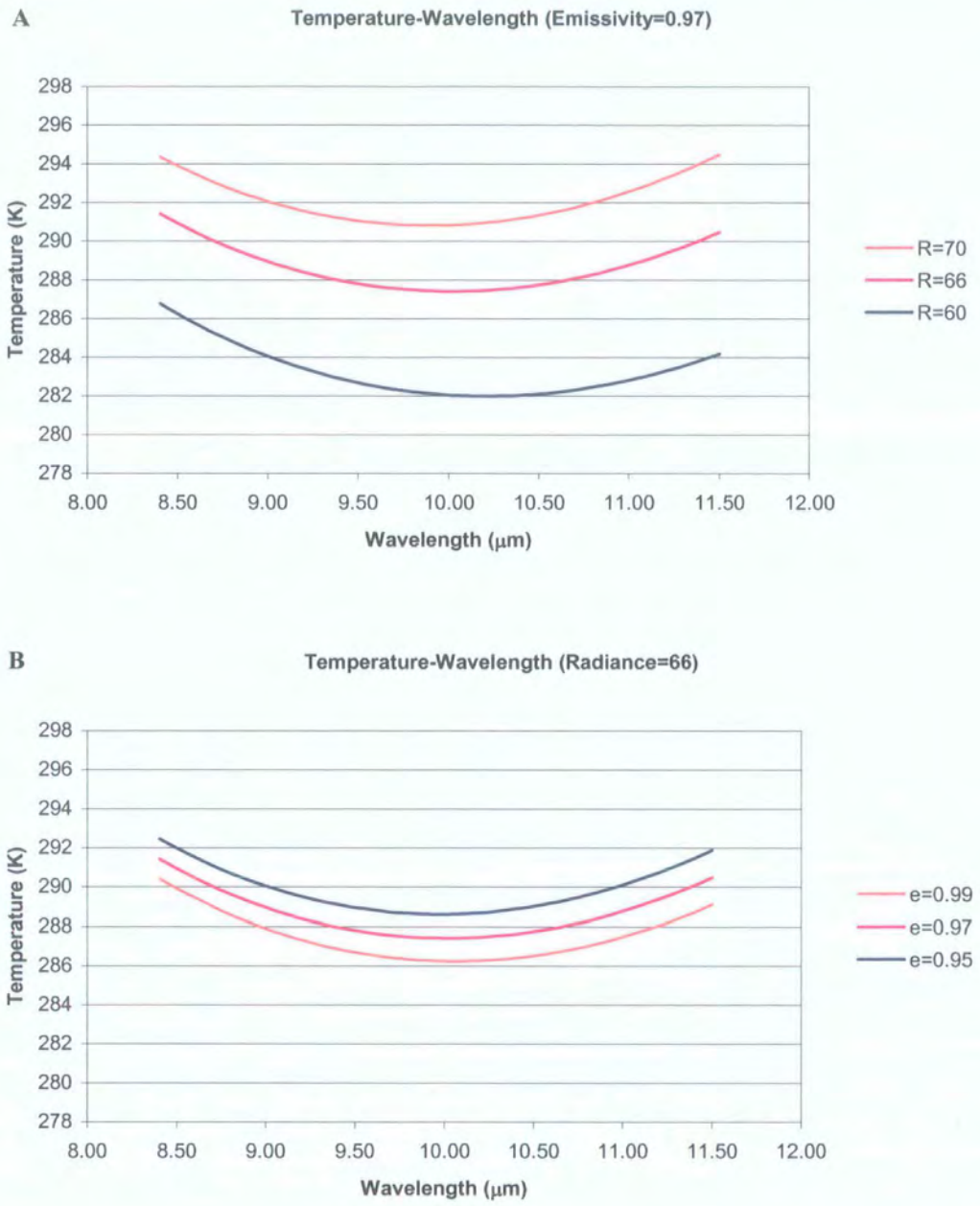

Figure 6.4: Sensitivity of temperature to variable wavelength at (A) variable radiance and (B) variable emissivity

The fourth analysis was performed to assess the sensitivity of temperature with respect to variable emissivity (Appendix F4). For this, values are substituted into the inverse Planck equation (Equation 6.2) for a constant wavelength of 9.95μm, chosen to represent the mean wavelength of the ATM thermal channel, with a constant radiance of 66 Wm^{-2}, chosen to represent the radiance calculated by Equation 6.1 using the mean parameter values recorded for the study sites. Results of the sensitivity analysis generate a 2^{nd} order polynomial solution with an inverse relationship between temperature and emissivity for constant wavelength and radiance (Figure 6.5).

Further analyses are performed, first by varying the radiance and then the wavelength. Results of the radiance variation show that an increase in radiance results in an increase in the associated temperature values (Figure 6.5A). Results of the wavelength variation are more complex with progressively shallower gradients with an increase in wavelength from 8.40μm to 10.00μm, and progressively steeper gradients observed from 10.00μm to 11.50μm (Figure 6.5B).

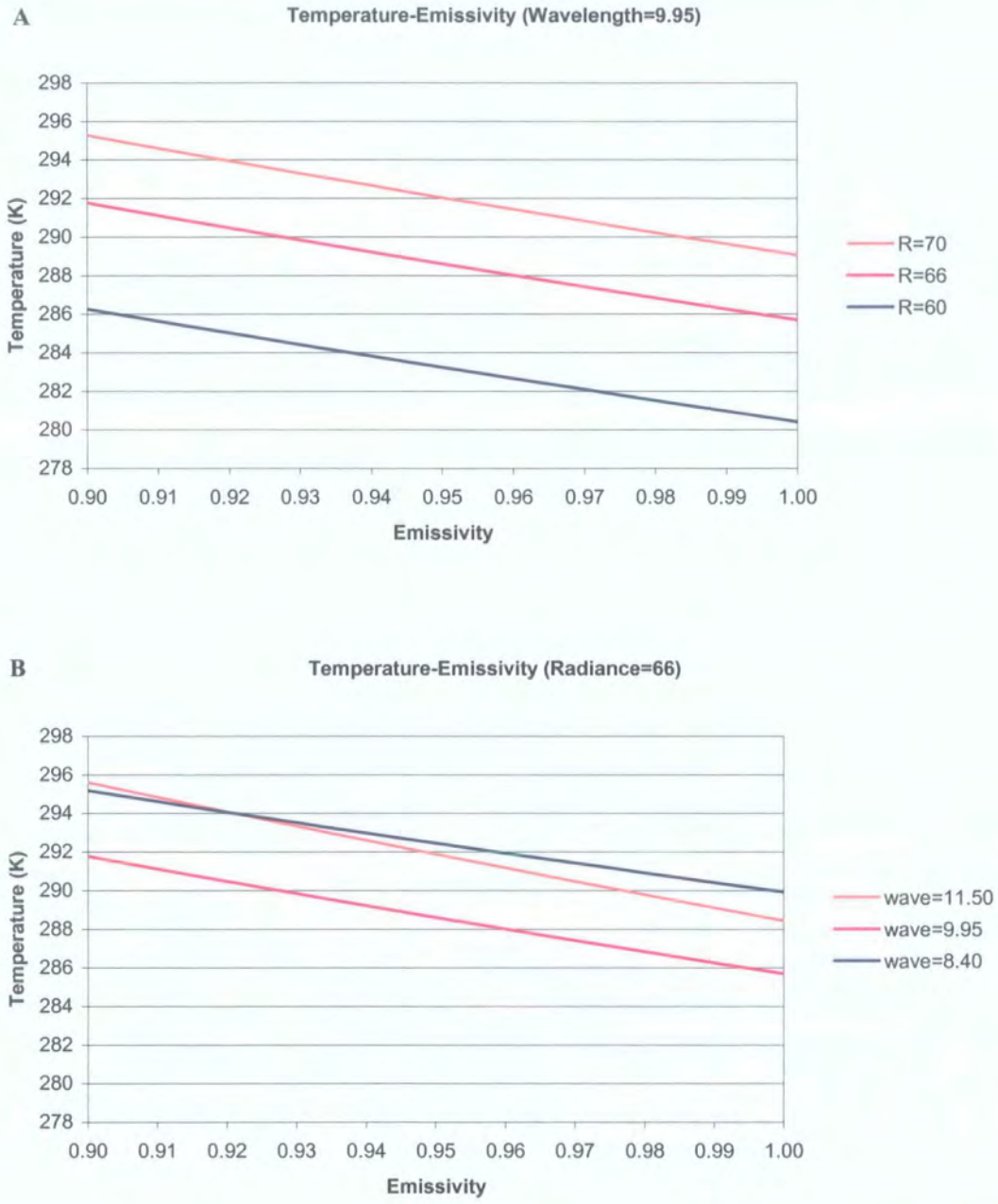

Figure 6.5: Sensitivity of temperature to variable emissivity at (A) variable radiance and (B) variable wavelength

From these sensitivity analyses, the range of emissivity values used appears to have little effect on calculated radiance (Figure 6.3) and temperature (Figure 6.5), with an uncertainty of ±0.03 emissivity resulting in an uncertainty of ±2.2K in temperature as is published in the literature (Fuchs & Tanner, 1966 and Schmugge *et al*, 1998). Emissivity values are known to be spectrally variable with wavelength in the thermal infrared region (Price, 1984 & Schmugge *et al*, 1991) but without having multiple channels within the thermal infrared, the true thermal emissivity of a surface cannot be determined. However, since the areas of most interest in the study sites are covered by vegetation of variable composition, structure and condition and there is only a slight variation in their associated emissivity values (Table 2.2), an emissivity of 0.97 can be assumed for the whole of the study sites as long as roads and buildings and other non-vegetated surfaces are omitted from analysis. Wavelength appears to have a greater influence on the calculated radiance (Figure 6.2) and temperature (Figure 6.4) and as such an assumed value of wavelength may be inappropriate. In addition, the spectral response of the ATM thermal channel shows a variable response across the 8.00μm-15.00μm range of thermal wavelengths (Figure 6.1). However, the mean spectral response occurs at a wavelength of 9.95μm and as a result, this wavelength is assumed for all further calculations on the ATM data using the Planck relationship.

The sensitivity analyses performed on the Planck Radiation Law have indicated that the assumed emissivity and wavelength values may have little affect on the calculation of temperature using the Planck relationship. As a result, users of the NERC Daedalus-1268 ATM sensor should be able to convert thermal radiance to temperature by substituting the radiance extracted from the ATM thermal channel and defining appropriate values for the wavelength of observation and the emissivity of the ground surface in the Planck relationship. However, there is great uncertainty in this process.

6.2 CONVERTING RADIANCE to TEMPERATURE USING THE PLANCK RELATIONSHIP

Thermal radiance can be converted to temperature using the Planck relationship (Equation 6.2) with respect to the wavelength of observation and surface emissivity. However, on closer inspection of the literature there was great uncertainty

on the definition of the parameters used by the various authors (Chapter 2.1.2). The greatest variation occurred in the units of measurement associated with radiance and wavelength, with additional discrepancies in the units and values of the physical constants. Further problems arose where some of the authors failed to state the units associated with specific parameters (Table 2.1). As a result, this posed a considerable problem for determining which description of the Planck equation should be applied for converting measured ATM radiance to ground temperature. A review of the literature revealed only three authors that state the complete set of units associated with radiance, temperature, wavelength and the physical constants, and also state the values of the physical constants used in the Planck equation:

1) ***Price (1989)*** defines radiance in $Wm^{-2}\ \mu m^{-1}$ with respect to temperature (K) and wavelength (μm) with values of $C1=3.74x10^{8}$ and $C2=1.439x10^{4}$

2) ***Qin & Karnieli (1999)*** define radiance in $Wm^{-2}\ \mu m^{-1}$ with respect to temperature (K) and wavelength (m) with values of $C1=3.74x10^{-16}\ Wm^{2}$ and $C2=1.439x10^{-2}$ mK

3) ***Kealy & Hook (1990)*** define radiance in Wm^{-3} with respect to temperature (K) and wavelength (m) with values of $C1=3.74151x10^{-16}\ Wm^{2}$ and C2=0.0143879 mK

Although Price (1989) and Qin & Karnieli (1999) use identical radiance and temperature units, there are variations in both the unit of wavelength and in the values of their physical constants. It is also apparent that there must be a discrepancy between Qin & Karnieli (1999) and Kealy & Hook (1990) since there is a variation in the units defined for radiance and yet the authors state identical units for the temperature and wavelength and also state identical values of their two physical constants. It is therefore necessary to assess the effect of these differences on the Planck equation in order to determine which Planck definition shall be applied to the thermal data measured by the ATM. This involved a simple technique of substituting values for emissivity (ε=0.97) and temperature (T=296K) into the equation together with a value of wavelength (λ=9.95, in the units appropriate to the authors' specification) and values of their associated physical constants (Equation 6.3).

Equation 6.3

$$L = \frac{\varepsilon C_1}{\lambda^5 \left(\exp\left(\frac{C_2}{\lambda T} \right) - 1 \right)}$$

PRICE (1989)

$$L = \frac{0.97 \times 3.74 \times 10^8}{9.95^5 \left(\exp\left(\frac{1.439 \times 10^4}{9.95 \times 296} \right) - 1 \right)}$$

$$L = 2.82 \times 10^1$$

QIN & KARNIELI (1999)

$$L = \frac{0.97 \times 3.74 \times 10^{-16}}{\left(9.95 \times 10^{-6}\right)^5 \left(\exp\left(\frac{1.439 \times 10^{-2}}{\left(9.95 \times 10^{-6}\right) \times 296} \right) - 1 \right)}$$

$$L = 2.82 \times 10^7$$

KEALY & HOOK (1990)

$$L = \frac{0.97 \times 3.74151 \times 10^{-16}}{\left(9.95 \times 10^{-6}\right)^5 \left(\exp\left(\frac{0.0143879}{\left(9.95 \times 10^{-6}\right) \times 296} \right) - 1 \right)}$$

$$L = 2.82 \times 10^7$$

If we refer back to the definition of radiance provided by the authors, Price (1989) and Qin & Karnieli (1999) state identical units of radiance and yet there is a factor of $1x10^6$ between the radiance values calculated above, which relates to the magnitude of the units of the other parameters. There is an additional problem in that the radiance calculated above for the Qin & Karnieli (1999) and Kealy & Hook (1990) definitions are identical and yet the units defined for radiance would suggest a factor of $1x10^6$ between these authors, i.e. converting from $Wm^{-2}\mu m^{-1}$ (Qin & Karnieli, 1999) to Wm^{-3} (Kealy & Hook, 1990). Although the discrepancy between the latter two authors would suggest that the units of the parameters are different from those used in their respective definitions of the Planck equation, the definition provided by Price (1989) is deemed the most reliable for temperature calculation with parametric definitions for radiance in $Wm^{-2}\mu m^{-1}$, wavelength in μm and values for $C1=3.74x10^8$ and $C2=1.439x10^4$. The Price (1989) definition is therefore applied to the ATM radiance to determine ground temperature. However, prior to its application users of the NERC ATM data must ensure that the ATM radiance is presented in the same physical units as defined by Price (1989).

6.3 CONVERSION of ATM RADIANCE to PRICE RADIANCE

When the header is extracted from each ATM image, the unit of measurement associated with the ATM radiance is $\mu Wcm^{-2}\ sr^{-1}\ nm^{-1}$, which is in stark contrast to

the units of Wm^{-2} stated in the Price (1989) definition of the Planck relationship. As a result, a conversion factor must be determined and applied to the ATM data to provide the appropriate radiance units for the determination of ground temperature. The conversion factor can be determined by comparing the magnitude of the radiance units from each source (Calculation 6.1).

Calculation 6.1

Source	ATM	PRICE
Radiance Units	$\mu W\ cm^{-2}\ sr^{-1}\ nm^{-1}$	$W\ m^{-2}\ \mu m^{-1}$
Magnitude	$\frac{10^{-6} \times 10^{0} \times (10^{-2})^{-2} \times (10^{-9})^{-1}}{10^{7}}$	$\frac{10^{0} \times (10^{0})^{-2} \times (10^{-6})^{-1}}{10^{6}}$

This calculation suggests that ATM radiance can be converted to Price radiance by multiplying by a factor of $1x10^{1}$. However, this calculation does not take into account the scaling factor that was introduced during the radiometric calibration process to ensure that the values of ATM radiance were recorded within the numerical range of 0-1. The ATM radiance therefore requires further division by this scaling factor, which is represented by a factor of $1x10^{3}$ that is detailed in the header of each ATM image. The above calculation must therefore incorporate this scaling factor prior to determining the conversion between ATM radiance and Price radiance (Calculation 6.2).

Calculation 6.2

Source	ATM	PRICE
Radiance Units	$\mu W\ cm^{-2}\ sr^{-1}\ nm^{-1}$	$W\ m^{-2}\ \mu m^{-1}$
Magnitude	$\frac{\text{scaling factor} \times 10^{-6} \times 10^{0} \times (10^{-2})^{-2} \times (10^{-9})^{-1}}{10^{7}}$	$\frac{10^{0} \times (10^{0})^{-2} \times (10^{-6})^{-1}}{10^{6}}$

The above calculation suggests that ATM radiance requires division by a factor of $1x10^{2}$ in order to represent Price radiance units. However, this calculation has not taken into account the *per steradian* (sr^{-1}) part of the ATM radiance units, a factor introduced to take into account the solid angle associated with observation from the sensor. However, there is great uncertainty as to whether steradian should be represented by 2π as in normal laboratory-based investigations where both northern and southern hemispheres of an object are observed, or should be represented by π when the northern hemisphere of the object is observed as in the case when the

ground surface is observed from the airborne platform. This latter approach is more plausible and as such a value of π was suggested for incorporation in the conversion between ATM and Price radiance (Wilson, *pers.comm*).

However, since there is such uncertainty in the literature on this issue, an empirical approach was adopted to assess the conversion between ATM radiance and Price radiance detailed in the previous discussion. Radiance was empirically determined for known ground temperature values using the Price (1989) definition (Equation 6.3) and comparing the calculated radiance with the ATM radiance extracted from the corresponding pixels, taking into account the conversion factor determined through Calculation 6.2 and the solid angle of observation (Table 6.1).

Temperature	Price Radiance	Extracted ATM Radiance	Price-converted ATM Radiance
296K	28.3	0.86	$0.86 \div 10^2 \times \pi = 2.7018$
288K	24.7	0.79	$0.79 \div 10^2 \times \pi = 2.4819$
299K	29.7	0.92	$0.92 \div 10^2 \times \pi = 2.8903$

Table 6.1: Comparison of Price and ATM radiance for known ground temperatures, calculated using wavelength of 9. 95μm and emissivity of 0.97

It would appear from the above table that even when the scaling factor and the solid angle are taken into consideration, the ATM radiance still does not equate to the expected Price radiance value. As a result, the thermal radiance measured by the NERC ATM cannot be directly inserted in the Price relationship to determine surface temperature, which has serious implications for users of the NERC ATM thermal data. The NERC ARSF is still reviewing this issue and hope to provide a solution in the near future to enable the determination of ground temperature directly from the measured ATM thermal radiance (Wilson, *pers.comm*).

Although the above discussion has outlined great uncertainty in the conversion of ATM radiance to Price radiance, this does not affect the remainder of the thesis where quantitative Apparent Thermal Inertia models were applied to ground temperature values of the study sites that were determined through application of an empirical line image calibration technique, which calculates a linear regression between the ATM radiance extracted for specific features and the corresponding known ground temperature values (Chapter 4.5.1.1). This technique provides day and night temperature images of the study sites on which to perform Apparent Thermal

Inertia modelling and to assess variations in the surface response potentially relating to features buried in the near-surface environment.

6.4 APPARENT THERMAL INERTIA MODELLING

Apparent thermal inertia can indicate volumetric variations in surface materials and may be particularly useful when attempting to locate features buried at shallow depths where there will be a variation in physical and thermal properties of the features compared to the surrounding matrix. Although thermal inertia cannot be measured directly from remote thermal observation, an Apparent Thermal Inertia (ATI) can be determined from the diurnal resistance of the surface to temperature change. ATI calculation requires the acquisition of thermal images at times when the surface displays the greatest difference in temperature response across the diurnal cycle with each thermal image calibrated to surface temperature via the empirical line method. ATI is then calculated for the co-registered image pair by subtracting the night temperature from the day temperature value for every pixel. ATI values are initially calculated using the temperature-calibrated diurnal image pairs from Bosworth before comparing the results performed with the uncalibrated image pairs to assess the necessity for temperature calibration.

ATI models are essentially driven by the parametric relationship under investigation and the type of auxiliary data available for incorporation in the model. A simple image-based approach can be used, as discussed in the previous chapter, using the day-night temperature difference of each pixel from a diurnal image pair. Alternative approaches can be adopted involving more complex mathematical relationships that require auxiliary detail on meteorological, topographical or surface characteristics.

The simplest approach to ATI calculation was initially conceived as part of the Heat Capacity Mapping Mission (HCMM) where ATI is calculated as a function of the diurnal temperature change measured across the surface (ΔT) with respect to surface albedo (A), Equation 6.4. This was expressed in Cracknell & Xue (1996) and as such shall be referred to the Cracknell & Xue (1996) model from this point forward.

Equation 6.4

$$ATI = \frac{(1-A)}{\Delta T}$$

A C++ program was written using the above equation, where the ATI is calculated on a pixel-by-pixel basis from the temperature change observed between co-registered diurnal temperature images and a value of the surface albedo (Appendix F5).

Surface albedo is a dimensionless measure of the reflectivity of the surface, or the fraction of incident solar radiation that is reflected by the surface (Barrett & Curtis, 1982, Sabins, 1986 & Elachi, 1987). Initially, the ATI is calculated with respect to a constant user-defined albedo value, which may be appropriate where surfaces have a homogenous composition. However, areas that have a heterogeneous nature may be poorly represented by a single albedo value. Albedo is affected by properties such as composition (Goetz, 1989 & Snyder *et al*, 1997), roughness (Verbrugghe & Cierniewski, 1998) and moisture content as well as view angle and solar zenith angle (Barnsley *et al*, 1997; Song, 1998 & Cresswell *et al*, 1999). Vegetation also affects surface albedo through variations in leaf and canopy geometries (Grover *et al*, 2000), leaf area index and fractional cover (Sharratt, 1998) and also canopy reclination (Song, 1998). Heterogeneous areas therefore require determination of surface albedo for every pixel in the image. A variety of methods for determining albedo are mentioned in the literature (Price 1977; Kahle *et al*, 1976; Gillespie & Kahle, 1977; Pratt & Ellyett, 1979; Watson, 1982; Price, 1985; Kahle & Alley, 1985; Xue & Cracknell, 1995 & Grover *et al*, 2000). However, none of the authors give any detail on the specific methods of calculation.

Since surface albedo cannot be easily determined for heterogeneous surfaces, all non-vegetated areas are masked from the images to ensure homogenous land cover. This reduces the variation in surface albedo values and enables the designation of a single albedo value to the remaining surface cover. Although albedo varies with structural properties of the vegetation, there is a narrow range of vegetation values published in the literature. However, to understand the sensitivity of ATI calculations to variations in albedo, a C++ program was written using Equation 6.4, where the ATI is calculated with respect to a specific temperature change, reflecting the range of diurnal temperature contrasts determined for the study site through the simple day-night temperature subtraction, and a range of albedo values from 0.00 to 1.00 in

increments of 0.01 (Appendix F6). Results of the sensitivity analysis are plotted as a graph of ATI against variable albedo (Figure 6.6).

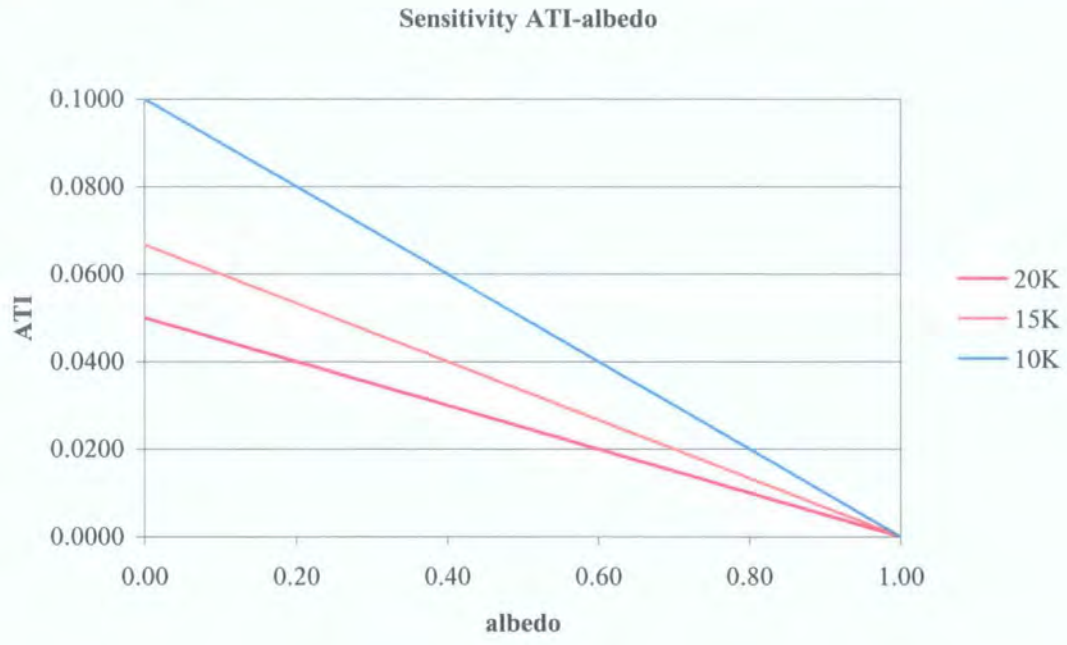

Figure 6.6: Sensitivity of ATI to variable albedo

The results from the sensitivity analysis show an inverse relationship between ATI and albedo, with a decrease in the gradient of the line on an increase in temperature contrast. Albedo values that are published in the literature range between 0.30 for green leaves (Song, 1998) to 0.16 for wheat (Barrett & Curtis, 1982) and vary between these values for different types of vegetation. From the above graph, such uncertainty in albedo value results in a relatively low uncertainty in ATI value with a decrease in uncertainty on increasing temperature contrast. Since the temperature contrast for a pixel is constant, a variation in the albedo value inserted into the Cracknell & Xue (1996) model (Equation 6.4) will result in a series of output images of identical visual appearance irrespective of the value of albedo. This is due to the image processing software scaling the output image values to fit the full radiometric resolution of the display. Although the albedo of the surface is therefore unknown for the study sites, a mid albedo value of 0.23 can be assumed where vegetation dominates the surface of the study sites.

The ATI model is applied to the diurnal thermal images to assess whether ATI modelling reveals any detail that is additional to that revealed on colour composite visualisation or on visualisation of the individual day and night thermal images. The ATI model is applied to the diurnal thermal images from only the Bosworth site since this is the only dataset that is calibrated to surface temperature due to the lack of ground temperature measurements during both Baildon Moor and Weardale image acquisition.

ATI is calculated for the diurnal thermal image pairs from June and August 1998 and March 2002 at the Bosworth site using the temperature-calibrated images the individual fields consisting of relatively homogeneous vegetation cover (Figure 6.7). Ambion field is covered with an agricultural crop of barley in 1998 and oil seed rape in 2002. Arena, Helipad, Picnic and South fields are all covered by fallow grass that vary height with the Arena field grass grown mainly for silage, the South field used for livestock grazing, the Picnic field used for public car parking with the Helipad field kept reasonably short at all times for a mixture of uses.

Figure 6.7: Field nomenclature for Bosworth site

ATI is calculated for only June and August data for Ambion field due to the very small temperature contrast occurring between the March images.

Results from the diurnal pairs of Ambion field (Figure 6.8) show that the linear old field boundaries and the ridge and furrow marks are greatly enhanced on ATI generation of both the June and August data. The June data shows a greater thermal contrast in the NW corner of the field that is not evident on either the day or night thermal images. The wind shear effect that dominates the August day thermal image appears to be present on the August ATI image, which suggests that the ATI shows mainly a surface temperature effect.

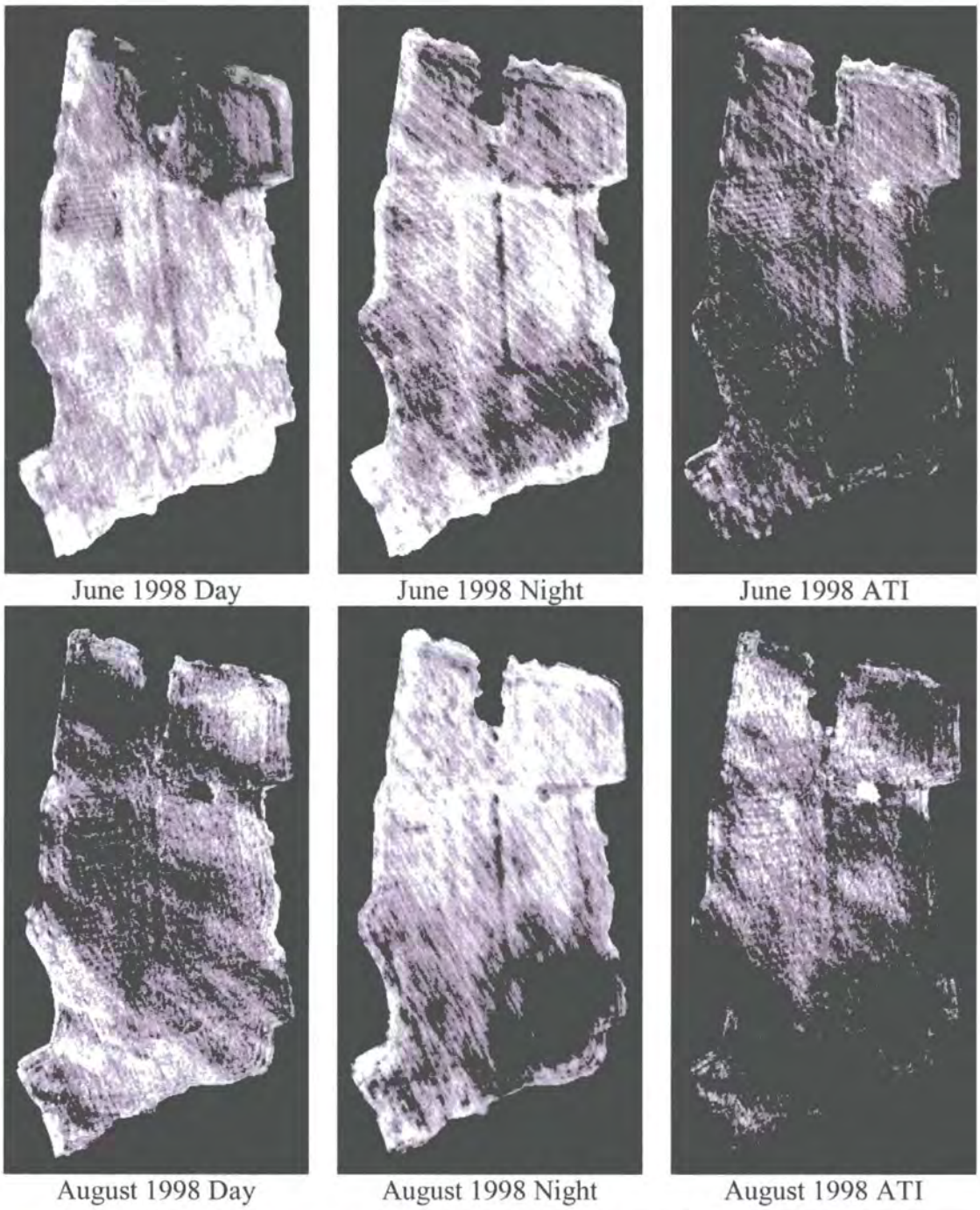

Figure 6.8: Cracknell & Xue (1996) ATI images for Ambion field at Bosworth

When the results from the Cracknell & Xue (1996) model are compared with the results of the simple image subtraction (Figure 6.9) there is a greater distinction in the main linear features on both June and August than is visible on the simple subtraction images. However, the images generated from the ATI model are similar to the images generated from the reciprocal of the simple image subtraction technique.

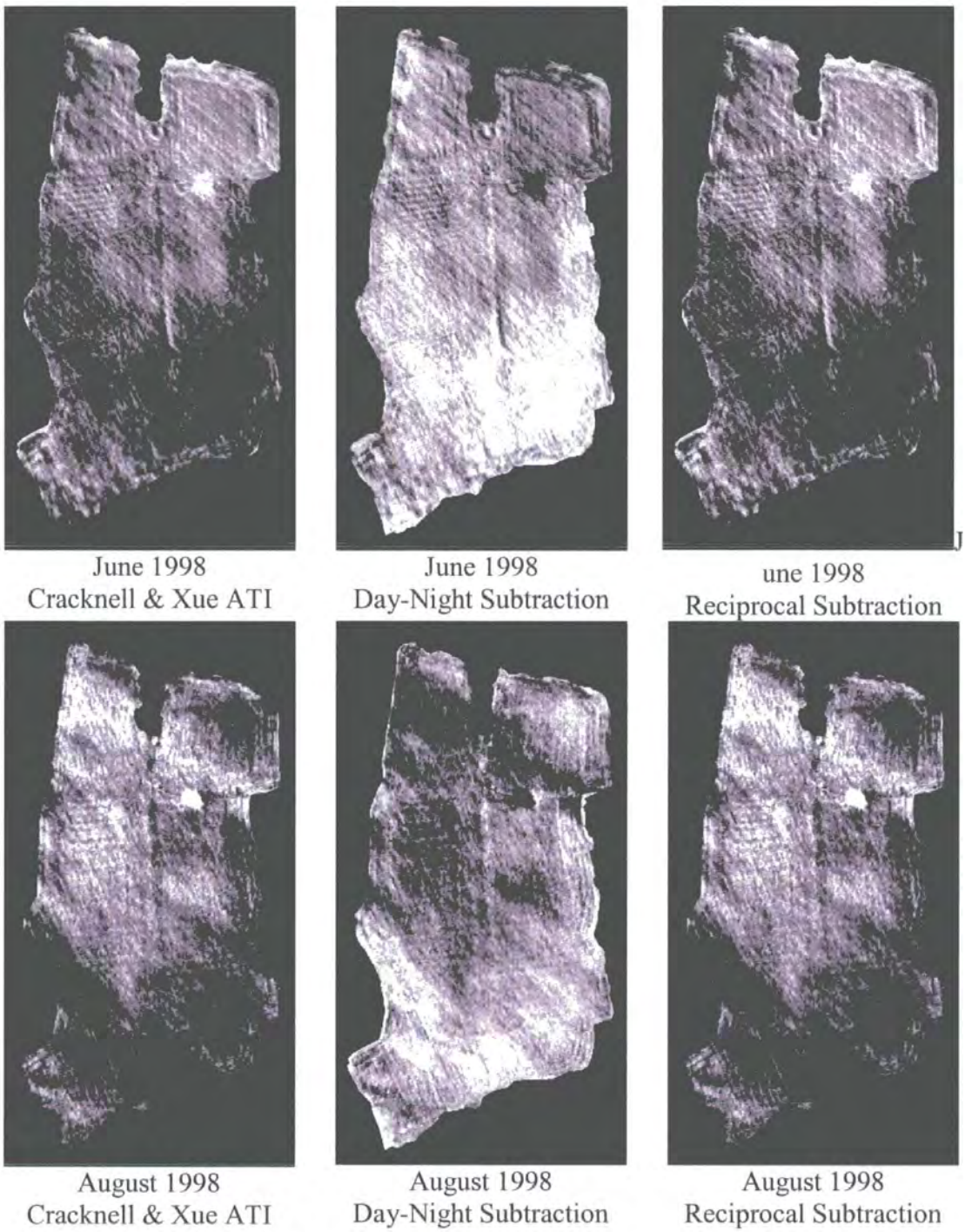

Figure 6.9: Comparison of results generated for Bosworth Ambion field from Cracknell & Xue (1996) ATI model and simple image subtraction

The results from the assessment of Ambion field suggest that there is little benefit for feature enhancement on application of the Cracknell & Xue (1996) model compared with taking a simple reciprocal of the image subtraction technique. This is mainly due to the inability to generate albedo values that accurately represent variations in individual pixel compositions of the barley field, and as a result of assuming a constant albedo value for every pixel, the numerator of the ATI model has a constant value and the ATI model takes the same form as the reciprocal image subtraction. The other fields in Bosworth have a much more homogeneous composition therefore the use of a single albedo value may be more appropriate.

Results from Arena field (Figure 6.10) show that in June when the grass is long ATI does not enhance feature detection. However, in August the grass has been shortened and there are a few linear features revealed in the south and east of the field on the day thermal image that are greatly enhanced by the ATI generation. Results from the Helipad field (Figure 6.11) show a linear feature on the June day thermal image when the grass is short, with a similar feature on the August day thermal image when the grass is longer. The Picnic field (Figure 6.12) has similar grass length in June and August, however, the June day thermal image reveals a linear feature that is enhanced on the ATI image that is not evident at any other time. The South field (Figure 6.13) has a more variable composition than the other fields with a couple of trees and patches of nettles and thistles that dominate the west section of the field. These are evident on all thermal images but are less evident in June when they have a similar height and similar day and night temperatures to the surrounding grass.

The results of the Cracknell & Xue (1996) ATI modelling of the grass fields show identical results to those produced by the simple reciprocal image subtraction technique. This is due to the use of a single albedo value for the entire image that generates a constant numerator of the algorithm, giving the ATI model the same form as the simple reciprocal subtraction technique.

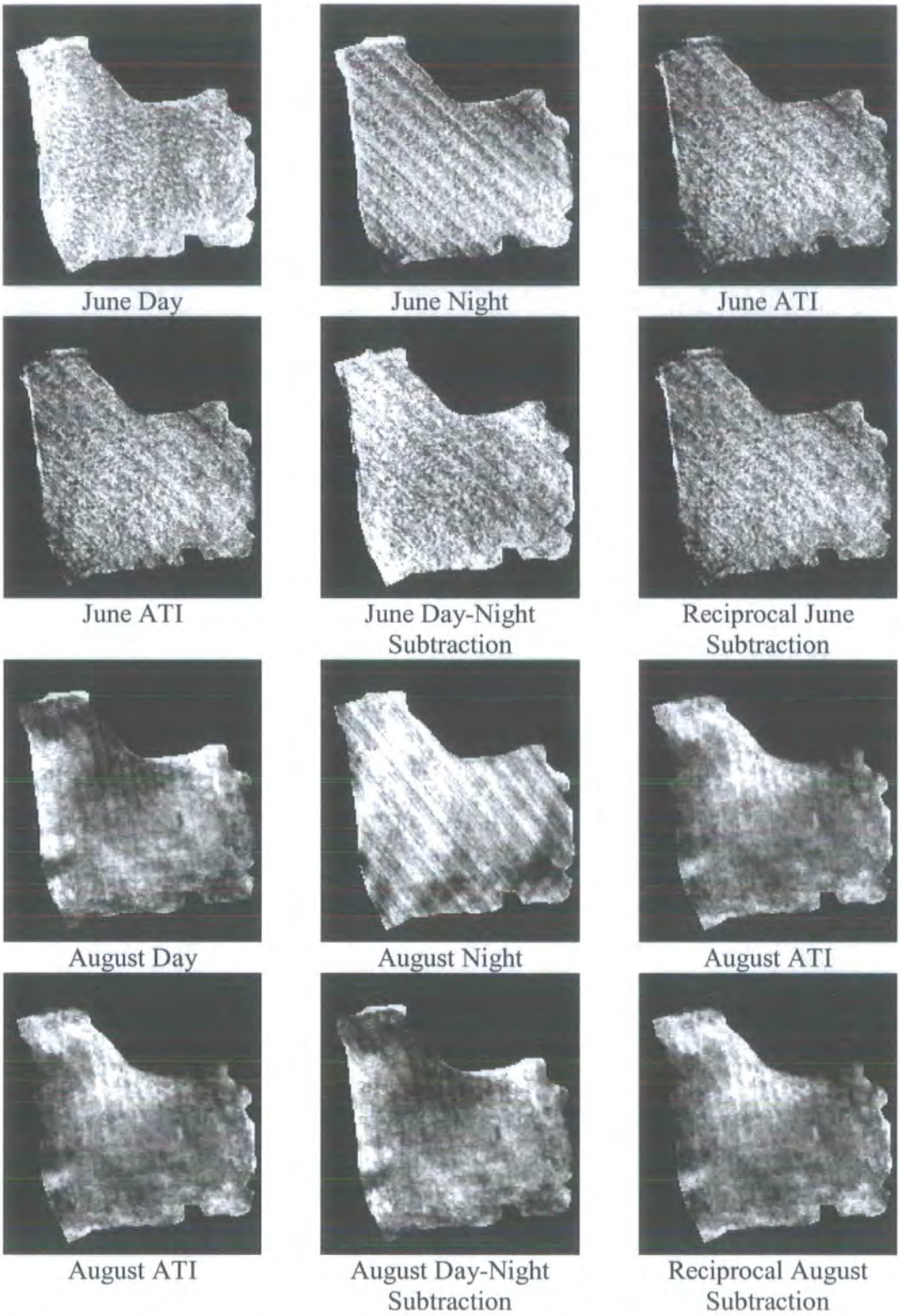

Figure 6.10: Comparison of results generated for Bosworth Arena field from Cracknell & Xue (1996) ATI model and simple image subtraction

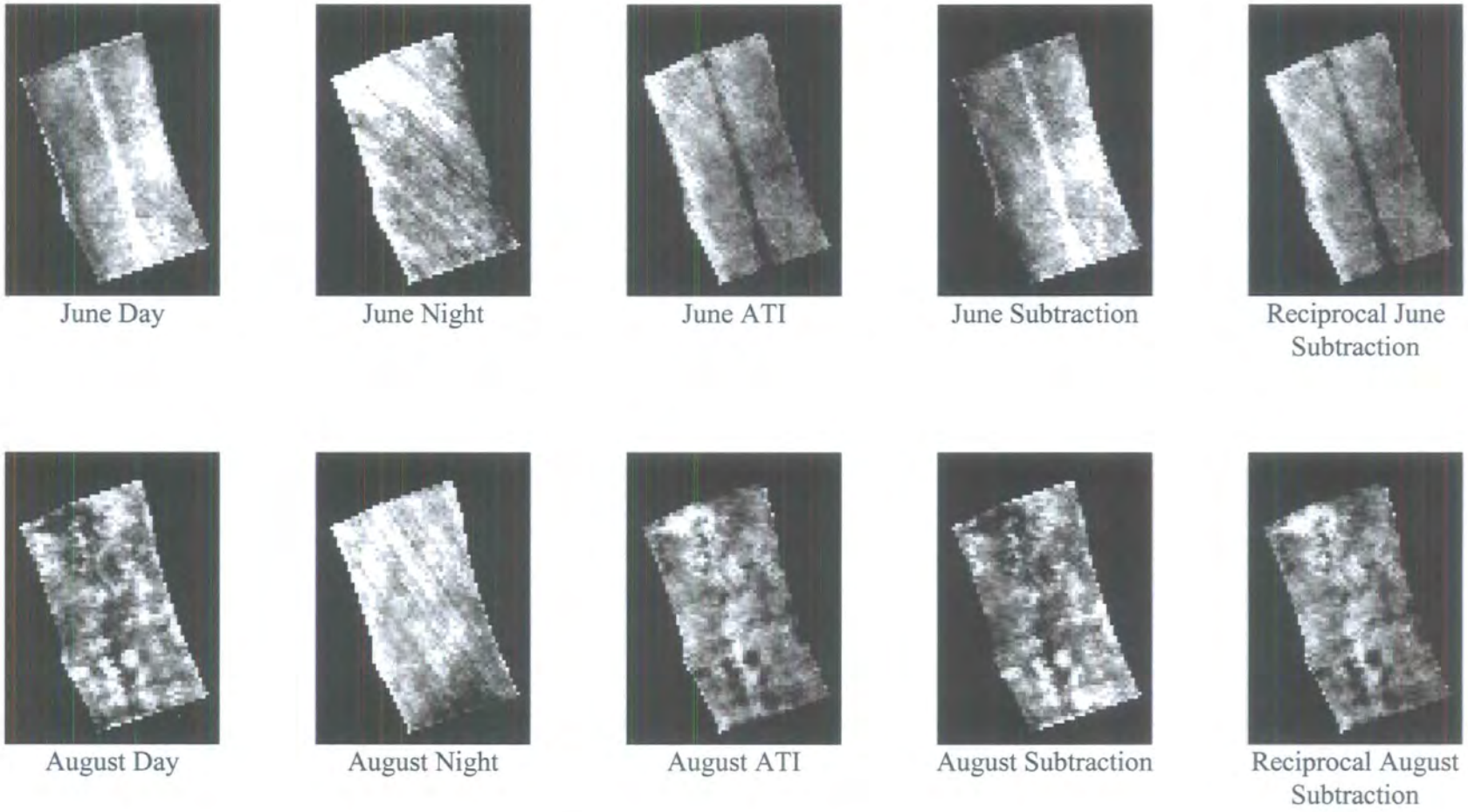

Figure 6.11: Comparison of results generated for Bosworth Helipad field from Cracknell & Xue (1996) ATI model and simple image subtraction

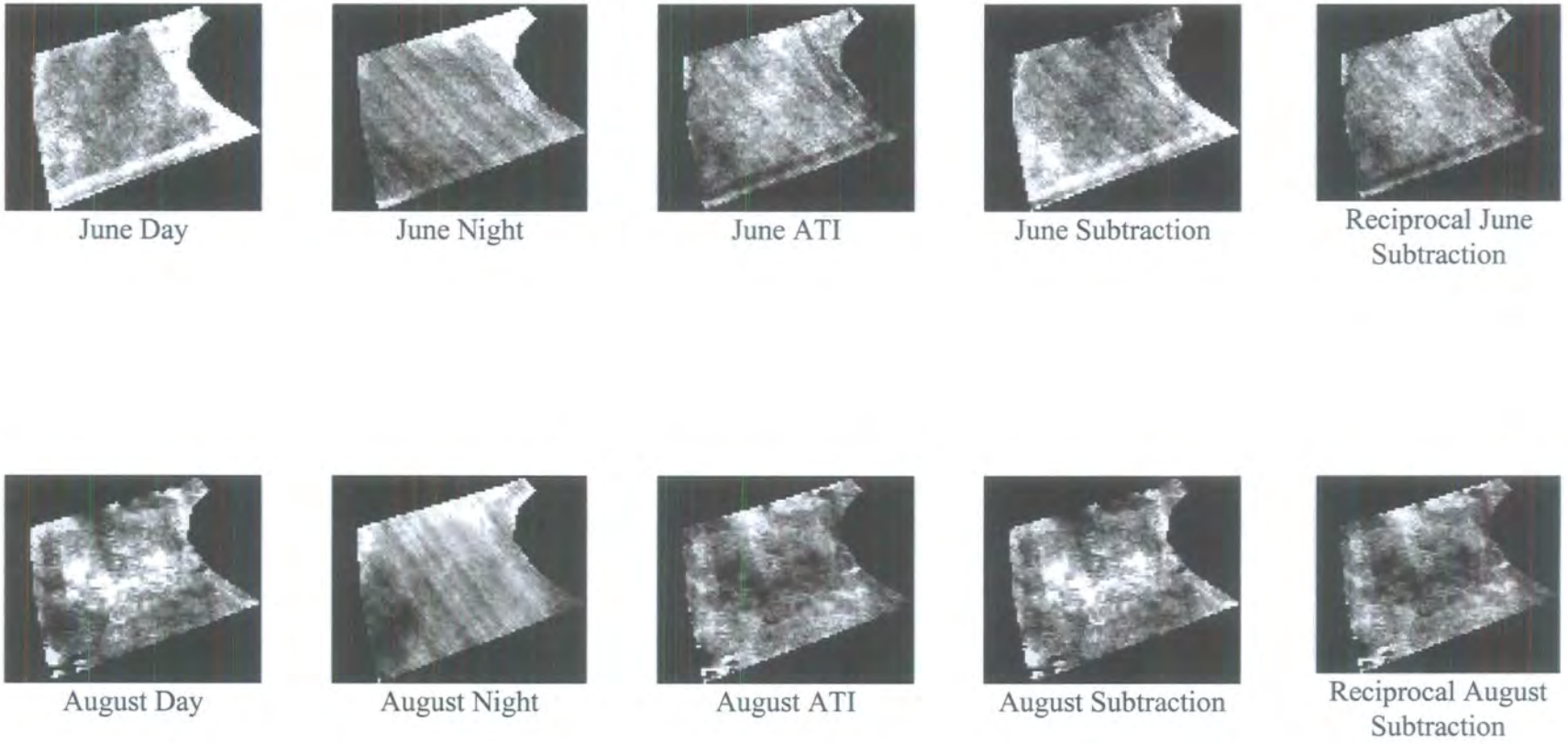

Figure 6.12: Comparison of results generated for Bosworth Picnic field from Cracknell & Xue (1996) ATI model and simple image subtraction

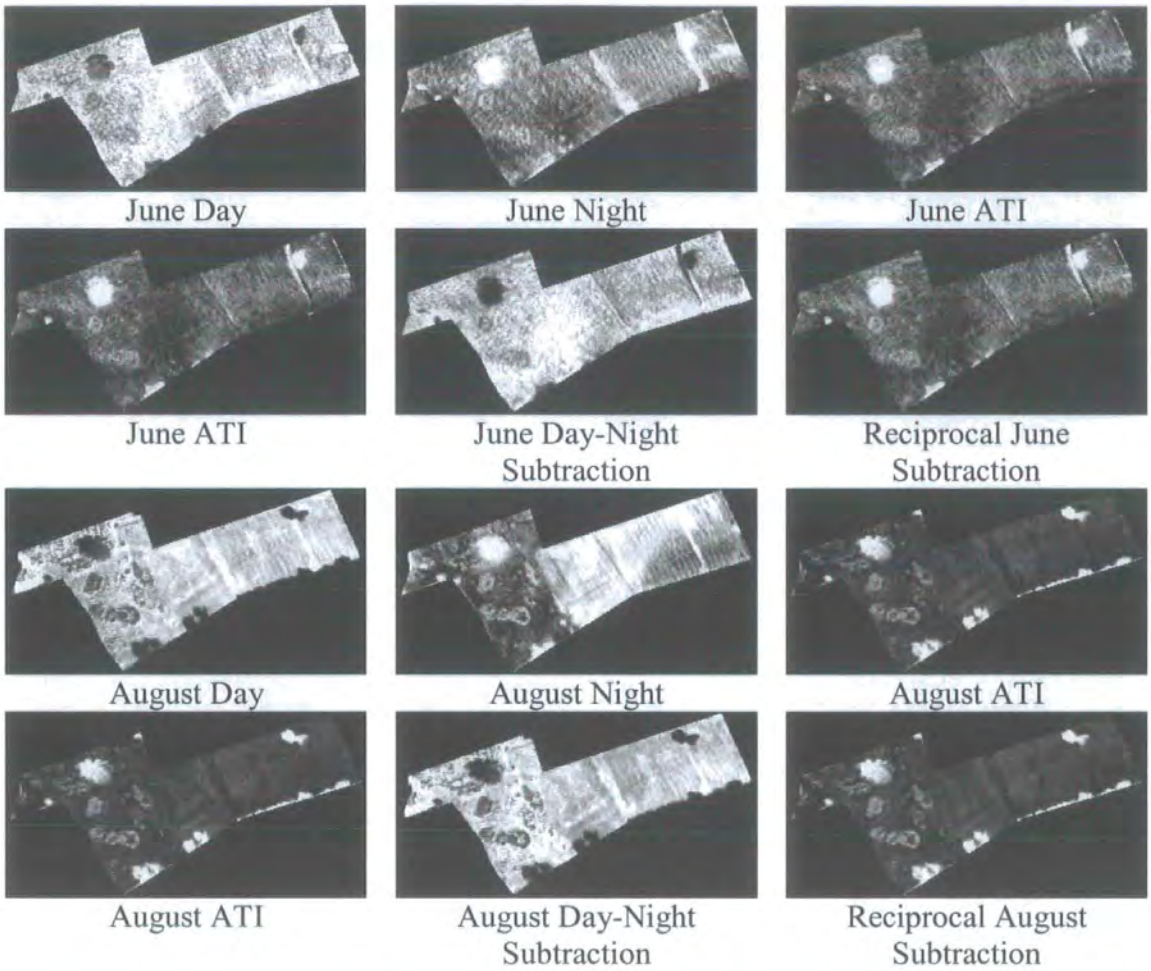

Figure 6.13: Comparison of results generated for Bosworth South field from Cracknell & Xue (1996) ATI model and simple image subtraction

The results from the individual fields of Bosworth, separated for homogeneous land cover, suggest that although the Cracknell & Xue (1996) model enhances feature detection within each field, the detail is identical to generation of a reciprocal of the day-night subtraction image due to the use of a constant albedo value on the numerator of the algorithm. This characteristic occurs at any stage in vegetation growth suggesting that the single albedo value that is assumed for the surface composition of all the fields may not represent fully any subtle variations in albedo occurring within the field due to slight variations in vegetation composition or structure. As a result this technique does not provide enough of an enhancement of the data for feature detection compared with the simple image subtraction technique.

There are a number of alterative models detailed in the literature that enable the calculation of ATI from the diurnal temperature. The Cracknell & Xue (1996) model forms the basis of most of the alternative ATI models, where variations arise in

the inclusion of different auxiliary parameters based on meteorological, topographic or surface parameters.

The model presented by Price (1977) gives a more complex formulation for ATI calculation by incorporating parameters on the solar constant (S), atmospheric transmittance (V), angular speed of rotation of the Earth (ω) and the ratio of the heat flux transferred between the atmosphere and the ground (α), as well as knowledge of the temperature difference and surface albedo (Equation 6.5).

Equation 6.5

$$ATI = \frac{2SV}{\sqrt{\omega}\sqrt{\left[1+\alpha+\sqrt{2\alpha}\right]}} \bullet \frac{1-A}{\Delta T}$$

The model presented by Kahle & Alley (1985) made slight modification to the Price (1977) model by including a parameter that takes into account additional detail on the latitude (λ) and solar declination (δ) associated with the timing and position of observation (Equation 6.6). The solar declination can be calculated using a pre-defined sun angle program from http://www.susdesign.com/sunangle (Appendix E) where detail is required on the geographical position and the precise date and time of observation.

Equation 6.6

$$ATI = \frac{2SVC}{\sqrt{\omega}\sqrt{\left[1+\alpha+\sqrt{2\alpha}\right]}} \bullet \frac{1-A}{\Delta T}$$

$$C = \frac{1}{\pi}\left[\sin\delta\sin\lambda\arccos(-\tan\delta\tan\lambda)+\cos\delta\cos\lambda\sqrt{(1-\tan^2\delta\tan^2\lambda)}\right]$$

Although the Price (1977) and Kahle & Alley (1985) models give greater characterisation of the ground surface during observation, it is quite common in many remote sensing studies that only partial detail may be available on meteorological and surface parameters and as a result the heat flux ratio remains undetermined in the model. Although this parameter is unknown, the model is applied to the temperature-calibrated diurnal images from the study sites by modifying the initial ATI C++ program to incorporate the C parameter derived from the detail provided in the ATM header files, and the known values of the solar constant, atmospheric transmittance

and the angular rotation of the Earth (Appendix F7). The results from the Kahle & Alley (1985) model are then compared with the results from the Cracknell & Xue (1996) and the standard image subtraction models to establish whether there are any visible variations in the thermal anomalies.

The results from the Kahle & Alley (1985) model appear to produce results that are identical to the Cracknell & Xue (1996) and reciprocal subtraction, suggesting that their model does not significantly enhance features detection under vegetation compared to the more simple techniques (Figure 6.14).

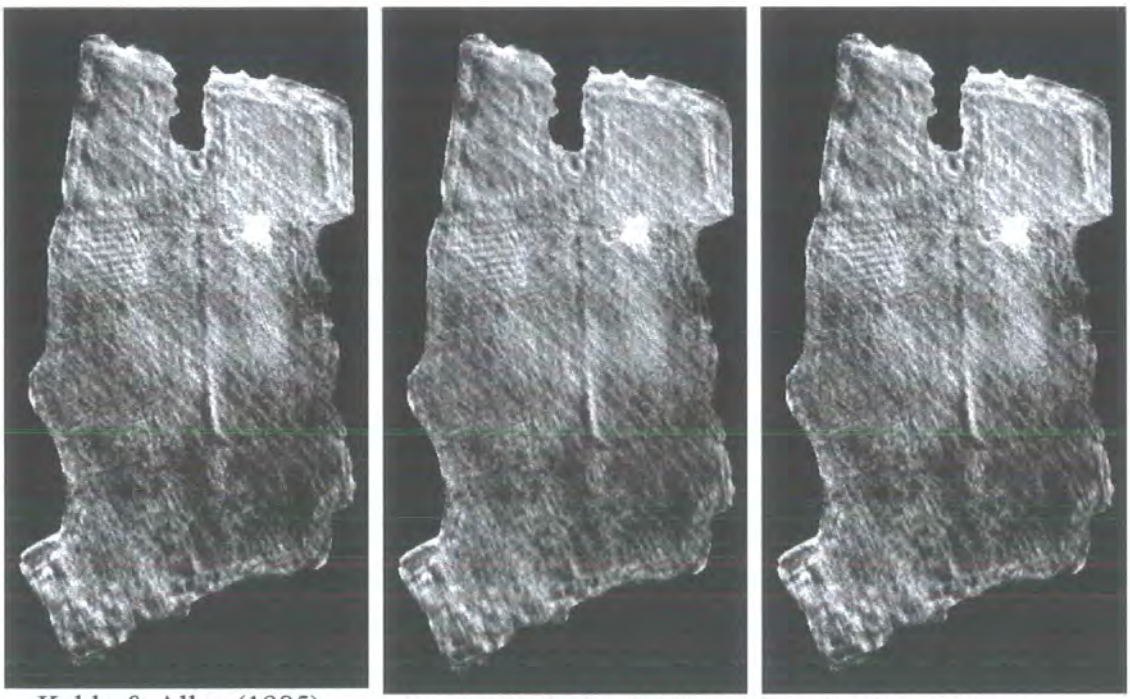

Kahle & Alley (1985) | Cracknell & Xue (1996) | Reciprocal Image Subtraction

Figure 6.14: Comparison of June 1998 results from Kahle & Alley (1985), Cracknell & Xue (1996) ATI models and the image subtraction technique for Bosworth Ambion field

Since detail is not available for calculation of the heat flux ratio between the atmosphere and the ground that is required for the Kahle & Alley (1985) model, alternative ATI models are investigated for their suitability in feature detection on the temperature-calibrated images of the study sites.

The model presented by Price (1985) simplifies the Price (1977) and Kahle & Alley (1985) models and requires additional detail on only the latitude (λ) and solar declination (δ) associated with the timing and position of observation, with application of a scaling factor to bring the values into the full radiometric resolution of the VDU image display (Equation 6.7). In this model the C parameter has a slight variation to that stated in the Kahle & Alley (1985) model, however, the values derived for a specific latitude and declination are identical.

Equation 6.7

$$ATI = 1000\pi \frac{(1-A)C_1}{T_{max} - T_{min}}$$

$$C_1 = \frac{1}{\pi}\left[\sin\delta \sin\lambda \sqrt{\left(1 - \tan^2\delta \tan^2\lambda\right)} + \cos\delta \cos\lambda \cos^{-1}\left(-\tan\delta \tan\lambda\right)\right]$$

The model is applied to the image data by modifying the initial ATI C++ program to incorporate the C parameter, which is derived using the detail provided in the ATM header files (Appendix F8). The results from the Price (1985) model are then compared with the results from the Kahle & Alley (1985), Cracknell & Xue (1996) and the standard image subtraction models to establish whether there are any visible variations in the revealed thermal anomalies.

The results from the Price (1985) model appear to produce results that are identical to the Kahle & Alley (1985), Cracknell & Xue (1996) and the reciprocal subtraction images, suggesting that the model does not significantly enhance feature detection under the vegetation compared to the more simple techniques (Figure 6.15). This similarity may relate to the image processing software stretching the output ATI values to fit the full radiometric resolution of the VDU display. However, the histograms also show a similarity in shape associated with each model output (Figure 6.16), suggesting that any of the models would provide adequate separation of thermal features within the vegetation surface.

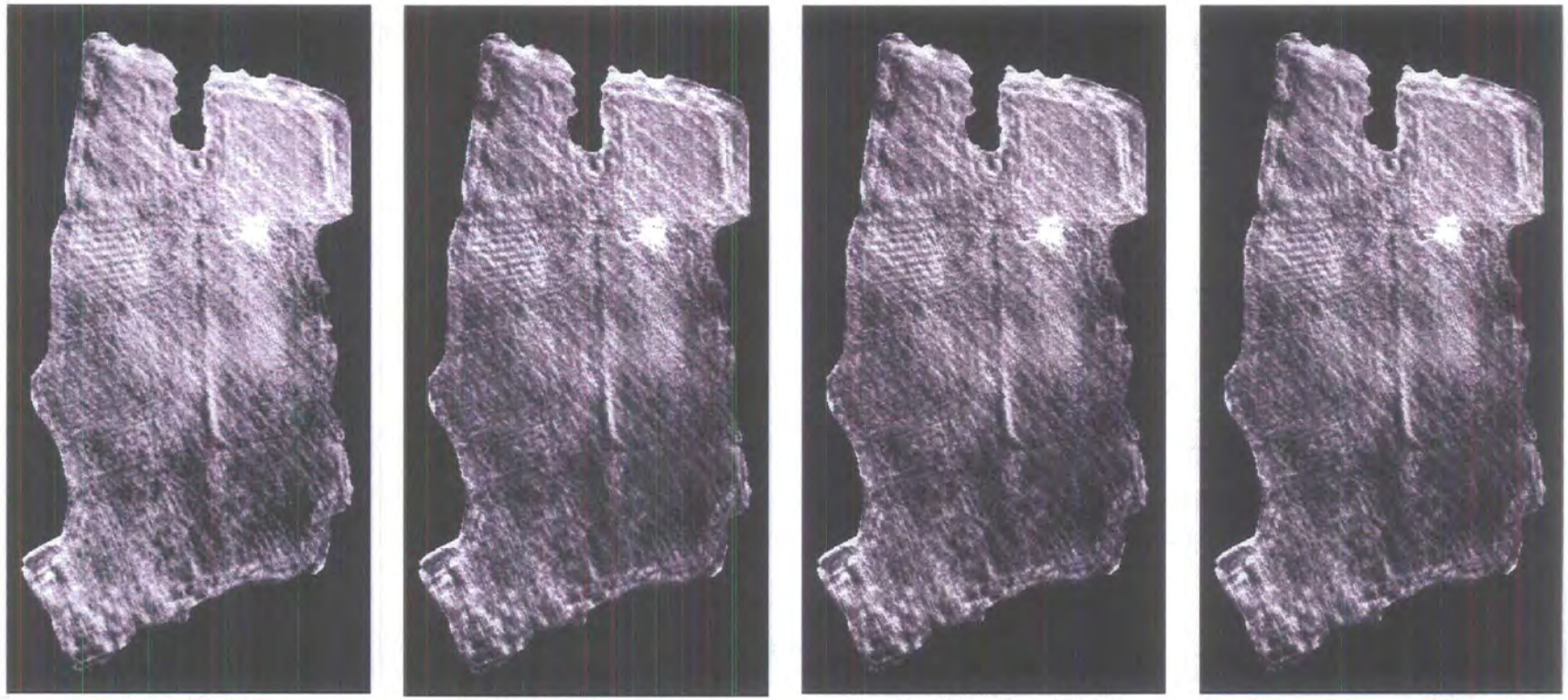

Price (1985) Kahle & Alley (1985) Cracknell & Xue (1996) Reciprocal Image Subtraction

Figure 6.15: Comparison of June 1998 results from Price (1985), Kahle & Alley (1985), Cracknell & Xue (1996) ATI models and the image subtraction technique on Bosworth Ambion field

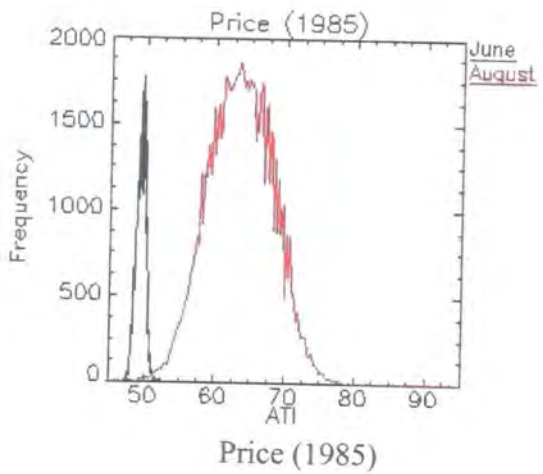

Price (1985)

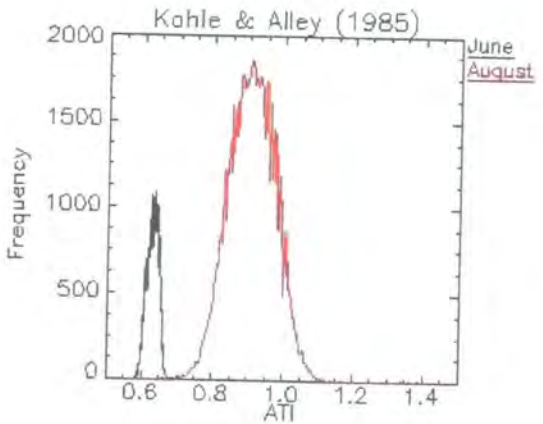

Kahle & Alley (1985)

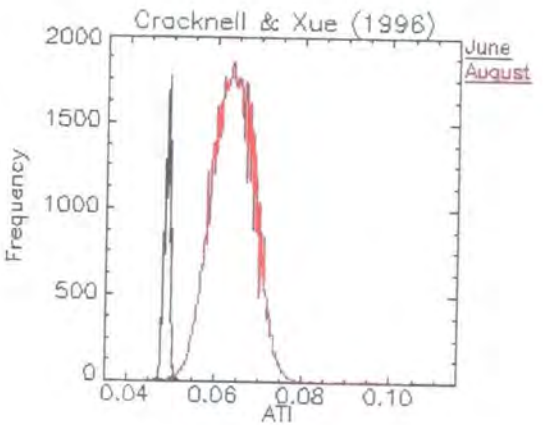

Cracknell & Xue (1996)

Figure 6.16: Comparison of histograms of model outputs for Bosworth Ambion field

The histograms in Figure 6.16 show that although there is a similarity in the shape of the model histograms, the absolute values of the calculated ATI values varies between the models (Table 6.2). Since the absolute temperature difference of each pixel is constant between the individual models, the variation must relate to the scaling factors associated with each model, which consist of numerous parameters that are assumed to be spatially invariant, although this may be an inappropriate assumption for characterisation of the natural vegetation surface. The Reciprocal Image Subtraction has no scaling factor applied to the data with values representing the reciprocal of the absolute temperature difference between the day and night images. The Cracknell & Xue (1996) model includes the estimated surface albedo value, which is constant across the whole image, with no additional scaling factors applied to the data. The Price (1985) model alters the scaling factor to incorporate the solar declination and latitude, with the Kahle & Alley (1985) model also including the solar constant, atmospheric transmittance and angular rotation of the Earth. The ATI values generated through the individual models are compared with ATI values presented in the literature. Unfortunately, Xue & Cracknell (1995) is the only paper where ATI values are actually published and although they use a much more complex ATI formulation, the range of values associated with the more complex model are similar to the range of values generated by the Cracknell & Xue (1996) model.

	June	August
Cracknell & Xue	0.060 – 0.065	0.065 – 0.095
Price	60 – 65	65 – 95
Kahle & Alley	0.85 – 0.925	0.9 – 1.4

Table 6.2: Comparison of absolute values from the ATI models on Bosworth Ambion field

The histograms generated for each model show a narrow range of values for the June data with a much wider Gaussian distribution occurring for the August data from Ambion field (Figure 6.16). This suggests that the ATI modelling technique shows seasonality in thermal response with the differences in value potentially relating to a variation in the condition of the vegetation between the observation dates. In order to test this hypothesis, ATI values are extracted from manmade objects that should not show seasonality in response due to consistent composition and condition between observation dates. The ATI images generated for the whole image area are

linked through their coordinates and coordinate systems. Regions of interest are then drawn around different manmade materials that should have consistent ATI values between observation dates (Figure 6.17).

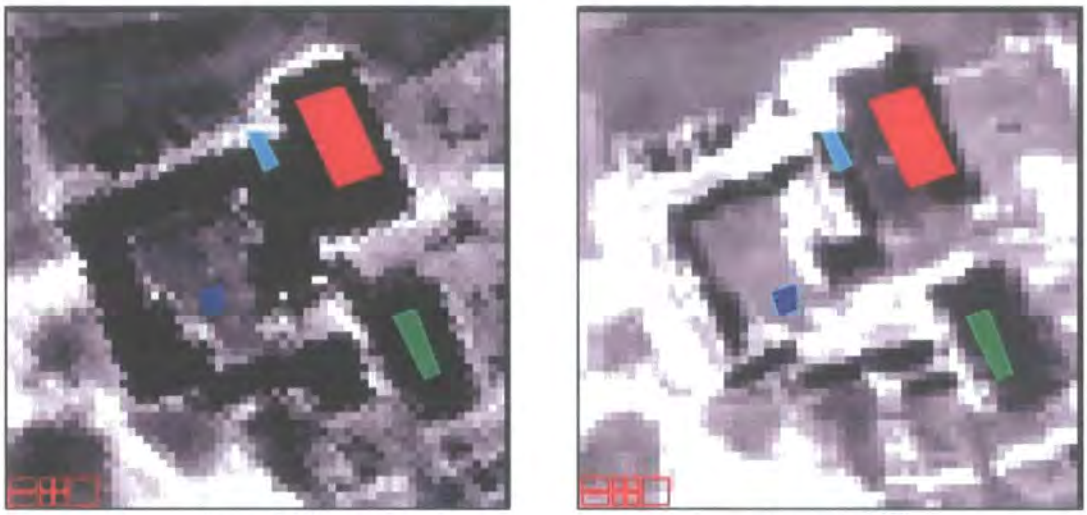

June ATI August ATI

Figure 6.17: Location of regions of interest for manmade objects at Bosworth

The defined regions enclose a tiled roof area of the main building (cyan), a tiled roof area of the garage (red), an area of flat thin roof of the café (green) and an area covered by flat paving slabs in the courtyard of visitor centre (blue). When the regions are displayed on both the June and August 1998 ATI images, it becomes apparent that there is a misalignment in the position of the edges of the buildings between the dates. This is mainly due to the ground resolution of the imagery (1m x 1m) and the variation in building shadow present during the daytime observation and the angle of observation of the ground surface, which hinder the selection of ground control points when the images were originally geocorrected (Chapter 4.4).

Histograms are extracted from the June and August ATI images for each of the materials. Since the manmade materials are unlikely to change in their composition or condition throughout time, it is expected that there would not be a variation in the range of ATI values observed between the dates, although the actual ATI values may vary between the observation dates due to variations in diurnal temperatures. When the June and August histograms are compared for each region, the August imagery consistently shows a wider range of values than is observed for June (Figure 6.18).

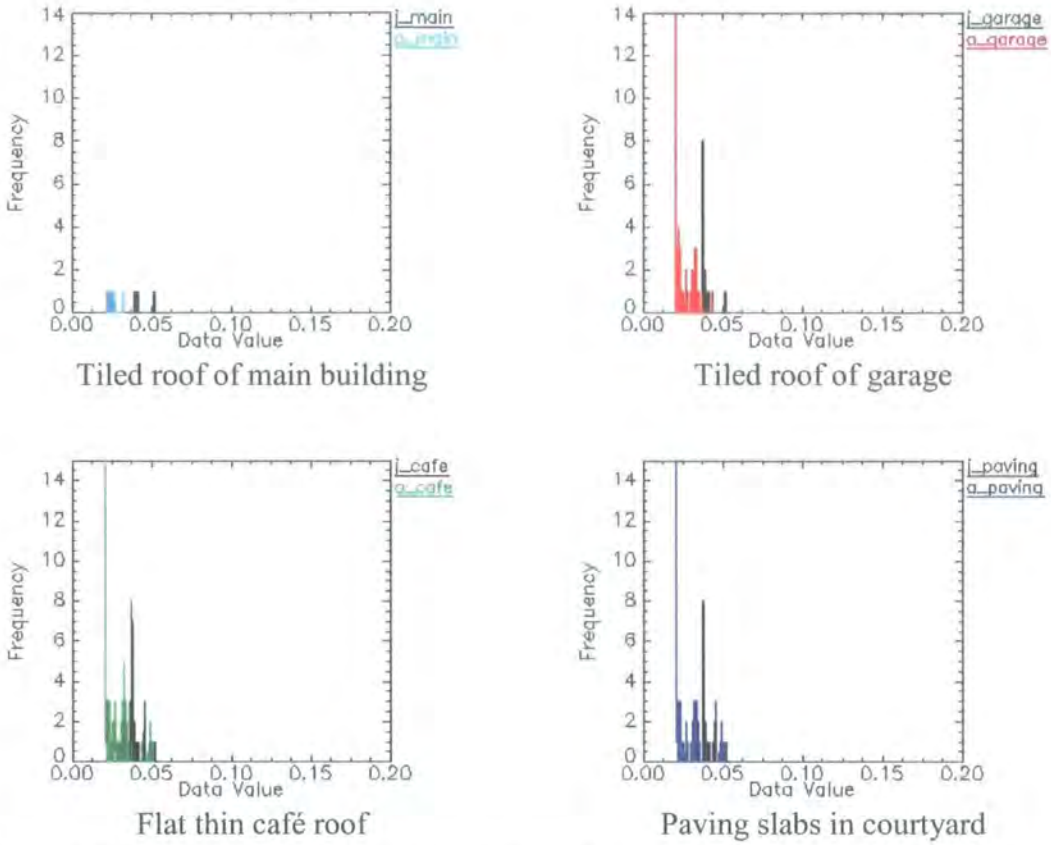

Figure 6.18: ATI histograms extracted from manmade objects at Bosworth

As a result of variation in the values associated with the manmade objects, the seasonality in the ATI values associated with the vegetated areas does not necessarily represent a change in the condition of the vegetation between the observation dates.

In June, the agricultural crop that dominates Ambion field has a fairly uniform structure and condition and as such, there is a fairly uniform temperature response observed across the field at the early stage in crop growth, suggesting that the vegetation may be sufficiently characterised by a single albedo value. Although the same agricultural crop is present in August, the crop is at a much later stage in maturity, resulting in patches of crops that are at a different stage in growth or that suffer from water stress. As a result, the single albedo value that is assumed for the whole field may be inappropriate in such situations, although the model outputs still show sufficient visual separation of the thermal features.

The ATI models are also applied to the temperature-calibrated images of the Arena, Helipad, Picnic and South fields. The histograms generated for these fields

show a similar distribution pattern to those generated for Ambion field with a wider range of ATI values of higher mean occurring in August (Figure 6.19).

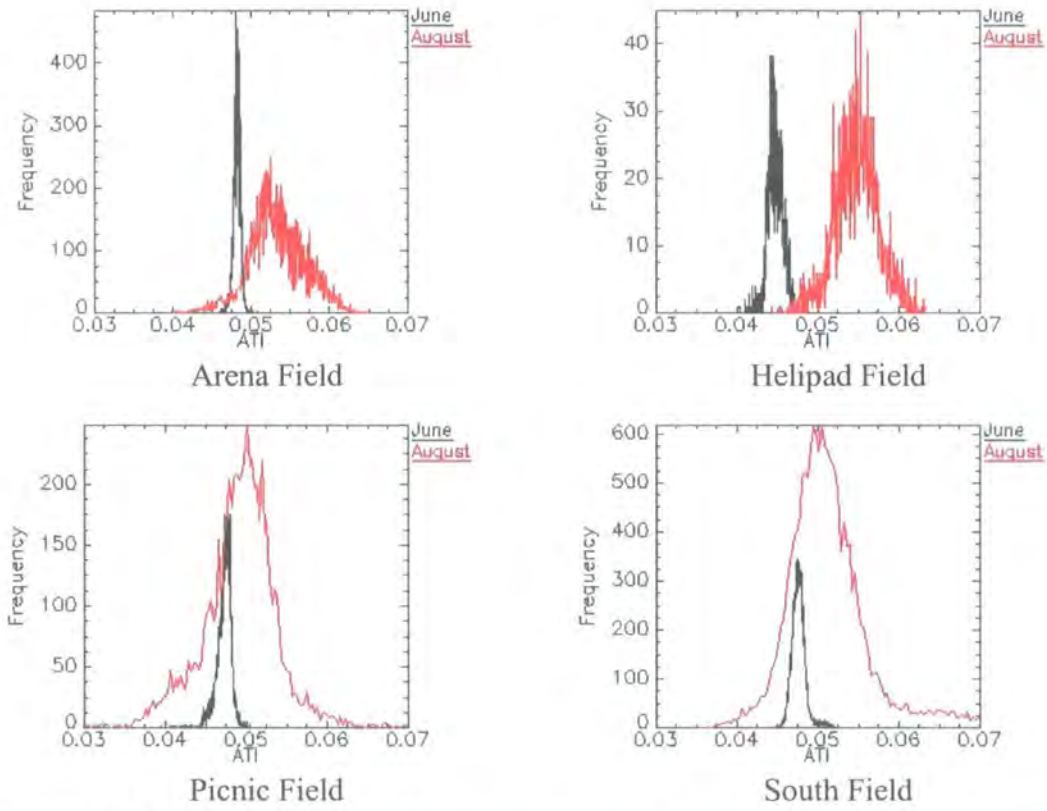

Figure 6.19: Bosworth field histograms generated from Cracknell & Xue (1996) ATI model

The results from the Arena field show a symmetrical distribution in June with a slight skew towards higher ATI values in August suggesting a higher resistance to temperature change possibly the result of a higher moisture content where the linear anomalies of low ATI values are evident (Figure 6.10). The results from the Helipad field show a slight bimodal distribution of the June data with a slight peak corresponding to the strong linear anomaly of low ATI values, with a more symmetrical appearance of the August data where few ATI anomalies are evident (Figure 6.11). The results from the Picnic field show a symmetrical distribution on the June data with a slight skew towards lower ATI values corresponding to a linear anomaly of low ATI value along the southern field boundary. The August data shows a more prominent skew towards lower ATI values that correspond with the anomalous patch of low ATI values on the topographic slope (Figure 6.12). The results from the South field show a much more prominent bimodal distribution pattern with a

secondary peak at higher ATI values corresponding to the trees, nettle and thistle patches occurring in the field. The peak is more pronounced in August when the nettle and thistle patches have grown to considerable height and have a much more anomalous ATI value compared with the surrounding grasses (Figure 6.13). Although the results from the histogram generation suggest that the ATI modelling may help differentiate features at later stage in grass growth where there is a tendency for a wider range of ATI values when the grass is longer, when the June ATI values are stretched to fit the full radiometric resolution of the VDU display, the shape of the resulting histogram is identical to that generated from August.

Although the ATI models show suitable visual enhancement of the features evident in the temperature-calibrated images from Bosworth, these techniques can only be performed on diurnal images where the day and night radiance values lie on the same scale, i.e. where a certain temperature has the same radiance value on the day and night images. As a result, the ATI modelling technique is only suitable for the diurnal image pairs from Bosworth where radiance is calibrated to ground temperatures.

When the results of the ATI modelling are compared with the results from the geophysical surveying, it is clear that the majority of features revealed by the ATI modelling do not coincide with features located on the magnetometry (Figure 6.20 and Figure 6.21) and resistivity (Figure 6.22 and Figure 6.23) with the only feature that does correspond to a geophysical anomaly being the ridge and furrow marks on the western section of Ambion field. Since the June 1998 or August 1998 ATI images show a poor correlation with the results of the geophysical survey in the fields covered with a late stage barley crop or tall grasses. This suggests that the ATI technique is sensitive to different properties than the geophysical techniques and that the ATI technique may represent a pure surface temperature effect rather than depth properties as a result of the vegetation cover. The ATI technique may therefore be unsuitable for detecting physical soil properties where the surface is covered with tall grasses or agricultural crop.

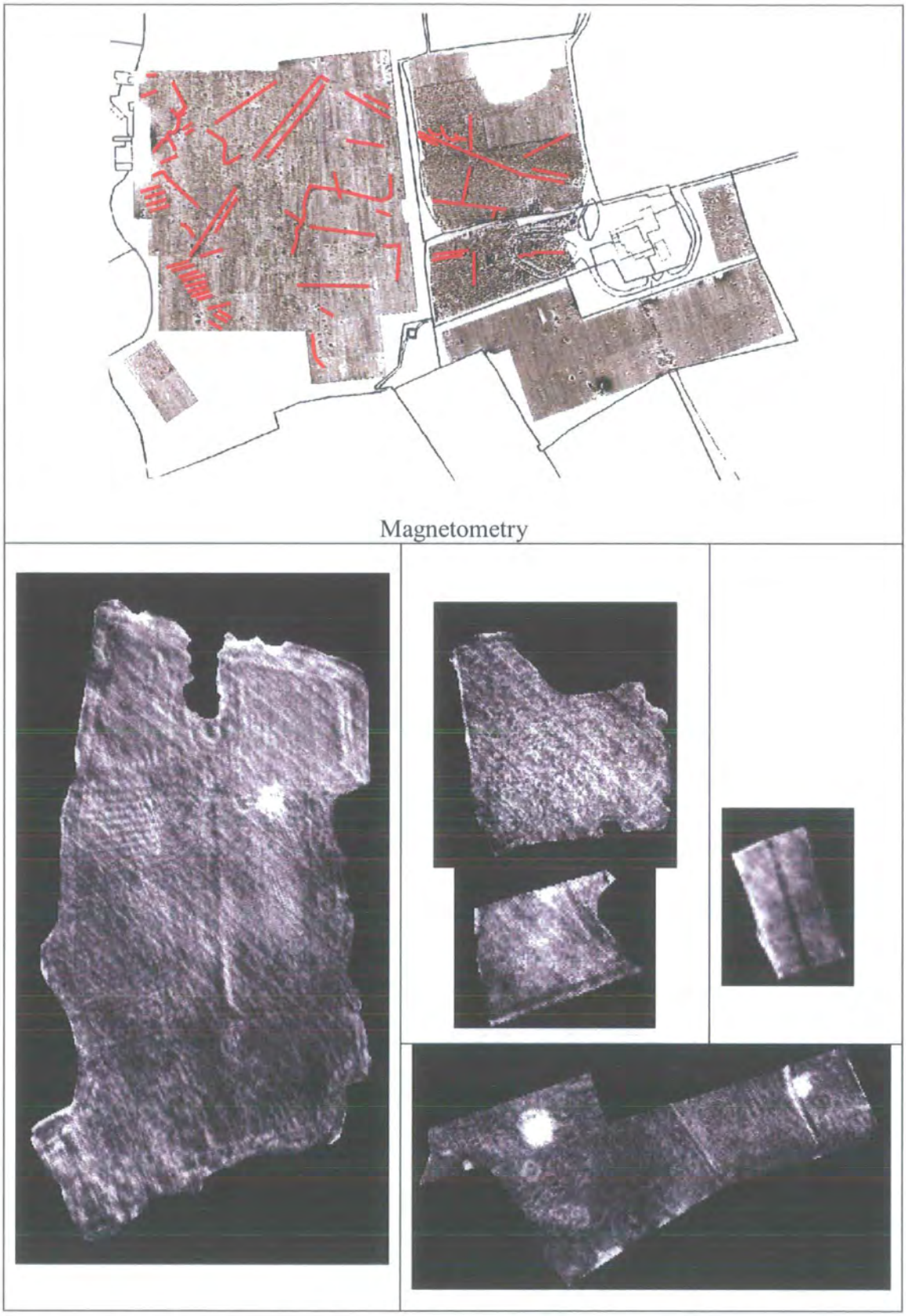

Figure 6.20: Comparison of Bosworth June 1998 Cracknell & Xue ATI with magnetometry

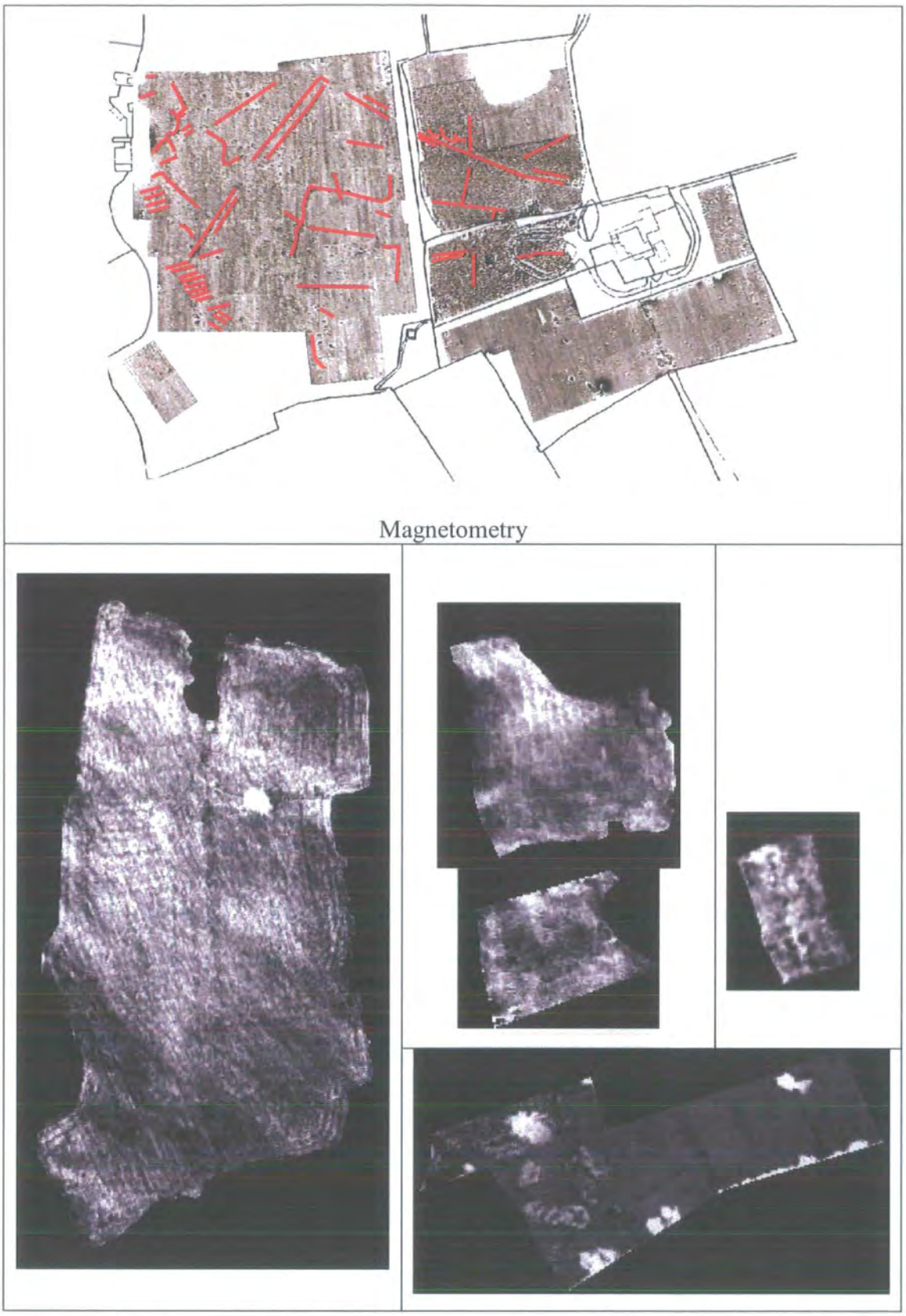

Figure 6.21: Comparison of Bosworth August 1998 Cracknell & Xue ATI with magnetometry

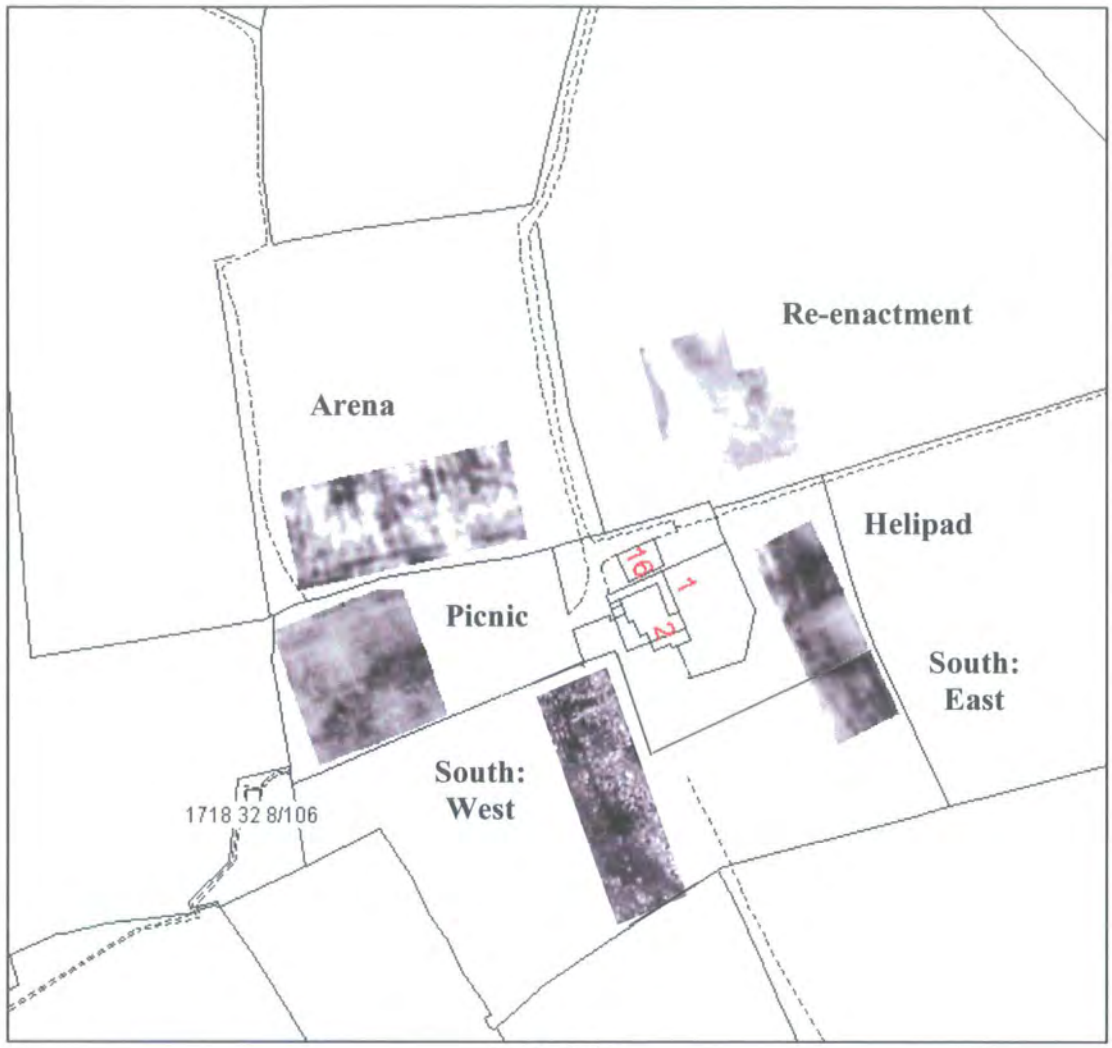

Resistivity

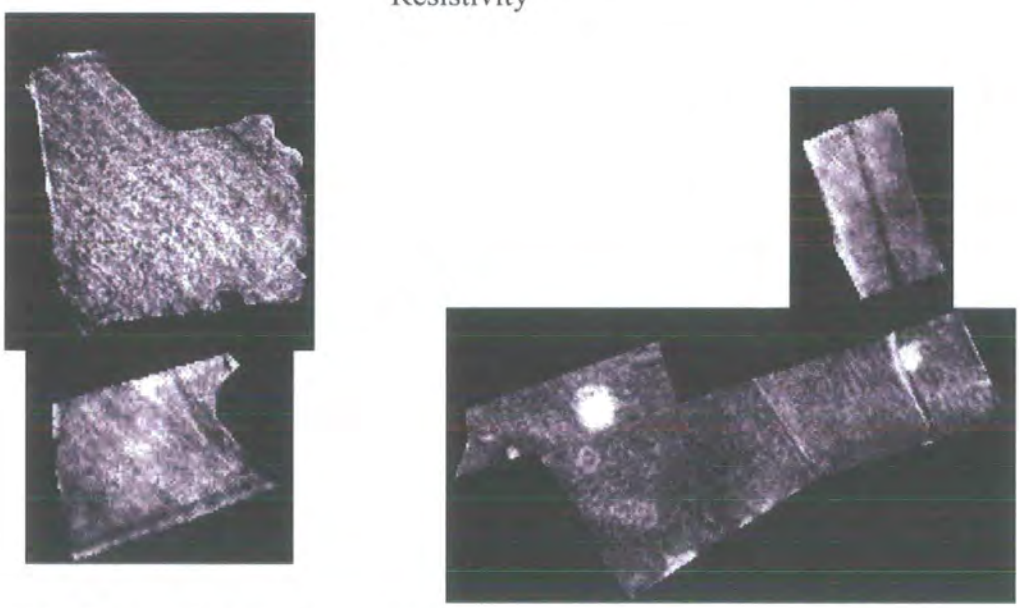

Figure 6.22: Comparison of Bosworth June 1998 Cracknell & Xue ATI with resistivity

Resistivity

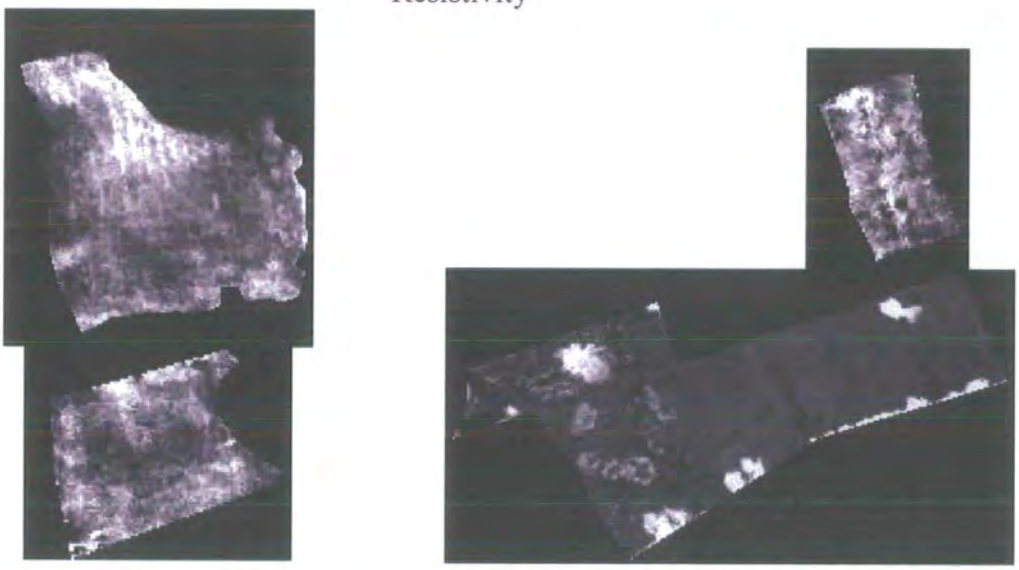

Figure 6.23: Comparison of Bosworth August 1998 Cracknell & Xue ATI with resistivity

6.5 SUMMARY of NUMERICAL MODELLING

It has been shown in the previous chapter that data acquired at thermal infrared wavelengths during the day adds considerable detail for characterising the surface when compared to the detail concurrently observed at visible, near-infrared and shortwave-infrared wavelengths. Similarly, thermal infrared data observed at night within the same 12-hour period adds additional detail to that observed during the day. However these characteristics are observed at single points within the diurnal cycle when materials with different compositions will often emit similar energies at thermal infrared wavelengths. As a result, single-point observations may conceal materials that have anomalous bulk compositions compared with the surrounding materials. Materials of different compositions will have different associated thermal properties and as a result will tend to display different heating and cooling patterns across the diurnal cycle in response to the solar input. A useful technique for enhancing material delineation is therefore to use the contrast in thermal response observed across the diurnal cycle, or the resistance to temperature change. This property is referred to as the thermal inertia of the material and physical thermal inertia values can give indications of bulk variations in material properties in response to material density changes. Although physical thermal inertia values cannot be measured directly from thermal observations, an Apparent Thermal Inertia (ATI) can be determined from the diurnal resistance of the surface to temperature changes, observed at times when the surface is at its maximum temperature during the day with a complementary thermal image acquired at night when the surface is at its minimum temperature. Since this technique requires the use of temperature images, the thermal infrared radiance response measured by the ATM must be calibrated to ground temperature values.

The Inverse Planck Radiation Law can be used to convert radiance to temperature with respect to the wavelength of observation, the surface emissivity and two physical constants. However, without accurate knowledge of surface emissivity, a sensitivity analysis was performed to assess the variation in calculated temperature values with variable emissivity. The results show similar temperature values when the emissivity values are varied between 0.90 and 1.00, which correspond to the range of values associated with the materials comprising the surface. The results are best summarised by a 2^{nd} order polynomial equation with an inverse relationship between temperature and emissivity for constant wavelength and radiance. Since there is little

variation in the output temperatures for this range of emissivity values, a single emissivity value of 0.97 is used in the Planck relationship to represent the mean value of the vegetation that covers the majority of the study sites. In addition to uncertainty in the precise value of emissivity associated with each individual pixel composition, the wavelength measured by the ATM has a range of values from 8.40μm to 11.50μm and so the sensitivity of Planck temperature is assessed with respect to a range of wavelengths. These results can also be summarised by a 2nd order polynomial equation but are more complex than for the emissivity analysis with the gradient of the relationship getting progressively shallower from 8.40μm to 10.00μm and then getting progressively steeper from 10.00μm to 11.50μm, but does not flatten out at 10.00μm, which is very close to the 9.95μm mid-channel wavelength of the ATM thermal channel.

The Inverse Planck Radiation Law is suitable for conversion of radiance to temperature only where specific units of radiance and wavelength are used in the calculation. The literature details a variety of unit combinations used in the Planck relationship with several authors omitting to state the specific units for each parameter. Although there are only three authors in the literature that state all parametric units, two of the authors state identical units for the temperature and wavelength and state identical values of the two physical constants, and yet state different parametric units for radiance. As a result, the definitions provided by the remaining author (Price, 1989) are deemed the most suitable for temperature calculation however the given units of radiance have a noticeable contrast to the units of radiance associated with the ATM data. The conversion between ATM radiance and Price radiance has proved to be more problematic that at first anticipated, even when taking into account the difference in magnitude of the radiance units, the scaling factor applied to the ATM radiance data to provide values in the 0-1 range and also the solid angle associated with measurement from the ATM sensor. As a result of the problems associated with the conversion between the ATM radiance and the Price radiance, the ATM radiance cannot be directly converted to ground temperature using the Price relationship.

Due to the uncertainty in the conversion between ATM radiance and ground temperature values further assessment of the thermal response of the study sites was

performed using the empirical line calibration images where ground temperature was determined through a linear regression between ground temperatures measured for specific features and the ATM radiance values extracted for the corresponding image pixels.

Quantitative Apparent Thermal Inertia (ATI) modelling can provide a useful technique for detecting features buried in the near-surface environment, where the buried features will have a volumetric variation in physical and thermal properties compared to their surrounding matrix that influences the ATI response of the ground. Since ATI modelling requires knowledge of the day and night temperature contrast observed for each pixel to reveal variations in bulk thermal characteristics, ATI modelling was applied to the empirical line calibrated images of the study sites, thus avoiding the uncertainty in the conversion between ATM radiance and Price radiance.

A variety of ATI models can be applied to the diurnal temperature images for assessment of thermal variations caused by potential features in the subsurface. These are essentially driven by the parametric relationship under investigation and the type of auxiliary meteorological, topographical or surface data available for incorporation in the model. The simplest formulation expressed in Cracknell & Xue (1996) uses the reciprocal of the temperature contrast and incorporates a measure of the surface albedo into the algorithm. Since no detail is known about the albedo values of the individual pixels within the image, a single albedo value is assumed for the whole area representing the mean albedo expected for vegetation, since all non-vegetated surfaces are omitted from analysis. The use of a single albedo value results in a constant numerator of the ATI model that is essentially identical to the reciprocal of a simple image subtraction. Although the values of the individual techniques are very different, the image processing software scales the values to fit the full radiometric resolution of the VDU display and as a result, the ATI image shows an almost identical pattern to the reciprocal subtraction image. This occurs at any stage in grass growth. However, there is more variability between these images where barley covers the surface with significant enhancement of feature at an early stage in barley growth (June) that are not evident on either day or night thermal images. The ATI image is again identical to the reciprocal subtraction image.

Alternative ATI models are applied to the data, where variations arise in the scaling factor to the Cracknell & Xue (1996) algorithm with different auxiliary meteorological, topographic and surface parameters incorporate in the algorithm. The Kahle & Alley (1985) model makes use of solar constant and atmospheric transmittance parameters as well as the rotation of the Earth and the ratio of the heat flux transferred between the atmosphere and the ground. In addition, their model includes a parameter that takes into account the latitude and solar declination associated with the timing and position of observation, which is given in the ATM image header files. Although this model uses the declination parameter that takes into account seasonal variation in the diurnal observations, the additional surface detail of the heat flux ratio between the atmosphere and the ground is unknown and as a result, the scaling factor remains constant for all pixels. As a result, the ATI image has an identical appearance to the Cracknell & Xue (1996) and reciprocal subtraction images. Since detail on the heat flux ratio between the atmosphere and the ground is unavailable, an alternative model presented by Price (1985) makes use of only the latitude and solar declination parameters. Since these parameters are constant for each pixel in the image and the albedo value remains constant, the results of the ATI model are again identical in appearance as the other models. Although the results of the ATI models are visually identical and the histograms extracted from each model have identical distribution patterns, the numeric values generated from each model are very different. However, there is a lack of numeric ATI values published in the literature with which to compare the results of the models.

The histograms generated for the June ATI data have a much narrower range of values than generated from the August ATI data, with higher mean values recorded for the August data from any of the fields under investigation. The June histogram generated for Ambion field has a uni-modal distribution pattern with values in the 0.045-0.50 range, which is similar to the values from the other grass-covered fields. The Helipad, Picnic and South fields all show a slight bi-modal distribution pattern with the minor frequency crest associated with the anomalous features revealed on the ATI imagery. The August histogram generated for Ambion field has a Gaussian distribution pattern with values in the 0.50-0.80 range, which have a higher mean value than the grass-covered fields. The grass-covered fields all have a fairly uniform uni-modal distribution pattern of the August data with a slight skew towards slightly

lower or higher ATI values associated with the more subtle anomalous features revealed on the ATI imagery. Although the results from the histogram generation suggest that the ATI modelling may help differentiate features at later stage in vegetation growth where there is a tendency for a wider range of ATI values, when the June ATI values are stretched to fit the full radiometric resolution of the VDU display, the shape of the resulting histogram is identical to that generated from August. This is somewhat puzzling since the ATI values extracted from manmade objects such as the tiled roofs of various buildings and the paving slabs also show a similar wider range of values for the August data and the histograms would be expected to show little seasonal variation. This suggests that there may be miscalibration of the data.

Although the ATI models have revealed features through the contrast between the day and night temperature response that are not evident on the individual thermal images, the technique is only applicable where the thermal radiance can be calibrated to temperature values. ATI is thought to represent variations in the bulk thermal properties of the surface, through the definition of thermal inertia, however, it is unknown whether an anomaly in ATI values may be caused by a subsurface feature or whether it may be due to variations in the surface vegetation, or indeed a combination of the two. In order to assess this issue, temperature profiles are measured continuously throughout the different stages in vegetation growth to determine the depth to which the diurnal heat penetrates the ground surface during vegetation growth and to assess whether this may be related to the surface ATI response. The characteristics of the thermal regime of the soil are dealt with at the start of the following chapter.

When the results of the ATI modelling are compared with the results of the geophysical surveying for variations soil properties beneath the surface, there is a poor correlation between the ATI anomalies and the geophysical anomalies at late stages in agricultural crop growth and also when the surface is covered by tall grass. This suggests that the ATI technique is sensitive to different properties than the geophysical techniques. In order to assess whether the ATI technique can be related to subsurface characteristics maybe at a different depth in the soil column than the geophysical techniques reveals, a series of soil samples are extracted across specific

features of variable ATI and geophysical response. The physical characteristics of the soil column are discussed after a discussion on the thermal properties of the soil column in the following chapter.

7 BOSWORTH SOIL CHARACTERISTICS

The thermal radiance values calibrated to ground temperature gives a snap-shot of the day and night thermal characteristics observed for the surface. However, the observed temperature response may not represent the true response of the soil to solar heating and will represent the combined effects of the soil and vegetation fractions comprising each pixel. In order to understand the effect of vegetation growth on the thermal regime of the underlying soil, contact soil temperature values were monitored from specific depths in the undisturbed soil column. A series of vertical thermal profiles were then generated at specific times in the vegetation growth cycle to determine the effect of vegetation growth on the thermal behaviour of the underlying soil. In addition to the thermal characteristics of the soil column, the physical properties of the soil were also determined in order to assess whether the observed variations in ATI value can indicate variations in true physical characteristics of the soil. The ultimate aim of the sampling technique is to bring together the soil characteristics and try and relate the contact temperature variations to the variations observed in the ATI response.

7.1 CONTACT TEMPERATURE MEASUREMENTS

The diurnal thermal response of surface materials under clear-sky conditions shows a minimum temperature in the pre-dawn time period, rising in response to solar heating to a peak at solar-noon, after which the temperature gradually decreases towards the minimum temperature at pre-dawn the following morning (Figure 7.1).

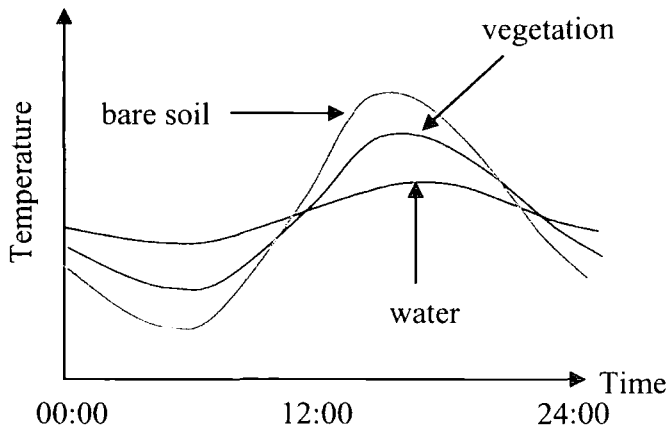

Figure 7.1: Schematic diurnal response of bare soil, vegetation and water

The amplitude of the temperature response varies with material composition in response to a variation in material thermal inertia. Where the ground surface is completely devoid of vegetation, the thermal response observed over the surface will tend to display a wide diurnal temperature range associated with the low physical thermal inertia values associated with pure soil. However, the composition, porosity and moisture content will affect the thermal inertia value of the particular soil, with sandy soils having lower values than those associated with clays for the same moisture content. The porosity of the soils also affects the thermal inertia with soils that have a higher moisture content having higher associated thermal inertia values (Pratt & Ellyett, 1979).

Where the ground surface is completely covered by vegetation, the thermal response will display a lower temperature range than that observed over bare soil due to a higher thermal inertia value associated with the vegetation. The type of vegetation present will also affect the thermal response with broad-leaved vegetation having higher thermal inertia values than cereal crops and as a result will tend to display lower diurnal temperature amplitudes. Where there is a combination of soil and vegetation components present at the surface, the thermal response of the surface will be represented by a combination of the heat fluxes associated with the individual soil and vegetation components.

Vertical temperature profiles were continuously monitored for a soil column throughout the growing season to observe the variations in surface temperature values with respect to the effect of the overlying vegetation. Vertical profiles were monitored at two specific locations to assess whether the variation in multispectral characteristics correlated with a variation in the physical thermal characteristics of the soil layer at two localities. The thermal profiling was also performed at the same localities under two different vegetation canopies, with pasture present in 2000 and barley present in 2001. This enables the assessment of the effect of vegetation structure on thermal characteristics of the soil.

Temperature probes, connected to a Tempcon® HOBO-H8 data logger (Appendix A5), were inserted with minimal soil disturbance, so as to preserve the structural integrity of the soil profile, at four individual depths in the soil column (0.00m, 0.10m, 0.20m and 0.50m) to assess the effect of vegetation growth on diurnal

and seasonal thermal regime of the underlying soil. Temperatures were monitored at 10-minute intervals from an early stage in crop development where the soil fraction dominated the pixel composition through a gradual increase in vegetation development until the crop reached full maturity and dominated the pixel composition. The temperatures recorded across the vegetation growth cycle were then downloaded, using BoxCarPro® 3.1v software, and the times for each recorded temperature value were converted into a minute count from the start of each day and also from the start of the year. The data was then analysed through development of a C++ program (Appendix F9) to identify trends in 1) the temperature maximum and minimum values, 2) the amplitude of the diurnal cycle and 3) the temperature patterns at depth with respect to the vegetation development. An assessment was also performed to identify trends in the timings when heat flux from depth exceeded that at the surface or near-surface soils. Results from the two localities were then compared to assess whether the observed variation in multispectral characteristics correlated with variations in physical thermal characteristics.

The thermal characteristics of the soil column were visualised as a series of graphs showing the temperature response at each depth through time. However, when the entire thermal profile from each location were visualised, there were sporadic periods during observation when the diurnal temperature response of the soil showed a much more muted thermal response with reduced maximum temperatures and diurnal amplitudes (Figure 7.3). In other cases the temperature continually fell during the diurnal cycle (Figure 7.4). Since the soil column was undisturbed during the periods of study with no pesticide spraying, fertilisation or ploughing, the variations in thermal characteristics is assumed to relate to an external factor such as meteorological conditions acting on the soil column. Ancillary meteorological data was therefore obtained for the entire period of observation to assess whether these sporadic thermal characteristics could be accounted for by variations in meteorological condition. The meteorological data was obtained from the archive of the British Atmospheric Data Centre (http://badc.rl.ac.uk) and provided detailed hourly and daily information on the amount of rain, the wind speed and wind direction that were recorded at the Church Lawford Saws meteorological stations located 20km south of the Bosworth study site (Figure 7.2).

Figure 7.2: Location of Church Lawford Saws meteorological station and the Bosworth study site

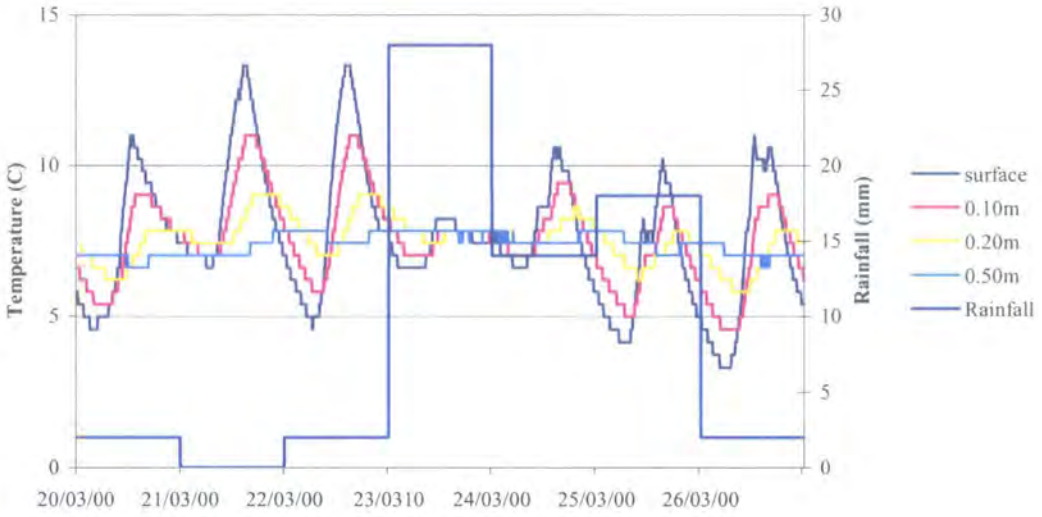

Figure 7.3: Thermal characteristics with overlay showing moderate daily rainfall

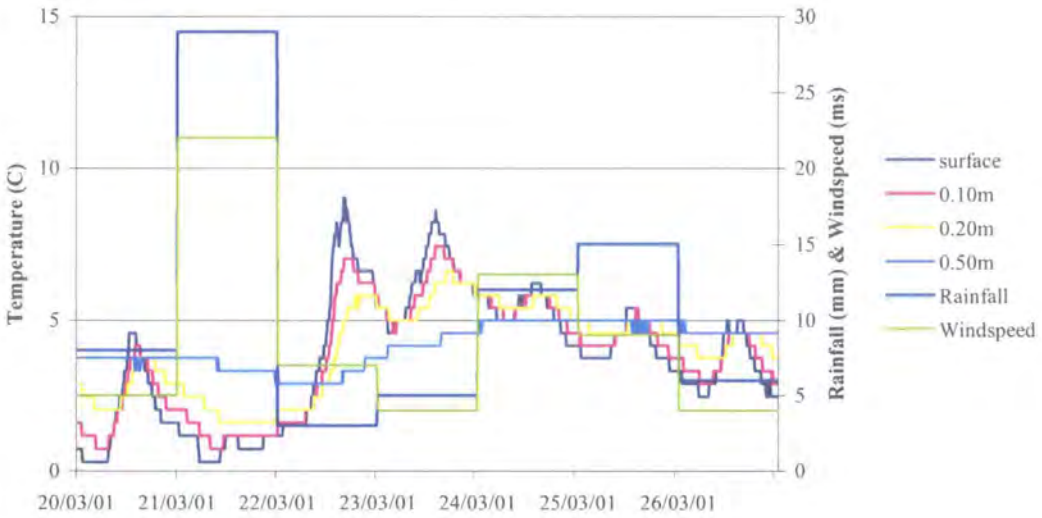

Figure 7.4: Thermal characteristics with overlay showing high daily rainfall and high wind speed

During periods of rain the soil column will retain moisture. Since moisture is known to have a higher thermal inertia, or higher resistance to temperature change than soils, the wet soils would be expected to display a smaller amplitude in the diurnal temperature range than would be observed for dry soils. When the meteorological rainfall and wind pattern data was examined, the dates where the soil exhibited a muted diurnal thermal response showed a strong correlation with dates exhibiting a significant amount of rainfall. There was also a strong correlation

observed between days where the soil showed a continual fall in temperature, indicated on the graph by a negative heating gradient, and days with significant rainfall and elevated wind speeds. The soils appeared to return to normal diurnal thermal characteristics a single solar heating and cooling cycle after rain ceased. However, under the same meteorological conditions, the soil under the pasture returned more quickly to normal characteristics than was observed under the barley. This may be a result of the different root systems of the different crops with a more complex network of roots in the cereal crop potentially locking more moisture in the soil column, and slowing the return of the soil to the characteristic diurnal response to solar heating.

In order to visually assess diurnal and seasonal trends in the thermal characteristics, specific diurnal cycles were chosen at different stages in crop development where the meteorological data showed a prolonged absence of rain and low wind speeds to remove variations caused by meteorological conditions. The typical thermal characteristics observed at the different stages in crop development, which are selected to represent the times associated with airborne image acquisition, are discussed in the following sections for the individual profiling locations. The trends in the observed thermal characteristics are then compared and contrasted in order to suggest the optimum times for thermal imaging of the soil surface under the specific vegetation canopies.

7.2 THERMAL PROFILE CHARACTERISTICS: SITE A

A continuous thermal profile was extracted from the mid-point of a feature that appeared as a linear anomaly on the day, night and ATI thermal images from both June and August 1998 but does not represent a geophysical anomaly (Figure 7.5). This feature corresponds with the position of an abandoned hedgerow boundary that was removed since generation of the 1st edition OS map. The temperature response of the soil was observed at four stages in vegetation development representing times when the surface was covered by vegetation at (i) and early stage in barley development when the soil fraction dominates, (ii) a middle stage in barley development during an increased stand height of the barley where equal fractions of the soil and vegetation components are present, (iii) a late stage in barley development where the vegetation dominates and is at its maximum stand height and (iv) a final

stage in barley development where the vegetation is at its maximum stand height and has reached maximum maturity prior to harvesting.

June 1998 Aerial Photograph

Magnetometry

June 1998 ATI

August 1998 ATI

Figure 7.5: Location of Site A thermal profile observed at Bosworth

The temperature response of the soil column is observed by plotting the temperature against time at four specific stages in vegetation development corresponding to the stage in surface vegetation growth present at ATM image acquisition. The main features of interest are the diurnal maximum and minimum temperatures and the amplitude of the temperature curve and the variations occurring

with respect to the depth of observation. These are discussed for the specific stages in crop development.

7.2.1 Stage I: Soil Fraction Dominates

The soil temperature observed under the pasture (Figure 7.6) shows a gradual decrease in the maximum temperature recorded through depth in the soil column. In addition, the peak temperatures occur at progressively later times in the day through depth suggesting a lag in the time that the soil at depth takes to respond to the penetrating solar heat flux compared with the surface soil. The soil shows a gradual increase in the minimum temperature recorded through depth, again occurring at progressively later times in the day and suggests a lag in the diurnal cooling through depth. The amplitude of the heating and cooling cycle decreases with depth. The rate at which the soil responds to solar heating decreases with depth, which is determined by the gradient of the morning temperature rise calculated from the ratio of the amplitude of the diurnal temperature variation with respect to the time between temperature extremes. Similar thermal characteristics are also observed when the surface is covered by barley at the early stage in crop development (Figure 7.7).

For both vegetation surfaces, the temperature response observed at the surface, 0.10m and 0.20m depths shows typical diurnal heating and cooling cycles, with the peak of the heating cycle occurring shortly after mid-day and the peak of the cooling cycle occurring in the early hours of the following morning. The graphs indicate that there is a lag in the time when the soils from the surface reach their maximum and minimum temperatures compared with those from depth, with the temperature extremes at the surface observed earlier in the day than those at depth. The temperature response measured at 0.50m does not show the typical diurnal heating and cooling characteristics observed at the shallower depths suggesting that the diurnal solar heating dissipates between 0.20m and 0.50m depth under either vegetation.

It is apparent that the values recorded under the barley are significantly higher than those observed at the equivalent depth under the pasture. This may be a direct result of variations in crop structure between the different vegetation types since the

ancillary meteorological data records consistently similar rainfall, wind speeds and air temperature values at this stage of pasture and barley growth (Table 7.1).

7.2.2 Stage II: Equal Soil and Vegetation Fractions

The soil temperature observed under the pasture (Figure 7.8) shows a decrease in the maximum temperature recorded through depth in the soil column with a lag in the heating of the soil at depth. In addition, the soil shows an increase in the minimum temperatures recorded at depth with a similar lag in the cooling of the deeper soils. The amplitude of the heating and cooling cycle decreases with depth and is much smaller than was observed at the earlier stage in vegetation growth. The rate of solar heating increases with depth, which is in direct contrast to the heating gradients observed at the earlier stage in pasture growth and may be a result of the vegetation interacting with and masking the underlying soil from solar heating. As for the earlier stage in vegetation development, the pasture shows a dissipation of heat between 0.20m and 0.50m depths, where the deeper soil at 0.50m shows no diurnal fluctuation. The barley shows the same maximum, minimum and amplitude patterns as the pasture and at the earlier stage in vegetation growth with a lag in heating and cooling with depth (Figure 7.9). However, the barley shows much higher temperatures than recorded at the equivalent depth under the pasture with a much greater diurnal temperature range for the specific depth (Table 7.2). Since the ancillary meteorological data records similar rainfall, wind speeds and air temperatures between the pasture and barley growth, the variation observed between the thermal characteristics of the pasture and the barley may be a direct result of a difference in vegetation root or leaf structure between the different vegetation types that influenced the direct solar heating of the soil.

7.2.3 Stage III: Vegetation Fraction Dominates

The soil temperature observed under the pasture (Figure 7.10) shows a decrease in the maximum temperature through depth with a more fluctuating pattern in minimum temperatures. Both parameters show a lag in the heating and cooling of the soil with depth with a fluctuation in the rate of heating with depth. The amplitude of the heating and cooling cycle decreases with depth and is much smaller than observed at the earlier stages in pasture growth. The temperature recorded at 0.20m

shows very little variation across the diurnal cycle suggesting that the vegetation masks the underlying soil from solar heating with the dissipation of heat just below 0.20m, which is shallower than observed at the earlier stages in pasture growth. The barley shows the same maximum, minimum and amplitude temperature patterns as the pasture with a similar lag in the heating pattern (Figure 7.11). The barley shows much lower temperatures than recorded at the equivalent depth under the pasture (Table 7.3). Since the ancillary meteorological data records similar rainfall, wind speeds and air temperatures between the pasture and barley growth, the variation observed between the thermal characteristics of the pasture and barley may be a direct result of a difference in vegetation root or leaf structure between the different vegetation types that influenced the solar heating of the underlying soil.

7.2.4 Stage IV: Mature Vegetation

The soil temperature observed under the pasture (Figure 7.12) illustrates one of the problems encountered when using the profiling equipment, where one of the probe connections becomes detached between periods of data download. When the data logger has been emplaced in the ground, it is then impossible to tell whether the probe connections have been broken until the data has been downloaded. The probes became detached at random intervals throughout the period of observation as the ground surrounding the logger moved. At this late stage in pasture growth, the probes at the surface and at 0.50m became detached from the logger and as a result no temperatures are recorded under the pasture. The remaining data shows an increase in minimum and maximum soil temperatures with depth with a lag in the heating and cooling of the soil. The amplitude of the heating cycle is identical at either depth with both depths showing a diurnal temperature fluctuation. The main variation between Stage III and Stage IV in pasture growth appears at 0.20m, where the Stage IV pasture shows a greater diurnal temperature range than the earlier stages which may be a result of foliage on the underlying soil. Temperatures are recorded at all depths under the barley (Figure 7.13). Although the soil at 0.20m shows higher maximum and minimum temperature than at 0.10m, there is a general decrease in the heating gradients with depth as the diurnal amplitude decreases. The barley shows much higher temperature than recorded at the equivalent depth under the pasture, which may be a result of the variation in leaf structure between the crops (Table 7.4).

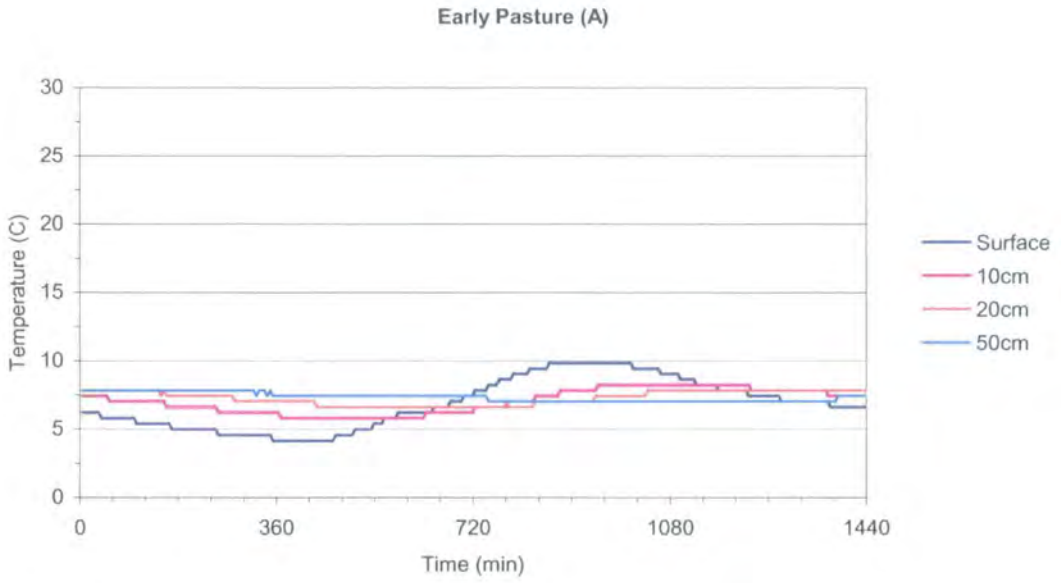

Figure 7.6: Diurnal thermal profiles at Site A under Stage I pasture 2000

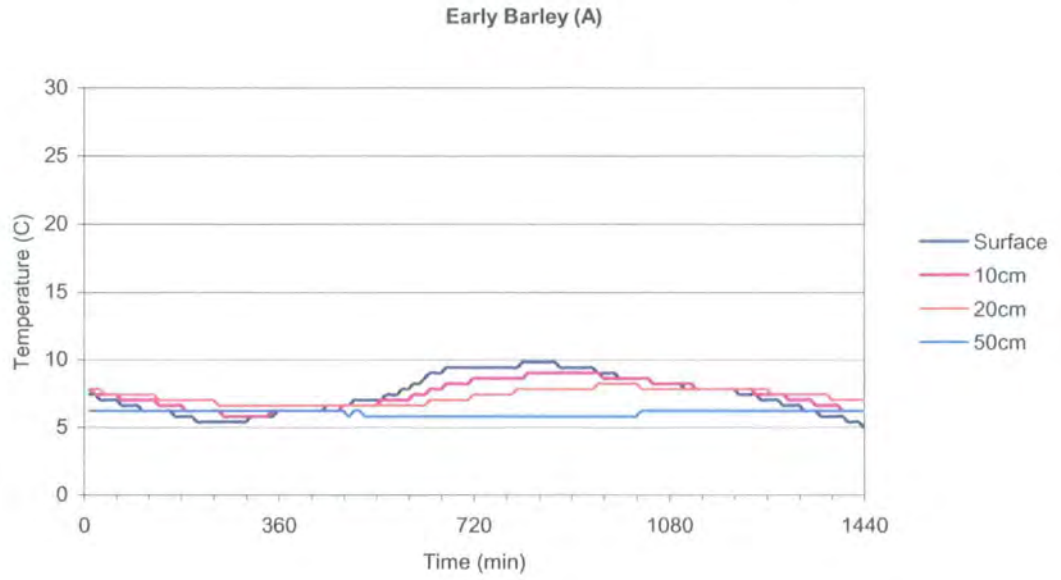

Figure 7.7: Diurnal thermal profiles at Site A under Stage I barley 2001

Early Pasture	Tmax	Tmin	tmax	tmin	ΔT	Δt	Rate
0.00m	9.82	4.15	859	464	5.67	395	0.0144
0.10m	8.23	5.81	949	629	2.42	320	0.0076
0.20m	7.83	6.62	1039	829	1.21	210	0.0058
Early Barley	Tmax	Tmin	tmax	tmin	ΔT	Δt	Rate
0.00m	7.43	2.46	719	459	4.97	260	0.0191
0.10m	6.62	3.31	729	499	3.31	230	0.0144
0.20m	6.22	4.57	789	589	1.65	200	0.0082

Table 7.1: Thermal characteristics of Bosworth Site A soil column at Stage I

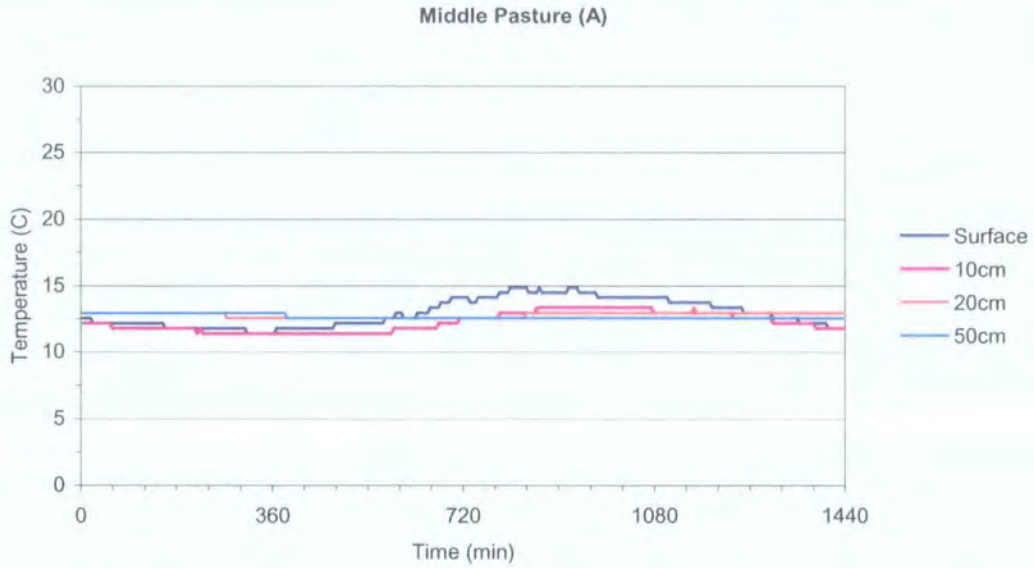

Figure 7.8: Diurnal thermal profiles at Site A under Stage II pasture 2000

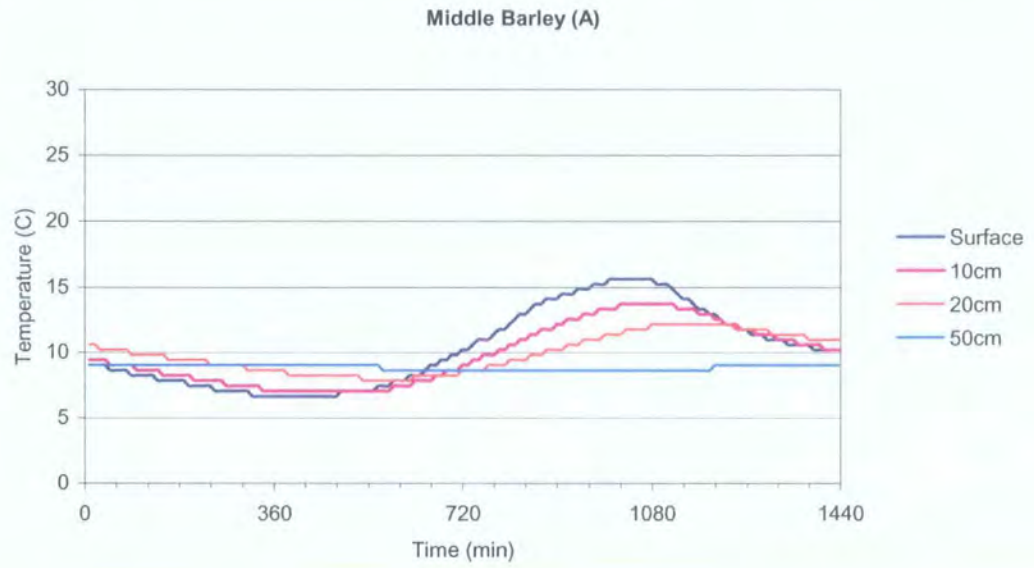

Figure 7.9: Diurnal thermal profiles at Site A under Stage II barley 2001

Pasture	Tmax	Tmin	tmax	tmin	ΔT	Δt	Rate
0.00m	14.85	11.38	918	363	3.47	555	0.0063
0.10m	13.32	11.38	848	583	1.94	265	0.0073
0.20m	13.32	12.55	918	833	0.77	85	0.0091
Barley	Tmax	Tmin	tmax	tmin	ΔT	Δt	Rate
0.00m	15.62	6.62	878	358	9.00	520	0.0173
0.10m	13.70	7.03	898	458	6.67	531	0.0126
0.20m	12.96	7.83	958	498	5.13	460	0.0115

Table 7.2: Thermal characteristics of Bosworth Site A soil column at Stage II

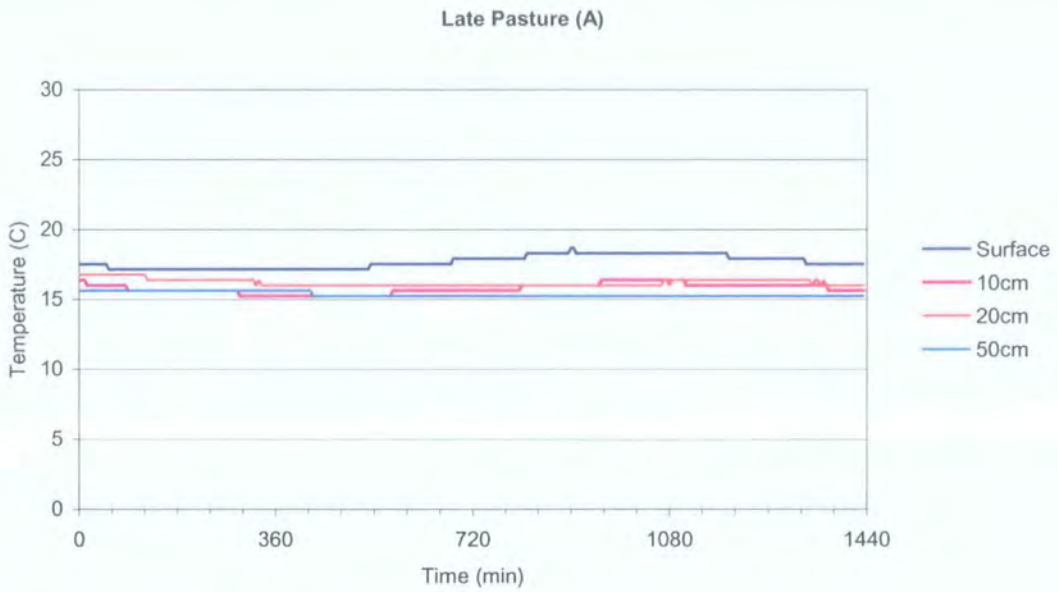

Figure 7.10: Diurnal thermal profiles at Site A under Stage III pasture 2000

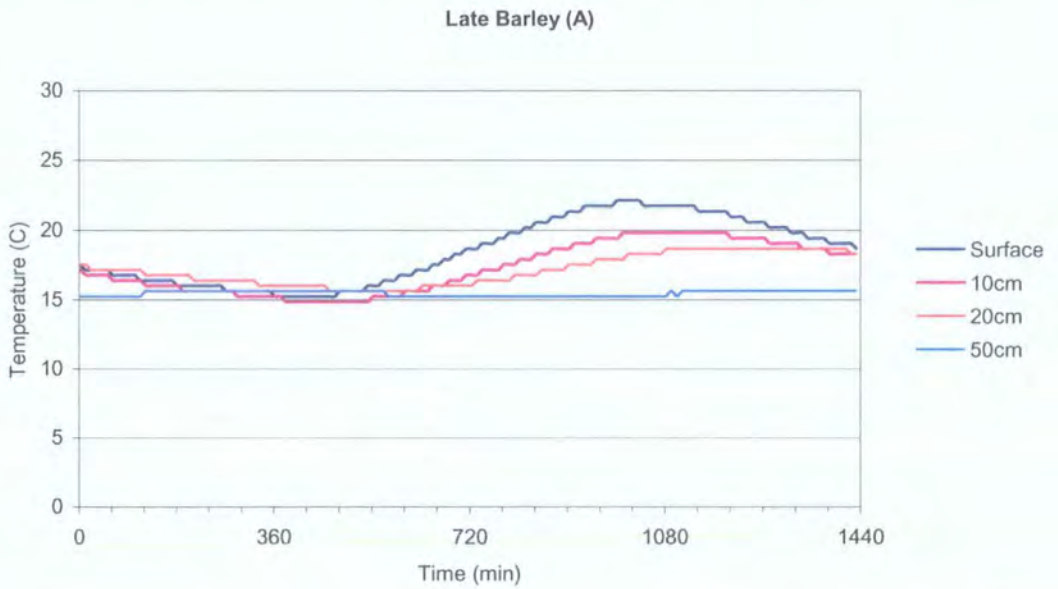

Figure 7.11: Diurnal thermal profiles at Site A under Stage III barley 2001

Pasture	Tmax	Tmin	tmax	tmin	ΔT	Δt	Rate
0.00m	18.66	17.14	900	530	1.52	370	0.0041
0.10m	16.38	15.23	955	570	1.15	385	0.0030
0.20m	16.38	16.00	1070	1065	0.38	5	0.0760
Barley	Tmax	Tmin	tmax	tmin	ΔT	Δt	Rate
0.00m	22.09	15.23	873	353	6.86	520	0.0132
0.10m	19.81	14.85	883	413	4.96	470	0.0106
0.20m	18.66	15.62	963	503	3.04	460	0.0066

Table 7.3: Thermal characteristics of Bosworth Site A soil column at Stage III

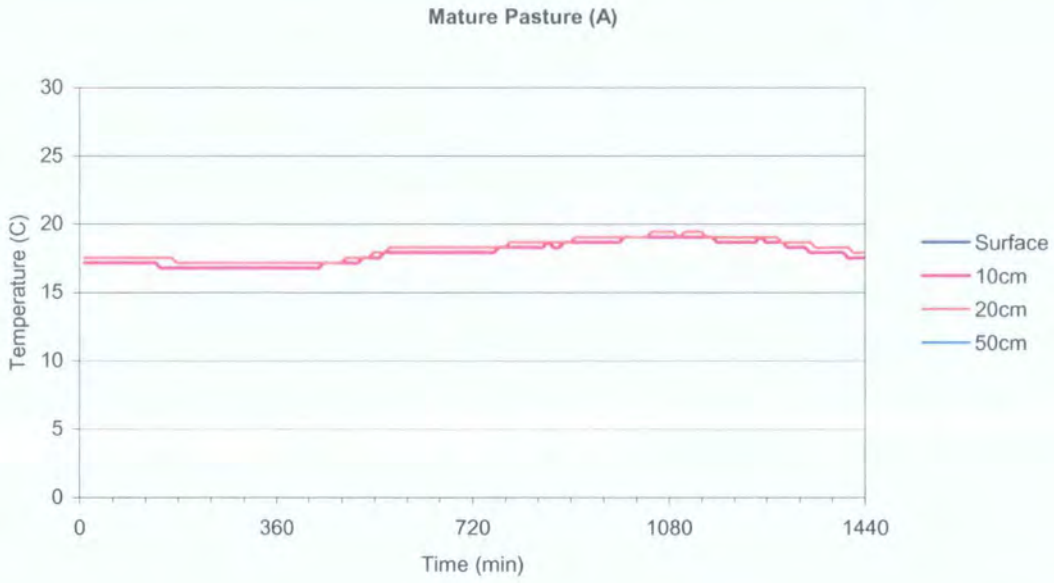

Figure 7.12: Diurnal thermal profiles at Site A under Stage IV pasture 2000

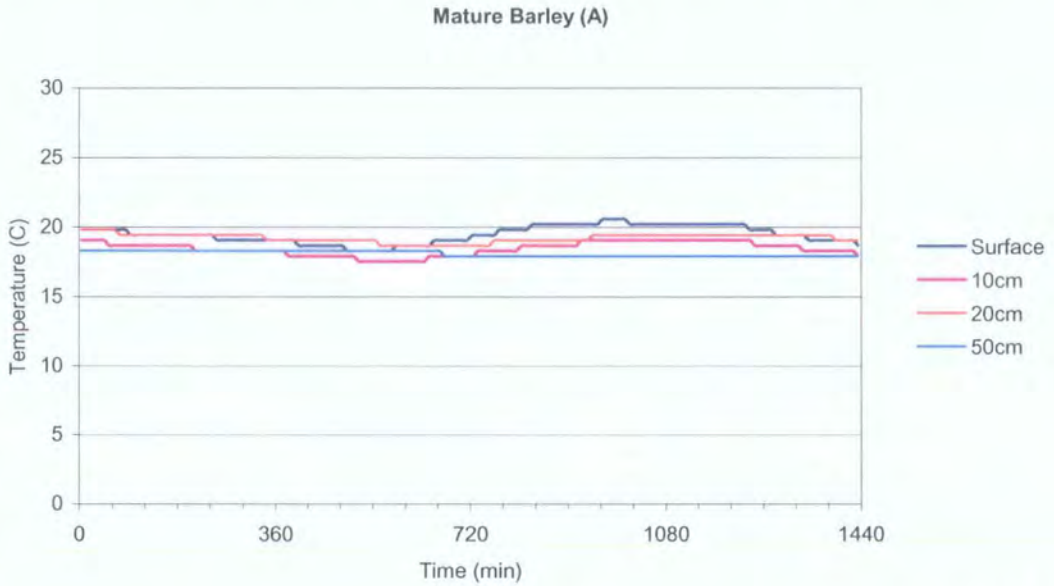

Figure 7.13: Diurnal thermal profiles at Site A under Stage IV barley 2001

Pasture	Tmax	Tmin	tmax	tmin	ΔT	Δt	Rate
0.00m	N/A	N/A	N/A	N/A	N/A	N/A	N/A
0.10m	19.04	16.76	997	437	2.28	560	0.0041
0.20m	19.42	17.14	1047	477	2.28	570	0.0040
Barley	Tmax	Tmin	tmax	tmin	ΔT	Δt	Rate
0.00m	20.57	18.28	923	573	2.29	430	0.0053
0.10m	19.04	17.52	923	633	1.52	290	0.0052
0.20m	19.42	18.66	943	753	0.76	190	0.0040

Table 7.4: Thermal characteristics of Bosworth Site A soil column at Stage IV

7.2.5 Summary of Site A Thermal Characteristics

The maximum temperatures recorded at Site A show an increase from Stages I-III under both pasture and barley, with maximum temperatures recorded at the surface higher than those at depth. The minimum temperatures are similar at Stage III and Stage IV under either crop with values under the barley initially lower than those recorded under the pasture at all depths. As the vegetation grows, the minimum temperatures recorded under the barley begin to exceed those recorded under the pasture at the equivalent depth. As a result, the amplitudes recorded under the barley are progressively lower than those recorded under the pasture, suggesting a greater resistance to temperature change of the soil under the cereal crop. The heat flux gradients determined under the barley show a progressive decrease with depth as the vegetation developed with the gradient at the surface exceeding that at depth. The values recorded under the pasture show a general decrease for a particular depth as the vegetation develops (Table 7.5). The ancillary meteorological data shows very similar meteorological conditions between the selected stages in crop development, therefore the variations in observed thermal characteristics may be a direct result of variations in the root systems, leaf or canopy structures associated with the different vegetation.

The data also shows that there are times during the diurnal cycles when the temperature from depth exceeds that observed at the surface. This gives an indication of potential times for remotely observing thermal heat flux characteristics from depth associated with buried structures, as opposed to those relating to surface characteristics. Temperatures recorded at depth are much higher than those recorded at shallower depths in the pre-dawn thermal regime. As the soil responds to solar heating, the temperatures recorded at depth appear slower to respond to heating than those at shallower depths. As a result, the cross-over in temperatures between the surface and 0.10m depth always precedes the timing of the cross-over observed between the surface and 0.20m. As the soil cools in the afternoon, the times between the cooling cross-over temperatures are very much shorter than those occurring for the morning heating, with surface temperatures decreasing progressively below those observed at 0.10m and 0.20m. The thermal cross-over times are progressively less distinct as the vegetation develops suggesting that the potential for observation of thermal characteristics from depth associated with buried structures decreases with

vegetation growth. From the thermal characteristics observed at this site, the maximum surface temperatures occur consistently between 14:00-15:00 local time with minimum surface temperatures occurring progressively later from 06:00-09:30 as vegetation developed. These values give an indication of the optimum times for thermal imaging of the surface under a particular stage in both vegetation canopies for use in apparent thermal inertia modelling. Times for optimum imaging of deeper properties become difficult to interpret from the date due to the wider range of times associated with the temperatures extremes from the deeper soils.

Pasture

Stage I	Tmax	Tmin	tmax	tmin	ΔT	Δt	Rate
0.00m	9.82	4.15	859	464	5.67	395	0.0144
0.10m	8.23	5.81	949	629	2.42	320	0.0076
0.20m	7.83	6.62	1039	829	1.21	210	0.0058
Stage II	Tmax	Tmin	tmax	tmin	ΔT	Δt	Rate
0.00m	14.85	11.38	918	363	3.47	555	0.0063
0.10m	13.32	11.38	848	583	1.94	265	0.0073
0.20m	13.32	12.55	918	833	0.77	85	0.0091
Stage III	Tmax	Tmin	tmax	tmin	ΔT	Δt	Rate
0.00m	18.66	17.14	900	530	1.52	370	0.0041
0.10m	16.38	15.23	955	570	1.15	385	0.0030
0.20m	16.38	16.00	1070	1065	0.38	5	0.0760
Stage IV	Tmax	Tmin	tmax	tmin	ΔT	Δt	Rate
0.00m	N/A	N/A	N/A	N/A	N/A	N/A	N/A
0.10m	19.04	16.76	997	437	2.28	560	0.0041
0.20m	19.42	17.14	1047	477	2.28	570	0.0040

Barley

Stage I	Tmax	Tmin	tmax	tmin	ΔT	Δt	Rate
0.00m	7.43	2.46	719	459	4.97	260	0.0191
0.10m	6.62	3.31	729	499	3.31	230	0.0144
0.20m	6.22	4.57	789	589	1.65	200	0.0082
Stage II	Tmax	Tmin	tmax	tmin	ΔT	Δt	Rate
0.00m	15.62	6.62	878	358	9.00	520	0.0173
0.10m	13.70	7.03	898	458	6.67	531	0.0126
0.20m	12.96	7.83	958	498	5.13	460	0.0115
Stage III	Tmax	Tmin	tmax	tmin	ΔT	Δt	Rate
0.00m	22.09	15.23	873	353	6.86	520	0.0132
0.10m	19.81	14.85	883	413	4.96	470	0.0106
0.20m	18.66	15.62	963	503	3.04	460	0.0066
Stage IV	Tmax	Tmin	tmax	tmin	ΔT	Δt	Rate
0.00m	20.57	18.28	923	573	2.29	430	0.0053
0.10m	19.04	17.52	923	633	1.52	290	0.0052
0.20m	19.42	18.66	943	753	0.76	190	0.0040

Table 7.5: Summary of thermal characteristics observed at Bosworth Site A

7.3 THERMAL PROFILE CHARACTERISTICS: SITE B

A continuous thermal profile was extracted from an area that showed no anomaly on the day, night and ATI thermal images from June and August 1998 and does not show a geophysical anomaly, thus representing background characteristics (Figure 7.14).

June 1998 Aerial Photograph

Magnetometry

June 1998 ATI

August 1998 ATI

Figure 7.14: Location of Site B thermal profile observed at Bosworth

This site is has a similar topographic slope to Site A, but is situated lower down the south-west facing slope of the field. The temperature response of the soil

column was observed at the same stages in vegetation growth as observed at Site A. However, initial equipment enabled acquisition of temperatures at only the surface, 0.20m and 0.50m depths until Stage III under the pasture, after which temperatures were additionally recorded at 0.10m. The temperature response of the soil column is observed by plotting the temperature against time at the same specific stages in vegetation growth as plotted for Site A.

7.3.1 Stage I: Soil Fraction Dominates

The soil temperature profile observed under the pasture (Figure 7.15) shows a gradual decrease in the maximum temperatures with depth, with a lag in the response of the soil from depth to solar heating. There is an increase in minimum temperatures with depth, with a similar lag in the diurnal cooling through depth. The amplitude of the heating and cooling cycle decreases with depth with a resulting decrease in the heating gradient of the deeper soils. This is similar to the characteristics observed at Site A under Stage I pasture. Although the temperatures under the barley are higher than under the pasture at Site B (Table 7.6) and also under the Stage I barley at Site A, the barley shows similar thermal characteristics to the Stage I pasture (Figure 7.16). As for Site A, the soil at 0.50m depth does not show a diurnal heating and cooling pattern under both pasture and barley, suggesting that the diurnal solar heating again dissipates between 0.20m and 0.50m depth. Since the same meteorological and vegetation conditions exist between the sites, the topographic aspect or physical properties of the underlying soils may be responsible for the thermal variations. The soil characteristics are discussed later in the Chapter.

7.3.2 Stage II: Equal Soil and Vegetation Fractions

The soil temperature profile observed under the pasture (Figure 7.17) shows a decrease in the maximum temperatures recorded through depth with a heating lag through depth. The soil shows an increase in the minimum temperatures at depth with a similar cooling lag of the deeper soils with an associated decrease in the amplitude with depth. The soil at 0.50m again does not show diurnal heating and cooling, suggesting dissipation of solar heating between 0.20m and 0.50m depth. These characteristics are very similar to those recorded at Site A for the Stage II pasture growth and also for the Stage I pasture at Site B. The maximum temperatures

recorded under the barley are higher than under the pasture with minimum temperature lower than under the pasture (Figure 7.18), but in excess of those recorded at Stage II barley at Site A. The amplitude again decreases with depth resulting in decreasing heating gradients with depth, similar to those observed under the same Stage II barley at Site A, however, these values exceed those determined under the Stage II pasture at this site (Table 7.7). Since the same meteorological conditions and vegetation condition existed between the sites, the variation in thermal response must be explained by an external factor, such as physical soil characteristics, which is discussed later in the chapter.

7.3.3 Stage III: Vegetation Fraction Dominates

The soil temperature observed under the pasture (Figure 7.19) shows a decrease in maximum temperatures and an increase in minimum temperatures recorded through depth, which are lower than those recorded for Stage III pasture at Site A. The amplitude and diurnal heating gradient decrease with depth and are higher than those recoded at for Stage III pasture growth at Site A. The temperature recorded at 0.50m again does not show a diurnal fluctuation suggesting solar heat dissipation between 0.20m and 0.50m depth, which is similar to observed at Site A. The barley shows the same maximum, minimum and amplitude temperature patterns as the pasture (Figure 7.20). The barley records higher maximum and lower minimum temperatures and than observed under the pasture (Table 7.8), with values lower than observed under Stage III barley at Site A. The barley also records higher amplitudes and diurnal heating gradients than under the pasture observed for Stage III barley at Site A. Since the same meteorological conditions and vegetation condition existed between the sites, the variation in thermal response must be explained by an external factor, such as physical soil characteristics, which is discussed later in the chapter.

7.3.4 Stage IV: Mature Vegetation

The soil temperature profile observed under the pasture (Figure 7.21) shows a decrease in the maximum temperatures through depth with an increase in minimum temperatures with a lag in the heating and cooling of the soils with depth. The amplitude and heating gradients decrease with depth, but remain higher than those recorded at Site A. The soil at 0.50m again does not show diurnal heating and cooling,

again suggesting the dissipation of heat between 0.20m and 0.50m. The soil temperature profile observed under the barley (Figure 7.22) shows a decrease in maximum temperatures and increase in minimum temperature with a similar lag in heating and cooling as for Stage I and Stage II barley. The amplitude and diurnal gradient decrease with depth beneath the barley and are consistently higher than those observed under the pasture (Table 7.9) and at Site A under Stage III barley. Since the same meteorological conditions and vegetation condition existed between the sites, the variation in thermal response must be explained by an external factor, such as physical soil characteristics.

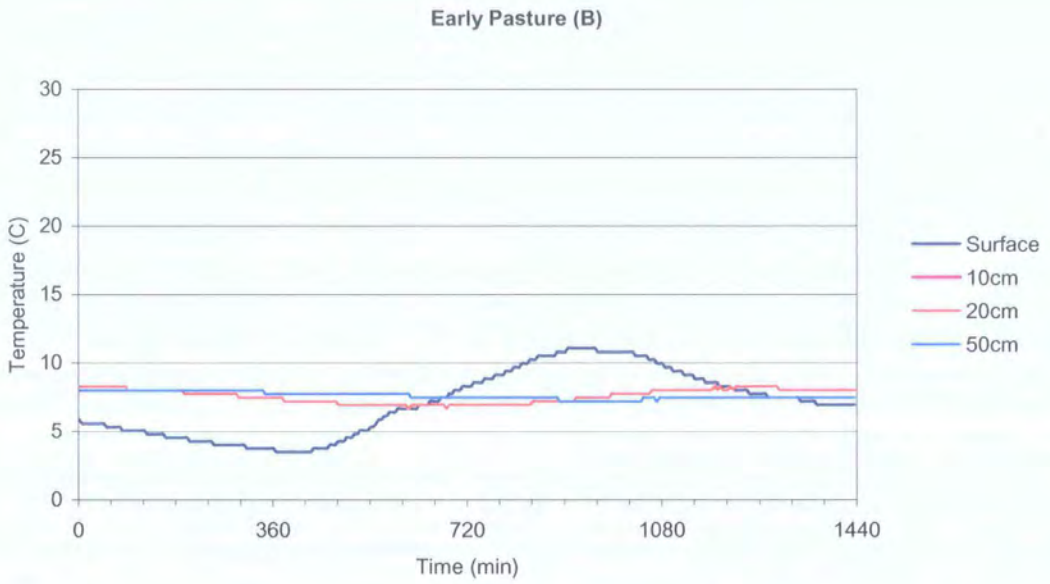

Figure 7.15: Diurnal thermal profiles at Site B under Stage I pasture 2000

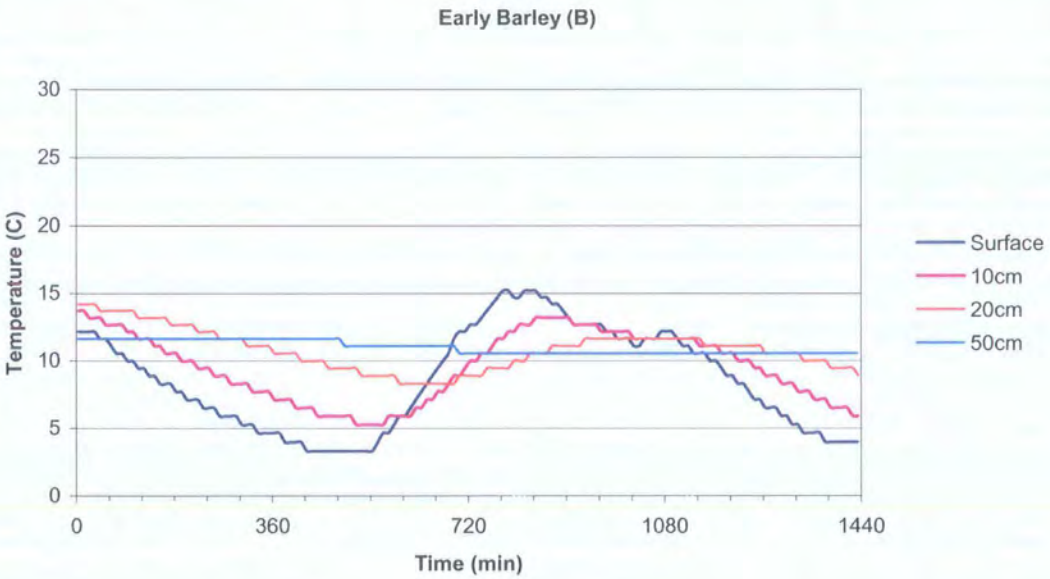

Figure 7.16: Diurnal thermal profiles at Site B under Stage I barley 2001

Pasture	Tmax	Tmin	tmax	tmin	ΔT	Δt	Rate
0.00m	11.08	3.51	907	432	7.57	475	0.0159
0.10m	N/A	N/A	N/A	N/A	N/A	N/A	N/A
0.20m	8.28	6.66	1177	682	1.62	495	0.0033
Barley	Tmax	Tmin	tmax	tmin	ΔT	Δt	Rate
0.00m	15.18	3.32	784	544	11.86	240	0.0494
0.10m	13.18	5.27	844	564	7.91	280	0.0283
0.20m	11.62	8.30	934	694	3.32	240	0.0138

Table 7.6: Thermal characteristics of Bosworth Site B soil column at Stage I

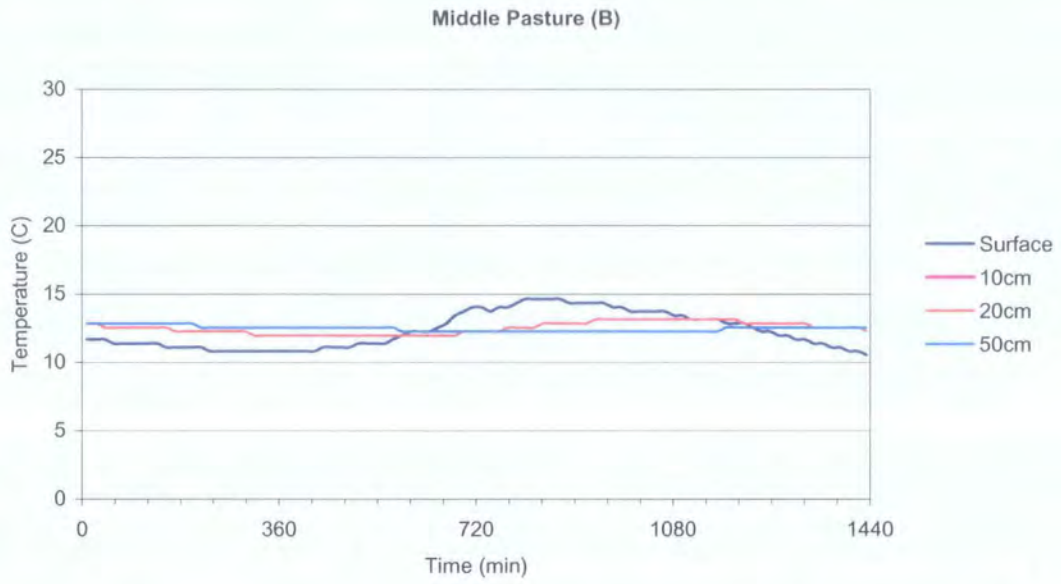

Figure 7.17: Diurnal thermal profiles at Site B under Stage II pasture 2000

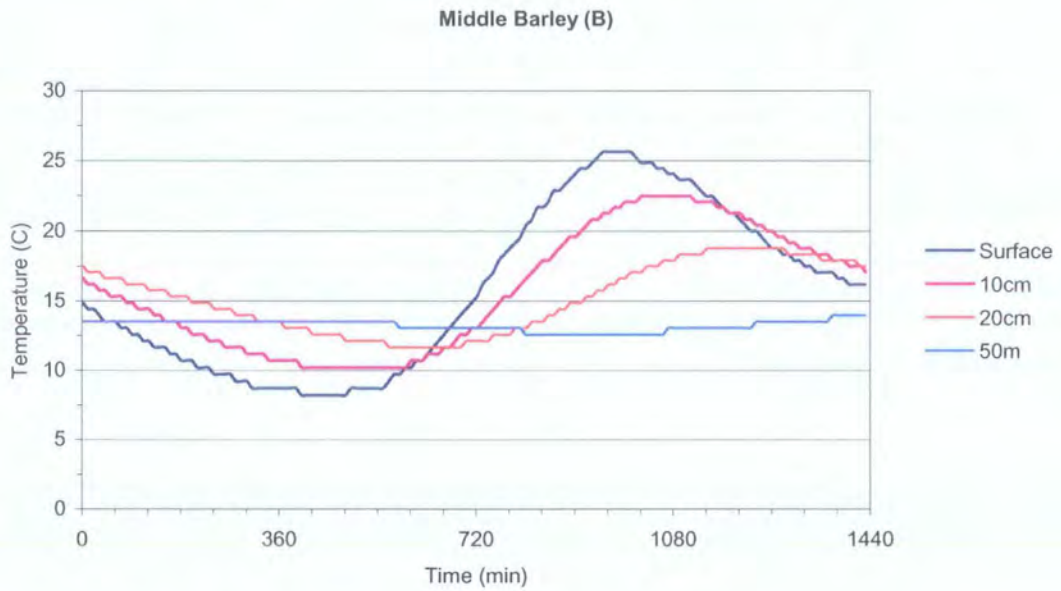

Figure 7.18: Diurnal thermal profiles at Site B under Stage II barley 2001

Pasture	Tmax	Tmin	tmax	tmin	ΔT	Δt	Rate
0.00m	14.62	10.80	809	425	3.82	384	0.0099
0.10m	N/A	N/A	N/A	N/A	N/A	N/A	N/A
0.20m	13.13	11.95	937	681	1.18	256	0.0046
Barley	Tmax	Tmin	tmax	tmin	ΔT	Δt	Rate
0.00m	25.60	8.18	951	481	17.42	470	0.0371
0.10m	22.43	10.18	1021	591	12.25	430	0.0285
0.20m	18.74	11.63	1141	691	7.11	450	0.0158

Table 7.7: Thermal characteristics of Bosworth Site B soil column at Stage II

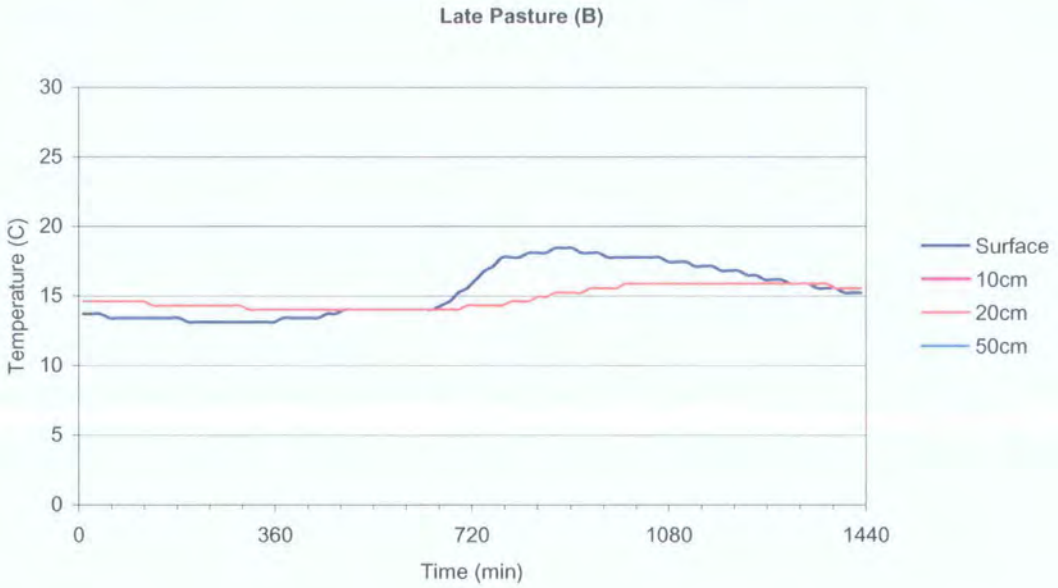

Figure 7.19: Diurnal thermal profiles at Site B under Stage III pasture 2000

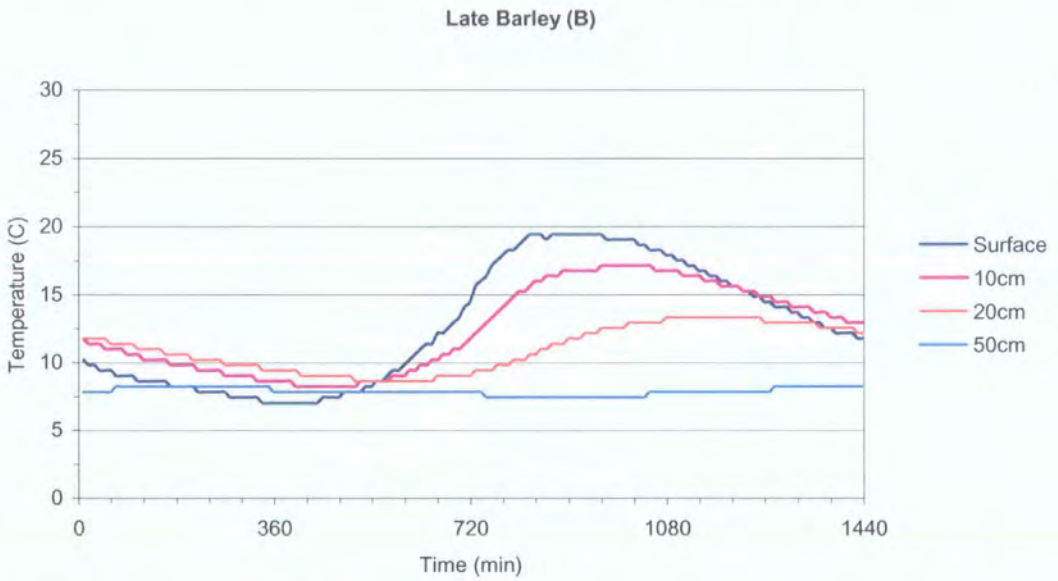

Figure 7.20: Diurnal thermal profiles at Site B under Stage III barley 2001

Pasture	Tmax	Tmin	tmax	tmin	ΔT	Δt	Rate
0.00m	18.43	13.13	872	360	5.30	512	0.0104
0.10m	N/A	N/A	N/A	N/A	N/A	N/A	N/A
0.20m	15.86	14.02	1000	696	1.84	304	0.0061
Barley	Tmax	Tmin	tmax	tmin	ΔT	Δt	Rate
0.00m	19.42	7.03	829	439	12.39	390	0.0318
0.10m	17.14	8.23	959	509	8.91	450	0.0198
0.20m	13.32	8.63	1079	649	4.69	430	0.0109

Table 7.8: Thermal characteristics of Bosworth Site B soil column at Stage III

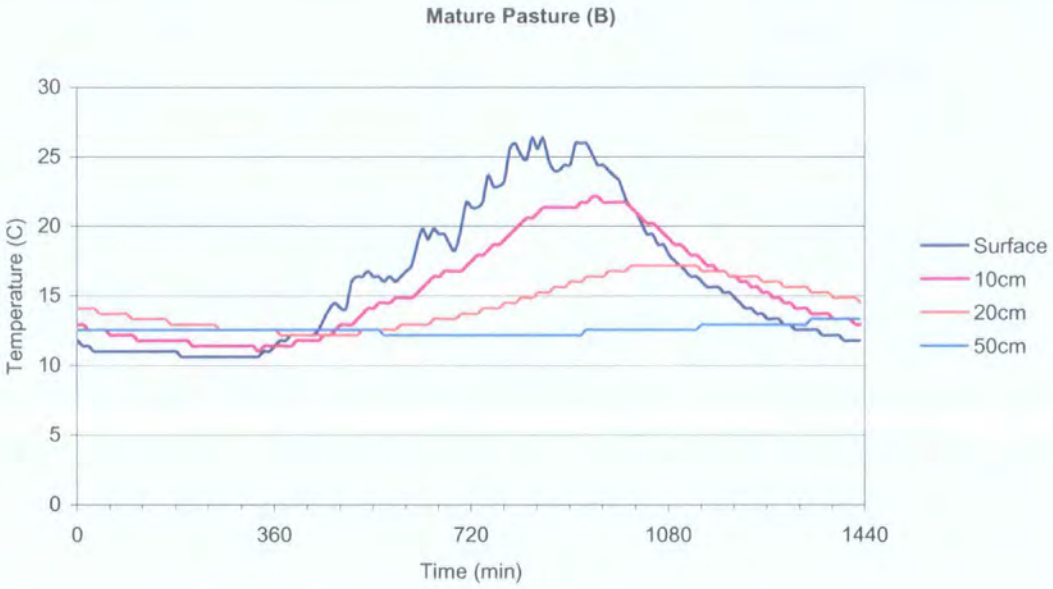

Figure 7.21: Diurnal thermal profiles at Site B under Stage IV pasture 2000

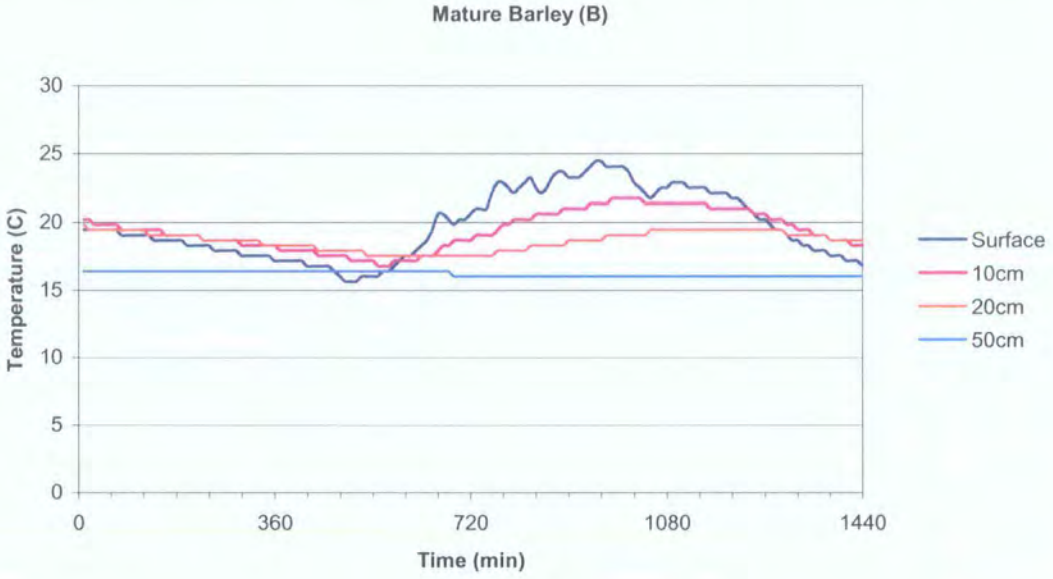

Figure 7.22: Diurnal thermal profiles at Site B under Stage IV barley 2001

Pasture	Tmax	Tmin	tmax	tmin	ΔT	Δt	Rate
0.00m	26.34	10.60	831	331	15.74	500	0.0315
0.10m	22.09	10.99	941	331	11.10	610	0.0182
0.20m	17.14	12.16	1011	511	4.98	500	0.0100
Barley	Tmax	Tmin	tmax	tmin	ΔT	Δt	Rate
0.00m	24.40	15.62	949	509	8.78	440	0.0200
0.10m	21.71	16.76	979	569	4.95	490	0.0121
0.20m	19.42	17.52	1049	759	1.90	290	0.0066

Table 7.9: Thermal characteristics of Bosworth Site B soil column at Stage IV

7.3.5 Summary of Site B Thermal Characteristics

The maximum temperatures recorded under the pasture at Site B increase throughout pasture growth with minimum temperatures increasing from Stages I-III. The maximum and minimum temperatures recorded under the barley at Site B show an increase from Stages I-II with a drop in values at Stage III followed by an increase to Stage IV. The maximum temperatures recorded under both vegetation canopies decrease with depth with an associated increase in minimum temperatures, which are lower under the barley until Stage IV. The temperature amplitude and heating gradients decrease with depth under both crops with higher values under the barley until Stage IV (Table 7.10).

As discussed for Site A, the there are times when the temperature at depth exceeds that observed at the surface, usually in the predawn thermal regime. The cross-over in temperature rise between the surface and 0.10m always precedes the cross-over between the surface and 0.20m as the soil from depth takes longer to respond to solar heating. The difference in time between these thermal cross-over points decreases as the vegetation develops and becomes less distinct and so the optimum timing for observing thermal heat flux characteristics from depth associated with potential buried structures becomes less distinct. The maximum surface temperatures occur consistently between 13:00-16:00 local time with minimum surface temperatures occurring progressively later from 05:30-08:30 local time, which is similar to the timing observed at Site A.

Pasture

Stage I	Tmax	Tmin	tmax	tmin	ΔT	Δt	Rate
0.00m	11.08	3.51	907	432	7.57	475	0.0159
0.10m	N/A	N/A	N/A	N/A	N/A	N/A	N/A
0.20m	8.28	6.66	1177	682	1.62	495	0.0033
Stage II	Tmax	Tmin	tmax	tmin	ΔT	Δt	Rate
0.00m	14.62	10.80	809	425	3.82	384	0.0099
0.10m	N/A	N/A	N/A	N/A	N/A	N/A	N/A
0.20m	13.13	11.95	937	681	1.18	256	0.0046
Stage III	Tmax	Tmin	tmax	tmin	ΔT	Δt	Rate
0.00m	18.43	13.13	872	360	5.30	512	0.0104
0.10m	N/A	N/A	N/A	N/A	N/A	N/A	N/A
0.20m	15.86	14.02	1000	696	1.84	304	0.0061
Stage IV	Tmax	Tmin	tmax	tmin	ΔT	Δt	Rate
0.00m	26.34	10.60	831	331	15.74	500	0.0315
0.10m	22.09	10.99	941	331	11.10	610	0.0182
0.20m	17.14	12.16	1011	511	4.98	500	0.0100

Barley

Stage I	Tmax	Tmin	tmax	tmin	ΔT	Δt	Rate
0.00m	15.18	3.32	784	544	11.86	240	0.0494
0.10m	13.18	5.27	844	564	7.91	280	0.0283
0.20m	11.62	8.30	934	694	3.32	240	0.0138
Stage II	Tmax	Tmin	tmax	tmin	ΔT	Δt	Rate
0.00m	25.60	8.18	951	481	17.42	470	0.0371
0.10m	22.43	10.18	1021	591	12.25	430	0.0285
0.20m	18.74	11.63	1141	691	7.11	450	0.0158
Stage III	Tmax	Tmin	tmax	tmin	ΔT	Δt	Rate
0.00m	19.42	7.03	829	439	12.39	390	0.0318
0.10m	17.14	8.23	959	509	8.91	450	0.0198
0.20m	13.32	8.63	1079	649	4.69	430	0.0109
Stage IV	Tmax	Tmin	tmax	tmin	ΔT	Δt	Rate
0.00m	24.40	15.62	949	509	8.78	440	0.0200
0.10m	21.71	16.76	979	569	4.95	490	0.0121
0.20m	19.42	17.52	1049	759	1.90	290	0.0066

Table 7.10: Summary of soil thermal characteristics at Bosworth Site B

7.4 SOIL COMPOSITIONAL CHARACTERISTICS

A soil is a layer of organic and inorganic weathered material that accumulates at the Earth's surface, reflecting the influence of the climate in which it developed, the relief of the land, the nature of the parent material or bedrock on which the soil developed and the effects of cultivation as well as the physical, chemical and biological processes involved in its formation (Duff, 1993). A soil profile is the vertical arrangement of the various discrete horizontal layers called horizons that make up any soil from the surface downward to the unaltered parent material or bedrock. A soil horizon is identified as a layer of soil that can be distinguished from adjacent layers by physical properties, such as structure, texture and colour, or through variation in its chemical composition. However, deeply cultivated soils may be more or less uniform throughout with little vertical variation in soil characteristics due to the effects of agricultural practise reworking the soils (Morgan, 1985). Soils consist mainly of combinations of solid particles, fluids and air. The particles forming the soils are separated into sand, silt and clay particles based on their particle size using the Wentworth classification scheme (Table 7.11) and the soils can then be classified using the Saxton textural scheme that is based on the fractions of sand, silt and clay components present within the soil (Figure 7.23).

Wentworth Size Class	Soil Particle Size (mm)
Sand	> 0.0625
Silt	0.0039-0.0625
Clay	<0.0039

Table 7.11: Soil particle size definition

Particle size analysis can be used to identify variations in soil properties that may be a result of the presence of infilled ditches, where the ditch soil has a different structure from the surrounding matrix. However, particle size is only one component of a complex set of interrelationships that characterise the physical and chemical properties of a soil, with the mineralogy of the soil components important for soil classification (Whalley, 1985). Variations in the composition of the soil can therefore suggest the presence of past anthropogenic activity, such as the presence of ash or organic-rich layers in the soil.

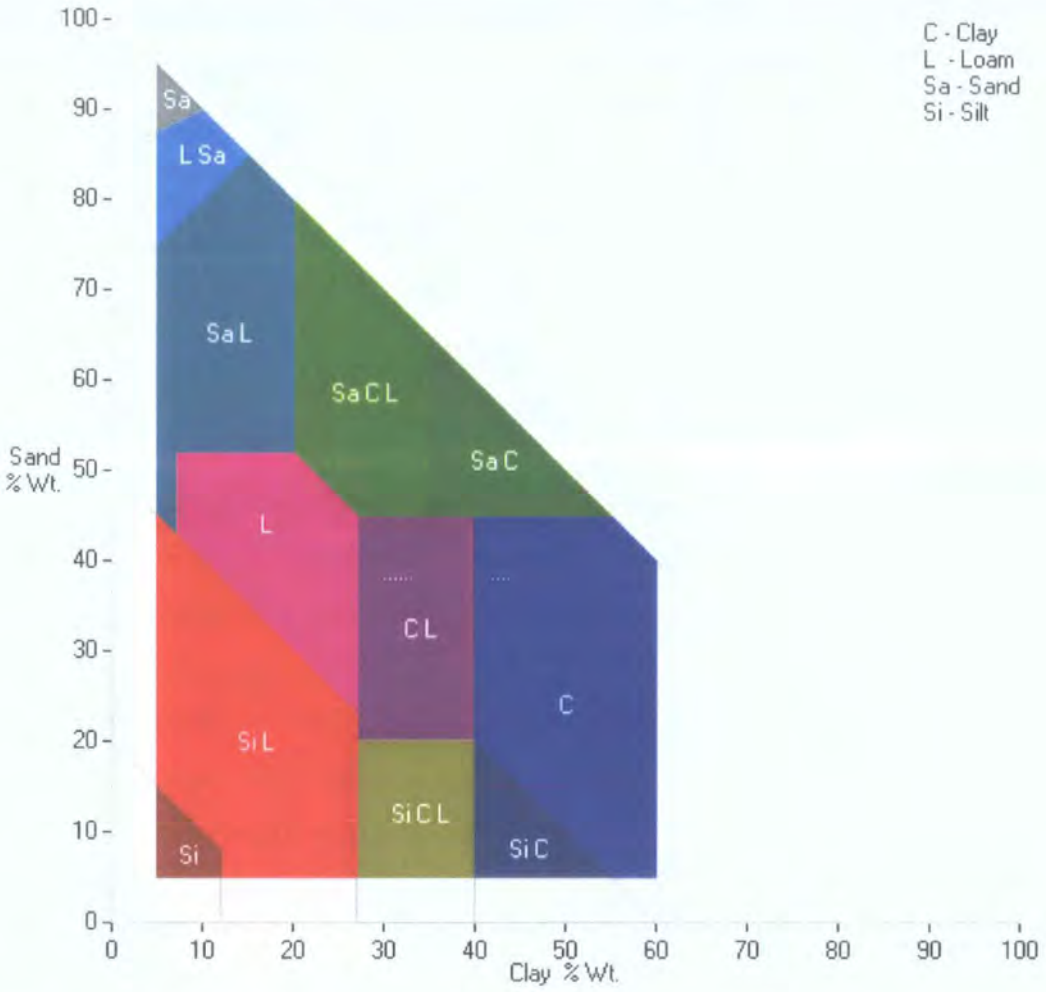

Figure 7.23: Soil classification scheme from Saxton (USDA Agricultural Research Service)

The particle size distribution and mineralogy of the undisturbed soil are permanent and unchanging characteristics, but variations in these characteristics can influence the permeability and porosity of the soil. These factors relate to the shape, angularity and surface texture of the soil particles, which can affect the retention of moisture contained in the soil pore spaces (Catt, 1985). Moisture has a high thermal inertia or a low diurnal temperature contrast and is represented by a dampening of the diurnal heating and cooling curve (Figure 3.2). Moist soils will therefore have a lower diurnal temperature contrast than dry soils enabling the differentiation of soils based on their variation in day and night temperature contrast (Pratt & Ellyett, 1979). When a feature is buried in the shallow subsurface, this causes a variation in the retention of soil moisture due to the differential compaction of the soils. As a result, the thermal regime of the soil above a feature may have a different response compared with that of the undisturbed soil matrix (Pickerill & Malthus, 1998). The moisture content of

the soil can affect the growth of vegetation above a feature due to the limitation in the availability of moisture into the root system of the vegetation and inflict stress on the crop (Morgan, 1985).

In order to establish whether the thermal variations observed in the soil column can be attributed to variations in the physical soil properties, soil profiles are extracted from the two positions where continuous thermal profiling was obtained, in addition to locations where variable spectral, thermal and magnetic response are apparent (Figure 7.24). There are five main features over which soils are extracted, with additional soil samples extracted at 5m and 10m lateral offset, where background characteristics are observed at the latter site. The main features are:

(A) - an anomaly seen at visible and near-infrared wavelengths

(B) - an anomaly seen at visible, near-infrared, thermal infrared wavelengths and the ATI images

(C) - an anomaly seen on August day and night thermal and magnetic images

(D) - an anomaly on day and night thermal, ATI and magnetic images

(E) - a location that has uniform characteristics

The intention was to extract complete 0.50m profiles from each location, however penetration of the soil layer using standard coring equipment was not possible due to the excessive amount of pebble material within the soil column at the Bosworth site. As a result, a 0.50m vertical trench was excavated, or down to the maximum depth where extraction was physically possible, with soils extracted at 0.05m intervals from the undisturbed soil face. Soils were extracted from the site once the crop had been harvested and access was permitted to the land, but prior to ploughing to ensure the soil underwent minimal reworking of its vertical and lateral characteristics to correspond with soil conditions associated with the imagery. Representative soil samples from each depth are analysed in the laboratory for particle size distribution (Appendix G1), moisture content (Appendix G2) and organic content (Appendix G3) and vertical profiles generated for each core sample. Lateral profiles are also generated across each feature from the adjacent soil characteristics for

comparison with the results from the ATI modelling to assess whether the variation in thermal response correlates with a variation in true physical soil characteristics of the features.

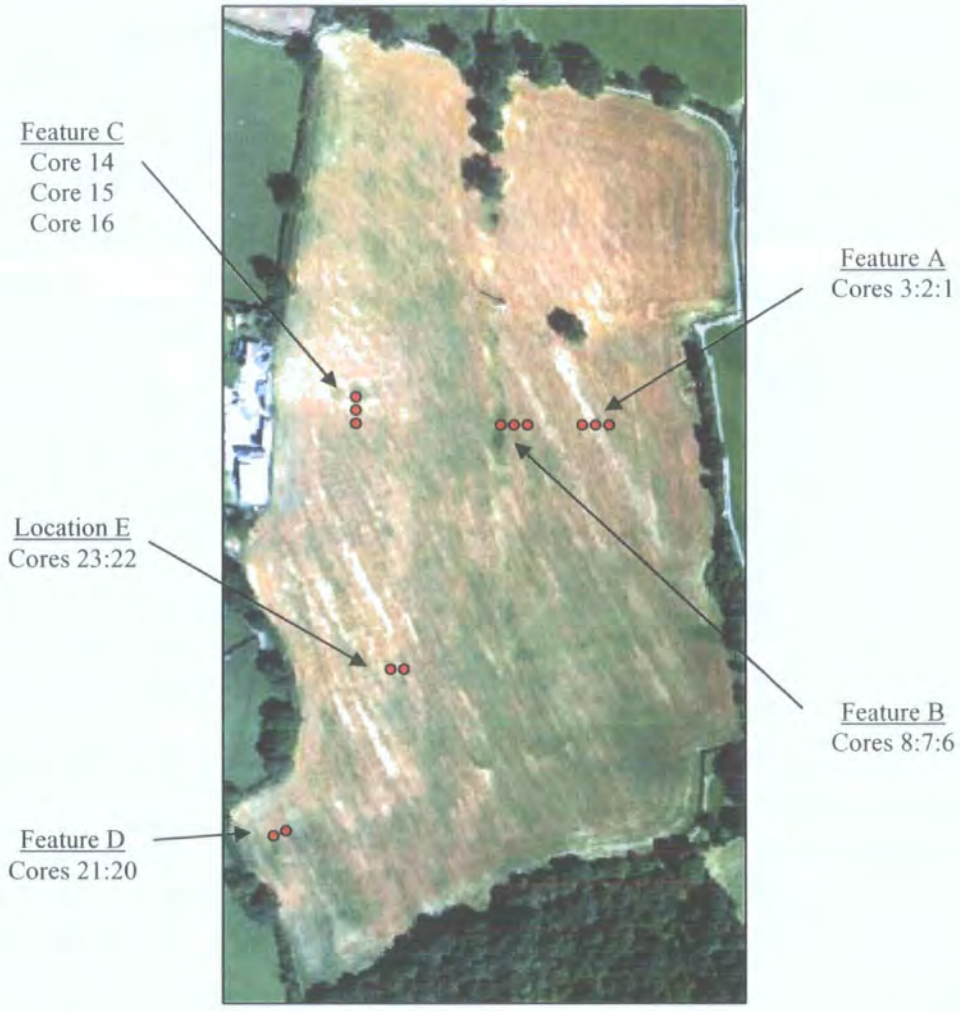

Figure 7.24: Location and nomenclature of Bosworth soil extraction profiles

7.4.1 Feature A

Feature A corresponds to an anomaly that is evident at visible and near-infrared wavelengths throughout the barley growth in 1998 but is not evident under the oil seed rape of 2002. Soil profiles are extracted from the feature (core 3), at a 5m eastern lateral offset (core 2) and at a 10m eastern lateral offset (core 1) for assessment of vertical and lateral trends in soil characteristics. The vertical soil profile extracted from the feature is visualised by plotting particle size distribution, moisture content and organic content through depth (Figure 7.25).

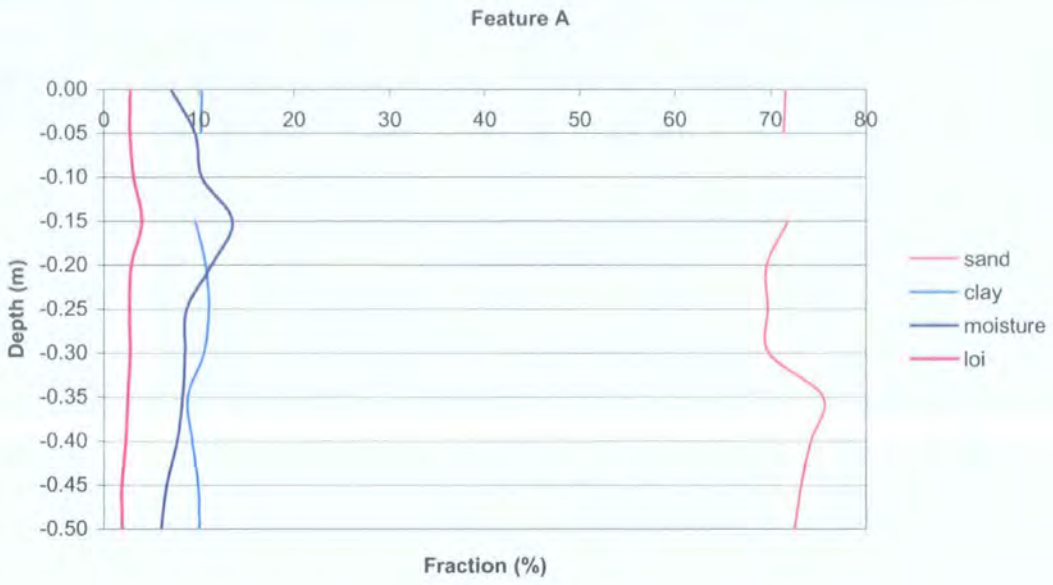

Figure 7.25: Vertical soil profile extracted from Bosworth Feature A

The soil profile from Feature A shows no variation in Saxton classification through depth with soils uniformly classified as sandy loams. The sand content is fairly uniform at shallow depths (<0.30m) with values in the 71.90%-69.60% range. There is a pronounced increase to 75.50% at 0.35m, below which the sand fraction gradually decreases but still remains higher than observed at shallower depths. The profile of the clay content shows the opposite pattern with a minimum value observed at 0.35m. The profile of the moisture content shows a more pronounced variation with depth with a gradual rise to 13.56% at 0.15m, below which values continually decrease. The organic content shows little variation with depth with a slight rise to 3.97% at 0.15m, below which values gradually decrease. The profiles of the sand and clay fractions suggest a change in physical characteristics between 0.30m-0.35m possibly relating to the plough depth where pebbles become visibly more widespread.

The soil profile extracted from above Feature A is compared with the adjacent soil profiles to assess any lateral trends in soil properties that may relate to the visible and near-infrared image anomaly (Insert A). Since the feature is evident at visible and near-infrared wavelengths then one would expect variations in moisture and organic differences associated with the feature, which affect vegetation growth. Since there was no volumetric ATI anomaly associated with the feature, the soil was not expected to show volumetric compositional variation associated with the feature if ATI corresponds to soil properties beneath the vegetation.

The results of the lateral soil profiles show very similar particle size distribution, moisture content and organic content across the feature at any depth, with no obvious variation in soil physical characteristics that can be related to the visible and near-infrared feature (see Insert A). This suggests that the visible and near-infrared feature is more likely to represent a surface vegetation effect.

7.4.2 Feature B

Feature B corresponds to an anomaly that is evident at visible, near-infrared wavelengths and on the day, night and ATI thermal images under the barley in 1998 but is not evident under the oil seed rape of 2002. This feature corresponds to the position of the field boundary hedgerow that has been removed since generation of the 1st edition OS map. Soil profiles are extracted from the feature (core 8), at a 5m eastern lateral offset (core 7) and at a 10m eastern lateral offset (core 6) for assessment of vertical and lateral trends in soil characteristics. The vertical soil profile extracted from the feature (Figure 7.26) gives no variation in Saxton classification through depth with soils uniformly classified as sandy loams, similar to Feature A.

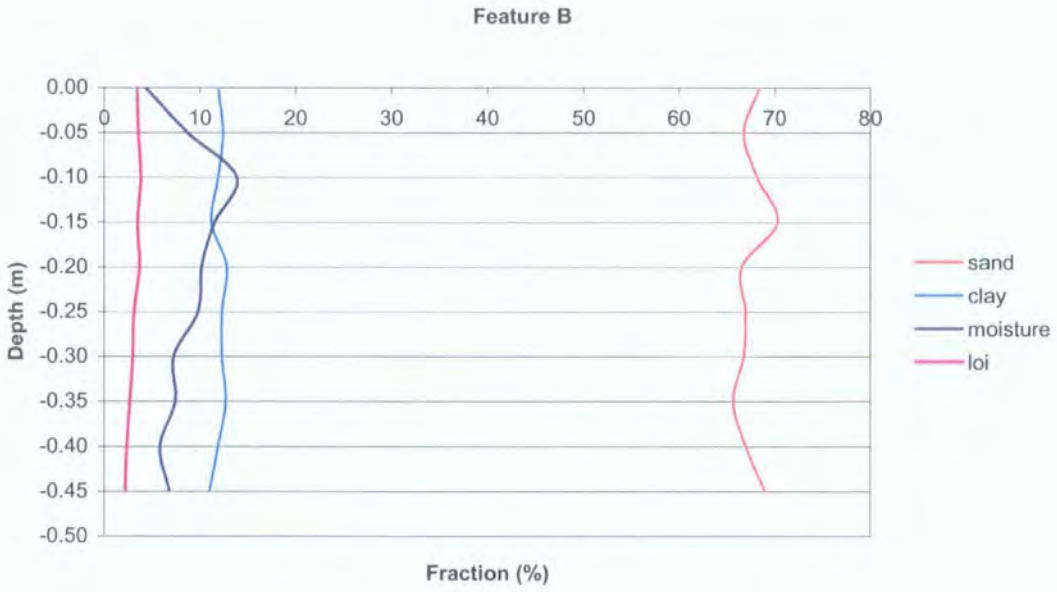

Figure 7.26: Vertical soil profile extracted from Bosworth Feature B

The profile of the clay content shows little variation through depth with values in the 11.00%-12.80% range, with a minimum value recorded at 0.15m and a peak at 0.20m, below which values continually decrease. The profile of the organic content

shows little variation with values in the 2.13%-3.78% range, with a slight peak at 0.10m, below which values continually decrease. The profile of the moisture content shows a more pronounced variation with values in the 4.29%-13.84% range, with a peak occurring at 0.10m, below which values again decrease. The sand fraction gradually increases to 70.20% at 0.15m, below which the values decrease to a minimum at 0.35m with a subsequent increase below this depth. The profiles of the clay, organic and moisture content suggest a variation in physical characteristics of the soil occurring between 0.10m and 0.20m depth. The sand content shows a strong variation at 0.35m similar to Feature A where the pebbles become more widespread and again possibly correlates to the plough depth.

The soil profile extracted above Feature B is compared with the adjacent soil profiles (Insert B). Since the feature is evident on the visible, near-infrared and day and night thermal images then one would expect to see an anomaly in soil properties at the surface and since there is also an ATI anomaly evident in June and August, then one would also expect to see a lateral variation in soil properties at depth, that is if the ATI corresponds to volumetric soil properties beneath the vegetation.

The results of the lateral soil profiles show very similar particle size distribution, moisture content and organic content across the feature with no obvious variation in soil physical characteristics relating to the feature (see Insert B). This suggests that the feature does not represent an anomaly in terms of the vertical properties of the soil and so the feature is more likely to represent a surface vegetation effect.

7.4.3 Feature C

Feature C corresponds to an anomaly seen at visible, near-infrared wavelengths and on day and night thermal images under a barley crop in August 1998 but is not evident under an oil seed rape crop during 2002. The anomaly is also evident on the geophysical image representing a variation in magnetic characteristics of the upper soil layer. Soil profiles are extracted from the feature (core 14), at a 5m southern lateral offset (core 15) and at a 10m southern lateral offset (core 16) for assessment of vertical and lateral trends in soil characteristics. The vertical soil profile extracted from the feature (Figure 7.27) shows a more variable Saxton classification

with depth with loams between 0.00m-0.10m, sandy loams between 0.15m-0.20m, loams between 0.25m-0.30m all sitting on a basal layer of clay loam.

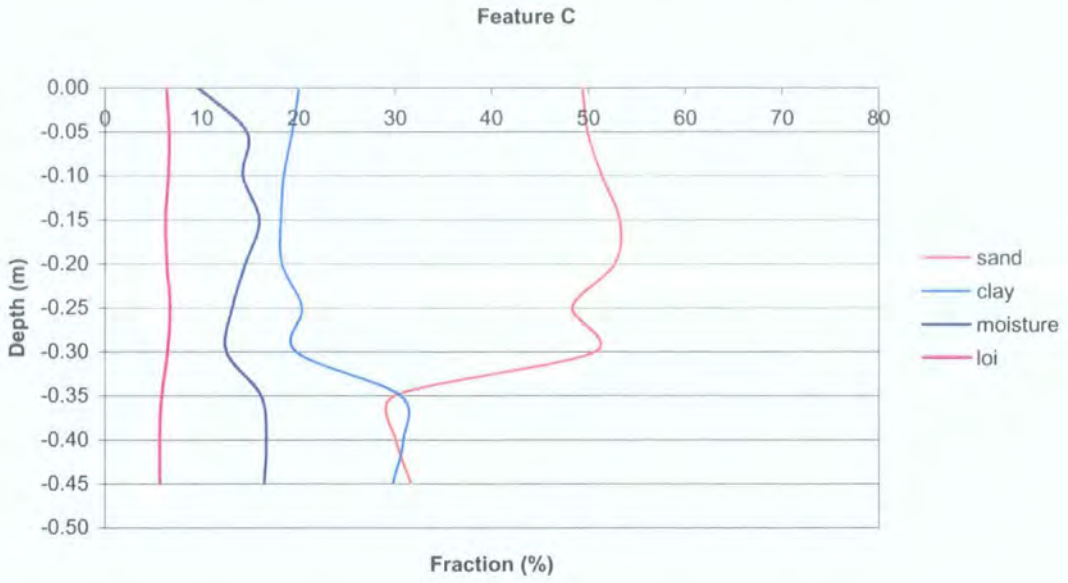

Figure 7.27: Vertical soil profile extracted from Bosworth Feature C

The profile of the clay fraction shows fairly uniform values until a dramatic increase in values from 19.80% at 0.30m to 30.60% at 0.35m. The moisture content gradually decreases with depth to a minimum of 12.57% at 0.30m, below which there is a slight jump to 16.67% at 0.35m followed by a gradual decrease. The profile of the organic content shows little variation through depth with values in the 5.59%-6.68% range, with a slight peak observed at 0.25m. The sand content is fairly uniform at shallower depths until 0.15m-0.30m where there is a much more variable response. There is a dramatic decrease from 50.70% to 30.10% at 0.35m with a gradual increase in sand content below this depth. From the profiles of the sand, clay and moisture content there appears to be a dramatic change in physical soil characteristics occurring between 0.30m and 0.35m. This is similar to the plough depth suggested from the results from Feature A and Feature B. However, since there is a magnetic anomaly evident at this position, the change in physical properties may relate to the presence of a physical feature at this depth in the soil column.

The soil profile extracted from above Feature C is compared with the adjacent soil profiles (Insert C). Since the feature is evident on the visible and near-infrared

channels in August 1998 then maybe one would not expect an anomaly in lateral sand and clay characteristics at the surface, otherwise the feature would be evident on the June 1998 images. Since there is no anomaly on the ATI images at this location, then one would not expect a variation in lateral properties if the ATI corresponds with soil properties beneath the vegetation. However, the presence of a magnetic anomaly at this position suggests a change in soil characteristics down to about 1.00m of observation depth.

The results of the lateral soil profiles show that there is a slight elevation in moisture content at 5m lateral offset to the feature (core 15) between 0.10m and 0.30m depths and little variation in organic content across the feature (see Insert C). There is an abrupt variation in sand and clay pattern across the feature below 0.35m where the core on the actual feature (core 14) shows greatly reduced sand and increased clay fractions. Although this depth corresponds a position to where pebbles become more widespread as for Feature A and B, the variation in sand and clay content is much more dramatic. Since the soil was fairly uniform above 0.35m depth, below which there was an abrupt change in lateral composition, and there was no volumetric ATI anomaly, then ATI may be associated with soils shallower than 0.35m if the parameter corresponds to soil properties beneath the vegetation.

7.4.4 Feature D

Feature D corresponds to an anomaly that is evident on the day, night and ATI thermal images throughout the barley growth in 1998 but is not evident under an oil seed rape crop during 2002. This feature is also represented by a magnetic anomaly. Soil profiles are extracted from the feature (core 20) and at a 5m south-western lateral offset (core 21) for assessment of vertical and lateral trends in soil characteristics. The vertical soil profile extracted from the feature (Figure 7.28) shows no variation in Saxton classification through depth with soils uniformly classified as sandy loams.

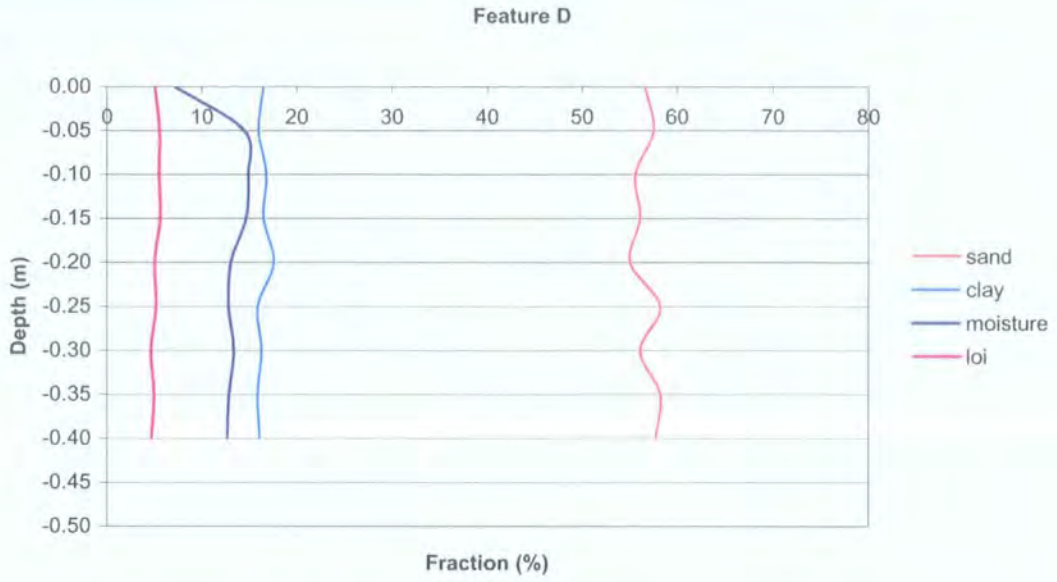

Figure 7.28: Vertical soil profile extracted from Bosworth Feature D

The profile of the organic content shows little variation with values in the 4.63%-5.62% range with a maximum at 0.15m. The profile of the moisture content shows a dramatic increase to 14.99% at 0.10m, below which the moisture content gradually decreases. The profile of the clay content shows little variation through depth with values in the 16.00%-17.70% range, with a maximum occurring at 0.20m. The profile of the sand fraction shows a narrow range from 55.00%-58.20%, with a gradual decrease to 0.20m from the surface below which there is a fluctuation in sand content. The soil profiles suggest a variation in characteristics between 0.10m and 0.20m depth, which is shallower than evident across the other features.

The soil profile extracted above Feature D is compared with the adjacent soil profile (Insert D). Ideally a further soil profile should have been extracted at 10m lateral offset for further evaluation, but this was not acquired. Since the feature is evident as an anomaly on the ATI images then one would expect to see an anomaly in soil properties at depth if the ATI corresponds to volumetric soil properties beneath the vegetation. The results of the lateral soil profiles show a slight increase in surface moisture content associated with the feature that may correlate with the day and night thermal anomaly (see Insert D). There is a slight increase in sand content between 0.10m and 0.20m associated with the feature (core 20), which may correspond with the ATI anomaly if ATI corresponds to volumetric soil properties beneath the vegetation.

7.4.5 Location E

Location E was situated at where the soil showed uniform characteristics throughout the images, thus corresponding to a position where the soil characteristics are not expected to show on the geophysical surveys. Soil profiles were extracted from the location (core 22) and at 5m western lateral offset (core 23) for assessment of vertical and lateral trends in soil characteristics. The vertical soil profile extracted from the feature (Figure 7.29) shows no variation in Saxton classification through depth with soils uniformly classified as sandy loams.

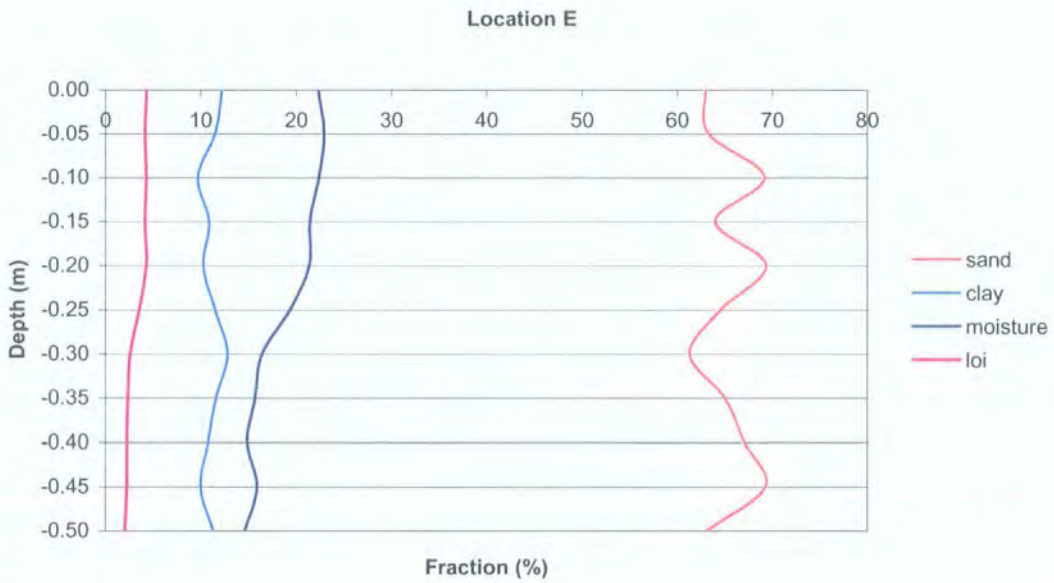

Figure 7.29: Vertical soil profile extracted from Bosworth Location E

The profile of the moisture content shows a gradual decrease from 22.95%-14.82% to depth, suggesting a greater retention of moisture at shallower depths. The profile of the organic content showed a fluctuation in values between 0.00m-0.20m with a gradual decrease in organic content below 0.20m. The profile of the sand content shows values in the 61.20%-69.30% range with a pronounced peak and trough fluctuation in values above 0.20m, with a decrease towards 0.30m, followed by a gradual increase with depth. The profile of the clay content mirrored that of the sand content with a decrease in clay content towards 0.10m that is followed by a gradual rise to 0.30m with subsequent decrease in values below this depth.

The soil profile extracted from Location E is compared with the adjacent soil profile (see Insert E). Since there is no anomaly on the imagery at this location then

would not expect there to be a variation in soil characteristics across the feature at any depth. The organic profile shows no lateral variation through depth. The moisture content is fairly uniform except at 0.25m and 0.30m where there is an increase in moisture of core 23. However, the sand profile shows an elevated value at 0.05m at core 23 and lowered values at 0.40m and 0.45m for this core. If the ATI represents volumetric variations in the soil properties then an anomaly would be expected at this location. Since this is not the case then the ATI is more likely to represent surface temperature variations of the vegetation and not of the underlying soil.

7.4.6 Summary of Compositional Characteristics

The compositional characteristics of the soil were examined by extracting a series of vertical soil profiles at 5m lateral intervals across the features showing variable spectral, thermal and magnetic characteristics. The soils were examined for particle size distribution, moisture and organic content at 0.05m vertical intervals from a trench of 0.50m at each location with examination of the variations in both vertical and lateral profile characteristics.

The anomaly evident at visible and near-infrared wavelengths (Feature A) suggests a surface vegetation difference with variations in moisture and organic content associated with the feature, which affect vegetation growth. Since there was no volumetric ATI anomaly associated with the feature, the soil was expected to show no volumetric compositional variation associated with the feature if ATI corresponds to soil properties beneath the vegetation. The results of the soil analysis showed that there is little variation in soil characteristics through depth associated with this feature, suggesting that the feature is likely to represent spatial variations in the vegetation characteristics.

The anomaly evident at visible and near-infrared wavelengths associated with the abandoned hedgerow boundary (Feature B) again suggests a surface vegetation difference with variations in moisture and organic content associated with the feature affecting vegetation growth. Since the feature was also marked by a thermal anomaly, a variation in surface moisture would also be expected with additional volumetric compositional variations at depth associated with the presence of the ATI anomaly, if ATI corresponds to soil properties beneath the vegetation. The results of the soil

analysis showed very little variation in soil characteristics by depth associated with this feature, suggesting that the ATI anomaly is more likely to represent an effect of temperature variations of the surface vegetation.

The anomaly seen in the August day and night thermal images (Feature C) suggests a difference in surface moisture content, which affects the heating and cooling of the moist surface. Since there was no volumetric ATI anomaly associated with the feature, the soil was expected to show no volumetric compositional variation associated with the feature if ATI corresponds to soil properties beneath the vegetation. However, there may be variations in composition at depth due to the presence of a magnetic anomaly, but it is possible that variations down to 1.00m observed by the magnetometry technique may not be evident in the 0.50m excavation trench. The results of the soil analysis showed that there was an anomaly in moisture content at the soil surface adjacent to the feature. Since the soil was fairly uniform above 0.35m and there was no volumetric ATI anomaly, then ATI may be associated with soils shallower than 0.35m if this parameter corresponds to soil properties beneath the vegetation, otherwise the variation in lateral compositional characteristics would have produced an ATI anomaly. However, the results from Feature B where there was an ATI anomaly and there were no compositional variations through depth strongly suggest that ATI may correspond to an effect of temperature variations of the surface vegetation.

The thermal day, night and ATI anomaly (Feature D) suggests a difference in surface moisture content, which affects the heating and cooling of the moist surface, and also volumetric compositional variations if ATI corresponds to soil properties beneath the vegetation. There may also be a variation in composition at depth due to the presence of the magnetic anomaly, but it was possible that variations down to 1.00m observed by the magnetometry technique may not be evident in the 0.50m excavation trench. The results of the soil analysis showed that there was a variation in surface moisture content that may be associated with the day and night thermal feature. There was also a volumetric variation in sand content between 0.10m and 0.20m that may correspond with the ATI anomaly. Since the variation in soil characteristics is only very slight between the two profiles (<4%) it is difficult to be confident that the ATI anomaly may relate to volumetric properties between 0.0m and

0.20m without extracting a further soil profile at 10m lateral offset and assessing the background characteristics. The results from Feature B suggested that the ATI anomaly is more likely to represent an effect of temperature variations of the surface vegetation and this may explain the ATI anomaly at Feature D.

Location E marks an area where no anomalies were apparent no the visible, near-infrared, thermal, ATI and magnetic images. The non-anomalous characteristics suggest that there should be no variation in moisture or organic content, since this would be expected to affect vegetation condition at the surface observed at visible, near-infrared and thermal wavelengths. Since there is a lack of an anomaly on the ATI images at this position, no difference in volumetric composition would also be expected if the ATI corresponds to soil properties beneath the vegetation. The results of the soil analysis showed no variation in organic content, as expected, although the soil did show a difference in moisture content between 0.25m and 0.30m with a variation in composition between 0.40m and 0.45m. Since there is no volumetric ATI anomaly at this location and the soil showed a clear compositional variation, then the ATI anomaly is more likely to represent an effect of temperature variations of the surface vegetation, as was suggested from the results from the other sites.

The results from these specific features suggest that visible, near-infrared and day and night thermal anomalies tend to correspond to variations in moisture content at the surface. There was a poor correlation between the magnetic anomalies and the soil characteristics at depth, suggesting that the variations down to 1.00m observed by the magnetometry technique are not evident within the 0.50m excavation trench. The results from the ATI assessment are more variable with suggestions that the ATI is likely to represent an effect of temperature variations of the surface vegetation. In order to assess the ATI characteristics more fully, the lateral properties of the soil are numerically compared with the ATI values recorded over the same features to assess whether the observed variations in ATI value can indicate variations in true physical characteristics of the soil. This is discussed in the following chapter and examines the necessity to determine the ATI for detecting subsurface soil characteristics beneath a layer of vegetation.

8 DISCUSSION

The main aims of the thesis are to investigate the use of multispectral airborne remote sensing techniques and ground geophysical prospection for detecting shallow ground disturbance beneath a layer of vegetation and to examine the relationship between airborne thermal radiance data and the characteristics of surface materials beneath a layer of vegetation. The vegetation effect is particularly important for detecting shallow ground disturbance in the UK where the majority of the ground surface is covered by agricultural crops that mask the underlying soil from direct observation from above the canopy.

The previous chapter assessed the dynamics of the heat flux in the soil-vegetation system at an instrumented site in Bosworth where accessibility to land enabled monitoring of the soil thermal characteristics beneath growing vegetation. The results from the study indicated that there was less of a contrast between the diurnal temperature extremes of the soil as the vegetation matures, suggesting that mature vegetation masks the underlying soil from direct solar heating processes. In addition, the contrast between the diurnal temperature extremes diminishes as the observation depth increases in the soil column with the dissipation of the diurnal heating and cooling pattern occurring between 0.20m and 0.50m in early stages of vegetation growth and occurring closer to 0.20m at later stages in vegetation growth. The results from the ground thermal observation suggests that if ATI can be used for assessing volumetric parameters, then the depth of diurnal heat penetration may be an important issue for detecting variations within the vertical soil layer occurring above these depths. The thermal characteristics also show the time when the surface is at its maximum temperature and when it is at its minimum temperature alters as the vegetation grows. From the extensive contact temperature measurements, the soil surface reaches its maximum temperature between 14:00-15:00 local time with minimum temperatures recorded progressively later from 06:00-09:30 the following morning as the vegetation grows. This will have implications on the appropriate times for thermal observation above the canopy for detecting features relating to soil properties.

The previous chapter also assessed the compositional properties of the soil column over specific features of variable visible, near-infrared and thermal characteristics. This was again performed at only the Bosworth site due to accessibility to the land for soil extraction for laboratory analysis and also since the diurnal thermal images acquired over this study site could be calibrated to ground temperature enabling ATI calculation. Although diurnal thermal images were acquired over Baildon Moor and Weardale, the lack of ground temperature measurements prevents calculation of ATI for these environmental settings. The results of the soil analysis from the specific features suggest that the anomalies at visible, near-infrared and day and night thermal wavelengths, which are more easily detected at early stages in vegetation development, tend to correspond to lateral variations in moisture content at the surface. This suggests that observation above the canopy at these wavelengths when the vegetation is under-developed may provide a suitable method of detecting variations in the very near-surface based on soil moisture differences between the disturbed and undisturbed soils.

However, one of the main issues of the research is to determine whether ATI can be used to detect volumetric variations within the soil column. If ATI represents volumetric variations as suggested by the inclusion of density in the definition of thermal inertia (Price, 1977) then one would expect a variation in the organic, moisture, sand or clay content, or a combination of all properties. When the lateral soil properties were assessed in the previous chapter with respect to the position of an ATI anomaly, the results suggested that since there was little lateral soil variation where the ATI feature occurs the ATI anomaly was more likely to represent an effect of variations in the temperature of the surface vegetation, probably relating to structural variations within the vegetation. However, these results were based on a purely visual assessment of the lateral soil properties with respect to the presence of anomalies evident on the ATI images.

A more quantitative approach for assessing whether ATI can be used to detect volumetric variations within the soil column can be performed by looking at the correlation between the ATI and soil characteristics across specific features. This is performed using a standard correlation technique where correlation coefficients are generated for the relationship between the lateral ATI values and soil properties for

each depth in the soil column. Specific features from the Bosworth study site are selected for discussion, due to limited soil sampling across the remaining features, providing some examples of feature of different ATI and multispectral characteristics. The correlation analysis is restricted to assessment of the features where soil profiles were extracted on the feature, at 5m and 10m lateral offset. As a result, the analysis can only be used to indicate possible trends in the data and is not statistically robust. The features assessed using the correlation analysis correspond to Features A, B and C that coincide with the position of soil extraction (Figure 7.24), with Feature B providing the only location where an anomaly is evident on the ATI imagery. When the ATI profiles are extracted across the specific features it is immediately apparent that the range of values observed for the June imagery is much smaller than that observed for the August imagery (Figure 8.1).

Since the thermal images were acquired under similar meteorological conditions, the variation in the range of ATI values between June 1998 and August 1998 for each feature was initially thought to represent the variations in the condition of the vegetation. In June 1998 the field was covered with an under-developed cereal crop of barley, but in August 1998 the cereal crop was fully mature. This implies that a greater resistance to temperature change is observed at a later stage in crop maturity. However, another possible explanation for the variation in ATI values is that the thermal images were not acquired when the surface displayed the maximum temperature contrast on each observation date. From the ground contact measurements it is known that the surface displays a maximum temperature between 14:00-15:00 local time, however, the day thermal image from August 1998 was acquired 10:00 suggesting that the surface would have still been heating up. When histograms were extracted for specific man-made features there was a clear variation in the range of ATI values observed between June 1998 and August 1998 (see Chapter 6.5). Since man-made materials are not expected to show seasonality in response, this suggests that there may be a miscalibration of the thermal images to ground temperature.

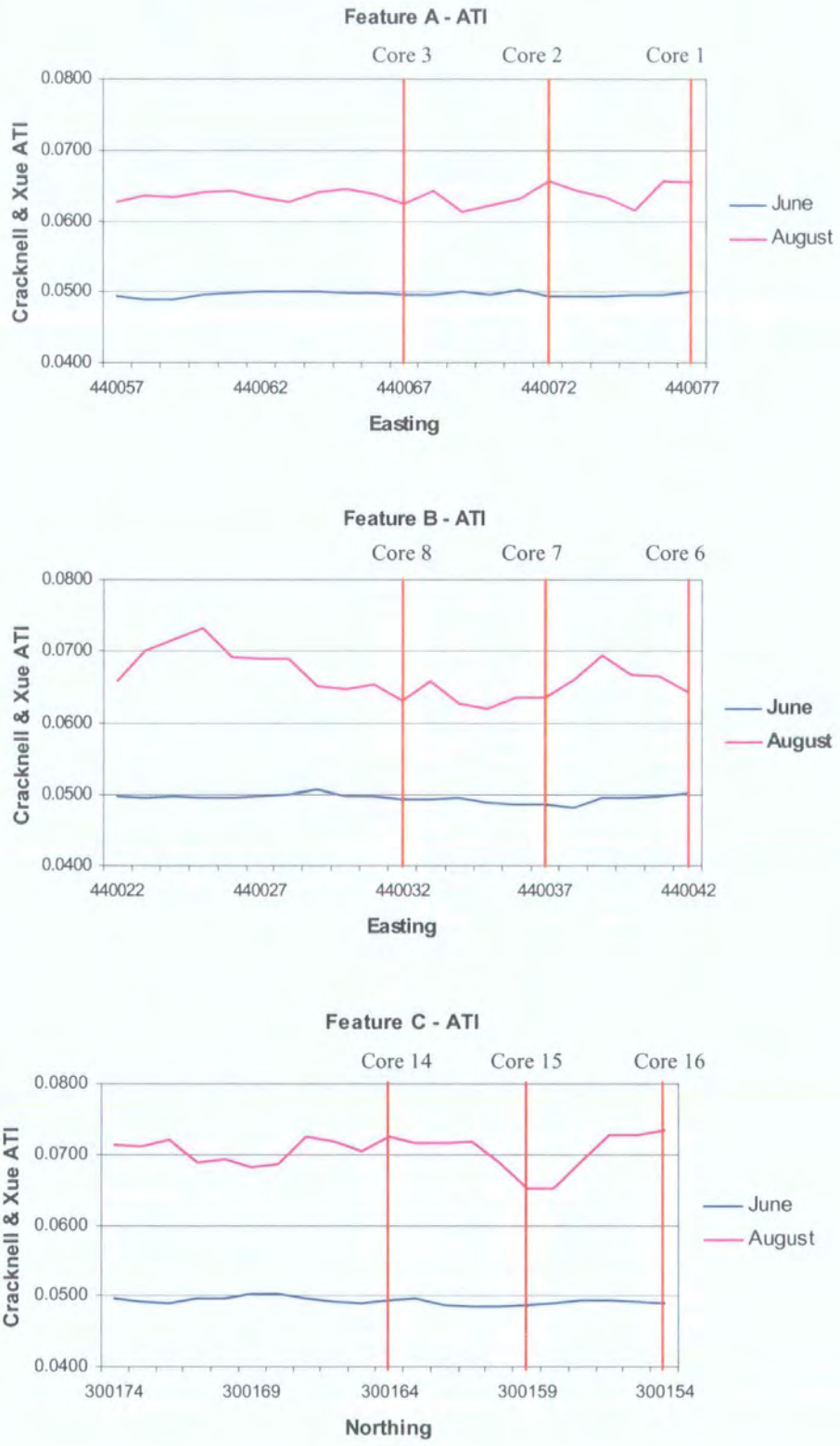

Figure 8.1: June and August ATI profiles across specific Bosworth features

Although there is a different range of ATI values between the observation dates, the correlation analysis relates the shape of the ATI profile to the shape of the soil profile across each feature.

Since there was no volumetric ATI anomaly associated with the Feature A, then one would not expect to observe a high correlation between the ATI and soil profiles if the volumetric ATI parameter corresponds to variations in soil properties beneath the vegetation. Results from the correlation analysis for Feature A (Table 8.1) suggest that the June 1998 ATI profile appears to be strongly correlated with the sand and clay profiles at 0.45m, with a high correlation with moisture content at 0.25m and organic content at 0.05m. The August 1998 ATI profile shows a negative correlation with the sand and clay properties near the surface at 0.05m, with a high correlation with moisture content at 0.30m and organic content at 0.40m. However, since this feature did not represent a visible ATI anomaly then the correlation between the ATI and volumetric soil properties may be purely coincidental and may be a result of the limited soil sampling.

JUNE under-developed barley

DEPTH	SAND	CLAY	MOISTURE	ORGANIC
0.00m	-0.34	0.54	0.20	0.56
0.05m	-0.02	-0.27	0.64	1.00
0.10m	N/A	N/A	0.58	0.99
0.15m	-0.73	0.67	-0.41	0.14
0.20m	-0.86	0.74	-0.88	0.96
0.25m	-0.99	0.98	0.99	0.98
0.30m	-0.98	0.94	-0.20	-0.98
0.35m	-0.93	0.92	-0.71	-0.37
0.40m	-0.86	0.85	0.56	0.03
0.45m	-1.00	0.99	-0.24	0.42

AUGUST mature barley

DEPTH	SAND	CLAY	MOISTURE	ORGANIC
0.00m	-0.98	0.91	-0.94	0.89
0.05m	-0.99	0.92	-0.67	0.22
0.10m	N/A	N/A	0.89	0.28
0.15m	-0.78	0.82	-0.96	-0.96
0.20m	-0.62	0.77	0.36	-0.15
0.25m	0.04	-0.06	0.28	-0.04
0.30m	-0.34	0.45	-1.00	0.05
0.35m	-0.49	0.51	-0.79	-0.97
0.40m	-0.62	0.63	-0.75	-0.99
0.45m	-0.17	0.00	-0.99	-0.84

Table 8.1: Correlation of ATI with soil properties across Bosworth Feature A

Since Feature B was marked by an ATI anomaly on the imagery then one would expect to observe a high correlation between the ATI and soil profiles if the volumetric ATI parameter corresponds to variations in soil properties beneath the vegetation. Results from the correlation analysis for Feature B (Table 8.2) suggest that the June 1998 ATI profile shows a strong correlation with the sand and clay profiles at 0.10m, with a high correlation with moisture content at 0.20m and organic content at the surface. The August 1998 ATI profile shows moderately high correlation values of –0.75 and 0.74 with the sand and clay profiles respectively at 0.15m, with a high correlation of 1.00 with moisture content at 0.05m and organic content at 0.25m. The strongest correlation between the ATI and soil profiles occurs at shallower depths than was apparent for Feature A where there was no ATI anomaly. The possible implications of this is that the anomaly on the ATI images at Feature B may correspond to variations in moisture content at the very near-surface at both stage in development of the barley crop, as was suggested by Pratt & Ellyett (1979). Although this is corroborated by the comparison between the resistivity survey, which is sensitive to soil moisture differences (Kearey & Brooks, 1991; Reynolds, 1997), and the ATI images in the grass-covered fields (Figures 6.22 and 6.23), the results are still inconclusive since Feature B shows a similar correlation pattern to Feature A where there was no ATI anomaly, which may again be a result of the limited soil sampling.

JUNE under-developed barley

DEPTH	SAND	CLAY	MOISTURE	ORGANIC
0.00m	-0.99	1.00	-0.04	1.00
0.05m	-0.89	0.94	-0.58	0.96
0.10m	-1.00	1.00	-0.15	0.97
0.15m	-0.96	0.96	-0.12	0.96
0.20m	-0.47	0.35	-1.00	0.89
0.25m	-0.80	0.88	0.14	0.53
0.30m	-0.99	1.00	-0.62	0.75
0.35m	-0.32	0.74	0.44	0.97

AUGUST mature barley

DEPTH	SAND	CLAY	MOISTURE	ORGANIC
0.00m	-0.42	0.46	0.83	0.58
0.05m	-0.08	0.21	-1.00	0.29
0.10m	-0.52	0.57	-0.92	0.32
0.15m	-0.75	0.74	-0.90	0.75
0.20m	0.50	-0.61	-0.45	0.86
0.25m	0.09	0.05	-0.76	1.00
0.30m	-0.38	0.52	0.34	0.96
0.35m	0.64	-0.18	-0.53	0.71

Table 8.2: Correlation of ATI with soil properties across Bosworth Feature B

Since there was no volumetric ATI anomaly associated with Feature C then one would expect to observe a low correlation between the ATI and soil profiles if the volumetric ATI parameter corresponds to variations in soil properties beneath the vegetation. Results from the correlation analysis for Feature C (Table 8.3) suggest that the June 1998 ATI profile shows a strong correlation with the sand and clay profiles at 0.45m, with high correlation with moisture content at 0.15m and organic content at 0.25m. The August 1998 ATI profile shows only a poor correlation with the sand, clay and organic profiles in the near-surface environment, with a high correlation with moisture content at 0.10m. The correlation pattern for this feature is similar in June 1998 when the barley crop is under-developed to that observed at Feature A, where there was also no ATI anomaly. However, the correlation pattern is different when the barley crop is more mature, which may be a result of canopy closure with Feature C representing soil moisture differences that may be masked from observation at Feature A. However, the reason for the variation between the features is inconclusive due to the limited soil sampling.

JUNE under-developed barley

DEPTH	SAND	CLAY	MOISTURE	ORGANIC
0.00m	-0.83	0.81	-0.37	0.40
0.05m	-0.85	0.82	0.25	0.62
0.10m	-0.56	0.49	-0.70	0.50
0.15m	-0.65	0.62	-0.99	0.38
0.20m	-0.52	0.58	-0.92	0.62
0.25m	-0.74	0.76	-0.22	1.00
0.30m	-0.82	0.81	-0.16	0.76
0.35m	-0.93	0.93	0.68	0.75
0.40m	-0.88	0.89	0.67	0.77
0.45m	-0.94	0.93	0.78	0.92

AUGUST mature barley

DEPTH	SAND	CLAY	MOISTURE	ORGANIC
0.00m	0.02	-0.06	0.58	-0.56
0.05m	-0.02	-0.04	-0.68	-0.33
0.10m	0.40	-0.47	-0.98	-0.46
0.15m	0.29	-0.33	-0.42	-0.57
0.20m	0.44	-0.38	-0.83	-0.33
0.25m	0.17	-0.14	-0.94	0.56
0.30m	0.05	-0.06	-0.92	-0.13
0.35m	-0.18	-0.18	-0.25	-0.16
0.40m	-0.07	-0.09	-0.26	-0.13
0.45m	-0.21	0.19	-0.10	0.17

Table 8.3: Correlation of ATI with soil properties across Feature C

Feature B is the only feature that showed an anomaly on the ATI images. However, the results from these correlation analyses between the ATI and soil profiles are inconclusive since there were similar correlation coefficients for features where an ATI anomaly existed and where there was no ATI anomaly. Price (1977) suggested that thermal inertia could be used to infer surface properties in the order of 0.10m depth. However, the results from this study suggest that thermal inertia may correspond to temperature effects of the surface vegetation that may be caused by variations in the structure of the vegetation.

When the ATI and soil characteristics are correlated using an alternative graphical matrix approach (Figure 8.2), the correlation in the data can be quickly assessed where clusters of points suggest homogeneous characteristics with outliers corresponding to anomalous characteristics. In the graphic matrix, points are plotted to represent the inter-relationship between the ATI and soil properties. The results of the graphical matrix approach show that there is little variation in the clustering of points between the June and August images for each feature. This suggests that there is little dependence of the seasonal ATI values on the soil characteristics. This is particularly noticeable for Feature B, which is the only feature corresponding to an anomaly on the ATI images. The results for this feature exhibit a strong clustering of points on both June and August graphs suggesting relatively homogeneous soil characteristics and this clustering pattern is very similar to that exhibited by Feature A. Since there is no anomaly on the ATI images associated with Feature A, this implies that ATI is unlikely to be affected by variations in the physical characteristics of the soil beneath the vegetation and is more likely to correspond to differences in the temperature response of the surface vegetation.

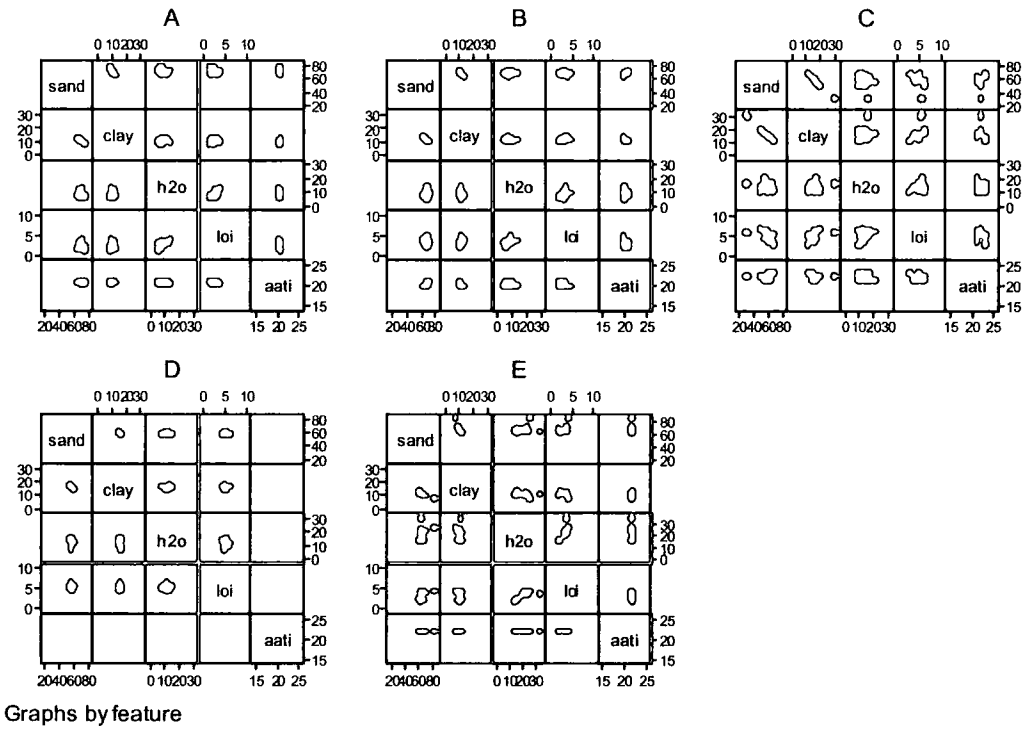

June ATI

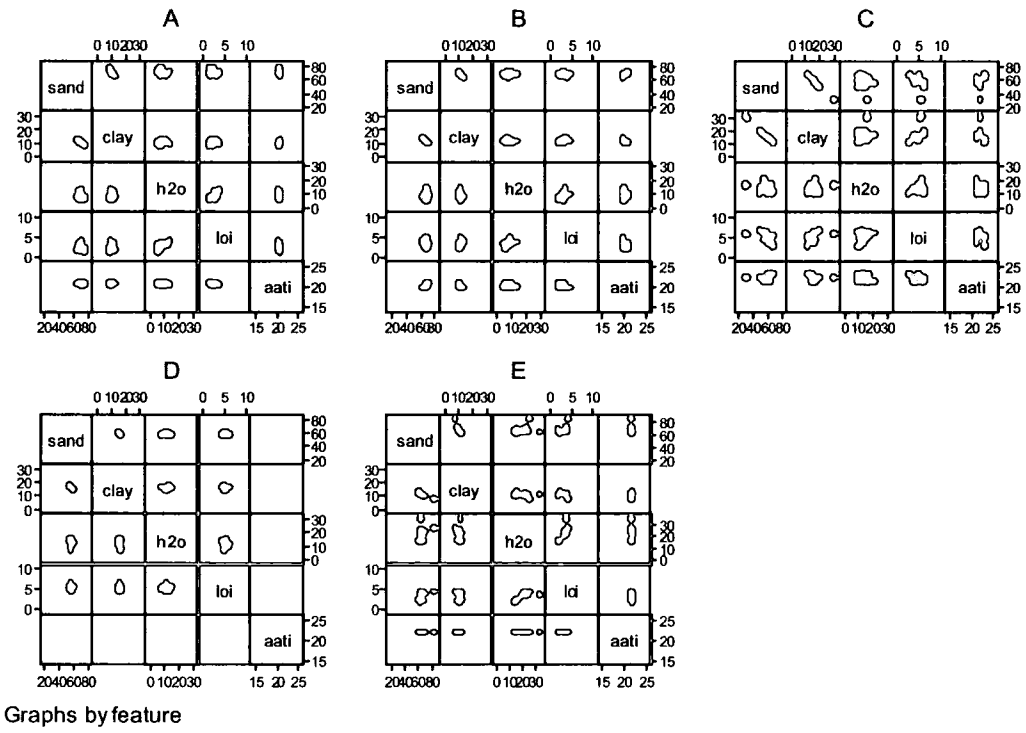

August ATI

Figure 8.2: Matrices generated for soil and ATI characteristics for each Bosworth feature

The results from the correlation analysis suggest that there is a poor correlation between the ATI and the sand and clay profiles, observed at the different times in the growth of the barley crop, with the ATI showing a strong dependence on the moisture content, as suggested by Pratt & Ellyett (1979). This is corroborated by results from field assessment where the magnetometry survey, which is sensitive to the composition of the soil materials (Scollar, 1990; Kearey & Brooks, 1991), show a poor correlation with the June ATI (Figure 6.20) and August ATI (Figure 6.21) images. The results from the resistivity survey, which is sensitive to moisture content (Kearey & Brooks, 1991; Reynolds, 1997), also corroborates the Pratt & Ellyett (1979) findings with a strong correlation with the June ATI (Figure 6.22) and August ATI (Figure 6.23) images. Although this discussion has focussed on the characteristics of the correlation between the ATI images and the soil characteristics at the Bosworth study site, this soil moisture effect concurs with the results from the Baildon Moor study site, where the thermal images of Baildon Moor show a series of circular mineshafts (Figure 5.35) where structural differences exist between the shaft and the undisturbed surrounding soil. These features also show anomalies in the resistivity profiles (Figure 5.44) suggesting a close relation between anomalies at thermal wavelengths with soil moisture differences.

From the above discussion, the method of applying ATI models to diurnal thermal images can provide useful detail on the moisture properties of the soil just beneath the surface when an open vegetation canopy, such as short grass or an under-developed barley crop, covers the soil. This has particular implications for geological and archaeological applications in the UK environment where the ground surface is predominantly covered by a layer of vegetation and features in the near-surface cause differences in the soil properties and may be masked from observation in visible and near-infrared wavelengths above the canopy. If the ATI modelling approach is to be used in such situations, a specific set of processing steps need to be defined so that the assessment can be executed efficiently.

First of all, it is important to acquire day and night thermal images at times in the diurnal cycle when the surface is at its maximum temperature and is also at its minimum temperature. Times when the surface is at its maximum and minimum temperatures are established from the time series obtained from ground based contact

measurements of soil temperature at the Bosworth site. From the heating curve observed during this experiment, the time when the surface is at its maximum temperature occurs between 14:00-15:00 local time with the time when the surface is at its minimum temperature occurring progressively later from 06:00-09:30 the following morning as the vegetation develops (Chapter 7.2.5). In practice it can be difficult to acquire images at such specific times, especially if the study site covers a large spatial area. There are also the logistical problems associated with flying at night and additional problems of ensuring that there are similar meteorological conditions between the day and night flights. If there are too many constraints on image acquisition then there is less chance that the images will be obtained at all. However, even with these factors taken into account and a thermal image pair acquired at appropriate time across the diurnal cycle, there still remains an issue of the time-scale involved in processing the data prior to assessment. Table 8.4 gives an indication of the processing steps involved for efficient modelling of the data, together with an example of the time involved for processing of a single flightline using each procedure.

DAY-NIGHT ATI MODELLING
Radiometric Calibration (specifically performed by NERC ARSF prior to handling)
Temperature Calibration Acquisition of ground temperature measurements over specific target materials simultaneously to flight (data logged automatically over 24-hour cycle) Empirical Line Calibration of thermal image using ground temperature values (30 minutes per image)
Geometric Co-registration Ground Control Point Collection (6 hours per day-night pair) NERC Automatic Geocorrection Software with subsequent GCP collection (4 hours per flightline)
ATI Modelling Cracknell & Xue (1996) model

Table 8.4: Processing steps for generation of ATI images using Cracknell & Xue (1996) model

The first step is to radiometrically calibrate the images. When using data from the Airborne Thematic Mapper, the images are radiometrically calibrated by the NERC Airborne Remote Sensing Facility prior to handling and require no additional radiometric calibration (Chapter 4.2). Following this, the thermal radiance is calibrated to ground temperature using temperature values recorded over specific

target materials simultaneously to the flight using an Empirical Line Calibration (Chapter 4.5.1.1). Once the day and night thermal images are calibrated to ground temperature, they require individual geometric correction so that the images have the geometric integrity of a map and can be directly lain on top of each other. This is best achieved using Ground Control Point Collection for small areas (Chapter 4.3.1) with an automatic approach for larger coverage using software supplied by NERC with additional geocorrection required to ensure direct overlay (Chapter 4.3.2). The day and night thermal images are then run through the Cracknell & Xue (1996) ATI model with an appropriate value for surface albedo for assessment of the surface characteristics.

However, the results from this research suggest that the ATI approach may not be entirely necessary for surface assessment under similar environmental conditions. In order to consider the necessity for ATI modelling, the results of the ATI technique were compared with the results of the visible, near-infrared and thermal visualisations. This shall be illustrated using specific examples of features occurring under different vegetation conditions from the Bosworth site. The variability between the multispectral, thermal and ATI response is demonstrated using Feature B representing the abandoned hedgerow in Ambion field where the surface is covered by a barley crop in 2001 (Figure 7.24) and a linear feature in the Helipad field where the surface is permanently covered by grass (Figure 6.11). These features are both evident on the June and August ATI images.

The abandoned hedgerow boundary shows a decrease in visibility between June and August on both natural colour composites (Figure 5.52) and near-infrared false-colour composite (Figure 5.53) as the barley matures. When the day and night thermal images are visualised, the feature is also evident on both images with a more prominent response at night (Figure 6.8). Although this feature is also evident on the June and August ATI images (Figure 6.8), this suggests that there is no real benefit to using the ATI approach for detection of this feature in the barley-covered field and suggests that the maximum detail relating to soil moisture may be extracted from visualisation of the night thermal image.

The linear feature in the Helipad field is evident on the June natural colour composites (Figure 5.52) and near-infrared false-colour composites (Figure 5.53) but

is completely absent from the same colour composites using the August data as the grass develops. This feature also displays a strong decrease in visibility on the day thermal images and is completely absent from both night thermal images (Figure 6.8). Although this feature is also evident on the June and August ATI images (Figure 6.8), the results closely match those of the day thermal image suggesting that there is once again no real benefit to using the ATI approach for detection of this feature in the grass-covered field and suggests that the maximum detail relating to soil moisture may be extracted from visualisation of the day thermal image.

It is clear from this assessment that the ATI approach may provide complementary information to the standard method of ground geophysical investigation. However, the results of the ATI modelling are similar to those established from visualisation of the visible, near-infrared or day and night thermal images in which case there is no real need for co-registration of the day and night thermal images and removes the problems involved in acquiring a diurnal thermal image pair. In order to get the maximum information from the data without the ATI modelling approach it is therefore important to understand the time-scale involved and the necessary processing steps required prior to assessment. Table 8.5 gives an indication of the processing steps involved for efficient assessment of the data, together with an example of the time involved for processing of a single flightline using each procedure.

QUALITATIVE ASSESSMENT
Radiometric Calibration (specifically performed by NERC ARSF prior to handling)
Atmospheric Correction Acquisition of ground spectral measurements over specific target materials simultaneously to flight (2 hours)
Geometric Correction Ground Control Point Collection (3 hours per flightline – minimum of 100 GCP per flightline) Automatic Geocorrection (2 hours per flightline)
Principal Component Analysis (1 hour per flightline)

Table 8.5: Processing steps for assessment of multispectral images

The processing steps are similar to those executed for the ATI assessment. The NERC Airborne Remote Sensing Facility radiometrically calibrates the data prior to handling. Atmospheric effects are then removed from the visible and near-infrared

wavelengths using an Empirical Line Calibration and ground spectral measurements recorded over specific target materials simultaneously to the flight. Geometric distortions are then removed from the data using Ground Control Point Collection for small areas or an automatic approach for larger coverage using software supplied by NERC. The spectral variability of the data is then assessed through a Principal Component Analysis (Chapter 5.5.3) for assessment of the surface characteristics.

The above discussion has shown that the day and night thermal images acquired by the single-band thermal system can be used to model the ATI of the surface and can give an indication of variations in moisture content in the soil beneath a layer of vegetation, which is shown through the strong correlation with the results of the resistivity survey, which is sensitive to soil moisture differences. Comparison of the ATI results with the resistivity survey gives particularly good results when the surface is covered by short grass or under-developed cereal crop. Although the ATI appears to be a useful complementary tool to conventional geophysical prospection techniques, there appears to be no real benefit for surface assessment than provided by visualisation of the visible, near-infrared and thermal wavelengths. In addition, the poor correlation between the volumetric ATI values and the soil characteristics extracted over specific feature suggest that the ATI technique may correspond to surficial surface temperature effects of the vegetation rather than characteristics of the soil beneath the vegetation.

9 CONCLUSIONS and RECOMMENDATIONS

The thesis has examined the use of multispectral and thermal airborne remote sensing techniques and ground-based geophysical prospection for detecting shallow ground disturbance beneath a layer of vegetation and has examined the relationship between thermal radiance data and the characteristics of surface materials beneath a layer of vegetation. The following section reviews the specific set of aims and objectives outlined in the introduction (Chapter 1) and discusses the relative outcomes, problems and possible solutions raised in each issue.

9.1 EVALUATION of AIMS and OBJECTIVES

The original aims of the study were:

1. To investigate the use of multispectral and thermal airborne remote sensing techniques and ground geophysical prospection for detecting shallow ground disturbance beneath a layer of vegetation

The research has concentrated on three environmental situations over which multispectral and thermal images were acquired. In order to show the variation in feature detection throughout the multispectral and thermal wavelengths, this can be illustrated by using one of these particular settings, that of the buried archaeology at the Bosworth study site, and examining the visibility of a particular feature at different wavelengths and times in vegetation growth. Images are displayed for two stages in the cereal crop growth with June representing a time when the surface was covered by an under-developed barley crop and August representing a time when the surface was covered by a mature barley crop. Additional images are displayed for March when the surface was covered with a leafy crop of oil seed rape. An abandoned hedgerow boundary is evident on natural colour and near-infrared false-colour composites at both stages in barley development, although the feature is less evident when the crop is more mature. The feature is clearly evident on the day and night thermal images at both stages in barley growth, with a more consistent visibility on the night thermal images. This feature is completely absent when the surface is covered by oil seed rape. The conclusion is therefore that features can be more easily

detected during an early stage in cereal growth, with a leafy crop being unsuitable for feature detection, with enhancement of visibility using night thermal radiance.

2. To examine the relationship between airborne thermal radiance data and the characteristics of surface materials beneath a layer of vegetation

This aim was investigated by considering the set of specific objectives outlined in the introduction and acquiring additional ground geophysical detail on the surface composition beneath the vegetation. The objectives outlined in Chapter 1 are discussed below together with comments on the individual issues.

2.1 To produce fully processed Daedalus-1268 Airborne Thematic Mapper images at visible, near-infrared, shortwave infrared and thermal infrared wavelengths provided by the NERC Airborne Remote Sensing Facility for the study sites

Radiometric, geometric and atmospheric correction was applied to the seasonal Bosworth images with removal of atmospheric effects, using ground spectral reflectance measurements synchronous to airborne acquisition over vast array of surface materials. Geometric distortion was removed through ground control point collection, which was simple to perform on the Bosworth and Baildon Moor images due to the availability of detailed base map data and a relatively small spatial coverage of the study site. The Weardale images were geometrically corrected using automatic geocorrection software provided by NERC that uses the coordinates of the platform recorded for each pixel. However, the output showed poor correlation with a base map, which may have been a result of the high topographic range occurring over the area. This dataset required additional ground control point collection and due to the large spatial coverage of the study site this proved to be very time consuming. It was not possible to remove atmospheric effects from the Baildon Moor images due to lack of coincidental ground spectral measurements nor from the Weardale images due to a combination of restricted access to land and equipment failure during acquisition. The results from this research suggest that it is not always possible to perform satisfactory atmospheric or geometric correction on the NERC ATM images and that it is not always easy to carry out some of the techniques. This has implications for other similar studies where staff input may be more restricted.

2.2 To provide co-registered day and night thermal images of the study sites

Accurate co-registration of the day and night thermal images ideally requires the use of identical ground control points from the day and night images for a similar warping effect with mosaicking along field boundaries where several images cover the study site. Problems arise where there may be different shadow effects such as occurring from buildings, hedgerows and trees. In addition, some features are not easily recognised on both day and night thermal images where there may be little temperature contrast compared to the surrounding materials. Sufficiently accurate co-registration was performed on the Bosworth images by using the same ground control points for each image. The ground control point collection method was more difficult to perform for the abandoned mineshafts on the Baildon Moor images due to the differential topographic shadow effects with a poor thermal contrast in some of the control point features on the night thermal images. The Weardale images showed very poor day and night co-registration suggesting that the onboard inertial navigation system of the airborne platform may not have been sufficiently integrated with the ATM pixel positions resulting in misalignment of the day and night images generated from the automatic geocorrection process. This has serious implications for using the NERC system for apparent thermal inertia studies, where the day-night contrast can only be sufficiently calculated using the ground control point geocorrection method and may be very time consuming for large study areas.

2.3 To provide co-registered multi-temporal images of the study sites

Accurate co-registration of the seasonal images also ideally requires the use of identical ground control points from the seasonal images for a similar warping effect with mosaicking along field boundaries where several images cover the study site. Again problems arise in differential shadow effects caused as the sun angle varies throughout year with respect to a particular feature. Problems also arise from differential vegetation growth with some features showing similar response to surrounding materials at different times in vegetation growth and substantial tree crown development and leaf area index masking underlying and surrounding materials. Co-registered images were produced for the Bosworth study site using the same ground control points for each image. Although there was a second day and night image pair acquired over Baildon Moor, the second dataset contained excessive noise and was unused. There were no additional images acquired over Weardale

preventing seasonal co-registration. As a result, co-registered images were provided for only the Bosworth study site and provided the only study site with which to assess the effect of vegetation growth on the visibility of features.

2.4 To calibrate airborne thermal radiance measurements to surface temperature values

Attempts to use the established Planck radiation law to convert the thermal radiance measured by the ATM to ground temperature produced inaccurate results for pixels whose ATM radiance and ground temperature were known. Even when the units of radiance measured by the ATM were converted into the same units used in the Planck relationship, there was still a discrepancy between the ATM radiance of known surface temperature and the Planck radiance calculated using the known temperature. The cause of this discrepancy is unknown. An alternative method was to use ground temperature measurements and convert the thermal radiance to temperature using an empirical line calibration method. This was performed for the Bosworth dataset where numerous ground temperatures were recorded over a range of materials using thermal probes. The thermal radiance acquired over Baildon Moor could not be converted to ground temperature due to a lack of coincidental surface temperature measurements for use in the empirical line calibration technique. Although surface temperatures were measured at Weardale, the temperatures showed little variation across the different materials and were unfortunately clustered on a single ATM image and were not spread across the three main ATM images that covered the study site. As a result the empirical line temperature calibration method was inaccurate for the Weardale dataset. The inability to easily calibrate the ATM thermal radiance to surface temperature poses a problem for thermal studies, especially where apparent thermal inertia requires accurate day and night temperature values for calculation of the temperature contrast of the surface. This suggests that the NERC ATM thermal data is inadequate for radiance calibration and also has implications for multitemporal work.

2.5 To assess the suitability of applying published Apparent Thermal Inertia Models to environmental applications

Apparent Thermal Inertia modelling requires accurate calibration of day and night thermal radiance, acquired when the temperature contrast of the surface is maximised,

to surface temperature values observed over specific target materials synchronous to airborne image acquisition. The results from the ATI modelling show that there is little variation in the output of the established ATI models (see Chapter 6.5). This is caused by variations in only the scaling factors between the Price (1977) and Cracknell & Xue (1996) models with the insufficient knowledge of the heat flux ratio between the ground and atmosphere in the Kahle & Alley (1985) model resulting in a similar constant scaling factor for each pixel. There is also insufficient detail on the albedo of the surface, which is incorporated in each of the tested models. The albedo of vegetation is known to vary throughout the diurnal cycle (Song, 1998) and with changes in vegetation structure (Grover *et al*, 2000). However, albedo remained at a constant value for all pixels in the models where there may have been small albedo differences due to lateral variations in vegetation characteristics. Albedo is also known to vary where the vegetation is affected by wind (Song, 1998) and this may be a strong factor for the August ATI imagery where the day image was dominated by wind shear. The simple Cracknell & Xue (1996) model gives an indication of similar thermal features to those revealed on the day thermal imagery at early stages in grass growth (see Chapter 6: Figures 6.10, 6.11 and 6.12) and on the night thermal imagery at any stage in barley development (see Chapter 6: Figure 6.8), suggesting there is no real benefit from performing ATI modelling on a surface covered by vegetation for detection of features where complete characterisation of soil and meteorological parameters can not be determined.

2.6 To conduct geophysical evaluation of the soil characteristics beneath vegetation at the study sites and compare the results with the airborne survey

Existing geophysical magnetometry and resistivity surveys performed on Bosworth by Leicestershire County Council were extended using the same sampling strategy. There were some features revealed on the magnetometry survey that were not evident on the resistivity survey, and vice versa. This is mainly due to a difference in the physical properties of the materials detected by each technique and may also be partly due to a difference in the investigative depth of each technique. Ridge and furrow marks that were evident on aerial photography, multispectral and thermal images in both sand-rich and clay-rich fields, the magnetometry survey did not reveal these features in the clay-rich field. This suggests a limitation of magnetic surveying in

clay-rich fields. The features revealed on the geophysical surveys cannot be correlated with features on the thermal images suggesting that the different techniques are either sensitive to different properties of the soil or that the different techniques may have different observation depths. However, the features revealed on the ATI images from Bosworth and the thermal images from Baildon Moor closely correlate with features on the resistivity surveys. This suggests that the thermal response is highly sensitive to soil moisture differences even beneath a layer of vegetation and concurs with laboratory analyses conducted by Pratt & Elllyett (1979). The implications from the comparison of the thermal and geophysical results are that the techniques reveal different features and so may be complementary. However, another important implication is that features revealed in one technique may not necessarily imply the presence in the other and so geophysics cannot be used to corroborate the anomalies seen in the airborne thermal imagery.

2.7 To assess the effect of vegetation on detection of near-surface geophysical or archaeological features

Dual-source soil-vegetation models (Norman *et al*, 1995; Anderson *et al*, 1997 and Kustas & Norman, 1999) may reveal differences in soil properties underlying the vegetation. However, these models require detailed parameters on specific vegetation and soil properties that have to have been obtained simultaneous to thermal image acquisition. As a result, these models were not applied to the data consequentially the effect of vegetation was based on a purely visual assessment of the imagery. The abandoned hedgerow boundaries in Ambion field are evident on the visible, near-infrared and diurnal thermal images at early stage in barley growth but are not evident under the oil seed rape. This suggests that oil seed rape is an unsuitable vegetation cover for detecting variations in soil properties as the leafy canopy masks the underlying soil from solar heating and introduces canopy-soil interactions that regulate the temperature over larger areas. The most suitable conditions for feature visibility appear to be when the surface is covered by short grass or when a cereal crop is not fully mature.

2.8 To analyse the dynamics of the soil-vegetation heat flux based on a time series obtained from ground based contact measurements of soil temperature

The undisturbed soil column shows typical diurnal heating and cooling pattern at depths shallower than 0.20m under barley and pasture that are at an early stage in development. The diurnal pattern does not occur in the soil at 0.50m under these conditions suggesting that the solar heat penetrates to a depth between 0.20m and 0.50m, which is deeper than the 0.10m suggested by Pratt & Ellyett (1979). When the barley reached full maturity, the diurnal heating and cooling pattern dissipates between 0.10m and 0.20m suggesting that the vegetation effects the solar heat penetration. Rain causes little variation between maximum and minimum soil temperatures with return to diurnal pattern a complete 24-hour cycle after the rain has ceased. Wind has a similar effect of dampening the diurnal curve under strong wind speeds, but the soil returns to diurnal pattern almost immediately the wind has ceased. However, when rain has dampened the soil and strong winds prevail then the soil takes longer to return to normal diurnal pattern than for either effect on its own. This implies that the most suitable conditions for which to conduct a thermal survey are at least 24-hours after significant rainfall when the soil displays its maximum temperature range.

2.9 To determine times when the temperature contrast within the soil column is optimised to conduct an effective thermal survey

Results from the instrumented site show that the temperature contrast observed at the surface is maximised by obtaining a day thermal image between 14:00-15:00 local time and a night thermal image around 06:00 local time the following morning. The temperature contrast observed at 0.10m in the soil column appears to exist when the day thermal image is obtained at 15:00-16:00 local time with the night thermal image showing minimised temperatures at 07:00. At 0.20m and 0.50m depths the times of maximum and minimum temperature is less well-defined with little variation in the diurnal temperature, which concurs with the thermal analysis conducted by Kahle (1980). Although the soil displays its maximum temperature between 14:00-16:00 for shallow depth throughout vegetation growth, the time when the soil is at its minimum temperature becomes progressively later as the canopy closes. To maximise the observed temperature contrast, it is also best to avoid times when the temperature from depth within the soil column is similar to that observed at the surface since there will be no variation in heat flux at different depths in the soil, and is best when the

temperature from the surface is higher in the morning than that at depth. If thermal images are acquired over a large surface area, then it may be more difficult to specify these times since there may be as much as an hour between acquiring the first and last thermal images over the study site. As a result, the thermal observations performed on the study sites were not acquired when there would have been the greatest contrast in temperature extremes of the soil and the ATI may therefore not represent the heat flux from depth beneath the vegetation.

2.10 To determine appropriate processing requirements for conducting assessment of disturbance occurring in the near-surface environment beneath a layer of vegetation using airborne image data

If airborne image data is to be used in similar environmental situations, then it is useful to determine the most appropriate processing requirements for assessing the presence of disturbance occurring in the near-surface environment. The processing requirements that proved most useful in the study examples are outlined below together with an indication of the relative time taken to perform such techniques. Initially the images require geocorrection to a standard coordinate system for overlaying of other airborne images or auxiliary coordinate data. This can be performed in areas where there is accurate ground control using GCP collection technique. Where accurate ground control is difficult, an alternative method is to perform automatic geocorrection using the supplied geocorrection software with optional use of a DEM of similar spatial resolution. However, in areas of large topographic range further ground control point collection is often required. This is essential for comparison with other imagery or auxiliary data such as ground-based geophysical surveys. If several images are required to provide complete coverage of the study site then the images are mosaicked together along field boundaries to minimise variations within the vegetation, assuming that the images are radiometrically normalised or atmospherically corrected to avoid variations in illumination or atmospheric conditions occurring between the images. Atmospheric correction is simple if ground visible and near-infrared spectral signatures are measured over numerous different target materials simultaneous to image acquisition. However, since it is imperative to select targets of sufficient surface area at locations spanning the entire study site for measurement simultaneous to airborne acquisition

and this may be difficult on larger study sites where atmospheric characteristics can change quickly. When assessing areas covered by vegetation, all pixels that are not covered by vegetation are excluded from assessment with contrast enhancement of the remaining areas. This process can be performed easily using standard image processing software. Where there is no possibility to atmospherically correct the images, the simplest method for rapid assessment of large vegetated areas is to perform Principal Component Analysis, which enhances the spectral contrast contained in the data, on the image channels that do not contain excessive noise.

When the ground is covered by short grass or cereal crop at an early stage in development, feature can be rapidly assessed by visualising natural colour composites or false-colour composites using the visible and near-infrared spectral channels. When the grass is longer or the cereal crop is more mature and dominates the pixel coverage, night thermal visualisation is the most useful for feature visibility with similar results at different stages in cereal crop growth. Night thermal visualisation also prevents the need to calibrate day and night thermal radiance to ground temperature values that are required for ATI modelling, since the result from the ATI modelling revealed no additional features. This is particularly useful where access may be restricted to land or where there may be problems with equipment failure when acquiring temperatures at ground level.

9.2 CONCLUSIONS

The thesis has established a working methodology for thermal image processing for detecting ground disturbance in the near-surface environment beneath a layer of vegetation. The results of this research have shown that although the day and night thermal images acquired by the single-band thermal system can be used to model the ATI of the surface and can give an indication of variations in moisture content in the soil, the ATI does not provide adequate detection of features that may be manifest as compositional changes in the soil column and may only be useful under specific vegetation conditions when the surface is covered by short grass or under-developed cereal crop such as barley. This has been revealed from observation of a partially open canopy of a barley crop and also at early stages in grass growth at the Bosworth study site and also when the surface is covered by moorland vegetation on Baildon Moor.

Although this research has indicated there is a potential for using airborne thermal radiance images to assess the surface characteristics beneath vegetation, the technique appears to reveal different features compared with those revealed on ground geophysical assessment with a poor correlation between volumetric ATI features and soil composition. As a result, the ATI approach appears to provide a useful complementary tool to conventional geophysical prospection techniques. However, the research has also concluded that there is no real benefit for using ATI modelling for feature location than is provided by visualisation of images acquired at visible and near-infrared wavelengths at early stages in vegetation development. The greatest benefit for feature location appears to come from acquisition of day thermal images when the surface is covered by an early stage in vegetation growth or by acquiring night thermal images when the surface is covered by an under-developed cereal crop such as barley. This suggests that thermal investigations can provide a useful complementary tool to conventional aerial photography or other multispectral techniques for detection of features in the near-surface environment beneath a layer of vegetation.

9.3 FUTURE RESEARCH DIRECTIONS

Although this research has indicated the potential for using single-band airborne thermal radiance images to assess the characteristics of the ground surface beneath vegetation, it has been shown that there are some limitations of this technique. As a result, there are several key considerations for future applications of thermal remote sensing techniques for detecting ground disturbance in the near-surface environment beneath a layer of vegetation.

The ATI models applied to the June and August images may have shown greater internal field variation if the albedo values associated with the vegetation could have been determined for each pixel. Albedo is known to vary with material composition and also shows a temporal fluctuation in value. The models could therefore be improved by incorporating spatially and temporally variable albedo, although documentation of such techniques proved elusive in the literature.

It is also essential that the day and night thermal images be acquired when the temperature contrast observed at the surface is at its maximum so that the resistance of the surface to temperature change may be associated with variations in volumetric properties through Apparent Thermal Inertia calculations. This requires the measure of temperatures over a variety of surface materials in order that the thermal radiance can be calibrated to ground temperature values. Since ground calibration is not always possible, acquisition of thermal radiance by a multispectral thermal instrument may enable calculation of surface temperature for use in Apparent Thermal Inertia Models. At present multi-band thermal data is difficult to obtain at spatial resolutions similar to those of the archaeological and geological features assessed in this study and studies for the UK academic community are restricted to use of the NERC single-band thermal system. However, future generations of spaceborne thermal instruments may one day provide the spatial and temporal resolutions for such environmental applications.

As a further approach, it would have been very useful to acquire a day and night thermal image pair when there was minimal vegetation cover of the surface. The results from the vegetation-free surface would have been compared with the results from the observations during vegetation growth to enable assessment of when in the

vegetation season the visibility of features would be maximised. Although a winter diurnal image pair was requested, by the time the data was flown the surface was covered by leafy oil seed rape, which completely masked the underlying soil from direct observation. Thermal imaging during vegetation-free conditions may have also shown a different correlation with the geophysical data and high correlation of features between the datasets may have suggested that thermal imaging of a vegetation-free surface may have optimised feature detection. As a result, the research had to concentrate on assessing the thermal characteristics from different stages in the vegetation growth, rather than having background soil characteristics with which to compare with the vegetation response.

In conclusion, this body of research has shown that single-band thermal imagery provided by an airborne system can give good results under specific vegetation conditions when the surface is covered by short grass or under-developed cereal crop and has shown to be a useful complementary tool to conventional aerial photography, other multispectral techniques or ground geophysical evaluation for detection of features in the near-surface environment beneath a layer of vegetation.

REFERENCES

ANDERSON, J.M. & WILSON, S.B. (1984) Review Article: The physical basis of current infrared remote sensing techniques and the interpretation of data from aerial surveys. *International Journal of Remote Sensing, 5,* p847-859

ANDERSON, M.C., NORMAN, J.M., DIAK, G.R., KUSTAS, W.P. & MECIKALSKI, J.R. (1997) A Two-Source Time-Integrated Model for Estimating Surface Fluxes Using Thermal Infrared Remote Sensing. *Remote Sensing of Environment, 60,* p195-216

ANTON, Y.A. & ROSS, Y.K. (1990) Emissivity of a Soil-Vegetation System. *Soviet Journal of Remote Sensing, 7,* p859-869

BARNSLEY, M.J., ALLISON, D. & LEWIS, P. (1997) On the information content of multiple view angle (MVA) images. *International Journal of Remote Sensing, 18,* p1937-1960

BARRETT, E.C. & CURTIS, L.F. (1982) Introduction to environmental remote sensing. *Chapman & Hall, London,* pp352

BECKER, F. (1987) The impact of spectral emissivity on the measurement of land surface temperature from a satellite. *International Journal of Remote Sensing, 8,* p1509-1522

BECKER, F. & LI, Z-L (1990) Toward a local split window method over land surfaces. *International Journal of Remote Sensing, 3,* p369-393

BELLERBY, T.J., NOEL, M. & BRANIGAN, K. (1990) A thermal method for archaeological prospection: preliminary investigations. *Archaeometry, 32,* p191-203

CARLSON, T.N., TACONET, O., VIDAL, A., GILLIES, R.R., OLIOSO, A. & HUMES, K. (1995) An overview of the workshop on thermal remote sensing held at La Londe les Maures, France, September 20-24, 1993. *Agricultural and Forest Meteorology, 77,* p141-151

CATT, J.A. (1985) Soil particle size distribution and mineralogy as indicators of pedogenic and geomorphic history: examples from the loessial soils of England and Wales. *In* Geomorphology and Soil. Richards, K.S., Arnett, R.R. & Ellis, S. (eds), *George Allen & Unwin, London,* p202-218

COLTON A.L. (1996) Effective Thermal Parameters for a Heterogeneous Land Surface. *Remote Sensing of Environment, 57,* p143-160

CRACKNELL, A.P. & XUE, Y. (1996) Thermal inertia determination from space – a tutorial review. *International Journal of Remote Sensing, 17,* p431-61

CRESSWELL, M.P., MORSE, A.P., THOMSON, M.C. & CONNOR, S.J. (1999) Estimating surface air temperatures, from Meteosat land surface temperatures, using an empirical solar zenith angle model. *International Journal of Remote Sensing, 20,* p1125-1132

CURRAN, P.J. (1985) Principles of Remote Sensing. *Longman, New York,* p36-43 (pp282)

DAAMEN, C.C. (1997) Two source model of surface fluxes for millet fields in Niger. *Agricultural and Forest Meteorology, 83,* p205-230

DALAN, R.A. & BANERJEE, S.K. (1996) Soil magnetism, an approach for examining archaeological landscapes. *Geophysical Research Letters, 23(2),* p185-188

DEARDORFF, J.W. (1978) Efficient Prediction of Ground Surface Temperature and Moisture, With Inclusion of a Layer of Vegetation. *Journal of Geophysical Research, 83, C4,* p1889-1903

DESVIGNES, G., TABBAGH, A. & BENECH, C. (1999) The Determination of the Depth of Magnetic Anomaly Sources. *Archaeological Prospection, 6(2),* p85-105

DONEUS, M. & NEUBAUER, W. (1998) 2D Combination of Prospection Data. *Archaeological Prospection, 5,* p29-56

DONNELLY, L.J. & McCANN, D.M (2000) The location of abandoned mine workings using thermal anomalies. *Engineering Geology 57,* p39-52

DONOGHUE, D.N.M & SHENNAN, I. (1988) The application of multispectral remote sensing techniques to wetland archaeology. *Geoarchaeology, 3,* p275-285

DUFF, D. (1993) Holmes' Principles of Physical Geography. *Chapman & Hall, London,* p275-288

ELACHI, C. (1987) Introduction to the Physics and Techniques of Remote Sensing. *John Wiley & Sons, New York,* pp413

EMERY, W.J. & YU, Y. (1997) Satellite sea surface temperature patterns. *International Journal of Remote Sensing, 18,* p323-334

ENGLISH HERITAGE: Proposed Battlefields Register: Bosworth 1485

FLYNN, L.P., HARRIS, A.J.L. & WRIGHT, R. (2001) Improved identification of volcanic features using Landsat 7 ETM+. *Remote Sensing of Environment, 78,* p180-193

FRANCA, G.B. & CRACKNELL, A.P. (1994) Retrieval of land and sea surface temperatures using NOAA-11 AVHRR data in north eastern Brazil. *International Journal of Remote Sensing, 15,* p1695-1712

FRENCH, A.N., SCHMUGGE, T.J. & KUSTAS, W.P. (2000) Discrimination of Senescent Vegetation Using Thermal Emissivity Contrast. *Remote Sensing of Environment, 74,* p249-254

FUCHS, M. & TANNER, C.B. (1966) Infrared Thermometry of Vegetation. *Agronomy Journal, 58,* p597-601

GOETZ, A.F.H. (1989) Spectral remote sensing in geology. *In:* Applications of Optical Remote Sensing, ASRAR, G. (editor), *John Wiley & Sons, New York,* p491-526

GIGLIO, L., KENDALL, J.D. & TUCKER, C.J. (2000) Remote sensing of fires with the RMM VIRS. *International Journal of Remote Sensing, 21,* p203-207

GILLESPIE, A.R. & KAHLE, A.B. (1977) Construction of a digital thermal inertia image. *Photogrammetric Engineering and Remote Sensing, 43,* p983-1000

GRIFFITHS, D.H. & BARKER, R.D. (1994) Electrical Imaging in Archaeology. *Journal of Archaeological Sciences, 21,* p153-158

GROVER, K.D., STEVEN. M.D., RONDEAUX, G. & CLARK, J.A. (2000) Estimating albedo from limited spectral and angular data. *International Journal of Remote Sensing, 21,* p155-165

GUOQUAN, D. & ZHENGZHI, L. (1992) The apparent emissivity of vegetation canopies. *International Journal of Remote Sensing, 14,* p183-188

HAPKE (1993) Theory of Reflectance and Emittance Spectroscopy. *Cambridge University Press, New York,* p358-385

HOOK, S.J. (1989) An evaluation of NS-001 and TIMS data for lithological mapping and mineral exploration in weathered vegetated terrain. *PhD Thesis (University of Durham, England),* pp306

IAQUINTA, J. & FOUILLOUX, A. (1998) Influence of the heterogeneity and topography of vegetated land surfaces for remote sensing applications. *International Journal of Remote Sensing, 19,* p1711-1723

IRVINE, J.M., EVERS, T.K, SMYRE, J.L., HUFF, D., KING, A.L., STAHL, G. & ODENWELLER, J. (1997) The detection and mapping of buried waste. *International Journal of Remote Sensing, 18,* p1583-1595

JIA, XIUPING & RICHARDS, J.A. (1999) Segmented Principal Components Transformation for Efficient Hyperspectral Remote-Sensing Image Display and Classification. *IEEE Transactions on Geosciences and Remote Sensing, 37,* p538-542

JONES, H.K, & ELGY, J. (1994) Remote sensing to assess landfill gas migration. *Water Management & Research, 12,* p327-337

JUPP, D.L.B. (1998) Directional radiance and emissivity measurement models for remote sensing of the surface energy balance. *Environmental Modelling & Software, 13,* p341-351

KAHLE, A.B., GILLESPIE, A.R. & GOETZ, A.F.H. (1976) Thermal Inertia Imaging: A New Geologic Mapping Tool. *Geophysical Research Letters, vol 3, no 1,* p26-8

KAHLE, A.B. (1977) A Simple Modal of the Earth's Surface for Geological Mapping by Remote Sensing. *Journal of Geophysical Research, 82,* p1673-1680

KAHLE, A.B. (1980) Surface Thermal Properties. *In:* Remote Sensing in Geology, SIEGAL, B.S. & GILLESPIE, A.R. (editors), *John Wiley & Sons, New York,* p257-73

KAHLE, A.B., SCHIELDGE, J.P. & ALLEY, R.E. (1984) Sensitivity of Thermal Inertia Calculations to Variations in Environmental Factors. *Remote Sensing of Environment, 16,* p211-32

KAHLE, A.B. & ALLEY, R.E. (1985) Calculation of Thermal Inertia from Day-Night Measurements Separated by Days or Weeks. *Photogrammetric Engineering and Remote Sensing, vol 51, no 1,* p73-5

KEALY, P.S. & HOOK, S.J. (1993) Separating Temperature and Emissivity in Thermal Infrared Multispectral Scanner Data: Implications for Recovering Land Surface Temperatures. *IEEE Transactions on Geoscience and Remote Sensing, 31,* p1155-1164

KEAREY, P. & BROOKS, M. (1991) An Introduction to Geophysical Exploration (2nd edition), *Blackwell Scientific Publications, Oxford,* p148-218

KORNFIELD, J. & SUSSKIND, J. (1977) On the Effect of Surface Emissivity on Temperature Retrievals. *Monthly Weather Review, 105,* p1605-1608

KUSTAS, W.P. & NORMAN, J.M. (1999) Evaluation of soil and vegetation heat flux predictions using a simple two-source model with radiometric temperatures for partial canopy cover. *Agricultural and Forest Meteorology, 94,* p13-29

LI, Z-H, BECKER, F., STOLL, M.P., WAN, Z. (1999) Evaluation of Six Methods for Extracting Relative Emissivity Spectra from Thermal Infrared Images. *Remote Sensing of Environment, 69,* p197-214

LILLESAND, T.M. & KIEFER, R.W. (2000) Remote Sensing and Image Interpretation. *John Wiley & Sons, New York,* pp724

LIN, J.D. (1980) On the Force-Restore Method for Prediction of Ground Surface Temperature. *Journal of Geophysical Research,* 85, p3251-3254

LŰCK, E. & EISENREICH, M. (1999) Geophysical prospection of archaeological sites in Brandenburg, Germany. *Archaeological Prospection, 6,* p125-133

MARMET, E., BINA, M., FEDOROFF, N & TABBAGH, A (1999) Relationships between Human Activity and the Magnetic Properties of Soils: A Case Study in the medieval Site of Roissy-en-France. *Archaeological Prospection, 6,* p161-170

MARSHALL, A. (1999) Magnetic Prospection at High Resolution: Survey of Large Silo-pits in Iron Age Enclosures. *Archaeological Prospection, 6,* p11-29

MATHER, P. (1999) Computer Processing of Remotely-Sensed Images. *John Wiley & Sons, Chichester, 2nd edition,* pp292

McMANUS, J., DUCK, R.W., & ANDERSON, J.M. (1999) The relative merits and limitations of thermal radiometric measurements in estuarine studies. *International Journal of Remote Sensing, 20,* p549-559

MORGAN, R.P.C. (1985) Soil degradation and erosion as a result of agricultural practise. *In* Geomorphology and Soil. Richards, K.S., Arnett, R.R. & Ellis, S. (eds), *George Allen & Unwin, London,* p380-395

MORI, M., KAMEI, H., NAKAI, M. & KUDO, H. (1999) High-density Resistivity Survey and Experimental Measurement of subsurface Temperature on Hirui-Otsuka Mounded Tomb in Ogaki, Japan. *Archaeological Prospection, 6,* p171-178

NASH, D.B. (1985) Detection of bedrock topography beneath a thin cover of alluvium using thermal remote sensing. *Photogrammetric Engineering and Remote Sensing, 51,* p77-88

NASH, D.B. (1988) Detection of a buried horizon with a high thermal diffusivity using thermal remote sensing. *Photogrammetric Engineering and Remote Sensing, 54,* p1437-1446

NOEL, M. & BELLERBY, T.J. (1990) Thermal archaeological surveying: a recording soil temperature probe. *Archaeometry 32,* p83-90

NOEL, M. & WALKER, R. (1990) Development of an electrical resistivity tomography system for imaging archaeological structures. *Archaeometry, 32,* p767-776

NORMAN, J.M., KUSTAS, W.P. & HUMES, K.S. (1995) Source approach for estimating soil and vegetation energy fluxes in observations of directional radiometric surface temperature. *Agricultural and Forest Meteorology, 77,* p263-293

OTTERMAN, J., BRAKKE, T.W., FUCHS, M., LAKSHMI, V. & CADEDDU, M. (1999) Longwave emission from a plant/soil surface as a function of the view direction: dependence on canopy architecture. *International Journal of Remote Sensing, 20,* p2195-2201

PICKERILL J.M. & MALTHUS, T.J. (1998) Leak detection from rural aqueducts using airborne remote sensing techniques. *International Journal of Remote Sensing, 19,* p2427-2433

PERRISET, M.C. & TABBAGH, A. (1981) Interpretation of thermal prospection on bare soils. *Archaeometry, 23,* p169-187

PLATT, C.M.R. & PRATA, A.J. (1993) Nocturnal Effects in the Retrieval of Land Surface Temperatures from Satellite Measurements. *Remote Sensing of Environment,* 45, p127-136

POWLESLAND, D., LYALL, J. & DONOGHUE, D.N.M (1997) Enhancing the record through remote sensing. The application and integration of multi-sensor, non-invasive remote sensing techniques for the enhancement of the Sites and Monuments Record. Heslerton Parish Project, N. Yorkshire, England. *Internet Archaeology, 2*

PRAKASH, A., GENS, R. & VEKERDY, Z. (1999) Monitoring coal fires using multi-temporal night-time thermal images in a coalfield in north-west China. *International Journal of Remote Sensing, 20,* p2883-2888

PRATT, D.A. & ELLYETT, C.D. (1979) The Thermal Inertia Approach to mapping of Soil Moisture and Geology. *Remote Sensing of Environment, 8,* p151-168

PRICE, J.C. (1977) Thermal Inertia Mapping: A New View of the Earth. *Journal of Geophysical Research, vol 82, no 18,* p2582-90

PRICE, J.C. (1980) The Potential of Remotely Sensed Thermal Infrared Data to Infer Surface Soil Moisture and Evaporation. *Water Resources Research, 16,* p787-795

PRICE, J.C. (1983) Estimating Surface Temperatures from Satellite Thermal Infrared Data – A Simple Formulation for the Atmospheric Effect. *Remote Sensing of Environment, 13,* p353-361

PRICE, J.C. (1984) Land surface temperature measurements from the split window channels of the NOAA-7 Advanced Very High Resolution Radiometer. *Journal of Geophysical Research, 89,* p7231-7237

PRICE, J.C. (1985) On the Analysis of Thermal Infrared Imagery: The Limited Utility of Apparent Thermal Inertia. *Remote Sensing of Environment, 18,* p59-73

PRICE, J.C. (1989) Quantitative Aspects of Remote Sensing in the Thermal Infrared. *In:* Applications of Optical Remote Sensing, ASRAR, G. (editor), *John Wiley & Sons, New York*, p578-603

QIN, Z. & KARNIELI, A. (1999) Progress in the remote sensing of land surface temperature and ground emissivities using NOAA-AVHRR data. *International Journal of Remote Sensing, 20,* p2367-2393

REGINATO, R.J., IDSO, S.B., VEDDER, J.R., JACKSON, R.D., BLANCHARD, M.B. & GOETTLEMAN, R. (1976) Soil water content and evaporation determination obtained

from ground-based and remote measurements. *Journal of Geophysical Research, 81,* p1616-1620

REYNOLDS, J.M. (1997) An Introduction to Applied and Environmental Geophysics, *John Wiley & Sons Ltd, Chichester*, p117-207, p417-490

ROBERTS, P. (1999) Report on Geophysical Survey, on the Scheduled Ancient Monument of Ambion Hill (No. 17084), Bosworth Field, Sutton Cheney, Hinckley & Bosworth District, Leicestershire. *English Heritage Report*

ROY, D.P., DEVEREUX, B., GRAINGER, B. & WHITE, S.J. (1997) Parametric geometric correction of airborne thematic mapper imagery. *International Journal of Remote Sensing, 18,* p1865-1887

RUBIO, E., CASELLES, V. & BADENAS, C. (1997) Emissivity measurements of several soils and vegetation types in the 8-14μm wave band: analysis of two field methods. *Remote Sensing of Environment, 59,* p490-521

SABINS, F.J Jr (1986) Remote Sensing and Interpretation (2nd edition). *W.H. Freeman and Company, New York,* p125-175

SAXTON, K.E. USDA Agricultural Research Service (http://www.bsyse.wsu.edu/saxton)

SCHMUGGE, BECKER & LI (1991) Spectral emissivity variations observed in airborne surface temperature measurements. *Remote Sensing of Environment, 35,* p95-104

SCHMUGGE, T., HOOK, S.J. & COLL, C. (1998) Recovering Surface Temperature and Emissivity from Thermal Infrared Multispectral Data. *Remote Sensing of Environment, 65,* p121-131

SCHOTT, J.R. (1989) Image Processing of Thermal Infrared Images. *Photogrammetric Engineering and Remote Sensing, 55,* p1311-1321

SCOLLAR, I, TABBAGH, A. HESSE, A. & HERZOG, I. (1990) Archaeological Prospecting and Remote Sensing. Topics in Remote Sensing 2. *Cambridge University Press, Cambridge*

SHARRATT, B.S. (1998) Radiative exchange, near-surface temperature and soil water of forest and cropland in interior Alaska. *Agricultural and Forest Meteorology, 89,* p269-280

SMITH, G.M. & MILTON, E.J. (1999) Technical Note: The use of the empirical line method to calibrate remotely sensed data to reflectance. *International Journal of Remote Sensing, 20,* p2653-2662

SNYDER, W.C., WAN, Z., ZHANG, Y & FENG, Y-Z (1997) Thermal infrared (3-14μm) bidirectional reflectance measurements of sands and soils. *Remote Sensing of Environment, 60,* p101-109

SONG, J. (1998) Diurnal asymmetry in surface albedo. *Agricultural and Forest Meteorology, 92,* p181-189

SUGITA, M,. HIYAMA, T. & IKUKAWA, T. (1996) Determination of canopy emissivity: how reliable is it? *Agricultural and Forest Meteorology, 81,* p229-239

SUITS, G.H. (1983) The Nature of Electromagnetic Radiation. *In* Manual of Remote Sensing Vol 1. SIMONETT, D.S & LILABY, F.T. (editors). *2nd edition, American Society of Photogrammetry, Virginia,* p37-61

SZEKIELDA, K-H. (1988) Satellite Monitoring of the Earth. *John Wiley & Sons, New York,* p231-6 (pp326)

VERBRUGGHE, M. & CIERNIEWSKI, J. (1998) Influence and modelling of view angles and microrelief on surface temperature measurements of bare agricultural soils. *ISPRS Journal of Photogrammetry & Remote Sensing, 53,* p166-173

VINCENT, R.K. (1975) The Potential Role of Thermal Infrared Multispectral Scanners in Geological Remote Sensing. *Proceedings of the IEEE, 63,* p137-147

WARNER, T.A., & CHEN, X. (2001) Normalization of Landsat thermal imagery for the effects of solar heating and topography. *International journal of Remote Sensing, 22,* p773-788

WATSON, K. (1975) Geological Applications of Thermal Infrared Images. *Proceedings of the IEEE, 63,* p128-137

WATSON, K. (1982) Regional thermal-inertia mapping from an experimental satellite. *Geophysics, vol 47, no 12,* p1681-7

WHALLEY, W.B. (1985) Scanning electron microscopy and the sedimentological characterisation of soils. *In* Geomorphology and Soil. Richards, K.S., Arnett, R.R. & Ellis, S. (eds), *George Allen & Unwin, London,* p183-201

WILSON, D.R. (1982) Air photo interpretation for archaeologists. *BT Batsford Ltd, London,* pp212

WRIGHT, R., FLYNN, L., GARBEIL, H., HARRIS, A.. & PILGER, E. (2002) Automated volcanic eruption detection using MODIS. *Remote Sensing of Environment, 82,* p135-155

XUE, Y & CRACKNELL, A.P (1995) Advanced thermal inertia modelling. *International Journal of Remote Sensing, 16,* p431-446

ZHAN, X., KUSTAS, W.P. & HUMES, K.S. (1996) An Intercomparison Study on Models of Sensible Heat Flux over Partial Canopy Surfaces with Remotely Sensed Surface Temperature. *Remote Sensing of Environment, 38,* p242-256

ZILIOLI, E., GOMARASCA, M.A. & TOMASONI, R. (1992) Application of terrestrial thermography to the detection of waste-disposal sites. *Remote Sensing of Environment, 40,* p153-160

Appendix A: INSTRUMENTATION

A1: AIRBORNE THEMATIC MAPPER

The Airborne Thematic Mapper (ATM) is a passive remote sensor designed to measure radiation from the Earth's surface from an airborne platform (Figure A1). It separates the incoming radiation into 11 spectral bands ranging from the visible (VIS) and near-infrared (NIR) and in particular provides two channels in the short-wave infrared (SWIR) and a single channel in the thermal infrared (TIR). Detail of the spectral characteristics of the ATM is shown in Table A1.

Figure A1: Daedalus AADS1268 Airborne Thematic Mapper, taken from http://www.nerc.ac.uk/arsf

Channel	Daedalus AADS1268 ATM
1	0.424 - 0.448
2	0.469 - 0.518
3	0.522 - 0.601
4	0.594 – 0.635
5	0.627 – 0.694
6	0.691 – 0.761
7	0.754 – 0.924
8	0.879 – 1.027
9	1.600 – 1.785
10	2.097 – 2.391
11	8.400 – 11.500

Table A1: Spectral characteristics of the Daedalus AADS1268 ATM

Radiation captured by the rotating scan mirror is split by dichroic filters into a number of radiation paths and are imaged onto detectors. VIS and NIR radiation is split by a prism before being imaged onto an array of silicon detectors (Channels 1-8). SWIR and TIR is split, imaged and recorded on single detector elements held within three individual liquid nitrogen cooled dewars (Channels 9-11). Unlike the VIS, NIR and SWIR channels, the TIR channel is calibrated by comparison in 'real-time' to two on-board black-bodies set to bound the high and low temperatures expected for the scene. These are imaged immediately before and after the scene pixels during every scan line and the temperature of the black-body responses recorded for radiometric calibration. However, the spectral response of the thermal channel varies across the thermal wavelength range (Table A2).

λ	Response	λ	Response	λ	Response	λ	Response	λ	Response	λ	Response	λ	Response
8.00	0.355	9.00	82.382	10.00	97.839	11.00	83.905	12.00	38.788	13.00	30.039	14.00	3.517
8.05	0.601	9.05	83.753	10.05	96.276	11.05	79.661	12.05	38.903	13.05	27.925	14.05	3.584
8.10	1.516	9.10	85.393	10.10	95.595	11.10	77.323	12.10	39.965	13.10	25.090	14.10	1.962
8.15	3.861	9.15	87.673	10.15	93.101	11.15	73.960	12.15	40.435	13.15	23.672	14.15	2.043
8.20	9.288	9.20	90.818	10.20	90.414	11.20	71.288	12.20	41.115	13.20	20.754	14.20	2.200
8.25	18.909	9.25	93.771	10.25	89.376	11.25	68.293	12.25	41.589	13.25	18.254	14.25	2.027
8.30	32.217	9.30	97.239	10.30	88.846	11.30	63.318	12.30	40.722	13.30	16.791	14.30	2.063
8.35	49.088	9.35	99.093	10.35	88.937	11.35	59.337	12.35	40.448	13.35	15.736	14.35	1.373
8.40	66.147	9.40	99.788	10.40	89.450	11.40	56.775	12.40	39.724	13.40	12.703	14.40	2.123
8.45	74.362	9.45	99.303	10.45	89.090	11.45	54.588	12.45	39.700	13.45	10.610	14.45	1.357
8.50	73.921	9.50	97.256	10.50	88.989	11.50	52.397	12.50	40.509	13.50	8.807	14.50	1.182
8.55	74.650	9.55	94.367	10.55	89.273	11.55	50.389	12.55	39.513	13.55	8.775	14.55	1.296
8.60	79.395	9.60	91.656	10.60	89.493	11.60	48.655	12.60	39.043	13.60	7.364	14.60	0.652
8.65	85.655	9.65	89.055	10.65	91.365	11.65	46.431	12.65	38.721	13.65	6.668	14.65	1.234
8.70	89.796	9.70	89.012	10.70	91.361	11.70	44.638	12.70	38.377	13.70	6.233	14.70	0.645
8.75	89.961	9.75	89.984	10.75	90.564	11.75	42.024	12.75	37.527	13.75	4.960	14.75	0.676
8.80	86.917	9.80	91.436	10.80	93.651	11.80	41.344	12.80	36.191	13.80	3.874	14.80	0.695
8.85	83.729	9.85	93.076	10.85	96.481	11.85	39.604	12.85	35.059	13.85	3.444	14.85	0.687
8.90	81.554	9.90	96.083	10.90	94.359	11.90	39.065	12.90	35.889	13.90	3.832	14.90	0.577
8.95	81.689	9.95	97.547	10.95	89.362	11.95	38.557	12.95	32.060	13.95	4.096	14.95	0.686

Table A2: Spectral response details of ATM thermal channel, obtained from Wilson pers. comm.

The scan mirror has three synchronised speeds (12.5, 25 and 50Hz) to optimise the scan-rate to more closely match data acquisition and coverage over the ground at various altitudes, thus avoiding under-sampling and over-sampling in the along-track direction. Ground spatial resolution will be dependent on the flying altitude of the aircraft with the instrument having a fixed IFOV of 2.5mrad (~0.14 degrees). The acquisition electronics of the Daedalus AADS1268 provided 8-bit A/D conversion with 16-bit A/D conversion introduced with the AZ-16 system, with an increased signal to noise ratio. Detail of the technical characteristics of the ATM is shown in Table A3.

Characteristic	Daedalus AADS1268 (1998)	AZ-16 (2001/2002)
Digitised FOV	73.72°	90°
Instantaneous FOV	2.5 mrad	2.5 mrad
Pixel Swath	716	938
Scan Rate	12.5, 25 and 50 Hz	12.5, 25 and 50Hz
Radiometric Quantisation	8 bit	16 bit
Spectral Units	uW.cm-2.sr-1.nm-1	uW.cm-2.sr-1.nm-1

Table A3: Technical characteristics of the Daedalus AADS1268 ATM, taken from http://www.nerc.ac.uk/arsf

The ATM is part of an Integrated Data System, provided to integrate the imagery provided by the scanners with the navigation and attitude data of the platform to ideally provide a fully geo-referenced digital data set without the need for ground control point collection. However, in some cases this is inadequate due to excessive motion of the platform caused by wind. The integrated system involves a fibre-optic gyro system providing 64Hz attitude information on pitch and roll angles and magnetic heading. The later 2001/2002 system also incorporated a 3-axial GPS mounted on the aircraft to provide 20Hz GPS attitude and position reference system which synchronises the GPS information with the scan line acquisition time. The flexible data recording on removable hard drives enables the ease of data transfer to CD prior to data transcription by the ground processing system. During data transcription, the GPS time-integrated information is incorporated into the data stream to enable navigational processing for geometric correction.

The ATM is deployed aboard a Dornier 228-101 research aircraft flown by the NERC Airborne Remote Sensing Facility. The Do-228 (Figure A2) is a non-pressurised twin turbo-propeller-powered research aircraft whose payload and configuration characteristics can accommodate a range of remote sensing and digital sensors.

Figure A2: The NERC aircraft (Dornier Do228-101 D-CALM), taken from http://www.nerc.ac.uk/arsf

A2: WILD RC-10 SURVEY CAMERA

The Wild RC-10 survey camera system is designed for taking near-vertical serial exposures from the air (Figure A3) and is capable of providing high definition black and white, colour or false-colour infrared imagery by interchanging the lens cones during flight, giving versatile aerial data acquisition. The lenses are colour corrected for the visible and infrared spectral ranges and enable exposures to be made at all the usual scales with various focal lengths up to the operational ceiling of the survey platform. The camera can be operated in either 'Basic' mode with minimal forward overlap of in 'Stereo' mode with up to 60% forward overlap with the standard output formats as negative and/or transparency film.

Figure A3: Wild RC-10 Survey Camera, taken from http://www.nerc.ac.uk/arsf

The camera is flown either as a complement to the remote sensing instrumentation, or on its own for high resolution photographic missions with alignment and levelling of the camera during flight enabled by a drift sight, remotely adjusting the camera attitude and correcting for aircraft roll, pitch and yaw.

The calibration specifications of the camera enable photogrammetric correction for lens distortion occurring across the aerial photograph with specified fiducal coordinates for the fiducal marks on the output photographs. Detail on the camera optics is provided along with the hard-copy output.

A3: GER1500 SPECTRORADIOMETER

The GER1500 from the Geophysical and Environmental Research (GER) Corporation is a light-weight, high performance field spectroradiometer measuring over the visible to near infrared wavelength range (Table A4). The instrument is very rapid scanning, acquiring single spectra in milliseconds. Its lightweight qualities mean that it can be used as a hand-held instrument, or alternatively mounted on a tripod for collecting measurements at different heights. The GER1500 can be used in one of three different modes. 'Stand-alone' mode allows the radiometer to be used without the need for a controlling PC, with up to 500 individual scans stored on the on-board memory. 'Single-beam' mode allows operation via a notebook PC, with near real-time spectrum display. 'Dual-beam' mode gives advanced functionality, allowing dual radiometer operation for target and reference scans simultaneously, thus reducing the effects of changing atmospheric conditions on data collection.

Parameters	**GER-1500**
Spectral Range	300-1100nm
Spectral Sampling	1.5nm
Spectral resolution	3nm
Field of View	3° or 15°
Quantisation	16 bit
Typical scan time under ideal field conditions	< 1 second
Power Source	Mains, NiMH rechargeable 12V gel cells
Size	15 cm x 8 cm x 26 cm
Weight	1.8 kg
Environmental Limits	-10°C to 50°C

Table A4: Technical characteristics of the GER1500 Spectroradiometer

A4: GER3700 SPECTRORADIOMETER

The GER3700 from the Geophysical and Environmental Research (GER) Corporation is a high performance single-beam field spectroradiometer measuring over the visible to short-wave infrared wavelength range (Table A5). The instrument is mounted on a tripod and is controlled by a notebook PC via a 2m serial cable. PC operation gives a distinct advantage, as it offers near real-time data display. The GER3700 can be accurately positioned using a laser positioning beam with a range of foreoptics available, making it suitable for a wide variety of applications.

Parameters	**GER-3700**
Spectral Range	300-2500nm
Spectral Sampling	1.5nm (300-1050nm) 6.5nm (1050-1900nm) 9.5nm (1900-2500nm)
Spectral resolution	3nm (300-1050nm) 11nm (1050-1900nm) 16nm (1900-2500nm)
Field of View	3° or 10°
Quantisation	16 bit (300-1050nm) 15 bit (1050-2500nm)
Typical scan time under ideal field conditions	< 1 second
Power Source	rechargeable gel cells
Size	33 cm x 33 cm x 11.5 cm
Weight	6.4 kg
Environmental Limits	-10°C to 50°C

Table A5: Technical characteristics of the GER3700 Spectroradiometer

A5: TEMPCON® HOBO-H8 DATA LOGGER

The HOBO-H8 data logger consists of a weatherproof unit with 4-external sensors (Figure A4) specified to measure a particular environmental parameter. To set up the unit, the socket head screws that hold the lid onto the case are removed. The dome nuts, which protect the connection points, are removed and the sensor cables inserted through the nut head and connected to the corresponding jack on the circuit board. The dome nuts are then screwed back onto their fittings on the outside of the case. Two blue dessicant cartridges, which turn pink when in need of replacement, are placed in the cavity at the top of the case to protect the unit from moisture. A lithium CR-2032 battery is placed under the lever, with the printed side facing away from the circuit board. The lid is then replaced ensuring that the O-ring, which lies in a groove on top of the case, is lubricated to provide a perfect seal between the lid and the base unit. Finally, the socket head screws are tightened to ensure unit is sealed and weatherproof ready for deployment.

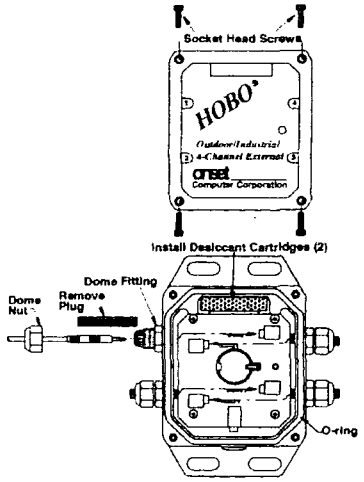

Parameter	HOBO-H8 4-Channel Data Logger
External Sensors	Input cable 0-20.1mA±1% sensitivity
Measurement Capacity	32,520 time-sampled measurements
Power Source	CR-2032 (lithium) replaceable battery
Size	14 cm x 13.7 cm x 3.2 cm
Weight	0.2 kg
Environmental Limits	-20°C to 70°C

Figure A4: HOBO-H8 outdoor 4-channel data logger with table of characteristics

To operate, the unit is connected to a PC by inserting the connector cable through the plug at the front of the unit and attaching the cable to the serial port on the PC, which has the BoxCar® Pro 3.5 software installed on it. The 'Launch' button is selected from the Logger menu to open the launch dialogue box (Figure A5).

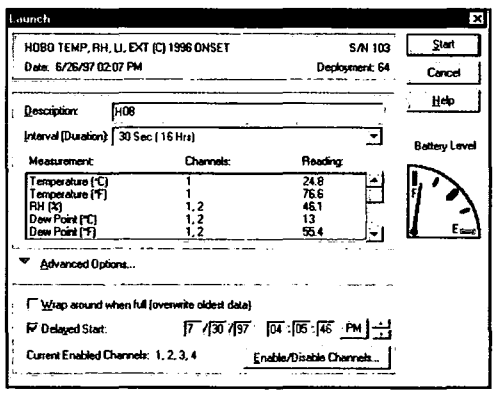

Figure A5: BoxCar® Pro 3.5 launch window enabling channel and sample-interval specifications

A description of the logger is entered as a logger reference. The time interval between measurements is selected from the drop-down menu, together with an indication of the total time the logger will collect data. The sensor channels are enabled or disabled by checking the appropriate channel number (corresponding to the number on the lid of the unit). It is also necessary to specify which type of sensor is used on each channel, so that the temperature can be measured correctly. The launch dialog box also gives a battery level indication, best to be above 30% before deployment. Once launched, the HOBO has a red light on the front that blinks brightly at every measurement, and weakly every two seconds if the interval between

measurements is longer than two seconds. The unit continues to take measurements until the battery life expires, or until the memory has reached its full capacity. The data can be downloaded at any time, by connecting the unit to the PC, as for the launch sequence, with selection of the 'Readout' button from the Logger menu. After the download, the user is prompted for a filename for data storage. The data is then exported to text file for analysis by selecting the 'Microsoft Excel' button from the Export menu and selecting the appropriate channels for data exportation.

Appendix B: ENVI PROCESSING

B1: BASIC IMAGE IMPORTATION

ENVI – File – Open Data File

1) Define Header for importation of raw image format

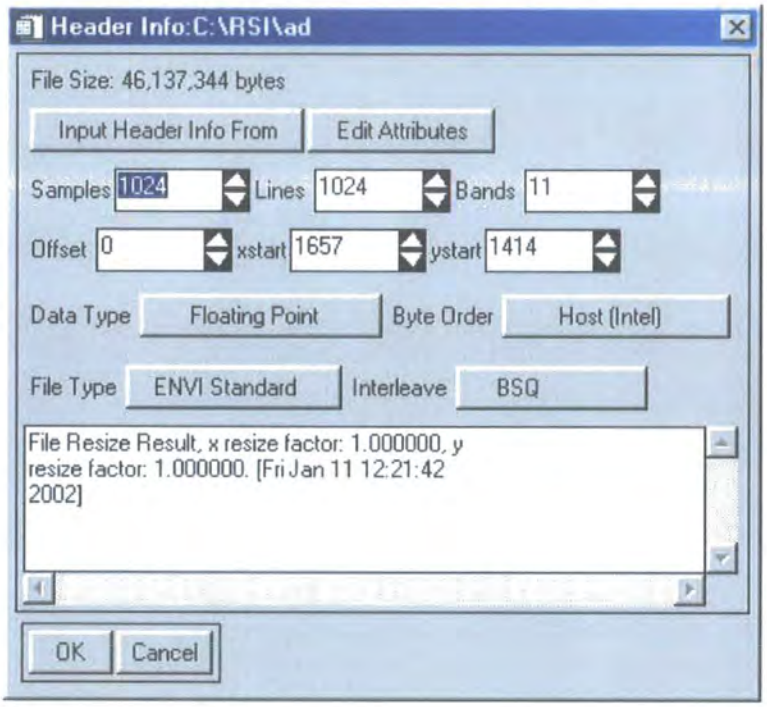

Samples	number
Lines	number
Bands	number
Offset	0
xstart	
ystart	
Data Type	float
Byte Order	Network IEEE
File Type	unknown
Interleave	BIL

B2: IMAGE VISUALISATION

ENVI – File Open Data File

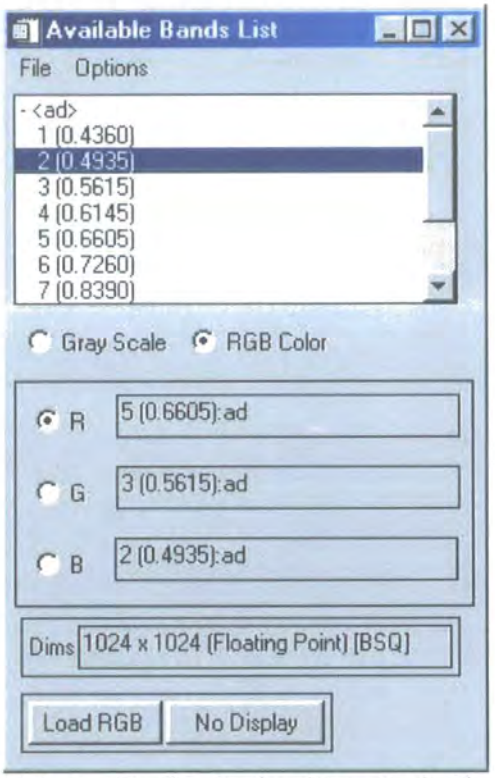

1) Image Band Selection (Grey Scale Single Band or RGB colour composite from open image file)

B3: EDIT FILE HEADER DETAILS

ENVI – File – Edit ENVI Header

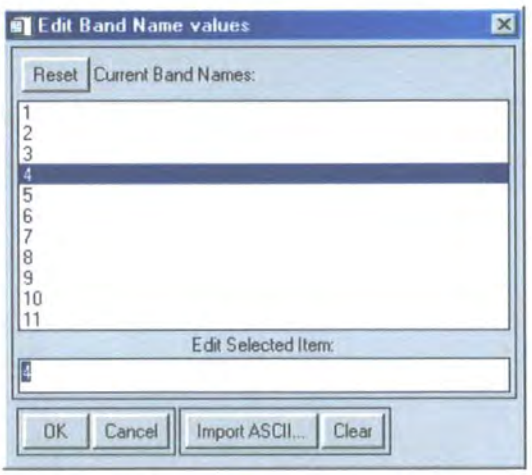

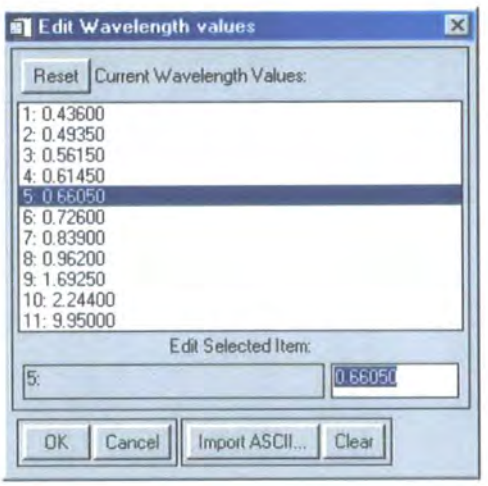

1) Edit Attributes - Band Names (left)
2) Edit Attributes – Wavelengths (right)

B4: DEFINE REGIONS of INTEREST for SPECTRAL EXTRACTION

On Open Image Display – Overlay – Region of Interest

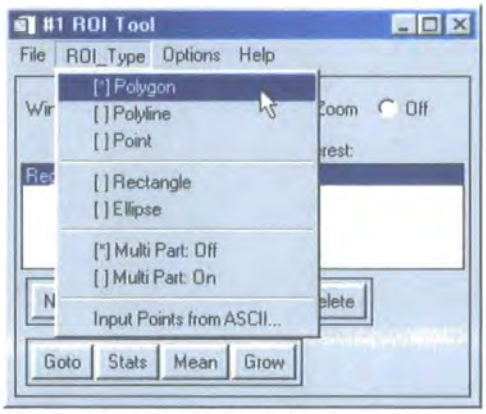

1) Select appropriate Window (Image, Scroll or Zoom) in to generate ROI (left)
2) Select type of polygon to generate (right)
3) Draw polygon on image window using Left Mouse
4) Close region with Right Mouse
5) Alter corners with Left Mouse (click & drag) then finalise with Right Mouse

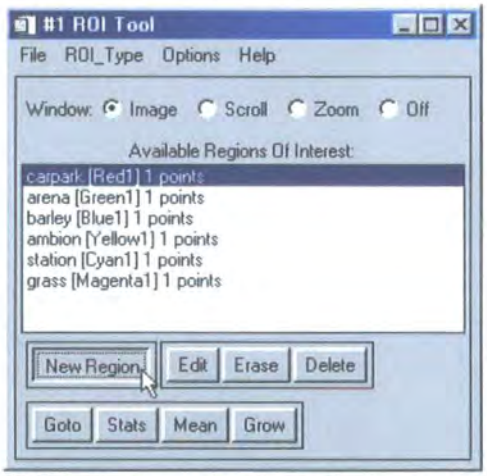

6) Select new region for each new target

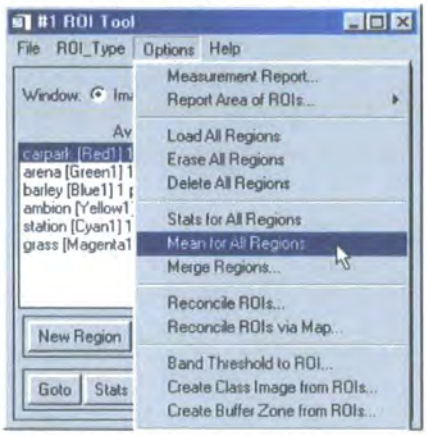

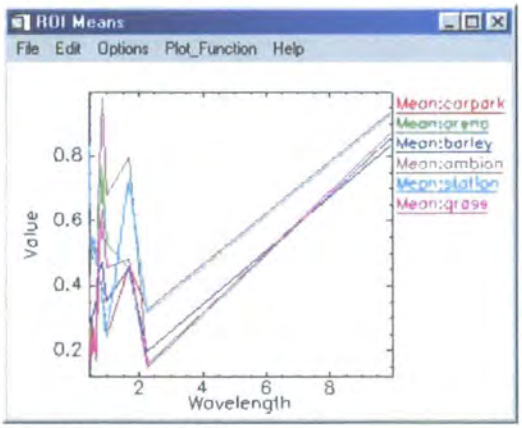

8) Extract mean spectral signature of each region of interest (left)
9) Mean spectral signatures are plotted on graph (right)

B5: EMPIRICAL LINE CALIBRATION

B5.1 ENVI – Basic Tools – Calibration Utilities - Empirical Line – Compute Factors and Calibrate

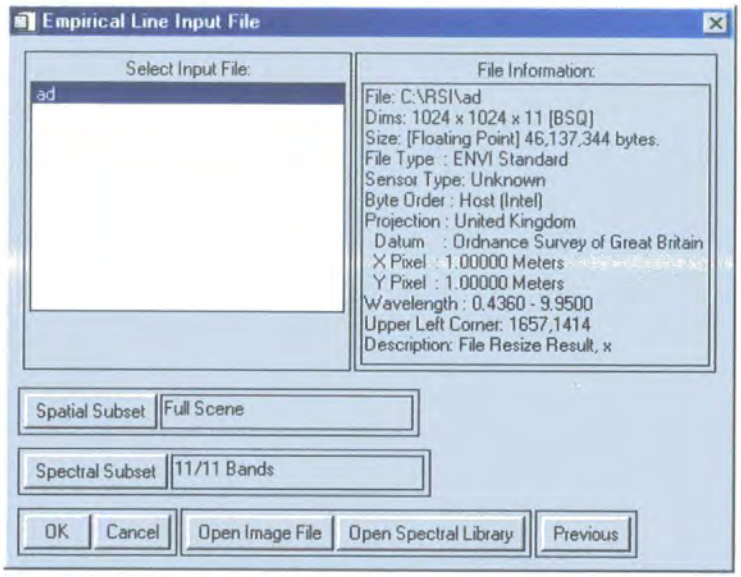

B5.2 Empirical Line Spectra – Data Spectra / Field Spectra– Import Spectra

1) Select to import either Data Spectra (left) or Field Spectra (right)

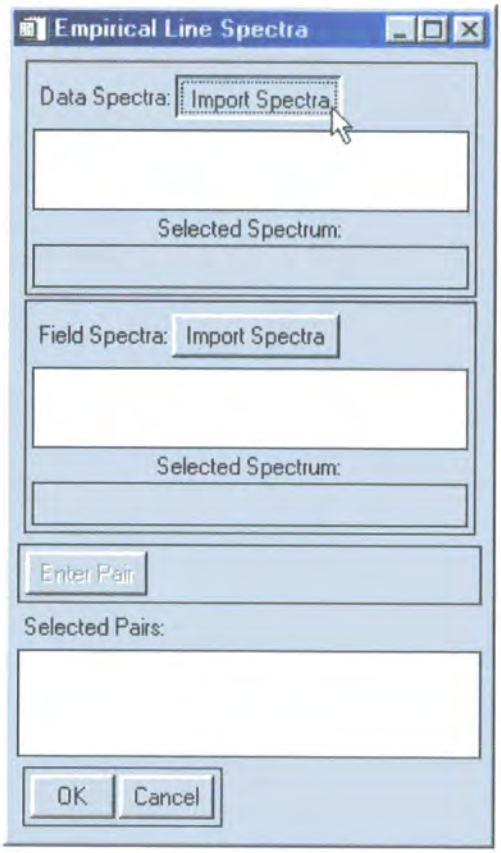

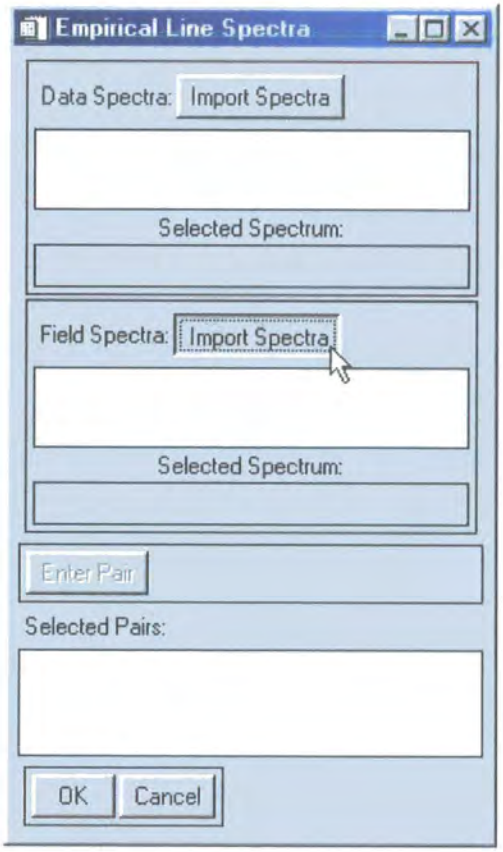

B5.3 Data Spectra Collection

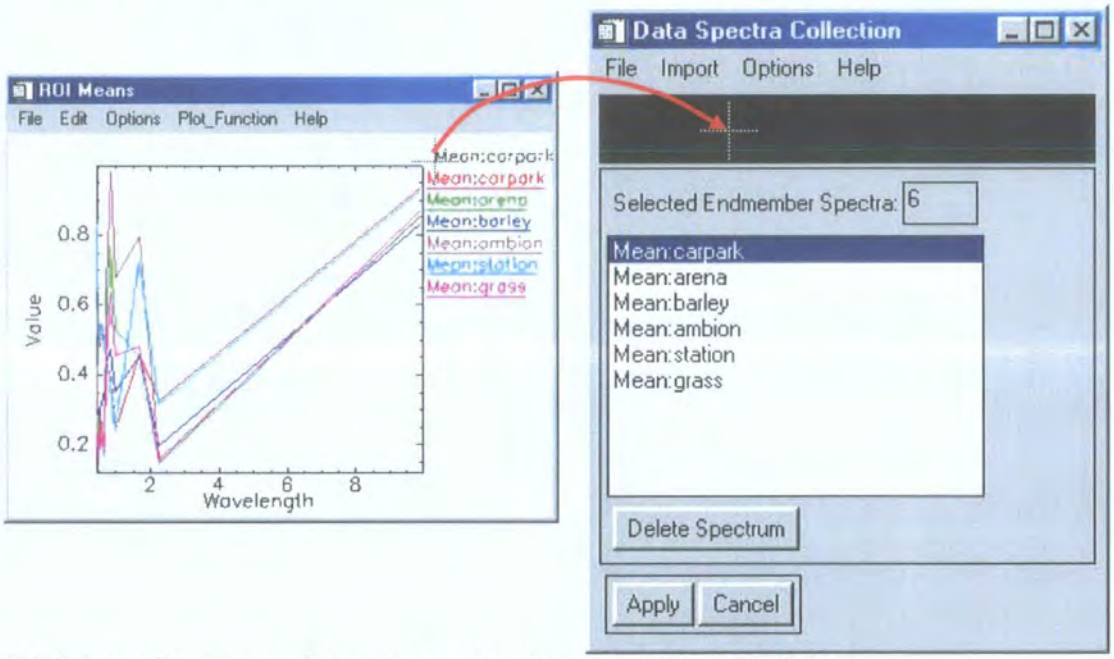

1) Click and Drag spectral signature to Data Spectral Collection window
2) Drop spectral signature into Data Spectral Collection black box
3) Apply desired spectra for calibration

B5.4 Field Spectra Collection – Import – from ASCII

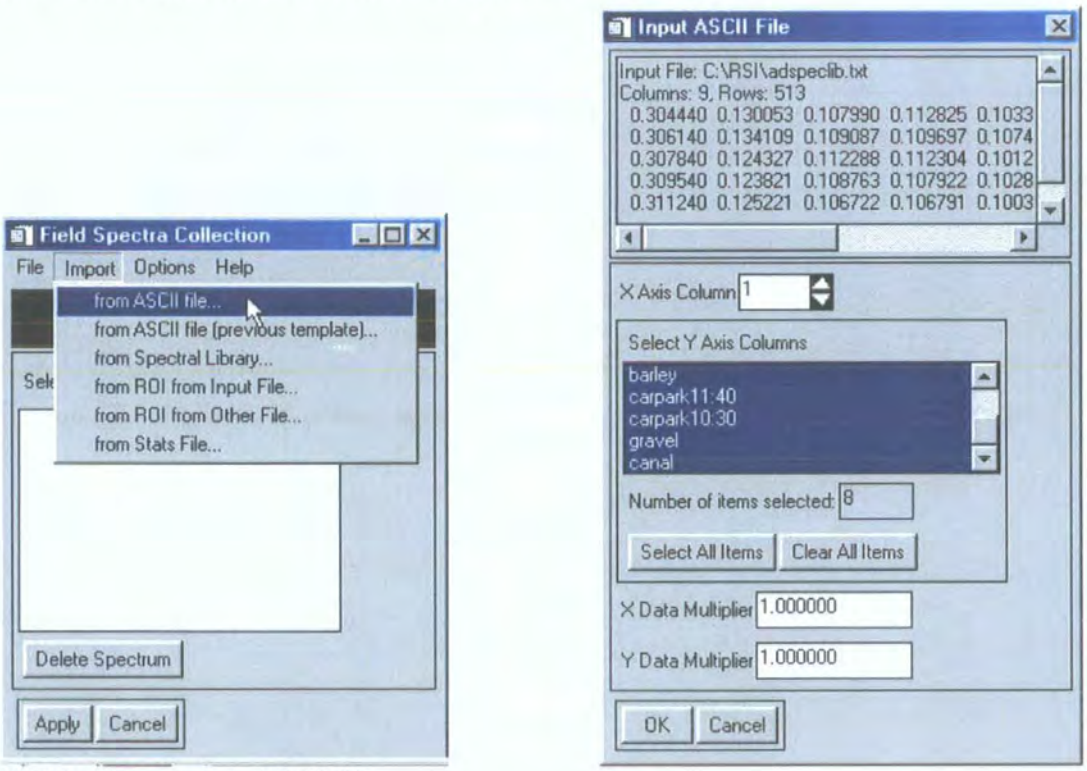

1) Select appropriate ASCII file
2) Select columns of data for importation

B5.5 Spectral Pairing for Empirical Line Calibration

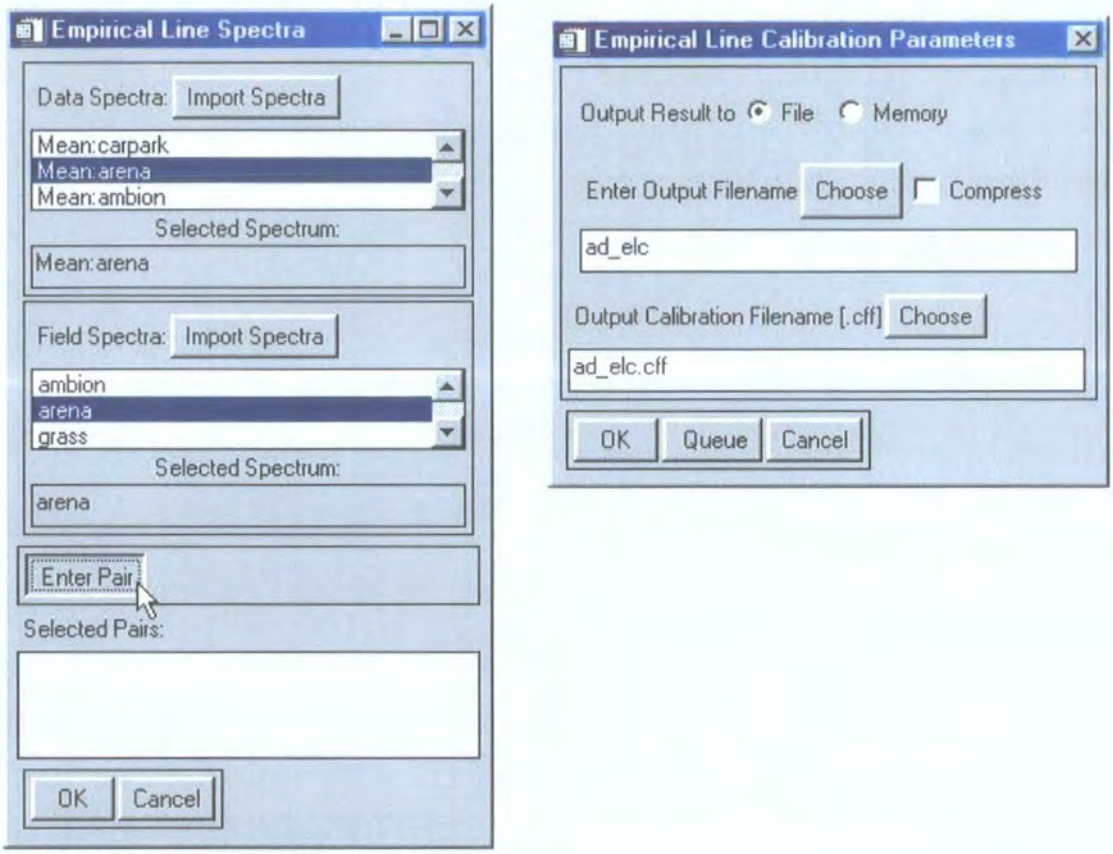

1) Click to select appropriate Data Spectra
2) Click to select appropriate Field Spectra
3) Select all pairs (left) then click OK
4) Empirical Line Calibration is performed to defined output file (right)

B6: IMAGE MASKING

B6.1 ENVI – Basic Tools – Masking – Build Mask

Mask Definition – Options – Import Band Data Range

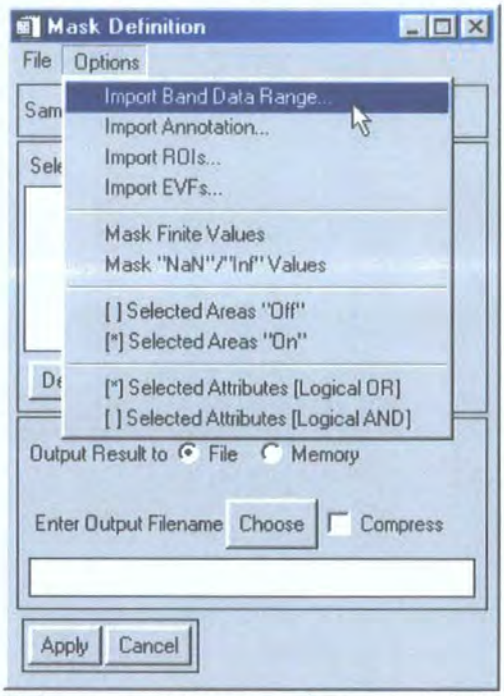

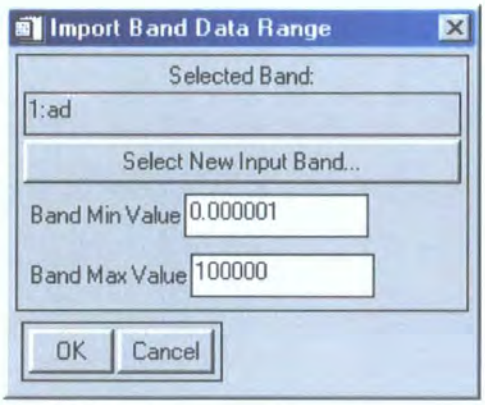

1) Image must be open prior to mask definition from data range
2) Select Band Minimum and Maximum Values as limits of retained data (right)
3) Select Output Filename

B6.2 ENVI – Basic Tools – Masking – Apply Mask

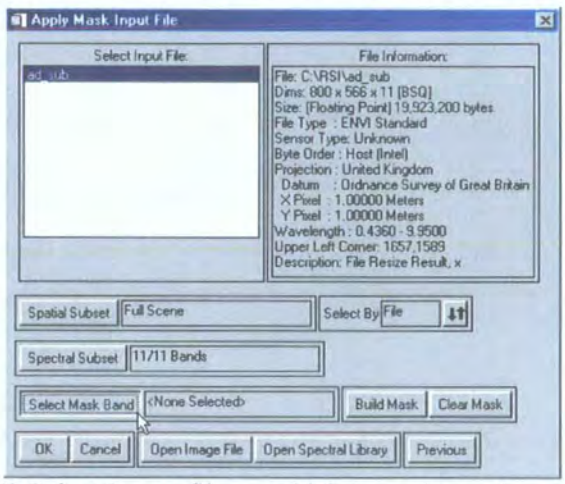

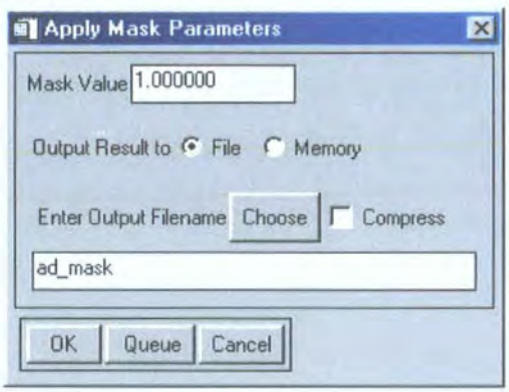

1) Select Image file on which to apply mask
2) Select Spatial and Spectral Subsets
3) Select Mask Band (mask must be open)
4) Select mask value=1 to retain masked area of image (right)
5) Select Output Filename

B7: BAND MATHEMATICS

ENVI - Basic Tools – Band Math

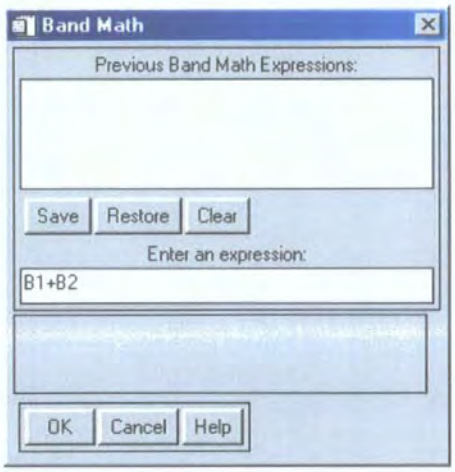

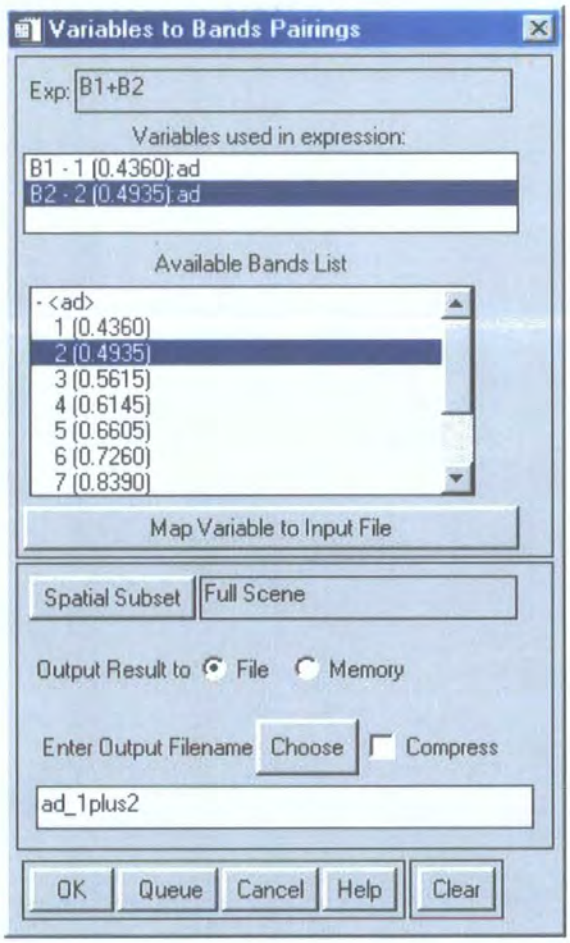

1) Enter mathematical expression (left)
2) Select representative bands from open images or masks (right)

B8: IMAGE RESIZING

ENVI – Basic Tools – Subset Image

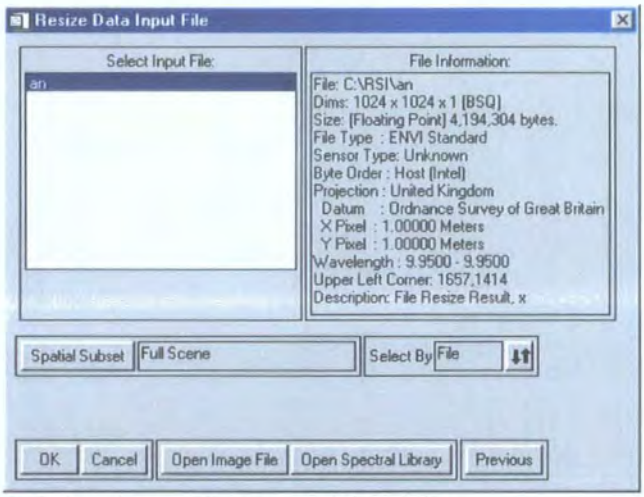

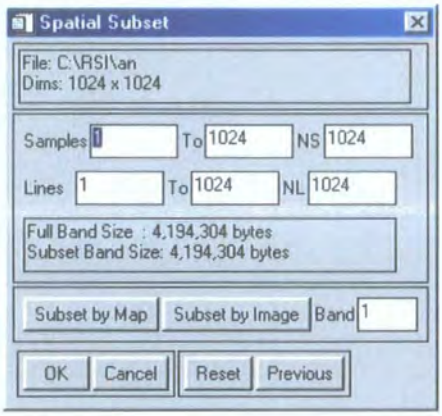

1) Select image file for spatial resizing
2) Spatial subset defined by Map coordinates or by Image (top right)
3) 'Previous' button allows image resizing using a previous example

4) Define rectangular area by dragging corners of red box
5) Alternatively define sample and lines and move red box over desired area
6) Save output file to removes 'non-value' pixels from analysis

B9: HISTOGRAM EXTRACTION

Image Display #1 – Enhance – Interactive Stretching

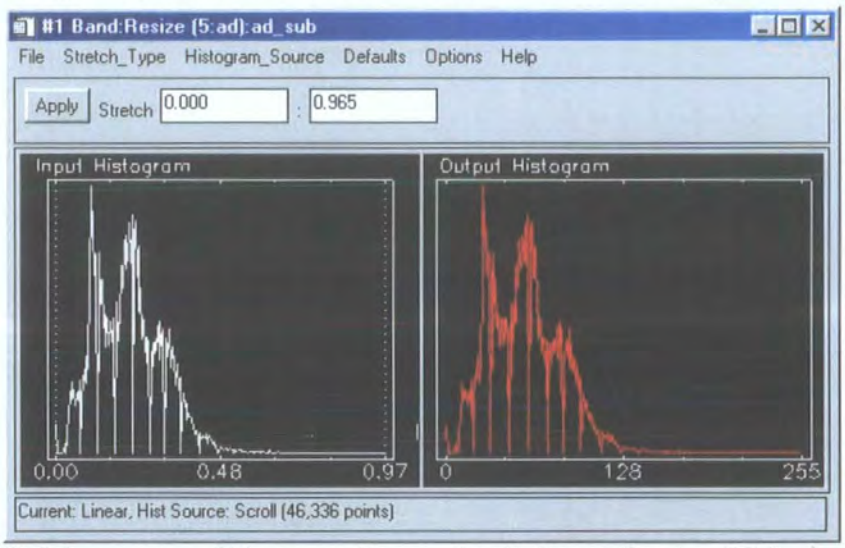

1) Select source of histogram (Image, Scroll, Zoom, Band or ROI)
2) Select Stretch-Tyoe (Linear, Piecewise Linear, Gaussian, Equalisation, Square Root, Arbitrary, User-Defined LUT)
3) Type range of values for stretch
4) Move Vertical Bars on Input Histogram for range of histogram for stretch

B10: PRINCIPAL COMPONENT ANALYSIS

ENVI – Transform – Principal Components – Forward PC Rotation – Compute New Statistics and Rotate

1) Select image file for forward PC rotation (selecting spatial or spectral subsets)

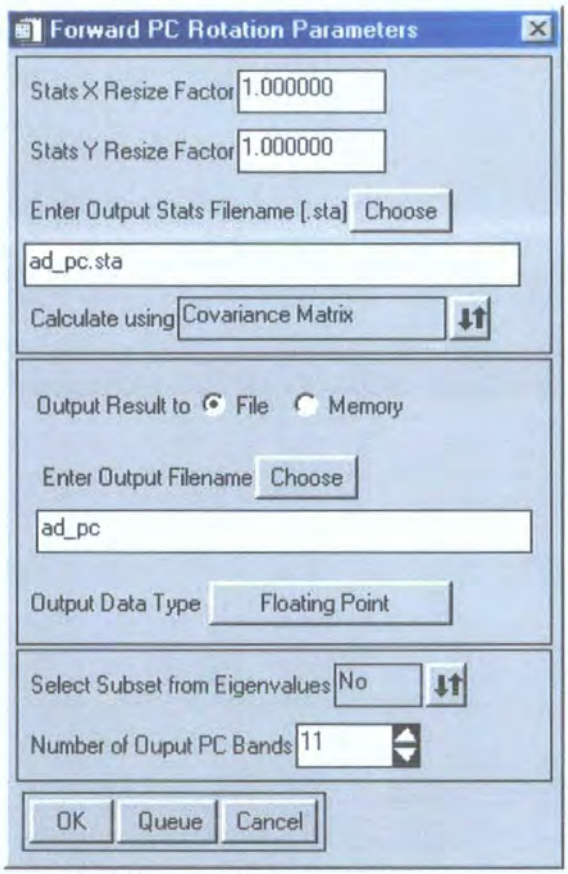

2) Define Forward PC Rotation Parameters
3) Enter Output Statistics Filename
4) Select to Calculate using either Covariance Matrix or Correlation Matrix
5) Select Output Filename
6) Select Output Data Type
7) Select Subset from Eigenvalues (NO) allowing definition of specific number of output PC Bands
8) Select Subset from Eigenvalues (YES) will display graph of eigenvalues graded from 1=data to 0=noise from which to select appropriate number of output PC bands (closest to 1)

B11: COMPUTE IMAGE STATISTICS

ENVI – Basic Tools – Statistics – Compute Statistics – Compute New Statistics and Rotate

1) Select image file for calculation of statistics (selecting spatial or spectral subsets)

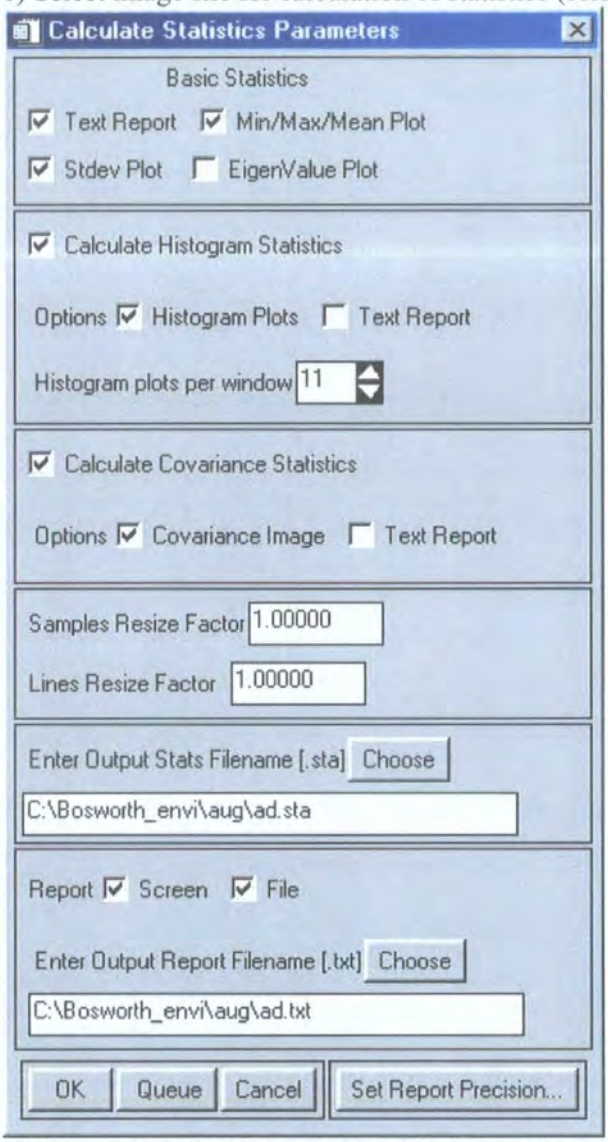

2) Select type of basic statistics with choice of text report, min/max/mean plot and/or stdev plot

3) Choice of selecting histogram statistics with choice of histogram plots and/or text report with choice of number of histogram plots per window

4) Choice of selecting covariance statistics with choice of covariance image and/or text report, which releases the choice of generating an additional eigenvalue plot on the basic statistics

5) Optional to enter an output stats filename (can be recalculated at any stage)

6) Select choice of writing statistics report to screen or file (entering appropriate filename)

Appendix C: ATM IMAGES & AERIAL PHOTOGRAPHS

C1 BOSWORTH IMAGES

June Aerial Photo Mosaic
Image Dimensions:
Vertical 0.566 km
Horizontal 0.800 km

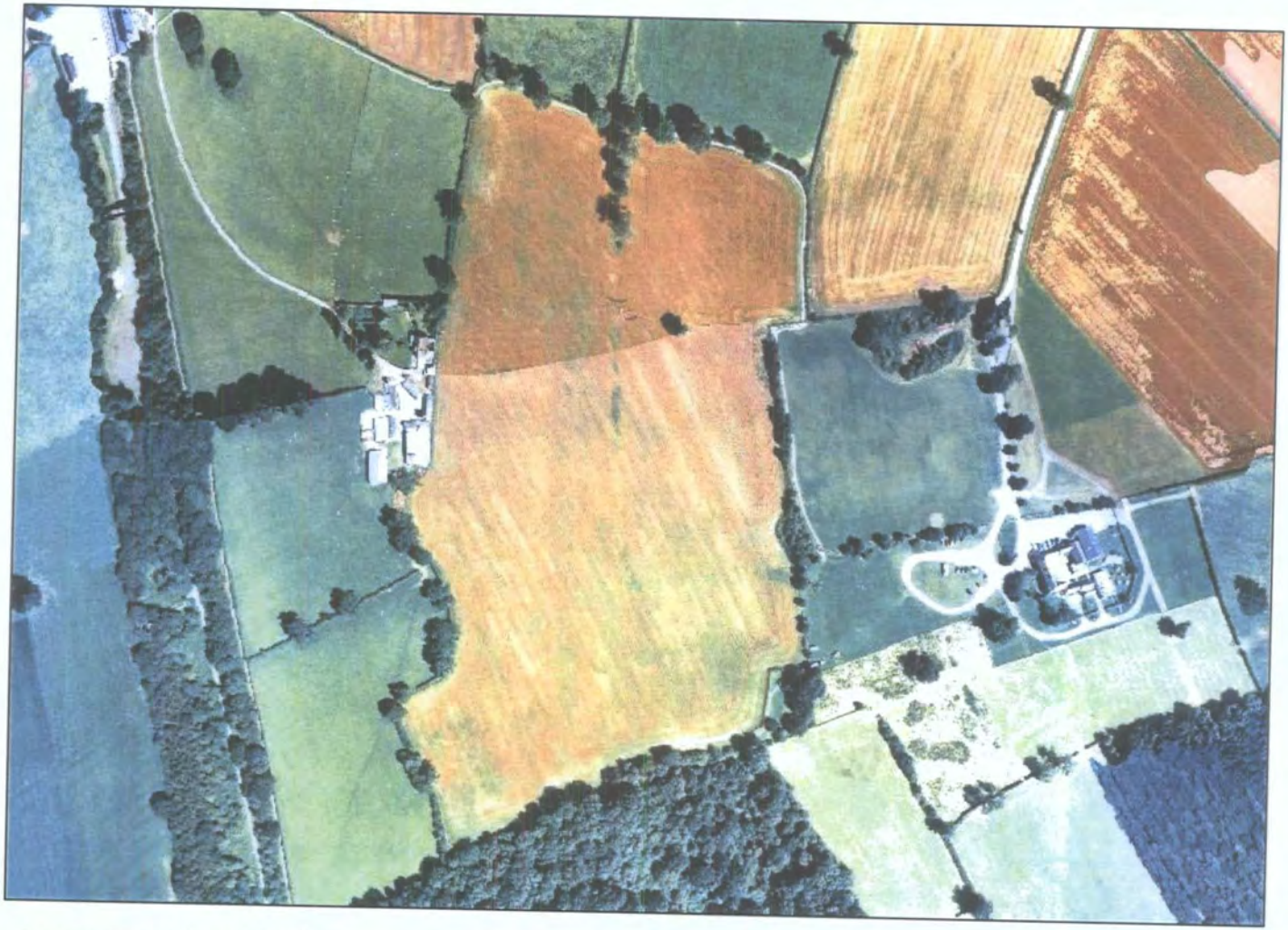

August Aerial Photo Mosaic
Image Dimensions:
Vertical 0.566 km
Horizontal 0.800 km

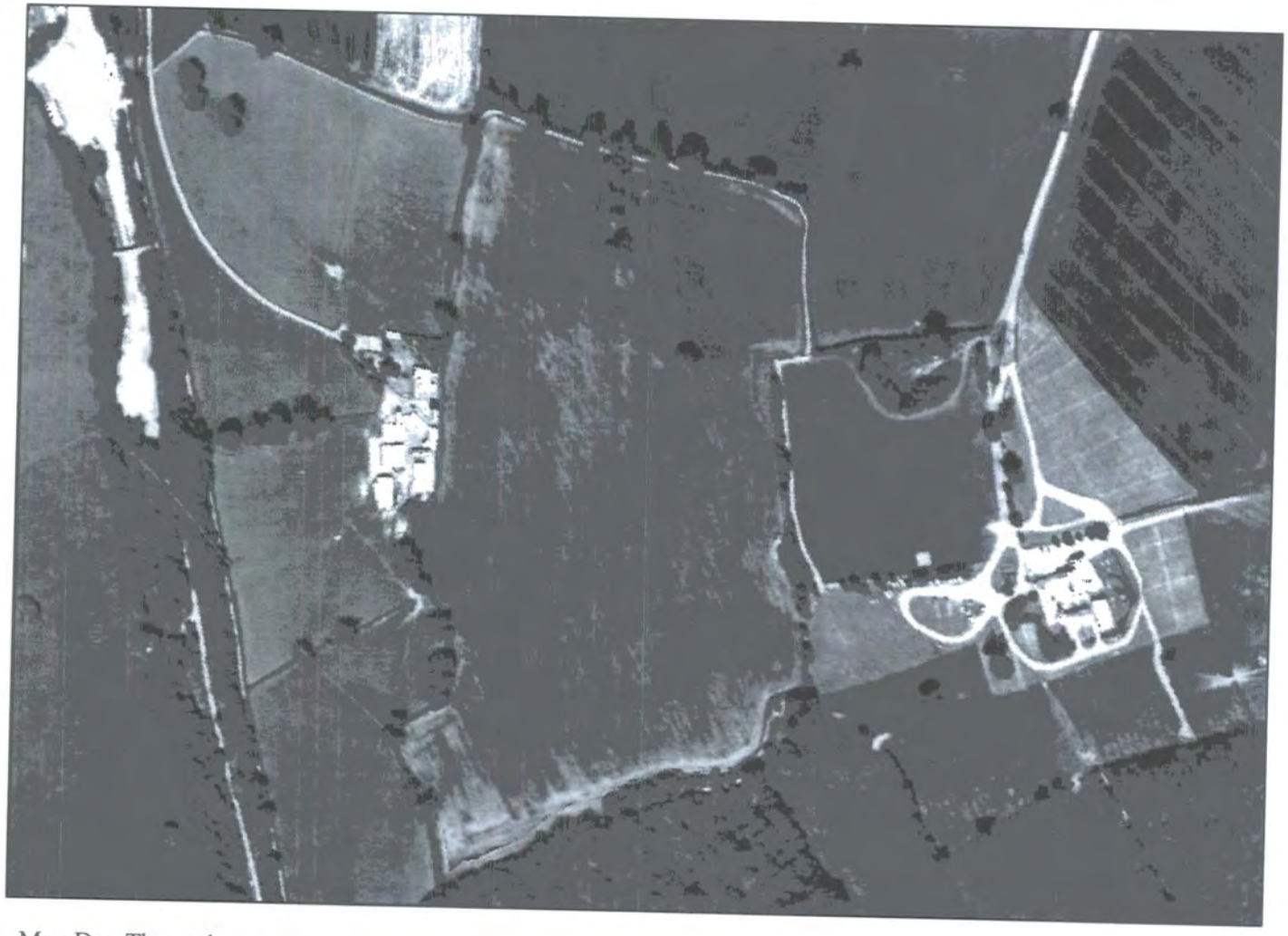

May Day Thermal
Image Dimensions:
Vertical 0.566 km
Horizontal 0.800 km

June Day Thermal
Image Dimensions:
Vertical 0.566 km
Horizontal 0.800 km

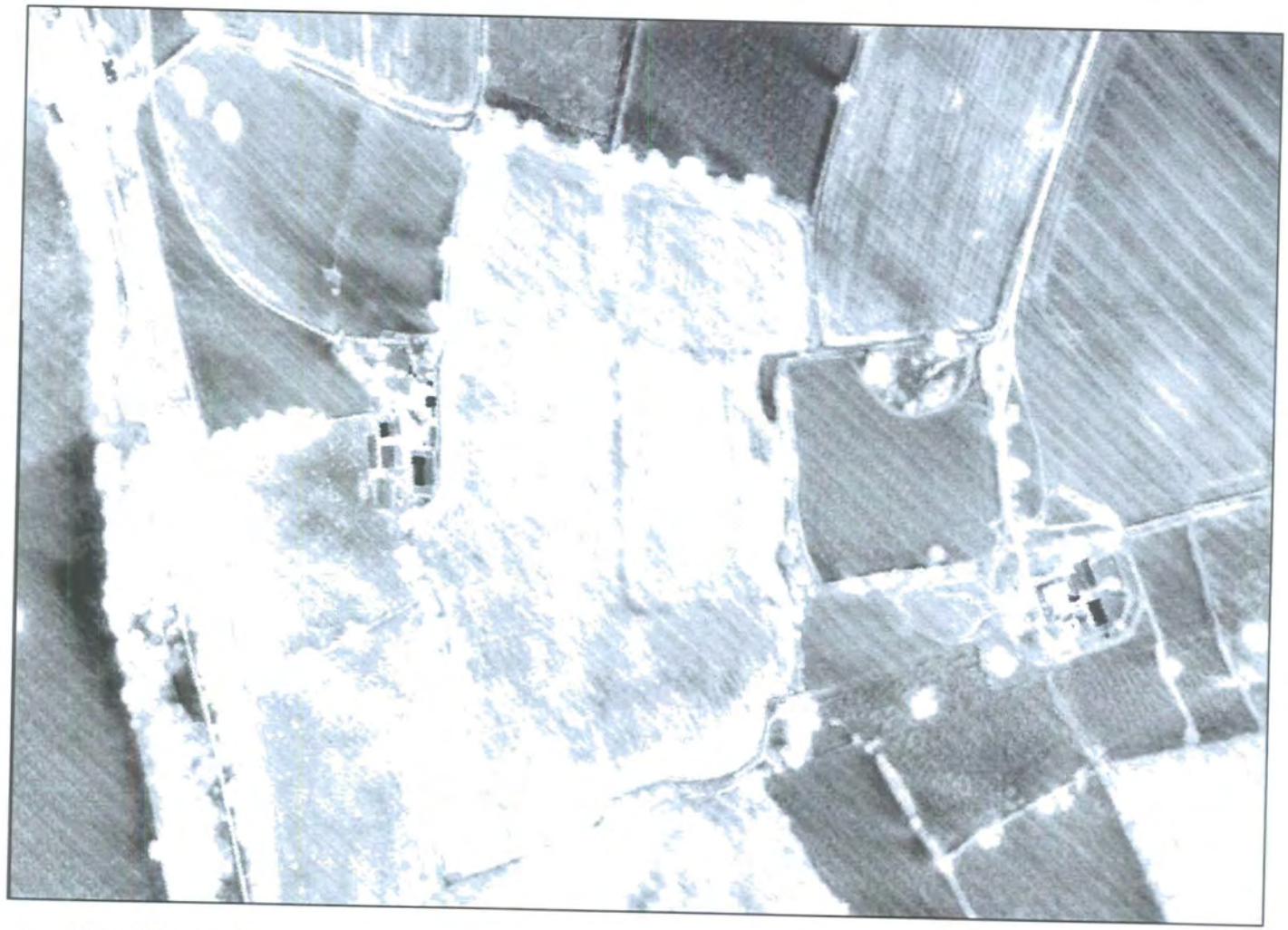

June Night Thermal
Image Dimensions:
Vertical 0.566 km
Horizontal 0.800 km

August Day Thermal
Image Dimensions:
Vertical 0.566 km
Horizontal 0.800 km

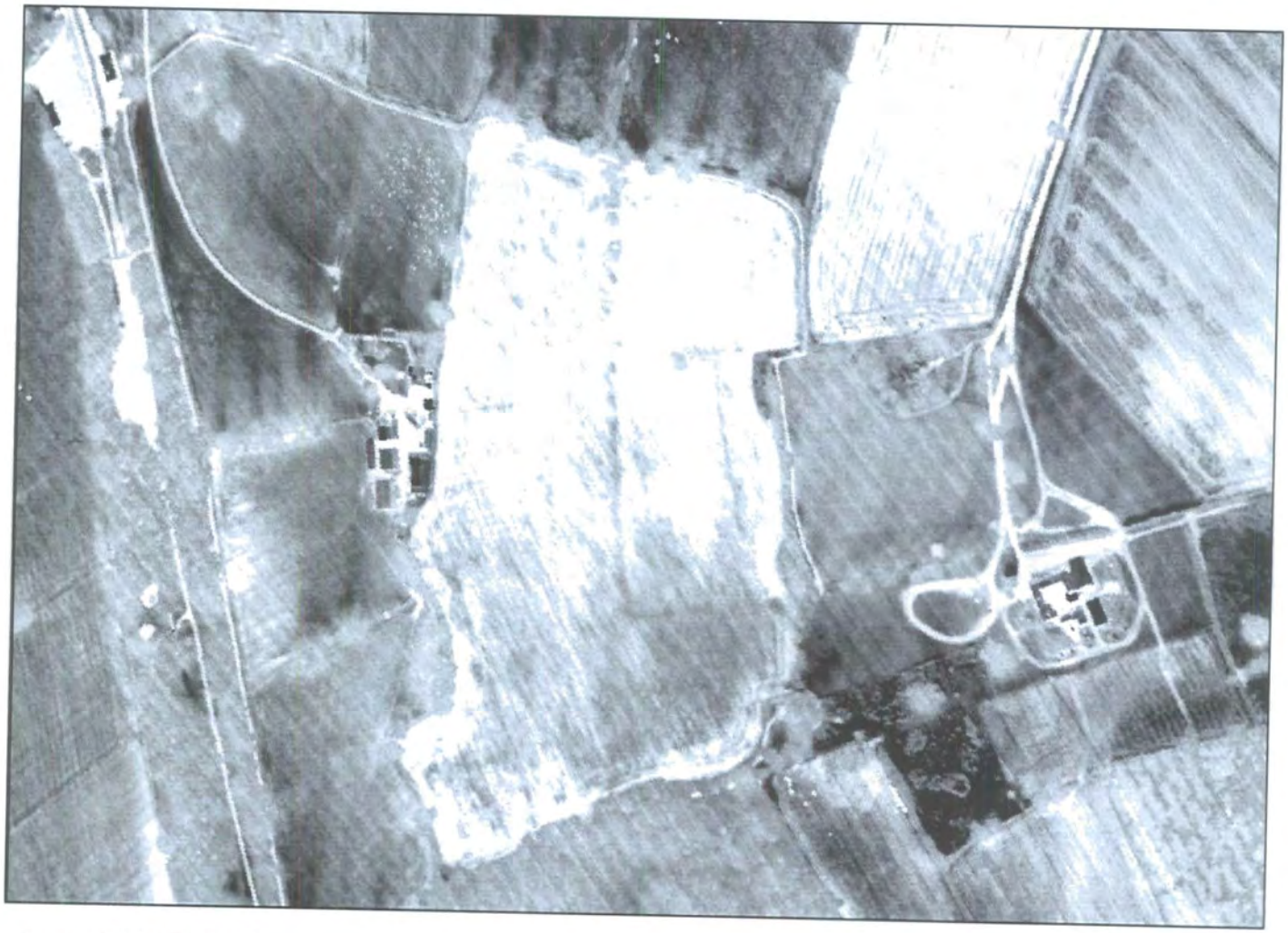

August Night Thermal
Image Dimensions:
Vertical 0.566 km
Horizontal 0.800 km

March Day Thermal
Image Dimensions:
Vertical 0.566 km
Horizontal 0.800 km

March Night Thermal
Image Dimensions:
Vertical 0.566 km
Horizontal 0.800 km

May Day Thermal Interpretation
Image Dimensions:
Vertical 0.566 km
Horizontal 0.800 km

June Day Thermal Interpretation
Image Dimensions:
Vertical 0.566 km
Horizontal 0.800 km

June Night Thermal Interpretation
Image Dimensions:
Vertical 0.566 km
Horizontal 0.800 km

August Day Thermal Interpretation
Image Dimensions:
Vertical 0.566 km
Horizontal 0.800 km

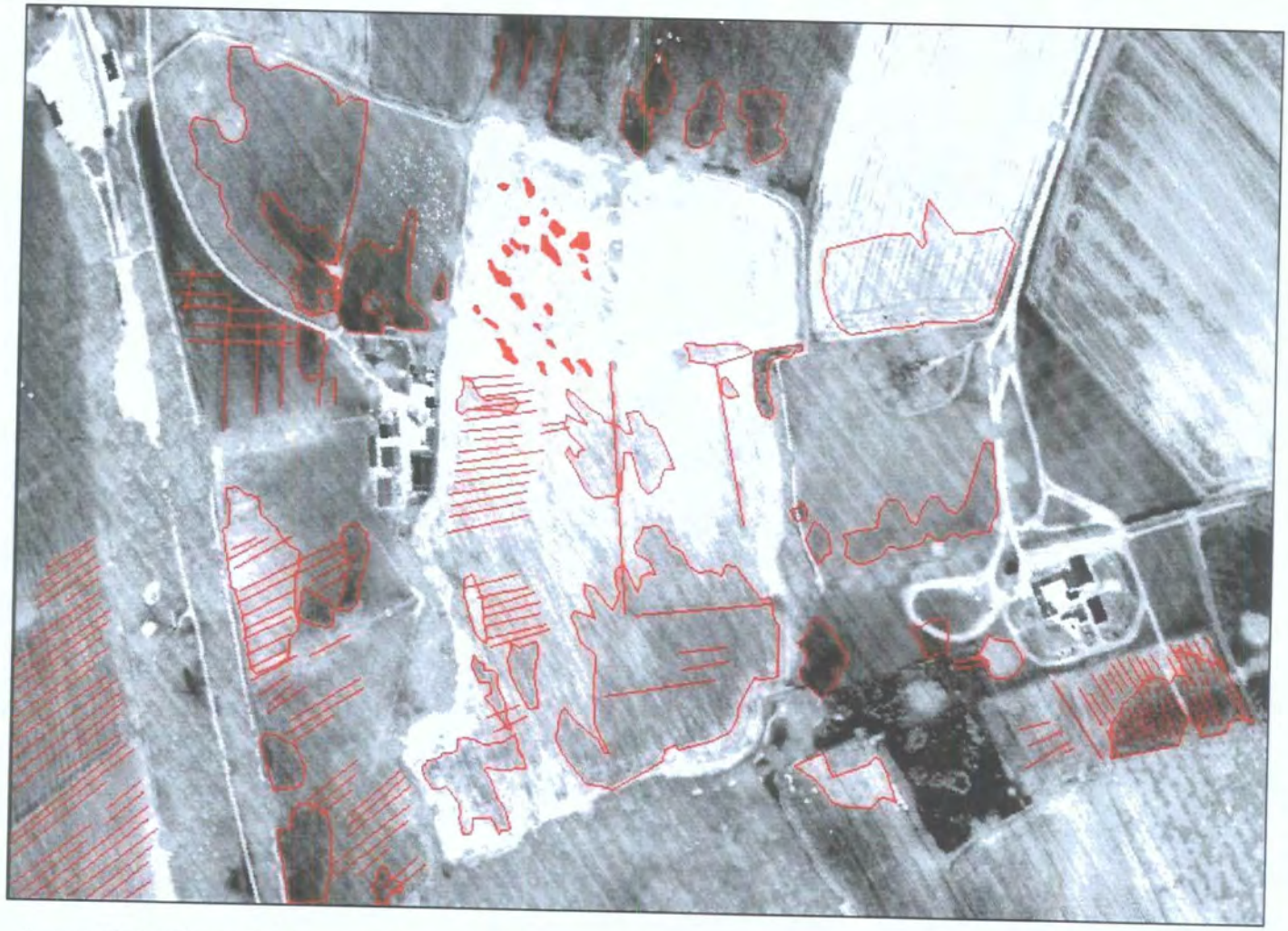

August Night Thermal Interpretation
Image Dimensions:
Vertical 0.566 km
Horizontal 0.800 km

March Day Thermal Interpretation
Image Dimensions:
Vertical 0.566 km
Horizontal 0.800 km

March Night Thermal Interpretation
Image Dimensions:
Vertical 0.566 km
Horizontal 0.800 km

C2 BAILDON MOOR IMAGES

May Natural Colour Composite Simulating Aerial Photograph

Image Dimensions:
Vertical 1.60 km
Horizontal 1.25 km

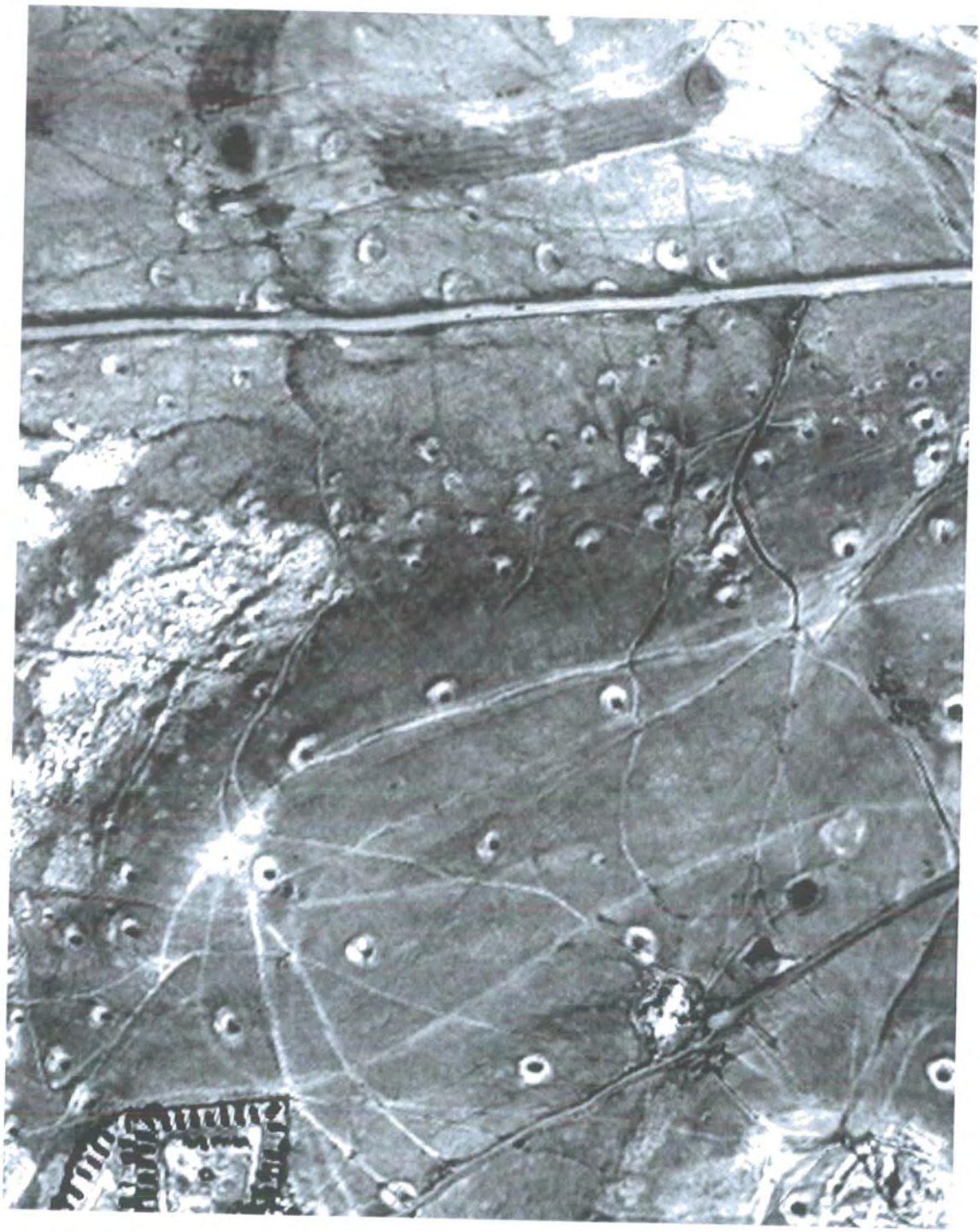

May Day Thermal Image

Image Dimensions:

Vertical	1.60 km
Horizontal	1.25 km

May Night Thermal Image

Image Dimensions:

Vertical	1.60 km
Horizontal	1.25 km

C3 WEARDALE IMAGES

August Natural Colour Composite Simulating Aerial Photo

Image Dimensions:
Vertical km
Horizontal km

August Day Thermal

Image Dimensions:
Vertical km
Horizontal km

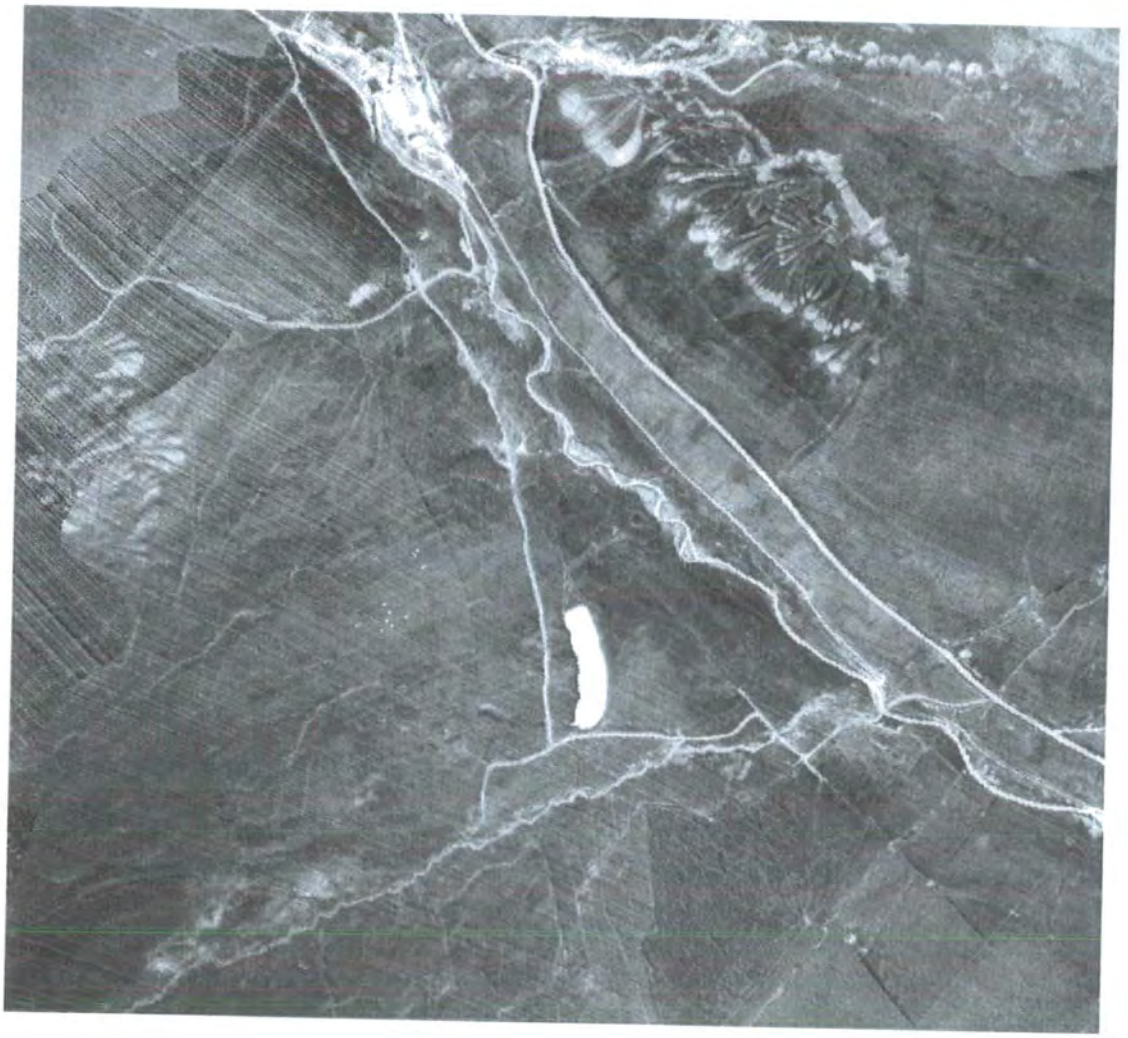

August Night Thermal

Image Dimensions:
Vertical km
Horizontal km

D1: BOSWORTH FLIGHT DETAILS

Flight	Day No	Time	Air Speed (kt)	Altitude (ft)	Lat Lower Limit	Lat Upper Limit	Long Lower Limit	Long Upper Limit	bbt1	bbt2
md1	139	12:12:59-12:16:00	105	2250	52.5752	52.5981	1.4547	1.4061	6.08	46.11
md2	139	12:19:00-12:22:04	105	2220	52.5718	52.6057	1.4524	1.3897	6.05	46.12
md3	139	12:26:00-12:29:04	105	1940	52.5796	52.6074	1.4471	1.3926	6.09	46.13
jd1	170	12:25:00-12:28:00	110	2010	52.5999	52.5791	1.3992	1.4392	7.02	39.03
jd2	170	12:32:00-12:34:00	110	2200	52.6105	52.5785	1.3918	1.4416	7.03	39.04
jd3	170	12:46:00-12:48:00	110	2140	52.6090	52.5806	1.3922	1.4447	7.04	39.04
jd4	170	12:53:00-12:55:00	110	2180	52.6084	52.5798	1.3838	1.4407	7.12	39.09
jn1	171	03:20:00-03:23:00	110	2290	52.6104	52.5799	1.3869	1.4429	4.70	28.61
jn2	171	03:27:00-03:29:00	110	2140	52.6035	52.5793	1.3974	1.4402	4.95	28.60
jn3	171	03:34:00-03:36:00	110	2350	52.6110	52.5795	1.3914	1.4442	5.24	28.64
ad1	217	09:39:00-09:41:00	110	2140	52.5810	52.6070	1.4108	1.4086	6.06	38.03
ad2	217	09:45:00-09:47:00	110	2330	52.5736	52.6084	1.4030	1.3990	6.07	38.04
ad3	217	09:51:00-09:53:00	110	2150	52.5789	52.6106	1.4227	1.4189	6.09	38.05
ad4	217	09:56:00-09:58:21	115	2110	52.5802	52.6073	1.4271	1.4233	6.09	38.05
ad5	217	10:03:00-10:05:00	110	2280	52.5714	52.6055	1.4111	1.4116	6.08	38.06
ad6	217	10:09:00-10:11:00	110	2270	52.5690	52.6085	1.3926	1.3901	6.10	38.06
ad7	217	10:15:00-10:17:00	110	2530	52.5742	52.6058	1.4164	1.4107	6.10	38.08
ad8	217	10:21:00-10:23:00	110	2190	52.5789	52.6061	1.4307	1.4281	6.11	38.08
ad9	217	10:30:00-10:31:00	110	2170	52.5800	52.6078	1.4069	1.4063	6.12	38.09

D1: BOSWORTH FLIGHT DETAILS (cont.)

Flight	Day No	Time	Air Speed (kt)	Altitude (ft)	Lat Lower Limit	Lat Upper Limit	Long Lower Limit	Long Upper Limit	bbt1	bbt2
ad10	217	10:36:00-10:38:00	110	2160	52.5727	52.6057	1.4199	1.4045	6.14	38.10
an1	218	04:12:00-04:15:00	110	2360	52.6094	52.5811	1.3925	1.4387	2.01	18.14
an2	218	04:20:00-04:23:00	110	2350	52.6081	52.5760	1.3771	1.4424	2.05	18.46
an3	218	04:28:00-04:31:00	110	2150	52.6086	52.5794	1.3799	1.4449	2.07	18.08
mard1	085	15:47:00-15:49:00	125	3250	52.6120	52.5690	1.4380	1.4373	N/A	N/A
mard2	085	15:51:00-15:54:00	125	3180	52.5610	52.6091	1.4067	1.4062	N/A	N/A
mard3	085	15:57:00-15:59:00	125	3190	52.6140	52.5699	1.4310	1.4320	N/A	N/A
mard4	085	16:01:00-16:04:00	125	3290	52.5709	52.6085	1.4105	1.4095	N/A	N/A
mard5	085	16:07:00-16:09:00	125	3280	52.6133	52.5710	1.4262	1.4278	N/A	N/A
mard6	085	16:13:00-16:15:00	125	3260	52.5644	52.6106	1.4128	1.4116	N/A	N/A
mard7	085	16:19:00-16:21:00	125	3210	52.6147	52.5704	1.4198	1.4220	N/A	N/A
mard8	085	16:25:00-16:28:00	125	3240	52.5643	52.6093	1.4178	1.4163	N/A	N/A
marn1	086	03:48:00-03:50:00	125	3180	52.6178	52.5702	1.4373	1.4362	N/A	N/A
marn2	086	03:54:00-03:56:00	125	3200	52.5663	52.6113	1.4169	1.4149	N/A	N/A
marn3	086	04:00:00-04:03:00	125	3220	52.6170	52.5702	1.4303	1.4325	N/A	N/A
marn4	086	04:05:00-04:08:00	125	3220	52.5661	52.6098	1.4113	1.4107	N/A	N/A
marn5	086	04:11:00-04:14:00	125	3200	52.6152	52.5706	1.4251	1.4273	N/A	N/A
marn6	086	04:17:00-04:20:00	125	3180	52.5716	52.6094	1.4097	1.4073	N/A	N/A
marn7	086	04:24:00-04:26:00	125	3240	52.6153	52.5701	1.4204	1.4222	N/A	N/A
marn8	086	04:30:00-04:32:00	125	3210	52.5667	52.6098	1.4060	1.4055	N/A	N/A

D2: BAILDON MOOR FLIGHT DETAILS

Flight	Day No	Time	Air Speed (kt)	Altitude (ft)	Lat Lower Limit	Lat Upper Limit	Long Lower Limit	Long Upper Limit	bbt1	bbt2
septn1	259	05:22:00-05:25:00	145	2650	53.8105	53.8578	1.8795	1.7890	0.08	16.10
septn2	259	05:28:00-05:31:40	135	2650	53.8648	53.7977	1.7276	1.8942	0.10	16.11
septn3	259	05:33:00-05:36:34	145	2650	53.7987	53.8679	1.9208	1.7687	0.09	16.12
septn4	259	05:38:00-05:42:00	135	3650	53.8702	53.8037	1.7344	1.8989	0.02	16.13
septn5	259	05:44:00-05:46:00	145	2650	53.7908	53.8200	1.9163	1.8583	0.02	16.14
septn6	259	05:47:00-05:49:39	145	3650	53.8164	53.8503	1.8475	1.7518	0.03	16.13
mayn1	123	03:59:00-04:30:00	135	3540	53.7865	53.8559	1.8975	1.7454	2.01	17.97
mayn2	123	04:05:00-04:09:00	125	3370	53.8675	53.8037	1.7411	1.8960	1.98	17.96
mayn3	123	04:10:21-04:14:00	130	3660	53.8030	53.8630	1.9212	1.7589	2.07	17.95
mayn4	123	04:15:00-04:19:00	125	3340	53.8775	53.8074	1.7552	1.9070	2.01	17.96
mayn5	123	04:22:00-04:24:00	125	3260	53.7942	53.8283	1.8855	1.8141	2.03	17.96

D3: WEARDALE FLIGHT DETAILS

Flight	Day No	Time	Air Speed (kt)	Altitude (ft)	Lat Lower Limit	Lat Upper Limit	Long Lower Limit	Long Upper Limit	bbt1	bbt2
augd1	240	14:08:00-14:11:30	115	4100	N/A	N/A	N/A	N/A	N/A	N/A
augd2	240	14:15:30-14:16:40	110	4030	54.7519	54.7840	2.1429	2.1075	N/A	N/A
augd3	240	14:20:00-14:23:30	120	3980	54.7954	54.7331	2.1154	2.1845	N/A	N/A
augd4	240	14:26:00-14:29:30	110	3950	54.7349	54.7954	2.2033	2.1363	N/A	N/A
augd5	240	14:33:00-14:36:30	115	4000	54.8036	54.7439	2.1481	2.2147	N/A	N/A
augd6	240	14:39:00-14:42:30	115	3950	54.7488	54.8157	2.2305	2.1570	N/A	N/A
augd7	240	14:45:00-14:48:30	115	4000	54.8094	54.7547	2.1841	2.2443	N/A	N/A
augd8	240	14:51:00-14:54:30	115	4000	54.7502	54.8054	2.2325	2.1722	N/A	N/A
augd9	240	14:57:00-15:00:10	115	4000	54.8040	54.7464	2.1587	2.2220	N/A	N/A
augd10	240	15:02:00-15:05:30	115	4000	54.7304	54.7868	2.1777	2.1153	N/A	N/A
augd11	240	15:11:00-15:14:41	115	4050	54.8010	54.7413	2.1411	2.2074	N/A	N/A
augd12	240	15:21:00-15:24:00	110	3900	54.7227	54.7808	2.1643	2.1002	N/A	N/A
augd13	240	15:29:00-15:30:41	115	3900	54.7952	54.7640	2.1267	2.1609	N/A	N/A
augd14	240	15:38:00-15:41:00	115	4050	54.7513	54.8115	2.2487	2.1818	N/A	N/A
augd15	240	15:45:40-15:48:00	115	4030	54.8040	54.7466	2.1591	2.2219	N/A	N/A
augd16	240	15:50:30-15:54:30	120	4070	54.7477	54.8074	2.2313	2.1655	N/A	N/A
augd18	240	16:04:00-16:06:30	115	4070	54.7432	54.8027	2.2264	2.1600	N/A	N/A

D3: WEARDALE FLIGHT DETAILS (cont.)										
Flight	Day No	Time	Air Speed (kt)	Altitude (ft)	Lat Lower Limit	Lat Upper Limit	Long Lower Limit	Long Upper Limit	bbt1	bbt2
augn1	241	02:02:00-02:05:00	115	4010	54.7774	54.7231	2.0947	2.1537	N/A	N/A
augn2	241	02:08:00-02:10:00	115	4000	54.7299	54.7460	2.1682	2.1523	N/A	N/A
augn3	241	02:14:20-02:16:30	115	4000	54.7297	54.7853	2.1657	2.1063	N/A	N/A
augn4	241	02:21:00-02:29:00	115	4100	54.7886	54.7339	2.1238	2.1853	N/A	N/A
augn5	241	02:26:50-02:32:00	115	4000	54.7399	54.7943	2.1976	2.1372	N/A	N/A
audn6	241	02:33:00-02:35:40	115	4000	54.7994	54.7459	2.1534	2.2161	N/A	N/A
augn7	241	02:38:40-02:40:50	115	4050	54.7524	54.8050	2.2256	2.1672	N/A	N/A
augn8	241	02:46:00-02:48:00	115	4000	54.8094	54.7558	2.1846	2.2434	N/A	N/A
augn9	241	02:51:00-02:53:30	115	4050	54.7545	54.8052	2.2351	2.1779	N/A	N/A
augn10	241	02:58:00-03:00:40	120	4100	54.7997	54.7478	2.1622	2.2203	N/A	N/A
augn11	241	03:05:00-03:07:30	115	4200	54.7431	54.7987	2.2039	2.1435	N/A	N/A
augn12	241	03:12:00-03:14:17	115	4100	54.7897	54.7436	2.1317	2.1815	N/A	N/A
augn13	241	03:18:30-03:21:17	115	4050	54.7324	54.7854	2.1758	2.1155	N/A	N/A
augn14	241	03:26:00-03:28:20	115	4100	54.7790	54.7260	2.1011	2.1623	N/A	N/A

D4: SUMMARY FLIGHT DETAILS for SUN ANGLE CALCULATION				
BOSWORTH	Date	Average Time	Average Latitude	Average Longitude
May Day	19-05-1998	12:20	52.59 N	1.41 W
June Day	19-06-1998	12:40	5259 N	1.41 W
June Night	20-06-1998	03:28	52.59 N	1.41 W
August Day	05-08-1998	10:08	52.59 N	1.41 W
August Night	06-08-1998	04:21	52.59 N	1.41 W
March Day	21-03-2002	16:07	52.59 N	1.41 W
March Night	22-03-2002	04:10	52.59 N	1.41 W
BAILDON MOOR	Date	Time	Average Latitude	Average Longitude
May Day	03-05-1997	12:10	53.83 N	1.82 W
May Night	04-05-1997	04:11	53.83 N	1.82 W
WEARDALE	Date	Time	Average Latitude	Average Longitude
August Day	22-08-2001	15:30	54.76 N	2.17 W
August Night	23-08-2001	02:45	54.76 N	2.17 W

Appendix E: SUN ANGLE

Solar declination calculated from known latitude, longitude, elevation and timing of study using sun angle calculator on http://www.susdesign/sunangle/index.html

SunAngle is an on-line tool that calculates solar angles and related information for a given location, date and time. The program runs on a web browser. As much information as possible should be entered into the inputs selection before calculation, the outputs appearing in the output section.

LATITUDE – in degrees N or S of equator in either decimal degree (45.5) or degree-minute-seconds (45d30m0s)
LONGITUDE – in degrees E or W in either decimal degree or degree-minute-seconds
DATE – indicate the month and date using pull-down menus
YEAR – indicate year using pull-down menu (although exact year matters very little)
ELEVATION - elevation compared to the surrounding terrain in meters or feet so relative elevation is zero if not require accurate sunrise/sunset outputs
TIME – indicate time using 12:34 or 1234 notation, indicating AM/PM/24 from pull-down menu
TIME ZONE – select time zone, i.e. GMT when daylight not active
TIME BASIS - time for clock (observations) or local solar time (sun cycle)
DAYLIGHT SAVING - if DST is in effect in locations

E1: BOSWORTH SUN ANGLE VALUES

MAY DAY INPUT			MAY DAY OUTPUT		
longitude	**1.41 W**		altitude angle	56.19	51.68
latitude	**52.59 N**		azimuth angle	17.98	40.83
date	May 19		clock time	12:20 pm	12:20 pm
year	1998		solar time	11:17 am	10:17 am
elevation	100 m		hour angle	10.52	25.52
time	**12:20 PM**		**declination**	**19.78**	**19.77**
time zone	(GMT +1)		equation of time	3.56	3.57
time basis	Clock time		time of sunrise	5:00 am	6:00 am
daylight savings	No	Yes	time of sunset	9:03 pm	10:03 pm

JUNE DAY INPUT			JUNE DAY OUTPUT		
longitude	**1.41 W**		altitude angle	60.39	56.47
latitude	**52.59 N**		azimuth angle	12.56	37.94
date	Jun 19		clock time	12:40 pm	12:40 pm
year	1998		solar time	11:33 am	10.33 am
elevation	100 m		hour angle	6.73	21.72
time	**12:40 PM**		**declination**	**23.42**	**23.42**
time zone	(GMT +1)		equation of time	-1.27	-1.27
time basis	Clock time		time of sunrise	4:38 am	5:38 am
daylight savings	No	Yes	time of sunset	9:35 pm	10.35 pm

JUNE NIGHT INPUT			JUNE NIGHT OUTPUT		
longitude	1.41 W		altitude angle	-8.01	-11.95
latitude	52.59 N		azimuth angle	147.68	161.07
date	Jun 20		clock time	3:28 am	3:28 am
year	1998		solar time	2:20 am	1:02 am
elevation	100 m		hour angle	144.76	159.76
time	3:28 AM		declination	23.43	23.43
time zone	(GMT +1)		equation of time	-1.41	-1.40
time basis	Clock time		time of sunrise	4:38 am	5:38 am
daylight savings	No	Yes	time of sunset	9:35 pm	10:35 pm

AUGUST DAY INPUT			AUGUST DAY OUTPUT		
longitude	1.41 W		altitude angle	39.51	30.97
latitude	52.59 N		azimuth angle	62.93	77.08
date	Aug 5		clock time	10:08 am	10:08 am
year	1998		solar time	8:56 am	7:56 am
elevation	100 m		hour angle	45.91	60.91
time	10:08 AM		declination	16.98	16.99
time zone	(GMT +1)		equation of time	-6.01	-6.02
time basis	Clock time		time of sunrise	5:28 am	6:28 am
daylight savings	No	Yes	time of sunset	8.54 pm	9:54 pm

AUGUST NIGHT INPUT			AUGUST NIGHT OUTPUT		
longitude	1.41 W		altitude angle	-9.48	-15.78
latitude	52.59 N		azimuth angle	134.43	147.93
date	Aug 6		clock time	4:21 am	4:21 am
year	1998		solar time	3:09 am	2:09 am
elevation	100 m		hour angle	132.64	147.46
time	4:21 AM		declination	16.78	16.79
time zone	(GMT +1)		equation of time	-5.94	-5.94
time basis	Clock time		time of sunrise	5:29 am	6:29 am
daylight savings	No	Yes	time of sunset	8.53 pm	9:53 pm

MARCH DAY INPUT			MARCH DAY OUTPUT		
longitude	1.41 W		altitude angle	26.42	32.55
latitude	52.59 N		azimuth angle	-50.28	-34.53
date	Mar 21		clock time	4:07 pm	4:07 pm
year	2002		solar time	2:54 pm	1:54 pm
elevation	100 m		hour angle	-43.54	-28.54
time	4:07 PM		declination	0.33	0.31
time zone	(GMT +0)		equation of time	-7.20	-7.21
time basis	Clock time		time of sunrise	7:03 am	8:03 am
daylight savings	No	Yes	time of sunset	7:22 pm	8:22 pm

MARCH NIGHT INPUT			MARCH NIGHT OUTPUT		
longitude	1.41 W		altitude angle	-25.29	-31.50
latitude	52.59 N		azimuth angle	129.39	144.94
date	Mar 22		clock time	4:10 am	4:10 am
year	2002		solar time	2:57 am	1:57 am
elevation	100 m		hour angle	135.67	150.67
time	4:10 AM		declination	0.53	0.51
time zone	(GMT +0)		equation of time	-7.05	-7.06
time basis	Clock time		time of sunrise	7:02 am	8:02 am
daylight savings	No	Yes	time of sunset	7:23 pm	8:23 pm

E2: BAILDON MOOR SUN ANGLE VALUES

MAY DAY INPUT			MAY DAY OUTPUT		
longitude	1.82 W		altitude angle	50.48	45.90
latitude	53.83 N		azimuth angle	20.73	41.35
date	May 3		clock time	12:10 pm	12:10 pm
year	1997		solar time	11:05 am	10:05 am
elevation	100 m		hour angle	13.53	28.53
time	12:10 PM		declination	15.76	15.74
time zone	(GMT +1)		equation of time	3.15	3.14
time basis	Clock time		time of sunrise	5:24 am	6:24 am
daylight savings	No	Yes	time of sunset	8:44 pm	9:43 pm

MAY NIGHT INPUT			MAY NIGHT OUTPUT		
longitude	1.82 W		altitude angle	-9.62	-15.13
latitude	53.83 N		azimuth angle	134.76	148.41
date	May 4		clock time	4:11 am	4:11 am
year	1997		solar time	3:06 am	2:06 am
elevation	100 m		hour angle	133.27	148.27
time	4:11 AM		declination	15.95	15.94
time zone	(GMT +1)		equation of time	3.21	3.21
time basis	Clock time		time of sunrise	5:22 am	6:22 am
daylight savings	No	Yes	time of sunset	8:45 pm	9:45 pm

E3: WEARDALE SUN ANGLE VALUES

AUGUST DAY INPUT			AUGUST DAY OUTPUT		
longitude	2.17 W		altitude angle	39.03	44.20
latitude	54.76 N		azimuth angle	-45.75	-27.30
date	Aug 22		clock time	3:30 pm	3:30 pm
year	2001		solar time	2:18 pm	1:18 pm
elevation	100 m		hour angle	-34.62	-19.62
time	3:30 PM		declination	11.63	11.64
time zone	(GMT +1)		equation of time	-2.82	-2.84
time basis	Clock time		time of sunrise	5:54 am	6:54 am
daylight savings	No	Yes	time of sunset	8:28 pm	9:28 pm

AUGUST NIGHT INPUT			AUGUST NIGHT OUTPUT		
longitude	2.17 W		altitude angle	-20.89	-23.38
latitude	54.76 N		azimuth angle	155.38	171.03
date	Aug 23		clock time	2:45 am	2:45 am
year	2001		solar time	1:33 am	12:33 am
elevation	100 m		hour angle	156.60	171.60
time	2:45 AM		declination	11.47	11.48
time zone	(GMT +1)		equation of time	-2.70	-2.71
time basis	Clock time		time of sunrise	5:55 am	6:55 am
daylight savings	No	Yes	time of sunset	8:26 pm	9:27 pm

E4: SOLAR DECLINATION VALUES from SUN ANGLE PROGRAM

Dataset	Lat (N)	Long (W)	Date	Time	Solar Declination
Bosworth May	52.59	1.41	19-05-98	12:20	19.77
Bosworth June Day	52.59	1.41	19-06-98	12:40	23.42
Bosworth June Night	52.59	1.41	20-06-98	03:28	23.43
Bosworth August Day	52.59	1.41	05-08-98	10:08	16.99
Bosworth August Night	52.59	1.41	06-08-98	04:21	16.79
Bosworth March Day	52.59	1.41	21-03-02	16.07	0.31
Bosworth March Night	52.59	1.41	22-03-02	04:10	0.51
Baildon Moor Day	53.83	1.82	03-05-97	12:10	15.75
Baildon Moor Night	53.83	1.82	04-05-97	04:11	15.94
Weardale Day	54.76	2.17	22-08-01	15:30	11.64
Weardale Night	54.76	2.17	23-08-01	02:45	11.48

F1 SENSITIVITY of PLANCK RADIANCE to VARIABLE WAVELENGTH, SPECIFYING TEMPERATURE and EMISSIVITY

```
#include <stdio.h>
#include <math.h>
#include <stdlib.h>
#include <string.h>
#include <memory.h>

main()
{
        float radiance=0.00;
        float wavelength_micron=0.00;
        float emissivity=0.00;
        float temperature;
        int C1=374000000;
        int C2=14390;
        float i;
        printf("\n Sensitivity of Planck Radiance to Wavelength\n");
        printf("\n Specify temperature in K: ");
        scanf("%f",&temperature);
        printf(" Specify emissivity: ");
        scanf("%f",&emissivity);
        for(i=8.40;i<11.55;i+=0.05)
        {
                wavelength_micron=i;
                radiance=(emissivity*C1)/((pow(wavelength_micron,5))*(exp((C2/(wavelength_micron*temperature))-1)));
                printf("wavelength\t%.2f\tradiance\t%.2f\n",wavelength_micron,radiance);
        }
}
```

F2 SENSITIVITY of PLANCK RADIANCE to VARIABLE EMISSIVITY, SPECIFYING TEMPERATURE and WAVELENGTH

```
#include <stdio.h>
#include <math.h>
#include <stdlib.h>
#include <string.h>
#include <memory.h>

main()
{
        float radiance=0.00;
        float wavelength_micron=0.00;
        float emissivity=0.00;
        float temperature;
        int C1=374000000;
        int C2=14390;
        float i;
        printf("\n Sensitivity of Planck Radiance to Emissivity\n");
        printf("\n Specify temperature in K: ");
        scanf("%f",&temperature);
        printf(" Specify wavelength: ");
        scanf("%f",&wavelength_micron);
        for(i=0.90;i<1.00;i+=0.01)
        {
                emissivity=i;
                radiance=(emissivity*C1)/((pow(wavelength_micron,5))*(exp((C2/(wavelength_micron*temperature))-1)));
                printf("emissivity\t%.2f\tradiance\t%.2f\n",emissivity,radiance);
        }
}
```

F3 SENSITIVITY of PLANCK TEMPERATURE to VARIABLE WAVELENGTH, SPECIFYING RADIANCE and EMISSIVITY

```
#include <stdio.h>
#include <math.h>
#include <stdlib.h>
#include <string.h>
#include <memory.h>

main()
{
        float radiance=0.00;
        float wavelength_micron=0.00;
        float emissivity=0.00;
        float temperature;
        int C1=374000000;
        int C2=14390;
        float i;
        printf("\n Sensitivity of Planck Temperature to Wavelength\n");
        printf("\n Specify spectral radiance in W m-2 micron-1: ");
        scanf("%f",&radiance);
        printf(" Specify emissivity: ");
        scanf("%f",&emissivity);
        for(i=8.40;i<11.55;i+=0.05)
        {
                wavelength_micron=i;
                temperature=C2/(wavelength_micron*(log((emissivity*C1)/(pow(wavelength_micron,5)*radiance))+1));
                printf("wavelength\t%.2f\ttemperature\t%.2f\n",wavelength_micron,temperature);
        }
}
```

F4 SENSITIVITY of PLANCK TEMPERATURE to VARIABLE EMISSIVITY, SPECIFYING RADIANCE and WAVELENGTH

```
#include <stdio.h>
#include <math.h>
#include <stdlib.h>
#include <string.h>
#include <memory.h>

main()
{
        float radiance=0.00;
        float wavelength_micron=0.00;
        float emissivity=0.00;
        float temperature;
        int C1=374000000;
        int C2=14390;
        float i;
        printf("\n Sensitivity of Planck Temperature to Emissivity\n");
        printf("\n Specify spectral radiance in W m-2 micron-1: ");
        scanf("%f",&radiance);
        printf(" Specify wavelength: ");
        scanf("%f",&wavelength_micron);
        for(i=0.90;i<1.00;i+=0.01)
        {
                emissivity=i;
                temperature=C2/(wavelength_micron*(log((emissivity*C1)/(pow(wavelength_micron,5)*radiance))+1));
                printf("emissivity\t%.2f\ttemperature\t%.2f\n",emissivity,temperature);
        }
}
```

F5 CALCULATION of ATI from CRACKNELL & XUE (1996) USING IMAGE DIURNAL TEMPERATURES, SPECIFYING ALBEDO

```
#include <stdio.h>
#include <math.h>
#include <stdlib.h>
#include <string.h>
#include <memory.h>

#define DIMENSION_REQUEST //can comment out for end of file instead of definition//

main()
{
        char inTd[30];
        char inTn[30];
        char out_ati[30];
        FILE *infileTd;
        FILE *infileTn;
        FILE *outfile;
// File specifications
        printf(" ATI Calculation (Cracknell & Xue, 1996)\n");
        printf("\n Specify day temperature file: ");
        scanf("%s",inTd);
        infileTd=fopen(inTd,"rb");
        if(infileTd==NULL)
        {
                printf("\n Error opening day temperature image file\n");
                exit(1);
        }
        printf(" Specify night temperature file (same dimensions as day): ");
        scanf("%s",inTn);
        infileTn=fopen(inTn,"rb");
```

```
        if(infileTn==NULL)
        {
                printf("\n Error opening night temperature image file \n");
                exit(1);
        }
        printf(" Specify output file for ati image: ");
        scanf("%s",out_ati);
        outfile=fopen(out_ati,"wb");
        if(outfile==NULL)
        {
                printf("\n Error creating output file\n");
                exit(1);
        }
//Parameter definitions
        long i;
        int pixels,lines;
        long repeatno;
        float imageTd;
        float imageTn;
        float outImage;
        float albedo;
        float ati;
        printf("\n Specify albedo to 2 decimal places = ");
        scanf("%f",&albedo);
#ifdef DIMENSION_REQUEST
        printf("\n Specify number of image pixels = ");
        scanf("%i",&pixels);
        printf(" Specify number of image lines = ");
        scanf("%i",&lines);
        repeatno=pixels*lines;
        for(i=0;i<repeatno;i++)
```

```
#else
        while(!feof(infileTd))
//Calculation of ATI
#endif
        {
                fread(&imageTd,sizeof(float),1,infileTd);
                fread(&imageTn,sizeof(float),1,infileTn);
                ati=(1-albedo)/(imageTd-imageTn);
                fwrite(&ati,sizeof(float),1,outfile);
        }
        printf(" ");
//Close files
        fclose(outfile);
        fclose(infileTn);
        fclose(infileTd);
}
```

F6 SENSITIVITY of CRACKNELL & XUE (1996) ATI to VARIABLE ALBEDO

```
#include <stdio.h>
#include <math.h>
#include <stdlib.h>
#include <string.h>
#include <memory.h>

main()
{
        float ati=0.00;
        float diurnal_temp=0.00;
        float albedo=0.00;
        float i;
        printf("\n Sensitivity of Cracknell & Xue (1996) ATI to Albedo\n");
        printf("\n Specify diurnal temperature change in K: ");
        scanf("%f",&diurnal_temp);
        for(i=0.00;i<1.00;i+=0.01)
        {
                albedo=i;
                ati=(1-albedo)/diurnal_temp;
                printf("albedo\t%.2f\tATI\t%.2f\n",albedo,ati);
        }
}
```

F7 CALCULATION of ATI from KAHLE & ALLEY (1985) USING IMAGE DIURNAL TEMPERATURES, SPECIFYING ALBEDO, DECLINATION and LATITUDE

```
#include <stdio.h>
#include <math.h>
#include <errno.h>
#include <stdlib.h>

#define DIMENSION_REQUEST //can comment out for end of file instead of definition//

main()
{
        char inTd[30];
        char inTn[30];
        char out_ati[30];
        FILE *infileTd;
        FILE *infileTn;
        FILE *outfile;
// File specifications
        printf(" ATI Calculation (Kahle & Alley, 1985)\n");
        printf("\n Specify day temperature file: ");
        scanf("%s",inTd);
        infileTd=fopen(inTd,"rb");
        if(infileTd==NULL)
        {
                printf("\n Error opening day temperature image file\n");
        }
        printf(" Specify night temperature file (same dimensions as day): ");
        scanf("%s",inTn);
        infileTn=fopen(inTn,"rb");
        if(infileTn==NULL)
        {
```

```
                printf("\n Error opening night temperature image file \n");
        }
        printf(" Specify output file for ati image: ");
        scanf("%s",out_ati);
        outfile=fopen(out_ati,"wb");
        if(outfile==NULL)
        {
                printf("\n Error creating output file\n");
        }
//C Calculation
        float declination;
        float latitude;
        float dec_rad;
        float lat_rad;
        float pi=3.141592;
        float C;
        printf("\n Calculation of C parameter (Kahle & Alley, 1985)\n");
        printf("\n Specify solar declination in decimal degrees = ");
        scanf("%f",&declination);
        printf(" Specify latitude in decimal degrees = ");
        scanf("%f",&latitude);
        dec_rad=declination/180;
        lat_rad=latitude/180;
        printf("\n Solar Declination in radians = %.2f\n Latitude in radians = %.2f",dec_rad,lat_rad);
        C=((1/pi)*((sin(dec_rad)*sin(lat_rad)*acos((-1)*tan(dec_rad)*tan(lat_rad)))+(cos(dec_rad)*cos(lat_rad)*pow((1-
(pow(tan(dec_rad),2)*pow(tan(lat_rad),2))),0.5))));
        printf("\n Kahle & Alley (1985) C parameter = %.4f\n",C);
//ATI Calculation
        long i;
        int pixels,lines;
        long repeatno;
        float ati;
```

```
        float albedo;
        float solar_c=1.98;
        float atmos_trans=0.75;
        float rot_angle=0.004363;
        float scale;
        float imageTd;
        float imageTn;
        printf("\n Calculation of Apparent Thermal Inertia (Kahle & Alley, 1985)\n");
        printf("\n Specify albedo to 2 decimal places = ");
        scanf("%f",&albedo);
#ifdef DIMENSION_REQUEST
        printf("\n Specify number of image pixels = ");
        scanf("%i",&pixels);
        printf(" Specify number of image lines = ");
        scanf("%i",&lines);
        repeatno=pixels*lines;
        for(i=0;i<repeatno;i++)
#else
        while(!feof(infileTd))
#endif
        {
                fread(&imageTd,sizeof(float),1,infileTd);
                fread(&imageTn,sizeof(float),1,infileTn);
                ati=((2*solar_c*atmos_trans*C)/pow(rot_angle,0.5))*((1-albedo)/(Tday-Tnight));
                fwrite(&ati,sizeof(float),1,outfile);
        }
        printf(" ");
//Close files
        fclose(outfile);
        fclose(infileTn);
        fclose(infileTd);
 }
```

F8 CALCULATION of ATI from PRICE (1985) USING IMAGE DIURNAL TEMPERATURES, SPECIFYING ALBEDO, DECLINATION and LATITUDE

```
#include <stdio.h>
#include <math.h>
#include <stdlib.h>
#include <string.h>
#include <memory.h>

#define DIMENSION_REQUEST //can comment out for end of file instead of definition//

main()
{
        char inTd[30];
        char inTn[30];
        char out_ati[30];
        FILE *infileTd;
        FILE *infileTn;
        FILE *outfile;
// File specifications
        printf(" ATI Calculation (Price,1985)\n");
        printf("\n Specify day temperature file?: ");
        scanf("%s",inTd);
        infileTd=fopen(inTd,"rb");
        if(infileTd==NULL)
        {
                printf("\n Error opening day temperature image file\n");
                exit(1);
        }
        printf(" Specify night temperature file of same dimensions as day?: ");
        scanf("%s",inTn);
        infileTn=fopen(inTn,"rb");
```

```
        if(infileTn==NULL)
        {
                printf("\n Error opening night temperature image file \n");
                exit(1);
        }
        printf(" Specify output file for ati image?: ");
        scanf("%s",out_ati);
        outfile=fopen(out_ati,"wb");
        if(outfile==NULL)
        {
                printf("\n Error creating output file\n");
                exit(1);
        }
//Parameter definitions
        long i;
        int pixels,lines;
        long repeatno;
        float imageTd;
        float imageTn;
        float outImage;
        float albedo;
        float ati;
        float declination;
        float latitude;
        float dec_rad;
        float lat_rad;
        float pi=3.141592;
        float C;
        printf("\n Specify solar declination in decimal degrees = ");
        scanf("%f",&declination);
        printf(" Specify latitude in decimal degrees = ");
        scanf("%f",&latitude);
```

```
        dec_rad=declination/180;
        lat_rad=latitude/180;
        printf("\n Solar Declination in radians = %.2f\n Latitude in radians = %.2f",dec_rad,lat_rad);
        C=((1/pi)*((sin(dec_rad)*sin(lat_rad)*acos((-1)*tan(dec_rad)*tan(lat_rad)))+(cos(dec_rad)*cos(lat_rad)*pow((1-
(pow(tan(dec_rad),2)*pow(tan(lat_rad),2))),0.5))));
        printf("\n\n C parameter = %.4f\n",C);
        printf("\n Specify albedo = ");
        scanf("%f",&albedo);
#ifdef DIMENSION_REQUEST
        printf("\n Specify number of image pixels = ");
        scanf("%i",&pixels);
        printf(" Specify number of image lines = ");
        scanf("%i",&lines);
        repeatno=pixels*lines;
        for(i=0;i<repeatno;i++)
#else
        while(!feof(infileTd))
//Calculation of ATI
#endif
        {
                fread(&imageTd,sizeof(float),1,infileTd);
                fread(&imageTn,sizeof(float),1,infileTn);
                ati=(1000*pi*C)*((1-albedo)/(imageTd-imageTn));
                fwrite(&ati,sizeof(float),1,outfile);
        }
        printf(" ");
//Close files
        fclose(outfile);
        fclose(infileTn);
        fclose(infileTd);
}
```

F9 **CALCULATION of MAXIMUM AND MINIMUM TEMPERATURES and their DIURNAL TIMES from a TIME-SERIES**

```
#include <stdio.h>
#define MAX_DATA_VALUES 143775
#define MAX_DATA_DAYS 200

// Storage for the imported data
typedef struct
{
        long YearMinute;
        float T[4];
        float deriv1[4];
        float deriv2[4];
}
LoggedDataStruct;
LoggedDataStruct LoggedData[MAX_DATA_VALUES];
long nLoggedValues=0;

// output values for day min/max
typedef struct
{
        int DayId;
        int DayMin[4];
        int DayMax[4];
}
OutputDataStruct;
OutputDataStruct OutputData[MAX_DATA_DAYS];
int nDays=-1;

// load tab-delimited text document where temperatures are recorded as time from start of year
// [Year Min, T(surface), T(0.10m), T(0.20m), T(0.50m)]
int LoadData(char*filename)
{
```

```
	FILE*f;
	if( (f=fopen("input.txt","r"))!=NULL)
	{
		nLoggedValues=0;
		while( (!feof(f)) && (!ferror(f)) )
		{
			fscanf(f,"%ld %f %f %f %f\n",
				&LoggedData[nLoggedValues].YearMinute,
				&LoggedData[nLoggedValues].T[0],
				&LoggedData[nLoggedValues].T[1],
				&LoggedData[nLoggedValues].T[2],
				&LoggedData[nLoggedValues].T[3]);
			nLoggedValues++;
		}
		fclose(f);
	}
	else
	{
		printf("Problem opening file.\n");
	}
	return -1;
}
// smoothing data removes peaks that are anomalously high compared with surrounding values
#define USE_SMOOTHING
//#undef USE_SMOOTHING

#define SMOOTH_WINDOW 7
#define SMOOTH_RANGE 3
float SmoothWeightings[SMOOTH_WINDOW]={0.1, 0.3, 0.5, 1.0, 0.5, 0.3, 0.1};

void CalcDerivatives(){
	long i;
	int d,j;
	float smoothed[MAX_DATA_VALUES],SmoothTotal=0.0;
```

```
#ifdef USE_SMOOTHING
        for(j=0;j<SMOOTH_WINDOW;j++)
                SmoothTotal+=SmoothWeightings[j];
#endif
        for(d=0;d<4;d++)
        {
                // Iterate for each depth in turn

#ifdef USE_SMOOTHING
                for(i=SMOOTH_RANGE;i<nLoggedValues-SMOOTH_RANGE;i++)
                {
                        smoothed[i]=0.0;
                        for(j=0;j<SMOOTH_WINDOW;j++)
                                smoothed[i]+=LoggedData[i+j-SMOOTH_RANGE].T[d] * SmoothWeightings[j];
                        smoothed[i]/=SmoothTotal;
                }
#endif

#ifdef USE_SMOOTHING
                for(i=SMOOTH_RANGE;i<nLoggedValues-SMOOTH_RANGE;i++)
                        // Use smoothed values while calculating derivatives
                        LoggedData[i].deriv1[d] =
                                                (smoothed[i]-smoothed[i-1])/
                                                (LoggedData[i].YearMinute-LoggedData[i-1].YearMinute);
#else
                for(i=1;i<nLoggedValues;i++)
                        // Use raw values while calculating derivatives
                        LoggedData[i].deriv1[d] =
                                                (LoggedData[i].T[d]-LoggedData[i-1].T[d])/
                                                (LoggedData[i].YearMinute-LoggedData[i-1].YearMinute);
#endif
        }
}
```

```
// calculate the times when soil temperature is at maximum and minimum in day
// for each soil depth
void TScan()
{
   int Depth;
        long i;
        for(Depth=0;Depth<4;Depth++)
        {
                int Today=-1;
                nDays=-1;
                for(i=0;i<nLoggedValues;i++)
                {
                        if( (int)(LoggedData[i].YearMinute / 1440) != Today)
                        {
                                nDays++;
                                OutputData[nDays].DayId=i;
                                Today=(LoggedData[i].YearMinute / 1440);
                                OutputData[nDays].DayMin[Depth]=i;
                                OutputData[nDays].DayMax[Depth]=i;
                        }
                        if(LoggedData[i].T[Depth] < LoggedData[OutputData[nDays].DayMin[Depth]].T[Depth])
                                OutputData[nDays].DayMin[Depth]=i;
                        if(LoggedData[i].T[Depth] > LoggedData[OutputData[nDays].DayMax[Depth]].T[Depth])
                                OutputData[nDays].DayMax[Depth]=i;
                }
        }
}
// calculate heating gradients for each soil depth
void Deriv1Scan()
{
   int Depth;
        long i;
        for(Depth=0;Depth<4;Depth++)
```

```
	{
		int Today=-1;
		nDays=-1;
		for(i=0;i<nLoggedValues;i++)
		{
			if( (int)(LoggedData[i].YearMinute / 1440) != Today)
			{
				nDays++;
				OutputData[nDays].DayId=i;
				Today=(LoggedData[i].YearMinute / 1440);
				OutputData[nDays].DayMin[Depth]=i;
				OutputData[nDays].DayMax[Depth]=i;
			}
			if(LoggedData[i].T[Depth] < LoggedData[OutputData[nDays].DayMin[Depth]].deriv1[Depth])
				OutputData[nDays].DayMin[Depth]=i;
			if(LoggedData[i].T[Depth] > LoggedData[OutputData[nDays].DayMax[Depth]].deriv1[Depth])
				OutputData[nDays].DayMax[Depth]=i;
		}
	}
}
// create output file with day, year day, temperatures and times in day for T min and T max for each depth
void OutputDays(FILE*f)
{
	int i,d;
	fprintf(f,"day\tyday\tgrad\ttmin\tTmin\ttmax\t\Tmax\n");
	for(i=0;i<nDays;i++)
	{
		fprintf(f,"%.2d\t%.3d ",i,(LoggedData[OutputData[i].DayMin[0]].YearMinute)/1440);
		for(d=0;d<4;d++)
```

```
                for(d=0;d<4;d++)
                        fprintf(f,"\t%.2f\t%4d\t%.2f\t%4d\t%.2f",
                        (LoggedData[OutputData[i].DayMax[d]].T[d]-LoggedData[OutputData[i].DayMin[d]].T[d])/
                        (LoggedData[OutputData[i].DayMax[d]].YearMinute-LoggedData[OutputData[i].DayMin[d]].YearMinute),
                        LoggedData[OutputData[i].DayMin[d]].YearMinute%1440,
                        LoggedData[OutputData[i].DayMin[d]].T[d],
                        LoggedData[OutputData[i].DayMax[d]].YearMinute%1440,
                        LoggedData[OutputData[i].DayMax[d]].T[d]);
                fprintf(f,"\n");
        }
}
// calculate time when inflexion point of heating/cooling for each depth
// create output file with day, year day and inflexion value and times of inflexion for each depth
void OutputDerivDays(FILE*f)
{
        int i,d;
        fprintf(f, "\n");
        for(i=0;i<nDays;i++)
        {
                fprintf(f,"%.2d\t%.3d",i,LoggedData[OutputData[i].DayMin[0]].YearMinute/1440);
                for(d=0;d<4;d++)
                        fprintf(f,"\t%.2f\t%4d\t%.2f\t%4d\t%.2f",
                        (LoggedData[OutputData[i].DayMax[d]].deriv1[d]-LoggedData[OutputData[i].DayMin[d]].deriv1[d])/
                        (LoggedData[OutputData[i].DayMax[d]].YearMinute-LoggedData[OutputData[i].DayMin[d]].YearMinute),
                        LoggedData[OutputData[i].DayMin[d]].YearMinute%1440,
                        LoggedData[OutputData[i].DayMin[d]].deriv1[d],
                        LoggedData[OutputData[i].DayMax[d]].YearMinute%1440,
                        LoggedData[OutputData[i].DayMax[d]].deriv1[d]);
                fprintf(f,"\n");
        }
}
```

```
int main(int argc,char* argv[])
{
        FILE*f_out;
        printf("File : '%s'\n",argv[1]);
        LoadData(argv[1]);
        f_out=fopen("output.txt","w");
        TScan();
        OutputDays(f_out);
        CalcDerivatives();
        printf("\n\n\n1st Derivatives\n\n");
        Deriv1Scan();
        OutputDerivDays(f_out);
        fclose(f_out);
        return -1;
}
```

Appendix G: SOIL ANALYSIS

G1 PARTICLE SIZE ANALYSIS

SOIL SAMPLE PREPARATION

- Weigh approximately 0.5g sample into a 50 ml tube
- Add approximately 20 ml of 20% Hydrogen Peroxide solution
- Cover tube with aluminium foil and place in a boiling water bath for 2 hours
- After 2 hours inspect the sample to make sure all organic matter has been dissolved
- Fill tube up to 40 ml with distilled water
- Centrifuge sample at 4000 rpm for 4 minutes
- Decant the supernatant liquid then refill to 40 ml with distilled water
- Centrifuge sample at 4000 rpm for 4 minutes
- Decant the supernatant liquid
- Add approximately 20 ml distilled water
- Add approximately 2 ml Sodium Hexametaphoshate solution and agitate sample to separate particles

PARTICLE SIZE INSTRUMENTATION (COULTER COUNTER)

- Run – Run cycle – New Sample – Start
- Instrument measures offset and will auto align once an hour
- Instrument takes a background reading (check that detector 100 measures ~15 flux)
- Add sample through a 2 mm sieve by washing tube with distilled water when software registers 'measure loading'
- Instrument will measure Obscuration and PIDS and after a minute click on done
- Enter sample details (group ID, sample ID) then run
- The sample undergoes 2 runs before generating a graph when the sample is finished
- **Individual Graph**
- Run file – open for overlay - add $01 file for the sample to generate graphical overlay
- Run file – average all
- **Average Graph**
- On graph of average select limits – suppress limits
- Graph – diff and cum <
- Run file – export for interpretation and visualisation in Microsoft Excel

DETERMINATION OF SAND, SILT AND CLAY FRACTION

- The cumulative volume is indicated for 22 different categories of particle diameter for each soil sample
- In order to determine the volume of particles in each category, the difference between adjacent categories is determined
- Clay (0-0.0039 mm), silt (0.0039-0.0630 mm) and sand (0.0630 – 2.0000 mm) volumes are then determined for each fraction by accumulating category values based on the Wentworth Scale

SAND	A1	A2	A3	B6	B7	B8	C14	C15	C16	D20	D21	E22	E23
0.00m	69.8	70.1	71.6	66.1	71.6	68.4	49.4	59.2	66.3	56.4	56.6	62.9	65.7
0.05m	67.8	67.0	71.4	66.1	72.8	66.7	49.9	56.7	61.0	57.7	57.5	63.2	84.2
0.10m	68.7	69.8		63.4	72.4	68.1	51.4	55.1	67.2	58.2	55.6	69.1	65.9
0.15m	66.3	69.6	71.9	65.6	71.4	70.2	53.2	57.1	64.7	59.2	56.1	63.9	62.8
0.20m	68.2	69.3	69.6	68.6	70.7	66.5	52.7	54.6	62.9	60.1	55.0	69.3	70.0
0.25m	68.3	71.0	69.7	67.3	70.9	66.9	48.3	57.2	68.2	55.8	58.2	64.5	63.7
0.30m	64.3	70.6	69.8	64.3	70.5	66.7	50.7	60.1	67.6	57.7	56.1	61.2	63.5
0.35m	69.0	75.2	75.5	67.6	68.7	65.6	30.0	58.6	67.5	59.2	58.2	64.9	62.8
0.40m	66.3	72.5	74.2		68.9	66.9	30.1	54.8	67.4		57.7	67.0	62.3
0.45m	66.9	75.9	73.2			68.9	31.7	60.8	68.4			69.2	62.3
0.50m		73.9	72.5					63.8				63.1	64.5

CLAY	A1	A2	A3	B6	B7	B8	C14	C15	C16	D20	D21	E22	E23
0.00m	11.2	10.9	10.4	13.0	10.6	11.9	20.1	16.1	12.8	16.4	16.6	12.2	10.5
0.05m	11.3	12.1	10.3	13.0	10.3	12.4	19.4	16.8	14.8	15.9	16.1	11.5	8.1
0.10m	11.4	10.9		13.9	10.4	11.9	18.5	17.5	12.1	15.6	16.9	9.7	10.7
0.15m	12.4	11.0	9.7	13.0	10.7	11.2	18.2	16.7	13.2	15.1	16.6	10.9	11.7
0.20m	11.8	11.2	10.8	11.7	11.0	12.8	18.3	17.2	14.0	14.7	17.7	10.3	9.7
0.25m	11.7	10.5	11.1	12.4	10.7	12.3	20.4	16.4	11.9	16.3	16.0	11.5	11.7
0.30m	12.7	10.6	10.6	13.6	11.1	12.3	19.8	15.3	11.5	15.3	16.4	12.8	11.9
0.35m	11.2	9.1	8.9	12.4	11.1	12.7	30.6	15.8	11.2	15.1	16.0	11.6	11.7
0.40m	12.0	9.9	9.4		11.1	11.9	30.9	17.8	11.5		16.2	10.8	11.9
0.45m	11.5	8.8	10.0			11.0	29.8	15.8	11.5			10.0	12.5
0.50m		9.6	10.1					14.0				11.3	11.6

G2 MOISTURE CONTENT

- Weigh clean/dry crucible to 0.0000g
- Add approximately 3-5g soil sample
- Weigh crucible + wet sample
- Dry in oven at 105°C overnight
- Weigh crucible + dry sample
- $MoistureContent(\%) = \left[\frac{(crucible + wet) - (crucible + dry)}{sample}\right] * 100$

H2O	A1	A2	A3	B6	B7	B8	C14	C15	C16	D20	D21	E22	E23
0.00m	5.80	5.01	7.05	7.00	7.23	4.29	9.66	9.67	10.50	9.12	7.19	18.26	19.51
0.05m	9.52	8.90	9.65	6.07	7.47	8.62	14.67	14.92	12.99	12.10	14.55	18.67	20.67
0.10m	11.60	11.08	10.34	8.15	8.90	13.84	14.27	18.03	14.65	14.89	14.99	18.29	18.64
0.15m	11.37	11.89	13.56	9.70	9.86	11.53	15.97	16.84	16.82	11.24	14.76	17.67	20.00
0.20m	11.24	11.94	11.40	9.52	10.94	10.16	14.54	20.90	17.46	12.19	13.14	17.62	19.08
0.25m	11.12	8.20	8.76	9.67	9.64	9.79	13.18	14.40	12.21	11.30	12.92	16.21	25.25
0.30m	7.61	7.62	8.58	7.70	8.56	7.25	12.57	14.01	11.17	10.56	13.45	14.06	18.60
0.35m	7.04	7.76	8.31	7.28	7.15	7.41	16.14	14.15	10.89	10.52	12.93	13.52	13.58
0.40m	7.50	6.90	7.72		6.44	5.81	16.67	14.24	9.98		12.75	12.90	13.92
0.45m	6.37	6.38	6.58			6.79	16.46	13.86	11.36			13.67	13.60
0.50m		6.02	6.01					11.88				12.73	13.43

G3 ORGANIC CONTENT (LOSS on IGNITION)

- Weigh crucible + dry sample
- Heat sample in furnace at 550°C for 4 hours
- Weight crucible + ignited sample
- $OrganicContent(\%) = \left[\frac{(crucible + dry) - (crucible + ignited)}{sample}\right] * 100$

LOI	A1	A2	A3	B6	B7	B8	C14	C15	C16	D20	D21	E22	E23
0.00m	3.20	3.03	2.77	3.55	3.25	3.37	6.35	6.27	4.76	5.69	5.06	4.24	3.88
0.05m	3.33	2.52	2.73	3.67	3.14	3.52	6.59	6.08	4.89	5.43	5.54	4.06	4.43
0.10m	3.83	2.93	3.10	4.11	3.12	3.78	6.53	6.24	4.81	5.67	5.51	4.19	3.87
0.15m	3.37	3.08	3.97	4.50	3.17	3.44	6.23	6.19	4.86	5.64	5.62	4.07	4.22
0.20m	2.95	2.76	2.87	4.73	3.61	3.64	6.35	5.95	5.02	5.49	5.03	4.19	4.00
0.25m	3.01	2.35	2.67	4.09	3.58	3.08	6.68	4.82	5.18	6.50	5.18	3.47	3.97
0.30m	1.76	3.65	2.72	3.69	3.22	2.93	6.41	4.81	3.08	5.28	4.63	2.51	3.71
0.35m	1.67	1.83	2.49	3.63	2.30	2.64	5.84	4.39	2.69	4.80	4.98	2.30	2.65
0.40m	1.74	1.58	2.29		1.99	2.32	5.59	4.19	2.70		4.71	2.18	2.57
0.45m	1.66	1.34	1.88			2.13	5.61	3.70	3.04			2.18	2.54
0.50m		1.38	1.91					4.00				2.00	2.46